



Proceedings of the 14th International Symposium on Space Terahertz Technology

Chris Walker[†] and John Payne[‡], Editors
[†] Steward Observatory, University of Arizona
[‡] National Radio Astronomy Observatory
Tucson, Arizona

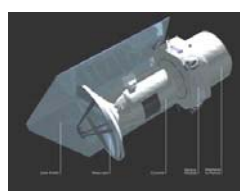
April 22-24, 2003
Loews Ventana Canyon Resort
Tucson, Arizona



SOFIA



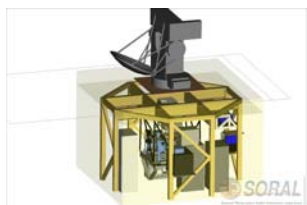
SAFIR



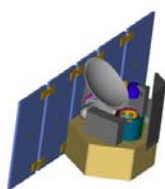
Herschel



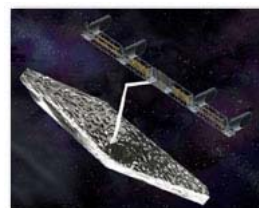
ALMA



AST/RO



GTO



TPF

Steward Observatory Radio Astronomy Lab
University of Arizona
Tucson, Arizona

National Radio Astronomy Observatory
Tucson, Arizona

Georgia Institute of Technology
Atlanta, Georgia

April, 2004



Proceedings of the 14th International Symposium on Space Terahertz Technology

Chris Walker[†] and John Payne[‡], Editors

[†] Steward Observatory, University of Arizona

[‡] National Radio Astronomy Observatory

Tucson, Arizona

April 22-24, 2003

Loews Ventana Canyon Resort

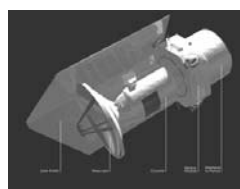
Tucson, Arizona



SOFIA



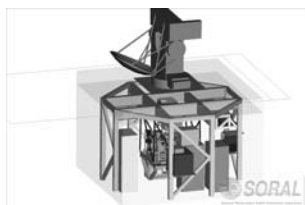
SAFIR



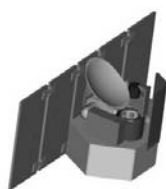
Herschel



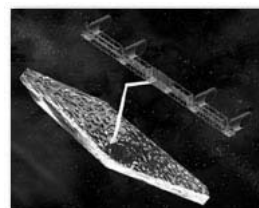
ALMA



AST/RO



GTO



TPF

Steward Observatory Radio Astronomy Lab

University of Arizona

Tucson, Arizona

National Radio Astronomy Observatory

Tucson, Arizona

Georgia Institute of Technology

Atlanta, Georgia

April, 2004

PREFACE

The fields of THz science and technology are now experiencing tremendous growth, both in the public and private sectors. Recent advances in theory, fabrication, and analytical tools permit for the first time the realization of devices, components, and systems that were only imagined just a short time ago. Much of this accelerated growth can be traced directly to the instrument requirements of space missions (*e.g. Herschel*). We will be benefiting from this work for years to come, both in future missions (*e.g. SOFIA* and *SAFIR*) and in enumerable remote sensing applications (spaceborne and terrestrial). THz science and technology is still in its infancy. The next decade should prove to be even more exciting and productive than the last!

The 14th International Symposium on Space TeraHertz Technology was held at the Loews Ventana Canyon Resort in Tucson, Arizona from April 22-24, 2004. There were a total of ~125 engineers and scientists in attendance from around the world. There were 12 oral sessions and a 3-day long poster session. A total of 55 papers were presented in the oral sessions and 35 in the poster session, for a combined total of 90 papers. The number of contributions in each subject area were roughly as follows:

Hot Electron Bolometers	15
SIS Mixers	18
Sources	18
Devices	8
Incoherent/Bolometers	2
Waveguide	9
Spectrometers	5
Systems	10
Optics	5

The Symposium would not have been possible without the support of the NRAO Tucson staff (in particular Jennifer Neighbours) and the students of the Steward Observatory Radio Astronomy Laboratory (Chris Groppi, Dathon Golish, and Abby Hedden). We also wish to thank Dr. John Papapolymerou and Peter Kirby of the Georgia Institute of Technology for their help in organizing the conference and the IEEE MTT Society for their support. Finally, the Chairs thank the SOC, session chairs, presenters, and all participants for making the 14th International Symposium on Space TeraHertz Technology an enjoyable and rewarding experience. We look forward to seeing you all in the future.

Christopher K. Walker
John M. Payne

14th International Symposium on Space Terahertz Technology

Session 1: HEB MIXERS I

Chair: Sigfrid Yngvesson

University of Massachusetts at Amherst

1.1. Review of HEB Heterodyne Detectors and Receiver Systems for the THz 1
Range: Present and Future

Sigfrid Yngvesson

University of Massachusetts at Amherst

1.2. Noise performance of NbN Hot Electron Bolometer mixers at 2.5 THz and its 11
dependence on the contact resistance

*J. J. A. Baselmans¹, M. Hajenius^{1,2}, J. R. Gao^{1,2}, T. M. Klapwijk², P. A. J. de Korte¹,
B. Voronov³, G. Gol'tsman³*

¹Space Research Organisation of the Netherlands (SRON), Groningen, The Netherlands

²Faculty of Applied Sciences, Delft University of Technology, The Netherlands

³Moscow State Pedagogical University, Russia

1.3. Fabrication and Noise Measurement of NbTiN Hot Electron Bolometer 20
Heterodyne Mixers at THz Frequencies

*Pourya Khosropanah¹, Sven Bedorf², Sergey Cherednichenko¹, V. Drakinskiy¹,
Karl Jacobs², Harald Merkel¹, Erik Kollberg¹*

¹Department of Microtechnology and Nanoscience, Microwave Electronics Laboratory,
Chalmers University of Technology, Sweden

²KOSMA, I. Physikalisches Institut, University of Cologne, Germany

1.4. Comparison of the Noise Performance of NbTiN and NbN Hot Electron 31
Bolometer Heterodyne Mixers at THz Frequencies

Harald F. Merkel, Pourya Khosropanah, Sergey Cherednichenko, Erik Kollberg

Microelectronics Department, Microwave Electronics Laboratory,

Chalmers University of Technology, Sweden

Session 2: SIS MIXERS I

Chair: Tony Kerr

National Radio Astronomy Observatory

2.1. Superconducting Hot-Electron Bolometer Mixer for Terahertz Heterodyne 33
Receivers

*Alexei D. Semenov¹, Heinz-Wilhelm Hübers¹, Heiko Richter¹, Konstantin Smirnov²,
Gregory N. Gol'tsman², Natalia Kaurova², Boris M. Vornov²*

¹DLR Institute of Space Sensor Technology and Planetary Exploration, Germany

²Moscow State Pedagogical University, Russia

2.2. Sideband-Separating SIS Mixer For ALMA Band 7, 275-370 GHz 41

Stéphane Claude

Institut de Radio Astronomie Millimetrique, France

2.3. Design Accuracy of the Resonance Frequency for the PCTJ SIS Mixer 52

Yasunori Fujii^{1,2}, Ken'ichi Kikuchi¹, Junji Inatani¹

¹National Space Development Agency of Japan, Japan

²Nihon Tsushinki Co., Ltd., Japan

- 2.4. Low noise SIS mixer for the band 1.1-1.25 THz of the Herschel space radio telescope** 54
A. Karpov¹, D. Miller¹, F. Rice¹, J. Zmuidzinas¹, J. A. Stern², B. Bumble², H. G. LeDuc²

¹California Institute of Technology

²Jet Propulsion Laboratory

- 2.5. Influence of Junction-Quality and Current Density on HIFI Band 2 Mixer Performance** 55

*R. Teipen¹, M. Justen¹, T. Tils¹, S. Glenz¹, C. E. Honingh¹, K. Jacobs¹, B. D. Jackson²,
T. Zijlstra³, M. Kroug³*

¹KOSMA, I. Physikalisches Institut, Universität zu Köln, Germany

²National Institute for Space Research (SRON), The Netherlands

³Dept. of Nanoscience, Faculty of Applied Sciences, Delft Univ. of Technology, The Netherlands

- 2.6. All-NbN SIS Mixers Using a Tuning Circuit with Two Half-Wavelength Distributed Junctions** 63

Y. Uzawa, A. Kawakami, M. Takeda, Z. Wang

Kansai Advanced Research Center, Communications Research Laboratory, Japan

Session 3: SOURCES I

Chair: John Payne

National Radio Astronomy Observatory

- 3.1. A 1600-1900 GHz Tunable Source** 64

Neal Erickson, Ron Grosslein, John Wielgus, Vern Fath, I. Mehdi, J. Gill

¹Department of Astronomy, University of Massachusetts

²Jet Propulsion Laboratory

- 3.2. W Band MMIC Power Amplifiers for the Herschel HIFI Instrument** 73

*Robert R. Ferber¹, Todd C. Gaier¹, John C. Pearson¹, Lorene A. Samoska¹,
Mary Wells¹, April Campbell¹, Gerald Swift², Paul Yocom², K. T. Liao²*

¹Jet Propulsion Laboratory, California Institute of Technology

²Northrop Grumman Space Technology (NGST)

- 3.3. Broadband Submillimeter Receiver and Source Development** 83

J. L. Hesler, D. W. Porterfield, W. L. Bishop, D. S. Kurtz, T. W. Crowe

Virginia Diodes Inc.

- 3.4. Design and Analysis of 500 GHz Hetero-structure Barrier Varactor Quintuplers** 84

Mattias Ingvarson, Arne Øistein Olsen, Jan Stake

Microwave Electronics Laboratory, Chalmers University of Technology, Sweden

- 3.5. 1400–1900 GHz Local Oscillators for the Herschel Space Observatory** 94

John Ward, Frank Maiwald, Goutam Chattopadhyay, Erich Schlecht,

Alain Maestrini, John Gill, Imran Mehdi*

California Institute of Technology, Jet Propulsion Laboratory

*Now at the Observatoire de Paris

Session 4: DEVICES

Chair: Art Lichtenberger

University of Virginia

- 4.1. HgCdTe Photoconductive Mixers for 3- 15 Terahertz** 102
Albert Betz¹, Rita Boreiko¹, Yongdong Zhou², Jun Zhao², Yusuf Selamer², Yong Chang², Renganathan Ashokan³, Charlie Bucker^{2,3}, Sivalingam Sivananthan²
¹Center for Astrophysics & Space Astronomy, University of Colorado
²Microphysics Laboratory and Department of Physics, The University of Illinois at Chicago
³Physics Institute of Wuerzburg, Germany
- 4.2. Transferred Substrated Heterojunction Bipolar Transistors for Submillimeter Wave Applications** 112
Andy Fung¹, Lorene Samoska¹, Peter Siegel¹, M. Rodwell², M. Urteaga², V. Paidi², Roger Malik³
¹California Institute of Technology, Jet Propulsion Laboratory
²Department of Electrical and Computer Engineering, Univeristy of California at Santa Barbara
³RJM Semiconductor
- 4.3. Novel Designs for Submillimeter Subharmonic and Fundamental Schottky Mixers** 118
Erich Schlecht, John Gill, Peter Siegel, John Oswald, Imran Mehdi
Jet Propulsion Laboratory
- 4.4. Design, Fabrication and Testing of Semi-conductor Tunable Antenna-coupled Intersubband Terahertz (TACIT) Detectors** 119
M. S. Sherwin^{1,3}, G. B. Serapiglia¹, Y. Dora^{1,2}, M. Hanson⁴, A. C. Gossard^{2,4}, W. R. McGrath⁵
¹Institute for Quantum Engineering Science and Technology (iQUEST), University of California at Santa Barbara (UCSB)
²Department of Electrical and Computer Engineering, USCB
³Department of Physics, USCB
⁴Department of Materials, UCSB
⁵Submillimeter-wave superconductive sensors group, Jet Propulsion Laboratory
- 4.5. SIR Chip for TELIS** 121
S. V. Shitov^{1,2}, V.P. Koshelets^{1,2}, P.A. Yagoubov, L. V. Filippenko¹, P.N. Dmitriev¹, O.V. Koryukin¹, An. B. Ermakov^{1,2}, R. W. M. Hoogeveen²
¹Institute of Radio Engineering and Electronics (IREE), Russian Academy of Sciences, Russia
²National Institute for Space Research (SRON), The Netherlands
- 4.6. Large RF Bandwidth Waveguide to Thinfilm Microstrip Transitions on Suspended Membrane for Use in Silicon Micromachined Mixer Blocks at THz Frequencies** 127
J. W. Kooi¹, Christian Drouet d'Aubigny², Chris Walker², Arthur W. Lichtenberger³
¹California Institute of Technology
²Department of Astronomy and Steward Observatory, University of Arizona
³University of Virginia

Session 5: INCOHERENT/BOLOMETRIC DETECTORS

Chair: Harvey Moseley

NASA - Goddard Space Flight Center

5.1. Photon Counting vs Photon Integration at SubMM Waves 128

Boris S. Karasik¹, Andrew V. Sergeev²

¹Jet Propulsion Laboratory, California Institute of Technology

²Wayne State University

Session 6: WAVEGUIDE

Chair: John Papapolymerou

Georgia Institute of Technology

6.1. Single Chip, Beam Combining, Interferometric Detector for Submillimetre-wave Astronomy 129

E. Campbell¹, S. Withington¹, G. Yassin¹, C. Y. Tham¹, S. Wolfe², K. Jacobs²

¹Department of Physics, University of Cambridge, UK

²Department of Physics, University of Cologne, Germany

6.2. Measurements and Simulations of Overmoded Waveguide Components at 70-118 GHz, 220-330 GHz, and 610-720 GHz 138

G. A. Ediss

National Radio Astronomy Observatory

6.3. A Broadband Waveguide Thermal Isolator 148

J. L. Hesler¹, A. R. Kerr², N. Horner²

¹University of Virginia, Department of ECE

²National Radio Astronomy Observatory

6.4. Silicon Laser Micromachining for the Development of Planar Waveguide-Based THz Structures 155

Peter Kirby¹, John Papapolymerou¹, Christian D'Aubigny², Chris Walker²

¹School of Electrical & Computer Engineering, Georgia Institute of Technology

²Department of Astronomy, University of Arizona

6.5. Design of a Dual Polarization SIS Sideband Separating Receiver Based on Waveguide OMT for the 275-370 GHz Frequency Band 159

A. Navarrini, M. Carter

Institut de Radioastronomie Millimétrique (IRAM), France

6.6. Symmetric Waveguide Orthomode Junctions 169

E. J. Wollack¹, W. Grammer²

¹Laboratory for Astronomy and Astrophysics, NASA/Goddard Space Flight Center

²National Radio Astronomy Observatory

Session 7: SPECTROMETERS

Chair: Rudolf Schieder

Physics Institute, University of Cologne

7.1. Optical Methods for Spectral Analysis of Future Heterodyne Instruments 177

R. Schieder

Physics Institute, University of Cologne, Germany

7.2. A Correlator Chip for Spaceborne Radiometry 178

Constantin Timoc

Spaceborne Inc., La Canada, California

Session 8: SYSTEMS

Chair: Chris Walker

University of Arizona

8.1. Deployment of TREND – A Low Noise Receiver User Instrument at 1.25 THz to 1.5 THz for AST/RO at the South Pole 179

Eyal Gerecht¹, Sigfrid Yngvesson¹, John Nicholson¹, Yan Zhuang¹, Fernando Rodriguez Morales¹, Xin Zhao¹, Dazhen Gu¹, Richard Zannoni¹, Michael Coulombe², Jason Dickinson², Thomas Goyette², Bill Gorveatt², Jerry Waldman², Pourya Khosropanah³, Christopher Groppi⁴, Abigail Hedden⁴, Dathon Golish⁴, Christopher Walker⁴, Jacob Kooi⁵, Richard Chamberlin⁵, Antony Stark⁶, Christopher Martin⁶, Robert Stupak⁶, Nicholas Tothill⁶, Adair Lane⁶

¹University of Massachusetts at Amherst

²Submillimeter Wave Technology Laboratory, University of Massachusetts at Lowell

³Chalmers University of Technology, Sweden

⁴Department of Astronomy and Steward Observatory, University of Arizona

⁵California Institute of Technology

⁶Smithsonian Astrophysical Observatory

8.2. Heterodyne Array Development at the University of Arizona 189

C. Groppi¹, C. Walker¹, C. Kulesa¹, G. Narayanan², K. Jacobs³, U. Graf³, R. Schieder³, J. Kooi⁴

¹SORAL, University of Arizona

²University of Massachusetts at Amherst

³University of Cologne, Germany

⁴California Institute of Technology

8.3. TELIS – Development of a New Balloon-Borne THZ/Submm Heterodyne Limb Sounder 204

R. W. M. Hoogeveen¹, P. A. Yagoubov¹, A. M. Maurellis¹, U. Mair², M. Krocka², G. Wagner², M. Birk², H.-W. Hübers³, H. Richter³, A. Semenov³, G. Gol'tsman⁴, B. Voronov⁴, V. Koshelets⁵, S. Shitov⁵, B. Ellison⁶, B. Kerridge⁶, D. Matheson⁶, M. Harman⁶, R. Siddans⁶, J. Reburn⁶

¹National Institute for Space Research (SRON), The Netherlands

²Remote Sensing Technology Institute, DLR, Germany

³Institute for Space Sensor Technology and Planetary Exploration, DLR, Germany

⁴Moscow State Pedagogical University, Russia

⁵Institute of Radio Engineering and Electronics (IREE), Russia

⁶Rutherford Appleton Laboratory (RAL), UK

8.4. Heterodyne Instrumentation Development for the Caltech Submillimeter Observatory 215

Jacob W. Kooi, Attila Kovacs, T. G. Phillips, J. Zmuidzinas
California Institute of Technology

8.5. CO(9-8) in Orion 216

Simon J. E. Radford¹, Ray Blundell², Scott Paine², Hugh Gibson², Dan Marrone²
¹National Radio Astronomy Observatory
²Smithsonian Astrophysical Observatory

8.6. Quasi-Optics for 640 GHz SIS Receiver of International-Space-Station-Borne Limb-Emission Sounder SMILES 217

Masumichi Seta¹, Axel Murk², Takeshi Manabe¹, Junji Inatani³, Richard Wyld⁴, Takeshi Miura³, Toshiyuki Nishibori³
¹Communications Research Laboratory
²Institute of Applied Physics, University of Bern, Switzerland
³National Space Development Agency, Japan
⁴Thomas Keating Ltd., UK

8.7. Meeting the Optical Requirements of Large Focal-Plane Arrays 227

Antony A. Stark
Smithsonian Astrophysical Observatory

Session 9: SIS MIXERS II

Chair: Karl Jacobs
University of Cologne

9.1. Influence of Temperature Variations on the Stability of a Submm Wave Receiver 237

Baryshev, A.^{1,2,3}, R. Hesper^{1,2,3}, G. Gerlofsma^{1,2,3}, M. Kroug⁴, W. Wild^{2,3}
¹Netherlands Research School for Astronomy (NOVA), The Netherlands
²Space Research Organization Netherlands (SRON), The Netherlands
³University of Groningen (RuG), The Netherlands
⁴DIMES, Delft University of Technology, The Netherlands

9.2. Quasiparticle Mixing and Josephson Electrodynamics in Non-uniform Parallel Junction Arrays 246

F. Boussaha, M. Salez, Y. Delorme, F. Dauplay, A. Feret, K. Westerberg, B. Lecomte
LERMA, Observatoire de Paris, France

9.3. Investigation of the Performance of 700 GHz Finline Mixers 247

P. Grimes¹, P. Kittara¹, G. Yassin¹, S. Withington¹, K. Jacobs²
¹Cavendish Laboratory, UK
²KOSMA, I. Physikalisches Institut, University of Cologne, Germany

9.4. Measurement of Gain Compression in SIS Mixer Receivers 257

A. R. Kerr¹, J. Effland¹, S.-K. Pan¹, G. Lauria¹, A. W. Lichtenberger², and R. Groves¹
¹National Radio Astronomy Observatory
²University of Virginia

9.5. Investigations into the Effect of Reflections at the RF and LO Ports of an SIS Mixer 265

Nicholas D. Whyborn
National Institute for Space Research (SRON), The Netherlands

Session 10: HEB MIXERS II

Chair: Johathan Kawamura

Jet Propulsion Laboratory

- 10.1. Development of NbN Terahertz HEB Mixer Devices and Films** 266
*Eyal Gerecht¹, Ashok K. Bhupathiraju¹, John Nicholson², Dazhen Gu², Yan Zhuang²,
Fernando Rodriguez Morales², Xin Zhao², Richard Zannoni², Sigfrid Yngvesson²*
¹National Institute of Standards and Technology
²Department of Electrical and Computer Engineering, University of Massachusetts at Amherst
- 10.2. Gain Bandwidth and Noise Temperature of NbTiN HEB Mixer** 276
*Gregory Gol'tsman, Matvey Finkel, Yuriy Vachtomin, Sergey Antipov,
Vladimir Drakinski, Natalia Kaurova, Boris Voronov*
Moscow State Pedagogical University, Russia
- 10.3. A 1.5 THz Hot-Electron Bolometer Mixer Operated by a Planar Diode-Based
Local Oscillator** 286
*Jonathan Kawamura¹, C.-Y. Edward Tong², Denis Meledin², Raymond Blundell²,
Neal Erickson³, Imran Mehdi¹, Gregory Gol'tsmann⁴*
¹Jet Propulsion Laboratory, California Institute of Technology
²Harvard-Smithsonian Center for Astrophysics
³Department of Astronomy, University of Massachusetts
⁴Physics Department, Moscow State Pedagogical University, Russia
- 10.4. Broadband Millimeter-Wave Bolometric Mixers Based on Ballistic Cooling in
a Two-Dimensional Electron Gas** 287
Mark Lee, L. N. Pfeifer, K. W. West
Bell Laboratories, Lucent Technologies
- 10.5. Bistability in NbN HEB Mixer Devices** 289
Yan Zhuang, Dazhen Gu, Sigfrid Yngvesson
Department of Electrical and Computer Engineering, University of Massachusetts at Amherst

Session 11: SOURCES II

Chair: Imran Mehdi

Jet Propulsion Laboratory

- 11.1. Heterostructure Barrier Varactor Frequency Triplers to 220 – 325 GHz** 299
Yiwei Duan, Qun Xiao, Jeffrey L. Hesler, Thomas W. Crowe
Department of Electrical and Computer Engineering, University of Virginia
- 11.2. THz-range Unipolar Ballistic Tunnel-Emission Transit-Time Oscillators** 307
J. East, Z. S. Gribnikov, N. Z. Vagidov, V. V. Mitin, G. I. Haddad
¹Department of ECE, Wayne State University
²Department of EECS, University of Michigan

11.3. F-Band (90-140 GHz) Uni-Traveling-Carrier Photodiode Module for a Photonic Local Oscillator 318

H. Ito¹, T. Ito¹, Y. Muramoto¹, T. Furuta¹, T. Ishibashi²

¹NTT Photonics Laboratories, NTT Corporation, Japan

²NTT Electronics Corporation, Japan

11.4. Optical Far-IR Wave Generation – An ESA Review Study 328

B. Leone¹, V. Krozer², M. Feiginov³, H. Roskos⁴, H. Quast⁴, T. Löffler⁴, G. Loata⁴, G. Döhler⁵, P. Kiesel⁶, M. Eckardt⁵, A. Schwanhäußer⁵, T. O. Klaassen⁶, P. Lugli⁷

¹ESA Directorate of Technical and Operational Support, ESTEC, The Netherlands

²Denmark Technical University, Denmark

³Technical University of Darmstadt, Germany

⁴University of Frankfurt, Germany

⁵University of Erlangen, Germany

⁶Delft University of Technology, The Netherlands

⁷University of Rome, Italy

11.5. Amplitude Noise in a Photomixer Using a UTC-PD in the 100 GHz Band 344

T. Noguchi¹, A. Ueda¹, H. Iwashita¹, S. Takano¹, Y. Sekimoto¹, M. Ishiguro¹, T. Ishibashi^{2}, H. Ito², T. Nagatsuma³*

¹Nobeyama Radio Observatory, Japan

²NTT Photonics Laboratory, NTT Corporation, Japan

³NTT Microsystem Integration Laboratories, NTT Corporation, Japan

*Present Affiliation: NTT Electronics Corporation

Session 12: OPTICS

Chair: Eric Mueller

Coherent Inc.

12.1. Propagating Partially Coherent THz Fields Using Non-Orthogonal Over-Complete Basis Sets 353

R. H. Berry, S. Withington, M. P. Hobson, G. Yassin

Cavendish Laboratory, University of Cambridge, UK

12.2. Experimental Verification of Electromagnetic Simulations of a HIFI Mixer Sub-Assembly 371

Willem Jellema¹, Paul Wesselius¹, Stafford Withington², Ghassan Yassin², J. A. Murphy³, C. O'Sullivan³, N. Trappe³, T. Peacocke⁴, Bruno Leone⁵

¹National Institute for Space Research (SRON), The Netherlands

²Cavendish Laboratory, University of Cambridge, UK

³National University of Ireland Maynooth (NUIM), Ireland

⁴UK Astronomy Technology Center (UKATC), UK

⁵European Space Agency (ESA/ESTEC), The Netherlands

12.3. A Novel Procedure for Designing Band-pass Filters using FSS Structures 383

Ge Wu¹, Volkert Hansen¹, Ernst Kreysa², Hans-Peter Gemuend²

¹Chair of Electromagnetic Theory, University Wuppertal, Germany

²Max Planck Institute for Radioastronomy, Germany

Session 13: POSTERS

Chair: Tom Crowe

University of Virginia

HEB MIXERS

13.1. A Hot-Spot Model for Membrane-Based HEB Mixer 393

Jean Baubert^{1,2}, H. Merkel², M. Salez¹, P. Khosropanah²

¹LERMA, Observatoire de Paris, France

²MC2, Chalmers University, Sweden

13.2. Noise Performance of Spiral Antenna Coupled HEB Mixers at 0.7 THz and 2.5 THz 405

K. V. Smirnov¹, Yu. B. Vachtomin¹, S. V. Antipov¹, S. N. Maslennikov¹, N. S. Kaurova¹,

V. N. Drakinsky¹, B. M. Voronov¹, G. N. Gol'tsman¹, A.D. Semenov²,

H. Richter², H.-W. Hubers²

¹Moscow State Pedagogical University, Russia

²DLR Institute of Space Sensor Technology, Germany

13.3. Improved NbN phonon cooled hot electron bolometer mixers 413

M. Hajenius^{1,2}, J. J. A. Baselmans², J. R. Gao^{1,2}, T. M. Klapwijk¹, P. A. J. de Korte²,

B. Voronov³, and G. Gol'tsman³

¹Department of Nanoscience, Delft University of Technology, The Netherlands

²Space Research Organization Netherlands, The Netherlands

³Moscow State Pedagogical University, Russia.

13.4. NbAu Bilayer Diffusion Cooled HEB 424

Harald F. Merkel, P. Khosropanah, S. Cherednichenko, T. Ottoson, J. Baubert, E. Kollberg

Department of Microtechnology & Nanoscience, Chalmers University of Technology, Sweden

13.5. Transition-Edge Operation of Tantalum Diffusion-Cooled Hot-Electron Bolometers 427

Anders Skalare, William R. McGrath, Bruce Bumble, Henry G. LeDuc

Jet Propulsion Laboratory, California Institute of Technology

13.6. Impedance and Bandwidth Characterization of NbN Hot Electron 431

Bolometric Mixers

F. Rodriguez-Morales, Sigfrid Yngvesson

Department of Electrical and Computer Engineering, University of Massachusetts

SIS MIXERS

13.7. Sideband-Separating SIS Mixer at 110 GHz for the Measurement of Atmospheric Ozone 439

Shin'ichiro Asayama¹, Takashi Noguchi², and Hideo Ogawa¹

¹Department of Earth and Life Sciences, College of Integrated Arts and Sciences, Japan

²Nobeyama Radio Observatory, Japan

- 13.8. Repeatability and Reliability of the 640 GHz SIS Mixer for JEM/SMILES** 442
K. Kikuchi, Y. Fujii, W.-L. Shan and J. Inatani
¹National Space Development Agency of Japan, Japan
²Nihon Tsushinki Co., Ltd., Japan
³Communications Research Laboratory, Japan
- 13.9. Observation of an Anomalous IF Peak at High Bias Voltage in 660-GHz SIS Mixers** 444
*M. J. Wang¹, W. L. Shan², W. Zhang², H. W. Cheng¹, T. Noguchi³, S. C. Shi²,
Y. Irimajiri⁴, T. Manabe⁴*
¹Institute of Astronomy and Astrophysics, Academia Sinica, Taiwan
²Purple Mountain Observatory, China
³Nobeyama Radio Observatory, NAOJ, Japan
⁴Communications Research Laboratory, Japan
- 13.10. SuperMix Aided Design of SIS Tunnel Junction Heterodyne Mixers** ---
Attila Kovács, Jacob W. Kooi, T. G. Phillips, J. Zmuidzinas
California Institute of Technology
- 13.11. Development of the HIFI Band 3 and 4 Mixer Units** 447
*G. de Lange¹, B. D. Jackson¹, M. Eggens¹, H. Golstein¹, W. M. Laauwen¹, L. de Jong¹,
S. Kikken¹, C. Pieters¹, H. Smit¹, and D. Van Nguyen¹, M. Kroug², T. Zijlstra²,
and T. M. Klapwijk²*
¹SRON National Institute for Space Research, The Netherlands
²Department of Nanoscience, Faculty of Applied Science,
Delft University of Technology, The Netherlands
- 13.12. Design of 129-174 GHz SSB SIS Mixer for Band 2 of New Generation Receiver of IRAM PdB Interferometer** 450
A. Navarrini and B. Lazareff*
Institut de Radio Astronomie Millimetrique, France
*Present Address: Radio Astronomy Lab, University of California
- 13.13. Scaled Model Measurement of the Embedding Impedance of a 660-GHz Waveguide SIS Mixer with a 3-Standard De-embedding Method** 453
W. Zhang¹, C.-Y. Edward Tong² and S.C. Shi¹
¹Purple Mountain Observatory, Chinese Academy of Sciences, China
²Harvard-Smithsonian Center for Astrophysics
- 13.14. Superconducting Microstrip Line Models at Millimeter and Sub-millimeter Waves and Their Comparison** 456
V. Belitsky, C. Risacher, M. Pantaleev, V. Vassilev
Group for Advanced Receiver Development, Onsala Space Observatory,
Chalmers University of Technology, Sweden
- SOURCES**
- 13.15. Local Oscillator Systems for (Sub)millimeter Spectroscopy** 476
A. Emrich, S. Andersson, J. Embretsen
Omnisys Instruments AB, Sweden

- 13.16. Equivalent Circuit for Photomixing in Resonant Laser-Assisted Field Emission** 478
M. J. Hagmann¹, M. S. Mousa², M. Brugat³, E. P. Sheshin⁴, A. S. Baturin⁴
¹Deseret Electronics Research Corporation,
²Department of Physics, Mu'tah University, Jordan
³Image Instrumentation Inc.,
⁴Moscow Institute of Physics and Technology, Russia
- 13.17. Effect of Finite Spectral Width on Photomixing in Resonant Laser-Assisted Field Emission** 481
M. J. Hagmann
Deseret Electronics Research Corporation
- 13.18. TeraHertz Quantum Cascade Laser Based on LO-Phonon-Scattering Assisted Depopulation** 484
Qing Hu¹, Benjamin S. Williams¹, Hans Callebaut¹, Sushil Kumar¹, John L. Reno²
¹Department of Electrical Engineering and Computer Science and Research Laboratory of Electronics, Massachusetts Institute of Technology
²Sandia National Laboratories, Dept 1123, MS 0601
- 13.19. Terahertz Backward Wave Oscillator Development** 486
Lawrence Ives¹, David Marsden¹, Malcom Caplan¹, Carol Kory¹, Jeff Neilson¹, S. Schwartzkopf²
¹Calabazas Creek Research, Inc.
²RWI, Inc.
- 13.20. Design and Operational Considerations for Robust Planar GaAs Varactors: A Reliability Study** 488
Frank Maiwald, Erich Schlecht, John Ward, Robert Lin, Rosa Leon, John Pearson, Imran Mehdi
Jet Propulsion Laboratory, MS 168-314
- 13.21. A Design Theory for a Terahertz-Frequency Quantum Oscillator that Operates in the Positive Differential Resistance Region** 492
Dwight Woolard¹, Peiji Zhao², H. L. Cui³
¹US Army Research Lab., ARO
²Department of Electrical and Computer Engineering, NCSU
³Department of Physics and Engineering Physics, Stevens Institute of Tech
- 13.22. A Multi-Subband Design Theory for a Terahertz-Frequency Double Barrier Quantum Well Oscillator** 495
Peiji Zhao¹, D. L. Woolard²
¹North Carolina State University
²Army Research Laboratory, Army Research Office

DEVICES

- 13.23. Beam Lead Fabrication for Submillimeter-wave Circuits Using Vacuum Planarization** 499

R. B. Bass¹, J. C. Schultz¹, A. W. Lichtenberger¹, J. W. Koo², C. K. Walker³

¹Department of Electrical and Computer Engineering, University of Virginia

²Division of Physics, Mathematics, and Astronomy, California Institute of Technology

³Department of Astronomy, University of Arizona

- 13.24. Wide Band Cryogenic IF Amplifiers for ALMA and Herschel Receivers** 502

Isaac López-Fernández, Carmen Diez, Juan Daniel Gallego, Alberto Barcia

Centro Astronómico de Yebes, OAN-IGN, Spain

INCOHERENT/BOLOMETER DETECTORS

- 13.25. Investigation of Superconducting Transition in the Molybdenum-Copper Thin Film Structure Showing the Proximity Phenomenon with the Purpose of Constructing TES Bolometer** 505

S. A. Kovtonyuk, A. G. Kovalenko, A. A. Chebotarev, A. N. Vystavkin

Institute of Radioengineering and Electronics of RAS, Russia

WAVEGUIDE

- 13.26. Full-Waveguide Band Orthomode Transducer for the 3mm and 1mm Bands** 508

Gopal Narayanan, Neal R. Erickson

Department of Astronomy, University of Massachusetts

- 13.27. Precision Measurements of the Properties of Thin-film Superconducting Microstrip Lines at 100-500 GHz** 513

Anastasios Vayonakis¹, Alexey Goldin², Henry Leduc², Chiyan Luo³, Jonas Zmuidzinas¹

¹California Institute of Technology

²Jet Propulsion Laboratory

³Massachusetts Institute of Technology

- 13.28. Propagation in Lossy and Superconducting Cylindrical Waveguides** 516

Ghassan Yassin, Choy Yoong Tham, Stafford Withington

Cavendish Laboratory, University of Cambridge, UK

SPECTROMETERS

- 13.29. Autocorrelation Spectrometers for (Sub)millimetre Spectroscopy** 520

A. Emrich, S. Andersson, J. Embretsén, J. Dahlberg, L. Landén, C. Tegnander

Omnisys Instruments AB, Sweden

- 13.30. Chip Set for Autocorrelation Spectrometer Applications** 522
L. Landén^{1,2}, J. Dahlberg¹, A. Emrich¹

¹Omnisys Instruments AB, Sweden

²Chalmers University of Technology, MEL, Sweden

- 13.31. THIS – A Quantum-Cascade-Laser Pumped Mid-Infrared Heterodyne Receiver** 525
Daniel Wirtz¹, G. Sonnabend², V. Vetterle¹, M. Olbrich¹, R. Schieder¹

¹I. Physikalisches Institut, Universität zu Köln, Germany

²NASA Goddard Space Flight Center

SYSTEMS

- 13.32. Heterodyne Receiver Requirements for the Single Aperture Far-Infrared (SAFIR) Observatory** 529

D. J. Benford¹, Jacob Kooi²

¹NASA – Goddard Flight Center, Code 685

²Caltech, MC 320-47

- 13.33. Cartridge-type receiver system on ASTE** 535

*Masahiro Sugimoto¹, Yutaro Sekimoto¹, Sozo Yokogawa¹, Takeshi Okuda¹,
Ken'ichi Tatematsu¹, Takashi Noguchi¹, Kotaro Kohno², Hideo Ogawa³,
Kimihiro Kimura³*

¹National Astronomical Observatory of Japan, Japan

²Institute of Astronomy, The University of Tokyo, Japan

³Department of Earth and Life Sciences, College of Integrated Arts and Sciences, Japan

- 13.34. Current Status of the Antarctic Submillimeter Telescope and Remote Observatory** 538
*Kecheng Xiao¹, Antony A. Stark¹, Adair P. Lane¹, Christopher L. Martin¹,
Wilfred M. Walsh¹, Christopher K. Walker², Jacob W. Kooi³*

¹Smithsonian Astrophysical Observatory

²University of Arizona

³California Institute of Technology

OPTICS

- 13.35. Efficient Side-band Ratio Measurement of a Submm Wave Mixer Using a Fourier Transform Spectrometer** 542

A. Baryshev^{1,2,3}, R. Hesper^{1,2,3}, G. Gerlofsma^{1,2,3}, M. Kroug⁴, W. Wild^{2,3}

¹Netherlands Research School for Astronomy (NOVA), The Netherlands

²Space Research Organization Netherlands (SRON), The Netherlands

³University of Groningen (RuG), The Netherlands

⁴DIMES, Delft University of Technology, The Netherlands

- 13.36. Transmission and Reflection Characteristics of Slightly Irregular Wire-Grids for Arbitrary Angles of Incidence and Grid Rotation** 543

Takeshi Manabe¹, Axel Murk²

¹Communications Research Laboratory, Japan

²Institute of Applied Physics, University of Berne, Switzerland

**REVIEW OF HEB HETERODYNE DETECTORS AND RECEIVER
SYSTEMS FOR THE THz RANGE: PRESENT AND FUTURE
(Invited talk)**

Sigfrid Yngvesson

**Department of Electrical and Computer Engineering
University of Massachusetts at Amherst, Amherst, MA 01003**

I. INTRODUCTION

The field of Heterodyne THz detectors using the hot-electron effect in superconductors was initiated through the pioneering Russian work by Gershenzon et al. [1]. Their version of this general type of detector came to be distinguished as the PHEB ('Phonon-Cooled Hot Electron Bolometer') after Dan Prober [2] proposed what is now known as the DHEB ('Diffusion-Cooled Hot Electron Bolometer'). Since that time, both types of HEB devices have demonstrated the order-of-magnitude lowering of the receiver noise temperature, as measured in several laboratories at frequencies from 1 THz to 2.5 THz, which had been anticipated. HEBs have also been part of the history of these ISSTT symposia since the very first one, although one won't find an HEB session or even HEB mentioned in a title for a paper at the 1st ISSTT: The present author "hid" a discussion on HEBs employing the semiconductor 2DEG medium in a paper entitled: "Integrated Tapered Slot Antenna Arrays and Devices" [3]. The first talks on the superconductor version of the HEB appeared at the 4th ISSTT. Since the 5th ISSTT, there have been entire sessions devoted to HEB topics, typically two at each conference. To-day, HEB receivers for up to 1.46 THz have been installed on radio telescopes, and are beginning to produce significant astronomical data in this frequency range which has not been well exploited for heterodyne measurements previously. HEB detectors now being developed will be launched on Herschel and flown in SOFIA, and it is appropriate to ask what their real potential is for future such systems; for example, how high frequencies will they realistically be used for, what are the anticipated actual requirements for LO power, etc. This talk will review the present status of the THz HEB heterodyne detector field, and attempt to make predictions for where it will go in the future. For brevity, the review will be organized around specific questions, to which I will give answers which obviously represent my own personal opinion. I hope at least some of the answers and comments will give rise to fruitful discussions.

II. STATE-OF-THE-ART OF HEB HETERODYNE DETECTOR TECHNOLOGY

A. Operating HEB systems above 1 THz.

There are presently to my knowledge three operating HEB heterodyne receivers systems above 1 THz (this frequency ought to be the dividing line at a THz conference!):

- 1) Kawamura et al. at the SMT0, on Mt. Graham here at the U. of Arizona. [4]
- 2) TREND on AST/RO at the South Pole, see Gerecht et al, this symp. (Figure 1) [5]
- 3) Radford et al, at Cerro Sairecabur, Chile. [6]



Figure 1. TREND at AST/RO

B. DSB Receiver Noise Temperature

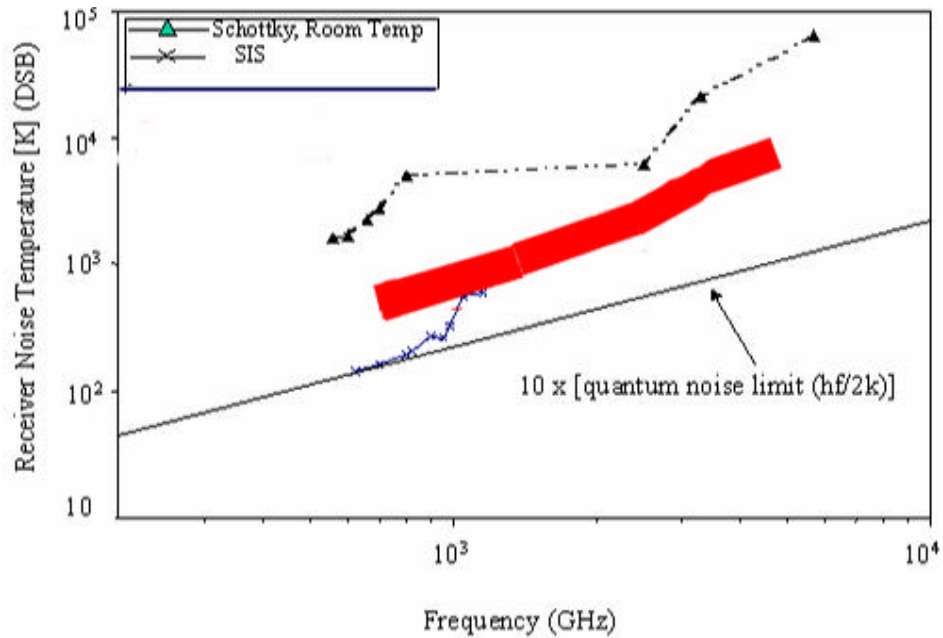


Figure 2. Representative DSB Receiver Noise Temperature Data from several Laboratories (the broad red band).

Figure 2 (above) reviews the state-of-the-art of DSB receiver noise temperatures (NTs) measured IN THE LABORATORY with HEB receivers.

The task is made easier by the fact that a number of laboratories have published NTs in about the same range, roughly within the red band in this figure.

The laboratories represented are listed in Table 1. Only PHEBs are presently represented among the operational systems on telescopes. The data above 2.5 THz (up to 5.3 THz) actually have only been demonstrated by a single program, the DLR/MSPU collaboration.

TABLE 1. Laboratories represented in Figure 1.

Laboratory	Type of HEB
Moscow State Pedagogical Univ. (MSPU), Moscow, Russia	PHEB, NbN, NbTiN
Chalmers Univ. of Technology (CUT), Göteborg, Sweden	PHEB, NbN, NbTiN
DLR Institute of Space Sensor Technology, Berlin, Germany	PHEB, NbN
SRON/Technical Univ. of Delft, The Netherlands	DHEB (Nb,Nb/Au), PHEB, NbN, NbTiN
KOSMA, Köln, Germany	DHEB (Nb), PHEB (NbTiN)
University of Massachusetts, Amherst and Lowell, MA, USA	PHEB, NbN
Yale University, New Haven, CN, USA	DHEB, Nb, Nb/Au, Al
Harvard/Smithsonian Center for Astrophysics, Cambridge, MA, USA	PHEB, NbN, NbTiN
National Institute for Standards and Technology (NIST), Boulder, CO, USA	DHEB, Nb
Jet Propulsion Laboratory, Pasadena, Ca, USA	DHEB, Nb, Ta; PHEB, NbTiN

C. HEB Receiver Systems "on the Way".

Some of the major HEB receiver systems which are under development are:

- 1) HIFI Band 6 (Herschel) 1.4 THz to 1.9 THz, CUT, JPL; Launch 2007; see Figure 3;
- 2) GREAT (for SOFIA), 1.4 THz to 5 THz, DLR, MPIfR, KOSMA, Operation 2005;
- 3) TELIS (balloon launched), 1.8 THz, DLR, SRON, RAL; First flight 2005.

We are clearly entering an era in which HEB low-noise receivers for up to at least 2.5 THz will be used in many systems. GREAT is also aimed at even higher frequencies, up to 5 THz. So, we can ask:

D) Will HEB receivers climb even higher in frequency?

Let's review why HEBs have always been considered promising for being extended to much higher frequencies than traditional technologies, such as Schottky diodes.

- 1) HEBs are “bulk” (or actually “surface”) devices. Parasitic reactances are very small, even at the highest THz frequencies.
- 2) HEBs rely on a) being able to absorb the THz radiation; this is guaranteed for superconducting film devices into the visible range due to the very short momentum scattering times (note that any superconducting portions of the devices also absorb THz radiation); and on b) being able to change their resistance as the electrons heat. These two properties do not depend on the frequency, once the frequency is above the bandgap frequency.
- 3) The majority of HEB receivers now use quasi-optical coupling. Some HEB receivers in the range up to maybe 2.5 THz are likely to be waveguide-coupled in the next few years. The highest THz frequencies are likely to continue to use quasi-optical coupling. Antennas can in principle be efficient (good radiation patterns, low ohmic losses) up to at least 30 THz, but *fabrication will be a greater challenge at the highest frequencies*.
- 4) A related challenge is that of providing the LO power: The “lower” THz range is likely to see broader use of multiplier LO sources, as these continue to improve. In the higher THz range laser sources will likely continue to dominate. Quantum Cascade Solid state lasers (QCLs) have had a breakthrough recently (see paper by Quing Hu et al, this symposium [7]; also Semenov et al [8] reported using a QCL to pump an HEB mixer at 4.3 THz). Realistic values of the LO power required for typical PHEBs at the dewar window are from 0.5 μ W to a few μ W.

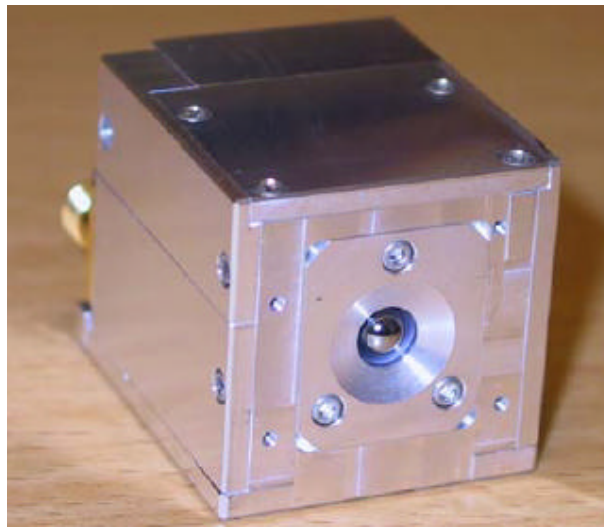


Figure 3. One of the HEB mixer blocks for HIFI

- 5) There are missions planned which need heterodyne detectors in the highest THz area, which are in the long-term planning stage, such as SAFIR [9].

II. BASIC QUESTIONS ABOUT HEBs

1) Optimum HEB material/cooling?

There is at least a temporary, practically motivated, answer to the question about which is the optimum HEB material, and which is the optimum cooling method (DHEB or PHEB): The systems which have been brought to fruition and have been installed on telescopes all use PHEBs. Also, the majority of all laboratory measurements in Figure 2 are for PHEBs. Laboratories which have tried both types, such as SRON, have achieved their lowest receiver NTs with PHEBs. This is not to say that the situation may not change. The DHEBs all use lower T_c materials, which according to theory should have lower output noise. If we examine the equation for the noise temperature of an HEB mixer, we can discern why the DHEBs may not prevail despite this advantage:

$$T_{R,DSB}=(L_c/2)(T_{FL}+T_J+T_{IF}) \quad (1)$$

Here, the temperature fluctuation term, T_{FL} , which is proportional to T_c^2 , tends to dominate. THz DHEBs tend to have larger conversion loss, however, which explains why PHEBs still have a lower (or similar) receiver NT. DHEBs tend to require less LO power, but are also much more sensitive to being biased at the exact optimum point, which is a practical disadvantage. Among PHEB materials, NbN has dominated for a while, although NbTiN may also compete, see several papers at this symposium.

2) HEB Models are as Good and Precise as those for SIS Receivers?

The answer to this question is unfortunately an emphatic NO at the moment. Here lies a major challenge for HEB researchers in the next few years. The program to accomplish this might proceed as follows: Step 1: Empirical models based on a variety of measured data; Step 2: Physical models will allow improved performance; Some suggestions based on our projects at UMass follow below.

3) New types of measurements to perform.

a) Impedance measurements with THz LO applied. This type of measurement has not been performed until recently. See Fernando Rodriguez-Morales's poster paper [10] at this symposium for some fresh results, one of which is shown below.

All *gain bandwidth* measurements of HEB devices have so far been performed at typical frequencies of 600 GHz. This is either below or barely above the superconducting bandgap frequency under typical operating conditions, and it is important to check what the gain bandwidth with actual THz LO applied is. An impedance measurement should be able to accomplish this, and also show any potential dependence on the LO frequency.

b) Receiver noise bandwidth measurements. There are still only a few measurements on the actual *receiver noise temperature bandwidth* (the IF bandwidth at which the receiver noise temperature becomes twice that at the lowest IF frequencies). It is predicted to be

about twice the gain bandwidth (i.e. 5 GHz to 7 GHz for NbN PHEBs) which has been verified in measurements at CUT and at UMass [10]. The UMass measurement demonstrated the use of a broadband MMIC IF amplifier for this test, see below:

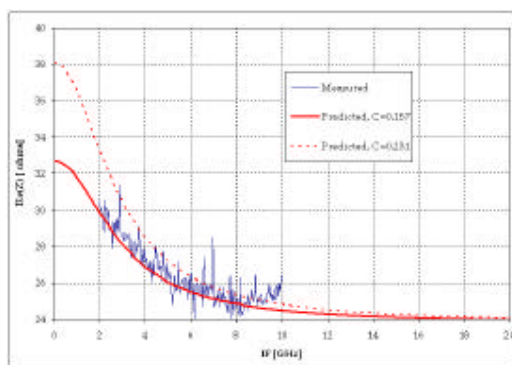


Figure 4. Measured IF impedance (real part) for an HEB device, vs frequency [10].

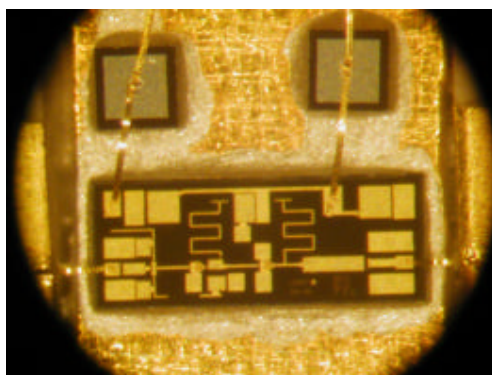


Figure 5. Broadband InP MMIC LNA used at UMass/Amherst (Courtesy of Dr. Sander Weinreb).

The *gain bandwidth* can also be measured at THz frequencies by employing a tunable THz sideband source. We are performing such measurements in collaboration with UMass/Lowell.

4) What is the effect of Quantum Noise on THz HEB mixers?

The author and Erik Kollberg of CUT began to tackle this unsolved question in a paper given at the previous ISSTT [11]. The main point is to use the Callen-Welton noise power expression for all components, including the HEB. A complication arises from the fact that all of the HEB absorbs THz radiation, while only a part of it is actually producing IF power. We have developed a simplified model to take this effect into

account, but further detailed work will need to go hand in hand with the development of physical hotspot models for the HEB (see below). A preliminary (unpublished) result is shown in Figure 6 below. We used data measured (crosses) by the DLR group [12], and also included their estimates of the optical input losses. We used the ratio of the resistances of the active and passive parts of the HEB, respectively, as an adjustable parameter. Although our calculations then fit the measured data, it is much too early to judge the correctness of the theory. Further measurements and theoretical investigations are ongoing.

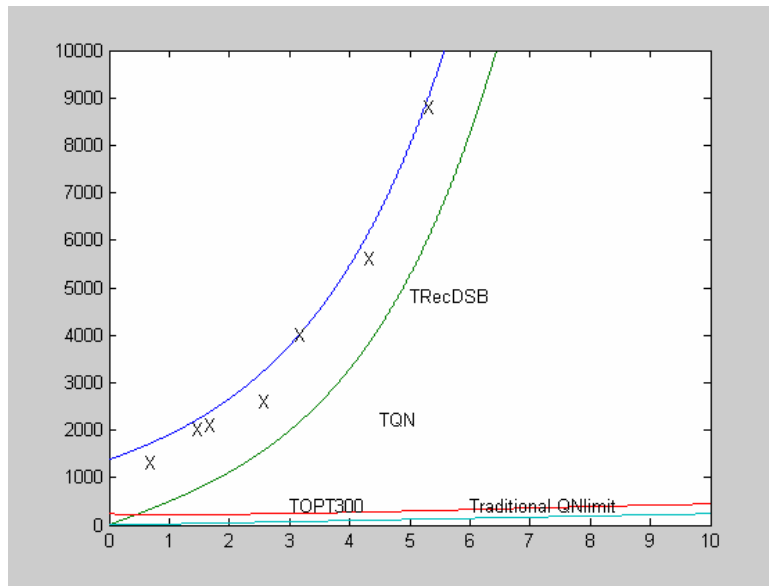


Figure 6. Calculated and measured DSB receiver NT for HEBs as a function of LO frequency.

5) *Physical HEB Models – Hot Spots!*

Erik Kollberg and I termed the type of model which has been used by essentially all HEB researchers since the beginning of the field of HEB mixers, the “standard model”, in reference to the standard model used by high energy particle physicists. Like the high energy physics standard model, it forms a consistent frame work against which to compare our measured data. In both fields, the standard models are known to be an incomplete picture of reality. We showed in a paper at the 10th ISSTT [12] that one can use adjustable parameters in the standard model to achieve good agreement with measurements for the variation of conversion loss, output noise, and receiver noise temperature, as a function of the LO power (or bias current, which is the same thing). However, the variation of those same quantities with bias voltage disagrees drastically with the standard model. So, everybody has realized that hot spot models make a lot more sense.

After much excellent work by several people, there is still no accepted hot spot model (for good review of some earlier work, see e.g. [12,13]). Again, a combination of careful measurements and theoretical work is expected to eventually solve this problem.

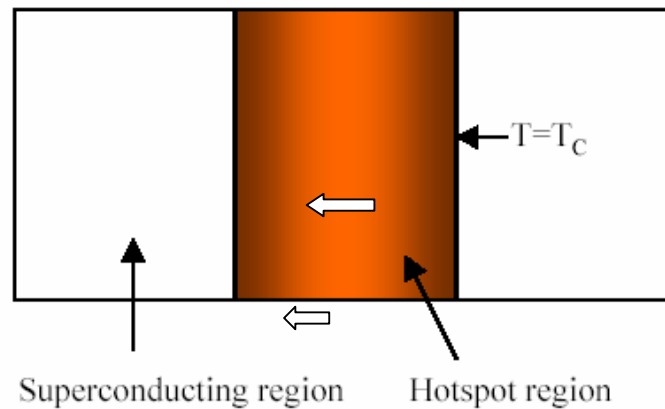


Figure 7. A hot spot model.

Much of the controversy has been centered on which parts of the HEB (see Figure 7) that actually produce an IF resistance (and thus voltage) in response to THz power. In a simplified picture of the hotspot, the inside of the hotspot is already in the normal state, and thus can not change its resistance. On the other hand, the SC regions outside the hot spot obviously can not change their resistance either. Which leaves the boundaries of the hotspot! Recent work by Harald Merkel et al. indicates that the active regions may spread further away from the actual boundaries than one would deduce from the simplified picture described above [14]. Some of the important features which have been recently added to the hotspot models are

- a) Since THz radiation is absorbed in the entire HEB, but only parts of it contribute to the conversion gain, there must be some loss in conversion gain compared with the standard model – this agrees with for example [12].
- b) Andreev Reflection (AR) of the electrons at the SC/hotspot boundary (also in [13]).
- c) A model for the very slow expansion/contraction of hot spots in the *unstable* (“*bistable*”) portion of the IV-curves [15], including AR..
- d) The models will now also need to explain the remarkable findings of the SRON group that devices with *higher* normal resistance have *lower* NT [16].

6) Are Superconducting HEBs all there is?

We should not forget that there are competing HEB or other types of devices which do not use SC films! Note the IF bandwidth record of 40 Ghz set by Mark Lee et al [17] with a “ballistic” 2DEG mixer! This receiver may have difficulties in reaching all the way to

the actual THz range due to charge-carrier inertia, though. Mark Sherwin’s TACIT detector [18] is resonant and would not have that problem. These devices, and Al Betz’s photoconductive HgCdTe mixers [19] are all worth watching.

III. CONCLUSION

Finally, I want to re-emphasize what is maybe the most important challenge for THz HEB researchers – how do we expand the frequency range of very low noise HEB mixers all the way to 30 THz? If we draw a receiver noise temperature diagram with a wider frequency scale as in Figure 8, then we see better what we are up against! Note that the photoconductive mixers at 30 THz (10 μm) reached close to the quantum noise limit long time ago, and that the Erbium-doped fiber amplifiers (they are masers!) are right on that limit at 1.5 μm wavelength. We have some work still remaining ahead of us!

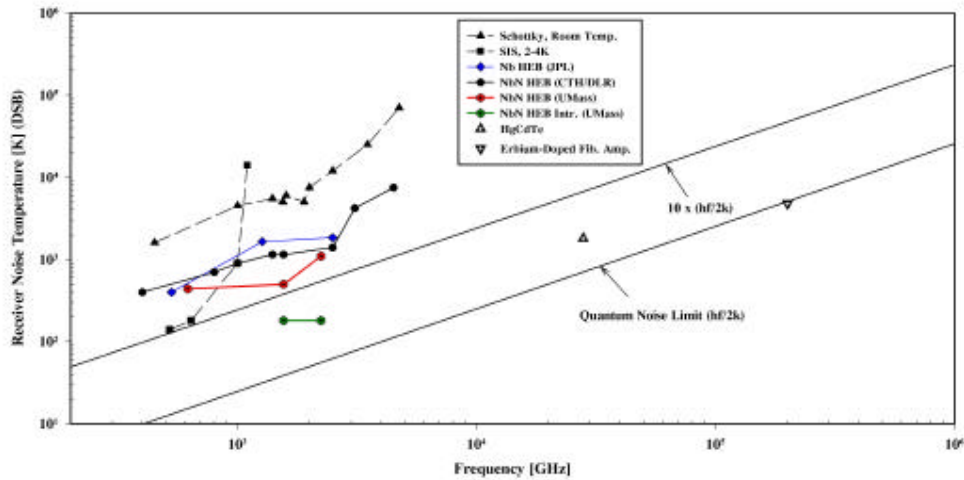


Figure 8. Receiver NT for different devices over a wide frequency range.

IV. ACKNOWLEDGEMENTS

THz HEB work at UMass/Amherst is supported by NASA through Contract NAS1-01058 with the NASA Langley Research Center, and grant NRA-00-01-SARA-012, as well as the National Science Foundation through its program for Advanced Technologies

and Instrumentation (ATI), Division of Astronomical Sciences, NSF award # AST 9987319.

V. REFERENCES

- [1] E. M. Gershenzon, G. N. Gol'tsman, I. G. Gogidze, Y. P. Gousev, A. I. Elant'ev, B. S. Karasik, and A.D. Semenov, "Millimeter and Submillimeter Range Mixer Based on Electronic Heating of Superconducting Films in the Resistive State", *Soviet Physics: Superconductivity*, 3, 1582, 1990.
- [2] D.E. Prober, "Superconducting terahertz mixer using a transition-edge microbolometer," *Appl.Phys.Lett.*, **62**, 2119, 1993.
- [3] K.S. Yngvesson, "Integrated Tapered Slot Antenna Arrays and Devices" *1st Intern.Symp.Space Terahertz Technol.*, JPL, Pasadena, CA, March 1990, pp. 176-186.
- [4] J. Kawamura et al., "First Light with an 800 GHz Phonon-Cooled HEB Mixer Receiver," p. 35-43, 9th ISSTT, 1998, pp.
- [5] E. Gerecht et al, "Deployment of TREND – A Low Noise Receiver User Instrument at 1.25 THz to 1.5 THz for AST/RO at the South Pole," this symposium
- [6] S. Radford, "CO(9-8) in Orion," this symposium.
- [7] Q. Hu et al., "THz QCL Based on LO-Phonon-Scattering Assisted Depopulation," this symposium.
- [8] A. Semenov et al., "Superconducting HEB Mixer for THz Heterodyne Receivers," this symposium.
- [9] D. Lester, "Looking Ahead to the Single Aperture Far-Infrared (SAFIR) Mission", this symposium.
- [10] F. Rodriguez-Morales and S. Yngvesson, "Impedance and Bandwidth Characterization of NbN HEB Mixers," this symposium.
- [11] E.L. Kollberg and K.S. Yngvesson, "Quantum Noise Contribution to the Receiver Noise Temperature of HEB THz Heterodyne Receivers," 13th ISSTT, 2002, pp. 73-84.
- [12] P. Khosropanah, "Modeling Hot Electron Bolometer Mixers", Licentiate thesis, Chalmers University of Technology, Dept. of Microelectronics (2000).
- [13] D. Wilms Floet, "Hotspot Mixing in THz Niobium Superconducting Hot Electron Bolometer Mixers," Ph.D. thesis, Technical University of Delft, Dept. of Applied Physics (2001).
- [14] H. Merkel et al., "Comparison of the Noise Performance of NbTiN and NbN HEB Heterodyne Mixers at THz Frequencies," this symposium.
- [15] Y. Zhuang, D. Gu and S. Yngvesson, "Bistability in NbN HEB Mixer Devices," this symposium.
- [16] Hajenius et al., "Current-Voltage and Resistance-Temperature Characteristics of Nb(Ti)N PHEB Mixers With and Without Contact Resistance," this symposium.
- [17] M. Lee et al., "Broadband Millimeter-Wave Bolometric Mixers Based on Ballistic Cooling in a 2DEG, this symposium.
- [18] M.S. Sherwin et al., "Design, Fabrication and Testing of Semiconductor Tunable Antenna-Coupled Intersubband Terahertz (TACIT) Detectors," this symposium.

Noise performance of NbN Hot Electron Bolometer mixers at 2.5 THz and its dependence on the contact resistance.

J.J.A.Baselmans¹, M.Hajenius^{1,2}, J.R. Gao^{1,2}, T.M. Klapwijk², P.A.J. de Korte¹, B. Voronov³, and G. Gol'tsman³

¹*Space Research Organisation of the Netherlands (SRON), Sorbonnelaan 2, 3584 CA Utrecht, The Netherlands*

²*Faculty of Applied Sciences, Delft University of Technology, Lorentzweg 1, 2628 CJ Delft, The Netherlands.*

³*Moscow State Pedagogical University, Moscow 119435, Russia*

Abstract - NbN hot electron bolometer mixers (HEBM) are at this moment the best heterodyne receivers for frequencies above 1 THz. However, the fabrication procedure of these devices is such that the quality of the interface between the NbN superconducting film and the contact structure is not under good control. The result is a low transparency interface between the bolometer itself and the contact/antenna structure. In this paper we report a detailed experimental study on a novel idea to increase the transparency of this interface. This leads to a record sensitivity and more reproducible performance. We compare identical bolometers, coupled with a spiral antenna, with different NbN bolometer-contact pad interfaces. We find that cleaning the NbN interface alone results in an increase in the noise temperature. However, cleaning the NbN interface and adding a thin additional superconductor prior to the gold contact deposition improves the noise temperature of the HEBM with more than a factor of 2. A device with a contact pad on top of an in-situ cleaned NbN film consisting of 10 nm of NbTiN and 40 nm of gold has a DSB noise temperature of 1050 K at 2.5 THz.

1. INTRODUCTION

The development of new space based [1] and airborne [2,3] telescopes will create new opportunities for sub-mm astronomy, as ground-based observatories suffer from limited atmospheric transmission in this spectral range. The desire for these instruments to perform high-resolution spectroscopy with a sensitivity close to the quantum limit drives the development of low noise THz mixers.

In the frequency range from 100 GHz to 700 GHz SIS mixers incorporating Nb/Al-ALOX/Nb SIS junctions with a niobium tuning circuit offer near quantum limited performance [4]. However, above that frequency, the Nb superconducting energy gap frequency, the sensitivity decreases drastically due to losses in the Nb stripline. Using either a low loss normal conductor or a superconductor with a larger bandgap for the tuning circuit is a possible way out and might extend the use of these devices to 1.2-1.4 THz, however, higher frequencies will be beyond their reach. Hence all practical mixers

in the THz range have to use Schottky-diode mixers with rather poor sensitivity and high local oscillator requirement. This is a serious issue regarding the practical use of these devices, for only very few powerful laser lines are available in the THz frequency range.

As a result the development of THz receiver has focused in the past years on Hot Electron Bolometer mixers (HEBm), initiated from the early work of Gershenzon et al. [5]. The major advantage of these type of mixers is that their RF frequency bandwidth is not limited by the superconducting energy gap. The HEB mixer can in principle operate from millimeter waves up to the far infrared without degradation in performance. Recently the practical usefulness of HEBm's at THz frequencies was shown with a successful application of a NbN based HEBm receiver in a radio telescope in Arizona [6].

Two types of bolometer mixers have been proposed and tested so far: The diffusion cooled HEBm [7] and phonon-cooled HEBm [5]. In both cases the bolometer consists of a small superconducting strip on a dielectric substrate connected to two contact pads which are part of a suitable antenna structure. Mixing in the bolometer is obtained by coherently adding the LO signal and RF signal with a small frequency difference. The envelope of the power spectrum oscillates with the difference frequency (IF-signal). As a result of RF and DC heating in the bolometer a normal conducting hot spot appears with a length dependent on the absorbed power. Hence the hot-spot length and thus the bolometer resistance oscillates with the IF frequency. The resistance change is detected using an external IF circuit. The difference between the two bolometer principles is how the hot electrons are cooled. In the diffusion cooled HEBm electrons loose their heat through out-diffusion to thermal reservoirs at the bolometer's edges. In the phonon cooled HEBm a material with a very fast electron-phonon interaction time constant, such as NbN, is used with the result that the electrons loose their energy by means of electron phonon interactions. The latter type of bolometers are at this moment the most promising; they have shown slightly better noise temperatures, have been studied more extensively and are more reliable than diffusion cooled devices [8].

However, to combine a high sensitivity with a high bandwidth extremely thin (~3 nm) NbN films are used in the fabrication of phonon cooled bolometers. Only very few labs in the world are able to produce sufficiently high quality NbN films, with a thickness of about 3.5 nm and a critical temperature above 9 K. The state of the art films at this moment come from Moscow state pedagogical university. Using these films on MgO substrate devices made in Chalmers have shown a DSB receiver noise temperatures of 1400 K at 2.5 THz on MgO substrates together with a 4.5 GHz gain bandwidth at the optimal bias point [9].

2. THE CONTACT INTERFACE IN NBN BASED PHONON-COOLED HEBM

Because most groups nowadays obtain their NbN films from elsewhere, it is inevitable that the NbN film is exposed to ambient atmosphere for a prolonged period, i.e. the bolometer fabrication is *ex situ*. To make this more clear we show, in Fig. 1, a schematic description of the conventional fabrication process of a NbN HEBm. This process is in principle identical to the one used by all labs including ours as reported in [6,10-16]. As stated the fabrication starts with a NbN film on a Si (or possibly MgO) substrate. In step 2 a contact pad of gold with a thickness of about 70 nm is deposited using conventional e-beam lithography with a PMMA based positive resist and lift off. This implies in most cases a short reactive ion etch with an Oxygen plasma to remove resist remnants on the NbN surface. Before the deposition of the gold a thin titanium layer (~5 nm) is deposited *in situ* to create a good adhesion of the gold. In step 3 the antenna structure, consisting of 5 nm Ti and 150 nm of gold, is deposited using the same method. In a last step the NbN is etched away except at the bolometer bridge location. A SEM micrograph of a finished bolometer with a spiral antenna is shown in Fig 2.

It is obvious that the surface of the NbN film is not very clean when the contact pad layer is deposited. The inevitable result is a limited interface transparency between the bolometer itself and the contact structure. This has important implications for the RF coupling between the bolometer itself and the contact antenna structure. Moreover, the bad control over the interface quality leads to a large spread in device performance for furthermore identical devices.

To underline this let us consider how the RF currents flow in some detail. For the RF currents the sheet resistance of the NbN layer is in the order of the normal state resistance, $R_N \approx 500 \Omega$ since $\hbar\omega \gg \Delta$. Hence the RF current flows through the gold antenna and contact pad and thus has to be transferred to the NbN bridge through the contact pad-NbN interface. This occurs over a distance which depends strongly on the

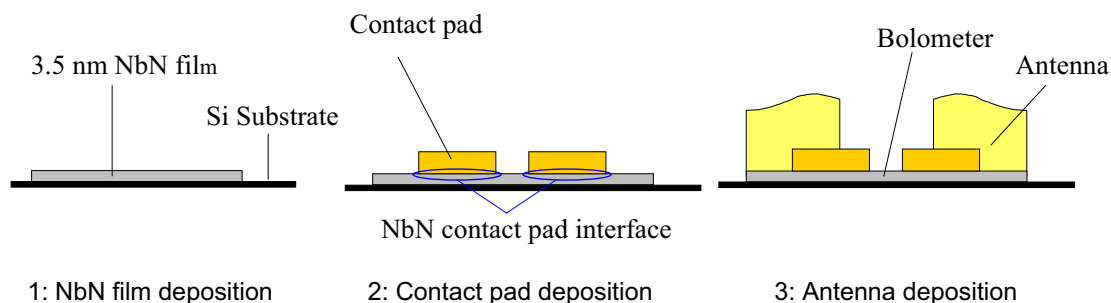


Fig 1. Schematical description of the conventional fabrication process of a NbN based phonon cooled hot electron bolometer mixer. In a last step 4 (not shown) the NbN is etched away except at the bolometer bridge location.

Table 1: Device parameters. In all cases a 6 sec. ex situ Oxygen plasma etch is included prior to the contact pad deposition.

Device	Contact pad-NbN interface	Contact pad material	R at 11K
A	No additional cleaning	5 nm Ti + 65 nm Au	$220 \pm 20 \Omega$
D	15 sec Argon etch	5 nm Ti + 65 nm Au (ex situ)	$70 \pm 10 \Omega$
H	15 sec Argon etch	5 nm Nb +45 nm Au (in situ)	$65 \pm 5\Omega$
G	15 sec Argon etch	10 nm NbTiN + 40 nm Au (in situ)	$55 \pm 5\Omega$

interface resistance and the impedances of the NbN and Au. The surface area in a real device (see Fig 2) associated with reasonable estimate of this distance of $0.2 \mu\text{m}$ is in the order of $1 \mu\text{m}^2$, witch results in $R_c \approx 20\text{-}100 \Omega$ for the RF current [13,17].

For the DC and IF currents the situation is different because $\hbar\omega \ll \Delta$, so $R_N=0$ and the NbN layer forms a short in parallel with the antenna structure. Hence these currents will flow through the NbN layer.

The possible influence of the bad NbN-contact pad interface has been noted before [13-15,17], however, cleaning the NbN-contact pad interface using an in-situ Argon etch of the NbN surface prior to the contact pad definition is reported to decrease the sensitivity of the device [13, 14]. One possible explanation is that a clean NbN-Au interface reduces the critical temperature of the NbN layer, i.e. the transition temperature of the NbN underneath the contact pad is lower than the NbN bridge [18].

3. DEVICES

In this article we study the effect of a possible contact resistance between the contact pad and the NbN film on the bolometer mixer performance. To do this we have made 4 different bolometer geometries which differ only in the way the NbN-contact pad interface is prepared. All devices are made in one process run on one single wafer consisting of a $300 \mu\text{m}$ thick Si wafer with a 3.5 nm NbN film deposited in Moscow. The size of the bolometer is $0.4 \times 4 \mu\text{m}$ and we use a spiral antenna because it is frequency independent, which enables a comparison of mixer properties at different frequencies which is important at this stage. Table 1 shows the 4 different geometries, denoted, A,D,G and H. Geometry A was made using the conventional fabrication process as shown in Fig 1. The NbN – contact pad interface has not been cleaned other than a short Oxygen etch necessary for a good lift-off process. The amount of oxygen etching was

calibrated to yield a minimum in interface resistance [11]. We associate this minimum with a total removal of e-beam resist remnants. A longer etch increases the interface resistance, probably due to the formation of an oxide layer at the interface.

For geometry D we use the same oxygen etch but afterwards we use a short Argon etch prior to the pad deposition, more or less identical to the process reported in [13,14,15]. However, a very short vacuum breach is necessary in our lab between the etch and the Au deposition (a few minutes). In geometry H we perform the same Ar etch but after that we deposit in-situ 5 nm of Nb. Geometry G is identical but in stead of Nb we deposit 10 nm of NbTiN. In all cases we have calibrated the Argon etch time for a minimum in device resistance (maximum interface transparency) and minimum NbN film damage. Further details on the fabrication and DC characterization of these devices can be found in Ref. [11].

4. EXPERIMENT

The bolometer chip is glued to a hyper-hemispherical Si lens *without* anti reflection coating and clamped to the mixer block that is thermally anchored to the 4.2 K plate of a L-He cryostat with 3 Zytex G104 heat filters, 1 at 77 K and 2 at 4.2 K and a 40 μm thick Mylar window. During the experiments the mixer block temperature is 4.35 K. As a local oscillator source we use a FIR laser at 2.5 THz, using CH_3OH at $2.2 \cdot 10^{-1}$ mBar pumped by a CO_2 laser at line 9p36. The LO power is coupled into the cryostat by means of a 6 μm mylar beam splitter. A rotatable grid is used to control the laser power. The device output is connected through a bias T to a 1.2 - 1.8 GHz HEMT amplifier with a noise temperature of $\sim 5\text{K}$. The output is further amplified at room temperature and filtered through a 1.35 ± 0.04 GHz band pass filter and detected using a power meter. The DSB receiver noise temperature was determined using the standard Y-factor technique. We

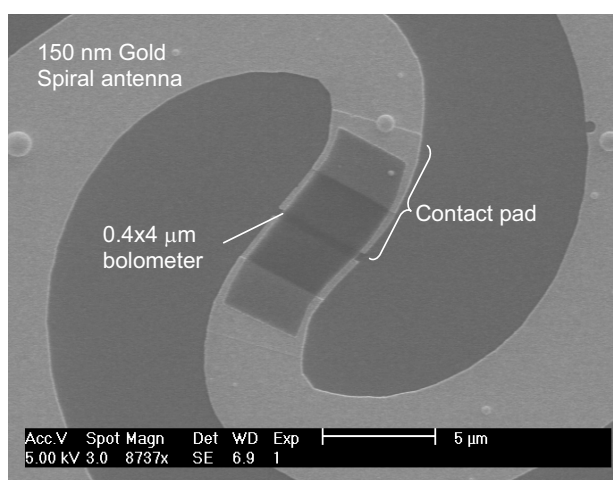


Fig 2. SEM micrograph of a NbN hot electron bolometer mixer with a Spiral Antenna. The dark region is remaining negative resist from the last processing step.

Table 2: DSB noise temperatures at 2.5 THz and estimated LO power for the devices reported in table 1.

Device	Minimum DSB noise temperature of two different devices	Estimated absorbed LO power at optimum bias point
A	4700 K, 4400 K	500 nW
D	4600 K, 8900 K	550 nW
H	2600 K, 3000 K	550 nW
G	2000 K, 2100 K	700 nW

use a mirrored hot/cold load consisting of Eccosorb at 295 K and 77K placed at exactly the same distance (30 cm) from the cryostat window at every experiment. The losses in the optics (beam splitter, window and heat filters) are measured to be 3.3 dB, the estimated lens losses (reflection and absorption) and lens antenna mismatch are estimated to be 2.2 dB, yielding a total loss of 5.5 dB in the RF optics. The air path between the hot/cold load gives an estimated additional loss of about 2 dB.

Due to the high LO frequency the Rayleigh-Jeans limit is no longer applicable to calculate the noise temperature from a measurement of the Y-factor. We use the Planck law to calculate the effective temperatures of the hot and cold load according to:

$$T_{eff} = \frac{hf}{k_b \left[\exp\left(\frac{hf}{k_b T}\right) - 1 \right]} \quad (1)$$

with T the hot (295 K) or cold (77 K) load temperature.

5. RESULTS

In Table 2 we summarize the results of the measured noise temperatures. For all geometries 2 identical devices have been tested and are quoted in the table. The unpumped and a few pumped I-V curves and of one of the devices of geometry A and G are shown in Fig. 3 together with the receiver noise temperatures at different bias points. In all cases the region over which the noise temperature was minimal was reasonably broad, in agreement with other experiments [16]. We observe that cleaning the interface alone, as done for geometry D, reduces the sensitivity when compared to geometry A, in agreement with Ref. [14]. However, adding a thin layer of superconductor in combination with a cleaning of the interface, as for geometry G and H, strongly reduces

the receiver noise temperature. The improvement is more than a factor 2 between geometry A and G.

Improving the optics of our system, by removing 2 heat filters, using an anti-reflection coated elliptical lens and using a direct hot/cold load 10 cm from the cryostate window, reduces losses in the air and the optics with about 3 dB. Using this improved setup enabled us to measure with a device with geometry G a DSB receiver noise temperature of 1050 K at 2.5 THz. The mixer block temperature was 4.4 K in this case, this somewhat higher temperature is caused by the reduced heat filtering. The improvement of a factor 2 in noise temperature is consistent with a reduction of 3dB in the losses.

The LO power absorbed is estimated using the isothermal technique. The LO power absorbed for device A is in agreement with the values reported in Ref. [9] Geometry G needs a little bit more LO power, probably due to a little bit of diffusion cooling associated with a more transparent bolometer-contact interface.

After the measurements of the noise temperature we have started a measurement of the Gain bandwidth at 650 GHz. The first preliminary results indicate that device G has a bandwidth that is about 1.5 to 2 times larger than that of device A. Hence it seems that cleaning the interface not only improves the noise but also the bandwidth.

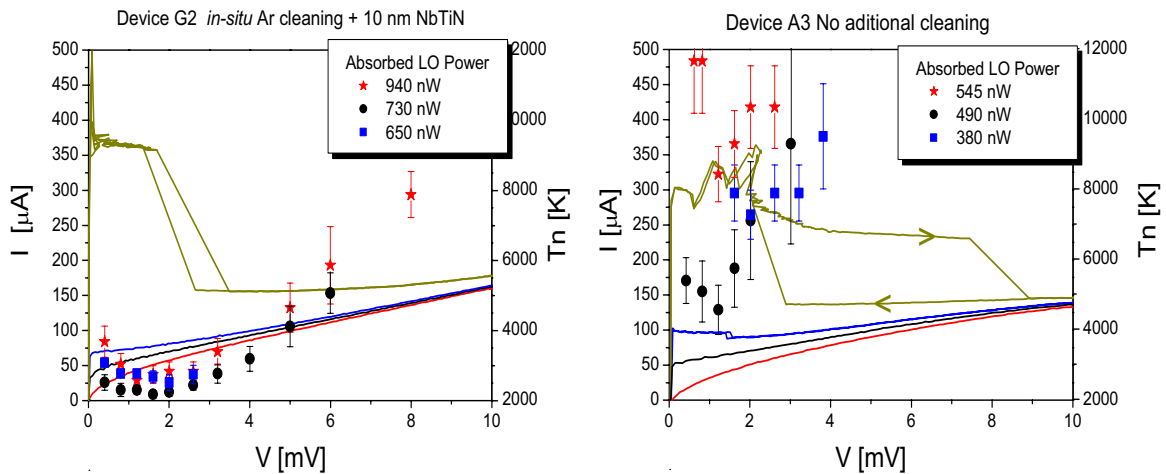


Fig 3. Unpumped and 3 pumped IV curves for 2 devices: G2 (left) with a clean NbN-contact pad interface and a contact pad consisting of 10 nm NbTiN + 40 nm Au. Right device A3 which did not receive any cleaning of the NbN film and a 65 nm Au contact pad. For the three pumped IV curves the noise temperatures are shown at different bias points.

6. CONCLUSIONS

We have studied the effect of the NbN-contact pad on the noise temperature of a NbN based phonon cooled HEBm. Cleaning the NbN - contact pad interface using Argon etching can improve the mixer noise temperature by a factor of 2 when compared to an identical device in which no interface cleaning was performed. However, to achieve this improvement an additional superconductor needs to be deposited on top of the NbN film underneath the contact pad to compensate the reduction of T_C associated with a stronger superconducting proximity effect due to the improved interface transparency. Using this strategy to fabricate a HEBm based on a 3.5 nm NbN film on a Si substrate we have achieved a DSB receiver noise temperature of 1050 K at 2.5 THz at a mixer block temperature of 4.4 K.

Acknowledgement: We would like to thank Willem Jan Vreeling for assistance, Pavel Yagoubov for assistance and the spiral antenna design and P. Khosropanah and H. Merkel for discussions at Chalmers. This work is supported partly by the European Space Agency (ESA) under Contract No. 11653/95/NL/PB

REFERENCES

- [1]: Herschel home Page at ESA:
<http://astro.estec.esa.nl/SA-general/Projects/First/first.html>
- [2]: SOFIA Home page: <http://sofia.arc.nasa.gov>
- [3]: TELIS home page: <http://telis.af.op.dlr.de/>
- [4]: B.D. Jackson, T.M. Klapwijk, "The current status of low-noise THz mixers based on SIS junctions". *Physica C* **327-276**, 368, 2002.
- [5]: E.M. Gershenzon, G.N. Gol'tsman, I.G. Gogidze, A.I. Eliantev, B.S. Karasik and A.D. Semenov, "Millimeter and submillimeter range mixer based on electron heating of superconducting films in the resistive state", *Sov. Phys. Superconductivity* **3**, 1582, 1990.
- [6]: C.-Y.E. Tong, J. Kawamura, T.R. Hunter, D.C. Papa, R. Blundell, M. Smith, F. Patt, G. Gol'tsman, E. Gershenzon, "Successful operation of a 1 THz NbN Hot-Electron bolometer receiver", *Eleventh int. symp. On Space THz. Techn. Ann Arbor, MI*, may1-2, 2000.
- [7]: D.E. Prober, "Superconducting terahertz mixer using a transition-edge microbolometer", *Appl. Phys. Lett.* **62**, 2119, 1993.
- [8]: J.R. Gao, P. Yagoubov, T.M. Klapwijk, P.A.J. de Korte, W.F.M. Ganzevles, and D. Wilms Floet, "Development of THz Nb diffusion-cooled hot electron bolometer mixers", *Millimeter and Submillimeter Detectors for Astronomy, Proceedings of SPIE, Vol. (2003), T.G. Phillips and J. Zmuidzinas editors*, 371-382, 2003.

- [9]: S. Cherednichenko, P. Khosropanah, E. Kollberg, M. Kroug, H. Merkel, "terahertz superconducting hot-electron bolometer mixers" *Physica C* 372-376, 407-415 (2002).
- [10]: P. Yagoubov, M. Kroug, H. Merkel, E. Kollberg, J. Schubert H.W. Huebers, S. Svechnikov, B. Voronov, G. Gol'tsman, and Z.Wang."Hot electron bolometer mixers based on NbN films deposited on MgO substrates", *Proc. Europ. Conf.on appl. Supercon. (EUCAS '99), Barcelona 14-17 september 1999*.
- [11]: M. Hajenius, J. J. A. Baselmans, J. R. Gao, T. M. Klapwijk, P. A. J. de Korte, "Current- Voltage and Resistance-Temperature Characteristics of Nb(Ti)N Phonon Cooled HEB Mixers With and Without Contact Resistance." *Fourteenth int. symp. On Space THz. Technol Tucson, Az, april 22-24, 2003*.
- [12]: A. D. Semenov, H.-W. Hübers, J. Schubert, G. N. Gol'tsman, A. I. Elantiev, B. M. Voronov, E. M. Gershenson, "Design and Performance of the Lattice-Cooled Hot-Electron Terahertz Mixer", *J. Appl. Phys.* **88**, 6758-6767, 2000.
- [13]: M. Kroug, S. Cherednichenko, M. Choumas, H. Merkel, E. Kollberg, H.W. Hübers, H. Richter, D. Loudkov, B. Voronov, G. Gol'tsman,"HEB Quasi-optical Heterodyne Receiver for THz Frequencies", *12th Int. Symp. On Space THz. Techn.*, 2001.
- [14]: S. Miki, Y. Uzawa, A. kawakami, Z. Wang,"IF Bandwidth and Noise Temperature Measurements of NbN HEB Mixers on MgO Substrates", *IEEE Trans. On Appl. Supercon.* **11** (1), 175, 2001.
- [15]: P. Khosropanah and H. Merkel, Private communication.
- [16]: P. Yagoubov, M. Kroug, H. Merkel, E. Kollberg, G. Gol'tsman, S. Svechnikov, E. Gershenson, "Noise temperature and local oscillator power requirement of NbN phonon-cooled hot electron bolometric mixers at terahertz frequencies", *Appl. Phys. Lett.* **73**, 2814, 1998.
- [17]: H.F. Merkel, P. Khosropanah, K. Sigfrid Yngvesson, S. Cherdinichenko, M. Kroug, A. Adam, E.L. Kollberg, "An active zone small signal model for hot electron Bolometric mixers", *12th Int. Symp. On Space THz. Techn.*, 2001.
- [18]: A.A. Golubov, "Proximity effect in dirty N/S multilayers", *Superconducting Superlattices and Microstructures*, I. Bozovic, ed., SPIE proc. 215 (SPIE, Bellingham, WA, 1994), p353.

Fabrication and Noise Measurement of NbTiN Hot Electron Bolometer Heterodyne Mixers at THz Frequencies

P. Khosropanah¹, S. Bedorf², S. Cherednichenko¹,
V. Drakinskiy¹, K. Jacobs², H. Merkel¹, E. Kollberg¹

¹ *Department of Microtechnology & Nanoscience,
Microwave Electronics Laboratory,
Chalmers University of Technology*

² *KOSMA, I. Physikalisches Institut, University of Cologne*

Abstract

The paper reports the latest development and the measured results of NbTiN hot electron bolometer mixers at THz frequencies. The devices are based on 4-7 nm thin NbTiN films, which were deposited by reactive magnetron sputtering of NbTi target in an Ar/N₂ atmosphere, on heated high-resistivity Si substrates over a 20 nm thick AlN buffer layer. The quality parameters of the film are transition temperature and normal-state resistivity, which were optimized by varying the sputtering parameters. The resistivity and the critical temperature of the films are about 400 $\mu\Omega\text{cm}$ and 9 K, respectively. Bolometers (4 μm wide and 0.7 μm long), integrated with logarithmic spiral antennas are fabricated. Mixer noise performance is tested in a quasi-optical receiver in 1.5-4 GHz IF band. The DSB receiver noise temperature of 700 K, 1100 K and 3000 K is obtained at 0.7, 1.6 and 2.6 THz LO frequencies, respectively.

1 Introduction

Currently superconducting hot electron bolometers (HEBs) are the most competitive devices for heterodyne detection in THz range [1]. Phonon-cooled NbN HEB mixer has become a relatively mature and reliable technology [2, 3]. It requires less than 1 μW of LO power [4] and offers about 1 K/GHz DSB receiver noise temperature up to 2.5 THz with 5-6 GHz IF bandwidth [5, 6, 7]. Noise measurements up to 5 THz

have been reported [8]. There are many active projects, which are planned to benefit from this technology in ground based (TREND [9], APEX [10]), airborne (SOFIA [11]) and spaceborne (Herschel [12]) observatories. HEB's noise performance above 2 THz will certainly improve with further development of THz antennas and waveguide techniques. Nevertheless, extension of the IF bandwidth and reduction of LO power requirements calls for new materials and approaches in HEB devices. Among others, NbAu bilayer HEBs [13], Ta HEBs [14] and 2-DEG semiconducting HEBs [15, 16] can be mentioned. Recently NbTiN thin films HEB mixers have been successfully fabricated and tested at 600 GHz and 800 GHz with DSB noise temperature of 270 K and 650 K at 1.5 GHz IF [17]. The gain roll-off frequency has been observed at 2.5 GHz (the film thickness was quoted to be 4 nm). Gain bandwidth measurements of NbTiN HEB mixers as a function of bias voltage can be also found in [18]. So far, Neither noise temperature nor noise bandwidth measurements at THz frequencies have been reported.

2 Device Fabrication

Bulk Niobium-titanium nitride (NbTiN) has a critical temperature of 16-17 K and a resistivity of around $90 \mu\Omega\text{cm}$ [19]. The properties of NbTiN show a strong dependence on the magnetron sputtering conditions and the film quality decreases as the film gets thinner. Thin (4-7 nm) NbTiN films are deposited on high resistive silicon substrate with 20 nm of AlN buffer layer, by DC reactive magnetron sputtering using a Nb_{78%}Ti_{22%} alloy sputtering-target (99.9% purity) in a mixture of Ar and N₂. The substrate was heated by a radiative heater below the substrate up to 400 °C during deposition. The typical sputtering conditions are listed in Table 1. The quality parameters of the film are transition temperature and normal-state resistivity, which were optimized by varying the sputtering parameters. Table 2 summarizes some of the parameters of four different films, which were chosen for fabrication of four batches of HEB devices. About 50 bolometers, integrated with different double slot and log

Parameters	Value
Base pressure	8.9×10^{-8} mbar
Gas flow rates	Ar 40 sccm N ₂ 10 sccm
DC power	300 W
Background pressure	0.63 Pa
Substrate temperature	400 °C
Deposition rate	0.5 nm/sec
Target-substrate distance	8 cm

Table 1: Typical sputtering condition for NbTiN film

Film ID	thickness (nm)	Deposition Temp. ($^{\circ}\text{C}$)	Critical Temp. (K)
CCN8-11	5-6	200	8
CCN8-1	6-7	375	7
CCN8-5	6-7	375	9
CCN8-15	4-5	400	10

Table 2: NbTiN films

periodic spiral antennas were fabricated in each batch. The fabrication is done by three consecutive electron beam lithography steps followed by metallization and lift off, where small contact pads, antenna and the large contact pads are patterned. 5 nm Ti followed by 80 nm of Au is deposited for small contact pads. The antenna and large pads are made from 5 nm of Ti and 200 nm Au. Then a resist mask is defined over the bolometer bridge by one more lithography step. This is to protect the NbTiN film in the bolometer bridge during the ion milling. In the last step the NbTiN is etched away using Ar ion milling from the whole wafer except the bolometer bridge and under the antenna and pads.

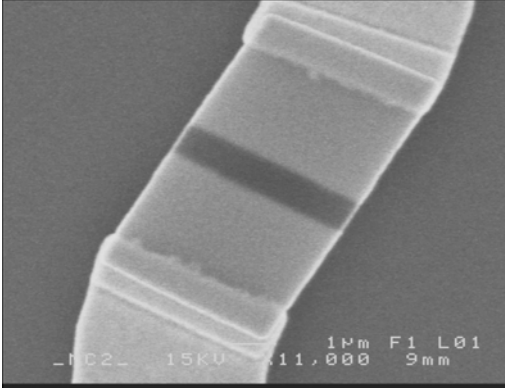


Figure 1: SEM picture of a $4\ \mu\text{m}$ wide $0.7\ \mu\text{m}$ long bolometer in the center of the spiral antenna.



Figure 2: SEM picture of a HEB integrated with a log periodic spiral antenna.

The scattering of the measured dc parameters (room temperature resistance and critical current) of devices within a batch is very small. This indicates that the film deposition have been quite homogeneous over the whole wafer. Four devices, one from each batch, have been singled out for RF measurement. All these bolometers are integrated with log periodic spiral antenna (Figure 1 and 2). Table 3 summarizes the room temperature resistance and the critical current of these devices.

Device ID	Film ID	Room Temp. Resistance (Ω)	Sheet Resistance (Ω/\square)	Critical Current (μA)
CCN8-1E	CCN8-11	310	1550	430
NbTiN1/1-5	CCN8-1	150	750	240
NbTiN2/1-9	CCN8-5	140	700	465
NbTiN3/2-17	CCN8-15	170	850	243

Table 3: NbTiN films

3 Noise measurement

The noise measurement setup is shown in Figure 3. The mixer chip is attached to the backside of a 12 mm diameter elliptical silicon lens, which is mounted on the cold plate of a liquid He cryostat (18 inch Infrared LabTM). The lens is coated with 28 μm Parylene, which acts as an anti-reflection coating optimized at 1.6 THz. Radiation comes through a 1.2 mm thick high-density polyethylene window. A 0.25 mm ZitexTM G108 filter is placed on the 4 K shield of the cryostat to block infrared radiation from entering the mixer. The local oscillator (LO) source for 0.7, 1.6 and 2.6 THz is a far infrared (FIR) laser. The LO and the RF beams are combined by a 12 μm thick Mylar beam splitter. The IF chain consists of an isolator and a 1.5-4 GHz low noise HEMT amplifier, which at 15 K temperature has about 2 K noise temperature in 2-4 GHz band and 5 K at 1.5 GHz. The IF signal is further amplified using two MiteqTM room temperature amplifiers and measured through a YIG-filter (30 MHz bandwidth) and a microwave power meter.

Figure 4 Shows the measured IV curves of device NbTiN2/1-9 as an example. Figure 5 has a closer look at the IV curve around the optimum operating point. The lowest receiver noise temperature was achieved at rather large area which was between 0.8-2.2 mV bias voltage and 40-56 μA bias current. This is due to the rather large length of the these devices (0.7 μm compared to 0.4 μm long NbN devices).

The so called Y -factor technique is used to determine the receiver noise temperature. Y is the ratio between the receiver output power when hot (room temperature 295 K) and cold (liquid Nitrogen temperature 77 K) black bodies are used as signal sources. The receiver noise temperature is calculated as:

$$T_{rec} = \frac{T_{CW}(295) - Y T_{CW}(77)}{Y - 1} \quad (1)$$

Here $T_{CW}(T)$ is the equivalent temperature of a black body at temperature T defined as [20]:

$$T_{CW}(T) = T \left[\frac{hf/k_B T}{e^{hf/k_B T} - 1} \right] + \frac{hf}{2k_B} \quad (2)$$

where h is the Planck constant, k_B is the Boltzmann constant, f is the RF frequency and T is the physical temperature.

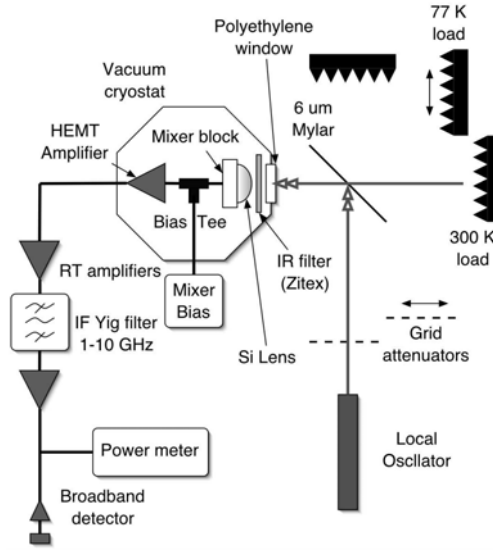


Figure 3: Noise measurement setup

Figure 6 shows the measured receiver noise temperature at 1.6 THz LO frequency versus IF frequency for all NbTiN mixers, mentioned above. As a comparison, a NbN mixer performance is also plotted. As one can see the NbTiN receiver noise temperature is almost the same as for NbN mixers at low IF frequency but the noise bandwidth is much smaller. Device (NbTiN3/2-17) was also measured at 0.7 and 2.6 THz LO frequencies (See Figure 7).

In our investigation we have used NbTiN films on AlN buffer layer (see §2). Gain bandwidth of NbTiN mixers on MgO buffer layer is discussed in [18]. The use of buffer layers for both NbTiN and NbN thin films has been reported in different papers. The superconducting critical temperature, transition width, normal state resistivity are observed to improve in these cases, compared to the films on bare substrates (Si, MgO, Quarts) [21, 22]. In HEB technology, T_c of superconducting films is not of that importance as for SIS mixers [23, 4]. Nevertheless, for ultra-thin films, where T_c is considerably lower than that for thick films or bulk material, a rise of 1-2 K for T_c can be quite important, since otherwise, it may not be possible to operate the mixers at 4.2 K (LHe) or 2 K (pumped LHe) temperature. Often, especially when substrate heating during film deposition is not available (or limited), the use of a buffer layer is the only way to obtain thin superconducting films with T_c above LHe temperature. There has been no report on NbTiN mixers without buffer layers. This is not the case for NbN HEB mixers. NbN HEB mixers with MgO buffer layers on both silicon and quartz substrates have been reported in [21, 22]. In both cases a deposition on 850 °C heated substrates was used. On quartz, the buffer layer results in an increase of the gain bandwidth by about 40 % (increase from 1.8 GHz to 2.5 GHz), while for silicon

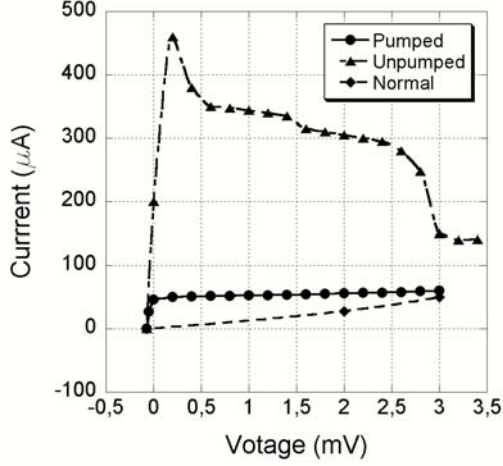


Figure 4: Unpumped, pumped and normal state IV curves of device No. NbTiN2/1-9.

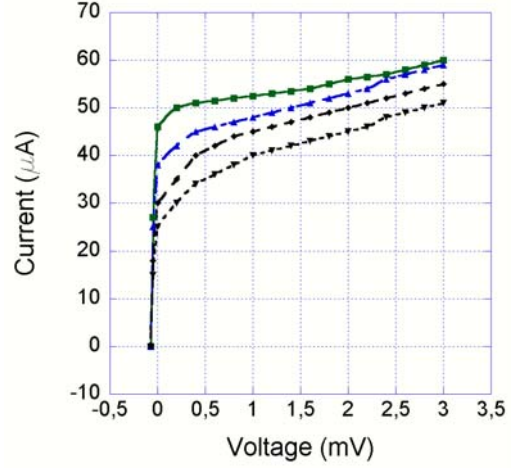


Figure 5: Pumped IV curves of device No. NbTiN2/1-9 around optimum operating point.

the gain bandwidth change is less (3.5-4 GHz to 4.7 GHz) and becomes comparable for NbN HEBs on bare MgO substrate. Earlier experiments have demonstrated that for 3-4 nm NbN films the electron temperature relaxation time (40 ps) is limited by the phonon escape time [2], while the electron-phonon interaction time is much less (10 ps at 10 K [24]). Similar investigation for NbTiN films has clearly shown that for thin NbTiN films on MgO buffer layer (silicon substrate) the phonon escape time remains a bottle-neck of the electron relaxation rate for temperatures above 10 K [18]. In NbN the electron-phonon interaction time is inversely proportional to electron temperature (i.e. $\tau_{e \rightarrow p} \propto T_e^{-1.6}$ [24]). So far, direct measurements of the electron-phonon time in NbTiN thin films has not been done.

In this paper we present noise bandwidth measurements of NbTiN HEB mixers. As it has been shown [25], the noise bandwidth for HEB mixers is larger than the gain bandwidth. The receiver output noise temperature is a sum of the Johnson noise, T_J (proportional to the electron temperature, and therefore to T_c), thermal fluctuation noise, $T_{FL}(f) = T_{FL}(0)/(1 + (f/f_0)^2)$ (proportional to the T_c^n , where n is close to 2, depending on the HEB model used [26, 27]), and IF amplifier input noise T_{IF} . Here, f and f_0 are the IF and the 3 dB gain roll-off frequencies, respectively.

$$T_{out}(f) = T_J + T_{FL}(f) + T_{IF} = T_J + \frac{T_{FL}(0)}{1 + (f/f_0)^2} + T_{IF} \quad (3)$$

The DSB receiver noise temperature (referred to the receiver input) is:

$$T_{rec}(f) = \frac{T_{out}(f)}{2G(f)} \quad (4)$$

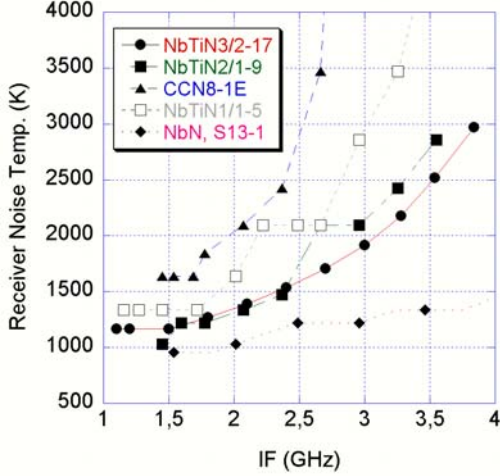


Figure 6: Measured receiver noise temperature vs. IF frequency at 1.6 THz LO frequency

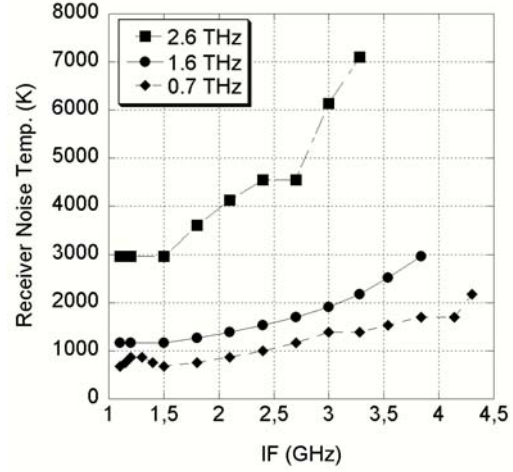


Figure 7: Measured receiver noise temperature vs. IF frequency at different LO frequencies using NbTiN3/2-17

where $G(f)$ is the SSB conversion gain. Since the gain dependence on the IF has a single pole Lorentzian shape, i.e. $G(f) = G(0)/(1 + (f/f_0)^2)$, then T_{rec} as a function of IF becomes:

$$T_{rec}(f) = T_{rec}(0) + \frac{(T_J + T_{IF})(f/f_0)^2}{2G(0)} \quad (5)$$

Finally, if the noise bandwidth f_N is defined as the IF where $T_{rec}(f_N) = 2 T_{rec}(0)$, then:

$$\frac{f_N}{f_0} = \sqrt{\frac{T_{out}(0)}{T_J + T_{IF}}} \quad (6)$$

The ratio between receiver output noise when mixer is in the superconducting state ($2T_{IF}$ is seen at the output) and in the operation point ($T_{out}(0)$ is seen at the output) is about 10 dB. From this together with the Y-factor measurement data, one can estimate that $T_{out}(0)$ is about 40 K. With $T_{out}(0) \approx 40$ K, $T_J \approx T_c = 8 - 9$ K and $T_{IF} \approx 2$ K, Equation (6) gives $f_N/f_0 \approx 2.2$. Experimentally, we obtained f_N to be 3-4 GHz for 0.7-2.6 THz LO frequency (see Fig 7). The reduction of HEB receiver noise bandwidth with LO frequency has been reported for NbN HEB mixers [28]. Taking the 2.5 GHz measured f_0 reported in [17], f_N/f_0 turns out to be about 1.2-1.6. Much smaller gain bandwidth for NbTiN HEB mixers on MgO buffer layer, 0.8 GHz at the optimal noise temperature bias point, was reported in [18]. Due to the observed dependence of the HEB mixers gain bandwidth on the deposition parameters and uncertainty of the film thickness (direct thickness measurements of the films 3-6 nm thick are very difficult), it becomes clear that to draw a conclusion

about the gain-to-noise bandwidth ratio for the NbTiN HEB mixers reported in this paper, independent gain bandwidth measurements are needed.

4 Summary and Conclusions

Four batches of NbTiN HEB devices have been fabricated based on 4-7 nm thick NbTiN film deposited on 20 nm AlN buffer layer on heated high resistive Si substrate, showing good reproducibility of the fabrication technique. The receiver noise temperature was measured 700, 1100 and 3000 K at 0.7, 1.6 and 2.6 THz LO frequencies respectively at 1.5 GHz IF using a NbTiN HEB mixer integrated with a broadband spiral antenna. The measured noise bandwidth was about 3-4 GHz. This results show that the noise of these NbTiN mixers are already comparable with our NbN mixers at low IF frequencies. However the IF bandwidth of NbN mixers is about 5-6 GHz, which is considerably higher than for NbTiN. One possible reasons for this difference is the thickness of the NbTiN film, which is about 4-5 nm compared to 3.5 nm for NbN. The thickness of the film is one of the key parameters, which determines the temperature relaxation time of the hot electrons in the bolometer and consequently the IF bandwidth [29]. The process for deposition of high quality (high critical temperature and low sheet resistance) and thinner (3-4 nm) NbTiN films has to be developed to improve the IF bandwidth. Nevertheless, comparison of the published data shows that AlN buffer layer results in larger gain bandwidth, that indicates better acoustic matching of NbTiN films to AlN than to MgO.

Acknowledgements

This work is initiated and funded by European Space Agency (ESA). The authors would like to thank Boris Voronov for the help with film thickness measurements.

References

- [1] E.M. Gershenzon, G.N. Gol'tsman, I.G. Gogidze, Y.P. Gusev, A.I. Elant'ev, B.S. Karasik, and A.D. Semenov. Millimeter and submillimeter range mixer based on electronic heating of superconducting films in the resistive state. *Sov. Phys. Superconductivity*, 3:1582, 1990.
- [2] S. Cherednichenko, P. Yagoubov, G. Ili'in, G. Goltsman, and E. Gershenzon. Large bandwidth of NbN phonon-cooled hot-electron bolometer mixers on sapphire substrate. In *proceedings of 8th International Symposium on Space Terahertz Technology*, pages 245–257, 1997.

- [3] M. Kroug, P. Ygoubov, G. Gol'tsman, and E. Kollberg. NbN quasi-optical phonon cooled hot electron bolometric mixers at THz frequencies. In *proceedings of 3rd European Conference on Applied Superconductivity*, page 405, 1997.
- [4] S. Cherednichenko, M. Kroug, H. Merkel, E. Kollberg, D. Loudkov, K. Smirnov, B. Voronov, G. Goltsman, and E. Gershenzon. Local oscillator power requirement and saturation effects in NbN HEB mixers. In *proceedings of 12th International Symposium on Space Terahertz Technology*, pages 273–285, 2001.
- [5] M. Kroug, S. Cherednichenko, H. Merkel, E. Kollberg, B. Voronov, G. Gol'tsman, H.W. Huebers, and H. Richter. NbN hot electron bolometric mixers for terahertz receivers. *IEEE Transactions on Applied Superconductivity*, 11(1):962–5, 2001.
- [6] S. Cherednichenko, P. Khosropanah, E. Kollberg, M. Kroug, and H. Merkel. Terahertz superconducting hot-electron bolometer mixers. *Physica C*, 372-376:407–415, 2002.
- [7] S. Cherednichenko, M. Kroug, P. Khosropanah, A. Adam, H. Merkel, E. Kollberg, D. Loudkov, B. Voronov, G. Goltsman, H. Richter, and H.-W. Hubers. A broadband terahertz heterodyne receiver with an NbN mixer. In *proceedings of 13th International Symposium on Space Terahertz Technology*, pages 85–94, 2002.
- [8] A.D. Semenov, H.-W. Hubers, J. Schubert, G.N. Gol'tsman, A.I. Elantiev, B.M. Voronov, and E.M. Gershenzon. Design and performance of the lattice-cooled hot-electron terahertz mixer. *Journal of Applied Physics*, 88(11):6758–67, 2000.
- [9] K. S. Yngvesson, C. F. Musante, Rodriguez F. Ji, M., Y. Zhuang, E. Gerecht, M. Coulombe, J. Dickinson, T. Goyette, J. Waldman, C. K. Walker, A. A. Stark, and A. P. Lane. Terahertz Receiver with NbN HEB Device (TREND)-a low-noise receiver user instrument for AST/RO at the south pole. In *proceedings of 12th International Symposium on Space Terahertz Technology, San Diego*, pages 262–285, 2001.
- [10] APEX: Atacama Pathfinder Experiment
<http://www.mpifr-bonn.mpg.de/div/mm/apex.html>.
- [11] H.-W. Huebers, A. Semenov, J. Schtibert, G. Gol'tsman, B. Voronov, E. Gershenzon, A. Krabbe, and H.P. Roser. NbN hot electron bolometer as THz mixer for SOFIA. In *Airborne Telescope Systems, 27-28 March 2000*, volume 4014 of *Proceedings of SPIE - The International Society for Optical Engineering*, pages 195–202, Munich, Ger, 2000.
- [12] Th. de Graauw and F.P. Helmich. Herschel-hifi: "the heterodyne instrument for the far-infrared". In *proceedings of Symposium "The Promise of the Herschel Space Observatory"*, Toledo, Spain, December 2000.

- [13] X. Lefoul, P. Yagoubov, M. Hajenius, W.J. Vreeling, W.F.M. Ganzevles, J.R. Gao, P.A.J. de Korte, and T.M. Klapwijk. Dc and if bandwidth measurements of superconducting diffusion-cooled hot electron bolometer mixers based on Nb/Au bilayer. In *proceedings of 13th International Symposium on Space Terahertz Technology*, pages 369–372, 2002.
- [14] A. Skalare, W. McGrath, B. Bumble, and H.J. LeDuc. Tantalum hot-electron bolometers for low noise heterodyne receivers. In *proceedings of 13th International Symposium on Space Terahertz Technology*, pages 245–248, 2002.
- [15] K.S. Yngvesson. Ultrafast two-dimensional electron gas detector and mixer for terahertz radiation. *Applied Physics Letters*, 76(6):777–9, 2000.
- [16] M. Lee, L.N. Pfeiffer, K.W. West, and K.W. Baldwin. Wide bandwidth millimeter wave mixer using a diffusion cooled two-dimensional electron gas. *Applied Physics Letters*, 78(19):2888–90, 2001.
- [17] C.E. Tong, J. Stern, K. Megerian, H. LeDuc, T.K. Sridharan, H. Gibson, and R. Blundell. A low-noise NbTiN hot electron bolometer mixer. In *proceedings of 12th International Symposium on Space Terahertz Technology*, pages 253–261, 2001.
- [18] G. Goltsman, M. Finkel, Y. Vachtomin, S. Antipov, V. Drakinskiy, N. Kaurova, and B. Voronov. Gain bandwidth and noise temperature of NbTiN HEB mixer. In *This proceedings: proceedings of 14th International Symposium on Space Terahertz Technology*, 2003.
- [19] N.N. Iosad, B.D. Jackson, T.M. Klapwijk, S.N. Polyakov, P.N. Dmitirev, and J.R. Gao. Optimization of RF- and DC-sputtered NbTiN films for integration with Nb-based SIS junctions. *IEEE Transactions on Applied Superconductivity*, 9(2):1716–19, 1999.
- [20] A.R. Kerr. Suggestions for revised definitions of noise quantities, including quantum effects. *IEEE Transactions on Microwave Theory and Techniques*, 47(3):325–9, 1999.
- [21] D. Meledin, C.E. Tong, R. Blundell, N. Kaurova, K. Smirnov, B. Voronov, and G. Gol'tsman. The sensitivity and the IF bandwidth of NbN hot electron bolometer mixer on MgO buffer layer over crystalline quartz. In *proceedings of 13th International Symposium on Space Terahertz Technology*, pages 65–72, 2002.
- [22] Y.B. Vachtomin, M.I. Finkel, S.V. Antipov, B.M. Voronov, K.V. Smirnov, N.S. Kaurova, V.N. Drakinski, and G.N. Gol'tsman. Gain bandwidth of phonon-cooled HEB mixer made of NbN thin film with MgO buffer layer on Si. In *proceedings of 13th International Symposium on Space Terahertz Technology*, pages 259–270, 2002.

- [23] J. Kawamura, Jian Chen, D. Miller, J. Kooi, J. Zmuidzinis, B. Bumble, H.G. LeDuc, and J.A. Stern. Low-noise submillimeter-wave NbTiN superconducting tunnel junction mixers. *Applied Physics Letters*, 75(25):4013–15, 1999.
- [24] Yu.P. Gousev, G.N. Gol'tsman, A.D. Semenov, E.M. Gershenson, R.S. Nebosis, M.A. Heusinger, and K.F. Renk. Broadband ultrafast superconducting NbN detector for electromagnetic radiation. *Journal of Applied Physics*, 75(7):3695–7, 1994.
- [25] H. Ekstrom, E. Kollberg, P. Yagoubov, G. Gol'tsman, E. Gershenson, and S. Yngvesson. Gain and noise bandwidth of nbn hot-electron bolometric mixers. *Applied Physics Letters*, 70(24):3296–3298, 1997.
- [26] B.S. Karasik and A.I. Elantiev. Noise temperature limit of a superconducting hot-electron bolometer mixer. *Applied Physics Letters*, 68(6):853–855, 1996.
- [27] P. Khosropanah, H. Merkel, S. Cherednichenko, J. Baubert, T. Ottoson, and E. Kollerg. NbTiN and NbN hot electron bolometer, a comparison. In *This proceedings: proceedings of 14th International Symposium on Space Terahertz Technology*, 2003.
- [28] S. Cherednichenko, M. Kroug, H. Merkel, P. Khosropanah, A. Adam, E. Kollberg, D. Loudkov, G. Gol'tsman, B. Voronov, H. Richter, and H.-W. Huebers. 1.6 THz heterodyne receiver for the far infrared space telescope. *Physica C*, 372-376:427–31, 2002.
- [29] S. Cherednichenko, P. Ygoubov, K. Il'in, G. Goltsman, and E. Gershenson. Large bandwidth of NbN phonon-cooled hot-electron bolometer mixers on sapphire substrate. In *proceedings of 8th International Symposium on Space Terahertz Technology*, pages 245–257, 1997.

Comparison of the Noise Performance of NbTiN and NbN Hot Electron Bolometer heterodyne mixers at THz Frequencies

Harald F. Merkel, Pourya Khosropanah, Sergey Cherednichenko, Erik Kollberg

Microelectronics Department, Microwave Electronics Laboratory, Chalmers University of Technology

Recently experimental data for the noise temperature of hot electron bolometers (HEB) based on NbTiN/AlN on high resistive Si have been obtained at 1.6THz. The noise, gain and IF bandwidth performance is compared to measured and extrapolated data for HEB on NbN thin films on Si with comparable device volume. In both cases, a hot spot model including Andreev reflection at the hot spot ends is applied. This yields IV curves, gain, noise and the IF bandwidth. These data are then compared with measurements. The parameters for NbTiN for a best fit to the experiments indicate a larger role of diffusion cooling ($0.55 \text{ cm}^2/\text{s}$ compared to $0.45 \text{ cm}^2/\text{s}$ for NbN) at about the same electron-phonon interaction time (50ps compared to 40ps for a 35 \AA thick film). Due to the lower resistivity of NbTiN (a $4 \mu\text{m} \times 0.4 \mu\text{m} \times 35 \text{ \AA}$ NbTiN device has 60Ω compared to 120Ω in NbN), antenna matching requires that the optimum device length in terms of receiver noise performance is located at $4 \mu\text{m} \times 0.75 \mu\text{m}$ (for a $60 \text{ \AA} \dots 70 \text{ \AA}$ thick film) compared to a $4 \mu\text{m} \times 0.4 \mu\text{m}$ (for a 35 \AA thick film). This increase in length results in an enlarged bias region where the device shows optimum noise properties (from 0.5 mV to 2 mV compared to 0.5 mV to 1 mV in shorter devices). The expected noise temperatures are about equal for NbTiN and NbN (500 K receiver noise at 1.6 T), measurements indicate 800 K for NbN and 1200 K for NbTiN. The gain figures indicate -12 dB for NbTiN compared to -11 dB for NbN, measurements yield -18 dB for NbTiN and -12 dB for NbN. This discrepancy may be explained by the presence of a AlN buffer layer detuning the antenna and therefore destroying the antenna pattern increasing the coupling loss between the laser and the mixer. Extrapolating the device resistances to zero device length indicates a residual resistance of 25Ω in most NbN devices. This increases the effective device length by 10% (corresponding to a current transfer zone under the antenna pads of 40 nm). This effect seems more pronounced in NbTiN since the measured film resistance indicates a 50% reduction of the sheet resistance compare with

NbN. The actual measured device resistance for a 60Å NbTiN yields a sheet resistance which is identical to NbN at 30Å. Therefore the contact resistance may be up to 100Ω indicating a 400nm increase of the effective element volume. The measured IF roll-off frequency is 3GHz for a 65Å thick NbTiN film. This compares to 4.5GHz for a 35Å NbN (extrapolated to 2.5GHz at 65Å thickness) indicating that NbTiN may be intrinsically somewhat faster than NbN in line with initial expectations. Obviously more work has to be done for NbTiN devices to yield the same performance level as NbN devices. NbTiN HEB are located in the crossover region between phonon and diffusion cooling.

SUPERCONDUCTING HOT-ELECTRON BOLOMETER MIXER FOR TERAHERTZ HETERODYNE RECEIVERS

Alexei D. Semenov^a, Heinz-Wilhelm Hübers^a, Heiko Richter^a, Konstantin Smirnov^c,
Gregory N. Gol'tsman^c, Natalia Kaurova^c, Boris M. Voronov^c

^a DLR Institute of Space Sensor Technology and Planetary Exploration, 12489 Berlin,
Germany

^c Moscow State Pedagogical University, 119891 Moscow, Russia

A number of on-going astronomical and atmospheric research programs are aimed to the Terahertz (THz) spectral region. At frequencies above about 1.4 THz heterodyne receivers planned for these missions will use superconducting hot-electron bolometers as a mixers. We present recent results of the terahertz antenna development of superconducting NbN hot-electron bolometer mixer for GREAT (German Receiver for Astronomy at Terahertz Frequencies, to be used aboard of SOFIA) and TELIS (Terahertz Limb Sounder). The mixer is incorporated into hybrid antenna consisting of a planar feed antenna, which has either logarithmic spiral or double-slot configuration, and hyper hemispherical silicon lens. The hybrid antenna showed almost frequency independent and symmetric radiation pattern with the beam-width slightly broader than expected for diffraction limited antenna. The noise temperature as well as its spectral dependence changes with the bolometer sizes that provides additional tool for mixer optimization. FTS spectra measured in the direct detection regime agreed with the noise temperature spectra.

Mixer and Antenna Design

Hot-electron bolometers (HEBs) were manufactured from a superconducting NbN film with a nominal thickness of about 3 nm. The film was deposited by dc reactive magnetron sputtering on a 350- μ m thick Si substrate. The HEB was incorporated in a planar feed antenna patterned from a 200 nm thick gold film. The bolometer had an area of one tenth of a square, i.e. the width amounted ten times the length. Given the normal sheet resistance ≈ 600 Ohm at the transition temperature of the NbN film, the resistance of the bolometer just above the superconducting transition should be 60 ± 6 Ohm as determined by the accuracy of the manufacturing process. However, the contact resistance between the HEB and the inner terminals of the antenna affected the actual device resistance. The contact resistance varied depending on the contact area and contact quality. Two types of feed antenna have been studied: self-complementary

logarithmic-spiral and twin-slot. We tested three logarithmic-spiral antennas with different sizes of the inner terminals and double-slot antennas optimized for several frequencies in the range from 1.5 THz to 3 THz. Antenna parameters are depicted in Fig.1 and specified in the Table. The substrate carrying the HEB and the feed was glued with its backside onto the flat optically polished side of an extended hemispherical 12 mm diameter silicon lens. The 3.5 mm extension of the lens together with the substrate thickness positioned the feed in the second elliptical focus [1]. The lens had a Parylene antireflection coating optimized for 2.5 THz [2]. The lens with the HEB was mounted in an Infrared Labs helium dewar with a wedged TPX vacuum window and a cold (77 K) quartz filter.

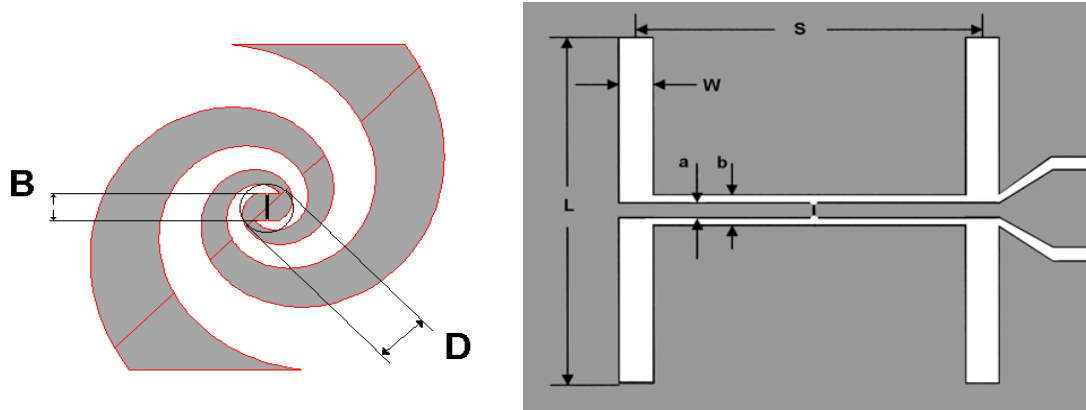


Fig. 1 Planar log-spiral (left) and twin-slot (right) antennas. Gold is shown gray. Black rectangle in the geometric center of the antenna depicts the bolometer. For log-spiral feeds: D is the diameter of the circle that demarcates the spiral structure of the feed from the contact pad area; B is the largest bolometer width that the feed may have embedded.

Table. Sizes in micrometers of studied log-spiral and twin-slot planar feeds.

Log-spiral feed			Twin-slot feed					
Antenna type	B	D	Antenna type	L	S	W	a	b
Sp_a	4	14	TW1	62	32	4	2	4
Sp_b	2.4	8	TW2	40	21	2.2	2.2	3.3
Sp_c	1.5	3.5	TW3	33.6	20	2.6	2	4
			TW4	46	24	3	2.2	3.3
			TW5	33.6	17.5	2.4	2	3

Experimental arrangement

The intermediate frequency (IF) signal was guided out of the mixer via the 50- Ω coplanar line. A circulator was used to feed the bias to the mixer and to transmit the IF signal to a low noise HEMT amplifier, which had either 1–2 GHz or 4–8 GHz bandwidth. The IF signal was filtered by an electrically tunable filter with a bandwidth of 75 MHz, further amplified and rectified with a microwave crystal detector. An optically pumped FIR laser providing lines at frequencies 0.69, 1.63, 2.53, 3.1 and 4.2 THz was used as a local oscillator (LO). Signal radiation and LO radiation were superimposed by a 6 μm thick Mylar beam splitter. The double sideband (DSB) noise temperature of the receiver was measured by the Y-factor method. Hot and cold loads (Eccosorb) at 293 K and 77 K alternatively covered the receiver beam. Output signal, that is the dc voltage at the crystal detector, was continuously readout by a computer, which performed statistical analysis of the signal and computed the noise temperature. The beam pattern of the hybrid antenna was measured at two LO frequencies, 1.6 THz and 2.5 THz, by moving a hot, point-like source in the far field of the receiver. The output heterodyne signal was registered as a function of the position of the source. FTS measurements were performed in the direct detection regime with the mixer kept at the middle of the superconducting transition. We used a simple cube interferometer with a 12-mm thick Mylar beam splitter and a mercury discharge lamp as radiation source. The mirror was moved with a step motor. Typically, ten or more computed spectra were accumulated and averaged in order to increase the sensitivity.

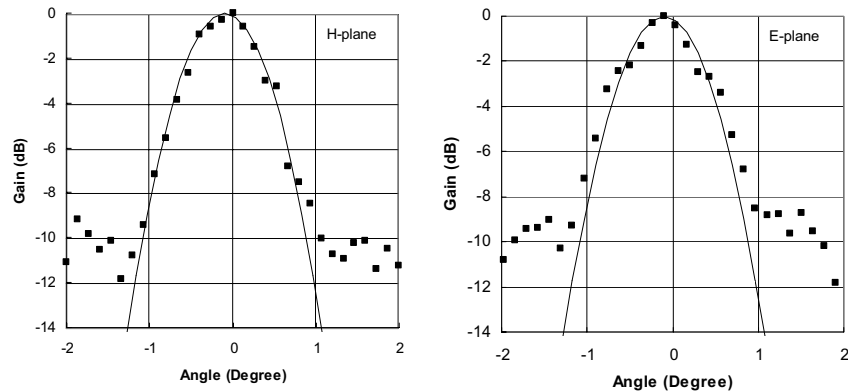


Fig. 2. Beam profile of the twin-slot antenna TW2 at 1.6 THz in the H- (left panel) and E- (right panel) planes. Solid lines show the Gaussian fit with the 3-dB width of 1.1° .

Antenna beam pattern

At 1.6 THz we found for the twin-slot feed antenna a 3-dB beam width of 1.1° in both E- and H-planes. The pattern was fairly symmetric (Fig. 2) with the side lobes appearing slightly below -10 dB. The log-spiral feed had at this frequency the same side

lobe level and also showed symmetric beam pattern (Fig. 4). The polarization of the antenna was elliptical with the middle value 1.3° of the 3-dB beam width. There was a 15% difference between the beam width in two main elliptical planes, indicating that at this frequency the twin-slot feed is probably the better choice than logarithmic-spiral. However, this changes at higher frequencies where the required dimensions of the twin-slot antenna become comparable to the size of the IF embedding circuitry. This brings parasitic impedances and destroys coupling [3] between the feed and the embedding circuitry.

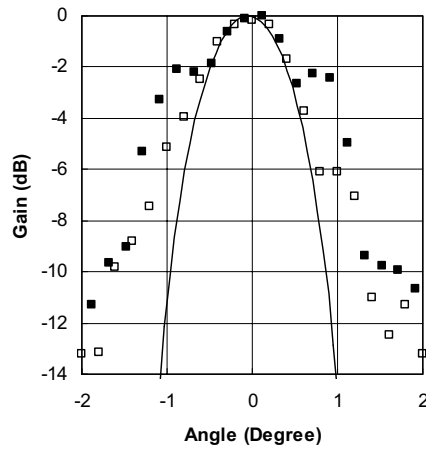


Fig. 3. Beam profile of the twin-slot antenna TW3 at 2.5 THz in the H-plane (filled symbols) and in the E-plane (open symbols). Solid line presents the Gaussian fit to the main lobe with the 1.5° beam width at -3 dB.

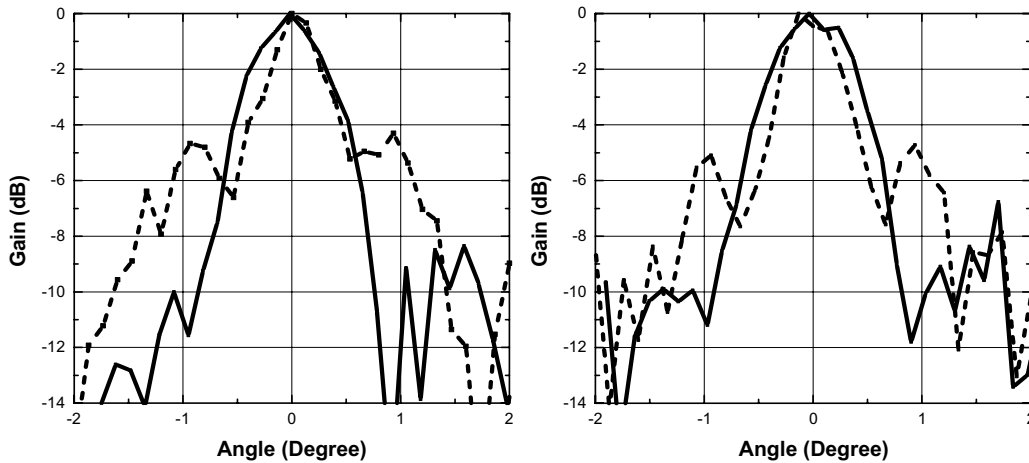


Fig. 4. Beam profile of the log-spiral antenna Sp_b at 1.6 THz (solid line) and 2.5 THz (dotted line) in main elliptical planes.

At 2.5 THz, we found (Fig. 3) higher side lobes (-3 dB) and wider beam pattern (1.5°) for the twin-slot feed. The log-spiral feed had at this frequency (Fig. 4) an almost symmetric circular polarized beam with a 3-dB width of 0.8° and side-lobes at -5 dB.

Spectral properties: Noise temperature

Generally, the noise temperature of a HEB mixer imbedded in the planar feed increases with frequency. That might be a manifestation of the detection mechanism [1] as well as the electrodynamics of the feed or optical coupling. We made an attempt to separate the contribution of the feed and the HEB geometry in that we measured the noise temperature as function of frequency for several identical feeds having bolometers with different planar dimensions. The length and the width of the bolometer were both changed proportionally in order to keep the number of squares and the impedance of the bolometer unchanged. Data shown in Fig. 5 suggest that the noise temperature grows faster for bolometers with larger width. This result seems to be a natural consequence of the skin effect in the bolometer. Indeed, the skin depth in our NbN films [1] is $\approx 0.57 \mu\text{m}$ at 2.5 THz that is noticeably smaller than the bolometer width.

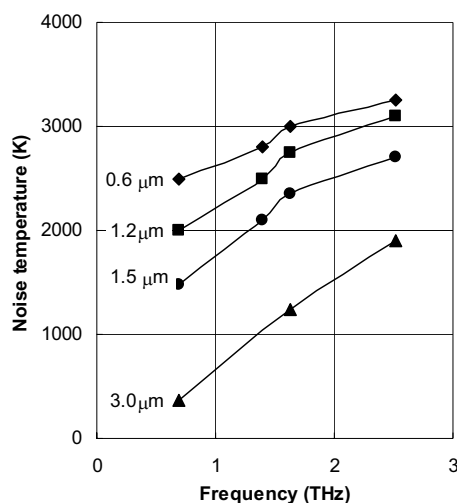


Fig. 5 Noise temperature for several bolometers with different width (shown in the plot) embedded in the log-spiral feed of the type Sp_a.

Although the noise temperature at a particular frequency tends to increase when the bolometer width decreases, this trend can be hardly treated numerically. Because of a very large spread of the noise temperatures between batches of identical mixers, the error bar would be larger than the expected variations. The reason for that is most likely poorly

controllable contact resistance between the bolometer and the inner terminals of the feed. The best noise temperatures at 2.53 THz (1.5 GHz intermediate frequency) were 1600 K for Sp_a with 3 mm bolometer width, 2200 K for Sp_b with 1.3 mm bolometer width, and 2600 K for Sp_c with 1.5 mm bolometer width. We shall note here that the power of the local oscillator required for optimal (lowest noise temperature) operation increases in proportion to the bolometer volume. We have directly measured the 2.5 μ W LO power in front of the cryostat window at the optimal operation of a 1.6- μ m wide bolometer imbedded in the Sp_b feed. Expected power for a 3- μ m wide bolometer is four times larger that might be crucial for applications relying on solid state LO sources.

The frequency dependence of the noise temperature for log-spiral feeds Sp_a and Sp_c is shown in Fig. 6. Typically, the feed Sp_a, which is capable to carry a larger bolometer, shows smaller noise temperature at any particular frequency. In order to compare electrodynamics of feeds and possibly avoid the effect of contact resistance, we used two different feeds with identical bolometers having the dimensions 1.5 x 0.15 μ m². The feed Sp_c with the spiral structure going down to a smaller radius (see Fig. 1 and Table) better performs at higher frequencies. According to [4], the upper cut-off frequency of a log-spiral feed should be (c is the speed of light and ϵ is the dielectric constant of the substrate)

$$v_0 = \frac{c}{5D\sqrt{(1+\epsilon)/2}} \quad (1)$$

For our Sp_a feed antenna $v_0 \approx 1.6$ THz that agrees within the accuracy of the cut-off definition with the data presented in Fig. 6. Following the same criteria, one should expect for Sp_c the cut-of at 6 THz.

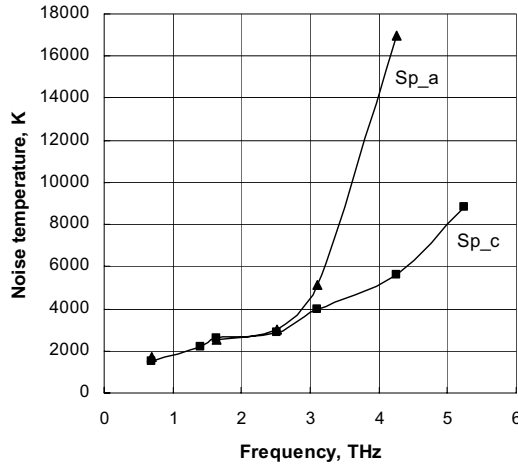


Fig. 6 Noise temperature of the log-spiral feeds Sp_a (triangles) and Sp_c (squares) with identical bolometers.

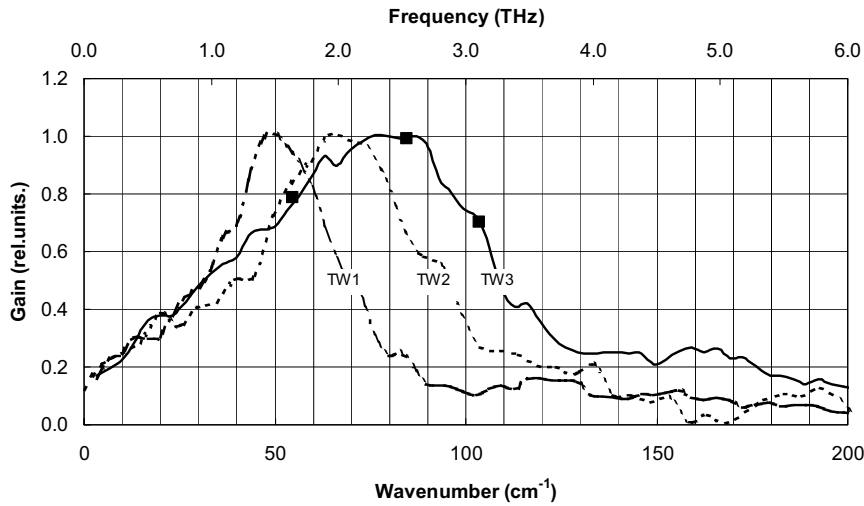


Fig. 7. Normalized to maximum FTS spectra of three twin-slot feeds. Dimensions are presented in the Table. Black squares show normalized noise temperature measured with the same TW3 feed.

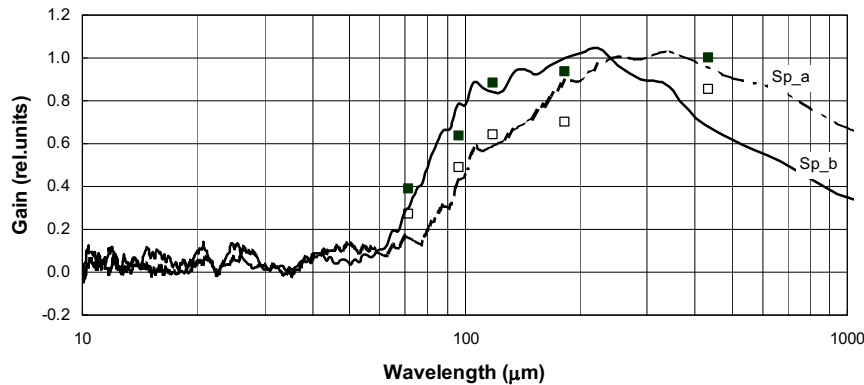


Fig. 8. Normalized to maximum FTS spectra of two log-spiral feeds (solid line Sp_b, dotted line Sp_a) and measured noise temperatures (closed symbols Sp_b, open symbols Sp_a).

Spectral properties: Fourier transform spectroscopy

FTS spectra of few twin-slot feeds are shown in Fig. 7. For all three, noise temperatures measured at available LO frequencies correspond well to the obtained FTS spectra. Black squares illustrate that for the TW3 feed. Our data shows, in agreement with [3], that the common design rule [5] $L = 1.95 \cdot S$ and $L = 0.33 \cdot \lambda_0$ does not properly

work at frequencies above 2 THz. In order to realize the required resonance frequency, the slot length and separation should decrease in excess to the wavelength.

Fig. 8 shows FTS spectra of log-spiral feeds. For this antenna type we also found reasonably good agreement between spectra and measured noise temperature. There is although a contradiction with common understanding of how the cut-off frequency should vary with the feed size. According to (1), the ratio of the smallest spiral diameters D (see Fig. 1 and the Table) dictates the cut-off frequency of the Sp_b almost twice as large as the cut-off frequency of the Sp_a . In fact we have found much smaller increase of the cut-off frequency.

In conclusion, we have studied spectral properties and beam pattern of log-spiral and twin-slot feeds at terahertz frequencies and found feed sizes resulting in reasonably good performance. Comparison of two types of fed antenna suggests that at frequencies above 2 THz the spiral feed, although it has not very practical elliptical polarization, provides better overall performance.

Acknowledgement

The work was partly supported by INTAS, K.S. acknowledges support through personal grant YSF 2002-408 by INTAS.

References

1. A.D. Semenov, H.-W. Hübers, J. Schubert, G.N. Gol'tsman, A.I. Elant'ev, B.M. Voronov, and E.M. Gershenson, *Design and performance of the lattice-cooled hot-electron terahertz mixer*, J. Appl. Phys **88**, 6758 (2000).
2. H.-W. Hübers, J. Schubert, A. Krabbe, M. Birk, G. Wagner, A. Semenov, G. Gol'tsman, B. Voronov, and E. Gershenson, *Parylene antireflection coating of a quasi-optical hot-electron-bolometric mixer at terahertz frequencies*, Infrared Physics & Technology **42**, 41(2001).
3. R.A. Wyss, A. Neto, W.R. McGrath, B. Bumble, H. LeDuc, Submillimeter-wave spectral response of twin-slot antennas coupled to hot electron bolometers, Proceedings of the 11th Int. Symposium on Space Terahertz Technology, Uni. Of Michigan, Ann Arbor, MI, May 2000, pp. 388-397.
4. J.D. Dyson, The equiangular spiral antenna, IRE Transactions on Antennas and Propagation **AP-7**, 181(1959).
5. W. Ganzevles, A quasi-optical THz mixer based on a Nb diffusion-cooled hot-electron bolometer, Ph. D. thesis, Delft University of Technology, 2001.

Sideband-Separating SIS Mixer For ALMA Band 7, 275-370 GHz

Stéphane Claude *

Institut de Radio Astronomie Millimetrique
300 Rue de la Piscine
38406 Saint Martin d'Herès
France

*Now at the National Research Council of Canada, 5071 West Saanich road, Victoria V8Y, B.C. Canada

Abstract

Following the design for a sideband-separating mixer using a quadrature waveguide hybrid and an in-phase waveguide power divider and SIS mixer chips [1] experimental results of a dual side-band separating SIS mixer (2SB) for Band 7, i.e. 275-370 GHz are presented. This mixer uses DSB mixer units that can be tested separately prior to the 2SB operation. Image rejection over the full Band 7 is better than -10 dB. The results are encouraging at a prototype level and some more qualifications tests remain to be done before the full production of the 128 + spare units. The design is suitable for scaling at any other frequencies below Band 7.

1. Introduction

One of the ALMA frontend requirements is to produce fixed-tuned single-sideband receivers with an image rejection better than -10 dB. In the case of a 2SB mixer, the IF bandwidth must cover 4 GHz per sideband. The SSB noise temperature specification is 133K for the 275-370 GHz band and 198 K over a maximum of 20% of the band. One of the method to reject the image is to use quadrature hybrid couplers in such a way that the Upper Side Band (USB) and the Lower Side Band (LSB) are simultaneously separated, as described in [1]. Design and experimental results are presented here for Band 7.

2. Concept

As described on Fig. 1 a sideband separating mixer consists of one quadrature hybrid coupler that will split the RF signal detected by the telescope in two and introduces a 90 deg phase difference between its outputs. The Local Oscillator (LO) is split in two with an in-phase power divider. At this point the LO and RF inputs are interchangeable. The LO and RF are combined through a -16 dB coupler before being coupled to the SIS mixer. The IF signals of both mixers are recombined through a quadrature hybrid where the 90 deg phase difference will separate the USB and LSB.

Having in mind the goal of producing front ends for 64 antennas, the design of 128 2SB mixers must be simple to machine, assemble and test. Therefore an E-plane split block technique is used to produce, in the same part, the quadrature hybrid, the in-phase power divider and the two -16 dB couplers. The mixers were chosen to be separate from the coupler in order to test them prior to the 2SB integration. And finally, the IF

signals are recombined with a commercial quadrature hybrid before amplification.

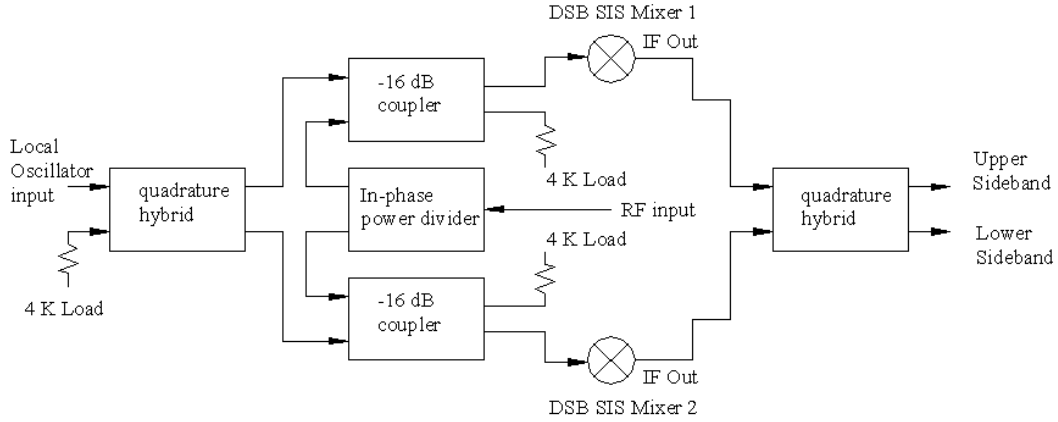


Fig. 1. Sideband-separating mixer.

As discussed by Kerr and Pan [2], the phase and amplitude imbalance is not very critical if image rejections better than -10 dB are to be obtained. For example, a 3dB amplitude imbalance and 30deg phase imbalance would lead to -10dB image rejection. However, the system must be kept symmetrical, in particular for the waveguides and the IF connections before the quadrature hybrid. Similar mixers input mismatch and gain are important too.

3. Design of the components

a. Waveguide quadrature hybrid

Hybrid couplers have been designed and manufactured for ALMA band 7 (275-370 GHz) and a scale model at 195-260 GHz has been fully characterized with the IRAM Vector Network Analyzer (VNA) [3] and [4].

A hybrid coupler is a 3dB power splitter with 90 deg phase shift between the two outputs. The two waveguides are coupled through the broad walls and are separated by shunt guides $\lambda_g/4$ long. There is a minimum of two shunt waveguides, separated by $\lambda_g/4$, producing a narrow band device, and the bandwidth can be increased with the number of shunts (see Fig 2). However, for keeping the same 3dB coupling the width of the slots has to be decreased if the number of slots is increased. Dimensions of a quadrature hybrid at mm wavelength are quite critical particularly for a series production of 128. Simulations have been carried out with CST Microwave Studio (CST MWS) [5] in order to optimize the slot width and number, and the separation between the waveguides. It was found that a good trade off to produce 3dB coupling over the ALMA band 7 while having slots that can be realistically made in series is to have 5 shunts 0.133 mm wide, 0.350mm apart. Each half of the split mixer blocks contains square waveguides 0.38x0.38 mm that are separated by a 0.20 mm wall.

The scale model has 5 shunts 0.189 mm wide, 0.497 mm apart. The 0.545 mm square waveguide in each block are separated by a 0.279 mm wall. Table 1 gives a summary of the coupler's dimensions.

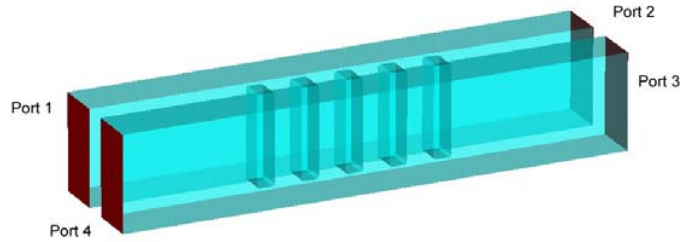


Fig 2 View of the hybrid coupler

Frequency band	Waveguide size (mm)	Slot width (mm)	Slot pitch (mm)	Waveguide pitch (mm)
195-260GHz	1.090x0.545	0.189	0.497	0.824
275-370GHz	0.760x0.380	0.133	0.350	0.580

Table 1 Dimensions of the 3dB coupler

The blocks were machined with CN milling machine at IRAM, except for the 5 slots. Since the 5 slots for the 320 GHz coupler cannot be easily machined the technique of spark erosion was used. In order to reduce sparking in the bottom of the main waveguides, there is 0.02mm step between the bottom of the slots and the bottom of the main waveguides. Fig 2 shows a 3D drawing of the coupler.

Amplitude measurement

The amplitude measurements made with the IRAM VNA at 195-260GHz fit nicely the simulation done with CST MWS (Fig. 3). These measurements were done by injecting a signal through port 1, and the detection was done at port 2 and 3 for amplitude imbalance. The isolation was measured between port 1 and 4. Input reflection coefficient S11 is better than -20 dB across the band for all 4 ports.

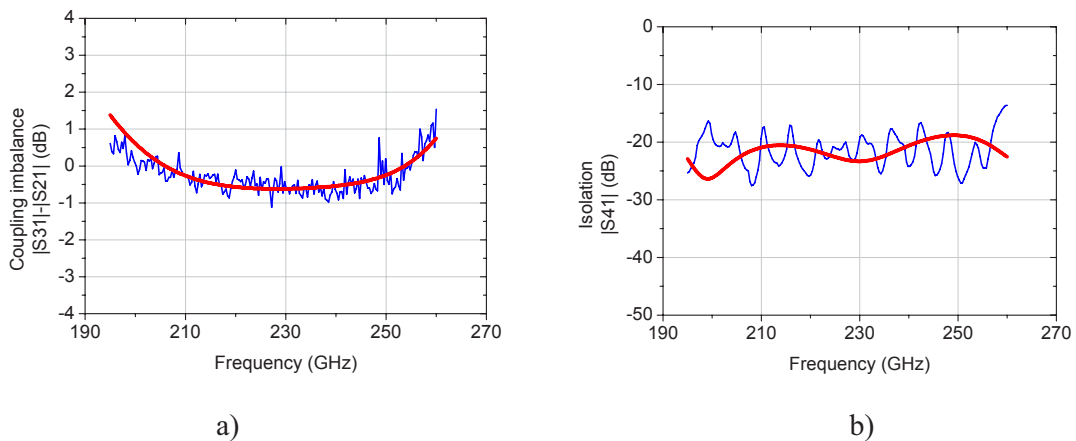


Fig 3 : CST MWS simulation (red smooth line) and measurement of a) amplitude imbalance and b)

isolation.

Phase Measurement

The phase measurements were made with the IRAM VNA at 195-260GHz. Using the transmission method, as for the amplitude measurement, requires moving the mm detector module of the VNA from port 2 to port 3. The mm detector module is linked to the VNA with a flexible coaxial cable that carries the 13th harmonic of the mm signal. Any movement of these cables will generate a phase shift. Therefore, a different method must be used to measure the phase difference between port 2 and 3. Instead, a reflection method can be used.

For that experiment, a -10 dB coupler was placed at port 1 so that emission and detection could be done at the same port. First, a load was placed at port 3 and a short circuit at port 2 so that the signal being detected at port 1 would have traveled the path port1-port2 twice. Second, the load and the short circuit were exchanged so that we detected twice the path port1-port3. The difference of these two measurements is equal to $2 \times \Delta\phi$ (modulo 2π). The phase imbalance is then $\Delta\phi$ (modulo π). Taking a linear fit in the data set we measure $\Delta\phi=82$ deg, mid-band (see Fig 4). In that case, only the loads are moved thereby no phase offset were generated by the measurements. However, as shown in Fig 4, the VSWR of the ports to which the loads are applied produce some modulation in the phase imbalance measurement.

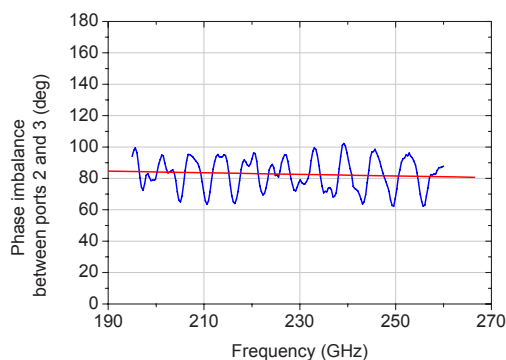


Fig 4: Phase imbalance measurement in transmission and linear fit.

b. -16 dB coupler

The coupler consists of two waveguides that are linked through the broad walls and are separated by shunt guides $\lambda_g/4$ long (See Fig. 5). There is a minimum of two shunt waveguides, separated by $\lambda_g/4$, producing a narrow band device, and the bandwidth can be increased with the number of shunts. For a given coupling, the slots widths have to be reduced if their number increases. A -16dB coupler at 320GHz will have two slots 0.060mm wide, representing the limit with present technology for reproducible high quality slots (see Table 2).

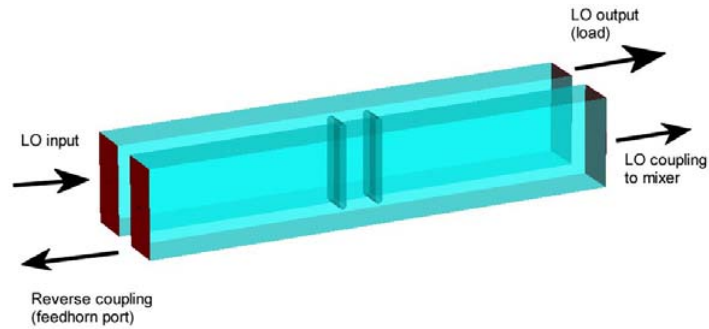
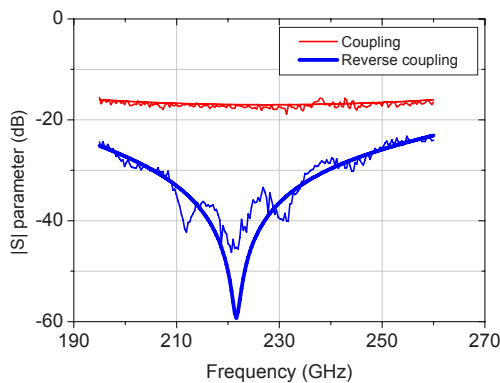


Fig. 5: View of -16 dB branch-guide LO coupler.

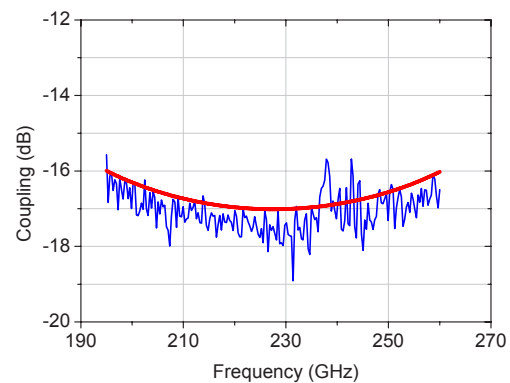
Frequency band	Waveguide size (mm)	Slot width (mm)	Slot pitch (mm)	Waveguide pitch (mm)
195-260GHz	1.090x0.545	0.080	0.440	0.875
275-370GHz	0.760x0.380	0.060	0.315	0.615

Table 2: Dimensions of the -16dB coupler

Simulations have been carried out with CST MWS in order to optimize the slot width and the separation between the waveguides. The resulting design covering Band 7 (275 GHz to 370 GHz) was tested with a scale model at 195GHz to 260 GHz, on the IRAM VNA. The coupling varies by 1dB across the band and the isolation is better than -10dB (see fig 6).



a)



b)

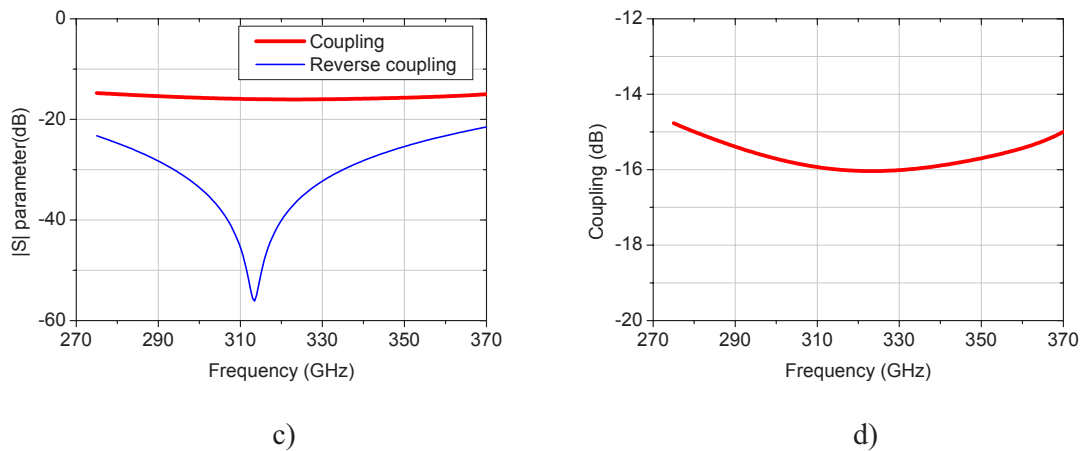


Fig. 6: a) and b) Simulation and measurements of the -16 dB branch-guide coupler covering the band 195-260 GHz; measurements are the noisy lines c) and d) show CST MWS simulation for the 275-370 GHz coupler.

The blocks (see Fig 7) were machined with a CN milling machine at IRAM, except for the 2 slots that were spark eroded. In order to reduce sparking in the bottom of the main waveguides, there is 0.02mm step between the bottom of the slots and the bottom of the main waveguides. The load, absorbing the unwanted LO signal, consists of a wedge glued in the waveguide made of Alkar 66 (carbon and iron loaded epoxy absorbing material).

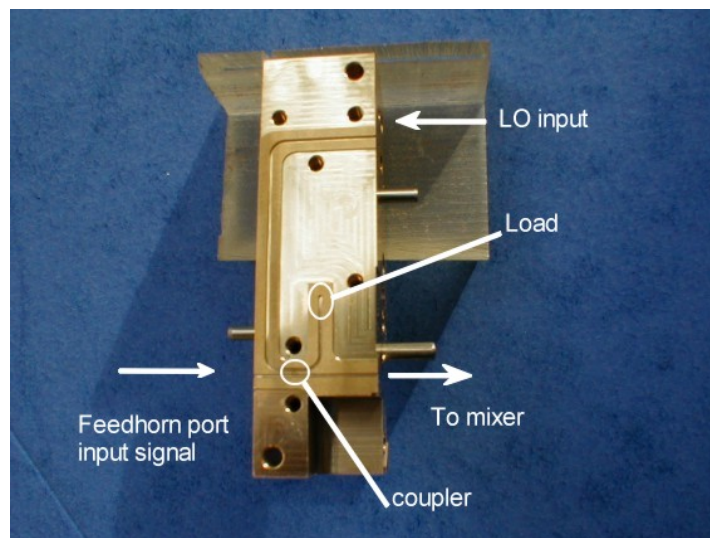


Fig. 7: One half of the 320 GHz coupler

c. DSB Mixer unit

The DSB mixers used in this experiment were designed by A.Navarrini [6]. In order to couple the LO signal to the mixer, the -16dB coupler was designed to be integrated with the back of the DSB mixer for reducing the input waveguide length (See Fig. 8 a). Two mixers coupler assemblies were measured as shown in Fig 8 b. It must be noted here that the two mixers did not have the best noise temperature in the batch but more importantly for this experiment had similar characteristics (I-V and noise temperature).

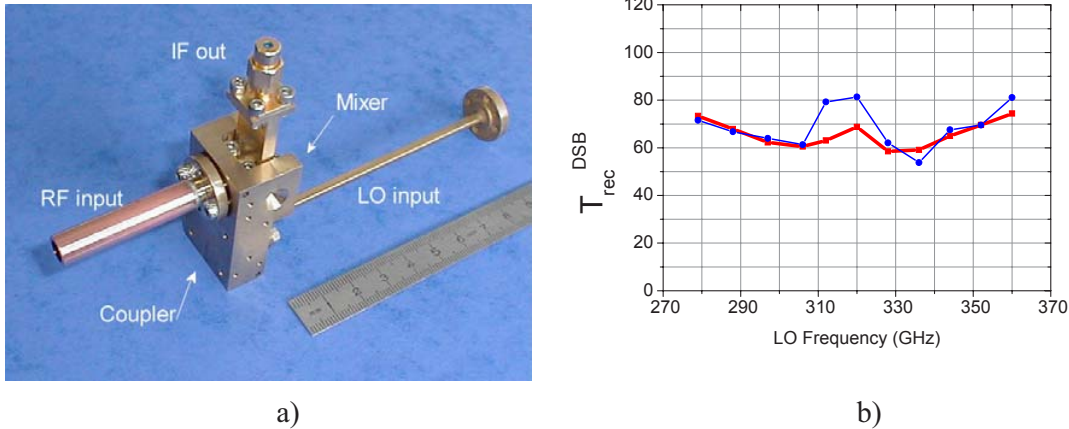


Fig 8: a) Mixer coupler assembly for DSB Mixer test and b) DSB mixer units noise temperature with 4-8 GHz IF bandpass filter

The mixer design used for this experiment was originally targeted for 2GHz IF bandwidth. Here, in order to meet the ALMA requirements the mixer IF was measured over a larger bandwidth and filtered over the 4-8GHz band. As shown on Fig 12 a) the actual bandwidth of the mixer is 4-6 GHz and the output IF cuts off rapidly beyond 6 GHz.

d. In-phase power splitter

The in-phase power divider consists of a Y junction with 5 mm radii and has a CST MWS simulated S11 better than -20 dB across the band..

4. Sideband separating mixer

All previously described elements can be put together to form a compact sideband separating mixer. One half of the coupler is shown in Fig 9 with the location of the LO in-phase power splitter, the signal quadrature hybrid and the two -16dB LO couplers all machined on a single piece of brass. For each coupler, the un-used waveguide branch was terminated by a load. Fig 10 shows the complete mixer assembly. The LO signal is brought in with an overmoded WR-10 waveguide followed by a waveguide transformer to WR-3. Note that such a transformer can be implemented in the coupler. This non essential added complication in the design was not considered for the present demonstration prototype. The two DSB mixers with the IF impedance transformers fit on opposite sides of the coupler connected to the output waveguide of each -16dB LO couplers. The size of the coupler is dominated by the alignment pins and

standard UG 387 flanges. Each mixer IF output are directly recombined by a quadrature hybrid coupler. The two output ports of the quadrature hybrid correspond to the separated USB and LSB signals and after going through a bias tee, an isolator, a 34 dB gain 4-8 GHz HEMT amplifier with a noise temperature of ~ 4 K [7], for each band, the signals are taken out of the cryostat for filtering and further amplification. A good symmetry must be maintained between the two signal paths from the waveguide and IF hybrid couplers.

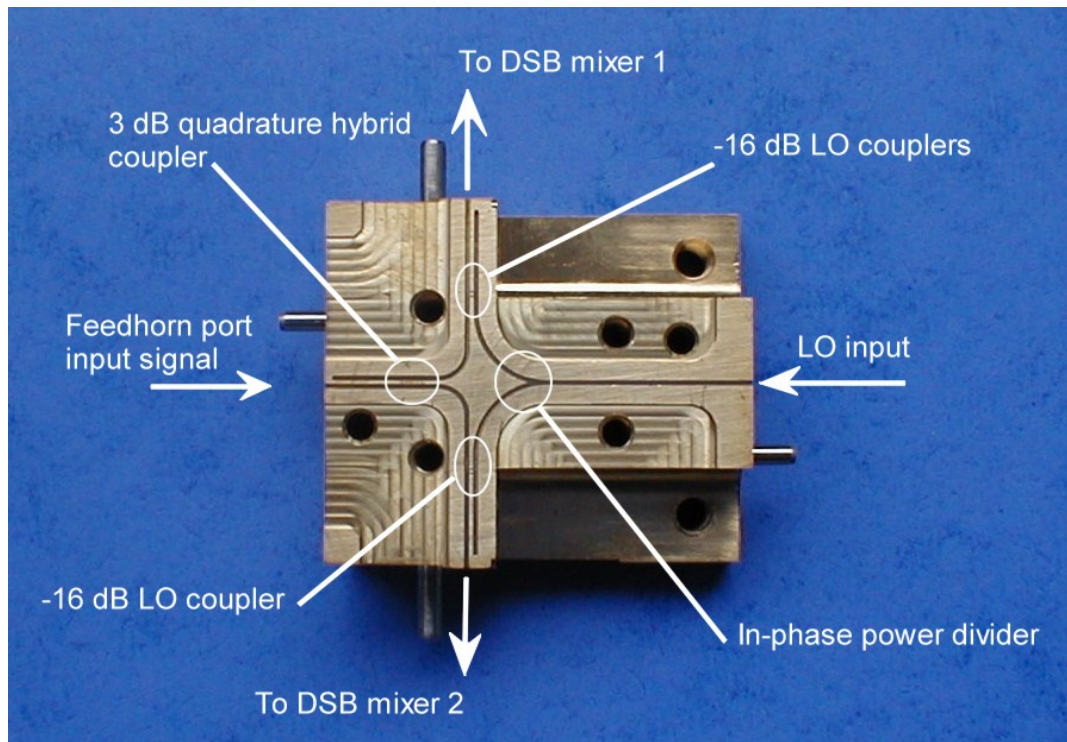
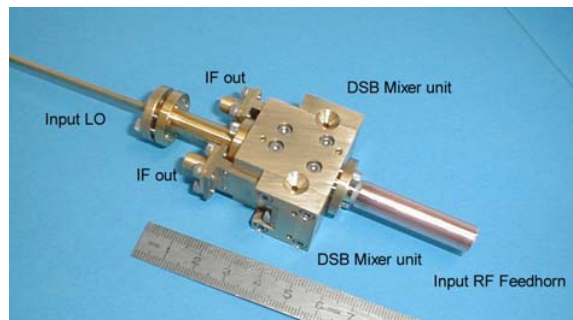


Fig 9: One half of the 2SB coupler.



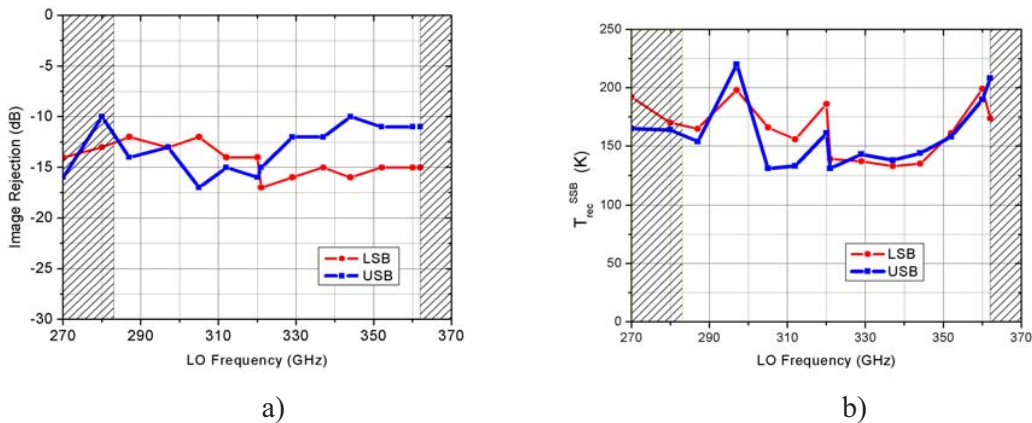
a)

b)

Fig 10: 2SB mixer assembly a) open 2SB Mixer, b) assembled 2SB Mixer

Two independent superconducting coils were used to suppress the Josephson currents. However, a good suppression was obtained with identical currents in both coils. A production mixer could have one coil in common, as described in [1]. Tuning the mixers with bias and LO power proved to be quite simple, and not much different to a single ended DSB experiment. Each mixer bias could be tuned independently, which proved to be useful for a few frequencies where the mixer responses were not identical. In addition, for the same bias value the pump current of each mixer was very similar, showing the symmetry of the LO splitter and the similarities in the mixers reflection coefficients. The image rejection was measured with the method described in [8] with a narrow band (35 MHz) filter at the IF output and a harmonic mixer to inject an RF signal. As shown in Fig 11, the image rejection is between -10 dB and -15 dB across the band. And the SSB receiver noise temperature is close to twice the DSB noise temperature of each individual single ended mixers, as expected for such a system. This noise temperature were obtained with a 4-8 GHz IF. In order to cover the IF bandwidth required by ALMA, 4-8GHz IF must be used. However, as shown of fig 12 a) the mixers have a narrower bandwidth. In order to estimate how the receiver noise would improve in a narrower band configuration, Fig 12 b) shows noise temperature measurement at 5 GHz IF with the 35 MHz bandpass filter used to measure the sideband ratio. The narrow band IF noise temperature is much improved compared to the 4 GHz wide band measurement. This effect is inherent of the DSB mixer units.

This experiment was done with two mixers having very similar DSB noise temperatures. Future experiments should show how important is the pairing of DSB mixers. That is particularly important for the production of a high number for ALMA. The yield must be determined for the matching of mixers since this would have a significant effect on the number of DSB mixer units to produce.



a)

b)

Fig 11 a) Image rejection for the LSB and USB ports of the mixer b) SSB receiver noise temperature with a 4-8 GHz IF. The haches represent frequencies that are out of Band 7.

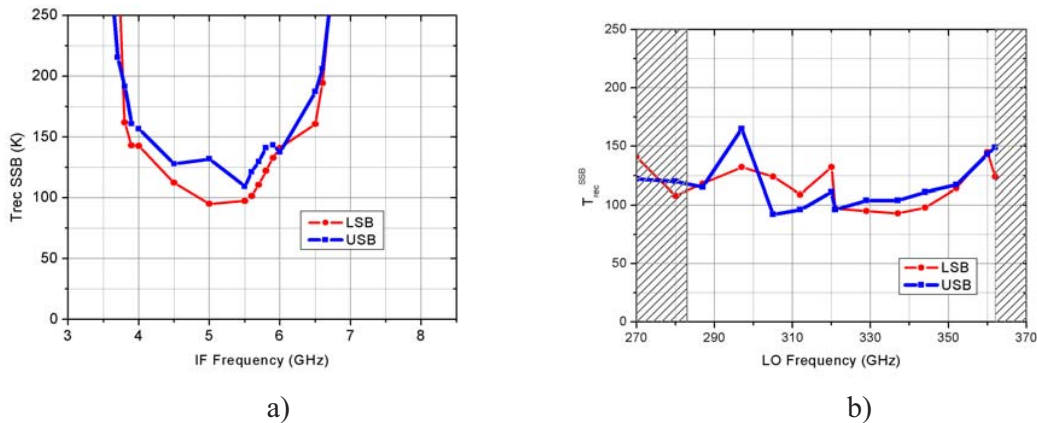


Fig 12: a) Trec SSB at LO=336GHz over the IF band with a 4-8 GHz band pass filter. b)SSB receiver noise temperature with a 5 GHz IF, 35 MHz passband. The haches represent frequencies that are out of Band 7.

5. Conclusion

A sideband separation mixer was designed and tested for ALMA Band 7 (275-370GHz). Performances of this demonstration prototype proved that the concept could be used on a telescope. Image rejection better than -10dB is meeting the ALMA specifications. However, the noise temperature and the IF bandwidth of the mixer have to be improved in order to meet the ALMA specifications. Also, the yield for the pairing of the DSB mixers must be measured.

Acknowledgments

The author wishes to thank the IRAM workshop for the high quality machining of the mixers and couplers, F. Mattioco for useful comments on the couplers measurements with the VNA and Sylvie Hallegen for contacting the SIS junctions in the mixers. Help of Lionel Degoud for the mixer measurements and useful advices from M.Carter and A. Navarrini were much appreciated as well as comments from B.Lazareff on this manuscript.

References

- [1] ALMA Memo #316
- [2] A.R.Kerr and S-K.Pan, "Design of Planar Image Separating and Balanced SIS Mixers", ALMA Memo #151, March 1, 1996.
- [3] F.Mattiocco and M. Carter, "80-360 GHz very wide band millimeter wave network analyzer", International Journal of Infrared and Millimeter Waves, Vol.16, No 12, 1995.
- [4] F.Mattiocco, M. Carter and B.Lazareff, "220-230GHz harmonic mixer for a full band sweep vector network analyzer", International Journal of Infrared and Millimeter Waves, Vol.21, No 11, 2000.
- [4] CST Microwave Studio. Bűdinger Str. 2 a, D-64289 Darmstadt, Germany.
- [6] A. Navarrini, B. Lazareff, D. Billon-Pierron, and I. Peron, "Design and characterization of 225-370 GHz DSB and 250-360 GHz SSB full height waveguide SIS mixers", Thirteenth International Symposium on Space Terahertz Technology, March 26-28, 2002, Cambridge, MA, USA.
- [7] Centro Astronómico de Yebes. Guadalajara, Spain.
- [8] A.Kerr, S-K.Pan, J.E.Effland, "Sideband Calibration of Millimeter-Wave Receivers", ALMA Memo

14th International Symposium on Space Terahertz Technology

#357, March 27, 2001.

Design Accuracy of the Resonance Frequency for the PCTJ SIS Mixer

Yasunori Fujii^{1,2}, Ken'ichi Kikuchi¹ and Junji Inatani¹

¹ National Space Development Agency of Japan, Tsukuba, Ibaraki 305-8505, Japan

² Nihon Tsushinki Co., Ltd., Yamato, Kanagawa 242-0018, Japan

Email: fujii@nitsuki.com

We are developing a 640 GHz SIS mixer for JEM/SMILES[1]. To tune out the junction capacitance, we use a resonance circuit designed by the parallel-connected twin junction(PCTJ) approach[2]. For a certain resonance frequency, the length between two junctions (L_j) depends on the junction capacitance. Since the junction has to be large enough for its reliable fabrication, L_j becomes short for the resonance at 640 GHz. In that case, the resonance frequency is not accurately calculated from a simple assumption that L_j represents the effective inductance, because the junction size and the microstrip width are no longer negligibly small compared to L_j . We investigated the relation between L_j and the actual resonance frequency by means of a simple circuit model of the PCTJ for our 640 GHz mixer.

Figure 1 shows a photo of our PCTJ circuit. The junction size is nominally $1\ \mu\text{m} \times 1\ \mu\text{m}$. A $6.6\ \mu\text{m}$ -wide microstrip connects the two junctions separated by L_j , which ranges over $7.45 - 11.45\ \mu\text{m}$. An analysis with a simple LCR circuit is not sufficient in that case, and we must take into account some spreading inductance of electric current. Our approach for that is to replace the superconductive PCTJ circuit with an approximate 3D structure of normal conductivity, which can be analyzed by means of a commercially available FEM tool. The replacement is done as follows:

- (1) The superconductive microstrip is replaced with a normal microstrip that has the same width, same characteristic impedance, and same electrical length as the original superconductive microstrip.
- (2) The SIS junction is replaced with a structure that has the same size, same capacitance, and same resistance, which is modeled with appropriate values for dielectric constant and conductivity.

The resonance frequency of that approximation model is derived from a 3D EM simulator (Ansoft HFSS), and it is compared with a result of a simple LCR

resonance model. An effective spreading inductance, that is necessary to get the derived resonance frequency, is calculated and shown in Figure 2.

The simulated mixer performance and measurement results will be also reported at the symposium.

References

- [1] SMILES Science Team and SMILES Mission Team, "JEM/SMILES Mission Plan", Version 2.1, November 2002 (available at <http://smiles.tksc.nasda.go.jp/index.shtml>)
- [2] T. Noguchi, S. C. Shi, and J. Inatani, "Parallel connected twin SIS junctions for millimeter and submillimeter wave mixers: analysis and experimental verification," *IEICE Trans. Electronics*, vol. E78-C, 481, 1995.

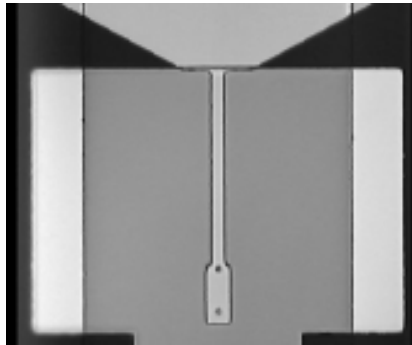


Figure 1. Optical microscope image of the 640 GHz PCTJ image.

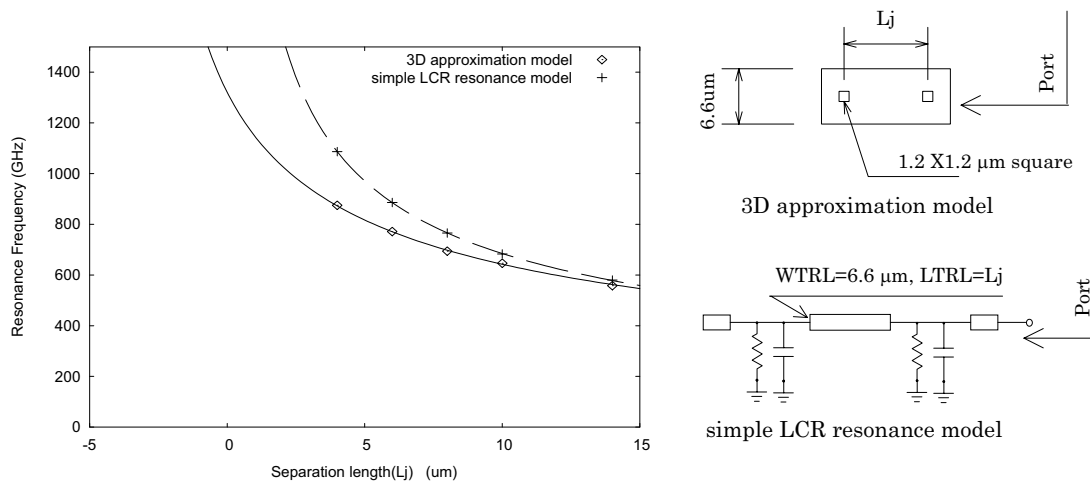


Figure 2. The resonance frequency as a function of junction separation length. Curves are the fits obtained with the expression $F_{res} \propto 1/\sqrt{(L_j + \Delta L_j)}$. For the case of 6.6 μm wide microstrip line, 1.2 X 1.2 μm square shape of junction, an acceptable fit is obtained with $\Delta L_j = 3.0 \mu\text{m}$.

Low noise SIS mixer for the band 1.1-1.25 THz of the Herschel space radiotelescope

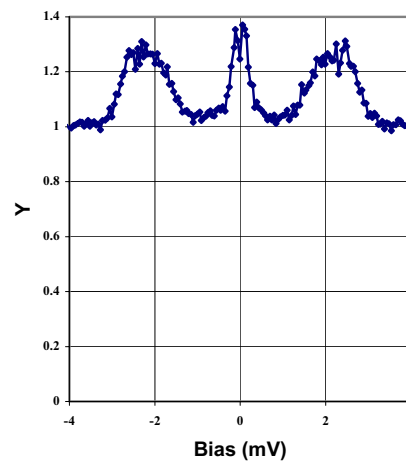
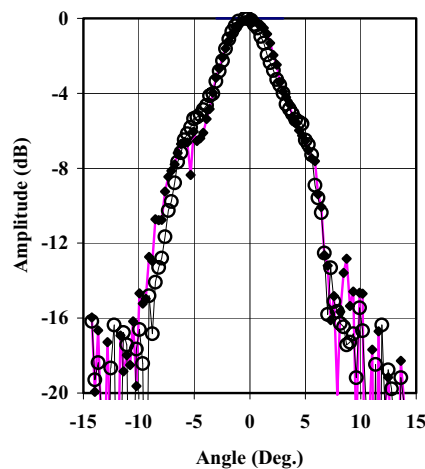
A. Karpov, D. Miller, F. Rice, J. Zmuidzinas
J. A. Stern*, B. Bumble*, H. G. LeDuc*

California Institute of Technology, Pasadena, CA 91125, USA
* Jet Propulsion Laboratory, Pasadena, CA 91109, USA

We report a further progress in development of SIS mixer for the 1.1-1.25 THz band of the heterodyne spectrometer of Herschel space observatory. The corrected receiver noise with the new mixer is close to 500 K with detection in entire 4-8 GHz IF band.

The quasi-optical SIS mixer has two Nb/AlN/NbN with the area of $0.25 \mu\text{m}^2$. The Josephson critical current density in the junction is 30-50 kA/cm^2 . The tuning circuit integrated with SIS junction has the base electrode of Nb and a gold wire layer. This approach simplifies the SIS junction technology, compared to a design using NbTiN base electrode. The junction base electrode and the ground of the tuning micro strip circuit are formed in one step. The frequency of operation of the mixer is well above the gap frequency of Nb, and it behaves here as a normal metal.

The measured mixer beam pattern is symmetrical and, in a good agreement with the design requirements, the $f/d = 4.2$. The receiver Y factor is measured in experiment with an ambient temperature and a liquid Nitrogen cooled loads. The maximum Y is about 1.26 at bias voltage about 2 mV. The receiver uncorrected DSB noise temperature is 750 K. A further experiment with the aim to reduce the loss in the mixer circuit at THz frequency by 30-60 % is under way.



INFLUENCE OF JUNCTION-QUALITY AND CURRENT DENSITY ON HIFI BAND 2 MIXER PERFORMANCE

R. Teipen*, M. Justen, T. Tils, S. Glenz, C. E. Honingh, K. Jacobs

KOSMA, I. Physikalisches Institut, Universität zu Köln
Zùlpicher Strasse 77, 50937 Köln, Germany

B. D. Jackson

National Institute for Space Research (SRON)
Landleven 12, 9747 AD Groningen, Netherlands

T. Zijlstra, M. Kroug

Dept. of Nanoscience, Faculty of Applied Sciences, Delft Univ. of Technology
Lorentzweg 1, 2628 CJ Delft, Netherlands

Introduction

The current density of Nb/Al₂O₃/Nb SIS junctions that are used as sub-millimeter wave mixers is a determining parameter in the device design. Integrated tuning circuits for single junction designs typically have a fractional bandwidth of $1/\omega RC$, with ω the angular frequency, R the junction normal state resistance and C the junction capacitance. As $RC \sim 1/j_c$ (j_c is the current density), for higher frequencies and/or larger bandwidths one would like to use a devices with higher current density.

Admittedly large bandwidth can also be achieved by parallel arrays of junctions with a lower current density¹. However a higher j_c will also improve the coupling for tuning circuits with normal metal lines that have some of loss, as are used at frequencies above the gap frequency of niobium (700 GHz). In addition at higher frequencies and for certain applications like array- or satellite mixers, one wants to avoid unnecessary complexity in the operation of the mixer, for example in tuning the magnetic field for an array of junctions.

For higher current densities it is observed that junctions start to exhibit a lower quality, expressed in the ratio of the sub-gap resistance ($R_{\text{sub-gap}}$) and the normal state resistance (R_N). This is attributed to an increasing number of imperfections in the barrier (pinholes). Dieleman² has shown that the additional sub-gap current through the pin-holes leads to a disproportionately high additional shot-noise generation in the SIS junction, because the charge transport through the pinholes is multiple Andreev reflections (MAR).

The increase in current density at the expense of quality leads to a trade off between improved coupling and higher junction noise in the optimization of a mixer design. For future design decisions it is important to obtain mixer data to verify the predictions of performance by the Quantum theory of mixing³ (QTM) that take into account the MAR in the barrier.

In the course of the development for HIFI⁴ Mixer Band 2 (636-802 GHz) KOSMA has access to twin junction devices with an integrated tuning structure consisting of a NbTiN ground plane and aluminum wiring, from two different fabrication facilities, DIMES^{5,6} and KOSMA⁷. The devices from DIMES have in general an excellent $R_{\text{sub-gap}}/R_n$ ratio of around 20 with current densities of 6-8 kA/cm², where devices from KOSMA have a high current density of 12-14 kA/cm² and an $R_{\text{sub-gap}}/R_n$ of around 7. We present measurements and analysis of comparable devices of both fabrication facilities. For the RF measurements we use a HIFI Band 2 fixed tuned waveguide mixer with a 4-8 GHz IF.

Device Design

The twin junction devices are of a standard design. The junctions are connected by a micro-strip line of suitable length and width to tune out both junction capacitances at the center frequency of the design band. This junction pair is connected to the antenna (in this case a waveguide probe) by an approximately quarter wavelength micro-strip-line that matches the junction pair impedance to the antenna impedance. The layout of the device is shown in Figure 1. The tuning structure has a superconducting NbTiN ground plane, and an aluminum wiring layer⁸.

The calculated coupling between the antenna and the devices as a function of frequency, dependent on device current density, is given in Fig. 2. The dimensions of the transformer part of the tuning structure are slightly adapted to achieve optimum coupling at each current density.

The DIMES device has an NbTiN ground plane with a resistivity of about 110 $\mu\Omega\text{cm}$ at approximately 20K and $T_c \sim 14.4\text{K}$. The aluminum wiring layer has a resistivity of approximately 1.2 $\mu\Omega\text{cm}$. The NbTiN ground plane of the KOSMA devices has

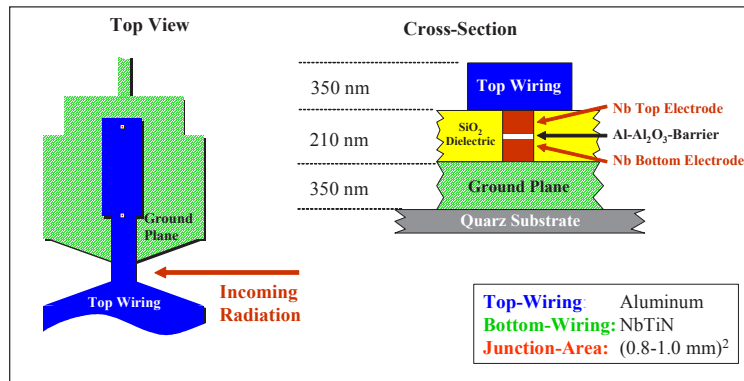


Figure 1: Realization of Twin-Junction-Device

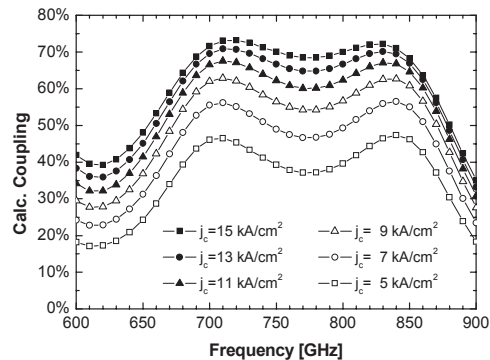


Figure 2: Impact of Current Density on calculated Power Coupling

a resistivity of $90 \mu\Omega\text{cm}$ and a T_c of 14.5 K. The aluminum wiring layer shows a resistivity of approximately $0.8 \mu\Omega\text{cm}$.

Measurement Setup

The devices are used in a standard fixed tuned waveguide mixer-block. The mixer-block is used in a HIFI Band 2 mixer unit, which contains a corrugated horn, a magnet and a 4-8 GHz IF coupling, including a bias tee.

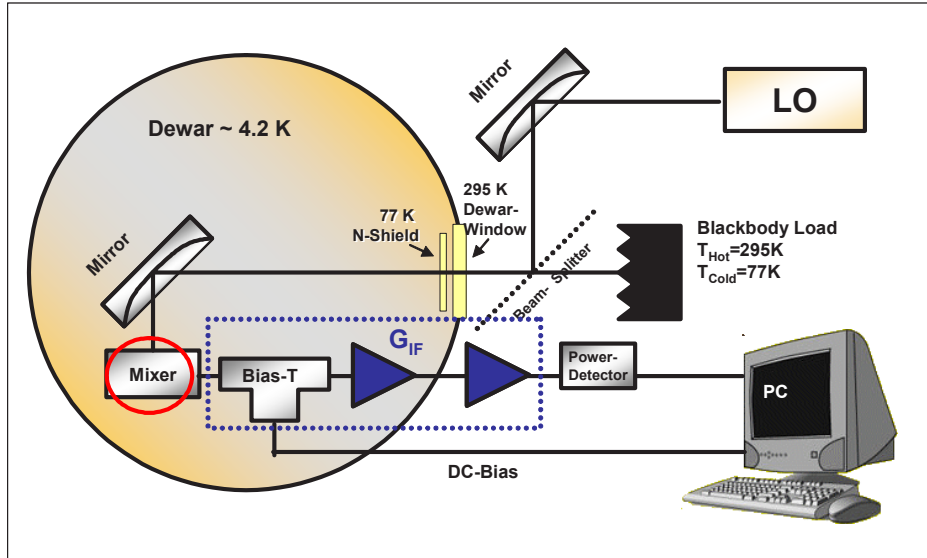


Figure 3: Sketch of the heterodyne Measurement Environment; measurements are made in a liquid helium Dewar, noise- and gain-contributions can be classified into three groups: beam-splitter and windows are the optics contribution, the mixer noise contribution, the contribution of the IF-chain, composed of bias-T, isolator, HEMT-amplifier and warm amplifiers.

The measurement set-up is shown in Figure 3. The mixer unit is mounted to the cold plate of a liquid helium dewar. The operating temperature of the mixer during all measurements is 4.3 K. We use a solid state LO source, a $10 \mu\text{m}$ Mylar beam-splitter and a standard 300K/77K load calibration unit. The IF output power is measured over the full 4-8 GHz bandwidth. The noise temperature of the IF-amplifier varies in different measurements and is calibrated with the shot-noise method.

Measurements

The devices of comparable area are characterized by DC-measurements. The DC-characteristics of three measured devices are shown in Figure 4. Clearly the differences in

current density can be seen in the higher current of the solid curve in the normal conducting branch above the gap frequency (a)). In b) the axes are scaled to see the differences below the gap. The sub-gap-current of the high-current density devices is clearly visible. Even if one would scale the current of the low current density devices to the values of the solid line, their sub-gap-current would be much lower.

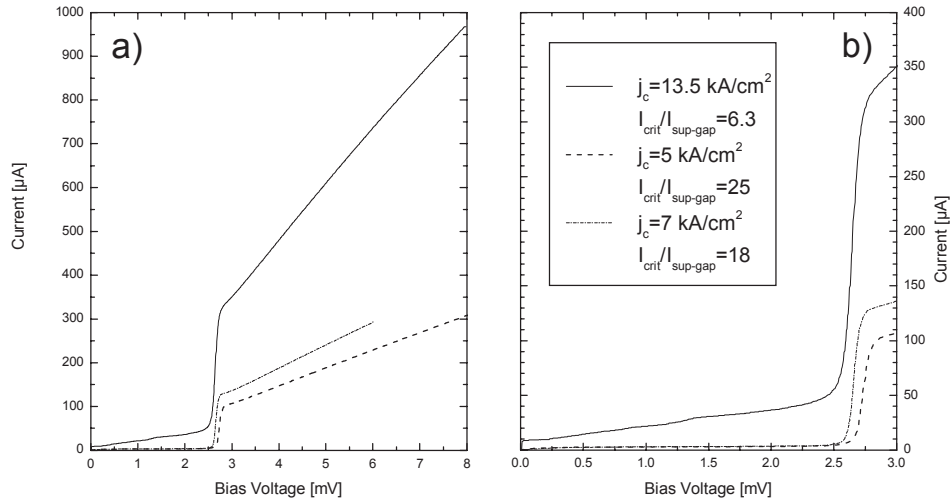


Figure 4: *I-V-Characteristics of measured junctions fabricated by DIMES ($j_c=5-7 \text{ kA/cm}^2$, $Q=25-18$) and KOSMA ($j_c=13.5 \text{ kA/cm}^2$, $Q=6.3$)*

The band pass of these devices is measured with a Fourier-Transform-Spectrometer (FTS). The data are plotted in Figure 5. The FTS-conversion is in arbitrary units scaled to comparable values.

The performance of the three devices is also characterized by their measured mixer noise and mixer gain. In the measurement setup which is shown in Figure 3, a total receiver noise temperature is obtained. The optics contribution has been measured separately in an FTS-measurement. The contribution of the IF-chain is determined by a shot-noise-fit, which is described below.

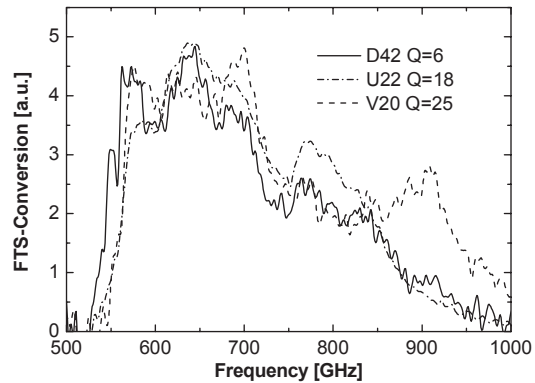


Figure 5: *Measured band path for three devices; all devices show the best coupling below and around 700 GHz*

After subtracting the optics- and IF-chain-contributions the corrected mixer gain and mixer noise are obtained which characterize the influence of the mixer-device itself. The corrected mixer noise and mixer gain are shown in Figure 6.

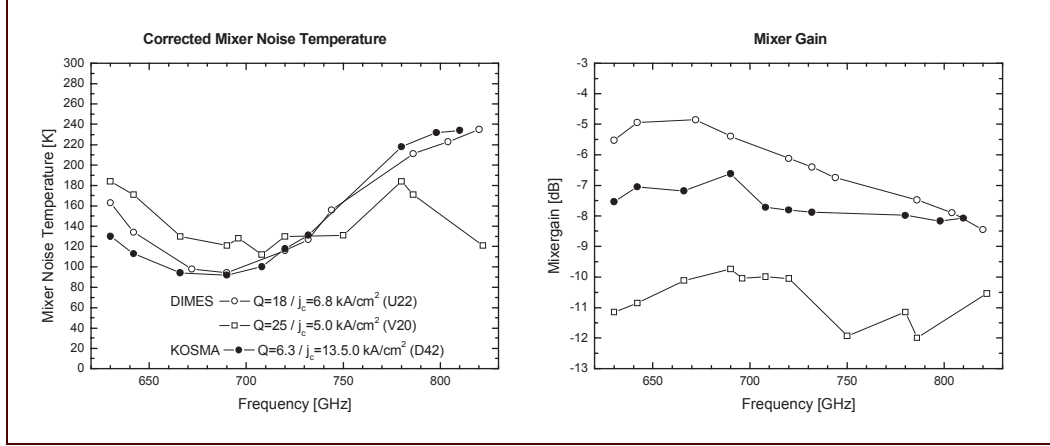


Figure 6: Mixer Noise Breakdown for three junctions

The devices U22 (DIMES) and D42 (KOSMA) show very similar values for the mixer noise although they have very different DC-characteristics (quality Q and current density j_c). The higher sub-gap-current of device D42 (KOSMA) apparently does not necessarily lead to a higher noise. The device with a lower current density U22 has a higher mixer gain in comparison to the high current density device D42. The third device V20 shows a wider bandwidth but does not have such good values for mixer noise and mixer gain.

In order to obtain information about the influence of the IF-noise, IF-gain and possible increase of output noise induced by the Multiple Andreev Reflection (MAR), the unpumped IF output power is analyzed. The calculated shot-noise power of the junction at the IF output is compared with the measured output power. For the shot noise power of the twin-junction devices, the formula

$$P_{\text{shot}}(V) = \frac{1}{\sqrt{2}} S_1(V) \cdot B \cdot \coth\left(\frac{eV}{2k_B T}\right) \cdot \frac{Y_L}{(dI/dV + Y_L)^2}$$

is used. Here B is the bandwidth, Y_L is the load admittance. The spectral noise density is defined after Dieleman et al.² $S_1(V) = 2e \cdot I_{\text{tun}}(V) + 2q_{\text{MAR}} \cdot I_{\text{MAR}}(V)$, where

$$I_{\text{tun}}(V) = \frac{2}{R_N e} e^{-\frac{\Delta}{k_B T}} \sqrt{\frac{2\Delta}{eV + 2\Delta}} (eV + \Delta) \cdot \sinh\left(\frac{eV}{2k_B T}\right) \cdot K_0\left(\frac{eV}{2k_B T}\right)$$

is used for the tunneling current⁹ for $eV < 2\Delta$ (with K_0 the zeroth-order modified Bessel function)

- $I_{MAR}(V) = I_{measured}(V) - I_{tun}(V)$ is the current carried by the MAR effect
- $q_{MAR}(V) = e \cdot (1 + r_{MAR} \cdot 2\Delta/eV)$ is the voltage-dependent effective charge of the MAR-carried current with r_{MAR} as fit-parameter. We introduce this “ratio of MAR-effect” in order to estimate, to which degree this effect has to be taken into account for the analysis of the measured devices.

Then the total output power is calculated according to the formula

$$P_{out}(V) = \left\{ P_{Shot}(V) + k_B B \left[T_{IF} + T_{ISO} \left(\frac{Y_L - dI/dV}{Y_L + dI/dV} \right)^2 \right] \right\} \cdot G_{IF}$$

where T_{IF} is the noise temperature of the HEMT-amplifier and bias-T, T_{ISO} is the temperature of the isolator and G_{IF} is the total gain of the IF-chain.

The resulting data for two devices – one of the DIMES devices (V20) and one KOSMA device (D42) – and their fit parameters are given in Figure 7:

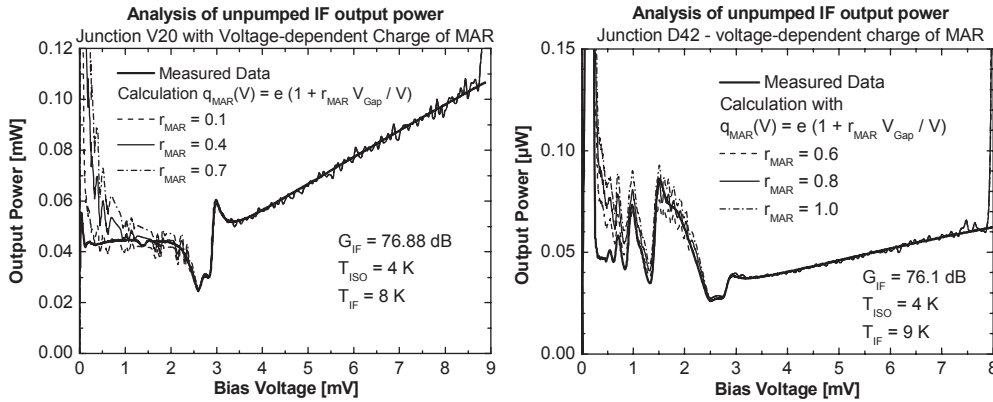


Figure 7: Calculation of shot noise of the junction and IF-noise for two devices in comparison with the measured IF-output power assuming a voltage-dependent charge for the MAR-carried current

It can be seen that the effect of MAR is stronger for the device D42 on the right hand side, which has the higher current density and the lower quality factor Q , as one would expect. The fit seems to be appropriate for voltages from around 1 mV to the gap-voltage. But for lower voltages the calculated power values are too high.

To obtain a better fit, the data were also analyzed assuming a constant effective charge for the MAR carried current ($q_{MAR}(V)=const$). If this constant effective charge has a value of $2e$, at the gap-voltage V_{Gap} , it has the same value as the voltage dependent ef-

fective charge for $r_{\text{MAR}}=1$, and for lower voltages it is below the voltage dependent function $q(V)$. The results are given in Figure 8.

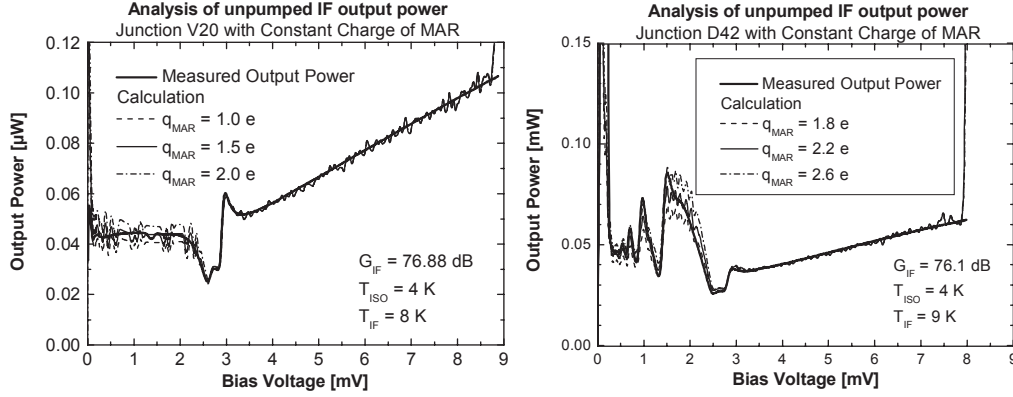


Figure 8: Calculation of shot noise of the junction and IF-noise for two devices in comparison with the measured IF-output power assuming a constant charge for the MAR-carried current

The approach with a constant charge over the bias voltage seems to describe the phenomena better than the previous one. For the DIMES-device the result is an effective charge of 1.5-e. The value for the KOSMA device is 2.2-e. These values are used in the further performance analysis.

Simulated mixer results

The measured DC IV-curves and results of the fit to the IF output power, including the MAR parameter, are used as input to the QTM. The actual embedding impedance of the devices is estimated using actual junction and layer parameters as obtained from DC-measurements. The Band center is shifted towards lower frequencies in agreement with the measured FTS results. We simulate the performance around 700 GHz where the best performance was measured for both devices. The results are given in Table 1.

Table 1: Simulated and measured mixer input noise temperature and mixer gain
The simulated mixer performance is calculated
with MAR-effect ($q_{\text{MAR}}/e \neq 1$) and without MAR ($q_{\text{MAR}}/e = 1$).

Device	q_{MAR}/e	T_{Mix} [K] simulated	G_{Mix} [dB] simulated	T_{Mix} [K] measured	G_{Mix} [dB] measured
U22 (DIMES)	1.5	70	-6.5	96	-5.4
	1	66	-6.5		
D42 (KOSMA)	2.2	96	-6.7	91	-6.9
	1	69	-6.7		

Discussion

It would be very desirable to have a reliable way of including the effects of the tunnel barrier imperfections in the performance simulation of high frequency (and high current density) Nb/Al₂O₃/Nb SIS mixers. If we compare the calculated output power using the formula $q_{\text{MAR}}(V) = e \cdot (1 + r_{\text{MAR}} \cdot 2\Delta/eV)$ with the measurements of the unpumped IF-output power, it is apparent that the effect of the MAR on the shot noise output is overestimated, even for the KOSMA device with a quality of 7. In addition we were only able to obtain a good fit between theory and measurement by removing the voltage dependence of the effective charge. The fit result indicates that only a part of the current in excess of the tunneling current is caused by MAR, and that there are still other charge transport mechanisms involved.

The fitted constant effective charge was used in the QTM as suggested in ². The inclusion of the MAR increases the calculated noise, but for the good quality junction the predicted noise is still a little low compared to the measured noise. For the bad quality junction the calculated noise is similar to the measured one.

Based on the measurements and analysis presented here we can conclude that one should take into account the MAR in the imperfect barriers in the analysis of the mixer results. Using the approach with the voltage independent, fitted, effective charge to estimate the influence of the MAR, the optimum design current density probably shifts to higher values than 10 kA/cm². To confirm if simulated results with the QTM including the MAR also yield a good prediction of measured mixer performance, we need to analyze more data.

¹ S.-C. Shi, T. Noguchi, J. Inatani, "Analysis of the Bandwidth Performance of SIS Mixers with Distributed Junction Arrays", Eighth International Symposium on Space Terahertz Technology, Harvard University, March 1997, p. 81-90

² P. Dieleman, T. M. Klapwijk, "Shot noise beyond the Tucker theory in niobium tunnel junction mixers", Appl. Phys. Lett. 72 (13), 1653 (1998)

³ J. R. Tucker and M. J. Feldman, Rev. Mod. Phys. 57, 1055 (1985)

⁴ See website <http://rhea.sron.nl/divisions/lea/hifi/>

⁵ Delft Institute of Microelectronics and Submicron Technology, Netherlands

⁶ The cooperation with DIMES was made possible under ESTEC Contract N° 11653/95

⁷ P. Pütz, S. Glenz, C. E. Honingh, K. Jacobs, "Progress in SIS Device Fabrication for HIFI Mixer Band 2 at KOSMA", Thirteenth International Symposium on Space Terahertz Technology, Harvard University, March 2002

⁸ B. D. Jackson, N. N. Iosad, G. de Lange, A.M. Baryshev, W. M. Laauwen, J.-R. Gao, and T.M. Klapwijk, "NbTiN/SiO₂/Al Tuning Circuits for Low-Noise 1 THz SIS Mixers", IEEE Transactions on Applied Superconductivity 11 (1), 653 (2001)

⁹ Th. v. Duzer, Ch. W. Turner, "Principles of Superconductive Devices and Circuits", Prentice Hall PTR, Second Edition, 1999

ALL-NbN SIS MIXERS USING A TUNING CIRCUIT WITH TWO HALF-WAVELENGTH DISTRIBUTED JUNCTIONS

Y. Uzawa, A. Kawakami, M. Takeda, and Z. Wang

*Kansai Advanced Research Center, Communications Research Laboratory
588-2 Iwaoka, Iwaoka-cho, Nishi-ku, Kobe 651-2492, Japan*

Abstract A tuning circuit with two half-wavelength distributed junctions has been tested in quasi-optical mixers using epitaxial NbN/MgO/NbN trilayers at frequencies above 700 GHz. The tuning circuit consisted of two half-wavelength distributed NbN/MgO/NbN tunnel junctions connected in parallel by a half-wavelength NbN/MgO/NbN microstrip line at a design center frequency of 870 GHz. The circuit was connected to the feed point of a center-fed twin-slot antenna by a quarter-wavelength impedance transformer. The mixer chips were installed in our quasi-optical receiver system and their performances were measured. Preliminary results showed double-side-band receiver noise temperatures of $6-9 \hbar f/k_B$ from 675 to 810 GHz for a mixer with the current density of only 6 kA/cm^2 (estimated $\omega C_J R_N$ product was about 30 at 750 GHz). The RF bandwidth was broader than that of a conventional full-wavelength distributed SIS mixer with the same current density. We are now redesigning and fabricating all-NbN SIS mixers to improve the performance at higher frequencies.

Acknowledgements This work was supported in part by the ALMA Joint Research Fund of the National Astronomical Observatory of Japan.

A 1650-1900 GHz Tunable Source

N.R. Erickson, R.M. Grosslein, J. Wielgus and V. Fath
Department of Astronomy
University of Massachusetts
Amherst, MA 01003

I. Mehdi and J. Gill
Jet Propulsion Laboratory
Pasadena, CA 91109

Abstract

A chain of multipliers has been built which for the first time produces an all solid state source up to 1.9 THz. The chain uses a tripler multiplying from near 300 GHz to 900 GHz and a doubler up to 1800 GHz. The 300 GHz source presently uses various multipliers and solid state drivers, with the goal of using a single cascaded pair of doublers driver by a power amplifier for the full band. All of the multipliers in this work use planar varactor or varistor diodes with a significant level of circuit integration. Output power exceeds 1 μ W at several points in the band and a peak of 3 μ W. The source is operated at a temperature of 90 K for best efficiency.

Introduction

The Herschel (FIRST) space mission requires LO sources with frequencies from 1.4 to 1.9 THz to operate HEB mixers in band 6. This band is broken up into two sub-bands, with the higher band of 1.7-1.9 THz being the subject of this work. The LO for these receivers is based on passive frequency multiplication from a initial band of 71-106 GHz where high power amplifiers are available. One way of multiplying to this band is to use a combination of three doublers and a tripler with a net multiplication of $\times 24$, with a starting frequency in the 71-79 GHz range. Another possibility is to use two triplers and one doubler ($\times 18$), and to start in the frequency range 94.5-105.5 GHz. The expected power level needed for these mixers is $\sim 1 \mu$ W, which is a fairly high power given the high frequency, and places fairly extreme requirements on the LO chain, given the present state of the technology. At 1.5 THz an HEB mixer has operated optimally from a 1 μ W solid state source [1], and this verifies the required power, although typical mixers at this time seem to use larger HEB devices (and more LO power) than the one used in this test.

In order to meet the requirements for flight qualification the source must use all-planar components with no mechanical tuning. At this time, planar diodes have shown excellent performance over moderate bandwidths and mechanical tuning is not really practical with most designs, so this requirement is not much of a limitation. Efficiencies actually exceed early expectations, and operating bandwidths do meet the goal. Diode

fabrication is quite consistent, and nearly all multiplier designs work very well, except that there are persistent errors in the exact frequency range covered relative to the design. Fairly complex circuits can be fabricated monolithically, on GaAs of any needed thickness and so the full set of tools are available to make the needed multiplier chains.

Within the range of multipliers that have been designed for this work there are many possible ways to realize either $\times 18$ or $\times 24$ net multiplication. In general if a chain uses a tripler it should be placed as the last stage because triplers are less suited to produce high output power than doublers. However, at the very high frequencies involved, a tripler circuit is harder to fabricate on GaAs, particularly if it is to be DC biased. In addition there are questions about the potential efficiency of such a high frequency tripler because of carrier velocity saturation which tends to reduce higher harmonics in the diode waveform. For these reasons this work is based on a doubler as the final stage, with a tripler as the driver. There is still a choice of initial stages, but two cascaded doublers have far higher output power potential than a single tripler, given that there is a good understanding of how to use series diode arrays in doublers but not in triplers. Thus this work is based on a $\times 2 \times 2 \times 3 \times 2$ chain.

Driver stages

While the plan is to use $\times 2 \times 2 \times 3 \times 2$, the first two doubler stages are not yet optimized and this work was primarily intended to test the feasibility of a tripler near 900 GHz driving a doubler. To provide full coverage, a variety of sources were used as drivers in the 280-320 GHz band. At the lowest frequencies a Gunn oscillator producing 50 mW from 140-146 GHz was used to drive a doubler. From 290-310 GHz a cascaded doubler- doubler was used, and at the highest frequencies a tripler was used. These drivers produced varying amounts of power and the final output varies considerably as a result, but it was possible to cover the full band.

All of the multipliers use planar diode arrays, and almost all of the devices used were developed for the Herschel work. The number of diodes used in the multipliers (and their size) depends on the expected power level. Both the doublers and triplers are very similar or identical to those described previously. All of the tests performed at ~ 90 K since Herschel will operate with a cold LO system at a temperature near 120 K.

The doubler used near 150 GHz was built some time ago using a UVa diode array [2, 3] and this device was intended to drive the chain at frequencies from 140-160 GHz, but the diode used was destroyed by overpower in early tests and no sufficiently similar replacement device was available. As a result the useful bandwidth was greatly reduced, and sufficient power was available only near midband. To avoid further loss of time the input power was limited to 150 mW which is probably well under the maximum that could be used. The typical output power was 45-50 mW in the midband. At frequencies below 146 GHz a Gunn oscillator was available producing 50 mW which exceeded the doubler output power, so this was used as a driver.

The planned second stage doubler uses a diode designed at UMass, and fabricated at JPL using 4 anode array. It is quite similar to a doubler described previously [2, 3] but with simpler construction. The diode array is connected to a beam lead capacitor with a 50 μm wide ribbon and these components are mounted to a waveguide block by soldering the diode in place. The construction is shown in Figure 1. While the block seemed to be properly constructed, there was a very large error in the operating frequency which tuned the block quite low in the band, and it was only marginally useful above 300 GHz. It is possible that the diode has excess capacitance, or that there is a design error in the block, but this is still unresolved. Despite this problem, there was still 10-15 mW output power from 275-300 GHz (at 90 K), which dropped rapidly above 300 GHz. This power was less than desired and certainly not enough for a flight multiplier chain, but sufficient for initial tests.

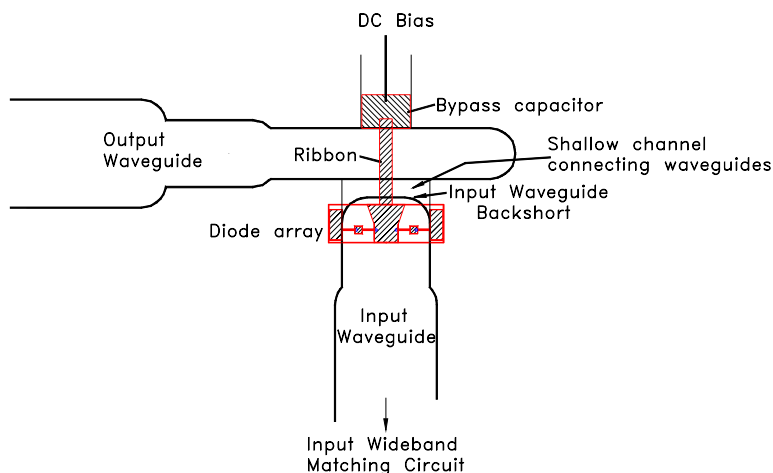


Figure 1. 280-320 GHz doubler using 4 diode array and beam lead capacitor for bias bypass.

As an alternative source for the frequencies above 300 GHz a tripler [4] was used which was built as prototype for later balanced triplers, including the 900 GHz stage in this work. This early design had limited bandwidth but good efficiency at the peak, which just happened to be from 300-320 GHz. The output power is estimated to be 8-9 mW at 90 K, which is considerably less than would be obtained from a doubler, but marginally adequate for this work. As a side note, this same tripler design is being used as the 320 GHz subharmonic LO on the EOS-MLS 640 GHz receiver.

900 GHz Tripler

The tripler was designed at UMass and the diode circuit was fabricated JPL. It is a balanced design very similar to the one mentioned above, and uses a pair of diodes. Provision is included within the chip for series biasing of the two diodes. A cross section

of the block and the device chip is shown in Figure 2. The block for the tripler was machined on a precision CNC micro-milling machine [5], with the very reduced height output waveguide made by broaching a slot with a 25 μm wide tool. Note that this waveguide steps up to near full height very close to the diode chip. The tripler is easy to assemble except that diode chip is very small and is only 12 μm thick. Thus the main problem is in picking up the chip, but with micro-manipulators this is fairly straightforward. The chip is simply glued into the block with the beam leads establishing the circuit ground, and the bias lead connected to an external bias circuit.

A prototype was built using a device that was 20 μm thick, rather than the design thickness of 12 μm . The tuning of these triplers is known to be sensitive to the thickness of the GaAs, and as expected this device tuned very low, relative to the design. However, it did operate at a frequency where a fairly powerful driver source was available, and so was useful in establishing the potential maximum output power that may be obtained. Tests were performed near a physical temperature of 90 K, which was convenient using LN₂, although actual operation in Herschel will be at 120-130 K. The peak output power was 1.0 mW near 810 GHz with ~18 mW input, which actually exceeded the expectation for this device. Bias conditions seemed moderate (2.3 V at 0.5 mA for the series pair) given the size and 4V (per diode) breakdown voltage for the device, but no long term testing was done to establish any safe operating limits.

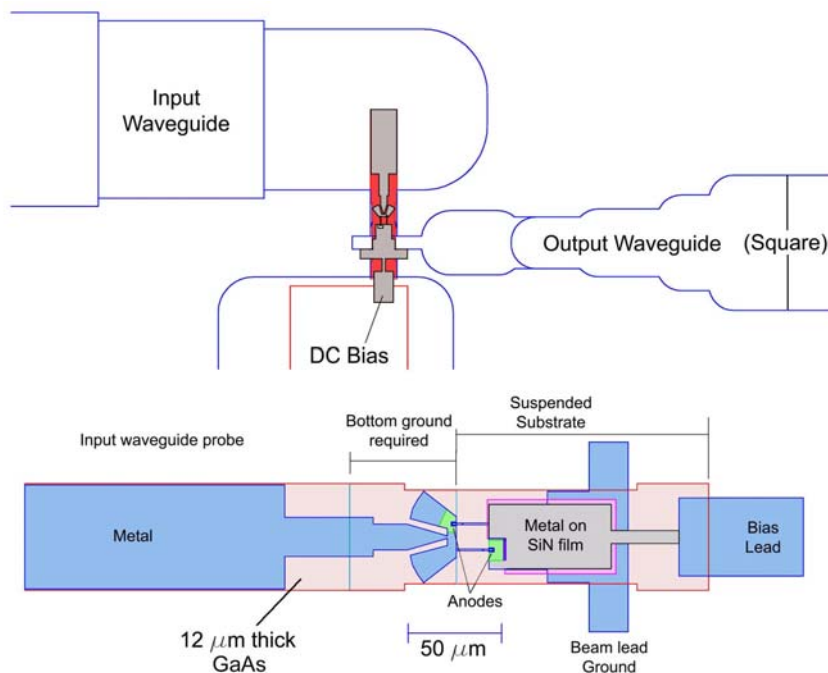


Figure 2. 900 GHz tripler cross section and the diode chip.

After these tests a second tripler was assembled with a 12 μm thick device and it appears to tune as expected, although there is not enough input power to properly pump it over the full band. Peak output power is lower, but this is largely because there is less input available, and only somewhat due to the higher frequency. A plot of the output power of both triplers over their respective bands is shown in Figure 3. Input power is not calibrated, but is typically 7-12 mW over the points tested. These tests were performed at a temperature near 90 K. Three drive sources were used, as described in the previous section.

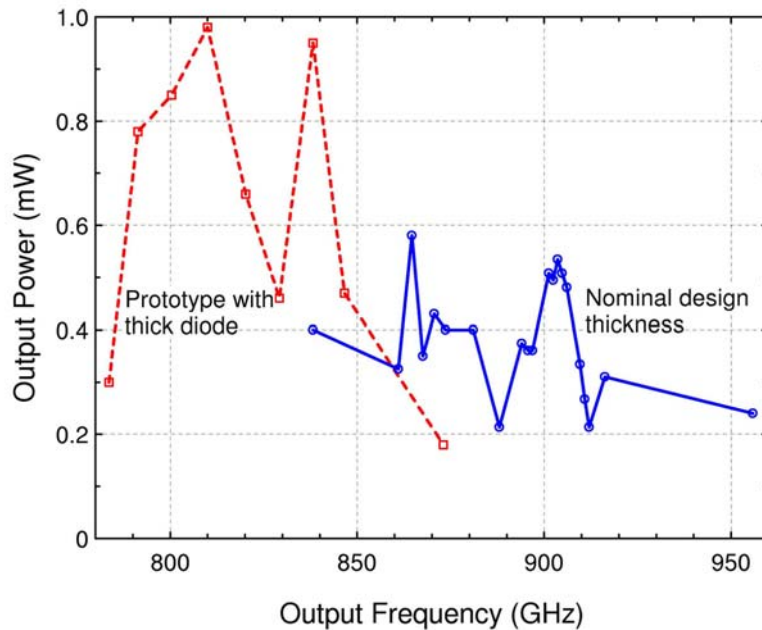


Figure 3. Output power from two triplers of the same design at 90 K with various drivers. The dashed curve is for a 20 μm thick device while the solid curve is for 12 μm thickness. Typical input power is 15-18 mW for points below 850 GHz and 7-12 mW above.

1.8 THz doubler

The doubler for 1.8 THz uses a balanced design in a resistive mode, with the diodes forward biased. The diodes are mounted in series in the output waveguide to simplify a layout with bias. The design is very much like that for 1.5 THz [6] except that the old design was on 3 μm thick GaAs with a 50 μm thick handling frame, while the new design has no frame, just 3 μm thick membrane for the circuit substrate with a 50 μm thick extension handle. The circuit has also been revised to improve the input match, and the overall bandwidth. The block was machined with the same CNC micromill as for the tripler, using end mills down to 50 μm diameter. The output waveguide transitions to square waveguide very close to the device chip, which is mainly required for optimal

impedance matching, but also aids the transition to a diagonal feed horn which is machined into the block. The input waveguide is internally 150 x 300 μm , but to reduce the loss of the input section, this was increased to a square 300 μm cross section at the flange. The same was done to the output waveguide for the 900 GHz tripler. While in principle this oversized cross section can work perfectly, there is some evidence in the test data that excitation of higher modes may be a problem.

The circuit is fairly easy to assemble, except that diode can not be positioned, or even touched, by hand, since the 3 μm thick GaAs is extremely fragile. The thicker “handle” region is strong enough to be useful for some purposes, but micro-manipulators are the preferred method of handling. Assembly simply requires positioning the chip properly and attaching the bias lead with conductive epoxy. The beam leads provide all of the remaining connections to the block, and the chip is fully suspended across the channel by its leads.

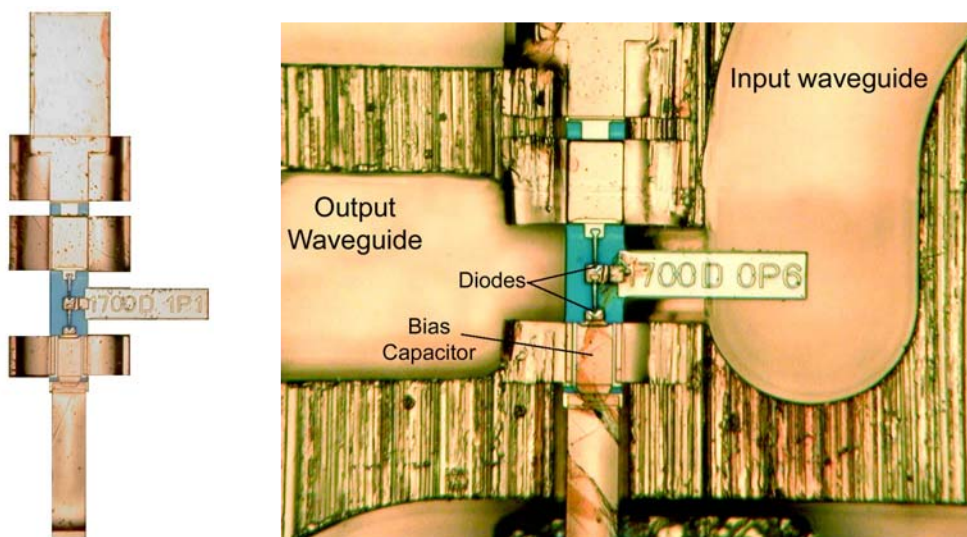


Figure 4. 1800 GHz doubler device and a detail of the complete block. The output waveguide at the left side of the photo is square and transitions to a diagonal horn.

All testing was done using the same 900 GHz tripler as a driver. The diodes were current biased at 0.2 mA, which appeared close to optimum for all input power levels. At this bias, V_{bias} is 1.8V with no drive to the doubler, at a physical temperature of 90 K. At the maximum input power this bias decreases by about 0.4 V. This bias change at constant current (ΔV_{bias}) is proportional to input power in the square law limit, which is quite broad for a biased detector. Up to the maximum input power, the output power varies as ΔV_{bias}^2 , equivalent to P_{in}^2 , which indicates that the doubler is very underdriven. This is expected since for the 1500 GHz doubler, an input power of 2 mW was required

to get the output into the regime where it is linear with input power. The plot in Figure 5 shows the output power and also a curve proportional to ΔV_{bias}^2 for the doubler over the range of frequencies tested. As can be seen, there appears to be a very close correspondence between these two quantities over the full band, and it is much easier to measure bias voltage than output power at the very low power levels involved, which approach the limit of sensitivity of the power meter [7] used.

Input power was not measured in any detail over the band, but the curve of Figure 3 (for the tripler output) may be used as an indication of the power available, since this was measured under the same conditions as in the doubler tests. Only the tripler with 12 μm thickness was used in these subsequent tests. As may be seen, the output power exceeds 1 μW for an input power of ~ 0.4 mW. This is fully consistent with the results for the 1500 GHz doubler. The highest power point of 3 μW also occurs for an apparent input power of 0.4 mW but, being at a band edge point for both devices, may result simply from a favorable interaction where the tripler delivers more power than into a matched load.

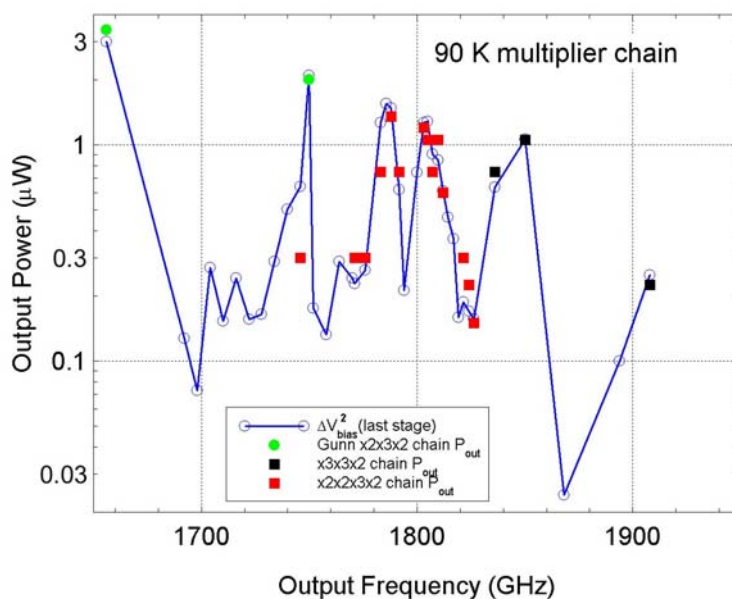


Figure 5. Output power from the 1800 GHz doubler, both measured (solid points) and estimated from the video response of the diodes (continuous line). Input power is as shown in Figure 3.

Figure 5 shows a general decrease in power at higher frequencies due to lower drive power, but the close correspondence between measured power and bias indicates that the output matching is quite flat. The input match shows no clear trend given the somewhat randomly spaced points and varying available power, but the power ripple is

higher than expected. It is possible that this results from a poor waveguide interface between the devices, either a poor flange joint, or significant mode conversion in the oversized waveguide. It is much higher than would be expected from the predicted VSWR of the two devices, since with a resistive doubler is actually fairly easy to get a good input match.

The properties of the various multipliers are summarized in Table 1. Efficiencies are well documented for the first two doubler stages but are only estimated for the last two stages. Efficiencies were not measured at room temperature for the higher stages, but it is expected that they operate similarly at room temperature because of the very high epilayer doping. The primary reason these tests were performed cold is to get the benefit of the increased power available near 300 GHz from the driver stages which use low doped diodes. Without this power the final stage would work too poorly to be even measurable.

Frequency	Number of diodes	Efficiency 90K	Epilayer doping
150 GHz	6	39%	1×10^{17}
300 GHz	4	28%	2×10^{17}
900 GHz	2	~5%	3×10^{17}
1800 GHz	2	~.2%	5×10^{17}

Table 1. Multiplier properties

While all details are not known, the overall $\times 24$ efficiency is a maximum of 7×10^{-6} . Because of the underdriven last stage, this would increase by a factor of ~ 3 at higher drive power, if the first two stages are operated in a power combined mode (two doublers in parallel with output combining). It is clear that the output power will not exceed $\sim 10 \mu\text{W}$ with the present limitations. With this method of operation there is potential for $\sim 1 \mu\text{W}$ output power above 2 THz with present technology, and in fact the required devices have been made as part of the same diode wafers used in this work.

Conclusions

A complete solid state source has been built for 1.8 THz using a net $\times 24$ multiplication, driven by a power amplifier. While tuning with good power is not continuous, there are a sufficient number of higher power points to indicate that a source with >200 GHz bandwidth and $>1 \mu\text{W}$ output is practical. It is likely that power combining will be needed for the first one or two stages in order to get sufficient power over the full band, but this is not inherently difficult, given the present state of planar technology. It appears that at least somewhat higher frequencies are feasible using the same approach.

Acknowledgement

This work was supported by NASA under contract 1239274 from JPL.

References

- [1] C.-Y. E. Tong., D. Meledin, D. Loudkov, R. Blundell, N. Erickson, J. Kawamura, I. Mehdi, and G. Gol'tsman, "A 1.5 THz Hot-Electron Bolometer Mixer Operated by a Planar Diode Based Local Oscillator", *IEEE MTT-S International Microwave Symposium Digest, 2003*, in press.
- [2] N. Erickson, T. Crowe, W. Bishop, R. Smith, S. Martin, "Progress in Planar Diode Balanced Doublers," *Tenth International Symposium on Space Terahertz Technology*, pp. 474-483, Mar. 1999.
- [3] N. Erickson, G. Narayanan, R.P. Smith, S.C. Martin, I. Mehdi, T.W. Crowe, and W.L. Bishop, "Planar Frequency Doublers and Triplers for FIRST," *Proceedings of the Eleventh International Symposium on Space Terahertz Technology*, pp. 543-551, May 2000.
- [4] N. Erickson, R. Smith, and S. Martin, "High Efficiency MMIC Frequency Triplers for Millimeter and Submillimeter Wavelengths," *IEEE MTT-S Int'l Microwave Symposium Digest*, Boston, June 2000.
- [5] G. Narayanan, N.R. Erickson, and R.M. Grosslein, "Low Cost Direct Machining of Terahertz Waveguide Structures," *Proceedings of the Tenth International Symposium on Space Terahertz Technology*, pp. 519-529, March 1999.
- [6] N. Erickson, G. Narayanan, R. Grosslein, G. Chattopadhyay, A. Maestrini, E. Schlecht, I. Mehdi, and S. Martin, "1500 GHz Tunable Source Using Cascaded Frequency Doublers," *Thirteenth International Symposium on Space Terahertz Technology*, pp. 177-186, Mar. 2002
- [7] N. Erickson, "A Fast, Very Sensitive Calorimetric Power Meter for Millimeter to Submillimeter Wavelengths," *Proceedings of the Thirteenth International Symposium on Space Terahertz Technology*, pp. 301-308, Mar. 2002.

W Band MMIC Power Amplifiers for the Herschel HIFI Instrument

Robert R. Ferber PhD, Todd C. Gaier PhD, John C. Pearson PhD, Lorene A. Samoska PhD,
Mary Wells, April Campbell
Jet Propulsion Laboratory, California Institute of Technology
4800 Oak Grove Drive, Pasadena, Ca 91125
Gerald Swift, Paul Yocom, K.T. Liao
Northrop Grumman Space Technology(NGST)
One Space Park, Redondo Beach, Ca 90278

ABSTRACT

This paper summarizes the development of W Band amplifiers for the Local Oscillator (LO) chains for the Herschel HIFI (Heterodyne Instrument for Far Infrared) Instrument. Key amplifier development issues and their solutions are presented, which have been applied on the way to realizing stable, wide-band amplifiers capable of producing 240 mW or greater RF power output across the 71 to 106 GHz frequency range. Development challenges addressed include: MMIC chip designs which initially had a variety of oscillation or “moding” propensities (mostly out-of-band), signal splitter and combiner development, matching of chip characteristics., power output control and leveling. The chosen design solutions are presented, including device, component and material selection for amplifier operation at cryogenic temperatures. Both room temperature and cryogenic (120 Kelvin) data is presented.

Keywords: GaAs, MMIC, mm-wave, W Band Amplifiers, Local Oscillator, Heterodyne Receiver, Herschel Space Observatory , radiometer

1. INTRODUCTION AND HIFI INSTRUMENT OVERVIEW

The HIFI receivers cover the frequency range of 480 GHz to 1900 GHz in six bands, using low noise superheterodyne receivers having superconducting HEB (Hot Electron Bolometers) or SIS (Superconductor-Insulator-Superconductor) mixers operating at about 2 Kelvin. These receivers, comprising the HIFI Instrument, will be the principal instrument of the Herschel Space Observatory. This European Space Agency observatory spacecraft is to be launched in 2007 to the L-2 Libration Point, where it will perform a 5 year mission to conduct a variety of astrophysics observations of star forming regions in the Milky Way Galaxy, as well as others.

NASA/JPL, with Northrop Grumman Space Technology(NGST,formerly TRW) as the principal contractor partner, is developing the amplifiers for the receiver local oscillator chains. The amplifiers, cooled to an operating temperature of approximately 130K, amplify a 0 dBm “W” Band signal up to + 23.6 dBm, or ~240 mW. The amplifier output is then coupled into a multiplier chain to produce the final LO injection signal in the range of 480 GHz to 1900 GHz.

This paper describes key amplifier development issues and their solutions, which have been applied on the way to realizing stable, wide-band amplifiers capable of

producing 240 mW or greater RF power output across the 71 to 106 GHz frequency range. The HIFI power amplifier design embodiment is based on an A-40 silicon-aluminum alloy package with six GaAs(Gallium Arsenide) HEMT(High Electron Mobility Transistors) MMIC(Monolithic Microwave Integrated Circuit) amplifier chips used in each amplifier. Development challenges addressed include: connector and package design to fit available space, MMIC chip designs which initially had a variety of oscillation or “moding” propensities (mostly out-of-band), signal splitter and combiner development and matching across the band, matching of chip characteristics for those chips installed in the parallel power combined arms of the amplifier, power output control and microstrip cavity moding. The chosen solutions to produce the desired results are presented, including device, component and material selection issues for amplifier operation at cryogenic temperatures. Cryogenic (120 Kelvin) and power output leveling performance data is also shown for the amplifier.

2. W BAND MMIC CHIP DEVELOPMENT & PROBLEM SOLUTIONS

In Figure 1 we show a two-stage, 71-84 GHz MMIC power amplifier, of similar type as those in Ref. [1], fabricated by NGST, using a 2 mil thick, 0.1 μ m GaAs PHEMT process. The design topology makes use of 4-way and 8-way microstrip power combiners to combine the FETs. The photograph indicates the two stages and the 8-parallel FETs combined in Stage 2. This type of cell is common for combining devices in parallel to achieve more power.

Early versions of this chip and similar chips for the HIFI Program produced oscillations in Ka-Band, which could not be corrected with off-chip bypass capacitors or other stabilization networks. The oscillations occurred between 30-50 GHz upon turn-on of the drain voltage, typically between $V_d=0.8$ V to $V_d=2.4$ V. The strongest oscillation observed was at 33 GHz. Since the oscillations

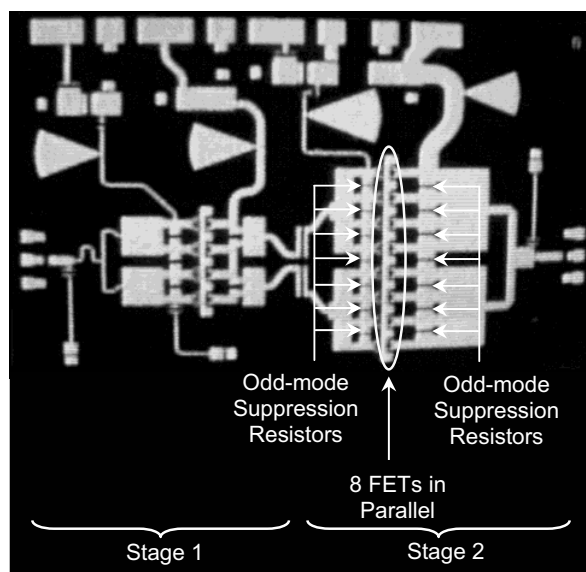


Fig. 1 Two Stage MMIC Power Amplifier Chip

occurred near the operating voltage of 2.5-3V and were expected to be more pronounced when cooled to the 120K operating temperature, we did simulations of the amplifier chips in order to understand and eliminate the oscillations. The analysis we have performed on the MMIC designs into the nature of the oscillations is described below. More details are found in Ref [2].

Two-port small-signal simulations of the amplifier chip in Figure 1 revealed no anomalies between 0-150 GHz, while the in-band stability factor, K , was greater than 2 between 60-85 GHz. In addition, the stability condition of each stage was carefully investigated to ensure that there was no overlap between the stability circles of one stage with the source mapping circles of the other stage. We then investigated two other ways to simulate the circuit, to cause the experimentally-verified oscillation at 33 GHz to appear in the simulations.

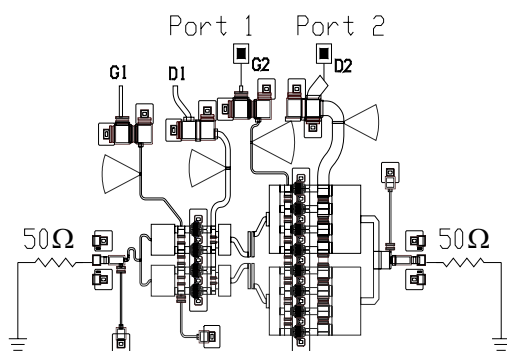


Fig. 2 Configuration for simulated K -factor analysis using the second stage bias lines as ports (Ref 3).

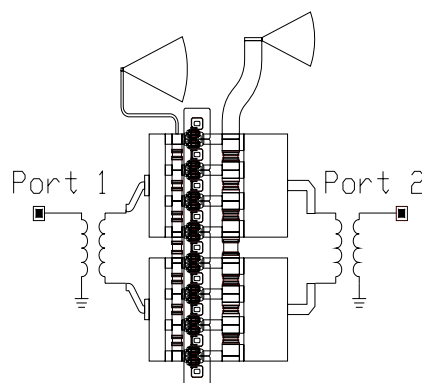


Fig. 3 Configuration for push-pull analysis of the second stage MMIC power amplifier.

We have performed two types of stability analysis. We focused our simulations on the second stage of the chip, since experimentally it appeared to be responsible for the 33 GHz oscillation. First, we performed a K -factor analysis using the bias lines in each stage of the amplifier chip as ports, as shown in Figure 2, according to Ref. [3]. The RF input and output of the circuit are terminated in 50 Ohms, while ports are inserted at the bias lines of the circuit. Port 1 is applied to the gate bias line while Port 2 is applied to the drain bias line. This method is usually applied to low frequency oscillations < 2 GHz, but it is also applicable to higher frequencies.

The second method we used to detect the instability in simulations was to apply a push-pull analysis to the second stage of the circuit, shown in Figure 3. In this method, the circuit is broken strategically at a point where the power is to be split into two legs, and an ideal transformer is inserted. The transformer serves to drive the two legs of the power splitter 180 degrees out of phase, thereby forcing an odd-mode condition. The transformer is applied at the input and output of the split circuit. Figure 3 shows the setup of the

problem in the linear simulator, and the K -factor is calculated between the input and output of *only* stage 2.

In order to make the instability more obvious in the simulations, we enhanced the value of transconductance, G_m , to twice its nominal value for the simulations. Although this is a relatively high value to use, such a theoretical exercise is more likely to make potential instabilities appear, and then correcting the circuit for large G_m values will make it more immune to stability problems. For HIFI, we are also planning to operate the circuit at cryogenic temperatures (120-130K), and we had observed an increase in G_m and circuit gain upon cooling.

The two analytical methods described above revealed that the 33 GHz oscillation was an odd-mode oscillation occurring because the damping of the odd-mode resistors separating the power-combined PHEMTs was insufficient to suppress instabilities. In simulation, we changed the value of the resistors from 50 ohms to 10 ohms, and moved the resistors closer to the PHEMTs. The simulations also indicated that a transient oscillation was present at 47 GHz, due to the first stage of the circuit. We made additional corrections to the first stage and also reduced the value of odd-mode suppression resistors to 10 ohms. In general, we have found that keeping the resistors very close to the PHEMTs is critical to making them work to eliminate instabilities.

The results of the simulations were applied to the MMIC circuit designs for HIFI, covering all the possible L.O. bands from 70-113 GHz, and several new circuit layouts were developed. New wafer fabrication runs were done at TRW(HPA3A & 4) and measurements of the chips were performed at JPL using a spectrum analyzer to check for instabilities up to 50 GHz. Whereas the original circuits exhibited 33 GHz and sometimes 47 GHz oscillations, all of the second-generation chips were stable and the oscillations were successfully removed using the methods described above.

3. HIFI AMPLIFIER DEVELOPMENT

Operation at cryogenic temperatures presents unique challenges for this Herschel HIFI application. Size, weight and power consumption also had to be addressed. An aluminum chassis is attractive because of low mass and high thermal conductivity. Yet, owing to its high coefficient of thermal expansion, aluminum becomes a difficult choice for this application where a 200 degree change in temperature will be experienced. Iron based alloys could have been employed to achieve a low coefficient of thermal expansion, but at the expense of high mass and low thermal conductivity. For this application, A40 Al-Si alloy was chosen as a compromise to achieve a moderate and acceptable coefficient of thermal expansion, good thermal conductivity, and low mass.

The five Herschel HIFI LO bands that must be covered span the frequency range of 71 to 113.5 GHz. The most obvious waveguide choice for this frequency range is WR-10, which has a nominal range from 75 to 110 GHz. Although 71 and 113.5 GHz are outside of the traditional WR-10 waveguide band, 71 GHz is still well above the WR-10 waveguide cutoff frequency (59 GHz), while 113.5 GHz is below the next higher order propagating mode in WR-10 waveguide (118 GHz). Since WR-10 waveguide was chosen

as the waveguide medium for all of the amplifier input and output ports, a common amplifier chassis design is used for all Herschel HIFI LO bands.

Figure 4 is a photograph of the Herschel HIFI W Band power amplifier. The WR 10 waveguide input port is visible on the chassis. The output port is on the opposite end.



Fig. 4 Amplifier Photograph

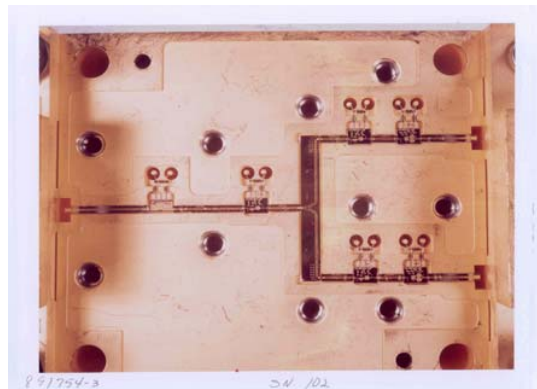


Fig. 5 Amplifier RF Cavity

Figure 5 shows the RF circuitry channelized inside the amplifier housing. Waveguide to microstrip transition is accomplished on the input port and on the output ports prior to power combining in the waveguide Magic “T” hybrid. The dc bias circuitry resides below the RF cavity and is brought up to the amplifier devices with glass bead feedthroughs, as can be seen in Figure 5. The six amplifier MMIC chips are clearly visible, along with the Wilkinson power splitter. The substrate material used for the microstrip elements is 125 micron quartz.

The TRW 0.1 micron GaAs process was chosen to achieve the required MMIC amplifier performance to well in excess of 100 GHz. The average G_m (transconductance) for the process is typically 695 mS/mm with F_t and F_{max} greater than 120 GHz and 200 GHz, respectively, Ref. [4]. The Herschel HIFI LO bandwidth specification imposed a

limit on the device size that could be employed to achieve power at such frequencies. A single power device might have been able to achieve close to the required 240 milliwatts from the amplifier, but this would have required that the amplifier be operated at drain voltages that might compromise long term reliability. For this reason, two power devices are operated in parallel, at reduced drain voltages to achieve the necessary 240 milliwatts output to drive the L.O. multiplier chains.

Several possible power combining approaches were examined for this application. These included Lange type hybrids, magic tee hybrids, branchline couplers, and Wilkinson and short slot hybrids. Figure 7 shows the various approaches considered. Figure 8 presents the results of the amplifier splitter/combiner trade studies.

For low loss power combining at the output of the amplifier, a waveguide magic tee hybrid was chosen. The magic tee hybrid provides close to full band performance. For this application, two tee-buttons were designed such that all five Herschel LO bands were addressed by use of only two magic tee designs.

A Wilkinson style power splitter was chosen because it is best suited for a low loss implementation in microstrip that is compatible with interconnecting substrates within the amplifier chassis. The five Herschel LO bands were covered with three Wilkinson designs.

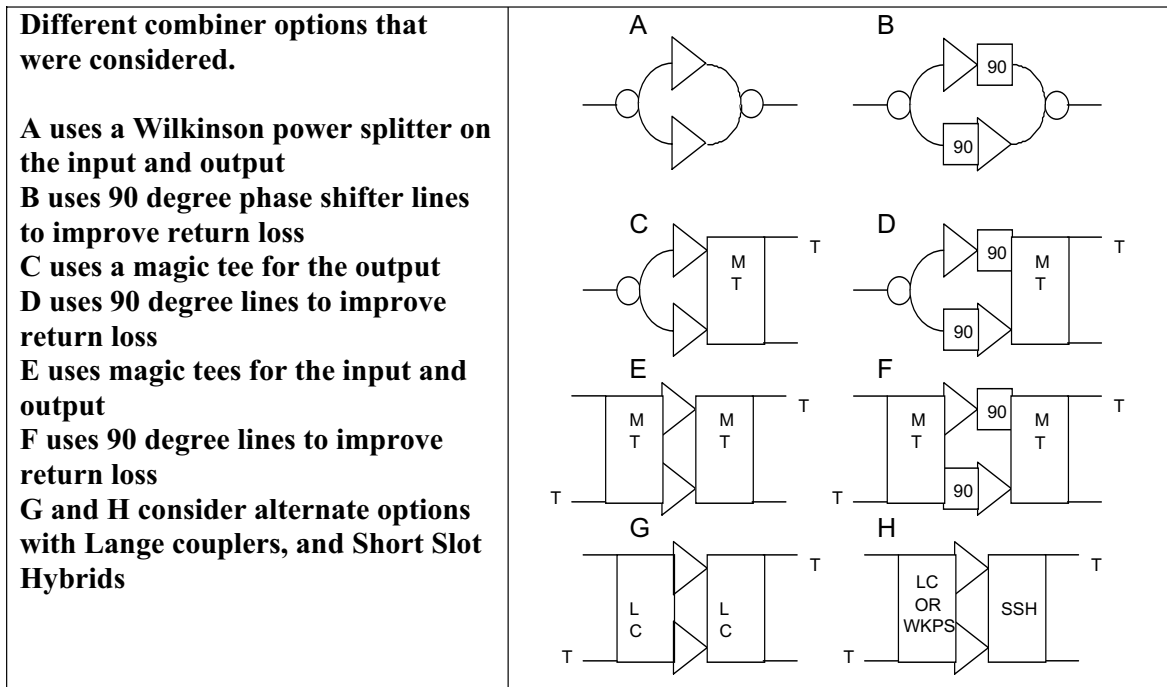


Fig. 7 Splitter/Combiner Options

Circuit	Advantages	Disadvantages
A	1) Low Cost 2) Allows single chip output	1) Moderate loss (1 dB?) 2) Output Return Loss not as good as "B"
B	1) Low Cost 2) Allows single chip output 3) Better Return Loss than "A"	1) More substrates needed 2) Better return loss than "A"
C	1) Magic tee provides good isolation 2) Magic tee is lower loss than Wilkinson	1) poorer output RL than "D" 2) Mechanical complexity
D	1) Magic tee provides good isolation 2) Magic tee is lower loss than Wilkinson	1) Mechanical complexity 2) Better return loss than "C"
E	1) Ideal for waveguide modules 2) Magic tee provides good isolation	1) Mechanical complexity
F	3) Ideal for waveguide modules 4) Magic tee provides good isolation	1) Mechanical complexity 2) Better return loss than "E"
G	1) Classic broadband balanced design 2) Good Output Return Loss	1) Lange Coupler Loss (2 dB?) 2)
H	1) Broadband 90 degree Hybrid 2) SSH works well with split block	3) Mechanical complexity 4) Less well characterized

Fig. 8 Splitter/Combiner Topology Design Trades

In-phase power combining and splitting techniques have the disadvantage that the resulting input and output return losses are for the most part, the same as the power-added gain of the devices that are being combined. Approach D of Fig. 7, using 90 degree phase delay for the combined devices, partially overcomes this disadvantage.

Consider the input Wilkinson power splitter when a 90 degree phase delay offset is included in one of the arms. The power is equally split, but the two signals arrive at the amplifier device offset by 90 degrees (at the design frequency). Reflections from the amplifier devices are also offset 90 degrees. On the return path, the same 90 degree phase delay offset is encountered and the reflected signals are 180 degrees out of phase when they arrive back at the power combiner. The reflected signals are then absorbed in the odd-mode isolation resistor, and ideally do not propagate any further. In this manner, excellent input and output return losses are achieved for the combined devices. An output isolator may not be required in this case.

Because the phase shift introduced by adding physical length in the combined arms is actually a time delay, the actual phase shift will vary as a function of frequency. As a

result, it was necessary to employ three different lengths of substrate to achieve sufficiently close to 90 degrees across the five Herschel HIFI LO operating bands.

4. AMPLIFIER PERFORMANCE

Room temperature amplifier performance example

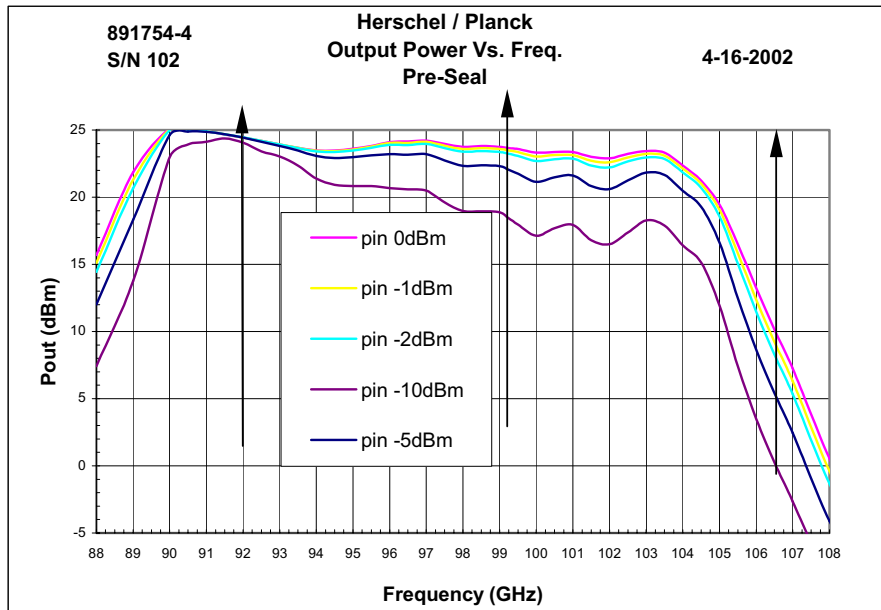


Fig. 9 Engineering Model(EM) Amplifier 102 Room Temperature Performance

Figure 9 shows the room temperature performance of Engineering Model(EM) amplifier serial no. 102. Greater than 23.6 dBm was achieved across the 92 to 106 GHz band, except for the high frequency edge of the band. Revised PA MMIC designs will correct this room temperature performance deficiency at the upper band edge.

Cryogenic performance example

Figure 10 shows the performance of EM amplifier serial # 102 at 120 Kelvin. A total of 9 EM amplifiers were built and all show repeatable and stable performance at room temperature and when cooled to temperatures as low as 60K.

5. POWER OUTPUT MODULATION AND CONTROL

A major challenge to the HIFI instrument is the adjustment of the local oscillator power so the mixers in the focal plane unit are optimally pumped. Additionally it is very useful as a diagnostic to be able to under or over pump SIS mixers. The result is a local oscillator subsystem requirement to be able to provide +3dB above the optimal and -10dB below the optimal LO power in something close to 0.5dB steps. Unfortunately no one knows what pump level the mixers really need or what the final in-flight or even in-lab

coupling will be. As a result, power output control flexibility over at least 15 dB is desirable in the local oscillator subsystem, as is extra power margin capability.

The power amplifier control unit(power supply) has the ability to adjust the amplifier drain voltage over 0V to +3.4 V in 2^{10} steps. The amplifier control module also has gate control with $-4V$ to $+2V$ adjustment in a nearly arbitrary 2^{16} steps. The output amplifiers are operated in saturation, so controlling the drain voltage changes the output voltage swing. With two additional wafer iterations and many MMIC design modifications, it has now been confirmed that the amplifier MMICs do not oscillate on chip under any bias condition that has been imposed. As a result, it was possible starting with the later EM amplifiers, to experiment using the drain bias to control the output power.

Figure 10 shows the 120K power vs output drain bias from less than 1V to more than 2.5V for S/N 102. All the other parameters (gates, input drains, RF level) were kept constant. From Figure 10, it can be shown that the output power increases slowly with turn on, then rapidly between 1.3 and 2.3V, and then saturates between 2.3 and 2.95V. We have found that the best power output, when at 120K, occurs at 3.1 (+/-0.1) V, however, long term operation at this high drain voltage may create a reliability liability, especially at high levels of RF input power.

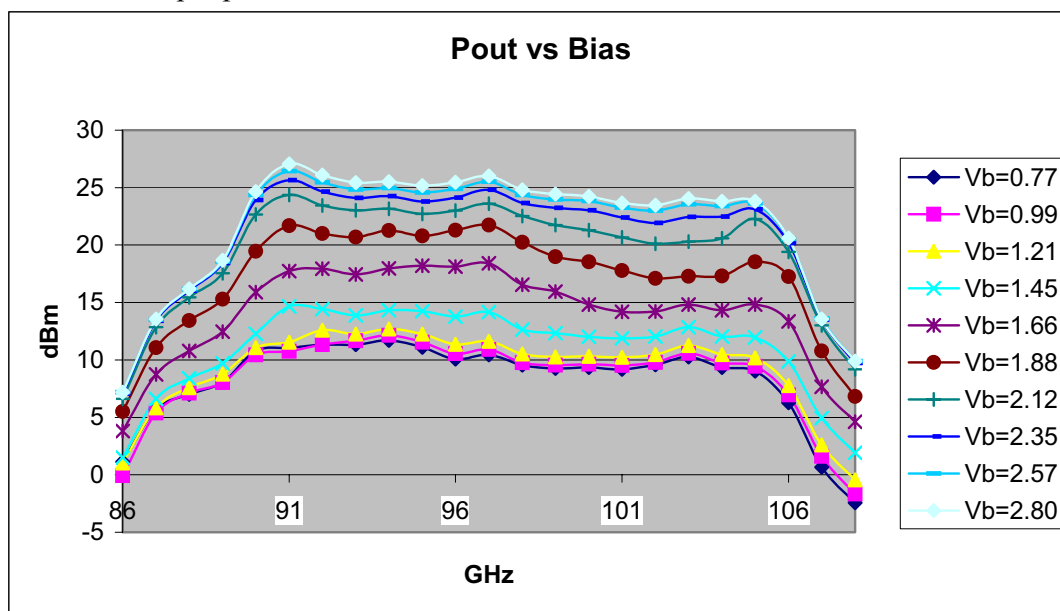


Fig. 10 S/N 102 power vs output drain voltage at 120K with +0dBm input

In order for the output power adjustment to function as desired, the power change with bias step needs to be evaluated. The bias supply can step in 3.3 mV steps, which correspond to approximately 60 steps between curves in Figure 12. The fastest change in output power is near 1.7 Volts, with S/N102 at 97 GHz between 1.45 and 1.65V. being the limiting case. This was 14.15 to 18.40 dBm or 4.25dB, which translates into a 0.072dB maximum step (if exponential). This is one order of magnitude finer than the 0.5dB

adjustability needed by the HIFI system. A more typical case is the 79 GHz points between 2.5 and 2.7V, where the power changes from 24.04 dBm to 24.62dBm. This is 0.58dB or 0.010dB/step(if exponential). If the step is evaluated in milliwatts of output power, these cases range from 0.6 to 1.0mW change per drain voltage step.

The data shows that the power amplifiers can be used to adjust the RF power output by more than 13dB by controlling one bias line(drain 2). The local oscillator control unit is currently designed with sufficient resolution to step the output power in steps of 0.08dB or less per step. The variability of the power amplifier dissipation (assuming we need 1V to 3V to adjust the power) would be on the order of 2 Watts.

6. SUMMARY AND CONCLUSIONS

The NASA/JPL Herschel HIFI Project, in partnership with TRW, has developed GaAs "W" Band power amplifier MMICs, which are stable at all frequencies(no in-band or out-of-band oscillations or other instabilities. These MMIC chip designs have been developed in three design types or categories for use in the power amplifiers developed for the Herschel HIFI instrument receiver L.O. chains.

Using these MMIC devices, multi-chip amplifiers have been developed for the HIFI Instrument L.O. chains. The power amplifiers utilize six MMICs to produce up to 240 mW(or more when operating at cryogenic temperatures) "W" Band RF output to drive the LO multiplier chains. The Herschel HIFI amplifiers include single MMIC amplifiers, 5 chip DM amplifiers, and the 6 chip Engineering Model amplifiers described in this paper. The 25 flight and flight spare amplifier deliveries are expected to be made to SRON(Space Research Organization, Netherlands) and ESA(European Space Agency) during 2003.

7.ACKNOWLEDGEMENT

This research was carried out at the Jet Propulsion Laboratory, California Institute of Technology, under a contract with the National Aeronautics and Space Administration.

8. REFERENCES

- [1] HWang, L. Samoska, T. Gaier, A. Peralta, H.H. Liao, Y. C. Leong, S. Weinreb, Y.C. Chen, M. Nishimoto, R. Lai, "Monolithic power amplifiers covering 70-113 GHz," *IEEE Trans. Microwave Theory Tech.*, vol. MTT-49, pp 9-16, Jan. 2001.
- [2] L. Samoska, Kun-You Lin, Huei Wang, Yun-Ho Chung, Michael Aust, Sander Weinreb, and Douglas Dawson, "On the Stability of Millimeter-Wave Power Amplifiers," *IEEE International Microwave Symposium Digest 2002*, Vol. 1, pp.429-432.
- [3] Steve C. Cripps, *RF power amplifiers for wireless communications*, Artech House, Boston, 1999.
- [4]Y.C.Chou, D.Leung, R. Lai, R. Grundbacher, D. Eng, J. Scarpulla, M. Barsky, P.H. Liu, M. Biedenbender, A. Oki, and D Streit, "Evolution of DC and RF Degradation Induced by High Temperature Accelerated Lifetest of Pseudomorphic GaAs and InGaAs/InAlAs/InP HEMT MMICs," *40th Annual International Reliability Physics Symposium, Dallas, Texas, 2002* pp. 241-247.

Broadband Submillimeter Receiver and Source Development

J.L. Hesler, D.W. Porterfield, W.L. Bishop, D.S. Kurtz and T.W. Crowe
Virginia Diodes, Inc.
Charlottesville, VA
www.virginiadiodes.com

This talk will describe recent developments in broadband fixed-tuned receivers and sources at millimeter and submillimeter wavelengths. These components rely on a strong fusion between novel integrated planar diode technology and innovative broadband circuit topologies. Using these methods excellent performance can be achieved over full-waveguide bands without the need for mechanical tuners or electrical bias.

Broadband multipliers have been developed over bands ranging from WR-12 (60-90 GHz) to WR-1.2 (600-900 GHz). As an example, a WR-3.4 tripler (220-330 GHz), pictured below, yields efficiencies of 2-4% over the band. WR-3.4 triplers optimized for different input power levels have been developed, with output powers ranging from $\frac{1}{4}$ mW to $1\frac{1}{2}$ mW for input powers from 15 mW to 50 mW. Broadband quintupler designs with efficiencies ranging from 0.2-0.6% have been developed. For example, a quintupler to 900 GHz has produced 66 μ W of output power using 20 mW of input power. A quintupler to 1.6 THz is currently under development.

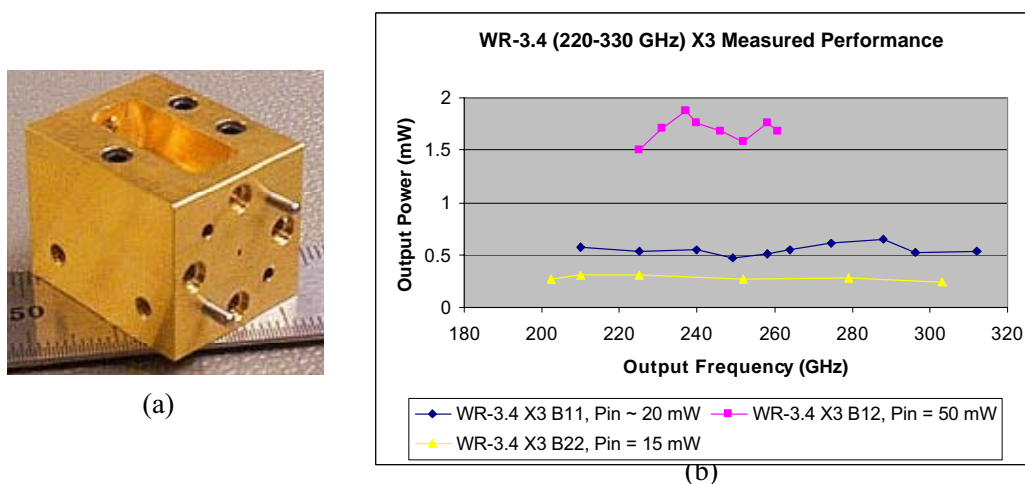


Fig. 1: (a) Picture of WR-3.4 Tripler, (b) measured performance.

A range of broadband receivers has also been developed, with RF bands ranging from WR-8 (90-140 GHz) to WR-1.7 (440-660 GHz). The subharmonic mixers use an LO at half the RF, and also provide LO noise suppression. Measurements at 600 GHz on a WR-1.7 subharmonic mixer have yielded a mixer noise temperature of 1550 K (DSB) and a conversion loss of 8 dB (DSB) using only 4 mW of LO power at 300 GHz. A WR-1.2 mixer covering the range from 600-900 GHz is currently under development.

Balanced varactor doublers are used to drive both the broadband multipliers and the mixers. A 300 GHz all-solid-state chain was used as the local oscillator for the 600 GHz mixer measurement. This doubler chain, with an output power in excess of 5 mW, consists of three cascaded doublers (at 75 GHz, 150 GHz and 300 GHz) driven by a commercially available millimeter-wave amplifier.

Design and analysis of 500 GHz heterostructure barrier varactor quintuplers

Mattias Ingvarson, Arne Øistein Olsen, and Jan Stake
Microwave Electronics Laboratory, Chalmers University of Technology,
SE-412 96 Göteborg, Sweden
E-mail: mattias.ingvarson@ep.chalmers.se

Abstract

We report on the design and analysis of heterostructure barrier varactor (HBV) frequency quintuplers with an output frequency of 500 GHz. The HBV is a symmetric varactor, thus only odd harmonics are generated and no DC bias is required. By incorporating several barriers in the device, the HBV is also capable of handling higher power levels than conventional varactors. This makes the HBV superior to the traditional Schottky varactor for high order frequency multiplier circuits. We present analytical, temperature dependent models, which can be used to calculate parameters such as optimum doping concentration, layer structure, device area and series resistance for HBVs, as well as to predict the performance with respect to conversion efficiencies and output power levels. These parameters are then further optimised by harmonic balance simulations in commercial microwave EDA tools, for which we have developed accurate device models. We investigate the influence of embedding impedance levels for optimum conversion efficiency by means of analytical expressions and harmonic balance simulations. Theoretical calculations predict a maximum diode conversion efficiency for a planar, six-barrier InGaAs HBV of more than 30%, for an input power level of 19 dBm. A waveguide circuit realisation of a 500 GHz HBV quintupler is presented.

1 INTRODUCTION

The heterostructure barrier varactor (HBV) [1] is a symmetric varactor consisting of a high band gap semiconductor (barrier), surrounded by moderately doped modulation layers of a semiconductor with a lower band gap. The barrier prevents electron transport through the structure. See Figure 1. When an external signal is applied to the HBV,

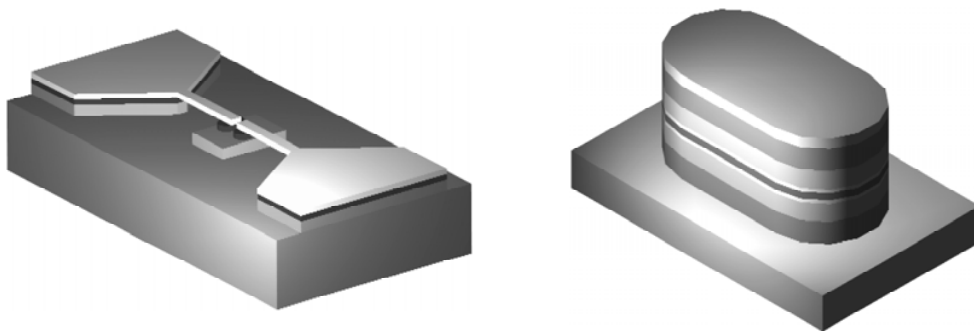


Figure 1 Schematic views of Chalmers planar HBV diode geometry (left) and a one-barrier HBV mesa (right).

are accumulated at one side and depleted at the other side of the barrier, causing a symmetric, voltage dependent capacitance. The symmetric C-V and anti-symmetric I-V characteristics of a typical HBV is shown in Figure 2.

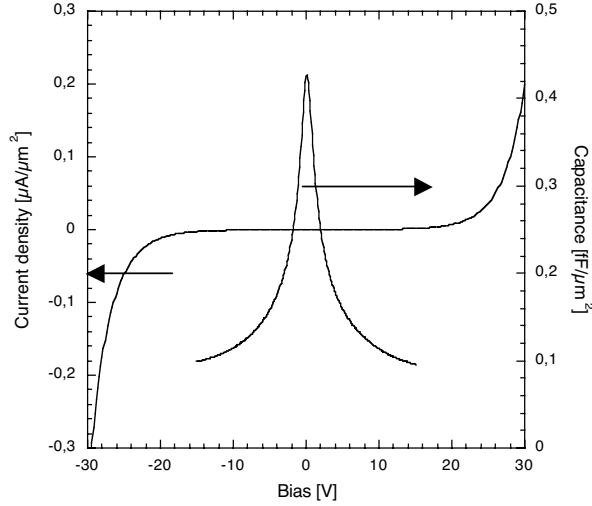


Figure 2. C-V and I-V characteristics of a typical HBV (CTH-ITME-1819).

The main advantage with HBVs is the possibility to tailor the layer structure of the device for various applications. The power handling capability can be increased by stacking several barriers epitaxially, or by series connecting mesas. The thickness and doping concentration of the modulation layers have a great influence on the dynamic cut-off frequency, which determines the conversion efficiency.

2 MATERIAL OPTIMISATION

2.1 Material system

HBVs are exclusively fabricated from III-V heterostructures, principally GaAs/AlGaAs on GaAs and InGaAs/InAlAs on InP. GaAs based HBVs exhibit high breakdown voltages but suffer from a low electron mobility and excessive leakage, which lowers the conversion efficiency significantly [2]. State-of-the-art HBVs are fabricated using $\text{In}_{0.53}\text{Ga}_{0.47}\text{As}/\text{In}_{0.52}\text{Al}_{0.48}\text{As}$ on InP [3]. This system offers higher electron velocities and the electron potential barrier is higher compared to GaAs based systems, which means lower leakage currents and, thus, higher conversion efficiencies of frequency multipliers.

2.2 Conversion efficiency

The conversion efficiency of an HBV is closely related to the dynamic cut-off frequency, which therefore needs to be maximised. The dynamic cut-off frequency is defined as

$$f_c = \frac{S_{\max} - S_{\min}}{2\pi R_s} \quad (1)$$

where S_{\max} and S_{\min} are the maximum and minimum elastances, respectively, and R_s is the series resistance. The diode conversion efficiency for quintupler operation can be approximated as

$$\eta \approx \frac{100}{1 + 200 \cdot \left(\frac{5}{3} \cdot \frac{f_p}{f_c}\right)^{1.5}} \% \quad (2)$$

where f_p is the pump frequency. For a typical HBV structure, the minimum elastance can be estimated as

$$S_{\min} = \frac{N}{A} \left(\frac{b}{\epsilon_b} + \frac{2s}{\epsilon_d} + \frac{2L_D}{\epsilon_d} \right) \quad (3)$$

where L_D is the extrinsic Debye length

$$L_D = \sqrt{\frac{kT\epsilon_d}{q^2 N_D}}. \quad (4)$$

In expressions (3) and (4),

N	number of barriers;
A	device area;
b	barrier thickness;
s	spacer layer thickness;
ϵ_b	dielectric constant of the barrier material;
ϵ_d	dielectric constant of the modulation layer;
k	Boltzmann constant;
T	device temperature;
q	elementary charge;
N_D	doping concentration in the modulation layer.

The maximum elastance S_{\max} during a pump cycle is determined by the drive level of the HBV, defined as

$$drive = \frac{\max(Q(t))}{Q_{\max}} \quad (5)$$

where Q_{\max} is the charge at the turn-on voltage, $V_{j,\max}$ [4]. Optimum performance is achieved with a maximum elastance swing, low conduction current and drive=1. Under these conditions, the maximum elastance is limited by

$$S_{\max} = \frac{N}{A} \left(\frac{b}{\epsilon_b} + \frac{2s}{e_d} + \frac{w_{\max}}{\epsilon_d} \right) \quad (6)$$

where w_{\max} is the maximal extension of the depletion region. For InP based HBVs, w_{\max} is determined by one of the following conditions:

1. depletion layer punch-through, i.e. $w_{\max} = l_D$ where l_D is the thickness of the modulation layers;
2. large electron conduction from impact ionisation at high electric fields;
3. current saturation, i.e. the saturated electron velocity in the material determines the maximum length an electron can travel during a quarter of a pump cycle.

For condition 2, w_{\max} can be calculated as

$$w_{\max} = \frac{\epsilon_d E_{d,\max}}{qN_D} \quad (7)$$

where $E_{d,\max}$ is the maximum electric field in the modulation layer at break-down. For condition 3, w_{\max} can be estimated as

$$w_{\max} \approx \frac{v_{\max}}{8f_p}, \quad (8)$$

where v_{\max} is the saturated electron velocity [5].

2.2.1 Series resistance

The series resistance R_s of a planar HBV can be estimated as

$$R_s = R_{\text{active}} + 2R_c + 2R_{cl} + R_{\text{spread.buffer}} \quad (9)$$

where

R_{active}	resistance of the active layers;
R_c	(ohmic) contact resistance;
R_{cl}	resistance of the contact layers;
$R_{\text{spread.buffer}}$	buffer layer spreading resistance.

The mesa resistance is estimated by

$$R_{\text{active}} = \frac{(N+2) \cdot l_D}{\mu_D N_D qA} \quad (10)$$

where μ_D is the low field mobility of the modulation layer. The contact resistance is

$$R_c = \frac{r_c}{A} \quad (11)$$

where the specific contact resistance, r_c , depends on the ohmic contact process used, and can be measured by the Transfer Length Method [6]. The resistance of the contact layers is estimated by

$$R_{cl} = \frac{l_{cl}}{\mu_{cl} N_{cl} q A} \quad (12)$$

where l_{cl} , μ_{cl} and N_{cl} are the thickness, low field mobility and doping concentration, respectively, of the contact layers. The buffer layer spreading resistance is the resistance between the two mesas used in the planar geometry, and can be estimated as

$$R_{spread,buffer} = \frac{l_{buff}}{\mu_{buff} N_{buff} q A_{buff}} \quad (13)$$

where l_{buff} and A_{buff} are the equivalent spreading length and area, and μ_{buff} and N_{buff} are the low field mobility and doping concentration, respectively, of the buffer layer between the mesas. l_{buff} and A_{buff} are extracted from FEM simulations performed by FEMLAB.

The low field mobility of the InGaAs contact and modulation layers as a function of doping concentration N and temperature T is calculated using the model reported by Sotoodeh *et al.* [7],

$$\mu(N, T) = \mu_{min} + \frac{\mu_{max} (300K)(300K/T)^{\theta_1} - \mu_{min}}{1 + \left(\frac{N}{N_{ref} (300K)(T/300K)^{\theta_2}} \right)^{\lambda}}, \quad (14)$$

where μ_{min} , μ_{max} , N_{ref} , λ , θ_1 and θ_2 are fitting parameters available for several III-V compounds.

2.2.2 Optimum doping concentration

By using expressions (3), (6) and (9), the dynamic cut-off frequency can be calculated from (1). Figure 3 shows the cut-off frequency versus doping concentration for an InP HBV structure with 2 to 8 barriers. In order to achieve feasible impedance levels, the area in these calculations is chosen so that

$$\frac{1}{2\pi f_p C_{max}} = 100. \quad (15)$$

From Figure 3 it can be seen that the optimum doping concentration in the modulation layers is around 10^{23} m^{-3} . However, it should be emphasised that no effect due to self-heating has been considered in the calculations for Figure 3. If too many barriers are stacked epitaxially the device temperature will be very high, which degrades the cut-off frequency [8]. Also, the area for each data point in Figure 3 is chosen according to (15), which means that the area is not constant.

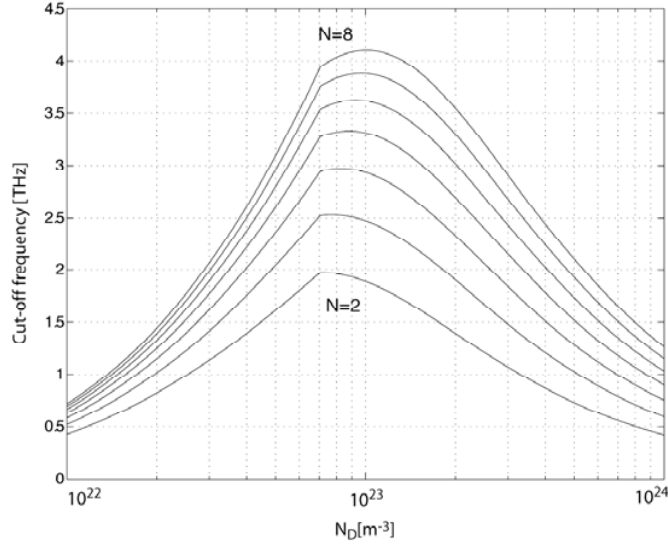


Figure 3 Cut-off frequency versus modulation layer doping concentration for an InP based HBV material with $N=2$ to $N=8$ barriers.

3 OPTIMUM IMPEDANCE LEVELS

This section investigates optimum embedding impedance levels for 500 GHz HBV quintuplers. First, analytical expressions are used to estimate optimum impedances for a given HBV structure, see e.g. [9]. These impedances are then optimised in Microwave Office, using an in-house HBV model, to predict the performance in terms of conversion efficiency and maximum voltage.

3.1 Harmonic balance simulations

This section presents the results obtained from harmonic balance simulations of HBVs for 500 GHz quintupler applications. All simulations have been carried out using Microwave Office, for which we have developed an accurate HBV diode model. The model is based on the following expression for the voltage across the device versus the charge stored in the HBV [10]:

$$V(Q) = N \left(\frac{bQ}{\epsilon_b A} + 2 \frac{sQ}{\epsilon_d A} + \text{Sign}(Q) \left(\frac{Q^2}{2qN_D \epsilon_d A^2} + \frac{4kT}{q} \left(1 - e^{-\frac{|Q|}{2L_D A q N_D}} \right) \right) \right). \quad (16)$$

The available input power level around 100 GHz is typically 100 mW or 20 dBm. We assume that the input losses can be limited to 1 dB, and thus the pump power at 100 GHz is set to 19 dBm in all following simulations.

In order to exemplify, we use the fictitious material OPT, optimised for 500 GHz quintupler applications. The material is $\text{In}_{0.53}\text{Ga}_{0.47}\text{As}/\text{In}_{0.52}\text{Al}_{0.48}\text{As}$ on InP. Table I summarises the specifications for the OPT material.

Table I. Data for the fictitious HBV batch OPT.

N	b [nm]	s [nm]	l_D [nm]	N_D [m ⁻³]	A [μm ²]	R_s [Ω]	C_{max} [fF]	f_c [THz]
2 x 3	13	5	250	9.2·10 ²²	37	10.4	13	4.3

3.2 Simulation results

Harmonic balance simulations predict a diode conversion efficiency to 500 GHz of approximately 31% for the OPT HBVs. The device area is chosen to 37 μm², in order to assure that the modulation layers are fully depleted when pumped with 19 dBm of input power at 100 GHz. Figure 4 shows the embedding impedances for maximum conversion efficiency for OPT HBVs. The loci of the optimum impedance levels are closely related to the device area. This means that diodes with the same area but different parameters such as doping concentration, material system, number of barriers etc. require very similar embedding impedances for optimum performance.

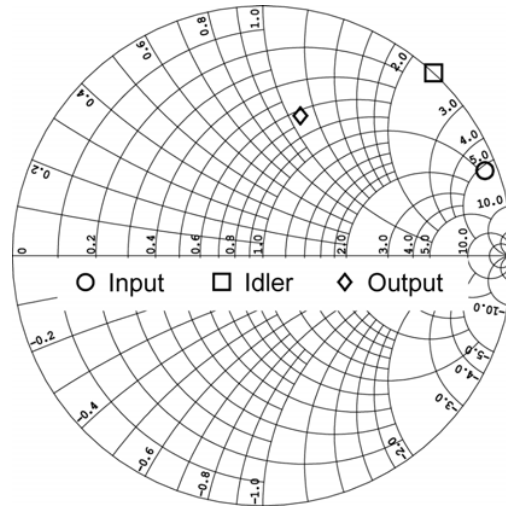


Figure 4. Optimum embedding impedances for OPT HBVs.

Figure 5 shows contour plots of the conversion loss for OPT HBVs, obtained from harmonic load pull simulations. The maximum conversion efficiency is 31%, corresponding to a minimum conversion loss of 5.1 dB. Each contour corresponds to an increase in conversion loss of 1 dB. From Figure 5 it is clear that the input matching is very crucial, whilst a non-optimum idler reflection coefficient will not have a very large impact on the circuit performance, as long as the reactance is kept smaller than the optimum value. An accurate impedance match at the input can be achieved by using moveable tuners.

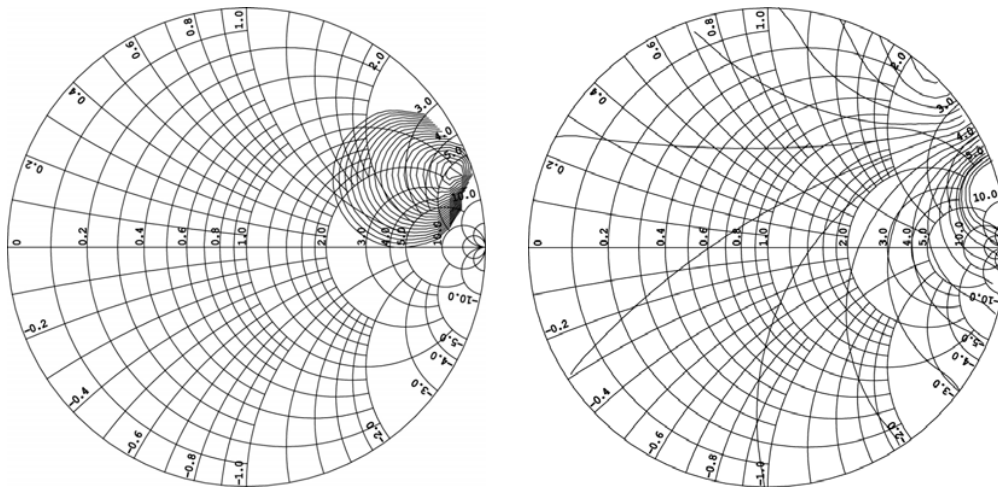


Figure 5. Conversion loss contours versus (left) input and (right) idler reflection coefficient. The minimum conversion loss is 5.1 dB and the contours correspond to an increase in conversion loss of 1 dB.

4 WAVEGUIDE CIRCUIT QUINTUPLER REALISATION

Given the relatively high frequency of operation, it is necessary to employ some kind of waveguide structure to realise a 500 GHz HBV quintupler. Figure 6 shows a possible microstrip waveguide circuit realisation, highly suitable for monolithic integration, where the HBV is embedded along with parts of the matching network on a common substrate. This design is based on the HBV tripler design reported by Olsen *et al.* [11]. The fifth and idler impedances are realised using microstrip components, whilst the fundamental frequency is matched using tuners in the input waveguide. It is also possible to use a backshort in the output waveguide to further adjust the embedding impedance levels. However, the aim is that the final version of this circuit shall be fixed tuned at the output. The microstrip circuit is placed in a narrow channel between the input and output waveguides. Beam leads are used to attach the circuit to the waveguide block. A membrane technique with a very thin supporting substrate, e.g. BCB, can be employed to realise this topology. The whole circuit will thus be positioned in air, and the medium will then support a more pure TEM-mode compared to the microstrip mode.

The standard type Archer waveguide has a reduced height across the diode, but this design uses a standard height waveguide. This makes the waveguide block very flexible, as only the microstrip circuit needs to be replaced when different designs are to be tested. A drawback with this approach is that the planar circuit elements exhibit higher losses compared to traditional waveguide elements.

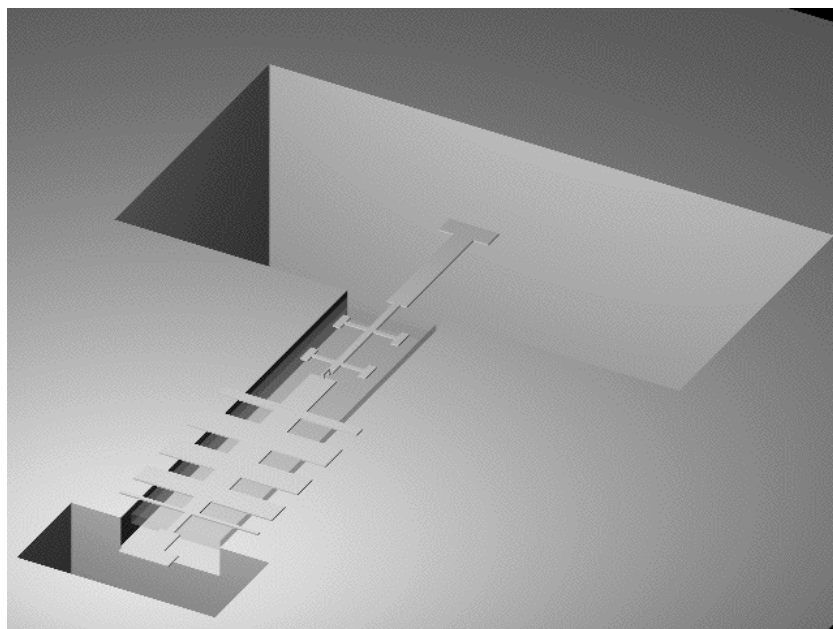


Figure 6. A possible microstrip/waveguide realisation of a 500 GHz HBV quintupler.

Figure 7 shows the simulated performance of an ideal element version of the quintupler circuit in Figure 6, when an OPT HBV is employed. The input power is 19 dBm at 100 GHz. The 3-dB bandwidth is approximately 5% and the conversion efficiency, as expected, 31%.

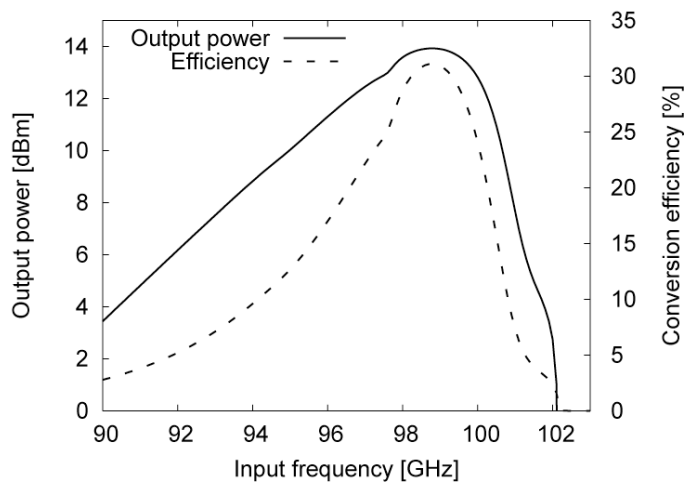


Figure 7. Simulated output power and conversion efficiency for an ideal element version of the circuit in Figure 6. The input power is 19 dBm, and an OPT HBV is used.

Conclusions

We have presented methods for the design and analysis of HBV frequency quintuplers with an output frequency of 500 GHz. HBVs were optimised using analytical, temperature dependent models. Optimum embedding impedances and estimated circuit performance were obtained from harmonic balance simulations in Microwave Office, for which HBV models have been developed. Finally, a possible microstrip/waveguide circuit realisation has been presented. An ideal element version of this circuit exhibits a maximum conversion efficiency of approximately 31% with a 3-dB bandwidth of 5%.

Acknowledgement

The authors would like to thank Professor Erik Kollberg for his continuous support and advice, and for being a great source of inspiration. This work is supported by the European Space Agency through the HBV Multiplier project, and the Swedish Foundation for Strategic Research, SSF.

References

- [1] E. L. Kollberg and A. Rydberg, "Quantum-barrier-varactor diode for high efficiency millimeter-wave multipliers", *Electronics Letters*, vol. 25, pp. 1696-1697, 1989.
- [2] J. Stake, L. Dillner, S. H. Jones, C. M. Mann, J. Thornton, J. R. Jones, W. L. Bishop and E. L. Kollberg, "Effects of Self-Heating on Planar Heterostructure Barrier Varactor Diodes", *IEEE Transactions on Electron Devices*, vol. 45, pp. 2298-2303, 1998.
- [3] X. Mélique, A. Maestrini, E. Lheurette, P. Mounaix, M. Favreau, O. Vanbésien, M. Goutoule, G. Beaudin, T. Nähri and D. Lippens, "12% efficiency and 9.5 dBm output power from InP based heterostructure barrier varactor triplers at 250GHz", IEEE MTT-S International Microwave Symposium. Digest, Anaheim, pp. 123-126, 1999.
- [4] J. Stake, S. H. Jones, L. Dillner S. Hollung and E. L. Kollberg, "Heterostructure Barrier Varactor Design", *IEEE Transactions on Microwave Theory and Techniques*, vol. 48, pp. 677-682, 2000.
- [5] E. L. Kollberg, T. J. Tollmunen, M. A. Frerking and J. R. East, "Current Saturation in Submillimeter Wave Varactors", *IEEE Transactions on Microwave Theory and Techniques*, vol. 40, pp. 831-838, 1992.
- [6] R. Williams, *Modern GaAs Processing Methods*, 2nd ed.: Artech House, 1990.
- [7] M. Sotoodeh, A. H. Khalid, and A. A. Rezazadeh, "Empirical low-field mobility model for III-V compounds applicable in device simulation codes", *Journal of Applied Physics*, vol. 87, no. 6, pp. 2890-2900, 2000.
- [8] B. Alderman, J. Stake, L. Dillner, D. P. Steenson, M. Ingvarson, E. Kollberg, C. Mann and J. Chamberlain, "A New Pillar Geometry for Heterostructure Barrier Varactor Diodes", Twelfth International Symposium on Space Terahertz Technology, 2001.
- [9] E. L. Kollberg, J. Stake and L. Dillner, "Heterostructure barrier varactors at submillimetre waves", *Phil. Trans. R. Soc. Lond.* vol. 354, pp. 2383-2398, 1996.
- [10] L. Dillner, J. Stake and E. L. Kollberg, "Modeling of the Heterostructure Barrier Varactor Diode", 1997 International Semiconductor Device Research Symposium, Charlottesville, pp. 179-182, 1997.
- [11] Ø. Olsen, M. Ingvarson, and J. Stake, "A Low Cost Fixed Tuned F-band HBV Frequency Tripler," presented at IEEE MTT-S International Microwave Symposium, Philadelphia, 2003.

1400 – 1900 GHz Local Oscillators for the Herschel Space Observatory

John Ward, Frank Maiwald, Goutam Chattopadhyay, Erich Schlecht, Alain Maestrini¹, John Gill, and Imran Mehdi

California Institute of Technology, Jet Propulsion Laboratory, MS 168-314,
4800 Oak Grove Drive, Pasadena, CA 91109

¹Now at the Observatoire de Paris, 61 avenue de l'Observatoire, 75014 Paris, France

ABSTRACT

JPL continues to develop robust planar, all solid-state sources to cover the 1414 to 1908 GHz band. These sources will be used as local oscillators to drive hot electron bolometer (HEB) heterodyne mixers on the Herschel Space Observatory to observe high-resolution spectra in the interstellar medium such as the N⁺ and C⁺ fine structure lines at 1461 and 1901 GHz, water lines at 1661, 1670, and 1717 GHz, and OH lines from 1834 to 1838 GHz. We report our current progress and present recent results. Results include a 175 K measurement of 88 μ W at 1544 GHz and a room temperature measurement of 1 μ W output power at 1810 GHz.

I. INTRODUCTION

The Herschel Space Observatory is a 3.5 meter diameter passively-cooled telescope scheduled to launch in 2007. Its three science instruments (PACS, SPIRE, and HIFI) will observe the cosmos from 450 to 5000 GHz (60 – 670 μ m) [1]. Band 6 of the Heterodyne Instrument for the Far-Infrared (HIFI) [2] is a heterodyne spectrometer to cover 1414 to 1908 GHz. Table 1 provides a brief summary of the four local oscillator chains that will be required to pump HEB mixers to cover this band. The design operating temperature of the local oscillators is 120 K.

When the development of heterodyne receivers for the Herschel Space Observatory was initiated, state-of-the-art submillimeter sources typically consisted of cascaded whisker-contacted Schottky-diode frequency multipliers driven by phase-locked Gunn oscillators [3,4]. Frequency tuning was achieved with mechanical tuners, and multipliers were mechanically fragile. Above about 900 GHz, the available power was too low to pump a mixer, and so compact solid-state sources gave way to massive FIR lasers, where changing frequencies implies changing the gas in the laser, and frequencies produced must be chosen from a finite list of available laser lines. The goal of the effort described here is to produce mechanically robust, low volume, low mass, solid-state sources to pump heterodyne mixers from 1414 to 1908 GHz. Furthermore, these sources must be electronically tunable over at least 140 GHz of bandwidth, and must be suitable for high-reliability space applications.

Band	Chain	Output Frequency	Goal Output Power
Band 6 Low	6a	1414 – 1584 GHz	2.1 μW
	6b	1472 – 1696 GHz	2.1 μW
Band 6 High	6c	1704 – 1908 GHz	2.1 μW
	6d	1704 – 1908 GHz	2.1 μW

Table 1. Requirements and nomenclature for the four local oscillator chains comprising band 6 of the HIFI instrument for HERSCHEL. The operating temperature is 120 K.

II. IMPLEMENTATION

The requirements given in Table 1 will be implemented by multiplying high-power W-band sources by three or four cascaded frequency multipliers. Table 2 shows three available power amplifier bands [5] and all configurations under consideration to multiply these bands up to the required output frequencies. Note that while the 6a and 6b chain configurations are fixed, there are several configurations under consideration to reach band 6 high.

All multiplier devices with output frequencies below 1 THz are based on the JPL substrateless process [6-8] in which the GaAs substrate under the integrated circuit is etched away to maximize conversion efficiency. The final, highest-frequency multipliers are based on the JPL membrane process [8,9], in which the circuit is fabricated on a 3 μm thick GaAs membrane. Figure 1 shows a membrane-based 1500 GHz balanced doubler with the device sitting inside the split waveguide block. A photo of the assembled multiplier chain along with the W-band power amplifier is shown in Figure 2. All multipliers employ balanced, multi-diode configurations to achieve high efficiency, high power, and broad bandwidth (approximately 8 to 13%) without any mechanical tuning. Low-loss waveguide matching circuits further contribute to the efficiency of these designs.

Power Amp	71 – 79.5 GHz 230 mW	88 – 99.5 GHz 230 mW	92 – 106 GHz 230 mW
x2x2x2x2		1408 – 1592 GHz Chain 6a	1472 – 1696 GHz Chain 6b
x2x3x3			1656 – 1908 GHz Band 6 high
x2x2x3x2	1704 – 1908 GHz Band 6 high		
x2x2x2x3	1704 – 1908 GHz Band 6 high		

Table 2. Possible configurations for band 6. The three columns represent available power amplifier bands, while the four rows show possible configurations of frequency doublers and triplers. Note that there are three different possibilities for band 6 high.

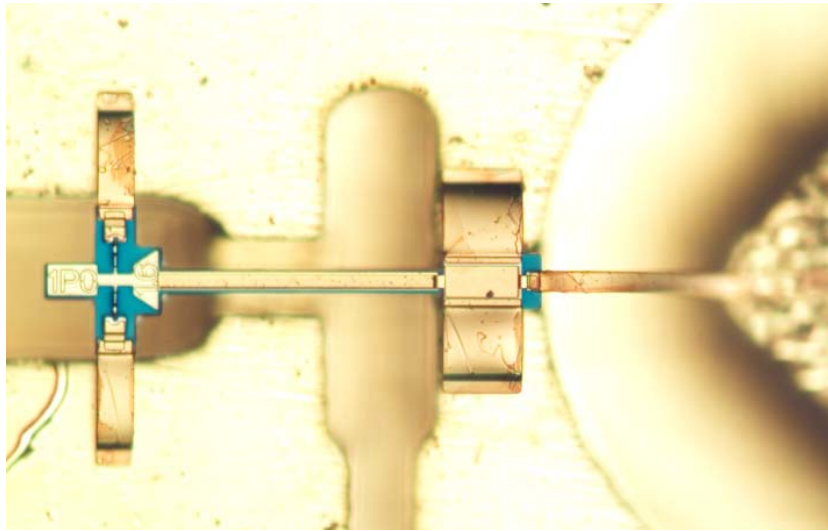


Figure 1. A 1500 GHz balanced doubler. The input signal at 750 GHz enters through a waveguide tuning circuit from the left. Two Schottky diodes are located in the input waveguide, with cathodes grounded by beam leads. The 1500 GHz output signal is launched into the output waveguide at the bottom of the picture toward an integrated diagonal horn. DC bias for the diodes is brought in from the right.

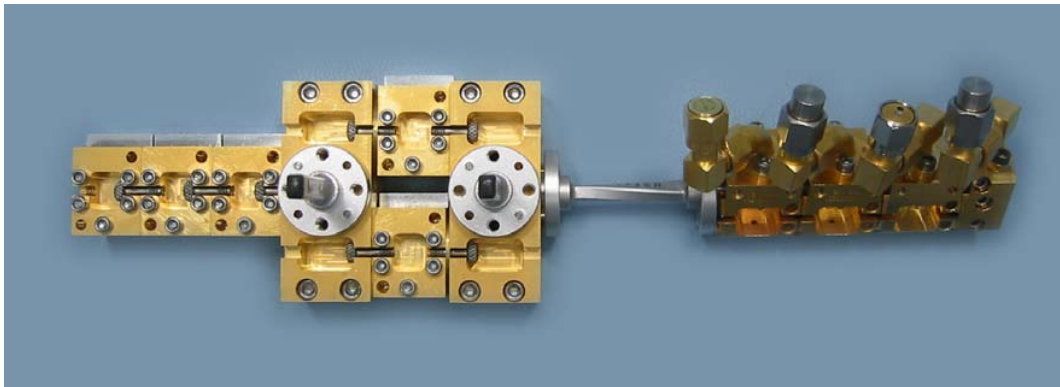


Figure 2. A 1500 GHz development local oscillator. From left to right: the 94 GHz input signal is amplified by a four-stage power-combined power amplifier, passes through a length of rectangular waveguide, and is multiplied up to 1500 GHz by four cascaded frequency doubler modules. The last multiplier includes an integrated diagonal horn, launching a Gaussian beam to the right. Note the absence of mechanical tuners: this source is electronically tunable over more than 100 GHz of bandwidth. Total length is about 20 cm.

III. RESULTS

Table 3 lists a summary of typical measured efficiencies and output powers for the multipliers being developed at JPL for the HIFI band 6 local oscillators. It should be noted that the measurement uncertainty ranges from less than 1 dB at the lowest frequencies and highest powers to about 3 dB for the highest-frequency measurements.

Figure 3 shows preliminary measurements of a 1500 GHz source. The W-band drive power into the first frequency doubler was 150 mW. The first two multiplier stages (200 and 400 GHz doublers) were originally developed for HIFI band 5 [6,7,10], the third stage 800 GHz doubler was a prototype for the 6b chain, and the final multiplier is the flight-model 1500 GHz doubler for the 6a chain. Although the frequency ranges of the stages are not optimally matched (low frequency performance should be improved by using all chain 6a multipliers) and none of the measurements were made at the nominal operating temperature of 120 K (multiplier efficiency improves with cooling, as clearly demonstrated in the figure), this chain is still able to meet the required output power over at least 120 GHz of bandwidth. The power needed to optimally pump an HEB mixer in this band has been experimentally demonstrated to be about 1 μ W [11]. To improve the long-term stability of this chain, the excess power across the band will be traded for increased lifetime by running at lower W-band input power, reduced diode current densities, and more conservative bias voltages. A more detailed look at this chain will be given in [12].

Output Frequency	Multiple	Intended Use	Typical Efficiency	Typical Power
176 – 199 GHz	2	Chain 6a, stage 1	30%	40 mW
352 – 398 GHz	2	Chain 6a, stage 2	20%	8 mW
704 – 796 GHz	2	Chain 6a, stage 3	Untested	
1408 – 1592 GHz	2	Chain 6a, stage 4	2%	30 μ W
184 – 212 GHz	2	Chain 6b, stage 1 Band 6 high, stage 1	30%	40 mW
368 – 424 GHz	2	Chain 6b, stage 2	Untested	
736 – 848 GHz	2	Chain 6b, stage 3	15%	1 mW
1472 – 1696 GHz	2	Chain 6b, stage 4	Untested	
552 – 636 GHz	3	Band 6 high, stage 2	Untested	
1704 – 1908 GHz	3	Band 6 high, stage 3 or 4	0.02%	1 μ W
152 – 159 GHz	2	Band 6 high, stage 1	Untested	
304 – 318 GHz	2	Band 6 high, stage 2	Untested	
608 – 636 GHz	2	Band 6 high, stage 3	Untested	
1704 – 1908 GHz	2	Band 6 high, stage 4	Untested	

Table 3. Multipliers being actively developed for band 6. Typical efficiencies and powers represent peak values for room temperature measurements, or values with several percent bandwidth at 120 K. Best measured peak powers at 120 K are about a factor of two higher in all cases except the 1704 – 1908 GHz tripler, which has only been tested at room temperature.

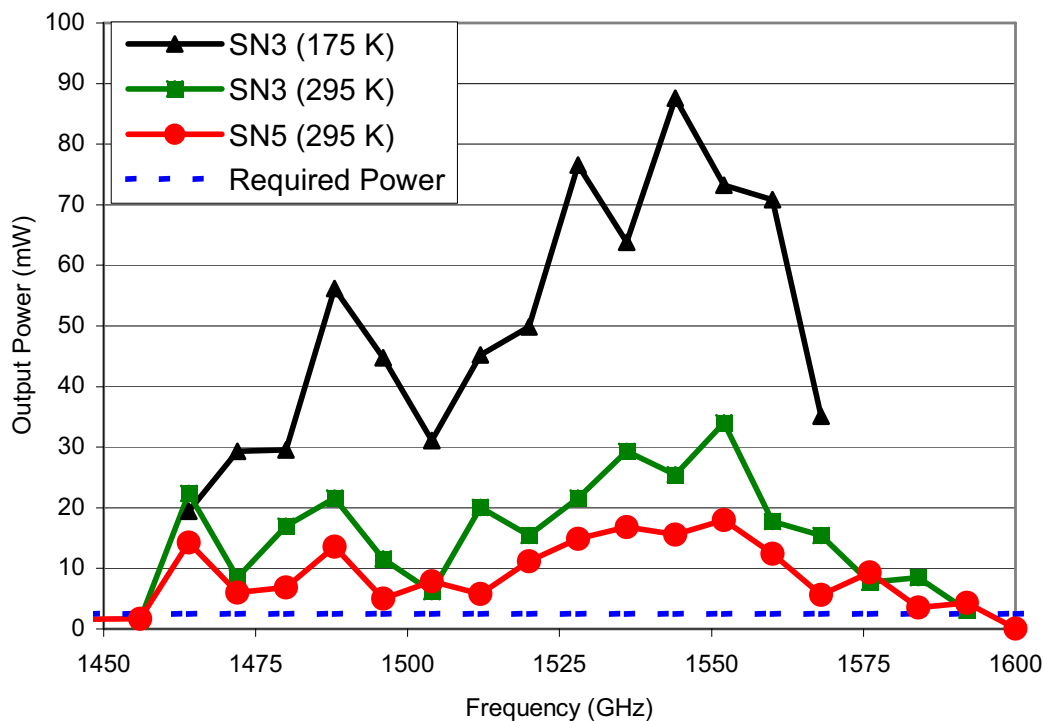


Figure 3. Output power as measured from a chain nearly identical to that shown in Figure 2. The W-band drive power into the first frequency doubler was 150 mW. The two measured multipliers use the exact same device geometry. Differences in the measured performance at room temperature are probably due to variations in fabrication and assembly, and coincidentally are representative of the overall measurement accuracy. The required power shown is the $2.1 \mu\text{W}$ specification for Herschel.

Implementing solid-state sources to cover the 1700 to 1900 GHz band is substantially more difficult than for the 1400 to 1700 GHz band. Not only do Schottky diode multipliers become less efficient at higher frequency, but also frequencies above 1700 GHz cannot be reached from currently available power amplifier bands with four cascaded frequency doublers. Therefore, at least one multiplier must be a tripler. Since the most difficult multiplier to design and build for this chain is the highest frequency stage, a tripler covering the 1700 to 1900 GHz range was designed and fabricated even before a solid-state 600 GHz driver chain was complete. Several triplers were assembled with devices of varying anode sizes, and were tested with a high-power 600 GHz backward-wave oscillator (BWO) at the University of Cologne. Figure 4 shows frequency sweeps of 3 different devices with 3 mW of input power, and Figure 5 shows the relation of output power to input power. All of these results were measured at room temperature, and it is expected that the performance will improve upon cooling. Based on these preliminary results, to obtain power levels that are sufficient for pumping HEB mixers in this frequency range, very high input power will be required. However, the devices used for these tests have anodes that are not perfectly formed, leading to high parasitic shunting capacitance. Moreover, there is significant uncertainty in the optical coupling between the BWO and the tripler, and the

tripler and the power meter. We believe that drive stages for this multiplier will have enough power to sufficiently drive this multiplier in the final implementation. A detailed description of this tripler will be given in [13].

IV. CONCLUSIONS

Mechanically robust, broadband, electronically tunable, lightweight, compact terahertz sources suitable for pumping heterodyne mixers for space applications have been developed and demonstrated. In particular, $88 \mu\text{W}$ of peak RF power were measured at 1544 GHz and 175 K. This represents a substantial improvement in capability for deploying THz heterodyne receivers. The high power available and convenient electronic tunability also open up possibilities of a host of other applications. The next challenge is to produce LO sources with sufficient efficiency and reliability to meet flight hardware requirements in the 1700 – 1900 GHz range.

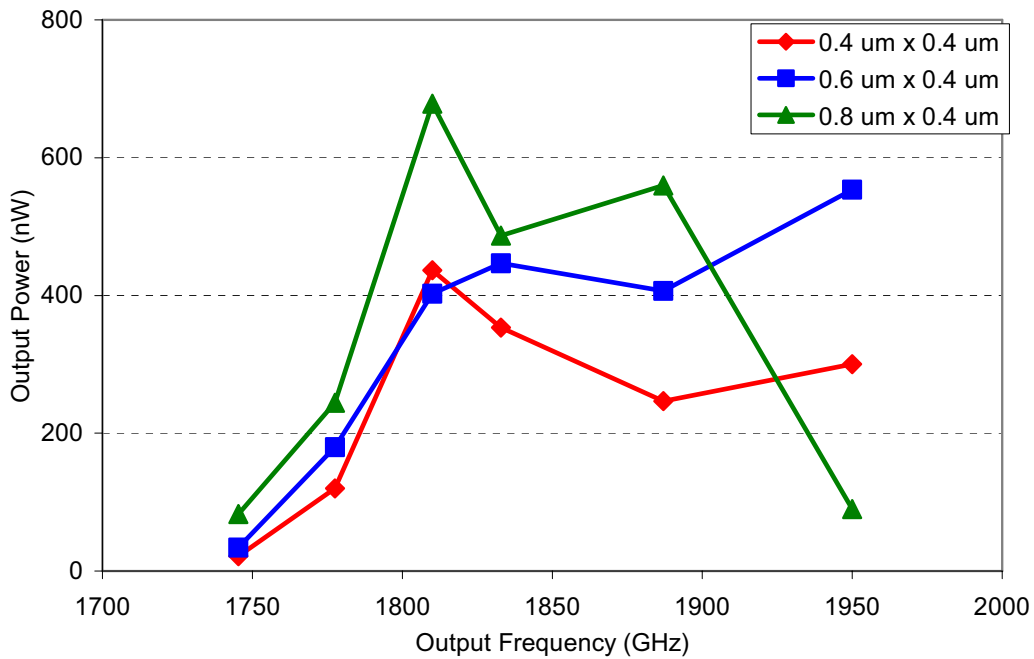


Figure 4. Measured frequency response of 1800 GHz tripler with approximately 3 mW input power at room temperature for devices with three different anode sizes.

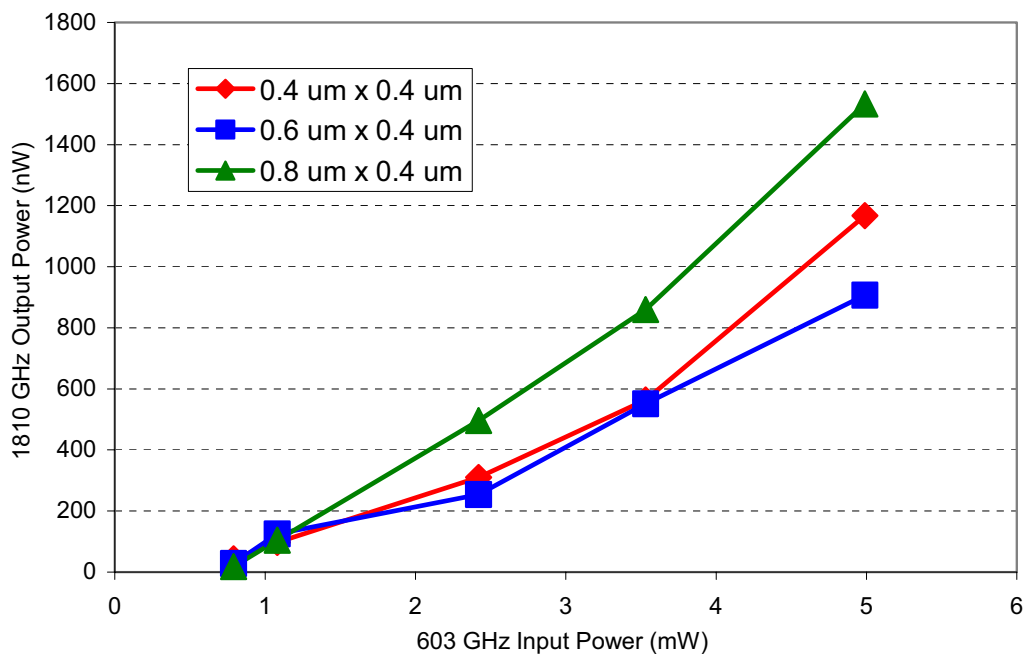


Figure 5. Measured output power of 1800 GHz tripler as a function of input power at room temperature for devices with three different anode sizes. The upward curvature shows that efficiency improves with increased input power: the multiplier is under-pumped, even with 5 mW of incident input power.

ACKNOWLEDGEMENTS

The authors wish to thank Katherine Ellis and Matt Dickie for their roles fabricating Schottky devices, and Peter Bruneau and James Crosby for fabricating the waveguide blocks. We also thank Ray Tsang and Alex Peralta for assembling the multipliers and Hamid Javadi, Brad Finamore, and David Pukala for testing them. The authors are grateful to Dr. Frank Lewen, Dr. Urs Graf, and Sandra Bruenken of the I. Physikalisches Institut der Universitaet zu Koeln for helping set up and conduct the measurements of the 1800 GHz triplers, and wish to thank Dr. J. Stutzki and Dr. G. Winnewisser for use of their laboratory. Technical discussions with Neal Erickson of the University of Massachusetts are gratefully acknowledged. The research described in this publication was carried out at the California Institute of Technology's Jet Propulsion Laboratory under a contract with the National Aeronautics and Space Administration.

REFERENCES

1. G.L. Pilbratt, "The Herschel Mission, Scientific Objectives, and this Meeting," Proceedings of The Promise of the Herschel Space Observatory Symposium, 12-15 December 2000, Toledo, Spain, eds. G. L. Pilbratt, J. Cernicharo, A. M. Heras, T. Prusti, R. Harris, ESA SP-460, pp. 13-20, 2001.

2. N. D. Whyborn, "The HIFI Heterodyne Instrument for FIRST: Capabilities and Performance," Proc. ESA Symp., The Far Infrared and Submillimetre Universe, ESA SP-401, 1997.
3. John E. Carlstrom, Richard L. Plambeck, and D. D. Thornton, "A Continuously Tunable 65-115 GHz Gunn Oscillator," IEEE Transactions on Microwave Theory and Techniques, Vol. MTT-33, No. 7, July 1985.
4. Neal Erickson, "High Efficiency Submillimeter Frequency Multipliers," IEEE MTT-S Digest, 1990.
5. Robert R. Ferber, John C. Pearson, Todd C. Gaier, Lorene A. Samoska, Frank W. Maiwald, Mary Wells, April Campbell, Gerald Swift, Paul Yocom, and K. T. Liao, "W-Band MMIC Power Amplifiers for the Herschel HIFI Instrument," Proceedings of the Fourteenth International Symposium on Space Terahertz Technology, Tucson, 22 April 2003.
6. E. Schlecht, J. Bruston, A. Maestrini, S. Martin, D. Pukala, R. Tsang, A. Fung, R. P. Smith, I. Mehdi, "200 and 400 GHz Schottky Diode Multipliers Fabricated with Integrated Air-Dielectric 'Substrateless' Circuitry," Proceedings of the Eleventh International Symposium on Space Terahertz Technology, Ann Arbor, Michigan, May 1-3, 2000.
7. E. Schlecht, G. Chattopadhyay, A. Maestrini, A. Fung, S. Martin, D. Pukala, J. Bruston and I. Mehdi, "200, 400 and 800 GHz Schottky Diode 'Substrateless' Multipliers: Design and Results," IEEE Int. Microwave Symp. Digest, pp. 1649-1652, Phoenix, AZ, May 2001.
8. Suzanne Martin, Barbara Nakamura, Andy Fung, Peter Smith, Jean Bruston, Alain Maestrini, Frank Maiwald, Peter Siegel, Erich Schlecht and Imran Mehdi, "Fabrication of 200 GHz to 2700 GHz Multiplier Devices using GaAs and Metal Membranes," IEEE MTT-S International Microwave Symposium, Phoenix, Arizona, May 20-25, 2001.
9. J. Bruston, S. Martin, A. Maestrini, E. Schlecht, P. Smith, and I. Mehdi, "The Frameless Membrane: a Novel Technology for THz Circuits," Proceedings of the Eleventh International Symposium on Space Terahertz Technology, Ann Arbor, June 2000.
10. Frank Maiwald, Erich Schlecht, Alain Maestrini, Goutam Chattopadhyay, John Pearson, David Pukala, and Imran Mehdi, "THz frequency multiplier chains based on planar Schottky diodes," Proceedings SPIE, Astronomical Telescopes and Instrumentation, Waikoloa, Hawaii, 22-28 August 2002.
11. C.-Y. Edward Tong, Denis Meledin, Raymond Blundell, Neal Erickson, Jonathan Kawamura, Imran Mehdi, and Gregory Gol'tsman, "A 1.5 THz Hot-Electron Bolometer Mixer Operated by a Planar Diode Based Local Oscillator," To appear in the 2003 IEEE MTT-S International Microwave Symposium Digest, 2003.
12. G. Chattopadhyay, J. Ward, H. Javadi, J. Gill, E. Schlecht, and I. Mehdi, "An All Solid-State Broadband Frequency Multiplier Chain at 1500 GHz," to be submitted to the IEEE Transactions on Microwave Theory and Techniques, 2003.
13. A. Maestrini, John Ward, John Gill, G. Chattopadhyay, Frank Maiwald, Katherine Ellis, Hamid Javadi, and I. Mehdi, "A Planar-Diode Frequency Tripler at 1.9 THz," To appear in the 2003 IEEE MTT-S International Microwave Symposium Digest, 2003.

HgCdTe Photoconductive Mixers for 3-15 Terahertz

Albert Betz^a, Rita Boreiko^a, Yongdong Zhou^b, Jun Zhao^b, Yusuf Selamet^b, Yong Chang^b, Renganathan Ashokan^b, Charlie Bucker^{b,c}, and Sivalingam Sivananthan^b

^aCenter for Astrophysics & Space Astronomy, University of Colorado, Boulder, CO 80309

^bMicrophysics Laboratory & Department of Physics, University of Illinois at Chicago, IL 60607

^cPhysics Institute of Wuerzburg, Germany

ABSTRACT

We are developing HgCdTe photoconductive detectors for use as heterodyne mixers in the 3-15 THz band ($\lambda=20-100 \mu\text{m}$). These planar devices have the potential for a high quantum efficiency $\eta > 0.1$, a fast time response $\tau < 50 \text{ ps}$, a relatively low LO power requirement of $P_{\text{LO}} = 10-50 \mu\text{W}$, and an operating temperature of 10-30 K. The required thickness of the intrinsic material is $< 10 \mu\text{m}$, and so devices can be readily fabricated in array formats with planar deposition techniques.

We are using molecular-beam-epitaxy (MBE) to fabricate two types of devices for applications initially between 5-15 THz ($\lambda=20-60 \mu\text{m}$). The first device is the well-known $\text{Hg}_{1-x}\text{Cd}_x\text{Te}$ alloy, while the second is a HgTe/HgCdTe superlattice (SL) grown on either CdTe/Si or CdZnTe (112)B substrates. The bandgap of the alloy is varied by adjusting the mole fraction x of CdTe in the range of $x = 0.17-0.22$, whereas the gap of the SL depends almost entirely on the thickness of the HgTe well layers interleaved between high-gap HgCdTe barriers.

The mixers are fabricated in series of three- and six-element linear arrays. The electrical contacts are deposited on the top surface as interdigitated electrodes (IDE). In the initial test arrays, either 4-, 6-, or 8- electrode fingers of $4 \mu\text{m}$ width span the active $200 \mu\text{m}$ width of the mixer. A trade-off between response speed and mixer impedance is made by adjusting the interelectrode separation. Signal and local oscillator (LO) beams are coupled to the photomixer optically. Typically the mixer size is $3-4 \lambda$ across, so no separate antenna is required.

1. Introduction

There are 3 planar technologies currently available for fabricating photoconductors for far-infrared applications. The first is an extension of extrinsic detector technology, but with doping densities 100 times higher. Ge can be doped with Ga at densities of 10^{16} cm^{-3} , in a manner analogous to highly doped As:Si detectors. At such densities, the detector has an absorption strength of 100 cm^{-1} , and so devices only $10 \mu\text{m}$ thick should have good quantum efficiencies. Conduction in the impurity band is blocked by an undoped layer, and hence these devices are called impurity-blocked-conduction (IBC) or

blocked-impurity-band (BIB) detectors. This technology appears most promising for the 70-200 μm band, but the devices will need cooling to $T \leq 2$ K [1]. Unfortunately, inherent difficulties in handling high purity Ge compounds have made Ge-IBC devices hard to make.

The second planar technology involves the creation of quantum-well structures in III-V materials such as InAs/GaSb and others [2,3]. The quantum well devices will have absorption strengths of 100 cm^{-1} in the 10-70 μm band, and a relaxed cooling requirement of about 10 K. Theoretically, one could also make zero-band-gap III-V alloys (e.g., InTlP, InTlAs, or InTlSb), but these materials have been difficult to fabricate epitaxially.

The third approach is the one favored here. It involves the II-VI group materials HgTe and CdTe, which can be used effectively in either zero-gap alloys or multiple-quantum-well (superlattice) structures [4]. Intrinsic HgTe/CdTe detectors, like extrinsic IBC devices, have minimal volumes, and hence higher radiation resistance compared to much larger extrinsic detectors with low doping. Most near-IR arrays are currently made with HgCdTe alloys, and in fact over 10^8 pixels have already been delivered by industry. This major investment by the industrial sector favors II-VI materials for either large-scale or mass-produced FIR arrays, should the technology prove applicable. Our goal is to demonstrate that II-VI technology is indeed applicable, initially between $\lambda = 40\text{-}65\ \mu\text{m}$, and later longward to $\lambda = 100\ \mu\text{m}$.

Our FIR project has 3 goals: (1) to fabricate high quality superlattice (SL) materials, (2) to fabricate discrete photoconductors and photodiodes from this material, and (3) to fabricate small linear arrays leading up to a 32×32 element direct-detection array. The array work will not be discussed further, but instead we will concentrate here on using discrete photoconductive devices as FIR heterodyne mixers. Some designs for such mixers were presented previously [5,6]. Now, two years later, we have successfully fabricated good quality SL materials and have made operating photoconductors and photodiodes for mid-infrared wavelengths. In fact, the new photodiodes are probably the first p-n junctions ever made in a II-VI superlattice material. While initial measurements are encouraging, further improvements in materials and device processing are needed before a FIR photoconductive mixer can be demonstrated.

2. Materials – Bandgap Engineering

Two approaches are available for fabricating II-VI materials with the 10-20 meV bandgaps needed for $\lambda = 50\text{-}100\ \mu\text{m}$ applications. The first is the well-known alloy approach in which the bandgap is tailored by varying the mole fraction x of CdTe in a HgCdTe alloy. This is the method used to fabricate all HgCdTe arrays to date, but none so far at FIR wavelengths. The second approach relies on the creation of a multiple quantum well structure called a superlattice (SL), in which HgTe (well) layers and CdTe (barrier) layers are alternated repeatedly. The bandgap of this composite structure is set primarily by the thickness of the well layer (HgTe). Absorption coefficients $\alpha > 1000\text{ cm}^{-1}$ are predicted for SL materials at FIR wavelengths, and so a superlattice thickness of $5\ \mu\text{m}$ should yield a 40% quantum efficiency (single pass).

2.1 Hg_{1-x}Cd_xTe Alloys

At 77 K, the band gap of the semimetal HgTe is -0.26 eV, and that of the semiconductor CdTe is 1.6 eV. These materials can be alloyed using various Cd fractions x to tune the bandgap E_g (eV) of Hg_{1-x}Cd_xTe to intermediate values (including zero) [7].

Figure 1 shows the cut-off wavelength, defined as $\lambda_c(\mu\text{m})=1.24/E_g(\text{eV})$, as a function of temperature for various fractional compositions x . It is evident that by choosing x between 0.16 and 0.17, a wide range of cut-off wavelengths in the FIR can be obtained. For the approximate 0.01 eV band gap needed for $\lambda=100 \mu\text{m}$ response, x would be close to 0.17. As the band gap approaches zero, small fractional changes in x lead to large fractional changes in the gap energy, and generally we need to control x to within 0.2% to have a 10% uncertainty in λ_c . It should be apparent that compositional gradients could lead to variations in the gap and thus a non-uniform response across an array detector. Nevertheless, we believe that by using molecular-beam-epitaxy (MBE), adequate composition control is available. As a test of this control, we successfully fabricated n-type alloy material with $x=0.165$ on silicon substrates.

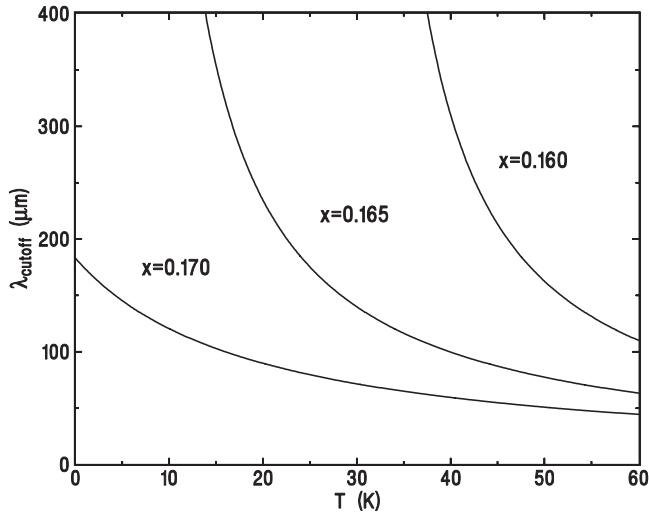


Figure 1: The cut-off wavelength is plotted against operating temperature for various Cd fractions x .

2.2 HgTe/CdTe Superlattices

A superlattice (SL) is a composite semiconductor consisting of a large number of alternating well and barrier layers – hence multiple quantum wells. HgTe/CdTe SLs form a new class called type-III SLs, because of the unique combination of a negative bandgap semimetal (HgTe) and a positive bandgap semiconductor CdTe. These layers are sequentially deposited on a CdZnSe or a CdTe/Si substrate to yield unstrained and strained-layer SLs, respectively (each has its uses). Figure 2 (a) shows a schematic cross-

sectional view of the SL structure deposited by precision MBE techniques. The overall thickness of the SL in the growth direction is typically 3-5 μm (about 200 layer pairs) to allow adequate absorption. The thicknesses of the individual layers, however, determine the optical properties. The lateral dimensions of the SL should appear to be at least λ , so that simple optical coupling can be used. (Note that Fig. 2 (a) is not to scale.) Figure 2 (b) shows the magnified cross-section of a superlattice made in 2001 at the UIC Microphysics Laboratory that shows excellent layer definition. (Dark spots are HgTe smearing likely caused by the sectioning process.)

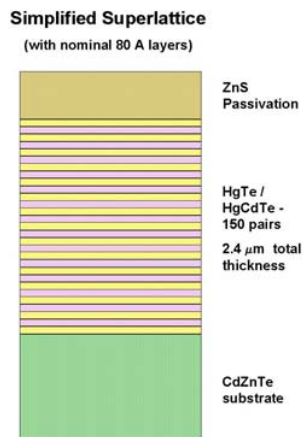


Figure 2 (a) - Schematic SL

TEM Image of HgTe/HgCdTe Superlattice

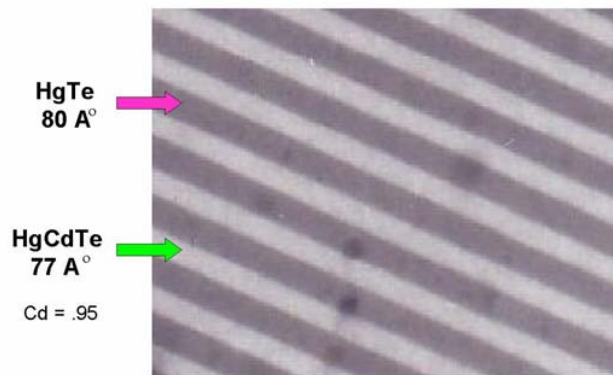


Figure 2 (b) - Actual SL

For detectors, superlattices have a number of advantages over alloy semiconductors:

- (a) the bandgap is easier to control because it depends on layer thickness rather than composition,
- (b) the large effective masses of electrons and holes in the growth direction lead to an order of magnitude (or more) reduction in tunneling currents,
- (c) carrier degeneracy effects (conduction band filling) near the long- λ band edge are less significant, and
- (d) a superlattice can suppress Auger recombination by intentionally inducing strain.

2.3 SL Design

The required thicknesses for the well (d_w) and barrier (d_b) layers of a SL are determined from band structure calculations, but can be summarized as follows. The band gap of a HgTe/CdTe superlattice depends almost entirely on the HgTe well thickness (d_w), because the barrier height of the semiconductor CdTe (or that of the $\text{Hg}_{0.05}\text{Cd}_{0.95}\text{Te}$ actually used), is much greater than the well depth of the semi-metal HgTe. Typically a barrier thickness of 50 Å is used in order to allow “perpendicular”

charge transport, while maintaining a sufficiently large difference in the parallel and perpendicular effective masses. For temperatures $T < 40$ K, when d_w is < 62 Å, the SL is a semiconductor with a normal band structure with the E1 subband $>$ H1 subband. At approximately 62 Å the band gap E_g reduces to zero, and when $d_w > 62$ Å, the band structure is inverted (i.e., the H1 subband is now the conduction band). Absorption coefficients for the regular and inverted regions of the same gap are approximately the same. Noteworthy is the very weak dependence of E_g on the HgTe width, especially in the inverted gap region. Another interesting result is that whereas E_g for fixed d_w decreases with cooling in the normal bandgap region, it increases with cooling in the inverted region. Figures 3 illustrates this behavior graphically. Although we are interested in only the lowest subbands, which determine the long wavelength properties of the SL material, the higher order subbands (such as the L1-E1, etc.) dictate the optical properties at shorter wavelengths. This is quite convenient, because we can use readily available instrumentation at near- and mid-IR wavelengths to evaluate material properties relative to theoretical predictions. The material does not even need to be cooled. Full details on the band structure calculations may be found in C. Becker *et al* [8].

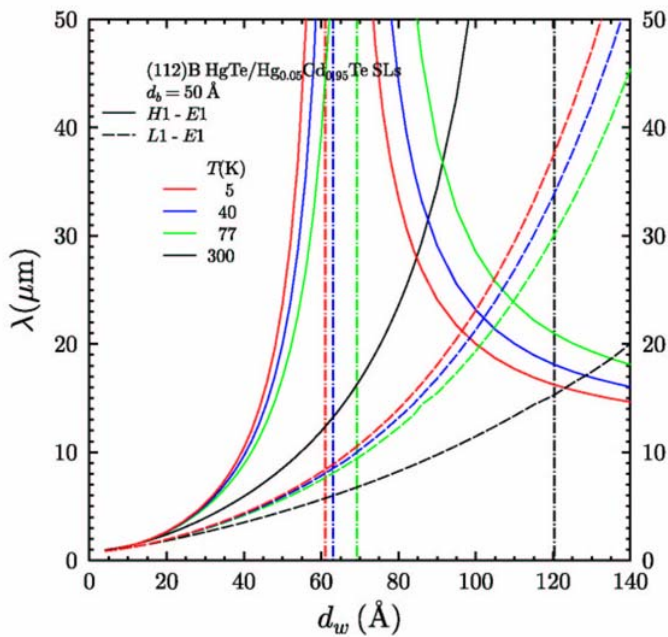


Figure 3 - Cutoff wavelength as a function of HgTe layer thickness. Inverted gap transitions are indicated by curves of negative slope. Vertical lines show thickness for zero gap at indicated temperature (from C. Becker *et al.* [8])

2.4 SL – Fabrication and Testing

The thickness required for the SL stack depends on the absorption coefficient of the material. Theoretical predictions, confirmed by FTIR absorption measurements at least in the mid-IR around 3-10 μm, indicate that the absorption coefficient at the H1-E1 band-edge is ~ 3000 cm⁻¹ for $\lambda_c = 45$ μm SL material. A total SL thickness of 3 μm would therefore suffice for near unity internal quantum efficiency (compared to a thickness >10 μm for a corresponding HgCdTe alloy). The calculations predict that the inverted band

region should have somewhat higher absorption than the normal band, although this point has yet to be verified experimentally.

A number of SL films were grown with various well depths to test the theoretical predictions for cut-off wavelength. To start we fabricated films for the mid-IR, because the wavelength response in the $\lambda = 3\text{-}20\ \mu\text{m}$ region is easy to measure with an available spectrometer. All the SL films grown at UIC are well characterized [9,10,11]. Crystal quality during growth is monitored through *in situ* spectroscopic ellipsometry and RHEED pattern techniques. The mechanical properties of the films are further investigated by x-ray diffraction and TEM measurements. Carrier mobility and concentration are measured by the Hall effect, while optical characteristics are determined by FTIR absorption and photoresponse spectra. The as-grown SL films usually have excellent mobilities around $3\times 10^4\ \text{cm}^2/\text{V}\cdot\text{s}$ to $1\times 10^5\ \text{cm}^2/\text{V}\cdot\text{s}$ at $T = 40\text{K}$, with the lower gap films having the higher mobility (as expected). All the SL material discussed here was grown n-type by introducing indium donors during the MBE growth process.

Finally, we should emphasize that two key tasks were accomplished regarding MBE growth of SL-based device structures. The first is the growth of multi-layer device structures with the SL-layers sandwiched between appropriately doped alloy layers with many graded hetero-interfaces. The structures were band-gap engineered to achieve good transport properties in the growth direction while suppressing tunneling currents. The second is the successful growth of SL structures on CdTe/Si substrates as well as lattice-matched CdZnTe substrates. MBE growth on CdTe/Si leads to a strained-layer SL that may be useful for suppressing Auger recombination.

3. Devices

3.1 Photoconductors

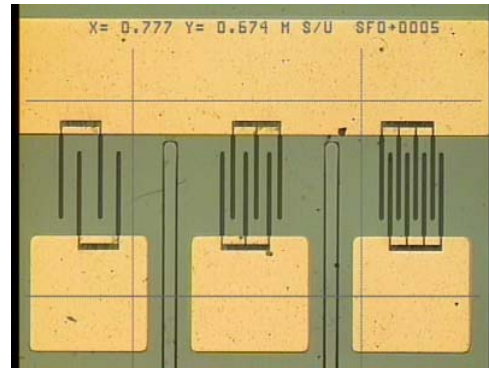
Once good quality SL films have been deposited, the easiest device to fabricate is the simple photoconductor (PC). Our first devices used conventional side contacts as shown in Figure 4a. Later an easier approach was adopted with top-surface interdigitated electrodes (IDE) as shown for three different electrode spacings in Figure 4b. The short inter-electrode spacing of the IDE devices leads to a fast transit time for carriers, and hence the broadest possible IF bandwidth when the device is used as a photomixer.

Superlattice Photoconductor



300 x 300 μm SL-PC with In+Au pads on HgTe/HgCdTe & Ti+Au on CdZnTe

(a)



(b)

Figure 4 - (a) Standard SL photoconductor (PC) with side contacts. (b) Three IDE style PC detectors with different electrode spacings. Active area per element is 200 μm \times 200 μm less regions blocked by electrodes. The light regions are electrode metalizations.

Figure 5 shows representative photoresponse spectra from two different SL materials. The peak intensity is defined by λ_p , while the -3 dB intensity is given by the cutoff wavelength λ_c on the long wavelength side. Spectra were measured at $T=77$ K using a Nicolet 870 FTIR which works out to $\lambda=25$ μm . The long wavelength limit of the FTIR will be upgraded to $\lambda=500$ μm in the near future. As mentioned above, for our initial SL experiments it is much easier to work with wide bandgap materials, whose optical properties can be verified with standard mid-IR instrumentation. After we are certain that fabricated devices match theoretical predictions, we can be more confident in designing subsequent SL devices optimized for FIR wavelengths.

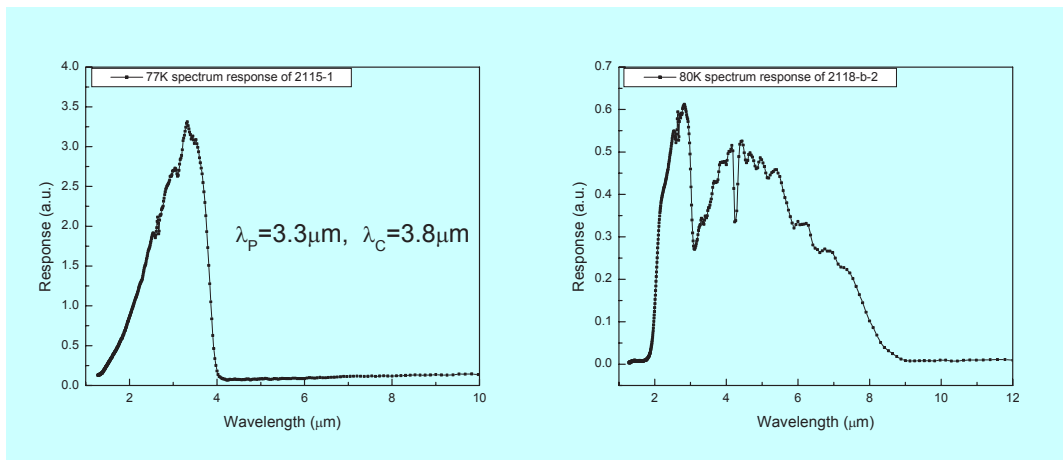


Figure 5 - (a) The 77 K relative spectral response of a 40 μm \times 40 μm device from SL2115 ($d_w=30$ \AA , $d_b=26$ \AA) with $\lambda_c=3.8\mu\text{m}$ and (b) that of a 580 μm \times 580 μm device from SL2118 ($d_w=45$ \AA , $d_b=25$ \AA) with $\lambda_c=7.4\mu\text{m}$.

3.2 Photodiodes

3.2.1 Standard process: p-type doping with As

Another device topology for photomixers is the reversed-biased photodiode (PD). The high field in the depletion region together with the short electrode spacing leads to a fast response time and high IF bandwidth. However, as the bandgap of the material is reduced toward zero, we must increasingly be concerned with tunneling currents. It remains to be seen whether PC or PD devices will prove superior as FIR mixers. The alloy and superlattice materials described above can be processed into photodiodes by the addition of a p-type layer onto the n-type material. The method currently favored for p-on-n in alloys is As-doping via ion implantation, although *in situ* As-doping during MBE material growth has also been used. Arsenic is favored here because of its relatively low thermal diffusion constant in HgCdTe. However, the As must be “activated” to occupy a Te site in the lattice if it is to function as an acceptor. This activation is readily accomplished by thermal annealing at $T = 250\text{-}300\text{ }^{\circ}\text{C}$ for 30-180 min. Although annealing causes no harm to alloy material, it is problematic for a SL which is itself grown at lower temperatures of $T=150\text{-}180\text{ }^{\circ}\text{C}$. To verify the deleterious effects of high temperatures on SL material, we ran a series of annealing experiments on samples from different SL batches. As expected, the $250\text{ }^{\circ}\text{C}$ anneal for 30 min caused noticeable interdiffusion between the SL layers, so much so that Hall mobilities dropped by a factor of 50 and the mid-IR absorption of the SL departed significantly from that measured for as-grown material. So now we must consider alternative methods for junction formation.

3.2.2 New Process: p-type doping with Au

Acceptors can also be introduced to II-VI compounds by substituting from the Group I elements (e.g., Li, Au, Ag, Cu). For p-type doping these elements would substitute for Hg or Cd in the lattice. Au is currently favored as an acceptor in II-VI heterostructures where the high temperature activation required by As is unacceptable. Au has a high thermal diffusivity, however, which needs to be controlled for good junction formation. The Microphysics Lab at UIC is currently working on p-type doping with Au under the Collaborative Alliance Technology program supported by the Army. Some preliminary, though encouraging, results have just been achieved with Au-doping to yield the first p-n junctions in a II-VI SL material. The junctions were formed by thermal diffusion of Au into n-type SL material at $110\text{ }^{\circ}\text{C}$, which is below the $180\text{ }^{\circ}\text{C}$ deposition temperature of the SL itself. The device structure is illustrated in Figure 6.

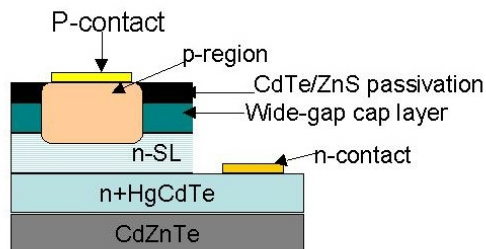


Figure 6 – Schematic cross-section of planar SL photodiode

Figure 7 shows the I/V curves of a junction grown on a sample of SL material. Although the R_oA values are far from the state of the art, they are quite encouraging for a first try. We believe improvements in the process technology will raise R_oA and detectivity closer to values achieved in alloys with As-doping. Our goal is not to compete with alloys, however, but to extend HgCdTe technology to the FIR where alloys are problematic. At this point - a little more than 2 years into the project - all the first-level technology challenges for SL-based photodiodes have already been met. However, much still needs to be done to realize the full potential of the device.

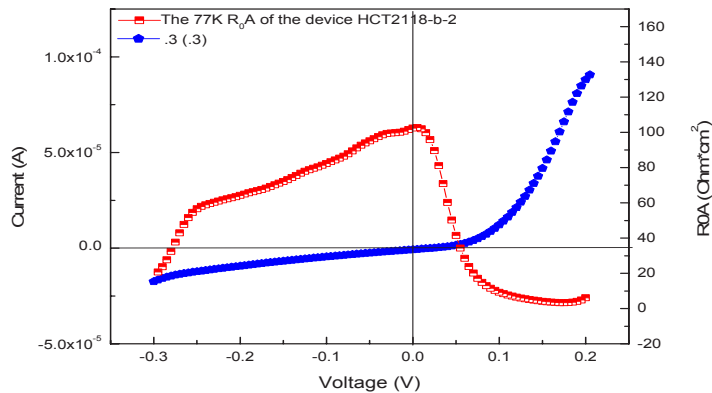


Figure 7 - The I-V and R_oA curves at $T=77K$ for a $580 \mu\text{m} \times 580 \mu\text{m}$ photodiode made from material SL-2118 with $\lambda_c=7.4 \mu\text{m}$ (see Fig. 5b).

Now that we can make SL devices, we are starting to test the speed of selected mid-IR detectors with IDE contacts. This is done by measuring the spectrum of the G-R noise power, which corresponds roughly to the expected IF bandwidth. Our goal is an IF bandwidth exceeding 3 GHz in a FIR device. Simultaneously, we are fabricating new SL materials with bandgaps closer to zero, so that FIR measurements can be started.

This work is supported by NASA Grant NAG5-10213.

References

- [1] E.E. Haller and J.W. Beeman, "Far Infrared Photoconductors: Recent Advances and Future Prospects", in Proc. Far-IR, Sub-mm, & Millimeter Detector Technology Workshop, J. Wolf, J. Farhoomand, and C.R. McCreight (eds.), NASA CP-211408 (2002), paper 2-06
- [2] M. S. Sherwin, C. Cates, B. Serapiglia, Y. Dora, J. B. Williams, K. Maranowski, A.C. Gossard, and W. R. McGrath, "Tunable Antenna-Coupled Intersubband (TACIT) Mixers: The Quantum Limit without the Quantum Liquid", in Proc. Far-IR, Sub-mm, & Millimeter Detector Technology Workshop, J. Wolf, J. Farhoomand, and C.R. McCreight (eds.), NASA CP-211408 (2002), paper 6-03

- [3] S. V. Bandara, S. D. Gunapala, D. Z-Y. Ting, S. B. Rafol, and J. K. Liu, "GaAs/AlGaAs Multi-Quantum-Well Based Far Infrared Detectors for Astronomy", in Proc. Far-IR, Sub-mm, & Millimeter Detector Technology Workshop, J. Wolf, J. Farhoomand, and C.R. McCreight (eds.), NASA CP-211408 (2002), paper 6-06
- [4] A.L. Betz, R.T. Boreiko, S. Sivananthan, and Y.D. Zhou, "Far-Infrared Focal Plane Arrays", in Proc. Far-IR, Sub-mm, & Millimeter Detector Technology Workshop, J. Wolf, J. Farhoomand, and C.R. McCreight (eds.), NASA CP-211408 (2002), paper 6-07
- [5] A.L. Betz and R.T. Boreiko, "Space Applications for HgCdTe at FIR Wavelengths Between 50-150 μm ", in *Materials for Infrared Detectors*, R.E. Longshore (ed.), Proc. SPIE Vol. 4454, pp. 1-9 (2001)
- [6] A.L. Betz, R.T. Boreiko, S. Sivananthan, and R. Ashokan, "HgCdTe Photoconductive Mixers for 2-8 THz", in Proc. 12th International Symposium on Space Terahertz Technology (JPL Publ. 01-18), pp. 92-101 (2001)
- [7] G.L. Hanson, and J.L. Schmit, Jour. Appl. Phys., **54**, 1639 (1983)
- [8] C.R. Becker, V. Latussek, G. Landwehr, and L.W. Molenkamp, "Inverted band structure of type III HgTe/Hg_{1-x}Cd_xTe superlattices and its temperature dependence", Phys. Rev. B, **68**, 035202 (2003)
- [9] Y.D. Zhou, C.R. Becker, R. Ashokan, Y. Selamet, Y. Chang, R.T. Boreiko, A.L. Betz, S. Sivananthan, "Progress in Far-Infrared Detection Technology", Proc. SPIE Volume 4795, p. 121 (2002)
- [10] Y.D. Zhou, C.R. Becker, Y. Selamet, Y. Chang, J. Zhao, R. Ashokan, R.T. Boreiko, T. Aoki, D.J. Smith, A.L. Betz, S. Sivananthan, "Far-infrared Detector Based on HgTe/HgCdTe Superlattices", Proc. II-VI MCT Workshop, San Diego (2002).
- [11] Y.D. Zhou, J. Zhao, R.T. Boreiko, Y. Selamet, Y. Chang, R. Ashokan, C. Bucker, A.L. Betz, S. Sivananthan, "HgCdTe for far-infrared heterodyne detection", SPIE Proc. (2003, submitted)

TRANSFERRED SUBSTRATE HETEROJUNCTION BIPOLAR TRANSISTORS FOR SUBMILLIMETER WAVE APPLICATIONS

Andy Fung, Lorene Samoska, Peter Siegel
California Institute of Technology-Jet Propulsion Laboratory, Pasadena, CA 91109, USA

Mark Rodwell, Miguel Urteaga, Vamsi Paidi
Department of Electrical and Computer Engineering, University of California, Santa
Barbara, CA 93106, USA

Roger Malik
RJM Semiconductor, Berkeley Heights, NJ 07922, USA

Abstract

We present ongoing work towards the development of submillimeter wave transistors with goals of realizing high frequency amplifiers, voltage controlled oscillators, active multipliers, and high-speed digital circuits. The approach involves fabrication of indium phosphide heterojunction bipolar transistors in a low parasitic transferred-substrate process, with the necessary requirements in uniformity and reliability for eventual space-borne applications. Transferred Substrate Heterojunction Bipolar Transistors (TSHBTs) have previously demonstrated record >20 dB measured unilateral power gain at 100 GHz, and high power gains in the 140-220 GHz band [1]. Single-transistor amplifiers have shown 6.3 dB gain at 175 GHz [2]. Thus far we have completed a first generation of TSHBTs with nominal emitter stripes of $1 \times 6 \mu\text{m}^2$. S-parameter measurements resulted in an extrapolated power gain cutoff frequency (F_{max}) of 150 GHz and current gain cutoff frequency (F_i) of 110 GHz, at an emitter current density of 94 kA/cm^2 and collector-emitter bias voltage of 1.25V. Future generations of TSHBTs will target improvements in speed, uniformity and reliability, through better semiconductor layer structure design and epitaxial material quality, reduction in transistor geometry size, and refinements in fabrication procedures.

Introduction and Background

Indium phosphide (InP) heterojunction bipolar transistors (HBTs) are one of the highest performance transistor technologies available. Advantages of this technology arise from the precise control of the semiconductor epitaxial structure that electrons traverse through, and the material properties of the epitaxy. In HBTs, electrons move in the direction of epitaxial growth, as a result, the environment of the electrons at each region of the transistor can be more easily and accurately controlled for optimal performance within the narrowest spatial dimensions. Some advantages resulting from this are that the epitaxial material for InP HBTs can be grown with a large bandgap emitter region to reduce injection of holes from the base into the emitter. Also an alloy or doping graded base region can be grown in the epitaxy to produce a built-in electric field to increase electron transport speed. Furthermore, a high voltage breakdown material such as InP can be grown epitaxially for the collector region so that the transistor may operate at higher voltages and subsequently produce higher output power amplifiers (see Figure 1). In contrast, in other high speed transistor technologies, such as high electron mobility transistors (HEMTs), the electrons travel perpendicular to the direction of epitaxial growth, confined to particular material layers of fixed properties. Modifications for material properties in the direction of electron transport to improve performance can only be done via processes after epitaxial growth, generally with less precision and more complications. Silicon Germanium HBTs, another high-speed technology, consist of semiconductor materials with lower breakdown voltages and are less suitable for power applications. InP HBTs are well suited for both high speed and high output power operation, which are desired for our applications.

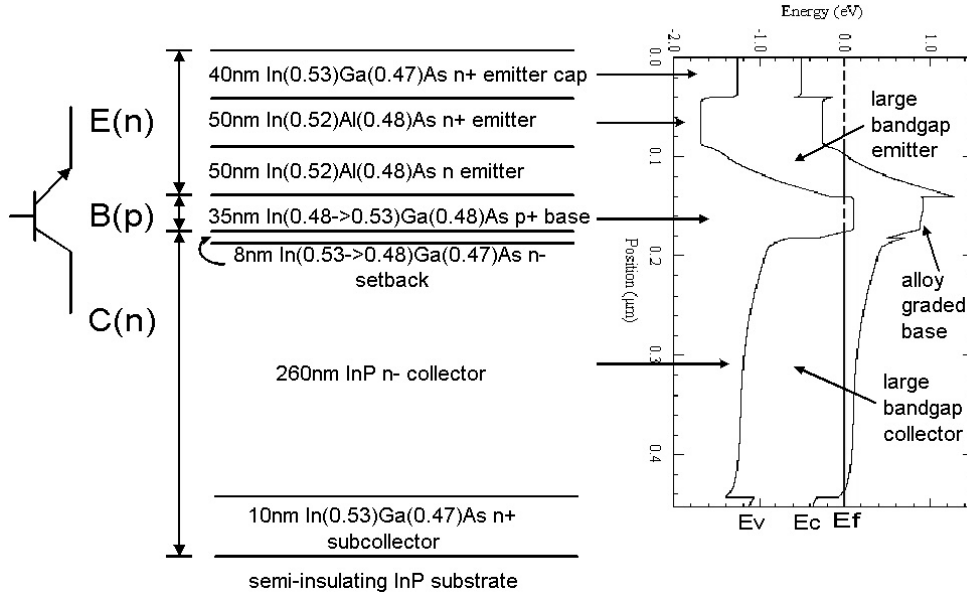


Figure 1: Schematic representations of an indium aluminum arsenide (InAlAs) emitter, indium gallium arsenide (InGaAs) base, InP collector, double heterojunction bipolar transistor (DHBT). The large bandgap emitter provides a larger energy barrier for holes from injecting from the base into the emitter in forward active operation. The base is alloy graded to provide a built-in electric field to speed electrons through the base into the collector. The collector is made of a large bandgap material to withstand larger voltages before breakdown. The energy (eV) versus position (μm) diagram is simulated using Bandprofiler developed by W. Frenley UT-Dallas.

Motivation

The goal of this effort is to develop the fastest reliable transistor process beyond what is available from industry, and have the capability to easily add features for performance not typically allowed in foundry services, which have rigid design rules. We are pursuing HBTs as they have shown thus far to have the highest power gain, >20 dB at 100 GHz [1] and higher power handling capability due to epitaxial engineering of the collector region of the transistor, in contrast to HEMTs. We expect that HBTs will provide more power per unit area at higher frequencies than HEMTs, and will yield higher transistor count ICs due to their particular fabrication procedures. To date, InP HBTs have demonstrated ICs with transistor counts approaching five thousand [3]. With the successful implementation of an ultra-high-speed and high-power HBT we plan to fabricate power amplifiers where they may be integrated into local oscillator chains for space heterodyne systems [4]. Additionally, voltage controlled oscillators can be fabricated to simplify local oscillator chains by reducing component count, and therefore DC power consumption (see Figure 2). Ultimately we would like to have a high yield process so that we can develop ultra-high speed mixed-signal ICs. Systems that we would like to utilize this technology in are for THz imaging systems, which are in development at JPL (see Figure 3) [5], and also future space hardware such as advanced autocorrelators for high-resolution remote sensing spectral analysis.

Transferred Substrate for Improving InP HBT Performance

The high frequency figures of merit of HBTs are the current gain cutoff frequency (F_t) and maximum frequency of oscillation (power gain cutoff frequency) (F_{max}). Physically, F_t can be expressed as,

$$F_t = 1/(2 \cdot \pi \cdot \tau_{\text{ec}}) \approx 1/(2 \cdot \pi \cdot (\tau_{\text{e}} + \tau_{\text{b}} + \tau_{\text{bc}} + \tau_{\text{c}})) \quad (1)$$

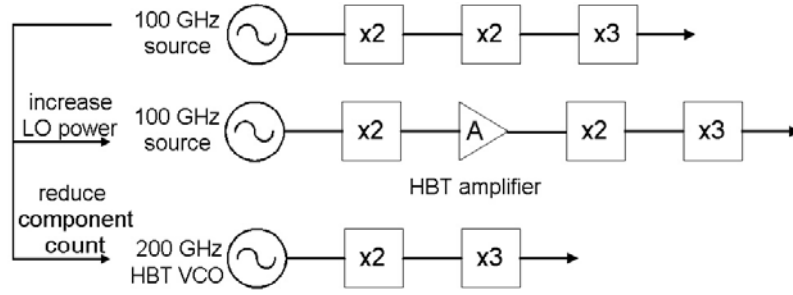


Figure 2: Block diagram of implementations of a 1.2 THz local oscillator (LO) chain. A baseline version is shown at the top. HBTs can be inserted along the chain to increase power. HBTs can also be used to produce high frequency voltage controlled oscillators to simplify LOs, reducing power consumption and mass.

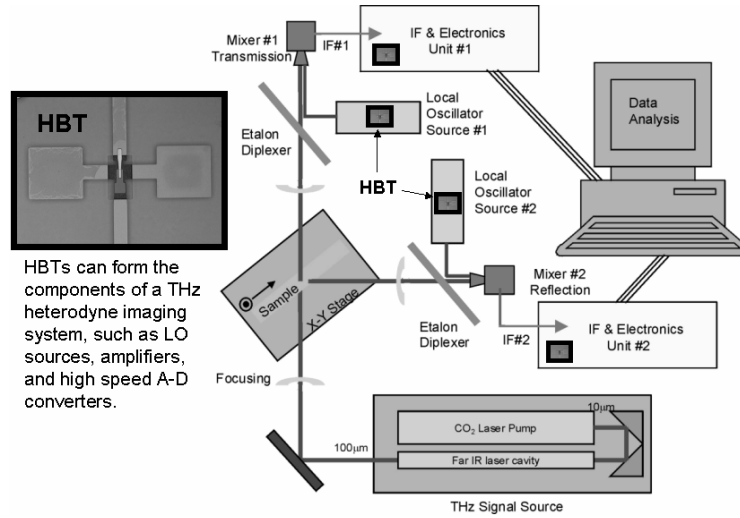


Figure 3: Schematic of a scanned pixel terahertz imaging system under development at JPL. HBTs are displayed in components where they can improve system performance.

where, τ_{ec} is the total emitter to collector delay time, τ_e is the emitter charging time, τ_b is the base transit time, τ_{bc} is the base-collector junction transit time, and τ_c is the collector charging time [6]. The power gain cutoff frequency can be approximated by,

$$F_{max} \geq (F_t / (8 \cdot \pi \cdot R_b \cdot C_{cb}))^{1/2} \quad (2)$$

where R_b is the complete base resistance from base contact to the base layer under the emitter, and C_{cb} is the full base to collector capacitance. F_{max} can be more accurately calculated with $R_b \cdot C_{cb}$ modeled by an effective time constant of a distributed network of the base-collector region [1]. Comparing the typical mesa HBT (Figure 4 (a)) and the Transferred Substrate HBT (TSHBT) (Figure 4 (b)), the TSHBT method overcomes the limitation of the base-collector overlap inherent to the mesa HBT since the collector contact is independently defined from the backside of the wafer. By minimizing C_{cb} , F_{max} is improved. To increase both F_t and F_{max} simultaneously, scaling in the vertical direction minimizes transit times in F_t , however this increases intrinsic and parasitic resistances and capacitances. To reduce these resistances and capacitances to increase both F_t and F_{max} the transistor must also be scaled in the horizontal direction and doped higher. Each of these fabrication degrees of freedom self limit each other to the point that they are allowed by material and equipment capabilities.

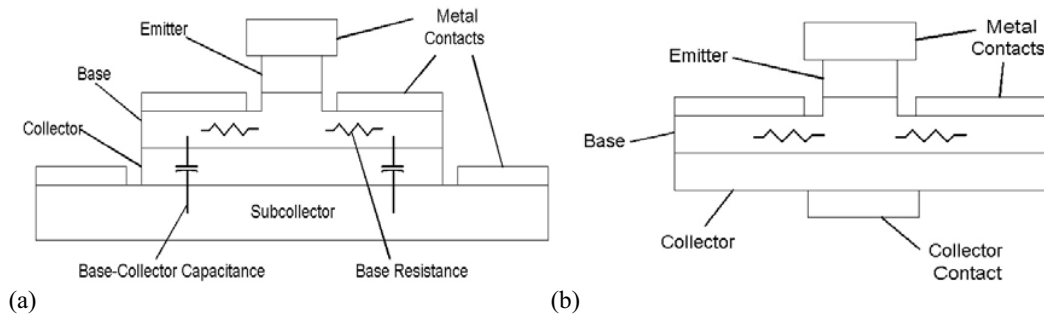


Figure 4: (a) Schematic cross section of a typical mesa HBT. (b) Schematic cross section of a TSHBT.

Experimentally, F_1 and F_{\max} are typically extrapolated from lower frequency measurements to the higher cutoff frequency values, due to the limited bandwidth of characterization setups. F_1 is determined from the current gain H_{21} and F_{\max} from Mason's unilateral power gain (U), both cutoff frequencies are determined from the frequency value where the gain curves reach 0 dB. H_{21} and U, as a function of frequency, are mathematically derived from S-parameter measurements over frequency. Cutoff frequencies are typically extrapolated from lower frequencies with a -20dB/decade gain behavior based on the single pole frequency response of the hybrid- π circuit model [7,8]. Recently, studies have indicated that the simple hybrid- π model may not properly fit certain HBTs operated in particular regimes [9,10]. Electron velocity modulation in the base-collector depletion region is suspected to be the cause of an observed reduction of the base-collector capacitance and of negative collector-base conductance [10]. In this report the measured data appears to fit the simple hybrid- π model, so for the purpose of comparisons, F_1 and F_{\max} are determined based on the standard extrapolation with a -20 dB/decade trend.

Development of Transferred Substrate InP HBTs at JPL

At JPL we are in collaboration with UCSB and RJM Semiconductor in an effort to develop advanced high speed and high reliability HBT processes for implementing high frequency amplifiers, VCOs and digital circuits for THz imagers and spectrometers. In the Microdevices Laboratory we recently fabricated the first wafer run of TSHBTs at JPL (Figure 5 (a)). The epitaxial material used for the TSHBTs is of a single heterojunction InAlAs emitter, and InGaAs base and collector design. The base is 400 Å thick carbon doped $5 \times 10^{19}\text{ cm}^{-3}$. DC measurements of the collector current versus collector-emitter voltage for different base current shows maximum small signal current gain β of 36 (Figure 5 (b)). From S-parameter measurements we deduce maximum F_1 and F_{\max} of 110 and 150 GHz, respectively, at an emitter current density of 94 kA/cm^2 (Figure 5 (c)). Through improvements in epitaxial designs, epitaxial material quality, and microfabrication processes, we expect to substantially improve TSHBT performance. Future transistors will utilize DHBT epitaxy for higher power handling capability [11,12].

The present TSHBT process includes nine stepper lithography mask steps, and two electron-beam lithography direct writes for the emitter and collector contacts. Important in the process is the deposition of a 5 μm thick low dielectric Benzocyclobutene (BCB) resin that serves as an intermediate substrate supporting the HBTs and passive components, from the ground plane. The integrated passive nichrome resistors and metal-insulator-metal capacitors provide for a full MMIC process (Figure 6). In developing the TSHBT process at JPL, a large-feature-size reduced-process-step HBT process for evaluating DC epitaxial material quality, and an RF mesa HBT process for developing all necessary topside wafer processes for TSHBTs have also been implemented [13]. Table 1 summarizes RF data we have measured thus far from both RF mesa and TSHBT processes. In the table the samples that are used have nominally the same epitaxial design. Wafer 1, 2 and 3 used in the mesa process differ in that wafers 1 and 2 have nominal base doping of $4 \times 10^{19}\text{ cm}^{-3}$ and wafer 3 has base doping of $5 \times 10^{19}\text{ cm}^{-3}$. Wafer 4, used in the TSHBT process is identical to wafer 3, except that there is no subcollector layer. Comparing the cutoff frequency values for wafers 3 and 4, F_{\max} has improved in the TSHBT sample.

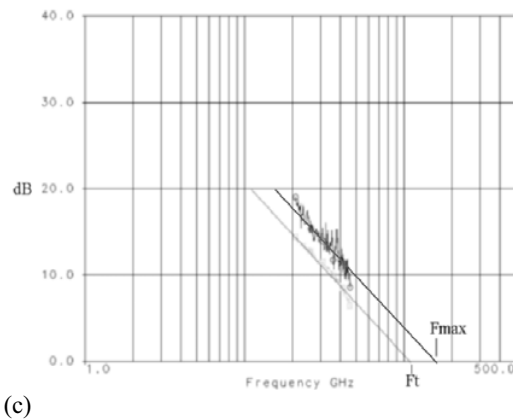
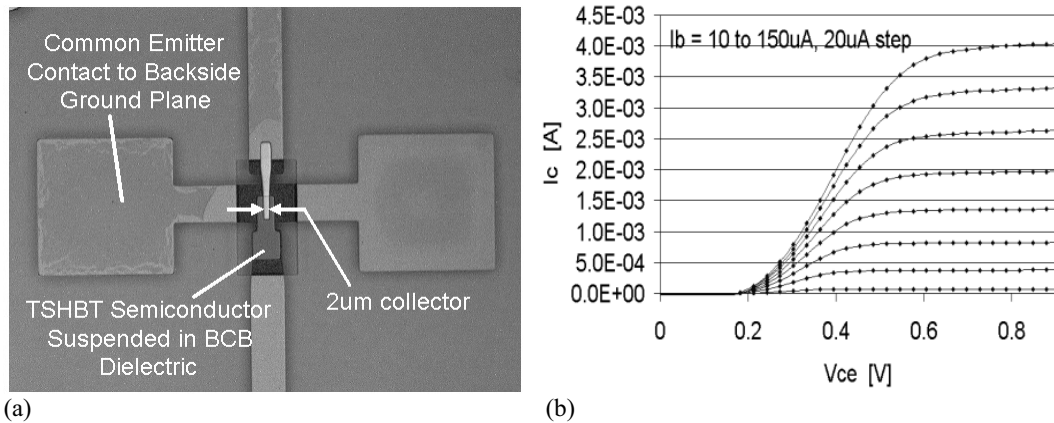


Figure 5: (a) Optical photo of an InP TSHBT. The emitter stripe is nominally $1 \times 6 \mu\text{m}^2$ and collector stripe is $2 \times 8 \mu\text{m}^2$ (b) DC I_c versus V_{ce} for different I_b of InP TSHBT. Maximum small signal β is 36. (c) Gain plots of an InP TSHBT deduced from S-parameter measurements. F_t and F_{max} are 110 and 150 GHz, respectively at an emitter current density J_e of 94 kA/cm^2 and V_{ce} 1.25V.

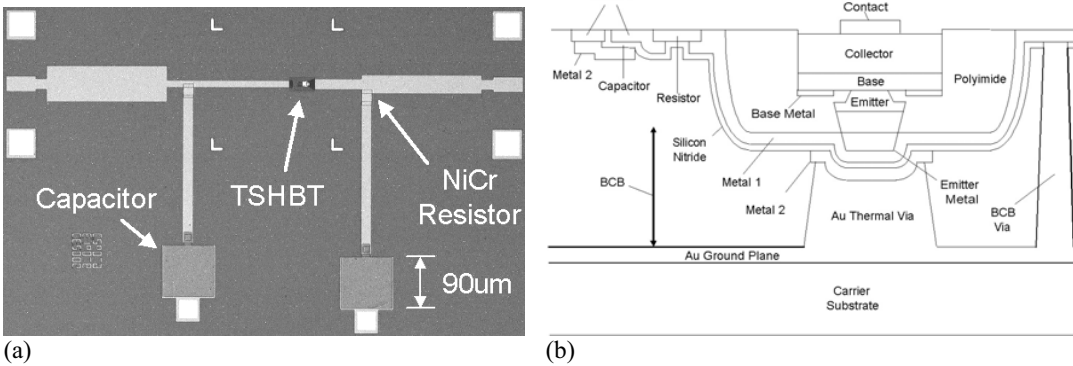


Figure 6: (a) Optical photo of a 200 GHz TSHBT amplifier during fabrication showing integrated TSHBT, resistors and capacitors. (b) Cross section (not drawn to scale) of transferred substrate MMIC process.

	Wafer 1, beryllium base, mesa HBT	Wafer 2, carbon base, mesa HBT	Wafer 3, carbon base, mesa HBT	Wafer 4, carbon base, TSHBT
F_t [GHz]	123	118	108	110
F_{max} [GHz]	118	100	119	150

Table 1: Summary of measured RF mesa HBTs and TSHBTs fabricated at JPL. F_t and F_{max} for each wafer sample are measured simultaneously under the same bias conditions at peak F_{max} . Mesa HBT emitter stripes are nominally $2 \times 10 \mu\text{m}^2$.

Conclusion

We are in a collaborative effort to develop an advanced high frequency HBT MMIC fabrication process in-house at JPL. This technology will provide performance beyond what is available in commercial processes, and will enable new instruments. In addition, with an in-house process we will have the flexibility to modify the process as necessary for the best possible performance, unlike foundry processes with rigid design rules. In the Microdevices Laboratory at JPL we have completed the fabrication of TSHBTs with F_t and F_{max} of 110 and 150 GHz, respectively. In fabricating these low-parasitic HBTs, we also developed a standard RF mesa HBT process and a large-size DC HBT process. In developing the RF mesa process, topside microfabrication procedures required in the TSHBTs are verified. The large-size DC HBTs are useful in that in the minimum process steps the electrical quality of epitaxial material can be examined prior to utilizing them in the more demanding transferred substrate or mesa processes. With improvements in epitaxial designs, epitaxial material quality, and microfabrication processes, we expect to substantially improve transistor performance and realize submillimeter-wave amplifiers.

Acknowledgments

The research and development presented in this paper was carried out at the California Institute of Technology - Jet Propulsion Laboratory, a federally funded research and development center under a contract with the National Aeronautics and Space Administration, and by MDA under contract DTRA01-01-0127, managed by DTRA. The authors thank Richard Muller, Paul Maker and Pierre Echternach, at JPL for providing electron beam lithography.

References

- [1] M.J.W. Rodwell, M. Urteaga, T. Mathew, D. Scott, D. Mensa, Q. Lee, J. Guthrie, Y. Betser, S.C. Martin, R.P. Smith, S. Jaganathan, S. Krishnan, S.I. Long, R. Pallela, B. Agarwal, U. Bhattacharya, L. Samoska, M. Dahlstrom, "Submicron scaling of HBTs," IEEE Trans. Electron Devices, vol. 48, Nov. 2001.
- [2] M. Urteaga, D. Scott, T. Mathew, S. Krishnan, Y. Wei, M.J.W. Rodwell, "Single-stage G-band HBT amplifier with 6.3 dB gain at 175 GHz," Proc. IEEE GaAs IC Symp., Oct. 2001.
- [3] <http://www.vitesse.com/news/20030113.shtml>, "Vitesse is First to Offer Indium Phosphide HBT Foundry Services Through MOSIS; Partnership Will Assist with the Adaption of the Emerging Technology," Jan. 2003.
- [4] J. Ward, F. Maiwald, A. Maestrini, G. Chattopadhyay, E. Schlecht, J. Gill, I. Mehdi, "1400-1900 GHz Local Oscillators for the Herschel Space Observatory," Proceedings 14th Inter. Symp. on Space Terahertz Tech., 2003 (to be published).
- [5] P.H. Siegel, "Submillimeter-Wave Camera," JPL New Technology Report NPO20718, June 1, 1999.
- [6] B. Jalali and S. Pearton, *InP HBTs Growth, Processing, and Applications*, Artech House Inc., 1995.
- [7] S. Sze (ed.), *Modern Semiconductor Device Physics*, John Wiley & Sons Inc., 1998.
- [8] A. Sedra and K. Smith, *Microelectronic Circuits 3rd Ed.*, Saunders College Publishing, 1991.
- [9] M. Urteaga and M.J.W. Rodwell, "Power gain singularities in transferred-substrate InAlAs/InGaAs-HBTs," IEEE Trans. Electron Devices, July, 2003 (to be published).
- [10] Y. Betser and D. Ritter, "Reduction of the base-collector capacitance in InP/GaInAs heterojunction bipolar transistors due to electron velocity modulation," IEEE Trans. Electron Devices Electron Devices, vol. 46, Apr. 1999.
- [11] Y. Wei, S. Lee, K. Sundararajan, M. Dahlstrom, M. Urteaga, M. Rodwell, "W-band InP/InGaAs/InP DHBT MMIC Power Amplifiers," IEEE MTT-S International Microwave Symposium, 2002.
- [12] Y. Wei, S. Lee, P.K. Sundararajan, M. Dahlstrom, M. Urteaga, M. Rodwell, "High current (100mA) InP/InGaAs/InP DHBTs with 330 GHz f_{max} ," Proceedings of 14th Indium Phosphide and Related Materials Conference, 2002.
- [13] A. Fung, L. Samoska, P. O'Brien, and P. Siegel, "Transferred Substrate Heterojunction Bipolar Transistors for Millimeter and Submillimeter Wave Applications," Proceedings FAR-IR, SUB-MM & MM DETECTOR TECHNOLOGY WORKSHOP, Wolf J., Farhoomand J. and McCreight C.R. (eds.), NASA/CP-211408, 2002 (in press). http://www.sofia.usra.edu/det_workshop/papers/session6/3-45fung_rev_ver.pdf

Novel Designs for Submillimeter Subharmonic and Fundamental Schottky Mixers

Erich Schlecht, John Gill, Peter Siegel, John Oswald, and Imran Mehdi

Jet Propulsion Laboratory, M/S 168-314, 4800 Oak Grove Drive, Pasadena CA 91109

E-mail: Erich.T.Schlecht@jpl.nasa.gov

Abstract

There is a demand for mixers operating in the submillimeter band between 300 and 1200 GHz for observation of various atomic and molecular lines. For Earth and planetary observations Schottky mixers have adequate sensitivity. Additionally, they have the substantial advantage of working with little or no cooling below room temperature, although their performance does improve at lower temperatures. Near term example missions is a proposal for water detection observations on Mars [1], and measurements of middle atmosphere trace gases and gas dynamics on Venus [2].

To meet these requirements, new mixers have been designed to take advantage of the frameless membrane technology developed at JPL [3]. Two circuit topologies have been used for the subharmonic mixers, one based on previous submillimeter subharmonic mixer designs [4], and the other based on the balanced doubler configuration [5]. These are expected to give single sideband noise temperatures at the diode of about 2500 K, with conversion loss around 13 dB. Single-diode single-ended mixers will also be described, and they are expected to give diode SSB noise temperatures near 1000 K, conversion loss about 8 dB.

- [1] Report of the NASA Science Definition Team for the Mars Reconnaissance Orbiter (MRO), available at http://mro.larc.nasa.gov/mro/MRO_SDTreport.pdf, Feb. 2001.
- [2] Solar System Exploration Survey, Space Studies Board of the National Research Council, "New Frontiers in the Solar System" available at <http://www.nas.edu/ssb/SSE-Survey-Report-Part-1.PDF>, July 2002.
- [3] S. Martin, B. Nakamura, A. Fung, P. Smith, J. Bruston, A. Maestrini, F. Maiwald, P. Siegel, E. Schlecht, and I. Mehdi, "Fabrication of 200 to 2700 GHz multiplier devices using GaAs and metal membranes," *2001 MTT-S International Microwave Symposium Digest*, pp. 1641-1644.
- [4] E.R. Carlson, M.V. Schneider, and T.F. McMaster, "Subharmonically pumped millimeter-wave mixers," *IEEE. Trans. Microwave Theory Tech.*, vol MTT-26, no. 10, pp. 706-715, Oct. 1978.
- [5] E. Schlecht, G. Chattopadhyay, A. Maestrini, A. Fung, S. Martin, D. Pukala, J. Bruston, and I. Mehdi, "200, 400 and 800 GHz Schottky diode 'substrateless' multipliers: design and results", *2001 MTT-S International Microwave Symposium Digest*, pp. 1649-1652.

Design, fabrication and testing of semiconductor tunable antenna-coupled intersubband Terahertz (TACIT) detectors

G. B. Serapiglia,¹ Y. Dora,^{1,2} M. S. Sherwin,^{1,3} M. Hanson⁴, A. C. Gossard^{2,4} and W. R. McGrath⁵

¹*Institute for Quantum Engineering, Science and Technology (iQUEST),
University of California at Santa Barbara (UCSB)*

²*Department of Electrical and Computer Engineering, UCSB*

³*Department of Physics, UCSB*

⁴*Department of Materials, UCSB*

⁵*Submillimeter-wave superconductive sensors group, Jet Propulsion Laboratory*

A new type of semiconducting sensor for frequencies in the range 1-5 THz is under development in this UCSB/JPL collaboration. The active region of the device is shown schematically in Fig.

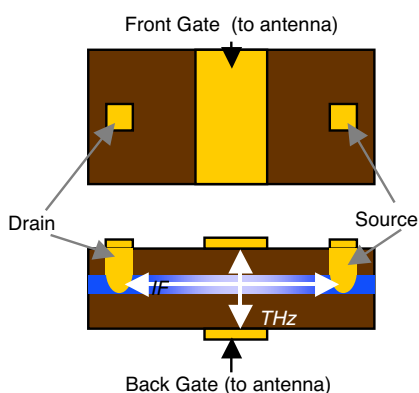


Figure 1: Schematic diagram of active region of a TACIT sensor.

1. THz radiation is coupled into a coplanar antenna (not shown). The antenna is terminated by a resonant absorber which is located between a front and a back gate. The absorber contains an electron gas bound in a quantum well. The Terahertz radiation is absorbed if it is resonant with the frequency of a transition between the quantized states, or subbands, of the quantum well. The absorbed radiation heats up the electrons in the quantum well, changing the resistance between a source and drain. It has been predicted that, when TACIT sensors are operated as heterodyne mixers, receiver noise temperatures of a few hundred K could be achievable at operating temperatures exceeding 20K, with $<1 \mu\text{W}$ of local oscillator (LO) power and IF bandwidths exceeding 10 GHz.¹ TACIT sensors can also be operated as fast, voltage-tunable direct detectors for THz radiation.²

In this contribution, we report on the design, fabrication and testing of TACIT sensors. A novel aspect of TACIT mixers is that they are four-terminal devices—the RF (THz) and IF (GHz) are coupled through separate contacts. This provides design flexibility as well as challenge. To our knowledge, no four-terminal THz mixers have been built. The current design is a modification of a design which is used successfully for superconducting hot-electron bolometers, which are two-terminal mixers. RF is coupled into twin slot dipole antennas which drive coplanar waveguide (CPW). The center conductor of one CPW line is connected to the front gate, the other to the back gate. The IF is coupled out on a microstrip line, which uses the same ground plane as the twin slot antenna. All lines are filtered to avoid RF leaking out along DC or IF lines.

Fabrication of TACIT sensors according to this design requires processing on both sides of the $<1 \mu\text{m}$ thick active region. We have based our process on the Epoxy Bond and Stop-Etch (EBASE) process developed at Sandia National Laboratories.³ Fig. 2 shows a prototype which has been fabricated and electrically tested. In this device, the twin-slot dipole antennas, ground plane, and filtered DC bias lines to the front and back gates, are visible through a submicron layer of GaAs.

This layer is bonded by epoxy to a carrier wafer of GaAs. The gold surface metallization shows the front gate, which is connected by a via to the center conductor of the underlying CPW line. Also shown are the IF and DC bias lines. All wire bonds are made to the exposed surface.

A processed device has been tested electrically by measuring source-drain current-voltage curves at a range of temperatures from 30 to 150 K. The theory of TACIT mixers¹ predicts that the mixer noise temperature is given by

$$T_N = \alpha^{-1}(8[\gamma^2 T_e] + 2T_e),$$

where T_e is the electron temperature (assumed to be much larger than the lattice temperature), α is the product of RF and IF coupling efficiencies, and $\gamma = 1/R(dR/dT_e)$, where R is the source-drain resistance. We will report on values of γ and αT_N extracted from electrical measurements using Eq. 1, and also discuss LO power requirements predicted based on these numbers. We will also discuss progress towards measurements of the NEP of fabricated devices, operating as direct detectors.

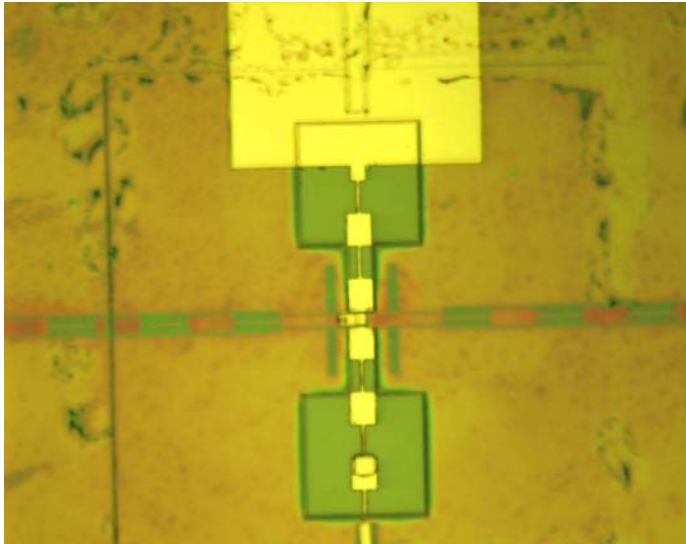


Figure 2: Photograph of prototype TACIT sensor. The thinnest visible gold lines are 1 micron wide.

This work is supported by NASA under contract NAG5 10299. We gratefully acknowledge helpful discussions with Dr. C. Cates and Dr. B. Thibeault.

1. Sherwin, M. S., Cates, C., Serapiglia, G. B., Dora, Y., Williams, J. B., Maranowski, K., Gossard, A. C. & McGrath, W. R., Tunable antenna-coupled intersubband terahertz (TACIT) mixers: the quantum limit without the quantum liquid. Proceedings of the far-IR, submm and mm detector technology workshop, Monterey April 1-3, 2002 (http://www.sofia.usra.edu/det_workshop/papers/manuscript_session6.html)
2. Cates, C. L., Briceno, G., Sherwin, M. S., Maranowski, K. D., Campman, K. & Gossard, A. C. A concept for a tunable antenna-coupled intersubband terahertz (TACIT) detector. *Physica E* **2**, 463-7 (1998).
3. Weckwerth, M. V., Simmons, J. A., Harff, N. E., Sherwin, M. E., Blount, M. A., Baca, W. E. & Chui, H. C. Epoxy bond and stop-etch (EBASE) technique enabling backside processing of (Al)GaAs heterostructures. *Superlattices and Microstructures* **20**, 561-7 (1996).

SIR Chip for TELIS

S.V. Shitov^{1,2}, V.P. Koshelets^{1,2}, P.A. Yagoubov², L.V. Filippenko¹, P.N. Dmitriev¹,
O.V. Koryukin¹, An.B. Ermakov^{1,2}, and R.W.M. Hoogeveen²

¹Institute of Radio Engineering and Electronics (IREE), Russian Academy of Sciences
Moscow, Russia

²National Institute for Space Research (SRON), the Netherlands

We report on first results of development a superconducting integrated receiver (SIR) chip for the 500-650 GHz channel of Terahertz Limb Sounder (TELIS) balloon project [1]. The general concept of the new device is quite similar to that used for superconducting integrated spectrometer presented last year at the Symposium [2]. The device comprises a double-dipole lens-antenna SIS-mixer pumped by an integrated Josephson-type phase-locked flux-flow oscillator (FFO), which provides the rf power also for a PLL harmonic mixer integrated on the same silicon chip of size 4 mm x 4 mm x 0.3 mm. The experimental chips (Fig. 1) are fabricated in IREE, Moscow [3].

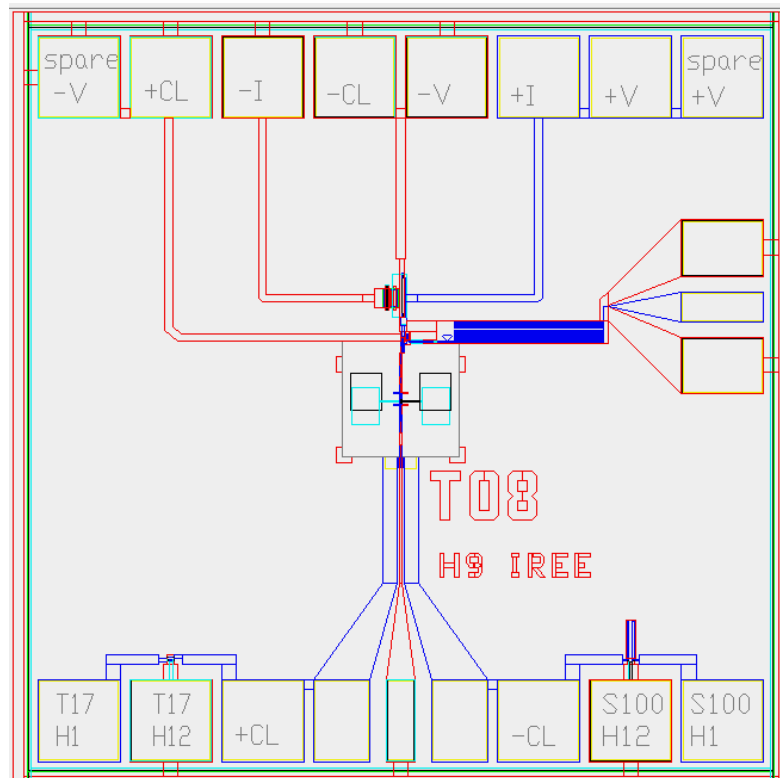


Fig. 1 General chip layout.

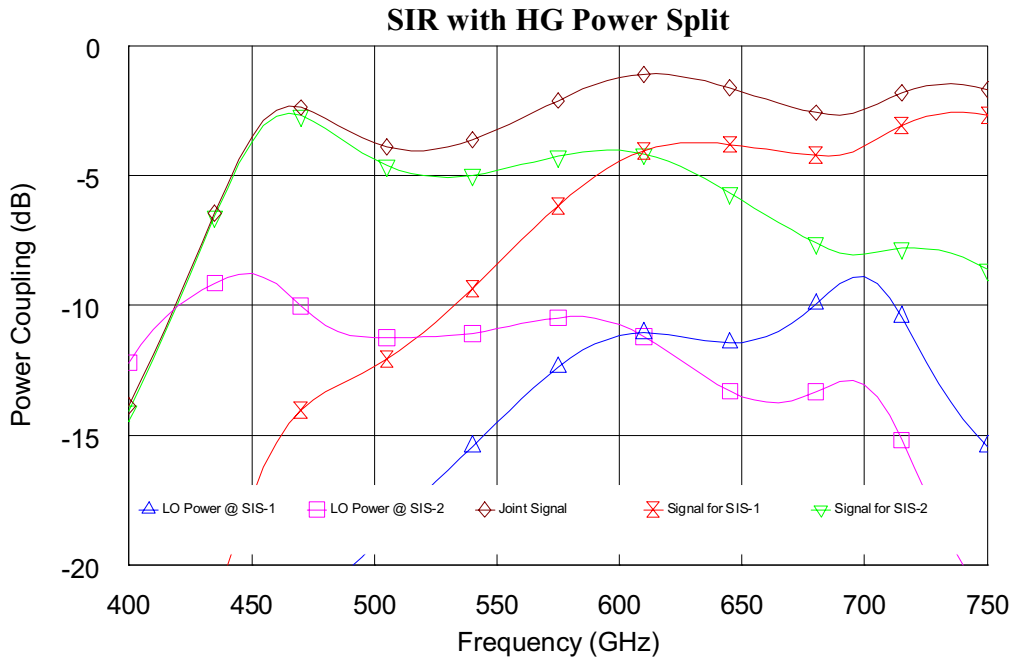


Fig. 2 Power split within the RF circuit of the chip for the case of external harmonic generator. Losses above the gap frequency are not included in the calculation.

A few new solutions are implemented in the SIR chip making it a new generation. To achieve the required instantaneous bandwidth of 500-650 GHz with emphasis on 600-650 GHz frequency range, a side-feed twin-SIS mixer with $0.8 \mu\text{m}^2$ junctions is implemented. The improved design of FFO is used suppressing the fine structure resonance phenomenon in the oscillator; the phase-lock/frequency-lock system eliminates industrial noise [4]. To reduce the magnetic field interference to the FFO, a folded control line feeder of the SIS mixer is placed opposite to the FFO, resulting in 10^{-3} suppression coefficient. The “Microwave Office” CAD tool is used for defining the chip characteristics as shown in Fig. 2 and Fig. 5.

A few batches of devices are produced in IREE and preliminary tested in SRON at dc and with a Fourier transform spectrometer (FTS). The FTS test presented in Fig. 3 demonstrates a possibility to obtain the required instantaneous bandwidth for the twin SIS mixer. However, we did not succeed yet in getting wide-band response for the single-SIS mixer as shown in Fig. 4.

The LO pump of both SIS mixer and harmonic mixer, however, is not flat and drops significantly above the boundary voltage of FFO unlike it was designed (Fig. 6). The reason for this behavior is not completely clear yet and has to be studied with the next design modification. We believe this problem can be solved, since SIR with a free-running FFO at 645 GHz has been tested successfully some time ago. A heterodyne experiment is under preparation.

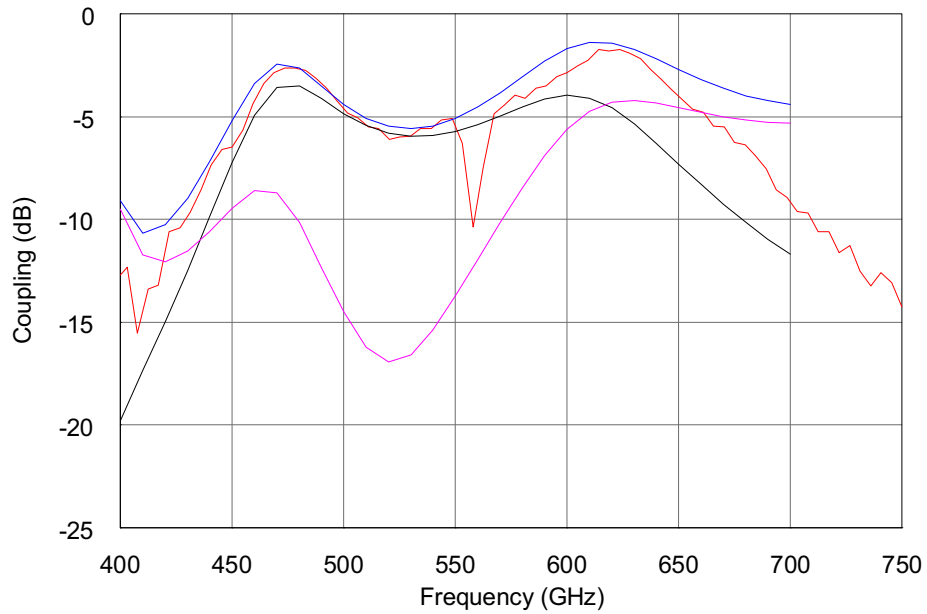


Fig. 3 FTS data (red curve) along with simulated response (smooth curves) calculated for twin-SIS mixer (blue) and for each of two junctions of the mixer (magenta and brown).

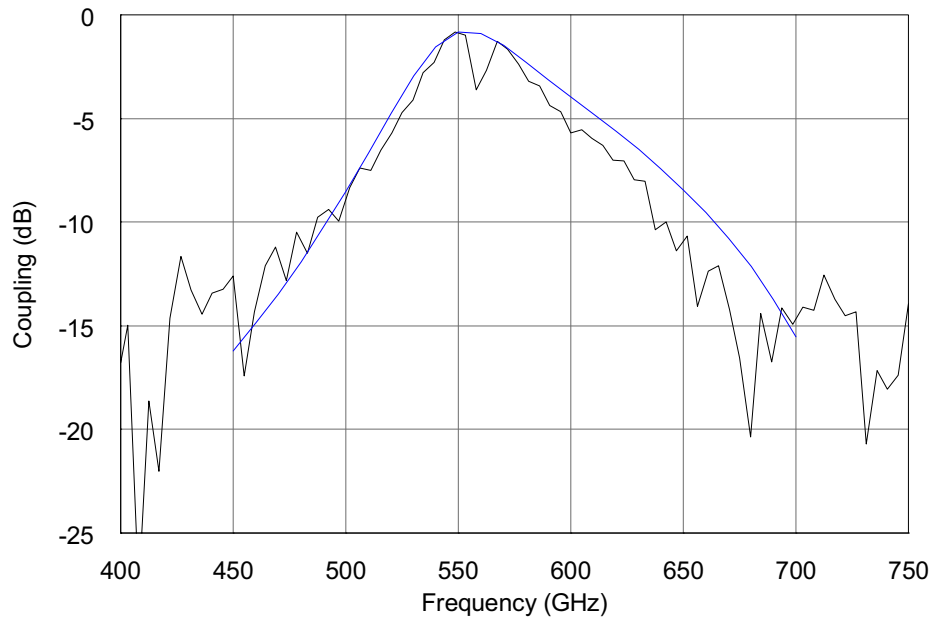


Fig. 4 FTS data (black curve) along with simulated response (smooth curve) calculated for single-SIS mixer (blue).

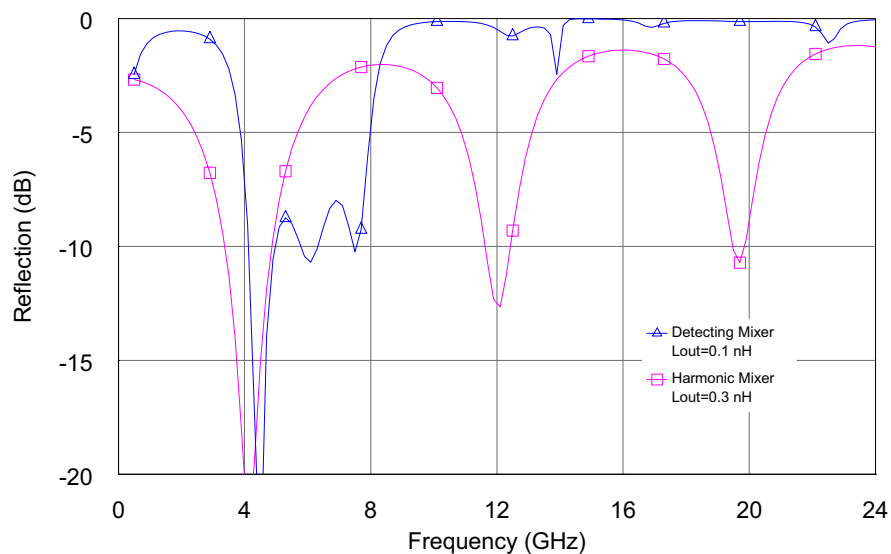


Fig. 5 Estimated IF port reflection for SIS mixer (triangles) and for harmonic mixer (squares) demonstrates 4-8 GHz coupling bandwidth for signal and good match for PLL reference source at 12 and 20 GHz, which is connected via an integrated transformer.

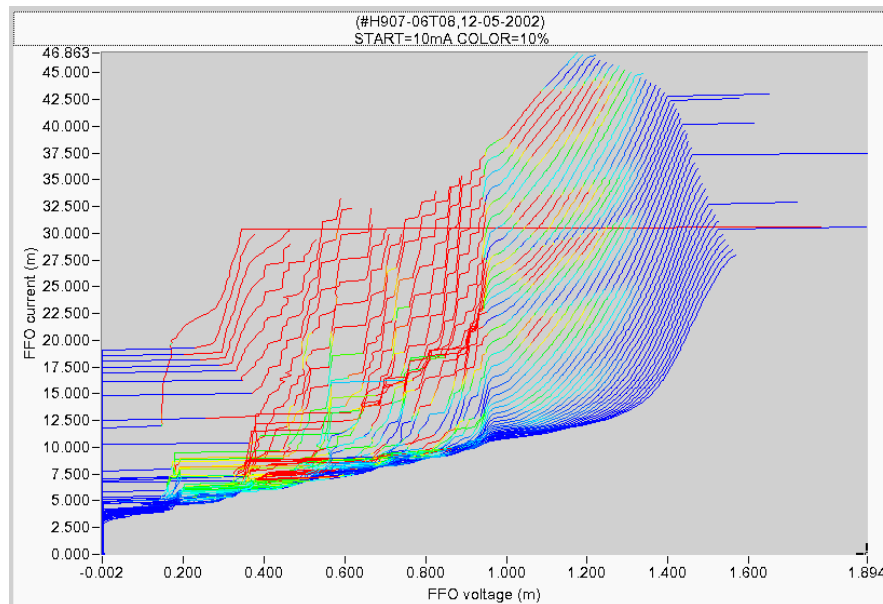


Fig. 6 IV-curves of FFO rainbow-colored by pump level of the SIS mixer. The red color corresponds to the sufficient pump of the SIS mixer; deep blue – no power.

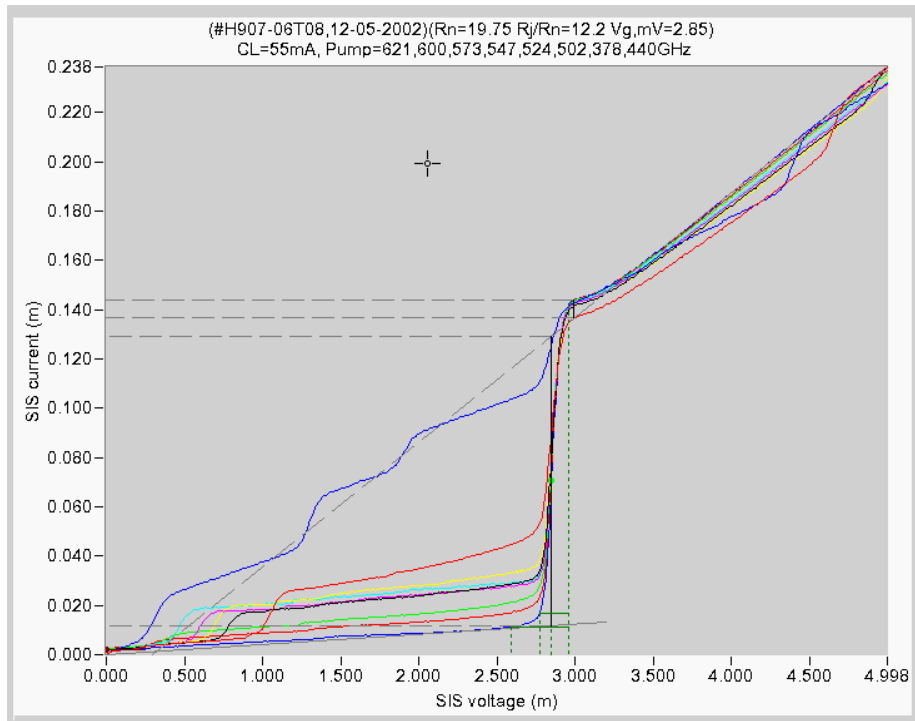


Fig. 7 Twin-SIS mixer pumped by FFO at different frequencies (listed at the top). IV-curves are colored for easier distinguishing.

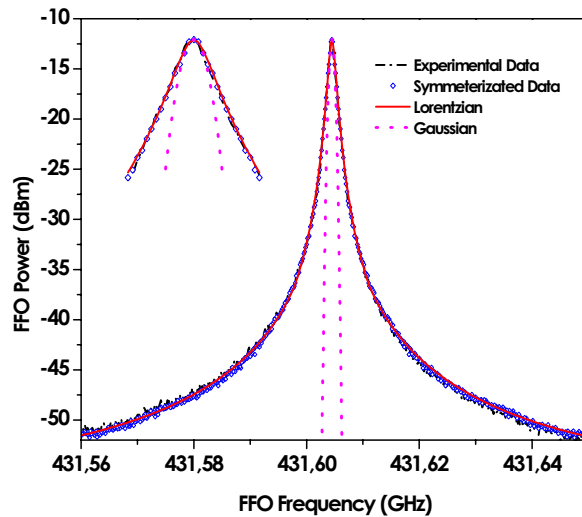


Fig. 8 Oscillation spectrum of the FFO demonstrates Lorencian shape.

Conclusion

Production of chips for TELIS is started satisfactory. Reliable small-junction ($A = 0.8 \mu\text{m}^2$, $R_n A = 25$) SIS mixers are tested to become the main line. Twin SIS mixer is shown to cover entire band 500-650 GHz (and even wider). The FTS response is found repeatable from sample to sample. However, its flatness has yet to be improved via circuit design fine-tuning. The single-junction SIS mixers appeared difficult to tune for the wide-band operation, but they can be used as the low-power (LO) narrow-band option for 600-650 GHz range. The LO power coupled from FFO drops down above the boundary voltage. This effect is not fully understood yet. The linewidth of FFO is found to be of Lorencian shape that means the wide-band noise is dominating and the external interference is negligible.

The work was supported in parts by INTAS project 01-0367, ISTC project # 2445, and the Nederlandse Organisatie voor Wetenschappelijk Onderzoek (NWO).

Reference

- [1] U. Mair, M. Krocka, G. Wagner, M. Birk, H.-W. Hübers, H. Richter, A. Semenov, P. Yagoubov, R. Hoogeveen, T. de Graauw, H. van de Stadt, A. Selig, V. Koshelets, S. Shitov, B. Ellison, D. Matheson, B. Alderman, M. Harman, B. Kerridge, R. Siddans, J. Reburn, "TELIS – development of a new balloon borne THz/submm heterodyne limb sounder", Presented at *13-th International Symposium on Space Terahertz Technology*, Harvard University, March 26-28, (2002), to be published in this *Symposium Proceedings*.
- [2] S. V. Shitov, V. P. Koshelets, P. N. Dmitriev, L. V. Filippenko, An. B. Ermakov, V. V. Khodos, V. L. Vaks, "A Superconducting Spectrometer with Phase-Locked Josephson Oscillator," *Proc. 13-th International Symposium on Space Terahertz Technology*, Harvard University, March 26-28, pp. 411-420 (2002).
- [3] L. V. Filippenko, S. V. Shitov, P. N. Dmitriev, A. B. Ermakov, V. P. Koshelets, and J. R. Gao, "Integrated superconducting receiver: fabrication and yield," *IEEE Trans. on Appl. Supercond.*, vol. 11, No 1, pp. 816-819 (2001).
- [4] V.P. Koshelets, S.V. Shitov, P.N. Dmitriev, A.B. Ermakov, A.S. Sobolev, M.Yu. Torgashin, P.R. Wesselius, P.A. Yagoubov, C. Mahaini, J. Mygind, "Externally Phase-Locked Local Oscillator for Submm Integrated Receivers: Achievements and Limitations," *Applied Superconductivity Conference ASC'2002*, Houston, USA, August 2002, Report 4EA10, to be published in *IEEE Trans. on Appl. Supercond.*

Large RF Bandwidth Waveguide to Thin-film Microstrip Transitions on Suspended Membrane for use in Silicon Micromachined Mixer blocks at THz Frequencies

J.W. Kooi¹, Christian Drouet d'Aubigny², Chris Walker², and Arthur W. Lichtenberger³

¹Dept. of Physics, Caltech, MS 320-47, Pasadena, Ca 91125.

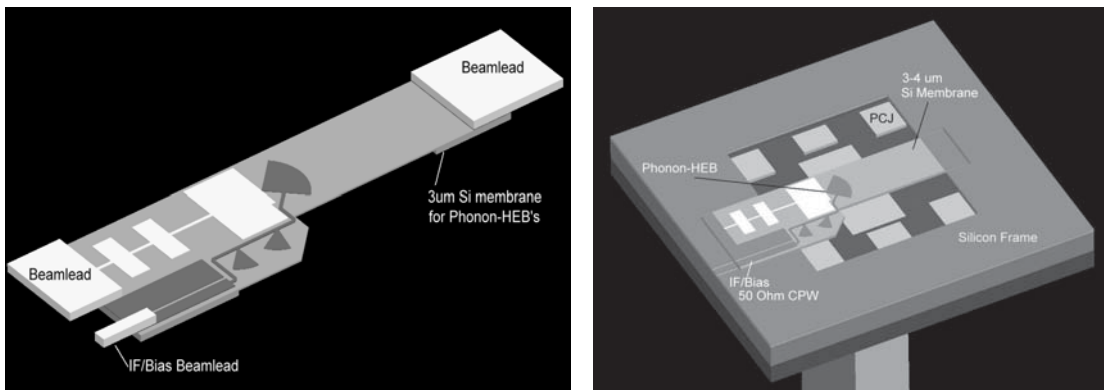
²Steward Observatory, University of Arizona, 933 N. Cherry Ave., Tucson, AZ 85721.

³Dept. of Electrical Engineering, Thornton Hall, University of Virginia, Charlottesville, VA 22903-2442.

With the advent of broad bandwidth low noise Hot Electron Bolometer (HEB) mixers at Terahertz frequencies, there is a need for a large RF bandwidth (scalable) waveguide to thin-film transition. At present nearly all HEB receivers operating above 800 GHz are implemented in quasi-optical (twin-slot, log-periodic, dipole) structures. This despite the fact that waveguide technology offers the prospect of higher throughput, better telescope coupling, and large format imaging arrays with well aligned beams on the sky.

There are several reasons for the use of open structure mixers in the THz regime. First, though there are many excellent fixed tuned waveguide probe designs in circulation, they nearly all are implemented in reduced half-height waveguide structures. Not only are these reduced height waveguides difficult and expensive to fabricate above 700 GHz, they also have significantly increased Ohmic loss when compared to a full height waveguide block at the same frequency. Secondly, even if a reduced height waveguide block at THz frequencies could be made, the actual device (usually mounted on a quartz substrate) becomes too small to handle or space qualify. Finally, up to now it has been difficult to realize a fixed tuned low loss full-height waveguide transition with a fractional bandwidth comparable to that of well designed quasi-optical (twin-slot) devices.

Fortunately, we are able to overcome these obstacles with the use of thin-film microstrip radial probe transitions on suspended membrane in full waveguide height silicon micro-machined mixers blocks. To maximize the RF bandwidth and coupling efficiency we utilize photonic crystal structures to suppress leakage directly above and below the membrane. It is seen that this work is applicable to both single element and multi-element array receivers. Membranes thickness is adapted to facilitate both phonon-cooled and diffusion cooled HEB's. Diffusion cooled HEB's on 1 μ m Silicon-Nitride have been fabricated at UVA, Phonon cooled HEB devices on NbTiN films are expected in the very near future. Detailed HFSS simulation results of the proposed design are presented.



Photon Counting vs Photon Integration at SubMM Waves

Boris S. Karasik

Jet Propulsion Laboratory, California Institute of Technology, Pasadena, CA 91109

Andrew V. Sergeev

Wayne State University, Detroit, MI 48202

Future needs of submillimeter wave astronomy include ultrasensitive detector arrays capable of achieving a noise equivalent power (NEP) $\sim 10^{-20}$ W/Hz^{1/2} at 0.1 K. Bolometric detectors using superconducting transition-edge sensors are considered as the most promising technology. An alternative way to achieve an equivalent sensitivity is to use photon-counting devices. The photon counting in the submillimeter wave range has been recently demonstrated by Astafiev et al. using quantum dots. Other proposals include various superconducting structures potentially capable of registering single quantum events. Besides achieving an unparallel sensitivity, both technologies will face a great challenge of maintaining a sufficiently large dynamic range limited by the cosmic background and the instrument bandwidth. The maximum optical loading for a bolometer directly decreases with the sensitivity ($P_{\text{opt.}} \sim \text{NEP}^2$). For the photon counters, handling high level of background radiation translates into high counting rate that can be engineered in some types of the devices. The readout electronics for an N-element array of counters should be, however, at least N times faster in order to detect individual photons from each element. Since the intensity of the cosmic background varies strongly over the submillimeter wave range, the trade-off between the sensitivity and the dynamic range will depend on the wavelength.

We will present an analysis of the potential performance of promising photon integrating and photon counting devices for subMM wave background limited narrowband applications. The emphasis will be made on a comparison of the hot-electron superconducting direct detectors and photon counters with other technologies.

This research was carried out by the Jet Propulsion Laboratory, California Institute of Technology under a contract with the National Aeronautic and Space Administration. The research at the Wayne State University was sponsored by a NASA grant.

Single Chip, Beam Combining, Interferometric Detector for Submillimetre-wave Astronomy

E. Campbell, S. Withington, G. Yassin, C. Y. Tham
Dept. Physics, Univ. Cambridge, UK

S. Wolfe, K. Jacobs
Dept. Physics, Univ. Cologne, Germany

Abstract

We present results from an interferometer using a single chip, beam combining, superconducting detector. The interferometer consists of back to back corrugated horns feeding a back to back finline transition. The beams are combined in microstrip using a directional coupler. The detector was illuminated by a coherent source in the far field at frequencies between 320 GHz and 380 GHz. The resulting beam patterns show fringes with excellent visibility and the correct angular separation.

1 Introduction

The millimetre and submillimetre regions of the spectrum offer a great deal to astronomers. Perhaps one of the most valuable aspects of millimetre astronomy is the Cosmic Microwave Background (CMB). Encoded within its anisotropies, both in its temperature and looking to the future its polarisation, lies a wealth of information on the structure of the early universe and constraints on cosmological parameters. Interferometers offer certain advantages for studying the CMB, firstly, they sample the Fourier domain directly. Secondly, they offer a huge range in angular resolution and finally they have excellent intrinsic noise rejection due to their ability to filter out signals at frequencies other than the fringe rate. There is also interest in putting

FIR interferometers into space [1]. Here they would escape the difficulties imposed by the Earth's atmosphere and could explore early galaxy formation as well as nearby planet and star formation.

Interferometry at radio wavelengths has previously been limited to heterodyne systems where the signal is downconverted to a lower frequency. These systems use front-end amplifiers that limit the bandwidth, however, at optical wavelengths beam combination is carried out directly [2]. In order to study the very small anisotropies of the CMB and to explore early structure formation we require very high sensitivity, excellent noise performance and large numbers of detectors. Here we present results from a single chip, beam combining interferometer operating at submillimetre wavelengths. The technologies we demonstrate here at 350 GHz can be applied from the millimetre through to the FIR. By combining the beams directly we avoid the bandwidth limited front-end amplifiers required by heterodyne systems and can take advantage of the broadband, high sensitivity behaviour of bolometric detectors [3]. Furthermore, this approach offers all the potential of sophisticated microwave signal processing techniques as well as the possibility of placing many detectors on a single substrate.

2 Interferometer Design

The interferometer consists of two back to back corrugated horns forming a single baseline of 83.4 mm. The horns feed into back to back finline transitions which couples each horn to superconducting microstrip. The beams are then combined using a -15 dB directional coupler leading to two SIS tunnel junctions behaving as direct detectors. The key dimensions of the interferometer are listed in Table 1.

The corrugated horns and waveguide were machined out of a split aluminium block which was later gold sputtered. At each aperture a parabolic mirror was placed to form a horn-reflector with a flat phase front at the projected aperture. This can be seen in Figure 1. The heart of the interferometer is the superconducting chip, see Figure 2. This combines the two finline transitions, the directional coupler and two Nb/AlO_x/Nb tunnel junctions all onto a single quartz substrate. Modelled using transverse resonance, spectral-domain analysis and the method of moments it was fabricated using photo-lithography and thin film sputtering techniques [4, 5]. Each finline is made of two niobium fins separated by a layer of silicon oxide 400 nm thick. These act to transform the high impedance of the waveguide to the low impedance of the microstrip.

Central to this design is that the beam combination is done before detection. This

is done using a -15 dB directional coupler which is shown in Figure 3. A directional coupler would not be used in an astronomical instrument, this would demand a more sophisticated correlator, for which there is plenty of room on the substrate. However, by using capacitive bridges to enhance the coupling, this design allows the system to demonstrate submillimetre beam combining interferometry without the need for the fabrication of dc blocks.

Another innovative aspect to this design was the use of two Nb/AlOx/Nb tunnel junctions, also visible in Figure 3. This offers the flexibility of allowing the tunnel junction on either arm of the directional coupler to act as the detector. By voltage biasing one of the junctions in the middle of the first photon step it acted as the detector while the other junction was biased above the gap so it behaved as a resistive load of around 21Ω . Since SIS tunnel junctions can detect photons both above and below the gap it was important to bias significantly higher than the gap voltage to make the junction a resistive load. SIS tunnel junctions were used as they have both high dynamic range and good sensitivity [6], however, an astronomical instrument would probably use TES detectors taking advantage of their greater sensitivity and noise performance.

The design we have implemented offers a significant amount of potential. The horns which are currently being used with parabolic mirrors to form horn-reflector antennas could be used to illuminate large aperture telescopes to achieve higher angular resolution. The large area of substrate could also be exploited to combine multiple baselines as well as implementing filtering and phase shifting, similar to the broadband correlation techniques being applied at microwave frequencies [7].

3 Theory

This interferometer implements pupil plane combination where afocal beams are superposed and the resulting intensity is measured by a single element detector. This differs from the more familiar image plane combination where beams are mixed in the focal plane forming an entire set of fringes that can be measured with an imaging array. In either case, however, the basic principle is the same, the signals from each of the two elements, E_1 and E_2 , are added and the time averaged intensity measured by the detector,

$$\begin{aligned} \langle (E_1 + E_2)(E_1 + E_2)^* \rangle &= \langle |E_1|^2 \rangle + \langle |E_2|^2 \rangle + \langle E_1 E_2^* \rangle + \langle E_2 E_1^* \rangle \\ &= \langle |E_1|^2 \rangle + \langle |E_2|^2 \rangle + \langle 2|E_1||E_2| \cos \phi \rangle \end{aligned} \quad (1)$$

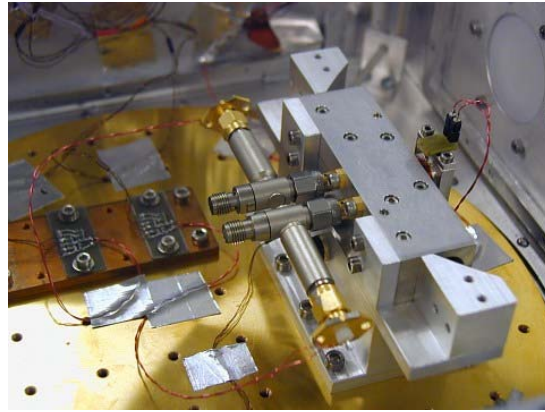


Figure 1: Exterior view of the interferometer. Two parabolic mirrors, two bias tees and the superconducting coil are clearly visible, attached to the split aluminium block in the centre.



Figure 2: Superconducting chip containing two finline transitions, a beam combining directional coupler and two SIS tunnel junctions

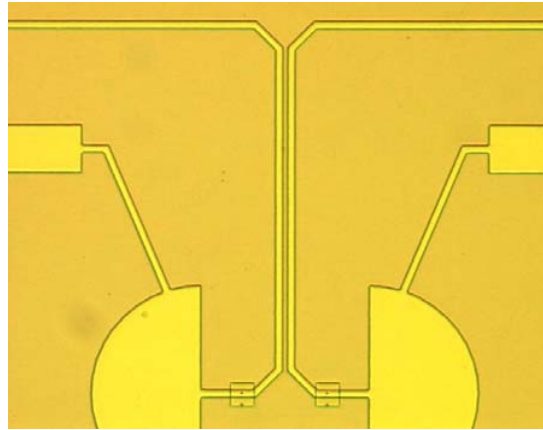


Figure 3: Close up view of the chip showing the microstrip from each finline coming together to form a directional coupler before entering radial stubs. Prior to each stub a SIS tunnel junction can be seen.

Diameter of horn aperture	10.8 mm
Axial length of horn	32.75 mm
Depth of corrugations	0.260 mm
Width of corrugation slots	0.210 mm
Width of corrugation walls	0.147 mm
Focal length of mirrors	19.3 mm
Distance between mirror centres	83.4 mm
Waveguide dimensions	0.700 × 0.350 mm
Substrate dimensions	6.50 × 0.55 × 0.08 mm
Resistance of tunnel junctions	21 Ω
Area of tunnel junctions	1.0 μm ²

Table 1: Key dimensions of the interferometer.

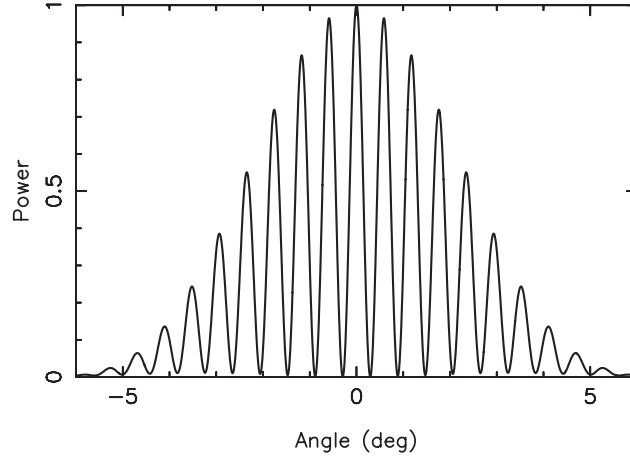


Figure 4: Expected fringe pattern from a 350 GHz source at a distance of five metres.

where ϕ is the phase difference between the two signals. In the case of a point source in the far field this is given simply by $\phi = \frac{2\pi B}{\lambda} \sin \theta$, where B is the baseline and θ is the direction of the source relative to the normal to the baseline.

Using modal matching the field at the horn aperture was calculated. Gaussian optics was then used to propagate this field in order to generate the beam pattern at five metres, the distance to the source. By combining the beam patterns of the two horns the predicted fringe pattern at a frequency of 350 GHz was calculated and is shown in Figure 4. The fringe separation, λ/B , is 0.59° .

4 Results

The Dewar containing the interferometer was placed on a motorised rotating table. The Dewar windows were illuminated by a 350 GHz source five metres from the detector, consisting of a Gunn oscillator and two varactor multipliers. On the front of the Dewar two polarising grids were mounted to allow the radiation entering each window to be attenuated independently. The beam patterns for each channel of the interferometer were measured in turn by blocking off the other channel and measuring the photon assisted tunnelling current as the table rotated. The junction of the channel being measured was biased in the middle of the first photon step and the other junction was biased well above the gap to act as a load. Synchronous detection was

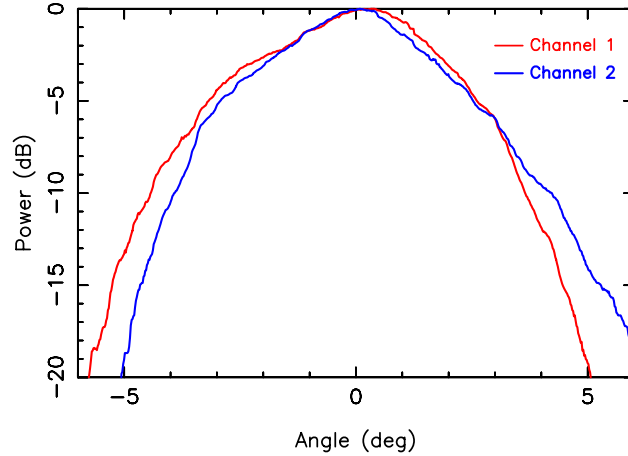


Figure 5: Measured beam patterns using a 350 GHz source at five metres. The two plots correspond to the two channels of the interferometer.

employed by electrically modulating the Gunn oscillator and using a lock-in amplifier. Figure 5 shows the beam patterns of both channels. In addition to some asymmetry the overlap differs from what is expected at this distance by about a degree. This is due to a small misalignment of the parabolic mirrors.

As mentioned earlier the beams from each channel are combined using a -15 dB directional coupler. The difficulty is that to achieve good visibility the signals from the two channels must be equal in magnitude. This was done by attenuating the beam entering the channel whose junction was being used as the detector. The results are shown in Figure 6. This shows two sets of fringes each with an angular fringe separation of 0.59° , as predicted, and visibility reaching 93%. The visibility can be improved even further by better alignment of the mirrors, increasing the distance of the source and careful adjustment of the attenuation. One set of fringes is centred around zero, while the other is offset. The shifted set of fringes is the result of placing a slab of dielectric in front of one of the Dewar windows. This acts as a delay line increasing the path length of one of the channels thereby causing the fringes to shift. This demonstrates the principle of fringe rotation and confirms that the system behaves as an interferometer.

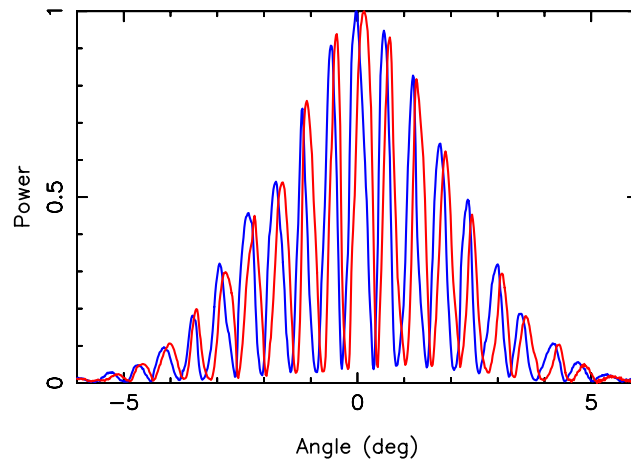


Figure 6: Two sets of interferometric fringes measured with a source placed at five metres. One of the sets of fringes is shifted due to the introduction of a dielectric slab in front of one of the Dewar windows.

5 Conclusion

These results show the successful design, manufacture and operation of the first ever single chip, beam combining interferometer. Excellent performance was seen over the entire frequency range of the source, 320–380 GHz. In terms of possible advances there is sufficient room on the substrate for a wide range of signal processing, allowing, for example, the measurement of multiple baselines. There is also the option of using TES detectors in combination with SQUID based readout electronics for improved sensitivity and noise performance.

References

- [1] D. T. Leisawitz, W. C. Danchi, M. J. DiPirro, L. D. Feinberg, D. Y. Gezari, M. Hagopian, W. D. Langer, J. C. Mather, S. H. Moseley, M. Shao, R. F. Silverberg, J. Staguhn, M. R. Swain, H. W. Yorke, and X. Zhang. Scientific motivation and technology requirements for the SPIRIT and SPECS far-infrared/submillimeter space interferometers. In *Proc. SPIE Vol. 4013, p. 36-46, UV, Optical, and IR Space Telescopes and Instruments, James B. Breckinridge; Peter Jakobsen; Eds.*, pages 36–46, July 2000.
- [2] J. E. Baldwin and C. A. Haniff. The application of interferometry to optical astronomical imaging. *Phil. Trans. R. Soc. Lond. A*, 360:969–986, 2002.
- [3] S. Ali, P. Rossinot, L. Piccirillo, W. K. Gear, P. Mauskopf, P. Ade, V. Haynes, and P. Timbie. MBI: Millimetre-wave bolometric interferometer. In *AIP Conf. Proc. 616: Experimental Cosmology at Millimetre Wavelengths*, pages 126–128, 2002.
- [4] G. Yassin, S. Withington, M. Buffey, K. Jacobs, and S. Wulff. A 350 GHz SIS antipodal finline mixer. *IEEE Trans. Microwave Theory Tech.*, 48:662–669, 2000.
- [5] G. Yassin and S. Withington. Electromagnetic models for superconducting millimetre-wave and submillimetre-wave microstrip transmission lines. *J. Phys. D:Appl. Phys.*, 28:1983–1991, 1995.
- [6] S. Withington, K. G. Isaak, S. A. Kovtonyuk, R. A. Panhuyzen, and T. M. Klapwijk. Direct detection at submillimetre wavelengths using superconducting tunnel junctions. *Infrared Phys. Technol.*, 36:1059–1075, 1995.
- [7] C. Holler. Broadband Correlator for AMI. In *ASP Conf. Ser. 257: AMiBA 2001: High-Z Clusters, Missing Baryons, and CMB Polarization*, pages 321–326, 2002.

Measurements and Simulations of Overmoded Waveguide Components at 70-118 GHz, 220-330 GHz and 610-720 GHz

G. A. Ediss

National Radio Astronomy Observatory*
Charlottesville, VA 22903

Keywords: waveguide, waveguide transitions, waveguide components, loss measurement

Abstract

For low-loss transmission of the LO in the ALMA Band 6 cartridges, overmoded waveguide may be used. In this paper, we report on the theoretical and measured losses of various sizes of waveguide in the frequency ranges 70-118 GHz, 220-330 GHz and 610-720 GHz.

Introduction

The use of overmoded waveguide for low-loss transmission dates back to the earliest usage of waveguide [1], [2], [3], [4]. This use is now quite standard in circular waveguide [5], [6] and in rectangular waveguide [7], [8], [9], [10], [11]. In this paper, we deal with the transmission of the fundamental mode (TE₁₀) in overmoded rectangular waveguide. This mode is the easiest mode to generate and control in signal sources and components such as couplers, hybrids, etc. as no mode converters are required. This will be used for the transmission of the LO from the final multiplier in the Band 6 multiplier chain, which will be on the 90 K or 20 K stage of the cartridge for thermal loading reasons, and the mixer, which will be on the 4 K stage. Depending on the thermal load conditions, these two components will be up to 200 mm apart. Due to waveguide losses and available/required power levels, losses should be as low as possible.

Theory

Loss, α , of the fundamental (TE₁₀) mode is given by [12]

$$\alpha = \frac{\lambda}{b \cdot \lambda_g} \cdot \left(\frac{\pi}{\lambda \cdot \eta \cdot \sigma} \right)^{1/2} \cdot \left[1 + \left(\frac{\lambda_g}{\lambda c} \right)^2 \cdot \left(1 + 2 \cdot \frac{b}{a} \right) \right] \cdot 8.676 \frac{\text{dB}}{\text{m}}$$

where λ is the free space wavelength; λ_g is the waveguide wavelength in waveguide of width, a , and height, b ; σ is the conductivity of the wall material and η is the impedance of free space ($120 \cdot \pi \Omega$). Figure 1 shows the theoretical loss for a frequency of 243 GHz as a function of waveguide width, a , for $a/b = 2$ (standard waveguide). The waveguide for Band 6 (WR3.7) is 0.94 x 0.47 mm (37 x 18.5 mils), for which the loss would be approximately 18 dB/m for copper ($\sigma = 4.00 \cdot 10^7$ S/m), and nearly 117 dB/m for stainless

*The National Radio Astronomy Observatory is a facility of the National Science Foundation operated under cooperative agreement by Associated Universities, Inc.

steel ($\sigma = 0.1 \cdot 10^7$ S/m), which is preferred for its thermal properties. These include the usual factor of 1.3** to account for surface roughness effects [13], and Tischer [13] also gives a further factor of 1.135** for an “anomalous skin effect” in copper. Using WR10 (2.54 x 1.27 mm, 100 x 50 mils) as the overmoded waveguide, the loss reduces to 3.8 dB/m and 26 dB/m, respectively.

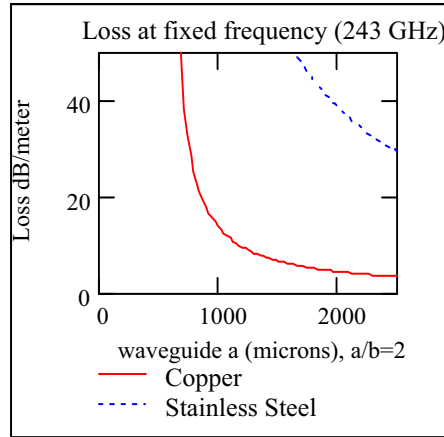


Figure 1

Losses will, of course, be reduced by a factor of approximately 3 to 4 upon cooling copper to about 4 K according to Wollack *et al.* [14], whereas for stainless steel the reduction is only about 25% [15].

Trapped Modes

One problem with using overmoded waveguide systems is the possibility of exciting unwanted modes that can cause resonant losses [14], [16], [17], especially in systems where two tapers from/to fundamental mode waveguide are used. The unwanted modes are reflected at some point in the tapers and are “trapped” causing deep, narrow resonances. The frequency spacing, δf , can be very fine, depending upon the total length between the reflection points, L [9]

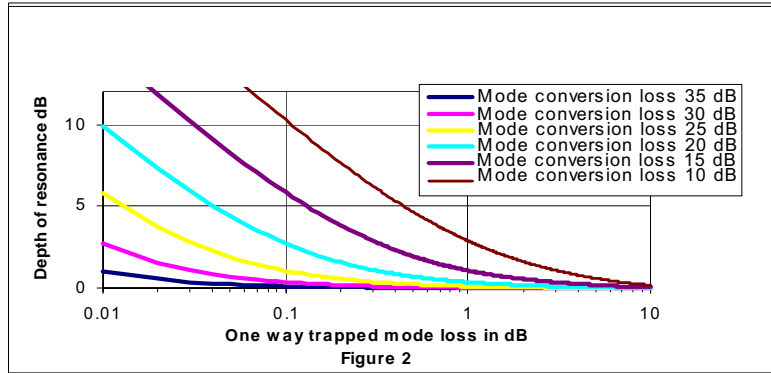
$$\frac{\lambda f}{f} = \frac{\lambda}{2L} .$$

The depth of the resonances is given by [10] as

$$\frac{P_{\min}}{P_{\max}} = \frac{1 - \frac{(2 \cdot P_c \cdot A)}{(1 + A)}}{1 + \frac{(2 \cdot P_c \cdot A)}{(1 - A)}}$$

where P_{\max} is the power transmitted through the system away from resonance, P_c is the power converted into the trapped mode (mode conversion), and A is the one-way power transmission of the trapped mode. (Note that equation (2) given in [9] is incorrect.) Calculations are shown in Figure 2.

** Losses in dB are multiplied by these factors.



For typical tapers, the mode conversion is -20 dB (or better), with a one-way mode loss of 2 dB, and the resonances are approximately 0.2 dB deep which is negligible. Cooling to 20 K, however, will reduce the one-way loss to about 0.67 dB which will increase the resonance depth to 0.5 dB. Also of concern for ALMA is any change in phase of the LO as it is tuned in frequency across a resonance. Unfortunately, it has not been possible to measure the phase with any of the present measuring systems.

Trapped modes will also be excited by any bends or twists included in the waveguide between the tapers. (H-plane bends are worse than E-plane bends in this regard for oversize waveguide with the usual E-field orientation [9][10]. The opposite is true for “Tall” guide (reciprocal a to b ratio), but “Tall” guide has more resonances.) Mode filters are difficult to use at these frequencies due to the small sizes and the large number of modes (WR10 has 14 modes at 300 GHz, 62 at 700 GHz), all of which can be excited above their cut-off frequencies by any discontinuities.

The width of the transmission resonances also gives an indication of the mode conversion level. [14] gives the conversion as

$$P_c = \frac{\pi}{2} \cdot \frac{\Delta f}{f} \cdot (1 - R_{min})$$

where R_{min} is the depth of the resonance, f is the resonant frequency, and Δf is the half-power width of the resonance.

QuickWave and CST Calculations

QuickWave [18] or CST [19] Finite Difference Time Domain EM simulators can be used to analyze such systems, but run into difficulty with such large structures (in wavelengths). As meshes with cell sizes of less than approximately 0.1 wavelengths should be used [20], complete structures cannot be analyzed due to memory limitations and calculation times. Partial structures can be analyzed (tapers, bends, etc.) which give some idea of the problems. In runs with bends, trapped modes are clearly seen and the change in their depth can be shown to be a function of material conductivity. QuickWave was used for the following. Figure 3 shows the calculated transmission of a 12.7 mm linear taper from WR3.7 to WR10 with 2.54 mm lengths of waveguide at each end, a 25.4 mm radius (center-line) 90-degree E-plane bend in WR10 and then a similar taper with waveguide sections back to WR3.7 for a perfect conductor. Figure 4 is the same geometry using a conductivity of $0.5 \cdot 10^7$ S/m (no surface roughness). Figures 5 and 6 show the phase for these two cases, respectively, and show that there are phase effects for deep resonances. For small resonances (< 1 dB), there are no phase effects. Similar effects can be achieved by inserting lossy material in the waveguide to obtain the same one-way path loss, but this can add extra reflections at the front and back surfaces of the material. Figure 7 shows the transmission and reflection of two lossless linear tapers of 7.62 mm length, from WR3.7 to WR10, back-to-back with a section of overmoded waveguide, WR10, of length 2.54 mm between them. Figure 7 also shows that tapers of sufficient length and perfect flange alignment have very little mode conversion. Figure 8 shows the results for two 1.27 mm long lossless tapers.

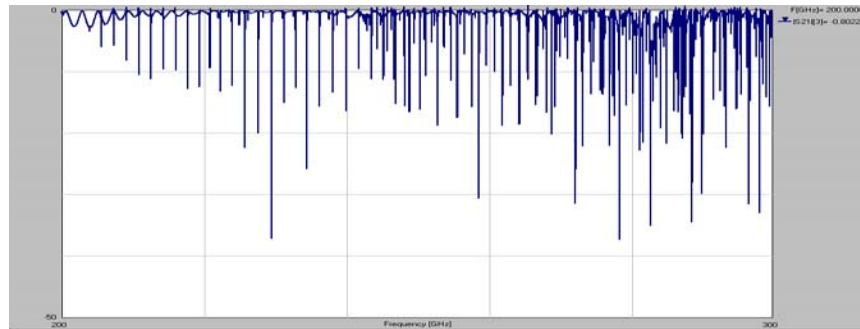


Figure 3. Calculated transmission (0-50 dB, 10 dB per division) as a function of frequency (200-300 GHz, 20 GHz per division) of a 12.7 mm linear taper from WR3.7 to WR10 with 2.54 mm lengths of waveguide at each end, a 25.4 mm radius 90 degree E-plane bend in WR10, and then a similar taper with waveguide sections back down to WR3.7 for a perfect conductor.

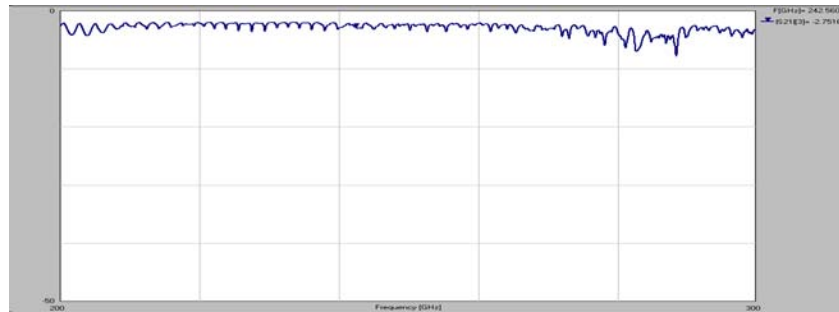


Figure 4. Calculated transmission (0-50 dB, 10 dB per division) as a function of frequency (200-300 GHz, 20 GHz per division) of a 12.7 mm linear taper from WR3.7 to WR10 with 2.54 mm lengths of waveguide at each end, a 25.4 mm radius 90-degree E-plane bend in WR10 and then a similar taper with waveguide sections back down to WR3.7 for a conductivity of $0.5 \cdot 10^7$ S/m.

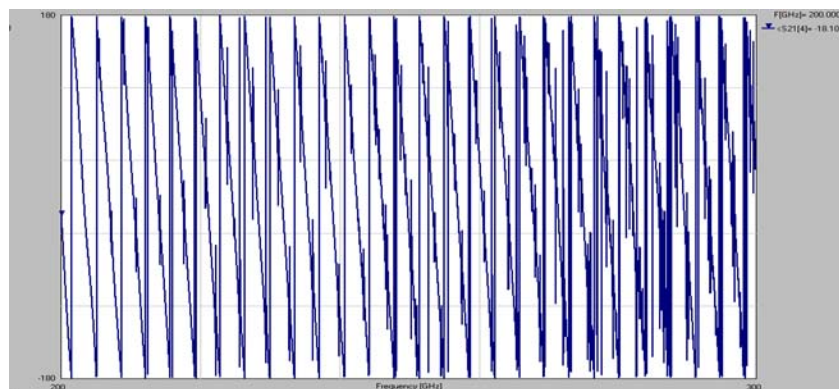


Figure 5. Transmission phase (+180 to -180 degrees) as a function of frequency (200-300 GHz, 20 GHz per division) of a 12.7 mm linear taper from WR3.7 to WR10 with 2.54 mm lengths of waveguide at each end, a 25.4 mm radius 90-degree E-plane bend in WR10 and then a similar taper with waveguide sections back down to WR3.7 for a perfect conductor.

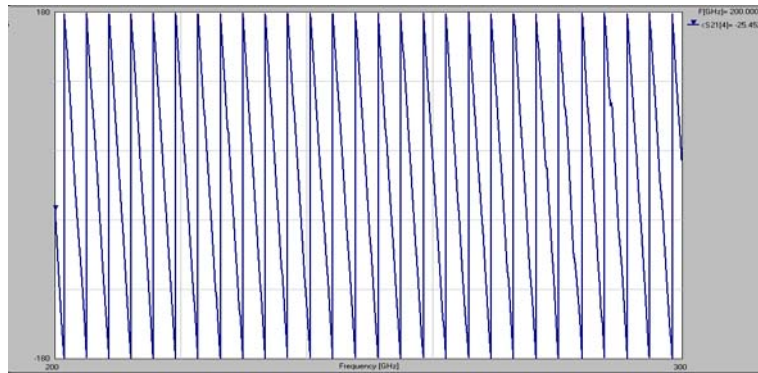


Figure 6. Calculated transmission phase (+180 to -180 degrees) as a function of frequency (200-300 GHz, 20 GHz per division) of a 12.7 mm linear taper from WR3.7 to WR10 with 2.54 mm lengths of waveguide at each end, a 25.4 mm radius 90-degree E-plane bend in WR10 and then a similar taper with waveguide sections back down to WR3.7 for a conductivity of $0.5 \cdot 10^7$ S/m.

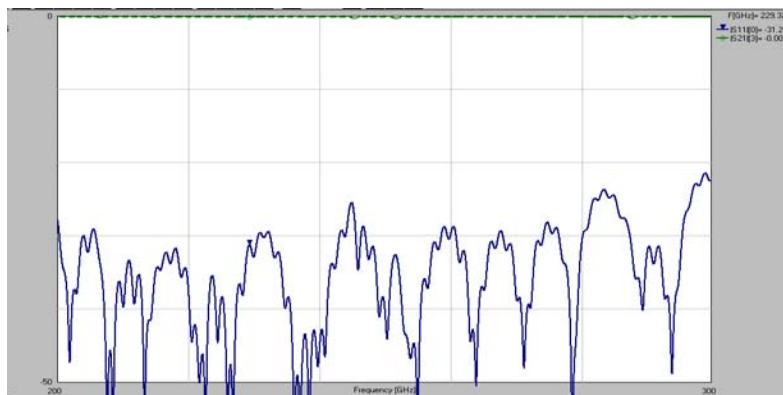


Figure 7. S11 and S21 for two lossless WR3.5 to WR10 tapers (7.62 mm long) back-to-back.

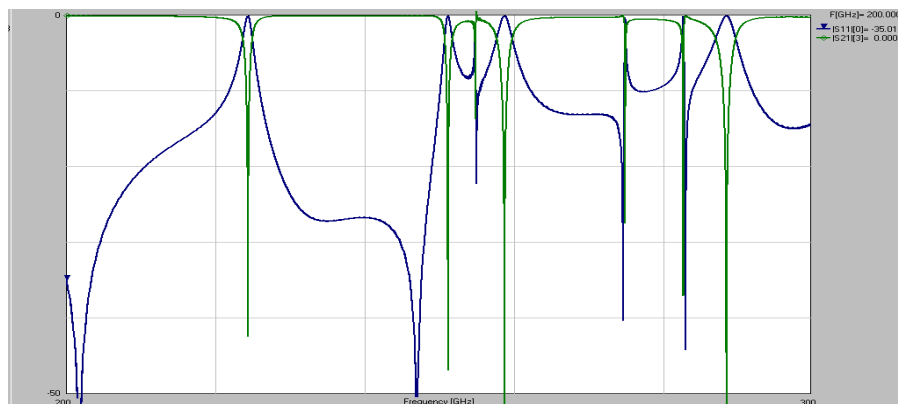


Figure 8. S11 and S21 for two lossless tapers WR3.5 to WR10 (1.27 mm long) back-to-back.

Scale Model Measurements at 69-118 GHz (Scale factor 7.14 from Band 9, 600-700 GHz)

In vector network analyzer (VNA) measurements on a scale model, the distance between the VNA (HP8510) heads is limited by the cable lengths to about 500 mm (equivalent to 70 mm at Band 9), and mounting bends and twists to simulate the final waveguide run may not be possible. Figure 9 shows the measured transmission of two tapers from WR10 to WR71.4, each 100 mm long placed back-to-back, which clearly shows resonances (theoretical loss 0.18 dB for aluminum, roughness factor included). In the scale model, aluminum was used for ease of manufacture, but the surface losses do not scale as required to simulate the Band 6 waveguide (increasing as the square root of the frequency), so that the resonances are much deeper than they would be in the final structure. The frequency scans were made with 801 points. Figure 10 shows the transmission for two tapers 300 mm long (theoretical loss 0.52 dB for aluminum, including roughness factor). Figure 11 shows the loss for a straight section of WR71.4 of length 190 mm placed in between two tapers (divided by the transmission of the tapers alone). This figure has both positive and negative resonances due to the shift in frequency of the resonances as the length is changed and the subtraction of the taper loss. The loss of the straight section matches well with the theoretical, including roughness factor (also shown in Figure 11).

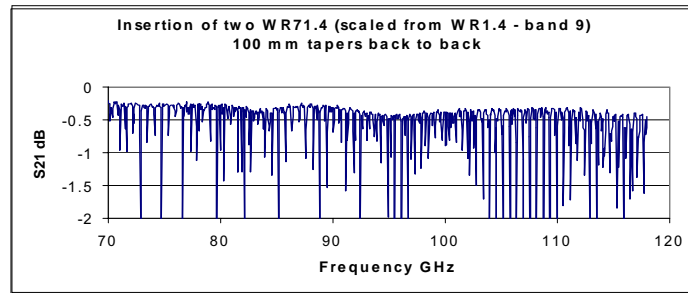


Figure 9

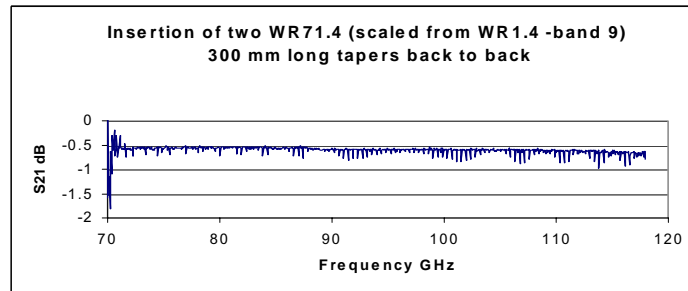


Figure 10

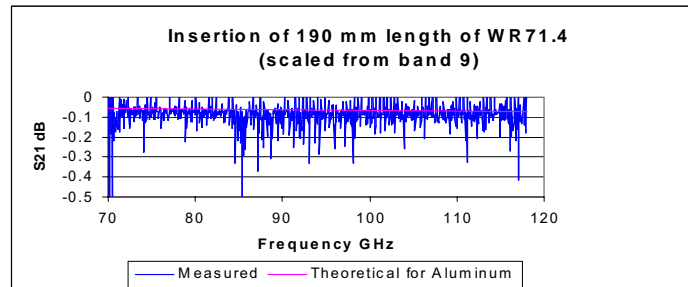


Figure 11

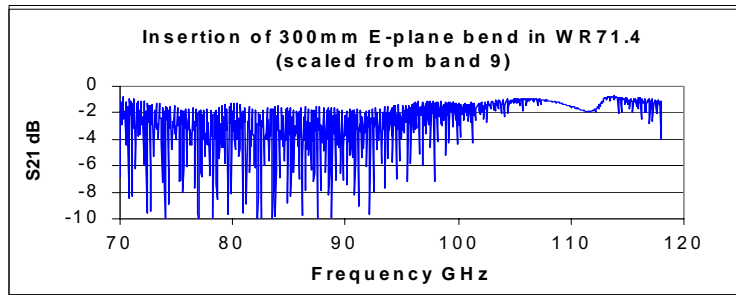


Figure 12

Figure 12 gives the insertion of a 300 mm long, (center-line) 90-degree, E-plane bend. Figure 13 gives the insertion of a 300 mm long (center-line), 90-degree, H-plane bend. (In both figures, the transmission of the tapers is subtracted.)

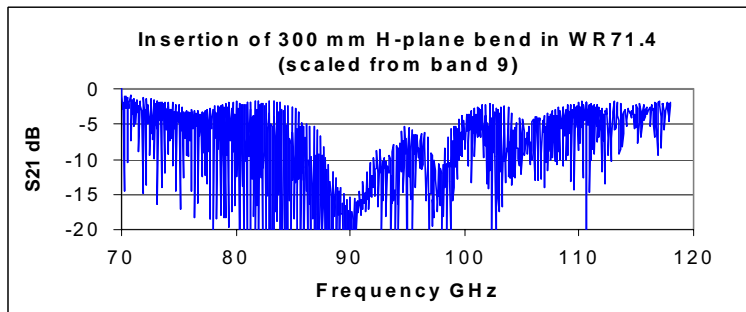


Figure 13

Measurements at 624-720 GHz with WR10 Components

Measurements at 624-720 GHz were made using a x6-multiplied Gunn (RPG [21]) and an overmoded power head (Anritsu 90-140 GHz [22]). The frequency was set by hand with no phase lock, and power levels were measured with and without the device under test between two WR3.4 to WR10 tapers (back-to-back). Figure 14 shows the measured and theoretical losses for a 152.4-mm length of WR10 stainless steel waveguide, and for the same waveguide after plating with 2.5 microns of copper. (12 mm at each end was copper-plated on the inside during attachment of the waveguide flanges; this is accounted for in the theoretical values.) The theoretical values include the 1.3 roughness factor for both, and the 1.135 skin-effect factor for copper but not for stainless steel [13]. There was insufficient power near 700 GHz to make any measurements.

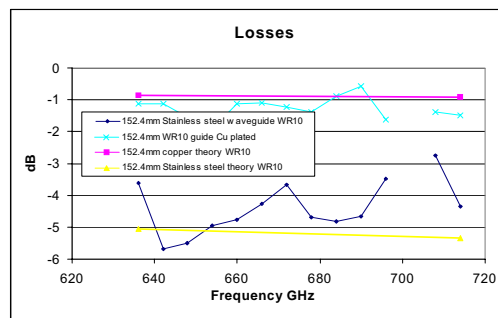


Figure 14

This clearly shows the improvement of plating copper or gold on the inside of the waveguide, but for very small waveguide (WR8 or smaller) or long lengths (100 mm or longer) this is extremely difficult. The sample was also measured at 75-110 GHz where it had 3.26-2.25 dB, unplated (compared to theoretical values, with roughness factor, and accounting for copper-plated sections at the ends, of 4.4 - 3.1 dB) and 0.63-0.47 dB, plated (theoretical values 0.76-0.54 dB with skin effect and roughness factors). The difference with the theoretical values can be explained if the waveguide is slightly larger than the nominal 2.54 by 1.27 mm. The losses of various components (H-plane bend {Aerowave [23]}, H-plane bend, E-plane bend and 90-twist {Baytron [24]}) are given in Figure 15. The reason for the difference between the two H-bends is unknown.

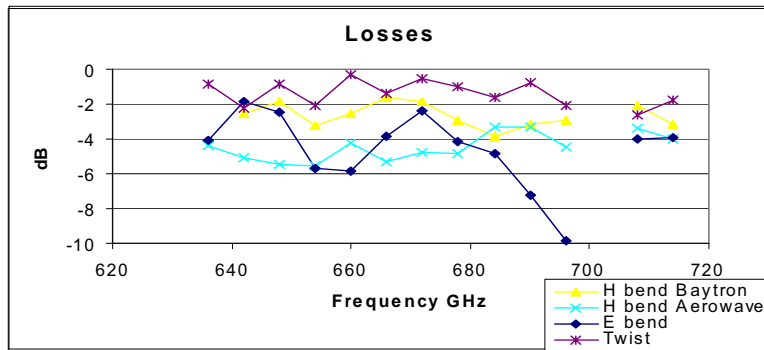


Figure 15

Two sections of WR1.4 (fundamental waveguide for this band) were made of brass in split-block technique and then gold-plated. One piece, 25.4 mm long, split in the narrow wall (incorrect wall) and one piece, 76.2 mm long, split in the broad wall. They had losses of 389 dB/m and 130 dB/m, respectively, at 684 GHz (theoretical value 130 dB/m with roughness factor).

Measurements at 220-330 GHz with WR10 Components

Measurements have been made in the range 220-330 GHz (0.5 GHz per point) using an HP8510 with WR3 extender heads (Oleson [25]). Again, spacing between the heads limits the size of structures which can be measured. Also, the system sensitivity and dynamic range are limited at these frequencies. Figure 16 shows the measured transmission of a taper from WR3.4 to WR10, 200 mm of waveguide followed by two H-plane bends and then one E-plane bend (all WR10 [24]) and then a taper from WR10 to WR3.4, divided by the system response with the heads connected directly together^{***}. This shows that at room temperature there are no major resonances. Note that the fluctuations below 220 GHz and above 300 GHz are due to the low power levels in these frequency ranges. No resonances were seen when the frequency range was reduced to 240-245 GHz (0.025 GHz per point). Also shown in Figure 16 is the measured loss of two tapers, back-to-back, which have a theoretical loss of 0.38 dB for copper, including roughness and skin-effect factors.

It was not possible to cool the waveguide run to determine if resonances become significant when cold.

Figure 17 shows the insertion loss of 150 mm of WR10, copper-plated, and stainless steel WR6 and WR5, measured between two tapers, over the frequency range 220-330 GHz, and compares it to the theoretical values (with roughness factors and skin-effect factors for copper-plated WR10) for those waveguides.

^{***} Full VNA calibration was not available on this instrument at the time it was used.

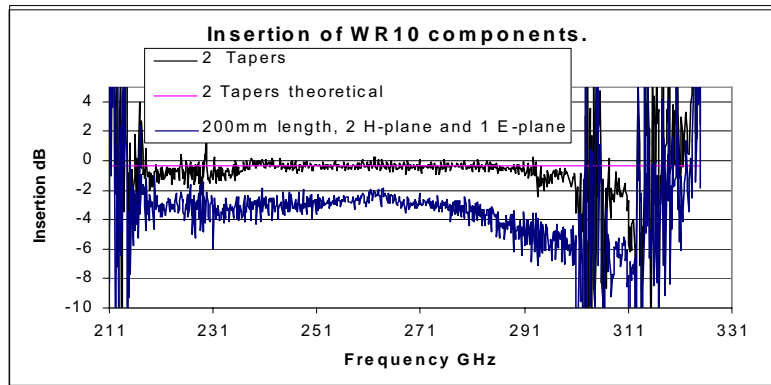


Figure 16.

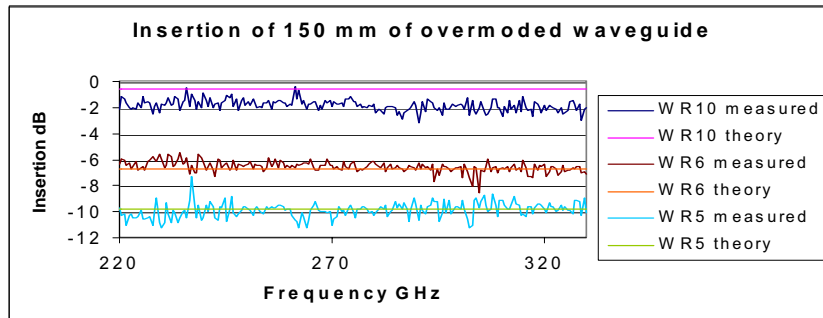


Figure 17. WR10 is copper-plated; WR6 and WR5 are stainless steel.

The excess loss of the WR10 is probably due to difficulties in plating, as measurements at 75-100 GHz show that this waveguide has twice the loss we usually measure for copper-plated stainless steel WR10.

Measurements of overmoded waveguide (WR10) made at IRAM for Band 7 at room temperature also show no resonances [26].

Conclusions

Overmoded waveguide is a possibility for low-loss LO transmission at Band 6, but trapped modes may be a problem when operated at cryogenic temperatures. Measured loss of straight waveguide compares well with theory when roughness and skin-effect loss factors are included. A simulation (at room temperature) of a 25.4-mm taper from WR3.4 to WR10, 150 mm of WR10 followed by a 25.4-mm taper back to WR3.4, had 1.0 dB loss with 0.3 dB resonances (20 dB mode coupling assumed), *i.e.*, maximum depth 1.3 dB, for copper (with roughness and skin-effect factors included), and 4.4 dB loss with 0.1 dB resonances if the WR10 section is unplated stainless steel (including roughness factor). To reduce phase problems, stainless steel may need to be used if the extra loss can be tolerated. Losses will reduce by approximately a factor of two when cooled to 90 K for copper, but the resonances will deepen (to approximately 0.6 dB loss with 2 dB resonances). Losses will reduce to 3.3 dB with 0.2 dB resonances for stainless steel.

Acknowledgment

I would like to thank Dr. J. Hesler (UVA) for allowing me to use the HP8510 with WR3 heads.

References

- [1] G. C. Southworth, "High frequency waveguides - general considerations and experimental results." *Bell System Technical Journal*, vol. 15 (1936), pp. 284-309.
- [2] J. R. Carson, S. P. Mead, and S. A. Schelkunoff, "Hyper-frequency waveguides - mathematical theory." *Bell System Technical Journal*, vol. 15 (1936), pp. 310-333.
- [3] S. A. Schelkunoff, "Transmission theory of plane electromagnetic waves." *Proc. Inst. Radio Eng.*, vol. 25 (1937), pp. 1456-1492.
- [4] L. J. Chu and W. L. Barrow, "Electromagnetic waves in hollow metal tubes of rectangular cross section." *Proc. Inst. Radio Eng.*, vol. 26 (1938), pp. 1520-1555.
- [5] S. E. Miller and A. C. Beck, "Low-loss waveguide transmission." *Proc. Inst. Radio Eng.*, vol. 41 (1953), pp. 348-358.
- [6] S. Weinreb, R. Predmore, M. Ogai and A. Parrish, "Waveguide system for a very large antenna array." *Microwave Journal*, vol. 20, no. 3 (March 1977), pp. 49-52.
- [7] T. N. Anderson, "State of the waveguide art." *Microwave Journal*, vol. 25, no. 12 (Dec. 1982), pp. 22-48.
- [8] F. J. Tischer, "Oversized waveguides and resonators for millimeter waves." *Int. J. Infrared and MM Waves*, vol. 9 (1988), pp. 18-27.
- [9] J. L. Doane and T. N. Anderson, "Oversize rectangular waveguides with mode-free bends and twists for broadband applications." *Microwave Journal*, vol. 32, no. 3 (March 1989), pp. 153-160.
- [10] J. L. Doane, "Low-loss twists in oversize rectangular waveguide." *IEEE Trans. MTT*, vol. 36, no. 6 (1988), pp. 1033-1042.
- [11] J. P. Quine, "E- and H-plane bends for high-power oversized rectangular waveguide." *IEEE Trans. MTT*, vol. 13, no. 1 (1965), pp. 54-63.
- [12] A. J. Baden Fuller, *Microwaves*. 2nd Ed., Pergamon Press, 1979.
- [13] F. J. Tischer, "Excess conduction losses at millimeter wavelengths." *IEEE Trans. MTT*, vol. 24 (1976), pp. 853-858.
- [14] E. J. Wollack, W. Grammar and J. Kingsley, "The Bøifot orthomode junction." ALMA Memo 425. <http://www.alma.nrao.edu/memos/html-memos/abstracts/abs425.html>
- [15] S. Weinreb, "Cryogenic performance of microwave terminations, attenuators, absorbers and coaxial cable," NRAO Electronics Division Internal Report No. 223, January 1982.
- [16] A. P. King and E. A. Marcatili, "Transmission loss due to resonance of loosely-coupled modes in a multi-mode system." *Bell System Technical Journal*, vol. 35 (1956), pp. 899- 906.
- [17] R. G. Meadows, "An absorption resonance method for measuring mode conversion coefficients of overmoded waveguide components." *Int. J. Electronics*, vol. 34, no. 6 (1973), pp. 837-848.
- [18] QuickWave FDTD EM simulator, QWED s.c. Zwyciezcow 34/2, 03-938 Warszawa, Poland. <http://www.qwed.com.pl/>
- [19] CST Microwave Studio, Sonnet Software, Inc., 1020 Seventh North St., Suite 210, Liverpool, NY 13088. Phone: 315-453-3096, fax: 315-451-1694. <http://www.sonnetusa.com/index.asp>
- [20] W. Gwarek (QuickWave), private communication.
- [21] RPG Radiometer Physics GmbH, Birkenmaarstr. 10, D-53340 Meckenheim, Germany. Tel: (49) 02225-999810, radiometer.physics@t-online.de
- [22] Anritsu ML83A with MP82B head. <http://www.anritsu.com>
- [23] Aerowave, Inc., 344 Salem St., Medford, MA 02155. Phone: (781) 391-5338.
- [24] Baytron (now Aerowave). See [23].
- [25] Oleson Microwave Laboratories, 355 Woodview Dr., Suite 300, Morgan Hill, CA 95037. Phone: (408) 779-2698, fax: (408) 778-0491. <http://www.oml-mmw.com/>
- [26] S. Claude. (IRAM), private communication.

A BROADBAND WAVEGUIDE THERMAL ISOLATOR

J. L. Hesler[†], A. R. Kerr[‡] and N. Horner[‡]

[†] University of Virginia Dept. of ECE
Charlottesville, VA 22902
e-mail: hesler@virginia.edu

[‡] National Radio Astronomy Observatory^{*}
Charlottesville, VA 22903

ABSTRACT

This paper describes a new, compact, waveguide thermal isolator. The isolator is based on a recently developed microwave bandgap joint, a periodic structure which suppresses microwave fields propagating between two parallel conducting surfaces. When such a structure is placed between a pair of waveguide flanges, the flanges can be separated by a few percent of a wavelength before the leakage and mismatch become significant. The thermal isolator is relatively immune to misalignment and cocking. Simulations and measurements on WR-10 thermal isolators indicate excellent performance over the entire waveguide band. The design is readily scalable to other waveguide bands.

Keywords: Waveguide components, waveguide transitions, thermal isolators

INTRODUCTION

When microwave or millimeter-wave equipment is operated at cryogenic temperatures, it is often necessary to make waveguide connections to it from room temperature. To reduce heat flow along the waveguide, some form of thermal isolation is normally used. Often, a length of thin-walled stainless-steel waveguide is used, but the attenuation of stainless-steel can be unacceptable, particularly at shorter wavelengths. The attenuation can be reduced by plating the inside of the waveguide with a few skin-depths of gold or copper, but this substantially increases the heat flow. An alternative approach is to use an abrupt thermal transition consisting of a small gap between the hot and cold sections of waveguide. Several designs for such thermal isolators have been described [1-3], but these tend to be sensitive to alignment and/or have resonance-free performance over less than a full waveguide band. This paper describes a waveguide thermal isolator which overcomes these drawbacks. The isolator, shown in Fig. 1, uses two flanged waveguide sections, separated by a small gap and supported by a G-10 glass-epoxy tube. It is based on a recently developed microwave bandgap joint, a periodic structure that suppresses microwave fields propagating between two parallel conducting surfaces [4]. When such a bandgap structure is placed between a pair of waveguide flanges, the flanges can be

^{*} The National Radio Astronomy Observatory is a facility of the National Science Foundation operated under cooperative agreement by Associated Universities, Inc.

separated by a few percent of a wavelength before the leakage and mismatch become significant. One advantage of this design over other thermal isolators is that it is relatively immune to cocking and misalignment.



Fig. 1. (a) The two waveguide sections of the isolator, showing the flat flange and the flange with the periodic bandgap structure. (b) The assembled thermal isolator and the individual parts. The waveguide sections are shown on the alignment mandrel used during assembly.

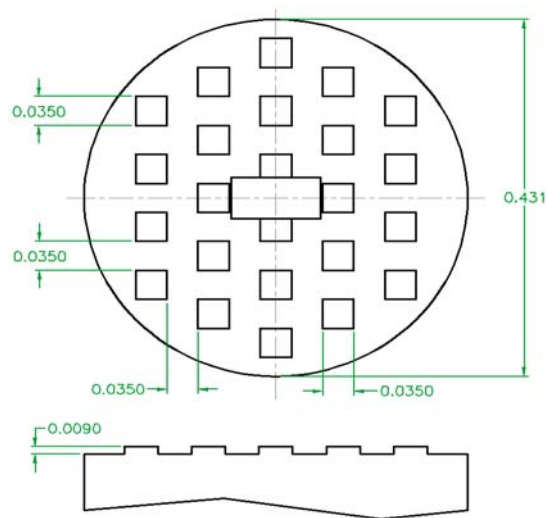


Fig. 2. Details of the periodic bandgap array for WR-10 waveguide (0.100" x 0.050"). Dimensions are in inches. The array is machined on only one side of the gap, the opposing flange being of the same diameter but flat.

DESIGN

An electromagnetic bandgap structure uses a periodic two-dimensional array of reflecting elements with approximately half-wavelength period. In this application, an array of metal posts is machined on the face of one flange of a pair, as shown in Fig. 1(a). Simulations with various array dimensions and gap widths were performed using QuickWave [5]. For the WR-10 (75-110 GHz) design described here, satisfactory results were obtained with 0.035" square pillars and a pitch of 0.070", adjacent rows being staggered by 0.035", as shown in Fig. 2. Simulation indicates that the height of the posts is not critical. All dimensions can be scaled with wavelength for operation in other bands.

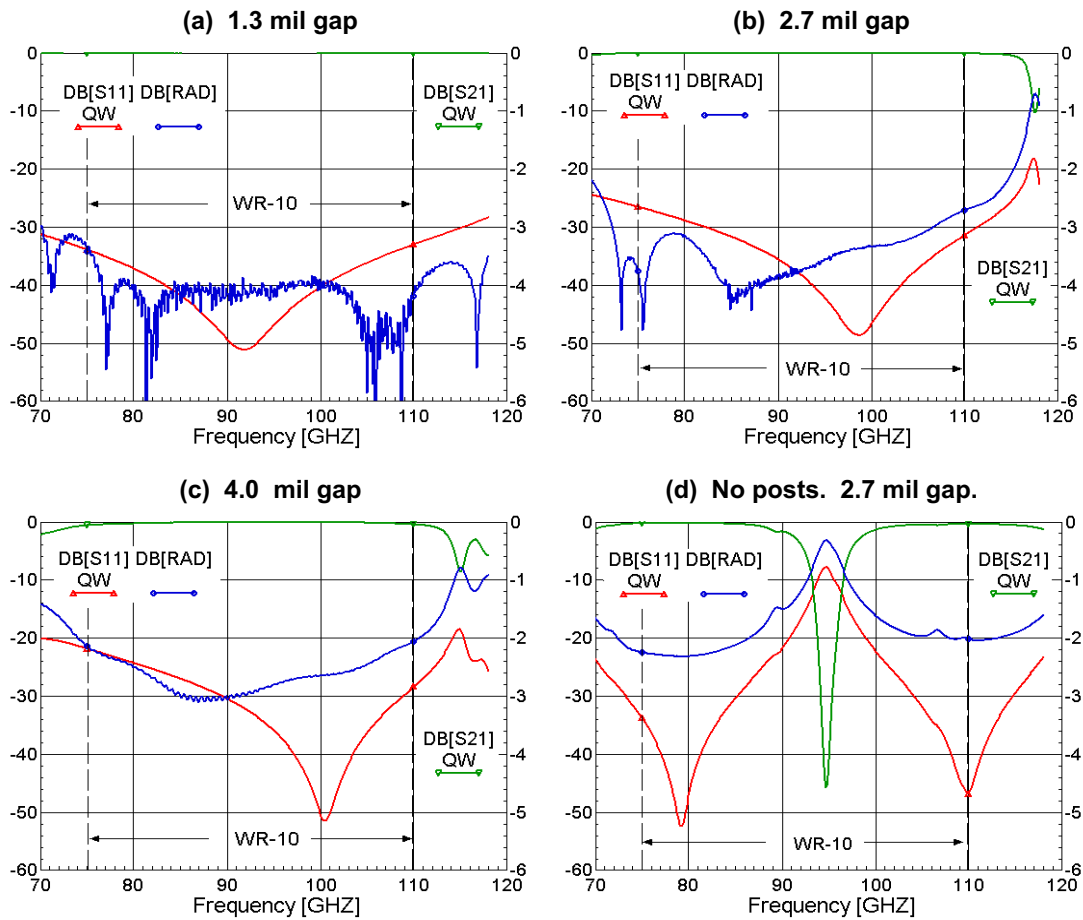


Fig. 3. Characteristics of the thermal isolator with different gap widths. (a) 1.3 mil gap, (b) 2.7 mil gap, (c) 4.0 mil gap, and (d) 2.7 mil gap without the periodic structure. Simulations using QuickWave: |S11| dB (—▲—), |S21| dB (—▼—), power radiated from gap dB (—◆—).

Figure 3 compares the performance of WR-10 thermal isolators using the bandgap array of Fig. 2 with gap widths 0.013", 0.027", and 0.0040", and also an isolator with gap width 0.0027" but without the bandgap array. For small gaps, the performance is nearly ideal. As the gap increases to 0.0027", the return loss remains better than 25 dB within waveguide band, and with a 0.004" gap the return loss is greater than 20 dB. It is clear that the gap between the flanges can be as large as 3% of a wavelength without serious degradation of the transmission and return loss over the full waveguide band. For the isolator without the bandgap array, a strong transmission minimum is present near the center of the band. It has also been observed that without the bandgap structure, the isolator is quite sensitive to misalignment and gap width, and is particularly sensitive to cocking.

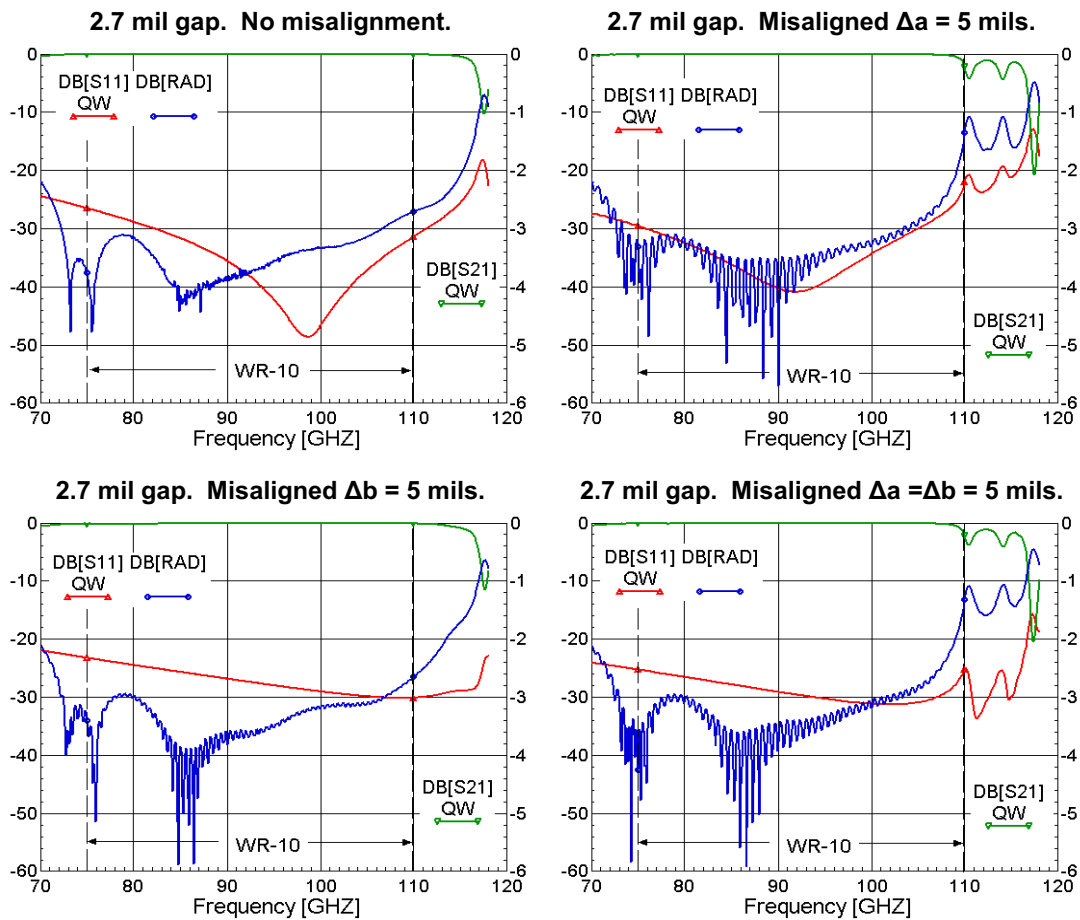


Fig. 4. Characteristics of the thermal isolator with different lateral misalignments. (a) No misalignment (same as Fig 3(b)), (b) 5 mil misalignment in the a direction, (c) 5 mil misalignment in the b direction, (d) 5 mil misalignment in both a and b directions. In all cases the gap width is 2.7 mils. Simulations using QuickWave: |S11| dB (\blacktriangle), |S21| dB (\blacktriangledown), power radiated from gap dB (\blacklozenge).

Figure 4 shows the effect of misalignments between the two flanges, and indicates that for reasonable machining tolerances good performance can be maintained.

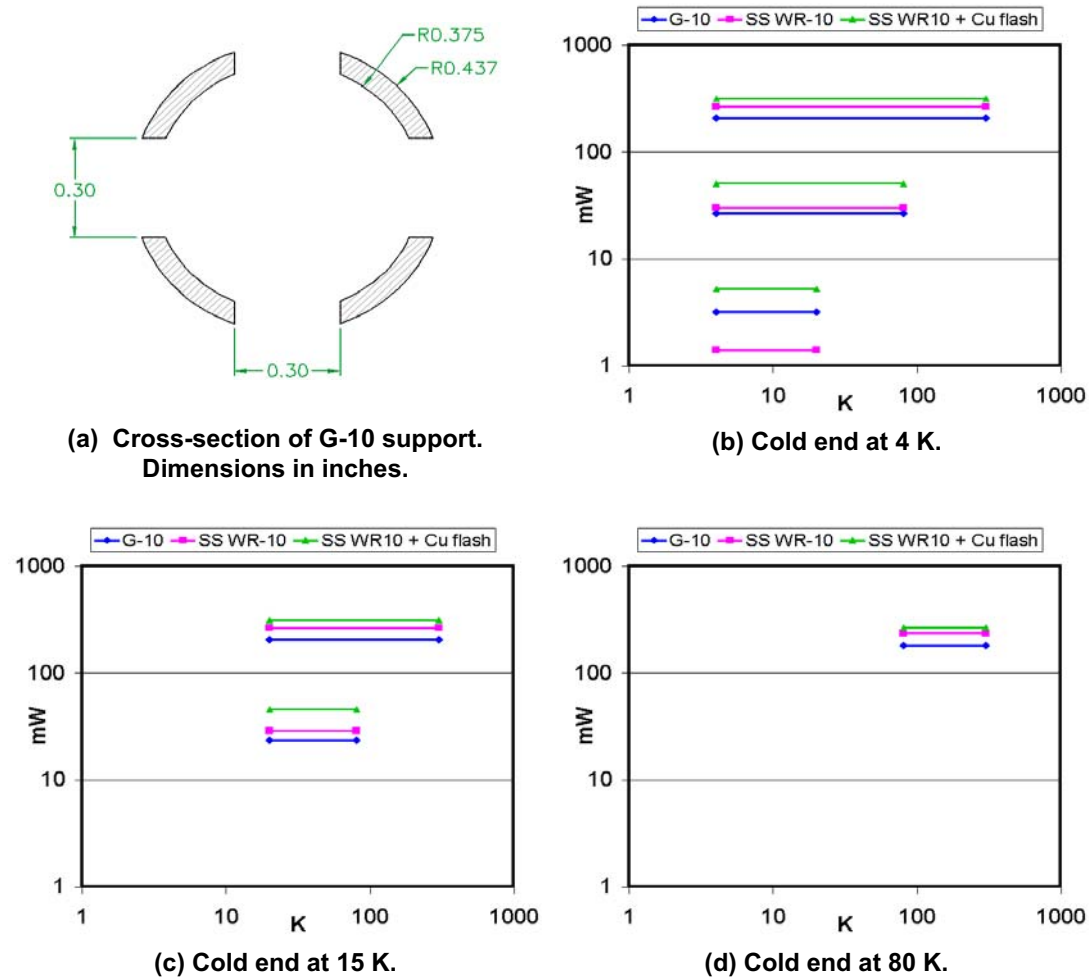


Fig. 5. Heat flow through the thermal isolator compared with that of plated and unplated stainless-steel waveguides of the same length (1.0"). (a) Cross-section of the G-10 support. The graphs show the heat flow when the cold end is at (b) 4 K, (c) 15 K, and (d) 80 K, for G-10 (—◆—), stainless-steel WR-10 with 10 mil wall thickness (—■—), and stainless-steel WR-10 with 10-mil wall thickness plated inside with 40 μ -in copper (—▲—).

HEAT FLOW CALCULATIONS

To compare the thermal performance of the isolator with that of a comparable length of stainless-steel waveguide, we consider the isolator supported as shown in Fig. 1(b) by a G-10 glass-epoxy tube of inside diameter 3/4" and wall thickness 1/16". Four 0.3" wide

slots were machined in the G-10 tube to reduce heat flow. The cross-section of the G-10 support is shown in Fig. 5(a). The stainless-steel WR-10 waveguide has a wall thickness of 0.010", and, in one example, it is plated inside with 40 μ -in of copper. The heat flow was calculated from the thermal conductivity $K(T)$ of the materials. Figs. 5(b)-(d) show the results of the thermal analysis. It is clear that the G-10 supported isolator is superior except when the isolator spans 4-20 K, in which range the unplated stainless-steel waveguide is superior thermally. For all other temperature spans (4-80, 4-300, 20-80, 20-300, and 80-300 K), the G-10 supported isolator has lower heat flow than the stainless-steel waveguide by a factor of 1.2-1.3. Compared with the copper-plated stainless-steel waveguide, the G-10 supported isolator has lower heat flow by a factor of 1.5-2.0. The RF loss of unplated stainless-steel WR-10 waveguide is \sim 1 dB/inch higher than that of coin silver waveguide as used in a gap type of isolator.

CONSTRUCTION

The two waveguide sections are glued into a thin-walled G-10 glass-epoxy tube, as shown in Fig. 1(b), using Armstrong A12 epoxy. To maintain alignment while the epoxy cures, a removable mandrel is inserted through both waveguides. Differential contraction between coin silver and G-10 is approximately 0.0012 inches/inch from 300 K to 4 K, so for cryogenic operation, the isolator can be made with no gap at room temperature. (The isolators described here were measured at room temperature, so the desired gap was set with a spacer during assembly.)

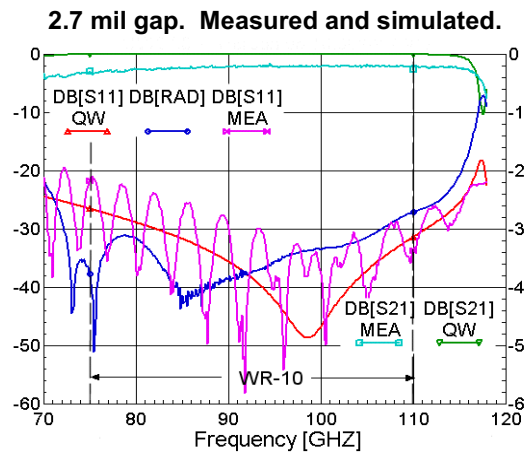


Fig. 6. Measured and simulated characteristics of the thermal isolator with a 2.7 mil gap. Measurements: |S11| dB (—X—), |S21| dB (—□—). Simulations using QuickWave (same as Fig. 3(b)): |S11| dB (—▲—), |S21| dB (—▼—), power radiated from gap dB (—◆—). The ripples on the measured |S11| data are caused by the interaction between the reflections at the two flanges (< -30 dB) and the gap itself.

MEASUREMENTS IN WR-10

Measurements were performed on the WR-10 thermal isolator using an HP8510 vector network analyzer. The measurements, shown in Fig. 6 for an isolator with a 0.0027" gap, agree well with the QuickWave simulations. The ripples in $|S_{11}|$ are caused by the interaction between the reflections at the two flanges (< -30 dB) and the gap itself. The measured midband loss is that of the coin silver waveguide used in the isolator.

CONCLUSIONS

The new waveguide thermal isolator has low return loss and insertion loss over the full waveguide band. It is relatively immune to cocking and misalignment, and does not exhibit the in-band resonances common in other waveguide gap designs. Its insertion loss is essentially that of the coin silver waveguide used in its construction, and is hence much lower than that of a comparable thermal isolator made of thin-walled stainless-steel waveguide. The design is readily scalable for operation in other waveguide bands.

ACKNOWLEDGMENT

This research was supported by the Army National Ground Intelligence Center through grant DASC01-01-C-0009.

REFERENCES

- [1] K. Tomiyasu and J. J. Bolus, "Characteristics of a New Serrated Choke," *IRE Trans. Microwave Theory Tech.*, vol. 4, no. 1, pp. 33-36, Jan. 1956.
- [2] S. Weinreb, H. Dill, and R. Harris, "Low-noise, 8.4 GHz, cryogenic GaAs FET front-end," VLBA Tech. Rep. No. 1, NRAO, Charlottesville, VA, Aug. 1984.
- [3] M. Davidovitz, "A Low-Loss Thermal Isolator for Waveguides and Coaxial Transmission Lines," *IEEE Microwave and Guided Wave Letters*, vol. 6, no. 1, pp. 25-27, January 1996.
- [4] J. L. Hesler, "A Photonic Crystal Joint (PCJ) for Metal Waveguides," *IEEE 2001 MTT-S Intl. Microwave Symp. Digest*, Phoenix, AZ, June 21-25, 2001, pp. 783-786.
- [5] QuickWave FDTD EM simulator, QWED s.c., Zwycieczów 34/2, 03-938 Warszawa, Poland.

Silicon Laser Micromachining for the Development of Planar Waveguide-Based THz Structures

Peter Kirby, John Papapolymerou

School of Electrical & Computer Engineering, Georgia Institute of Technology, USA

Christian D' Aubigny and Chris Walker

Department of Astronomy, The University of Arizona, USA

Abstract – This paper describes an approach toward the development of low cost terahertz components. The approach utilizes laser micromachining on a silicon substrate to form rectangular waveguide structures. We discuss the design and fabrication of a 600 GHz bandpass filter employing the laser micromachining technique. We will discuss the measurement plan to produce the first measurement of a laser micromachined waveguide bandpass filter at 600 GHz.

Introduction

Increasing focus has been placed on the use of Terahertz (THz) frequency signals. Currently the frequency range is used mostly for astronomy purposes, but has great promise in imaging, especially in medical imaging as THz signals do not have the harmful effects associated with traditional X-Rays. In order to bring this technology to the forefront, an in-expensive and highly repeatable production of THz components needs to be established. While some of the components may be fabricated using traditional metallic waveguide or by using established etching techniques on silicon to form the waveguide, none offer the accuracy, versatility or potential inexpensive production as does the laser micromachined approach.

Laser Machining

Although very small metallic waveguide structures can be manufactured using mechanical machining techniques, they can be costly and could be difficult for mass production and could be come impossible to manufacture as frequency increases and the size of the waveguide and associated components decrease. The alternative is to use well developed micromachining techniques to form the needed waveguide. This approach has already been applied [1, 2, 3] section waveguide sizes of WR-10 and WR-4 with measurements reported, but these techniques are limited in the 3-dimensional shapes they can form. What we propose is using laser micromachining [4] as this technique is able to create very small features, different depths of etch and must is not constrained to any crystalline plane and is highly repeatable for frequencies up to ~ 10 THz.

The laser machining technique is based on the illumination of a silicon substrate with an argon-ion laser that locally heats a portion of the substrate inside a chlorine ambient. At the onset of melting, volatile silicon chlorides are formed and, as a result, controlled thin shavings can be removed plane by plane with no change in the etch rate. With this technique, THz waveguide structures that were extremely difficult, if not impossible, to fabricate with classical machining techniques can be developed. The structures can be three-dimensional and of any shape with an accuracy of one micron.

600 GHz Bandpass Filter

Our efforts to prove the validity of this technique and approach are to initially be proven in the 600 GHz frequency range. This range was selected due in part for its ability to be measured with a network analyzer. For the bandpass filter design we elected to use a classic waveguide cavity filter [5] having 3 poles yielding a 15 GHz (2.5%) bandwidth. These simulations of these were carried out using Ansoft's HFSS simulator. The waveguide size for the filter was selected to be WR-1.4 (14 by 7 mils). The simulation results are shown in figures 1 and 2.

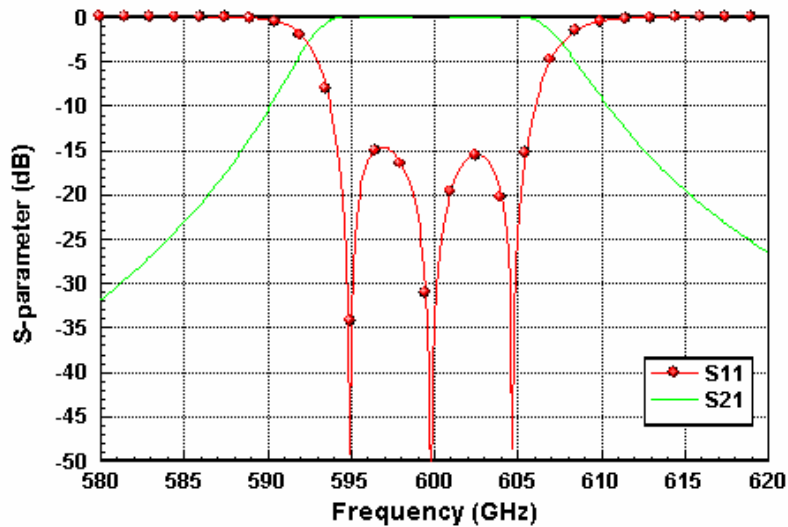


Figure 1 Simulated S-parameters of the 3 pole laser machined waveguide filter.

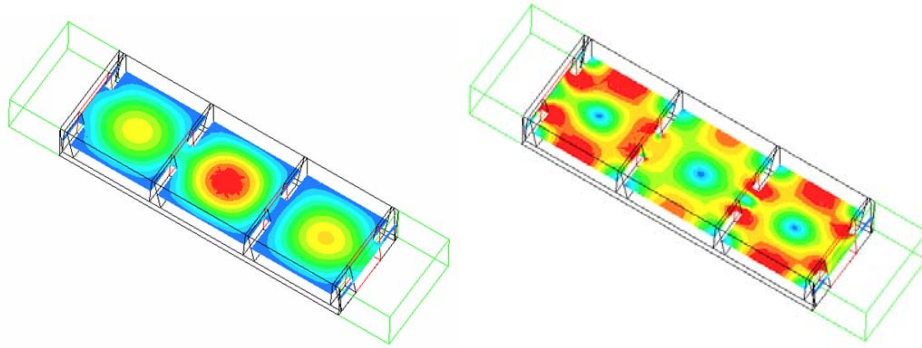


Figure 2 Simulated E-Field (left) and H-Field (right) of the 3 pole laser machined waveguide filter.

The fabrication of the filter using the laser etching technique can potentially be done in two ways, the first by creating two halves or a ‘split-block’ and bond the two halves together, the second approach is to laser etch the entire waveguide and simply use a ‘lid’ style approach. We have elected to use the latter approach to avoid any alignment issues. The fabrication results of the filter can be seen in the SEM image from a top view perspective in figure 3 without the lid attached.

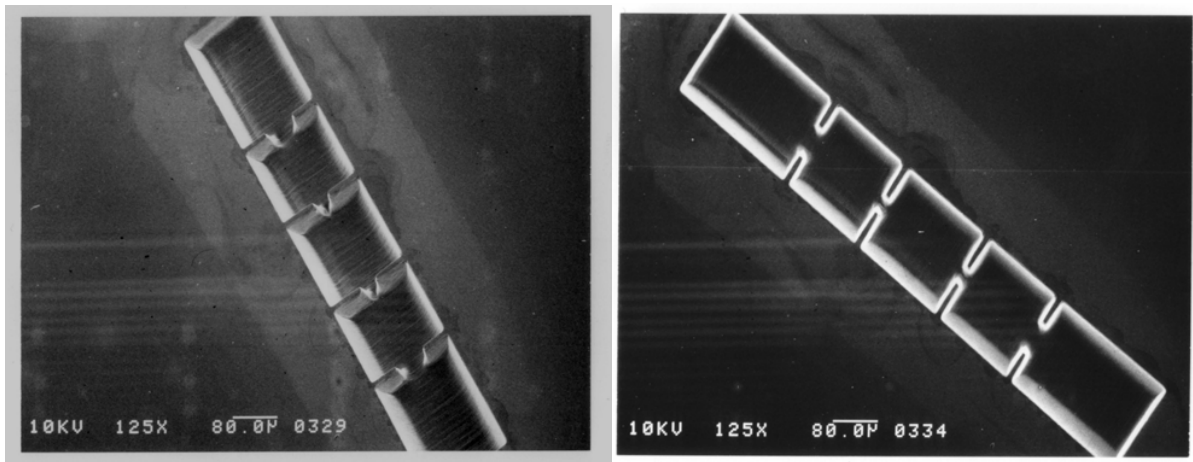


Figure 3 SEM picture of the 3 pole laser machined waveguide filter

After the laser fabrication the filter was sputtered with a titanium layer followed by a gold layer. Additionally the ‘lid’ for the filter was sputtered with the same combination of metals. These two pieces were then bonded together using a Karl Suss SB6 bonding machine.

Measurement Plan/Results

For the measurement of the 600 GHz bandpass filter, we intend to use the Network Analyzer at Jet Propulsion Laboratories in Pasadena, California. Specially designed metallic waveguide filters have been manufactured in order to select the harmonic content for our frequency band. The difficulties of a measurement at this frequency with alignment issues are compounded by the fact that we are trying to interface a waveguide made in silicon without flanges to a metallic interface. In order to facilitate this interface a custom package will be built around the finished silicon waveguide filter. This will not only provide a rigid package for the filter, helping to avoid handling damage, but will also be outfitted with precision round flanges that will directly interface with the measurement system.

Conclusions

We have discussed laser micromachining of THz components and its advantages over mechanically machined and traditional etched waveguides. A proposed 600 GHz bandpass waveguide filter was proposed for the purpose of proving the laser machining approach. Simulation and initial fabrication results were shown. A measurement plan has been proposed for demonstrating the effectiveness of this approach.

References

- [1] C.E. Collins, J.W. Digby, R.D. Pollard, R.E. Miles, G.M. Parkhurst, J.M. Chamberlain, D.P. Steenson, N.J. Cronin, L.S. Karatzas and J.W. Bowen, "W-band measurements of 100 μm height micro-machined air-filled rectangular waveguides," *IEEE MTT-S Microwave Symposium Digest*, Vol.3, pp. 1439 -1442, Jun 1997.
- [2] V. Lubecke, K. Mizuno and G.M. Rebeiz, "Micromachining for Terahertz application," *IEEE Trans. Microwave Theory Tech.*, Vol. 46, pp. 1821-1831, Nov. 1998.
- [3] W. R. McGrath, C. Walker, M. Yap and Y. Tai, "Silicon Micromachined Waveguides for Millimeter-Wave and Submillimeter-Wave Frequencies," *IEEE Microwave and Guided Wave Letters*, Vol 3, No. 3, March 1993.
- [4] C.K. Walker, G. Narayanan, H. Knoepfle, J. Capara, J. Glenn and A. Hungerford, "Laser Micromachining of Silicon: A New Technique for Fabricating High Quality Terahertz Waveguide Components," *Proc. Eighth International Symposium on Space Terahertz Technology*, Harvard University, March 1997, pp. 358-376.
- [5] G. Matthaei, L. Yound and E.M.T. Jones, *Microwave Filters, Impedance-Matching Networks, and Coupling Structures*, MA, Artech House: 1980.

Design of a Dual Polarization SIS Sideband Separating Receiver based on waveguide OMT for the 275-370 GHz frequency band

A. Navarrini*, M. Carter

*IRAM (Institut de Radioastronomie Millimétrique)
300, rue de la Piscine, 38406 St. Martin d'Hères Cedex – France*

*Present address: Radio Astronomy Lab, University of California, Berkeley, CA, USA

Abstract

We report on the design of a wideband waveguide Orthomode Transducer (OMT) integrated with two 90° waveguide hybrid couplers and four 16 dB branch-guide LO directional couplers for the 275-370 GHz frequency band. The device allows the sideband separation for each of two mutually orthogonal polarizations to be achieved by employing four fixed-tuned SIS DSB mixer-units. The central part of the system is based on a Bøifot type junction OMT as realized by Wollack [1], and is similar to the design discussed by Narayanan [2]. The proposed device takes advantage of the -3 dB splitting operated over one polarization of the RF input power that is delivered in the two side arms of the Bøifot orthomode junction by a thick septum parallel to the E-field of the considered polarization; the RF signals of the split polarization are added through two 16 dB branch-guide couplers to the signals of a Local Oscillator (LO) that enter the Bøifot orthomode junction side arms with a phase difference of 90° . The RF and LO are applied in two fixed-tuned DSB SIS mixers whose IF outputs are recombined in a 4-8 GHz IF 90° quadrature hybrid, so that the resulting downconverted upper (USB) and lower (LSB) sideband of the considered polarization are separated. The LO quadrature hybrid, the 16 dB waveguide couplers, and the idea of assembling these elements to get a single polarization sideband separating receiver (2SB) are adopted from the work of Claude [3]. The RF signal of the orthogonal polarization passing the septum is divided using an in-phase power divider and delivered through side arms perpendicular to the previous. The sideband separation for this second polarization is realized using the same scheme as for the first polarization.

The advantage of the device is to exploit the -3 dB splitting operated over each of two mutually orthogonal polarizations by the waveguide OMT junction and power divider, as required for sideband separation, and to avoid the problem of signals recombination of classical waveguide OMTs. Both the OMT junction and the in-phase power splitter have been optimised using a 3D electromagnetic simulator. Return loss better than 16 dB, and transmitted power to the four side arms within 0.1 dB of the reference value at -3 dB of the single polarization input excitation are expected over the RF band of design. Because of symmetry properties, the structure has not cross-polarization. Although the 3D structure looks complex, the proposed device can easily be constructed using conventional split-block techniques with reliability and cost-effectiveness.

I. Introduction

Most of cryogenically cooled millimeter and submillimeter wave receivers in radio astronomy are based on Double Side Band (DSB) SIS mixers that have noise performances approaching the quantum limit. In a DSB receiver the atmospheric noise contribution coupled in the image band during a radioastronomical measurement

degrades the system sensitivity for spectral line observation. Backshort-tuned Single Side Band (SSB) mixer that reject the image sideband, or mechanically tuned interferometer that provide image sideband filtering can be used to reduce the SSB system noise temperature, which is the figure of merit of spectroscopic observations.

An alternative to these systems is offered by the sideband separating receiver (2SB) based on fixed-tuned DSB mixers. A 2SB receiver provides at its output two separated IFs, one containing the down-converted RF signal from the Upper Side Band (USB), the other from the Lower Side Band (LSB), each with a high rejection of the respective image band. With respect to SSB mixers or tuned interferometer, a 2SB receiver offers the advantage of not having moving parts, and has twice more IF band.

To increase further the capacity and versatility during astronomical observation, dual polarization operation is often required or, in some cases, mandatory (e.g. ALMA project). The easiest way to separate linearly polarized signals with orthogonal polarizations is obtained with a quasi-optical system based on a grid consisting of free-standing parallel wires. The polarization with E-field parallel to the wires is reflected by the grid, while the perpendicular polarization is transmitted. Although the wire grid is intrinsically wideband it has important drawbacks. In fact, it is large and bulky and requires two well aligned feed-horns along the optical path of the two wave polarizations resulting from the well aligned wire grid. In a practical implementation of a receiver, the wire grid should reside inside the cryostat, which correspondingly increase the size of the required dewar.

An alternative to the wire grid is represented by the waveguide orthomode transducers (OMT). Waveguide OMTs are more compact and less sensitive to mechanical vibrations than wire grid based systems. Moreover, they require the use of only one dual-polarized broadband corrugated feedhorn, thus the optical alignment is much facilitated and the instrumental polarization offset is reduced. Therefore, waveguide OMT are the favoured solution for focal plane imaging arrays.

OMTs are classified in three different groups with increasing geometrical complexity and manufacturing difficulties, and with increased performances (see Bøifot [4]). A broadband waveguide OMT has been realized by Wollack [1] for ALMA band 3 (86-116 GHz) using a design rescaled from a lower frequency model based on the Bøifot junction. The main disadvantage of Wollack's OMT is the use of pins located at the entrance of the waveguide side arms. Pins act as capacitive posts that tune out the discontinuity of the holes created by the side arms in the common waveguide. However, the complexity of assembling the pins in the block make them unsuitable for scaling the OMT at higher frequencies. In a more recent design of Narayanan the discrete compensation pins have been replaced with capacitive steps at the side arm apertures that are easier to fabricate and allow to achieve equivalent performance as the original Wollack design.

Starting from the design published by Wollack we have carried out 3D electromagnetic simulations using the FDTD package CST Microwave Studio [5] and optimised a new type of broadband Bøifot type junction OMT based on a thick septum that resulted in a design similar to that discussed by Narayanan. With respect to that design, our junction OMT does not require the use of short capacitive steps that have been replaced by standard multistep transitions on the side arms. Finally, the polarization with E-field

parallel to the septum that is split in the Bøifot junction side arms results in low return loss over a wide band. A multi-step power divider has been optimised in the main arm of the OMT to split the linear polarization passing the septum, having E-field perpendicular to the septum itself, in two full-height waveguides perpendicular to the Bøifot junction side arms. The resulting four arms system consisting of the OMT junction with their side arms plus the main arm power divider is the central part of our dual polarization 2SB. The sideband separation for the polarization parallel to the septum is obtained by adding each of the Bøifot type junction OMT side arm to a LO provided by a 90^0 hybrid followed by a 16 dB branch-guide coupler. A similar configuration is used to achieve the sideband separation for the orthogonal polarization.

In the whole, the proposed device contains: (i) an improved Bøifot type junction OMT with a thick metallic septum; (ii) an optimised multistep power divider; (iii) four 16 dB branch guide couplers; (iv) two 90^0 hybrid couplers.

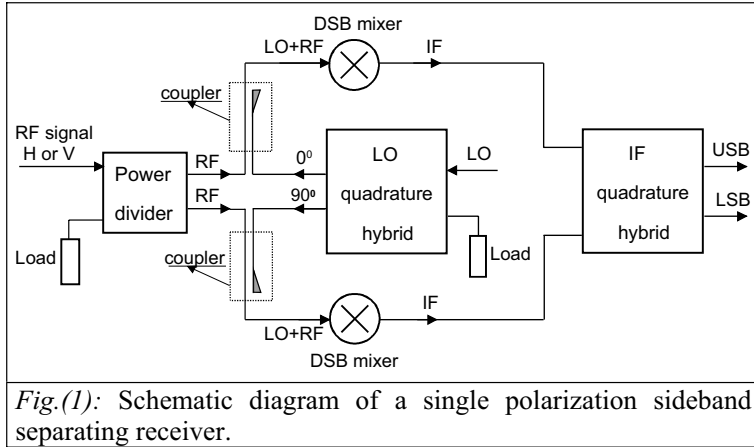
The 275-370 GHz dual polarization 2SB can be realized by using 4 fixed-tuned DSB mixers at the ends of the proposed device. The device consists of 6 mechanical blocks that can be assembled to form a compact structure together with the 4 mixers.

The present paper is organized as follows: in section II we introduce the concept of a classical single polarization 2SB in which the required circuits for combining and phasing the signal and LO power are realised in full height rectangular waveguide. In section III we discuss our design of the Bøifot orthomode junction integrated with the multistep power divider in the main waveguide arm, and present the results of electromagnetic simulations for such structure. Finally, in section IV we present the design of the whole structure of the dual polarization 2SB and discuss the construction of the mechanical blocks.

II. Single Polarization 2SB

Sideband separating receivers have been widely used at microwave frequencies for many years. The schematic of a 2SB is shown in Fig.(1). Here, a single polarization of the incoming RF signal enters an in-phase power divider and is split in two parts. Before being applied to the DSB mixers, the two signals are added through a coupler to the power of LOs with 90-degree phase difference coming from an LO quadrature hybrid. The IF outputs are combined in a IF quadrature hybrid at whose output ports the downconverted upper (USB) and lower (LSB) sidebands appear separately.

Claude [3] has realized a single polarization 2SB integrating fixed-tuned DSB SIS mixers for the 275-370 GHz band. Its receiver setup is shortly discussed here as some of its basic elements are also employed in the design of our dual polarization sideband separation receiver. This includes a waveguide power divider, a waveguide quadrature hybrid coupler providing a 3 dB power splitting with 90^0 phase shift from the two outputs, two branch-guide 16 dB LO directional couplers, two SIS mixers, and a commercial 4-8 GHz IF quadrature hybrid (in our design the quadrature hybrid is used in the LO section instead of the RF section). The two full height waveguides of the broadband LO hybrid are coupled through the broad walls and are separated by five shunt guides $\lambda_g/4$ long.



Two $\lambda_g/4$ long shunt guides are used in the 16 dB couplers. The couplers were realized by splitting the blocks on the E-plane; this facilitates their integration with other components. All the elements of the network were designed and tested at IRAM.

III. Bøifot type orthomode junction and in-phase power divider

III-a Design of orthomode junction

The twofold symmetric Bøifot junction was chosen as starting point for the OMT junction design investigated in this work. Different geometries were considered in turn with varying septum types and waveguide junction dimensions. The electromagnetic structures were optimised with CST Microwave Studio in the 275-370 GHz frequency to achieve the following requirements:

a) return loss < -15 dB for the two polarizations; b) transmitted power to the four side arms within 0.1 dB of the reference value at -3 dB of the single polarization input excitation; c) cross-polarization level below -40 dB. The latter specification is required in a practical implementation of a receiver because it is desirable for the cross-polarization induced by the OMT to be stable and less than the level arising from the feed assembly and telescope which is rarely below that figure. Very low cross-polarization levels are achievable with our design, with values that in principle are zero as a consequence of the symmetry of the designed structure, and that in practice depend on the amount of misalignments that are determined by specified mechanical tolerances. Although a detailed study of the influence of all possible contributions to the cross-polarizations has not been performed we point out that the typical cross-polarization levels in classical waveguide OMT are much lower than the those induced by a standard wire grid (\approx -30 dB) and are also sufficiently low for most astronomical applications.

A 3D view of the final orthomode junction design is shown in Fig.(2). Further details are illustrated in Fig.(3). The square waveguide at the input (dimensions $0.76 \times 0.76 \text{ mm}^2$) can support the propagation of 4 modes in the frequency band of interest: TE_{10} , TE_{01} , TE_{11} and TM_{11} , with cut-off frequencies of respectively, $\nu_{c,TE10}=\nu_{c,TE01}=197 \text{ GHz}$, $\nu_{c,TE11}=\nu_{c,TM11}=279 \text{ GHz}$. The excitation of the higher order modes TE_{11} and TM_{11} is excluded for symmetry reasons. In fact, the main and side-arm junctions are twofold symmetric about the horizontal and vertical guide planes, thus TE_{11} and TM_{11} excitation can be avoided in the square mixer common arm of the junction as long as this condition is realized during fabrication and assembly. The alignment of the septum inside the

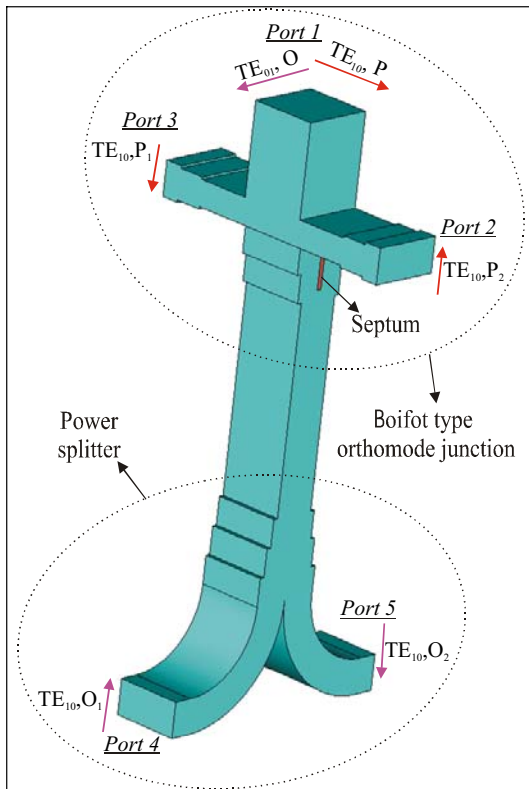
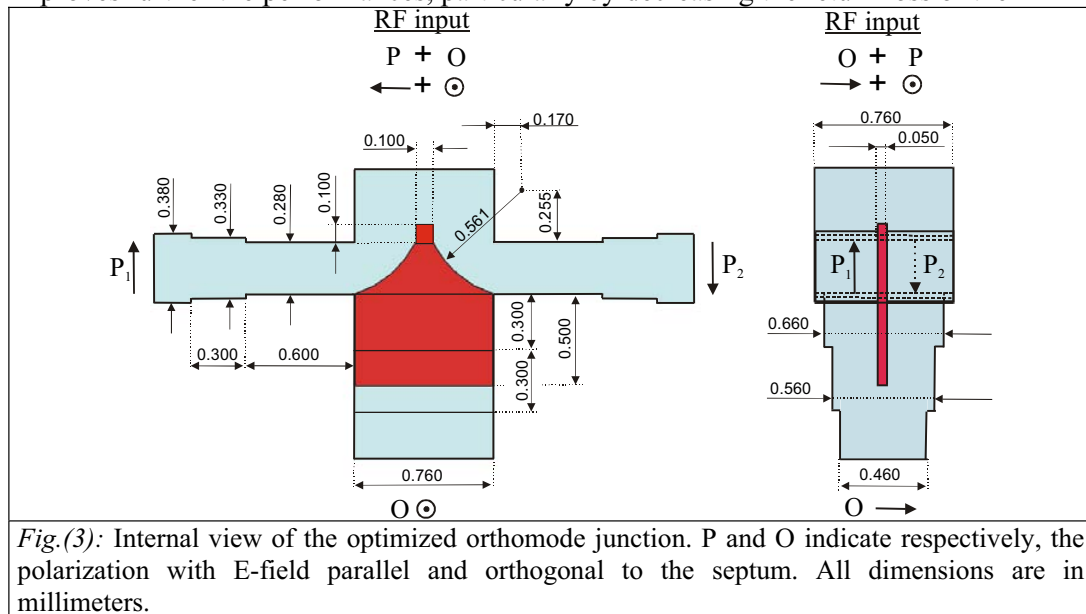


Fig.(2): Three-dimensional view of the designed Bøifot type orthomode junction with power splitter. The RF signal coming from the feed-horn enters the square waveguide from the top (Port 1). The RF power coupled at the square waveguide entrance into the TE_{10} mode (polarization P, parallel to the septum) is equally split between two side-arms (Port 2 and 3). The RF signal coupled into the TE_{01} mode (polarization O, orthogonal to the septum) is divided, after passing the septum, by a power splitter with E-plane bend side arms perpendicular to the previous (Port 4 and 5).

orthomode junction and of the input square waveguide at the interface with the flange of the circular-square waveguide transition (or the feed-horn including such transition) previous the OMT, is critical to minimize the excitation of the TE_{11} and TM_{11} modes. When proper assembly is realized only the desired fundamental modes TE_{10} and TE_{01} , with E-field excitation respectively, parallel (P) and orthogonal (O) to the septum will propagate. Referring to Fig.(2), the polarization of the RF signal at the input (Port 1) with E-field parallel to the septum will be divided on the side arms at the septum location (Port 2 and Port 3). The RF signal with input polarization perpendicular to the septum will pass the septum itself and will be divided by the power splitter in two side arms (Port 4 and Port 5). Higher order modes whose excitation is not excluded by symmetry reasons are created by the discontinuity due to the side arm apertures and septum. Although their cut-off frequencies fall outside the useful frequency band and the modes are evanescent, their reactances must be compensated by a proper choice of the septum geometry and orthomode junction dimensions. In general, the thinner the septum, the easier the structure is to compensate. Decreasing the septum thickness δt makes its realization more difficult, decreases the return loss of both input polarizations, increases the transmission through the main arm of the polarization perpendicular to the septum at values closer to -3 dB, and increases also

the transmission of the polarization parallel to the septum that should not be passed (the cross-polarization level which is intrinsically very low in this structure). The adopted septum thickness of $\delta t = 50 \mu\text{m}$ is a compromise between the bigger values required to facilitate its manufacturing from one hand, and the smaller values necessary to achieve better performances from the other hand. The ratio between septum thickness and lateral dimension of the square waveguide results in a value of $\delta t/L \approx 0.066$ (in the original Wollack design $\delta t/L \approx 0.024$). The adopted septum geometry consists of a circular tapering from full waveguide lateral size down to a narrow square section tip that properly feed

the symmetric side arms allowing for wide band performances. We found using simulations that the advantage of circularly tapered septum tip over the more standard triangular type as used by Wollack is the decreasing of return loss for the parallel polarization with a corresponding improved “flatness” of the -3 dB transmitted power on the junction side arms. The short and narrow square section at the septum tip end improves further the performances, particularly by decreasing the return loss of the



orthogonal polarization. The finite septum tip end width makes the design robust against possible off-axis misalignments parallel to the septum itself.

In the septum region next to the junction side arms, the main waveguide arm can be thought of as divided in two independent parallel waveguides separated by the metallic septum itself. Because of the reduced dimensions, the two waveguides support in the frequency band of interest, the propagation of only one mode with E-field orthogonal to the septum. The mode with E-field parallel to the septum is evanescent in such region and is quickly attenuated. Therefore, the length of the septum controls the attenuation of the evanescent modes: increasing its length, the transmission in the main arm of the mode with E-field parallel to the septum (cross-polarization) decreases, but the return loss for the orthogonal polarization increases. To keep such return loss below the -15 dB specification and reduce the transmission of the unwanted polarization we have decided to implement a symmetric multistep transition at the side arm junction from square to reduced height waveguide (dimensions $0.76 \times 0.46 \text{ mm}^2$) along the main waveguide arm. This reduces drastically the transmission of the polarization with E-field parallel to the septum without degrading the return loss performances. In addition, the reduced waveguide dimension prevents the excitation of TE_{11} and TM_{11} modes within the operating frequency range due to possible misalignment. In fact, the cut-off frequency of such modes is pushed outside the upper limit of the band ($v_{c,TE11}=v_{c,TM11}\cong 381.1 \text{ GHz}$).

The side arm waveguides next to the septum have dimensions $0.76 \times 0.28 \text{ mm}^2$ and are 0.60 mm long (see Fig.(3)). To reduce the ohmic losses in these sections, their lengths have been chosen to have the shortest possible values for which the transmission of the polarization coupling to the side arms results unaffected. Decreasing the side arm waveguide heights shifts to lower frequency the useful band for the return loss of the polarization parallel to the septum, while improving its cross polarization and the return loss of the polarization orthogonal to the septum. The side arms are transformed with a multistep transition to the standard $0.76 \times 0.38 \text{ mm}^2$ adopted for the full height waveguide dimensions of the ALMA Band 7 DSB SIS mixers [6] foreseen for integration with the proposed device.

III-b Power Splitter

The Bøifot type orthomode junction is connected through a reduced height waveguide to the power splitter as shown in Fig.(2). Such long waveguide section (2.24 mm) is required by mechanical assembly reasons of the various blocks constituting the device. A multistep transition to square waveguide is used before the power divider. The -3 dB splitting junction is characterized by two full height waveguides ($0.76 \times 0.38 \text{ mm}^2$) joined at the square waveguide section that are E-plane bended with radius of 1.5 mm. This bending radius is sufficient to decrease the amplitude of the reflection coefficient at the square waveguide input below -30 dB over the 275-370 GHz band.

III-c Predicted performances

The entire 5-port structure shown in Fig.(2) has been simulated without taking into account the effects of ohmic losses (only perfect conductors were considered). The results are illustrated in Fig.(4). Return loss below -16 dB are obtained for both polarizations over the whole RF band of interest with zero cross polarization level. The coupling amplitude between the fundamental TE_{10} mode at port 1 and the fundamental mode at one of the side arms of the Bøifot junction has a value of -3 dB and variations

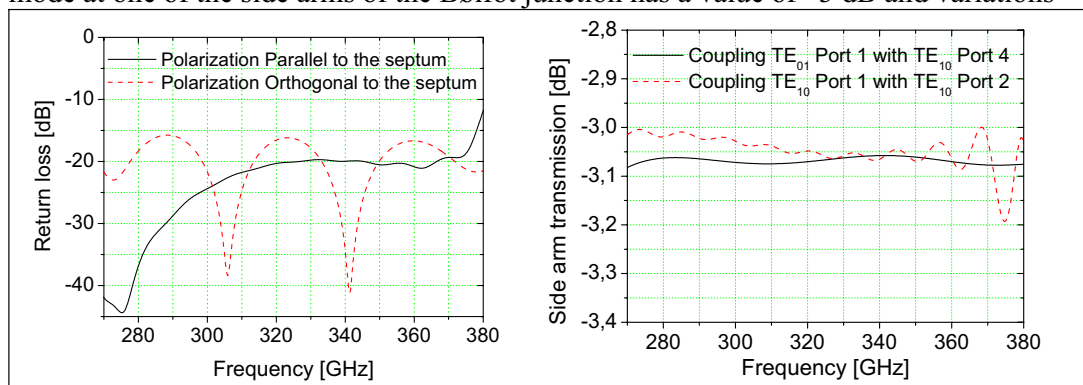


Fig.(4): Result of simulations of the 5-port device illustrated in Fig.(2). *Left*): Amplitude of reflection coefficient at the input (Port 1) for polarization parallel, and orthogonal to the septum. *Right*): Solid line: Coupling amplitude between fundamental mode at Port 1 with E-field orthogonal to the septum and fundamental mode at Port 4 (or 5). Dashed line: Coupling amplitude between fundamental mode at Port 1 with E-field parallel to the septum and fundamental mode at Port 2 (or 3).

within 0.1 dB around this optimum. A similar result is obtained for the orthogonal polarization at the input that couples to the power splitter side arms.

IV. Dual polarization 2SB

A schematic diagram of the dual polarization sideband separating receiver, based on the device illustrated in Fig.(2), is shown in Fig.(5). Here, the RF signals of the split polarization parallel to the septum (P) are added through 16 dB couplers to the signal of a

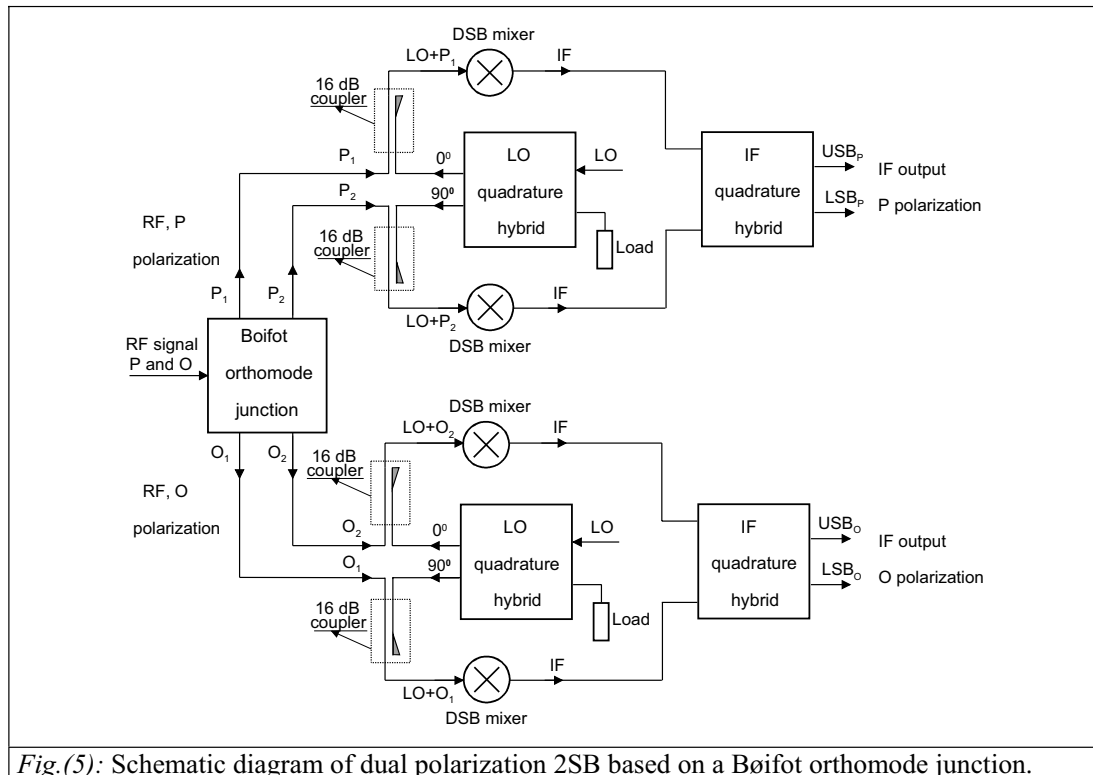


Fig.(5): Schematic diagram of dual polarization 2SB based on a Bøifot orthomode junction.

LO that enter the Bøifot orthomode junction side arms with a phase difference of 90^0 . The RF and LO are applied in two fixed-tuned DSB mixers whose IF outputs are recombined in a IF 90^0 quadrature hybrid, so that the resulting downconverted upper (USB_P) and lower (LSB_P) sidebands of the considered polarization are separated. The sideband separation for the orthogonal polarization (O) passing the septum is realized using the same scheme as for the other polarization, and the downconverted upper (USB_O) and lower (LSB_O) sidebands results at the output.

IV-a Design of waveguide circuitry

The dual polarization 2SB design follows closely the schematic diagram illustrated in the above figure, and is based on two independent LO sources, each driving the two DSB mixers of each single polarization sideband separating SIS receiver. A view of the RF waveguide circuitry of the whole device is shown on the left of Fig.(6). Here, the RF input signal enters the square waveguide from the top. Each of the two orthogonal polarizations are split by the Bøifot type orthomode junction and power splitter. Two

waveguide quadrature hybrid couplers and four 16 dB branch-guide directional couplers are employed to inject the LO in the RF signal paths with the proper phase. The two full height waveguide side arms at the output of the Boifot type orthomode junction as well as the two waveguide branches following the 90° LO hybrid coupler must have the same electrical path length to allow a proper phase balancing at the two SIS mixer input P_1 and P_2 . The two waveguides exiting the power splitter and the two waveguide branches following the second 90° LO hybrid coupler must also have the same electrical path length before entering the two SIS mixer input O_1 and O_2 .

IV-b Design of mechanical assembly

The waveguide circuitry discussed above can be realized using 6 mechanical parts (3×2 half blocks) made of brass to allow easy machining. A view of the compact split-block mechanical assembly of the three different half blocks showing the internal waveguide circuitry is presented on the right of Fig.(6). The whole device comprises four 16 dB

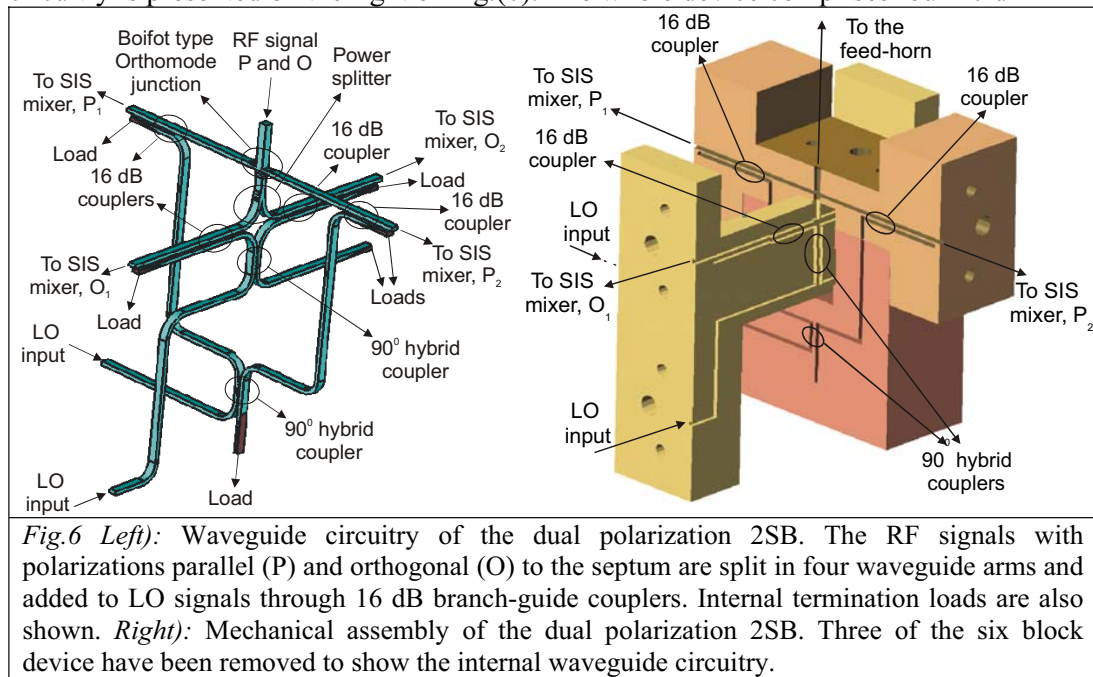


Fig.6 Left): Waveguide circuitry of the dual polarization 2SB. The RF signals with polarizations parallel (P) and orthogonal (O) to the septum are split in four waveguide arms and added to LO signals through 16 dB branch-guide couplers. Internal termination loads are also shown. *Right):* Mechanical assembly of the dual polarization 2SB. Three of the six block device have been removed to show the internal waveguide circuitry.

branch-guide couplers, two 90° hybrid couplers as well as the orthomode junction and power splitter. Once assembled, the device will have external dimensions $40 \times 40 \times 40 \text{ mm}^3$. A beryllium copper septum (not visible) can be positioned between hollow surfaces of two split-blocks. The blocks can be realized using a standard CNC, except for the slots of the waveguide couplers that require to use spark-erosion technique.

A view of the whole RF section of the dual polarization 2SB including the ALMA Band 7 feed-horn and SIS mixers is shown on Fig.(7). Each mixer includes its IF matching circuit and a magnetic field concentrator to suppress the Josephson currents. The dimensions of the six mechanical blocks have been chosen to allow their assembling with the ALMA feed-horn and the ALMA Band 7 mixers.

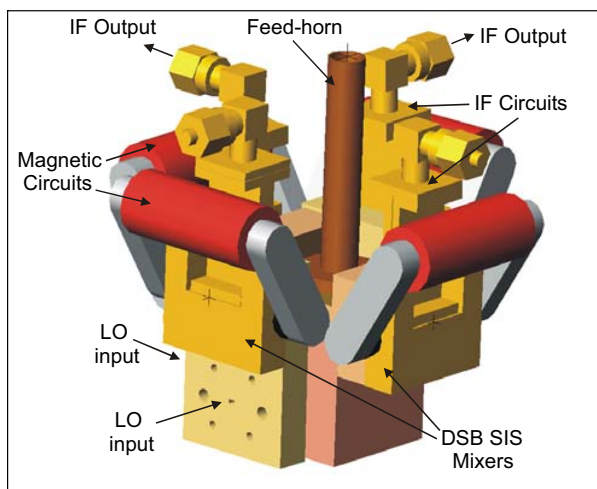


Fig.7: View of the mechanical assembly of the dual polarization 2SB showing the feed-horn and the 4 DSB ALMA Band 7 SIS mixers including its magnetic circuits and IF outputs.

V. Conclusions

A dual polarization sideband separating receiver using a waveguide OMT has been designed for the 275-370 GHz frequency band. This is based on a Bøifot type orthomode junction that integrates a 50 μm thick septum. The RF section of the device comprises, other than the OMT, a power divider, two 90° LO waveguide hybrid couplers and four 16 dB branch-guide LO directional couplers. The whole system is composed of 6 mechanical blocks that are assembled to form a compact structure. Its advantage is to exploit the -3 dB splitting operated over each of two mutually orthogonal

polarizations by the waveguide OMT junction and power divider, as required for sideband separation, and to avoid the problem of signals recombination of classical waveguide OMTs. The device can be constructed using conventional split-block techniques with reliability and cost-effectiveness.

Acknowledgements

We are grateful to Bernard Lazareff (IRAM) and to Renzo Nesti (Astrophysical Observatory of Arcetri, Italy) for helpful discussions. This work has been supported by IRAM (Grenoble, France).

References

- [1] Wollack, E., Grammer, W., and Kingsley, J., "The Bøifot Orthomode Junction", ALMA Memo n. 425, May 2002.
- [2] Narayanan, G. and Erickson, N.R., "A Novel Full Waveguide Band Orthomode Transducer", Proceedings of the 13th International Symposium on Space Terahertz Technology, Cambridge, MA, USA, March 26-28, 2002, p. 505-514.
- [3] Claude, S. "Sideband Separating SIS Mixer For ALMA Band 7, 275-370 GHz", 2003, this conference, Tucson, AZ, USA.
- [4] Bøifot, A. M., "Classification of Orthomode Transducers", 1991, European Transactions on Telecommunication and Related Technologies, vol. 2, n. 5, pp 503-510.
- [5] CST Microwave Studio. Bødinger Str. 2 a, D-64289 Darmstadt, Germany.
- [6] Navarrini, A., Lazareff, B., Billon-Pierron, D., and Peron, I., "Design and characterization of a 225-370 GHz DSB and a 250-360 GHz SSB full height waveguide SIS mixers", Proceedings of the 13th International Symposium on Space Terahertz Technology, Cambridge, MA, USA, March 26-28, 2002, p. 33-40.

Symmetric Waveguide Orthomode Junctions

E.J. Wollack¹ and W. Grammer²

National Radio Astronomy Observatory²
949 North Cherry Avenue, Tucson, AZ 85721

Laboratory for Astronomy and Astrophysics¹
NASA/Goddard Space Flight Center
Greenbelt, MD 20771
email: edward.wollack.1@gsfc.nasa.gov

ABSTRACT – Imaging applications at millimeter and submillimeter wavelengths demand precise characterization of the amplitude, spectrum, and polarization of electromagnetic radiation. The use of a waveguide orthomode transducer (OMT) can help achieve these goals by increasing spectral coverage and sensitivity while reducing exit aperture size, optical spill, instrumental polarization offsets, and lending itself to integration in focal plane arrays. For these reasons, symmetric OMTs are favored over a traditional quasi-optical wire grid for focal plane imaging arrays from a systems perspective. The design, fabrication, and test of OMTs realized with conventional split-block techniques for millimeter-waveguide bands are described. The design provides a return loss of ~20 dB over a full waveguide band. The observed cross-polarization and isolation are better than ~40 dB for tolerances readily achievable in practice. Prototype examples realized in WR10.0 and WR3.7 waveguide bands are presented.

Keywords: Orthomode Transducer, Polarization Diplexer, Waveguide Techniques

INTRODUCTION:

Receiver systems for radio astronomy require high-performance polarization-discrimination components. We report on the fabrication and performance of a wideband linear polarization diplexer for millimeter wavelengths. The designs considered here build on the concepts laid out by Brain (1978) at the Marconi Research Laboratory and first reported in a true split-block configuration by Boifot (1991). This two-fold symmetric junction achieves full waveguide band performance by limiting the excitation

of TE_{11} and TM_{11} in the square common-port. This was a key step toward the development of a wide bandwidth topology amenable to manufacture at millimeter wavelengths. These properties have lead to use of this configuration use in full-waveguide band receivers at centimeter and millimeter wavelengths (Cazzatello et al., 1996; Wollack, 1996). More recently, variations on these ideas have been explored with machinable apertures replacing the discrete compensation pins (Narayanan & Erickson, 2002; Nesti, 2002). In additions, see Uher, et al. (1993) for a comprehensive review of wide- and narrow-band OMT designs.

The two-fold symmetric OMT can be viewed as a variant on the turnstile junction where two of the ports have been folded parallel to the common-port [4]. The two ports that form the main-arm are separated by a thin septum, combined, and transformed to standard-height waveguide. For the other polarization, this septum forms a pair of back-to-back "mitered" bends which feed the symmetric side-arm ports. The pin number, diameter, and location are a compromise between tuning the septum reactance produced in the side-arm ports and allowing a low impedance return path for the main-arm currents.

To lowest order, throughout the structure, the propagation constant and impedance are constant. Although other implementation can be envisioned, this approach minimizes the frequency dispersion between the output ports. The main and side-arm junctions are two-fold symmetric about the horizontal and vertical guide planes, thus, TE_{11} and TM_{11} excitation can be avoided in the square common-arm of the junction to the extent that this condition is realized during fabrication and assembly.

This polarizer configuration can achieve relatively low fabrication cost while maintaining superior full waveband performance. The key strengths of this approach are as follows:

Fabrication:	2-piece split-block
Design Bandwidth:	$1.15 < f / f_c < 1.95$
Return Loss:	$\sim 20\text{dB}$ (typical) at millimeter wavelengths
Isolation:	$> 40\text{dB}$ (typical); limited by symmetry of junction
Phase Balance:	$< 20\text{deg}$ phase error (typical); $1.2 < f / f_c < 1.9$

We observe that the broadband phase balance is a direct consequence of the homogenous propagation constant in the structure. The functional form of the residual phase error is approximately parabolic with frequency.¹ For broadband polarimetry, these properties have the potential to enable a substantial improvement in continuum receiver technology over current approaches.

¹ This has been experimentally verified in the present design topology by equalizing the side- and main-arm path lengths with a waveguide shim and measuring the phase difference between the two output ports.

Symmetric OMTs: $\lambda \approx 3\text{mm}$ and 1mm Designs

We present details for prototype 3mm and 1mm two-fold symmetric waveguide OMTs. See Table 1 for a summary of mechanical specifications. A W-band (ALMA Band-3) prototype device with standard 3/4"-round flange interfaces is depicted in Figure 1. To achieve clearance between the side- and main-arm port flanges, the side-arm power combiner was realized at the interface of a 1:1 to 2:1 transition and a 65° miter was used in the main-arm port. This miter design provides full waveguide-band performance without the discontinuity jutting above the plane of the split-block and minimized the guide lengths for the indicated constraints. This was convenient for testing the basic properties of the prototype junction. The mixer block to OMT interface will determine the final package geometry.

The side-arms were realized in 2:1 guide and are combined in a 1:1 guide which is adiabatically transformed to a standard height. Placing the impedance transformer after the side-arm power combiner relaxes the tolerances required to maintain the phase match before the signals are recombined. For additional loss considerations see Appendix A. A discrete compensation approach related by symmetry to a miter bend is employed for the side-arm power combiner as described [4,5].

The split-block housing was fabricated out of brass. The main-arm output section was defined by multiple pass EDM (Electric-Discharge-Milling). The septum was made out of $61\mu\text{m}$ beryllium-copper shim stock. The septum is integrated into the 2:1 Chebyshev stepped main-arm transformer. A $\sim 100\text{mm}$ length of $125\mu\text{m}$ diameter copper-clad steel magnet wire was threaded through the holes to realize the compensation "pins". After assembling the blocks and septum, the wires are potted into the upper block and trimmed. The resulting configuration is insensitive to variation in applied force and allows disassembly of the block if desired.

The performance indicated in Figure 2 is with four pins and the nominal septum placement used to compensate the junction. Measurement frequencies are normalized to the WR10.0 cutoff, $f_c = 59.01\text{ GHz}$, to facilitate comparison of the response. TRL (Thru-Reflect-Line) was used to calibrate the HP85106D network analyzer. The common-arm termination is a sliding conical load with a return loss $\sim 40\text{dB}$. The data presented are uncorrected for the resultant measurement errors. The observed insertion losses for

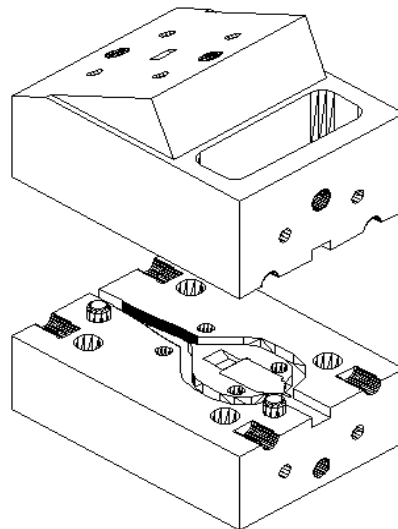


Figure 1: WR10.0 OMT Assembly.

bright and bondable pure gold plated housings are also indicated. The overall performance is in agreement with a HFSS [9] model of the structure.

The preliminary electrical characterization of a set of prototype WR03.7 full-band orthomode transducers was also performed. The design is derived from the junction previously described and is intended as a proof-of-concept for a ~1mm (ALMA Band-6) OMT. Two pairs of split-block housings were fabricated from leaded brass, to verify reproducibility of the approach. The main arm output sections on one set were formed using EDM, and on the other set by electroformed copper inserts. In a production design, the fabrication details will be modified to suit the details of the mixer block interface. The septum was produced by photolithographic etching on a 36 μ m thick beryllium-copper sheet. Copper-stainless steel magnet wire with a diameter of 61 μ m was used to compensate the junction. All components were subsequently gold plated. Further optimization of the side-arm return loss for atmospheric window is possible and would potentially result in improved overall coupling efficiency.

The measured performance indicated in Figure 3 was taken with the nominal septum placement and four wires compensating the junction. Measurement frequencies are normalized to the WR03.7 cutoff, $f_c = 159.6$ GHz. Oleson WR03.4 millimeter-wave test set were used to measure the device's S-parameters. Data were taken both in the WR03.4 and WR03.7 waveguides with TRL (Thru-Reflect-Line) calibration. For the WR03.4 calibration, a 2:1 transition with return loss less than 25dB was used mate to the native WR03.7 OMT guide. Within the experimental error, quantitatively consistent results were obtained with both calibration approaches. The ~0.2dB ripple observed in the loss estimate results from the finite directivity of the VNA heads. The observed isolation was limited by the test set in use and will be addressed in subsequent efforts. This suite of measurements indicates that the structures have repeatable parameters during manufacture.

CONCLUSIONS:

The performance of two-fold symmetric millimeter wave orthomode junctions is presented. Isolation >40 dB and return loss ~20 dB are typically observed. The ohmic contribution to the insertion loss is within a factor of ~two of the theoretical for pure gold at room temperature and improves modestly upon cooling to cryogenic temperatures. Components based upon these designs have been incorporated into state-of-the-art broadband low-noise receivers for radio astronomy. Direct integration of the OMT and sensor will be of increased importance in reaching the fundamental limits for wideband waveguide polarization applications.

REFERENCES:

- [1] Brain, J.M. "The Design and Evaluation of a High Performance 3 M Antenna for Satellite Communication," *The Marconi Review*, Fourth Quarter, 1978, pp. 218—236; Henderson, R.I., BAE Systems, private communication, 2002, Great Baddow, Chelmsford, UK.
- [2] Boifot, A.M., Lier, E., Schaug-Pettersen, T., "Simple and Broadband Orthomode Transducer," 1990, *Proc. IEE*, vol. 137, no. 6, pp. 396 400; Boifot, A.M., "Classification of Ortho-Mode Transducers," 1991, *European Transactions on Telecommunications and Related Technologies*, vol. 2, no. 5, pp. 503—510.
- [3] Cazzatello, G.F., Barbiero, M., Giglia, C.G.M., Klooster, C.G.M., "Wide-Band Dual-Polarized Feeds," 1996, *Workshop on Large Antennas in Radio Astronomy*, ESTEC, Noordwijk, Netherlands, pp. 159—171.
- [4] Wollack, E., "A Full Waveguide Band Orthomode Junction," 1996, NRAO, EDIR Memo Series, #303.
- [5] Wollack, E.J., Grammer, W., and Kingsley, J., "The Boifot Orthomode Junction," May 2002, NRAO, ALMA memo series #425.
- [6] Narayanan, G. and Erickson, N.R., "Design and Performance of a Novel Full-Waveguide Band Orthomode Transducer," 2002, 13th Symposium on Space THz Technology, Cambridge MA.
- [7] Nesti, R., Private Communication, 2002, Osservatorio Astrofisico di Arcetri, Firenze, Italy.
- [8] Uher, J., Bornemann, J., Rosenberg, U., *Waveguide Components for Antenna Feed Systems: Theory and CAD*, 1993, Artech House, Norwood, MA, section 3.8, pp. 371—445.
- [9] Hewlett Packard EEsop Division, Hewlett Packard High Frequency Structure Simulator (HFSS), Santa Rosa, CA 95403.
- [10] Montgomery, C.G., Dicke, R.H., Purcell, E.M., *Principles of Microwave Circuits*, 1987, IEE Electromagnetic Waves Series, vol. 25, Peter Peregrinus, London, chapter 12. (First published 1948, MIT Radiation Laboratory Series, Vol. 8, McGraw-Hill, New York.)

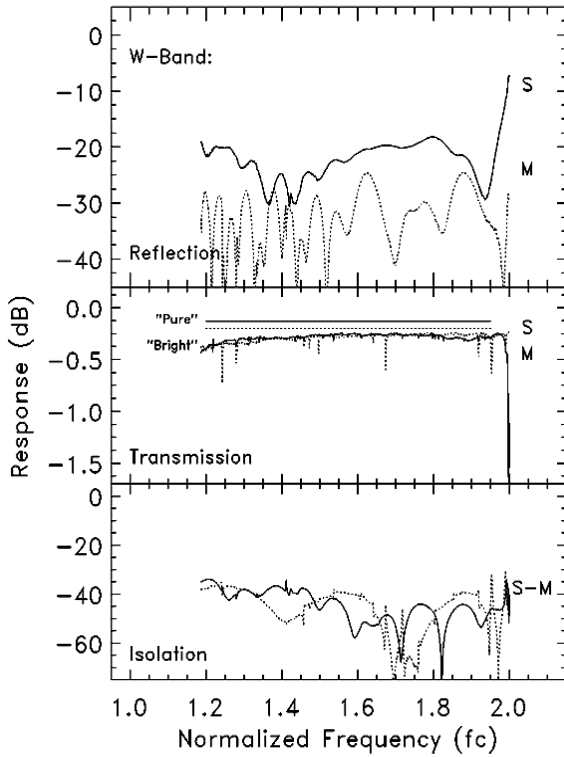


Figure 2: WR10.0 OMT ($f_c=59.01$ GHz). The solid and dashed lines are respectively the side- and main-arm responses for reflection and transmission. The solid isolation line is with a load on the common-arm; the dashed line is with a short on the common-port.

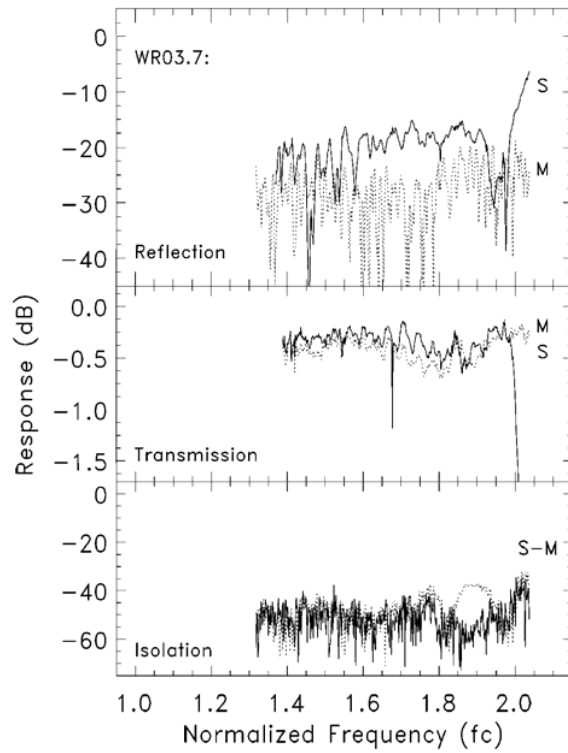


Figure 3: WR03.7 OMT ($f_c=159.6$ GHz). The solid and dashed lines are respectively the side- and main-arm responses for reflection and transmission. The solid isolation line is with a load on the common-arm; the dashed line is with a short on the common-port.

Wave Band	Output Guides [WR]	Guide Broadwall a_0	Sidearm: Power Combiner Angle	Power Combiner Transformer Ratio	Flange Geometry	OMT Mass [gm]	Spit-Block Envelope L x W x H [mm ³]
Q ($\lambda_0 \approx 7$ mm)	22.4	5.69 mm (0.224")	$\pi/4 : \pi/4$	0.5 : 1.0	19.1 mm (0.750") Sq	45 (Al)	44 x 28 x 26
Q ($\lambda_0 \approx 7$ mm)	22.4	5.69 mm (0.224")	$\pi/2 : \pi/4$	0.5 : 1.0	19.1 mm (0.750") Rd.	149 (Brass)	45 x 29 x 28
W ($\lambda_0 \approx 3$ mm)	10.0	2.54 mm (0.100")	$\pi/2 : \pi/4$	1.0 : 2.0	19.1 mm (0.750") Rd.	110 (Brass)	32 x 22 x 28
- ($\lambda_0 \approx 1$ mm)	3.7	.94 mm (0.037")	$\pi/2 : \pi/4$	1.0 : 2.0	9.5 mm (0.375") Rd.	24 (Brass)	14 x 17 x 14

Table 1: Orthomode Junction Design and Layout Summary.

APPENDIX A: Waveguide Loss Considerations

Since standard flanges do not scale with guide size, in practice, the flange interface area can significantly influence the overall component size. For wavelengths greater ~ 5 mm, physically small compensation structures are desirable to minimize overall device mass and volume. For wavelengths less than ~ 5 mm, physically large matching and potentially overmoded structures are desired to control loss and improve overall manufacturability. With adequate attention to detail, the benefits of reduced ohmic loss can be realized while mitigating the potential spurious effects of mode conversion [5].

In light of these considerations, we briefly consider the scaling laws for the ohmic component of the loss which result from a finite electrical conductivity, σ . In limit the skin depth, $\delta = (2/\omega\mu\sigma)^{1/2}$, is small compared to the metallization thickness and wavelength, the loss can be estimated by perturbation of boundary conditions [10]. The power loss per unit length in the guide is,

$$\alpha = -\frac{1}{P} \frac{dP}{dz} = \frac{1}{P} \operatorname{Re} \left\{ \int_{\text{cross section}} \vec{S} \cdot \hat{n} \, dA \right\}$$

$$\cong \frac{R_s}{2P} \oint_{\text{walls}} dl \left| \vec{H} \times \hat{n} \right|^2$$

For the dominate mode for a rectangular guide with broadwall dimension a_o and sidewall height b_o ,

$$\alpha = \frac{R_s}{2P} \left[\int_{\text{broadwall}} dx \left(\frac{\beta^2}{k_c^2} \sin^2 k_c x + \cos^2 k_c x \right) + \int_{\text{sidewall}} dy \right]$$

$$= \frac{2R_s}{\eta} \left[\frac{1}{2b_o} + \left(1 - \frac{\beta^2}{k^2} \right) \frac{1}{a_o} \right] \frac{k}{\beta}$$

where $k = (\epsilon\mu)^{1/2} \omega$, the propagation constant is $\beta = (k^2 - k_c^2)^{1/2}$, and $k_c = \pi/a_o$ is the mode cutoff wavevector. For a good metal, the ratio of the surface resistivity, $R_s = 1/\sigma\delta$, over the impedance of free space, $\eta = (\mu/\epsilon)^{1/2}$, is small compared to unity. It is convenient to define the following dimensionless function,

$$\xi \equiv \frac{\pi}{2} \frac{\eta}{R_s} \frac{\alpha}{k_c}$$

$$= \left(\frac{a_o}{2b_o} + 1 \right) \frac{k}{\beta} - \frac{\beta}{k}$$

This allows a practical separation of the geometric and material contributions to the attenuation for the dominate mode. This quantity is plotted in Figure 4 with the guide aspect ratio as a parameter. As the sidewall height is increased, the loss is correspondingly reduced by accepting a smaller the single mode bandwidth. This basic behavior is reminiscent of the unloaded cavity quality factor, Q_o , which in the thermal dynamic limit scales as the characteristic size of the system in wavelengths. We recall, for a cavity with TE₁₀ illumination,

$$\begin{aligned} 1/2Q_o &\cong \frac{R_s}{4\omega U} \left[\int_{length} dz \oint_{walls} dl \left| \vec{H} \times \hat{n} \right|^2 + 2 \int_{ends} dA \left| \vec{H} \times \hat{n} \right|^2 \right] \\ &= \frac{2R_s}{\eta} \left[\frac{1}{2k b_o} + \left(1 - \frac{\beta^2}{k^2} \right) \frac{1}{k a_o} + \left(\frac{\beta^2}{k^2} \right) \frac{1}{k l_o} \right] \end{aligned}$$

where l_o , the length of the rectangular waveguide, imposes a discrete symmetry on the resonant responses. In the limit the cavity length tends to infinity, the contribution of the ends relative to the sidewalls drops. Similarly, a discrete excitation spectrum is possible in the limit b_o is large enough to allow multimode propagation. This general picture can be extremely useful in considering the effects of transmission and isolation resonances in the multi-mode limit. In practice, the necessity to control these effects presents a challenge for achieving ultra low-loss wide-band performance for guide aspect ratios significantly larger than 1:1 without the use of mode filters in homogenous structures.

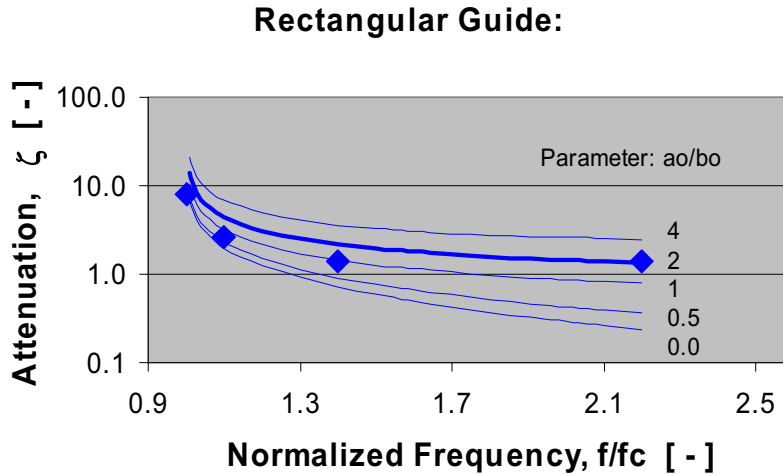


Figure 4: Normalized Waveguide Attenuation versus Frequency. The geometric dependence of attenuation constant is plotted with the broadwall over guide height as a parameter. The bold line depicts the normalized attenuation of a standard 2:1 guide. The diamonds indicate the onset of TE₁₁ and TM₁₁ mode propagation for the aspect ratios indicated.

Optical Methods for Spectral Analysis of future Heterodyne Instruments

R.Schieder

**Physics Institute, University of Cologne
Zùlpicher Str.77, D-50937 Cologne, Germany**

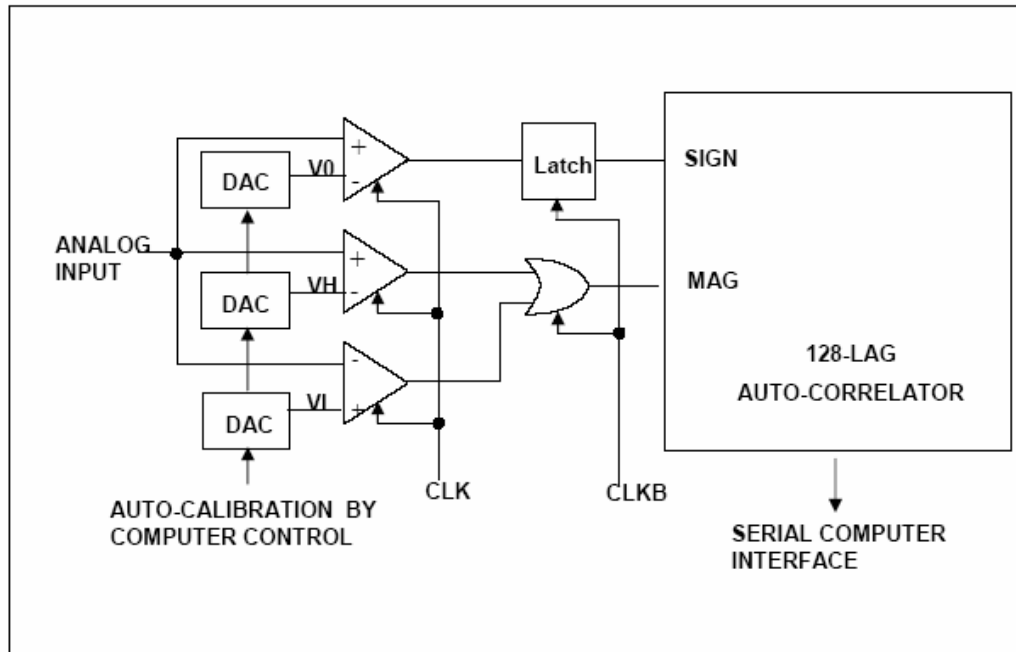
Today, submm- and THz-receivers are now state of the art in radio-astronomy. Consequently, the availability for wide bandwidth back-ends is becoming increasingly important. But, at the same time, also imaging receivers are now operational in several places, so that the availability of large numbers of such spectrometers is now developing into one of the major bottle-necks. In recent years, large bandwidth (~1 GHz) acousto-optical spectrometers (AOS) became available with small weight and low power consumption so that their applicability particularly for space programs is now of increasing interest. But also at ground-based observatories numerous AOS are in use very successfully. For the particular needs of array-receivers the development of array-AOS represents an important step which allows to operate four low resolution spectrometers in one small optical unit. Such spectrometer will fly for example aboard the ESA cornerstone mission Herschel for the heterodyne instrument HIFI. Nevertheless, imminent programs like SOFIA will require spectrometers with even more bandwidth and in fairly large numbers, which are presently not available with any well approved technology. Acousto-optics can provide more than presently available bandwidth, most likely up to 4 GHz, but it requires the usage of new materials and new laser sources. The latest results of a dedicated investigation are indicating that such spectrometers are feasible, and ideas for future array-systems might become reality within the next few years. When considering systems further up in frequency towards the FIR or mid-IR frequency range, even more bandwidth is required. For this, other optical methods like the application of optical modulation of single frequency lasers with the IF output of a heterodyne receiver can lead to a new generation of lower resolution instruments when using Fabry-Perot Etalons for the spectral analysis. Such systems may also be converted into array-spectrometers by fairly simple optical methods. Details of such ideas and first preliminary results will be discussed.

A Correlator Chip for Spaceborne Radiometry

Constantin Timoc
Spaceborne Inc.

Summary

The S2000S128C is a digital correlation spectrometer comprising a digitizer and an auto-correlator on a single chip. The digitizer is used in conversion of noise-like signals to 2-bit/4-level digital signal. The S2000CS128 is provided with 4 frequency counters which contain information necessary for auto-calibration of the digitizer. The digitizer includes 16-bit DACs used to set the threshold voltages for comparators during auto-calibration by a computer software. The computer is connected to the digitizer through a serial interface. The auto-correlator calculates 128 points of the correlation function of two digitized signals. The spectrometer employs a 4-level quantization scheme with weighting factors of $(-3,-1,+1,+3)$ and a modified 2×2 bit multiplication table to achieve a sensitivity of 87%. The S2000S128C uses parallel processing with a time multiplexing factor of 2 to achieve an effective signal bandwidth of 2 GHz at a clock frequency of only 2 GHz. Each lag comprises a 2×2 bit multiplier, a 4-bit accumulator, a 32-bit counter, and a 32-bit buffer shift register. Several chips can be cascaded to construct spectrometers with more than 128 lags. The chip is powered from a 1.8 V supply and dissipates 4.5 W at a sampling frequency of 2 GHz



Deployment of *TREND* - A Low-Noise Receiver User Instrument at 1.25 THz to 1.5 THz for AST/RO at the South Pole

Eyal Gerecht^a, Sigfrid Yngvesson^a, John Nicholson^a, Yan Zhuang^a, Fernando Rodriguez Morales^a, Xin Zhao^a, Dazhen Gu^a, Richard Zannoni^a, Michael Coulombe^b, Jason Dickinson^b, Thomas Goyette^b, Bill Gorveatt^b, Jerry Waldman^b, Pourya Khosropanah^c, Christopher Groppi^d, Abigail Hedden^d, Dathon Golish^d, Christopher Walker^d, Jacob Kooi^e, Richard Chamberlin^e, Antony Stark^f, Christopher Martin^f, Robert Stupak^f, Nicholas Tohill^f, and Adair Lane^f

^aUniversity of Massachusetts at Amherst

^bSubmillimeter Wave Technology Laboratory, University of Massachusetts at Lowell

^cChalmers University of Technology, Gothenberg, Sweden

^dDepartment of Astronomy and Steward Observatory, University of Arizona

^eCalifornia Institute of Technology

^fSmithsonian Astrophysical Observatory

ABSTRACT - We have developed and constructed a low noise receiver user instrument based on HEB technology, *TREND* (*Terahertz REceiver with NbN HEB Device*). The plan was to install *TREND* on the 1.7 meter diameter AST/RO submillimeter wave telescope at the Amundsen/Scott South Pole Station during the austral summer season of 2002/2003. The frequency range of 1.25 THz to 1.5 THz was chosen in order to match the best windows for atmospheric transmission and interstellar spectral lines of special interest. The South Pole Station is the best available site for ground-based THz observations due to the very cold and dry atmosphere over this site.

The *TREND* team is now able to report that this receiver has been installed on schedule and met our goals for its performance. *TREND* is thus ready to perform astronomical observations in the upcoming austral winter season as soon as the weather becomes suitable for THz work. The first spectral lines which will be observed are the CO J= 11→10 line at 1.27 THz and the 1.46 THz line of NII. *TREND* is an NbN Hot Electron Bolometer (HEB) type receiver, and the double sideband noise temperature at 1.27 THz has been measured on the telescope to be 1,200 K. The local oscillator is a CO₂ laser pumped, amplitude stabilized CD₃OH gas laser. The *TREND* receiver will pioneer observations from a ground-based telescope at frequencies well above 1 THz. This is also the first time that a receiver can potentially perform an extensive study of the ubiquitous NII ion, first noted by COBE.

I. INTRODUCTION

A number of significant technological research efforts aimed at the development of terahertz low-noise heterodyne instruments are under way in laboratories around the world. Instruments that will be operational in a few years include the far infrared space telescope (HERSCHEL) and other platforms in the upper atmosphere (SOFIA, balloons). Low-noise receivers based on HEB devices deployed on ground-based telescopes at the best available sites are becoming operational now, however. It has only recently been realized that observations above 1 THz are feasible at such sites. Ground based telescopes can be dedicated to specific tasks for longer periods of time compared with facilities in space. Furthermore, larger diameter telescopes, such as the 8 meter one under construction at the South Pole, will be superior to air and space borne dishes in terms of angular resolution. Presently, the 1.7 meter diameter AST/RO submillimeter wave telescope is operated at the South Pole by the Smithsonian Astrophysical Observatory, and has successfully performed observations up to the 800 GHz (350 μm) window for several years.

NbN HEB THz receivers have been under development at the University of Massachusetts for a few years and are now ready to be used for astronomical observations. *TREND* (“*Terahertz REceiver with NbN Device*”) is a low-noise heterodyne receiver for the 1.25 THz to 1.5 THz frequency range. The receiver takes advantage of the atmospheric transmission windows in the above frequency range, as well as the availability of AST/RO.

II. SITE CONSIDERATIONS

The Antarctic Plateau, with an altitude of 2847 meters, is unique among observatory sites for unusually low wind speeds, absence of rain, and an extremely cold and dry atmosphere. The *median* Precipitable Water Vapor (PWV) value is less than 0.3 mm during the austral winter season. Available atmospheric models can be used with the measured amount of PWV to predict the atmospheric transmission in two windows near wavelengths of about 200 μm , occurring from about 1.25 THz to 1.4 THz, and from 1.45 THz to 1.6 THz. Expected *median* transparency at frequencies corresponding to important spectral lines is from 5% to 11%, and on unusually good days may reach values 2 or 3 times higher. Atmospheric transmission measured with an FTS instrument from the South Pole site [2] is shown in FIG. 1. These measurements show good atmospheric transparency and confirm the above model predictions. It is clear that installing a low noise terahertz receiver at the South Pole site is thus well justified.

We have identified two spectral lines, located in the above atmospheric windows, which are of special interest. The first is the NII (singly ionized nitrogen) line, at 1461.3 GHz (205.4 μm), which is the second strongest spectral line overall in a typical galaxy (only CII at 156 μm is stronger). NII

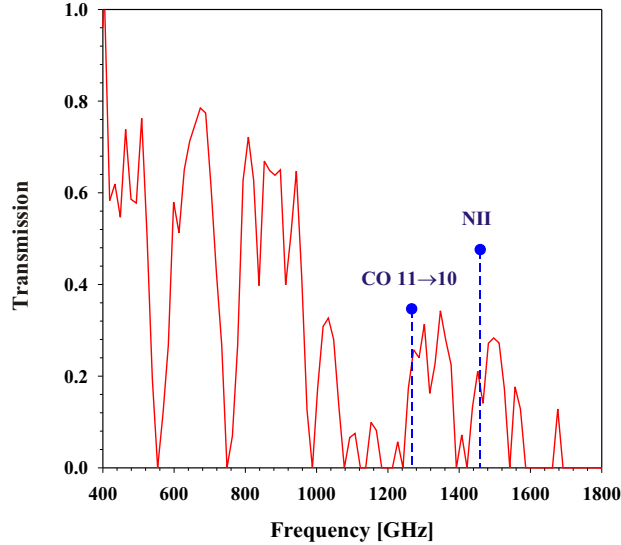


FIG. 1. Atmospheric transmission at the South Pole measured with an FTS [2].

should be ubiquitous in the warm interstellar medium (WIM) of our galaxy. The other line is the $J=11 \rightarrow 10$ line of CO at 1267.014 GHz. It is important to observe higher order CO lines and compare these with the well studied millimeter lines of CO in warmer, denser sources. The locations of the above lines relative to the atmospheric transmission spectrum are marked in FIG. 1.

III. RECEIVER DESIGN

We have chosen the quasi-optical coupling design for our phonon-cooled HEB (PHEB) mixers. Typical state-of-the-art DSB receiver noise temperatures for PHEB receivers measured at about 1.5 THz are in the range of 500-1000 K [1,3]. NbN HEB mixers are also very insensitive to changes in bias conditions and LO power and should be easy to adapt to the observing logistics at AST/RO, where all observations in the austral winter season are performed by one or two “winter-over” operators. Whereas multiplier LO sources are expected to be available in the future, a laser LO was chosen for *TREND*, since it is a mature technology in the terahertz regime and will lend itself well to a future upgrade of the system to incorporate a multi-pixel focal plane array.

Active Device

Phonon-cooled HEB mixers are typically fabricated from NbN films on either silicon or MgO substrates. The MgO substrate potentially results in a wider IF bandwidth than for NbN on silicon. The IF bandwidth requirement for *TREND* (1 – 2 GHz) can be satisfied by using silicon substrates,

however, and our devices for *TREND* were fabricated on this substrate. We have developed devices using (1) UV lithography and (2) e-beam writing. Devices fabricated with UV lithography at UMass/Amherst are $1\ \mu\text{m}$ (length) \times $4\ \mu\text{m}$ (width) whereas a set of smaller devices, written with e-beam at Chalmers University of Technology, are $0.4\ \mu\text{m}$ \times $4\ \mu\text{m}$. The $1\ \mu\text{m}$ long devices have somewhat higher resistance ($200 - 400\ \Omega$) and recent devices have shown noise temperatures from 1,500 K to 2,000 K. The shorter e-beam devices are better matched to the antenna and have yielded noise temperatures below 1,000 K as discussed below.

Quasi-Optical Coupling

In our NbN HEB development work, we have made use of a quasi-optical coupling scheme consisting of a 4 mm diameter elliptical silicon lens, coupled to a self-complementary toothed log-periodic antenna on a silicon substrate. The optimum polarization direction is frequency-dependent for log-periodic antennas. We have therefore chosen a twin-slot antenna designed for a center frequency of 1.3 THz for the *TREND* receiver, as shown in FIG.2. This antenna is linearly polarized, perpendicular to the slots. The bandwidth of similar twin-slot antenna HEB mixers has been shown to be wider than required for matching the entire 200 μm atmospheric window, about 1.25 to 1.6 THz. Our NbN HEB mixers show no saturation due to thermal noise, and also no direct detection effects.

The beamwidth of the quasi-optical system is primarily determined by the diameter of the elliptical lens and has been measured for an earlier version as reported in [4]. The 3 dB beamwidth of the *TREND* lens/antenna combination was determined to be 3.6 degrees roughly in the center of the band (1.4 THz) by using ring-shaped cut-outs in the hot load while doing Y-factor measurements. The

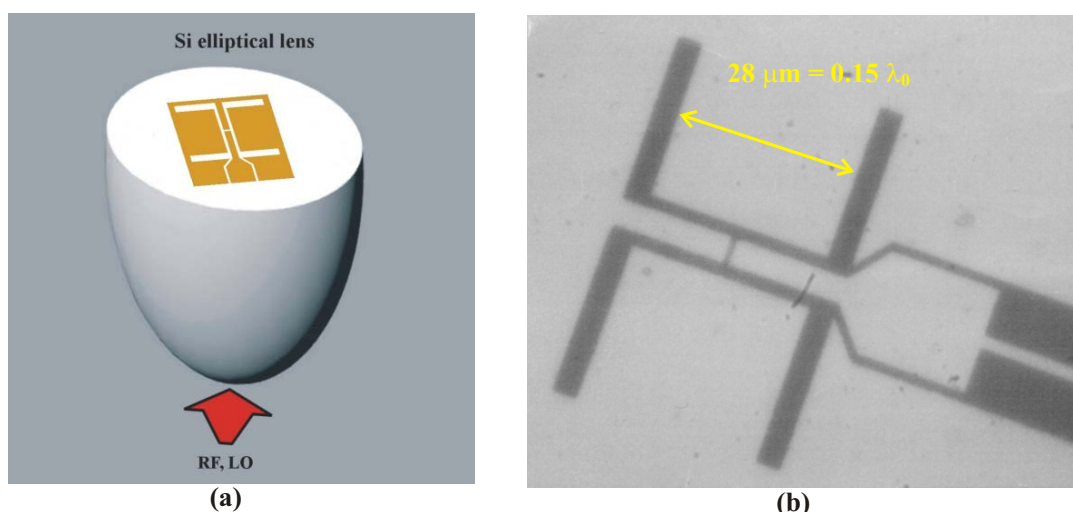


FIG.2. (a) A quasi-optical design illustration; (b) A photograph of the twin-slot antenna. The PHEB device in the center is too small to be seen.

beamwidth varies linearly with the wavelength, and the focusing optics for the LO and sky beams on the AST/RO telescope were designed to match the measured beam width of the *TREND* system in the center of the band, see below for further details on the optics.

Laser Local Oscillator

The LO source is a model # SIFIR-50 FPL terahertz gaseous laser system that was designed and built by the Coherent/DEOS company [5]. As other terahertz gas lasers, it is pumped by a CO₂ laser. In the case of the *TREND* laser, the pump laser is sealed, and is expected to be able to operate at least 10,000 hours before it needs to be refilled with gas, a feature which facilitates operation at a remote site. The pump laser is RF excited and thus does not require a high-voltage power supply. Its maximum power output is 50 W on one of the strongest lines. The CO₂ laser is grating tuned through a PZT translator, and is actively frequency locked to one of the resonance frequencies of a high-Q temperature-stabilized Fabry-Perot resonator. The terahertz laser uses a thermally compensated design for amplitude and frequency stability. Its cavity length can be adjusted either by a micrometer or a PZT translator. All of the above components are integrated into a rugged, transportable package, with dimensions of about 185 cm × 50 cm, and height of about 25 cm. The laser system requires liquid cooling. FIG. 3 shows a photograph of the *TREND* laser system while being tested at AST/RO.

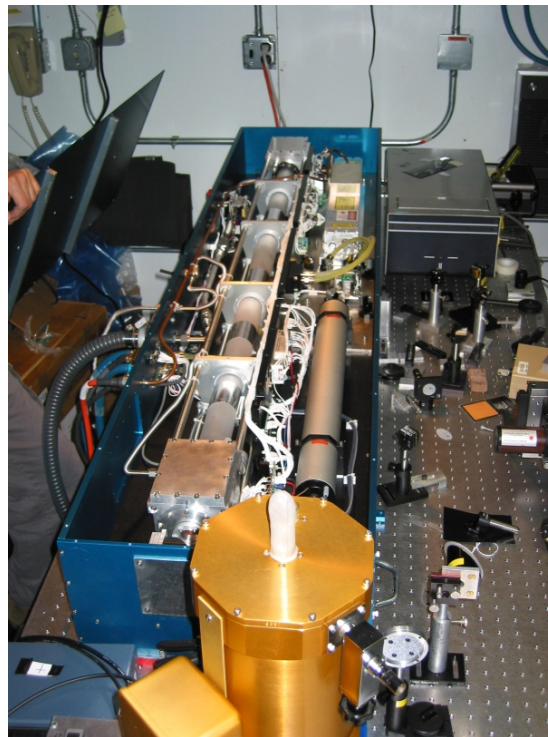


FIG.3. Photograph of the *TREND* laser system with the laser cover off.

It is usually possible to find a terahertz laser line which matches a particular line in the ISM, within the IF bandwidth of typical HEB mixers (about 5 GHz). However, some portions of the terahertz range may not have a strong laser line available. At the present time, the best known laser line sufficiently close to the required frequency of 1461.31 GHz for NII is a line produced by CD₃OH at 1459.3913 GHz (205.423 mm wavelength), which yields a convenient IF of 1.7 GHz. The output power on this line in stable operation is about 1 mW, which is sufficient since we found that less than 10 μW of laser power at the dewar window was needed to pump the mixer to its optimum point. We use a 6 μm thick beam splitter, which reflects about 1 % of the power. The CD₃OH laser line demonstrates some of the constraints on obtaining a laser local oscillator at a specific terahertz frequency. The center of the CO₂ pump laser line (10P36) is offset from the center of the CD₃OH line to be pumped. Since the offset is larger than the free spectral range of the particular pump laser used, the laser cannot be operated at the optimum pump frequency. This results in lower than typical laser gain and thus less output power. There are actually two lines in CD₃OH which are pumped by the same pump line; the second one is located at about 215.8 μm, with the same polarization as the 205.4 μm line. We distinguish between the two lines by using a silicon etalon, which has different attenuation for the two lines. CD₃OH has an additional line (with a different CO₂ pump line) measured to be at 1265.513 GHz. This line matches that of the J = 11 → 10 transition of CO, with a conveniently low IF of 1.5 GHz.

The *TREND* Laser power is actively stabilized to ±0.01 dB (±0.25 %) over many minutes by a feedback system which senses the DC bias current of the HEB device directly, and applies this signal through an amplifier/filter circuit to the FIR laser PZT translator, thus keeping the operating point very stable. The time-constant of this circuit is about 10 seconds. Additional long term stabilization is achieved by controlling the continuous flow of the gas in the FIR laser using a gas manifold.

Mixer Block and Biasing

We have designed a new mixer block that is compatible with other mixer blocks used at the AST/RO facility. The mixer block contains the lens, the substrate on which the NbN device and the antenna were fabricated, and a circuit board that supplies the DC bias and connects the mixer through a capacitor to the IF amplifier. FIG.4 shows the present configuration of the bias circuit, as well as photographs of the mixer block. The bias scheme utilizes a total of five wires plus ground (three wires plus ground inside the dewar). Chip resistors of about 2 kΩ are placed in series with all leads, while chip capacitors inside the mixer block shunt transients to ground. Furthermore, the DC ground is separate from the mixer block/IF ground. This bias scheme protects the devices and minimizes line and other pickup. The bias electronics was built at the University of Arizona. The IF amplifier is a 1-2 GHz balanced amplifier design, which was originally designed at CalTech and has been used on earlier AST/RO receivers. The noise temperature contribution of the IF chain is about 5 K.

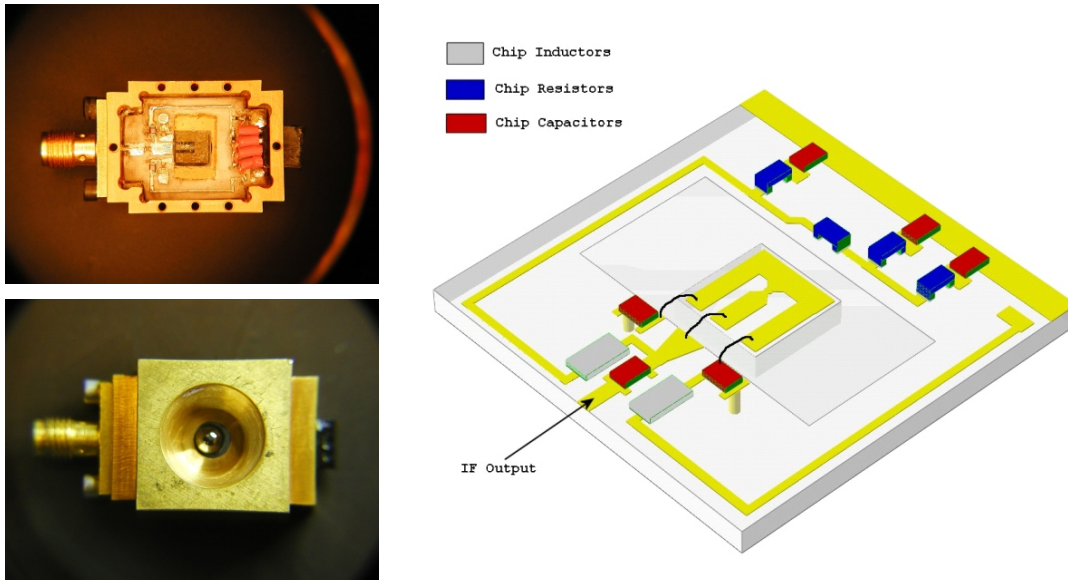


FIG.4. Photographs of the mixer block and a drawing of the bias circuitry.

IV. OPTICAL SYSTEM FOR *TREND* AT AST/RO

The AST/RO telescope has provisions for four different receivers, each occupying a receiver pallet/optical breadboard of size $75\text{ cm} \times 75\text{ cm}$. FIG.5 shows the position of the *TREND* receiver on one of these pallets. The laser is located on a separate optical breadboard in the ceiling, together with a HeNe laser for alignment, a pyroelectric detector for power monitoring, and an attenuator/polarizer (two crossed wire grids). The laser beam is guided to the receiver by mirrors L1 through L5. The “sky beam” from the telescope is guided through a hole in the ceiling onto a rooftop mirror system, which is used to select the particular receiver one wants to use for observing. It is then directed to the *TREND* receiver through three further mirrors. A $6\text{ }\mu\text{m}$ thick mylar beam splitter is located in front of the dewar window that allows low-loss transmission of the sky beam, while reflecting only a small fraction of the laser LO beam toward the *TREND* cryostat window. Most of the laser power is dissipated in an LO “beam dump”. This flexible arrangement eliminates the need for a diplexer for the LO injection. The *TREND* cryostat is mounted on an x-y translator system for alignment with the two beams. Further alignment degrees of freedom are available by turning the elliptical injection mirrors (L5 and R3, the closest mirrors for the respective beams). We have constructed two optical paths for the LO beam to compensate for the different polarization of the LO beam at the two frequencies of operation (see FIG.5).

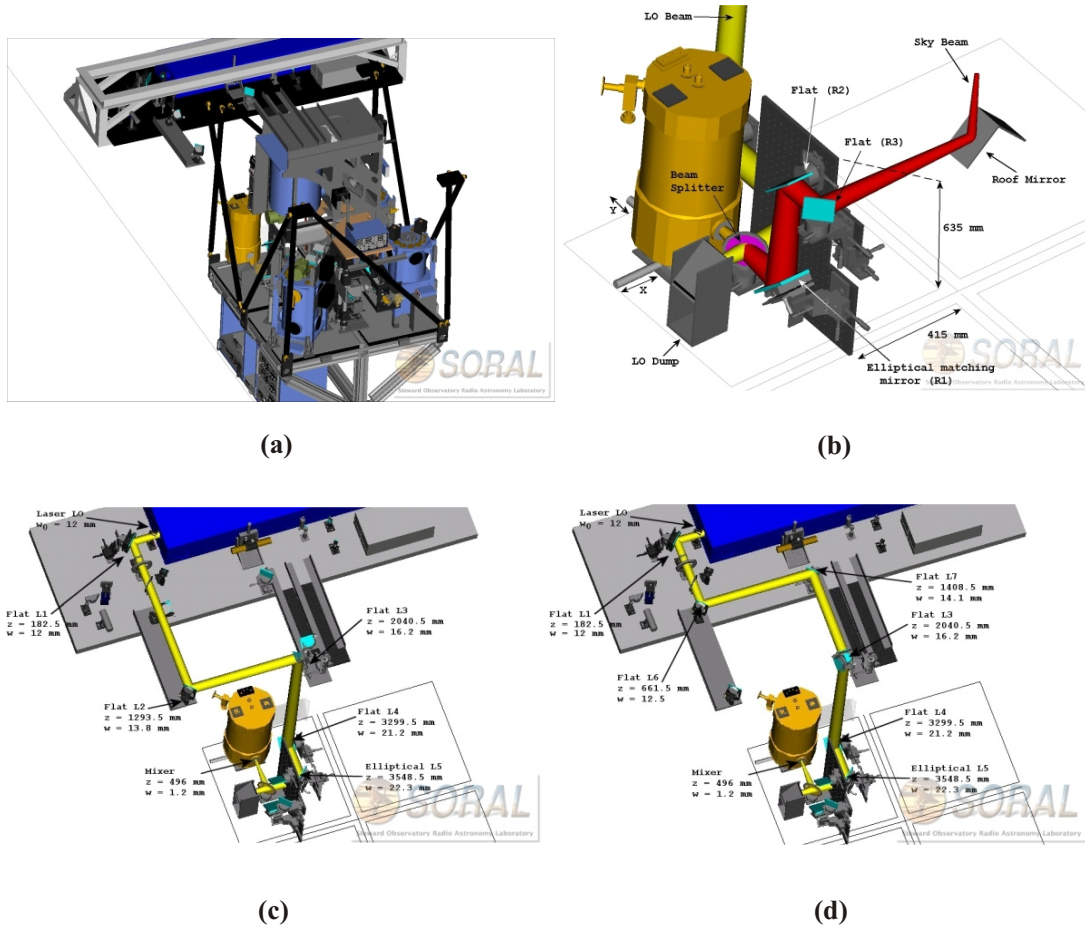


FIG.5. Optical system for the *TREND* receiver at the AST/RO telescope. (a) 3-D simulations of the receiver room; (b) *TREND* dewar with LO and Sky beams; (c) LO beam configuration for the 205 μm line; (d) LO beam configuration for the 237 μm line.

V. RESULTS AND CONCLUSION

Four mixer blocks with PHEB devices were constructed and transported to AST/RO. The mixer blocks are readily exchangeable and provide redundancy in case a device fails during the winter season. The best noise temperature results measured at UMass with one of the smaller devices are shown in FIG.6. These measurements show that the receiver covers the required tunable bandwidth with about a 30 % variation in receiver noise temperature across the band. The minimum of the noise temperature agrees with the design frequency of the twin-slot antenna, centered at 1.3 THz, and the bandwidth is what is expected for this antenna. The best double sideband total receiver noise temperature

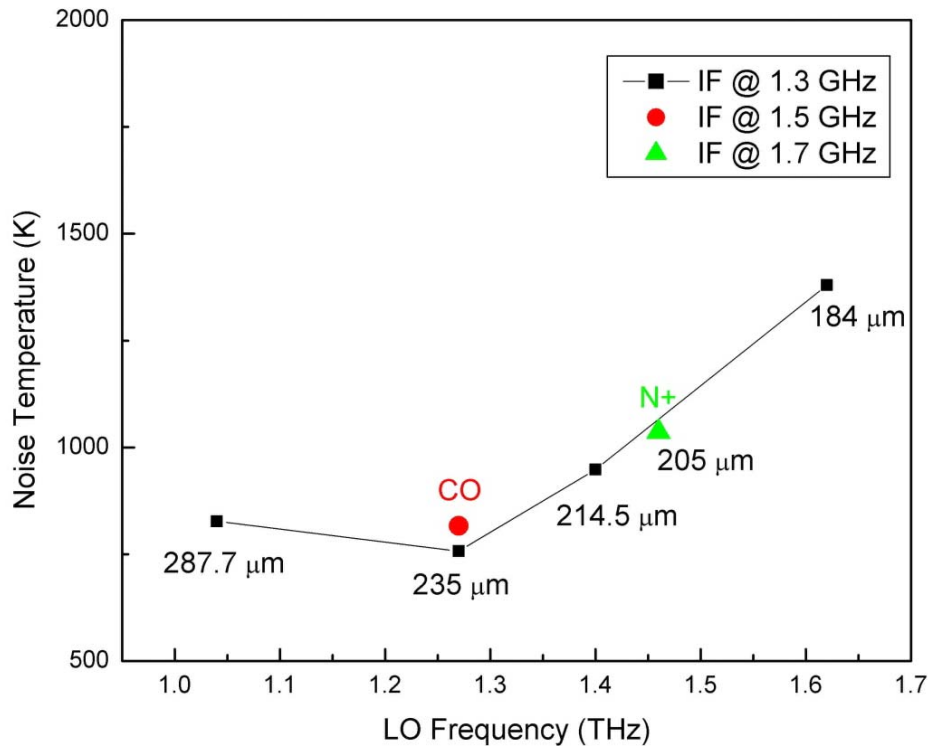


FIG.6. Double sideband receiver noise temperatures at different LO frequencies measured on one of the PHEB devices fabricated by e-beam. The IF was 1.3 GHz. A measured point at the IF for the CO 11→10 line is also plotted. The noise temperature point for the NII line was found by interpolation.

measured on the telescope was 1200 K at the 237 μm line. Other measurements in the laboratory prior to shipping the *TREND* system showed that the noise temperature was essentially unchanged for a 1 dB variation in LO power, when the bias voltage was low (about 0.6 mV). The total noise output power varied by 2.5 dB for the same change in LO power. Such variations do not occur on the telescope system since the LO power is actively stabilized in a way that maintains a constant bias current. We also measured short term fluctuations of the output power and derived the Allen variance from such data. Due to space limitations, we will defer the publication of this data to a future paper.

In conclusion, we have shown that a complex, laser-pumped, HEB receiver system can be transplanted from the laboratory to a fairly remote site and demonstrate similar performance to that measured in the laboratory. The system will now be used for actual observations as the best terahertz weather conditions at the South Pole usually occur during the months of June through August.

ACKNOWLEDGMENTS

We gratefully acknowledge support for this project from the NSF program for Advanced Technologies and Instrumentation (ATI), Division of Astronomical Sciences, NSF award # AST 9987319.

REFERENCES

1. E. Gerecht, C.F. Musante, Y. Zhuang, K.S. Yngvesson, T. Goyette, J. Dickinson, J. Waldman, P.A. Yagoubov, G.N. Gol'tsman, B.M. Voronov, and E.M. Gershenzon, "NbN Hot Electron Bolometric Mixers - A New Technology for Low Noise THz Receivers," *IEEE Trans. Microwave Theory Tech.*, vol. 47, pp. 2519-2527, Dec. 1999.
2. Chamberlin R A, Martin B, Martin C, Stark A A, "South Pole Submillimeter Fourier Transform Spectrometer [4855-83]", in *Millimeter and Submillimeter Detectors*, Proceedings of SPIE (Volume 4855), Kona, Hawaii, 2002),
3. See for instance Merkel, H., Khosropanah, P, Cherednichenko, S, and Kollberg, E., "Comparison of Noise Performance of NbTiN and NbN Hot Electron Bolometer Heterodyne Mixers at THz Frequencies", this symposium.
4. Yngvesson et al., "Terahertz Receiver With NbN HEB Device (*TREND*) - A Low-Noise Receiver User Instrument for AST/RO at The South Pole", 12th Intern. Symp. Space THz Technology, San Diego, CA, Febr. 2001, p. 262.
5. Coherent/DEOS, 1280 Blue Hills Ave, Bloomfield, CT 06002.

Heterodyne Array Development at the University of Arizona

C. Groppi, C. Walker, C. Kulesa, The University of Arizona

G. Narayanan, The University of Massachusetts

K. Jacobs, U. Graf, R. Schieder, Universität zu Köln

J. Kooi, California Institute of Technology

ABSTRACT

Over the past four years, SORAL and its collaborators have been developing two SIS heterodyne array systems for astronomical telescopes: the PoleStar 4 beam array for the 850 GHz atmospheric window, and DesertStar 7 beam array for the 350 GHz atmospheric window. PoleStar was delivered to the AST/RO telescope at the South Pole during the austral summer of 2000, and is now in normal operation. Desert Star is undergoing lab testing and engineering on the Heinrich Hertz Telescope now. We will present an overview of the system designs, techniques for local oscillator multiplexing, bias control, optics, cryogenics and results from system characterization and commissioning. Techniques used in the construction of these arrays are being extended, with the ultimate goal of building fully integrated heterodyne arrays with hundreds of pixels.

PoleStar: An 810 GHz Array Receiver for AST/RO

A 4-pixel array receiver constructed to operate in the astrophysically important 810 GHz atmospheric window was assembled and tested at the Steward Observatory Radio Astronomy Lab (SORAL) and installed on the Antarctic Submillimeter Telescope and Remote Observatory located at the South Pole (AST/RO) at the South Pole (Groppi et al. 2000). The cold, dry conditions at the South Pole, coupled with its relatively high altitude (~10,500 ft.) make it an excellent location for observations at submillimeter wavelengths. AST/RO has a 1.7 m aperture and was designed to take advantage of these conditions (Stark et al 2001). The almost ideal atmospheric conditions and the resulting observing efficiency available from the South Pole motivated us to build an 810 GHz



Figure 1: PoleStar in the lab during front-end testing.

All system electronics fit into a single transportable equipment rack. A He-Ne laser is mounted on the optics plate here for optics alignment.

array for use on AST/RO. Figure 1 is a photograph of the receiver front-end as it appeared in the lab before deployment.

Pole Star Optical Design

The purpose of the optical system is to re-image AST/RO's focal plane onto a compact 2x2 array of lenses located in the array cryostat and to efficiently inject local oscillator power into each mixer. Focal plane re-imaging is achieved by a pair of parabolic mirrors and two flats. A quasi-optical LO power divider is used to split the focused LO beam into 4 equal parts. The power dividing is accomplished by two, low-loss, ~50% crystalline quartz beam splitters. Each beam splitter is paired with a flat mirror to give the emerging beams the proper horizontal and vertical offsets. After including all loss mechanisms, we estimate that 18% of the incident LO power is in each LO beam at the output of the power divider.

LO diplexing is handled with a 0.5 mil Mylar beamsplitter. A 2x2 array of HDPE lenses then focuses the beams into the mixer feedhorns. Initially, we used a Martin-Puplett interferometer as an LO diplexer, but we later decided to replace it with a simple Mylar beamsplitter. While the MPI theoretically couples 100% of both the LO and sky power, they are very sensitive to misaligned beams. Even a 0.5 degree beam squint can cause 3 dB of loss in both LO and sky power, adding close to 600K of noise (Martin et al. 1977). The Mylar diplexer is not sensitive to mixer squint, and adds very little loss as long as the Mylar thickness is kept small.

JPL Local Oscillator

The first major upgrade to PoleStar was the replacement of the LO chain with whisker contacted multipliers with a state-of-the-art planar diode LO chain with 100 GHz power amplifiers before the first doubler. This LO chain uses multipliers developed for the Herschel HIFI project, designed and built jointly by JPL and UMass (Mehdi et al. 2003). The source is a 100 GHz Gunn Oscillator from J. Carlstrom. This is followed by two 100 GHz power amplifiers in series, then a 200 GHz doubler, a 400 GHz doubler and an 800 GHz doubler. The multipliers are self biased and tunerless. Measured power output at the operational frequency of 807.3 GHz is in excess of 250 μ W. After the LO upgrade, it was possible to saturate all the mixers using only a 0.5 mil Mylar beamsplitter. In addition, the

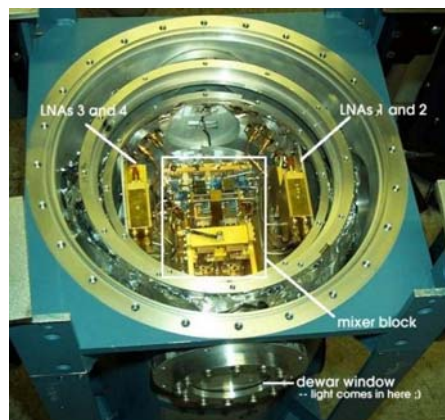


Figure 2: The inside of the PoleStar cryostat.

The 4 L-band Low-Noise IF amplifiers are mounted on the 15K radiation shield, and the mixers, lenses and bias tees are mounted on the 4K working surface.

self-biased tunerless operation makes the system much easier to use for the winter-over operators. Figure 3 shows the JPL/UMass LO chain installed on PoleStar.

Cryostat

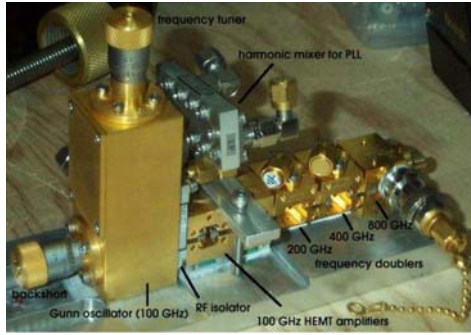


Figure 3: The JPL/UMass LO chain added to PoleStar.

This was added during the Austral summer of 2001. This chain puts out 0.25 mW at 807.3 GHz, enough to saturate all the mixers with a 0.5 mil thick Mylar LO diplexer. This LO chain is based on Herschel HIFI technology, using planar tunerless multipliers and 100 GHz power amplifier modules.

reduce thermal load. While polyethylene is not as good an anti-reflection coating as Te on for crystalline quartz, it is easy to apply, robust and inexpensive. This window is based on the design successfully used on the SPARO polarimeter used on the VIPER telescope also at the South Pole (Dotson et al. 1998). This window has virtually no loss at 810 GHz, and dramatically improved the dewar hold time and vacuum compared to earlier windows. With all 4 mixers and amplifiers mounted in the cryostat, the measured hold time is ~3 days.

Mixers

The SIS mixers used in PoleStar were made by KOSMA. Each mixer uses a Potter horn with a circular to half height rectangular waveguide transition to couple radiation to a Nb SIS junction. The junctions achieve low noise (~450 - 650K) performance through the use of an on-substrate Al tuning structure and a fixed waveguide backshort. The mixers have embedded magnets to suppress the Josephson effect. A four-wire bias system is used to ensure stable operation of the mixers. The inductive stub tunes out the capacitance of the SIS junction over the entire operating band, eliminating the need for mechanical backshort and E-plane tuners. Each mixer is extremely compact, with a small, square cross-section allowing easy stacking in recilinear arrays. A novel magnet probe design with a rear-

The Pole STAR cryostat (Figure 2) was constructed by Precision Cryogenics and is based on the successful Caltech Submillimeter Observatory (CSO) hybrid design. It uses a CTI model 350 coldhead to cool the outer and inner radiation shields to ~77 and ~12 K, respectively and a 4 liter liquid helium can to maintain the mixers at their operating temperature. This same basic design is used for all AST/RO and CSO receivers. In the single pixel AST/RO receivers, 30.5 mm diameter, Te on coated, crystalline quartz windows are used at 300 and 77 K. Zitex is used as the IR filter on the 12 K radiation shield. With a good vacuum, hold times of ~6 days can be achieved. At 77 K, we use an additional layer of Zitex. For the 300K vacuum window, we use a 0.3 in. thick z-cut crystalline quartz vacuum window with polyethylene anti-reflection coating, and diamond dust coating on the inner surface to

mounted electromagnet spool allows the mixers to be packed directly against each other. These mixers are prototype designs for the KOSMA effort to build mixers for Herschel HIFI instrument's band 4. Developments pushed by this effort promise to reduce mixer noise temperatures to below 300K at 800 GHz in the next few years.

Pole Star Array AOS

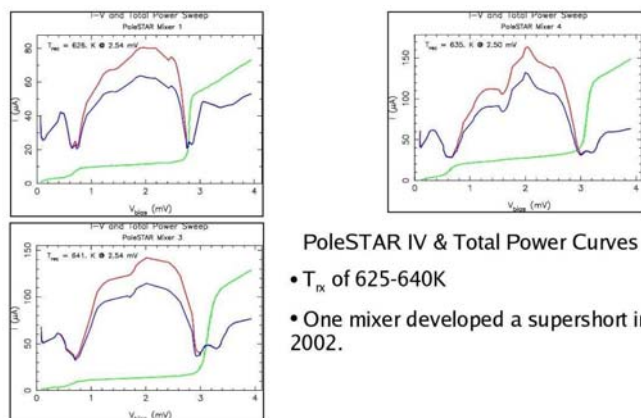
The Array AOS (aAOS) built by KOSMA provides four independent spectrometer channels, each with ~ 1 MHz of spectral resolution over a 1 GHz bandwidth. At 810 GHz, these numbers translate to 0.37 and 370 km/s respectively. It uses a single laser, a 4-channel, lithium niobate Bragg cell, and a custom CCD to achieve its performance parameters. The aAOS has been successfully tested on the IRAM 30m and CSO. This spectrometer also benefits from KOSMA's contribution to the Herschel HIFI instrument, through their contract to provide a multi-channel spectrometer system for the instrument (Schieder et al. 2003).

Pole Star Bias Control Hardware

The SIS junctions, the electromagnets used to suppress quantum-generated mixer noise, and the Low Noise Amplifiers (LNAs) all require noise-free, accurate electrical biasing for reliable operation. On single-pixel receivers, providing the appropriate biasing voltages and currents is handled adequately by individual boxes with manual potentiometers and LCD panels on the front. With the advent of array receivers, however, the sheer number of boxes required makes this kind of control impractical. The PoleStar bias system uses proven circuit design used on single pixel receivers at AST/RO and the Heinrich Hertz Telescope. We replace the manual potentiometers in these designs with a Xicor digital potentiometer, and package 4 channels of bias on a single Euro 96 card. These modular 4 channel cards can be plugged into a backplane in a 19" equipment rack, allowing easy extensibility. All digital communications with the bias system are done through a bi-directional optically isolated connection with the control computer. The I²C bus used for digital communications has a separate clock line. The digital lines, including the clock, are only active when changing a bias setting. The voltages and currents for the SIS junctions, magnets and amplifiers, the total power from the 4 channel total power box and the cryostat temperature information are read through a A/D card in the control computer. Signals from the bias system are multiplexed with Burr-Brown analog multiplexers, and read through a single BNC output. The I²C signals needed by the electronics is generated at the parallel port of an otherwise normal rack mounted PC running the Linux operating system. An Intelligent Instrumentation PCI-20428W multi-purpose Data Acquisition (DAQ) card is used for non-I²C control of the instrument.

Noise and stability measurements

Figure 4 shows the LO pumped IV curves of each of the three mixers currently functioning as of summer 2003, together with IF power sweeps. The fourth mixer has developed a super short and will be replaced during the Austral summer of 2003-2004. The red curve shows the IF power output when a HOT (290K) load is placed in front of the receiver. The blue curve shows the response with a COLD (77K) load. After two seasons of upgrades, PoleStar



PoleSTAR IV & Total Power Curves
 • T_{ix} of 625-640K
 • One mixer developed a supershort in 2002.

Figure 4: Post-upgrade IV and total power curves from the three functioning mixers.

is now working with noise temperatures close to those measured in the lab at Cologne with an optimized test receiver. After the installation of the new LO system with Mylar diplexer, the crystalline quartz window and properly leveling input power to both the total power box, up/down converter and aAOS, mixer noise temperatures are between 625K and 640K. Even with three pixels, the receiver is almost 15 times faster for mapping than WANDA, the single pixel 810 GHz facility receiver. Receiver stability measurements on Pole STAR were made by monitoring the IF output power of two of the receivers over ~1000 sec. The IF power variation was about 1 part in 1000 over this period.

First Light on AST/RO

Pole STAR was installed on AST/RO during a three week period from mid November to early December 2000. Figure 5 shows spectra taken with PoleSTAR in its latest configuration, with all upgrades. Spectra from the three functioning mixers are shown, also towards NGC 6334. The instrument has been at the South Pole continuously since the Austral summer of 2000.

Lessons Learned

In the process of building, deploying and operating PoleSTAR, we have learned several lessons that we can apply to all our future designs of heterodyne array receivers. Several components in the initial PoleSTAR design did not work as expected, and advances in technology have allowed us to improve receiver performance and reliability. Initially, one of the most pressing problems in developing an array for high frequency operation was the difficulty of obtaining LO power. At the time PoleSTAR was deployed, our LO source produced only 40 μ W of power. This forced us to use a MPI LO diplexer since we could

not afford to waste any LO power. While theoretically capable of delivering 100% of both the LO and sky power, small optical misalignments destroy their performance. While other solutions exist, especially for a fixed tuned receiver (Silicon etalons, meandering waveguide feeds), advancements in LO technology made this problem moot. We benefited from the enormous development effort created by work for the Herschel/HIFI instrument, which has increased available LO power by almost an order of magnitude since PoleSTAR was deployed. The new, more powerful LO is easier to align and use, is more robust, and the optics simplifications allowed for an improvement of more than 500K in receiver noise temperature.

PoleSTAR also went through three iterations of vacuum windows before we found one with suitable performance. Anti-reflection coated crystalline (z-cut) quartz has the lowest loss of any material suitable for large diameter vacuum windows. Optimally, Teon is used for the AR coating because its dielectric constant is the closest to the square root of the quartz. At the time of deployment, no company we could find would coat a vacuum window with

Teon. We decided to make a window out of high density polyethylene (HDPE), 0.5 in thick with pockets milled out for each beam. A solid window would have unacceptable loss at 810 GHz. By milling pockets leaving a membrane of 2λ thickness behind, the window spanned the 4 in. window aperture, with acceptable loss. While this window did work, it added ~200K to the receiver noise temperature and was subject to cracking. We next tried a window made from Zotefoam PPA-30 nitrogen blown Teon foam. This low dielectric constant material holds a vacuum, and has very low loss at 350 GHz. No measurements existed at 810 GHz, but the resulting window was very inexpensive and more robust than the HDPE window. We found the loss to be less, but this window still added ~150K to the receiver noise temperature. The loss of a slab of Zotefoam rises rapidly above 400 GHz, possibly due to scattering off the foam cells. We finally chose a z-cut crystalline quartz window with polyethylene AR coating as discussed in section . This vacuum window cost over \$3000 US, but is the only solution that offers good performance at 800 GHz over a 4 in. cryostat window aperture.

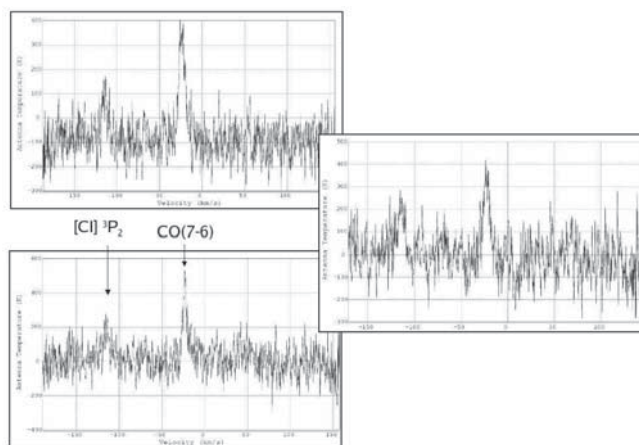


Figure 5: PoleStar spectra after upgrades.

Both [CI] and CO(7-6) are visible in all three spectra, taken during the Austral summer of 2002 toward NGC6334. Since no measurement of beam precession had been done, pointing is not known well for this observation.

Desert Star: a 7 pixel 345 GHz Heterodyne Array Receiver for the Heinrich Hertz Telescope

DesertSTAR is a 7 beam, 345 GHz heterodyne array receiver for the Heinrich Hertz Telescope (HHT) on Mt. Graham, AZ. The instrument uses x ed-backshort Superconductor-Insulator-Superconductor (SIS) mixers with a broadband waveguide probe. Instantaneous bandwidths of 2 GHz can be achieved over the entire 345 GHz atmospheric window. A cryostat with a Joule-Thompson (JT) mechanical refrigerator allows continuous operation and 1.8W of cooling capacity at 4K, and provides the needed temperature stability for low-noise operation. Local Oscillator (LO) distribution is accomplished with a novel phase grating that yields high efficiency and power uniformity in a hexagonally symmetric geometry. The computer controlled bias system is an evolution of a proven design that is simple, portable to any computer platform, and readily extensible to over 100 channels. It provides control and monitoring of bias, temperature and vacuum from any X-windows capable machine, and writes an instrument status web page visible with any web browser. The 2 GHz Intermediate Frequency (IF) bandwidth allows the future addition of a wide-band backend optimized for extragalactic observations, with ~ 1700 km/s of velocity coverage. The system will increase mapping speed at the HHT by a factor of ~ 16 compared to the current 345 GHz receiver system.



Figure 6: A picture of DesertStar mounted on the right angle of the HHT .

This photograph was taken during an engineering run in June, 2003.

DesertSTAR was designed for use as a facility instrument for the Heinrich Hertz Telescope, located at 10,500 ft. on Mt. Graham in southeastern Arizona. The telescope is a 10m Cassegrain design with Carbon Fiber Reinforced Plastic (CFRP) primary reflector panels and backup structure. The quadrupod and the subreflector are also CFRP. The CFRP construction provides very good stiffness, plus the temperature stability necessary to operate 24 hours per day (Baars et al. 1999). The surface of the main reflector has an RMS roughness of ~ 13 μm , measured with holography. DesertSTAR will be mounted on the right Nasmyth platform, bolted directly to the

telescope angle. Figure 6 is a photograph of DesertSTAR on the right Nasmyth angle of the HHT during an engineering run in June, 2003. The angle opening itself limits the

maximum number of pixels. With the $2F\lambda$ spacing of the pixels in DesertSTAR, the outer beams clear the angle at the 4ω level. The beams on the sky are $22''$ FWHM, with $44''$ center-to-center spacing, arranged in a close packed hexagonal arrangement. This configuration maximizes the number of beams through telescope angle on the HHT, while still preserving ~ 20 dB isolation between pixels.

Optics

Given that an array receiver is already a very complicated system, we chose to make the optics of DesertSTAR as simple as possible. Experience with the PoleSTAR 810 GHz array has shown that in practice, complex optical circuits are difficult to implement in practice with array receivers. With an array architecture

based on individual mixers mounted in the focal plane, it is difficult to control the beam boresight to the required tolerances. Other arrays, like CHAMP (Gusten 2000) and SMART (Graf 2000) have gone through great pains to ensure alignment of optical components and mixers. We have chosen to eliminate all optics from the system that require extremely tight tolerances on mixer beam boresight, and minimize the number of lenses and mirrors. The beam from each diagonal horn is matched to the telescope with separate High Density Polyethylene (HDPE) lens mounted directly to the mixer housing, decreasing the chances of mixer squint due to horn-lens misalignment. The beams then reflect off a single, cold 45° mirror and directly illuminate the tertiary of the telescope.

Most designs use a curved mirror to cross the beam bundle at the location of the vacuum window to minimize window size and then use another curved mirror to parallelize

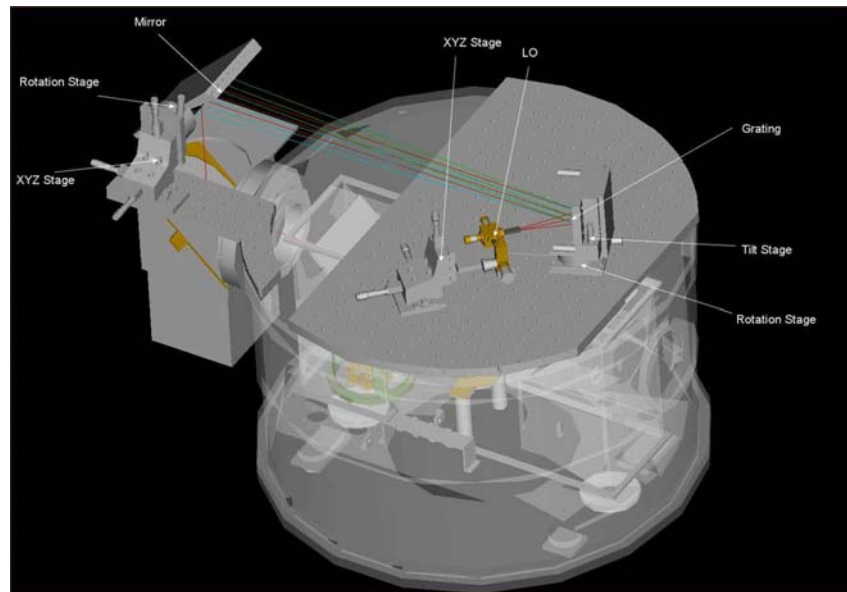


Figure 7: A cutaway CAD drawing of DesertStar.

This shows the LO distribution optics, mixer array and internal mirror. Since the beam bundle is not crossed anywhere in the system, optics complexity is minimized. Figure courtesy Dathon Golish.

expanding beams. We chose to keep the beams parallel throughout at the cost of increased vacuum window size. A new material, ZoteFoam PPA-30, made it possible to construct a 4.5 in. clear aperture vacuum window with extremely low loss and good vacuum properties. ZoteFoam PPA-30 is a closed-cell polyethylene foam blown with dry nitrogen gas. A 1" thick window 8" in diameter (1.75" glue surface, 4.5" clear aperture) is sufficient to hold vacuum with no other materials present, with acceptable deformation under vacuum, and no noticeable helium permeability or outgassing problems. While loss is significant at high frequencies, the performance from 300-400 GHz is quite good. The transmission of the DesertStar window is 96%-98% from 300-400 GHz, adding noise of ~10K. This is about twice the added noise of a 0.5 mil Mylar window or a Polyethylene coated crystal-line quartz window, but can span large openings and is economical. It has been in use as a window material in an instrument at the South Pole (AKBAR) for over two years with no reliability problems (Kuo et al. 2002).

Local Oscillator

Local oscillator power delivery is another difficult problem for array receivers. LO power must be efficiently and equally divided into each pixel. While many waveguide techniques are available, they are complicated, difficult to implement and lossy at high frequencies. Quasi-optical techniques can also be lossy and complicated, with difficult alignment issues. Recent work by the Cologne and MPIfR groups in Germany have led to the development of both transmissive and reflective phase gratings that form multiple LO beams from a single input beam through diffraction.

Our LO distribution system uses a novel reflective grating design from the University of Cologne (Heyminck et al. 1998). This design creates a 7 beam array with hexagonal symmetry with 80% efficiency and is superimposed on a parabolic mirror. This optic then acts as a collimating mirror for the LO beam, and also forms the 7 beam array. The phase grating has an operational bandwidth of ~10% centered on 345 GHz. A simple Mylar beam-splitter acts as the LO diplexer. Figure 7 is a cutaway CAD drawing of the LO optics and receiver optics.



Figure 8: A photograph of three mixers installed in the JT cryostat before testing.

Cryogenics

DesertSTAR was designed to allow for cooled optics and have room for a second sub-array. To achieve these goals, we designed a cryostat, with a 28" cold plate, a large 4K volume for cold optics, and a large 4K cooling capacity. The cryocooler is based on the proven NRAO JT refrigerator, used for the facility receivers at the NRAO 12m telescope. The unit has a 180W capacity at 77K, a 1.8W capacity at 4K, a 20K helium precooler stage and a self-cleaning JT expansion valve. The refrigerator is mated to a commercial Balzers cold head, and driven by a custom NRAO compressor. Cooldown tests show stable 4K operation is achieved in ~13 hours. In addition, we have used a resistive heater on the 4K cold plate to measure a cooling capacity of 1.44W. This measurement was made with full infrared (IR) loading on the cold plate. Calculations show that the total heat load including amps and infrared loading is 0.9W. The IR heat load is dumped to the 77K shield with a Gore-Tex GR IR filter. Since cryogenic testing began in 2000, we have experienced no failures of the cryogenic system.

Mixers and Cold Electronics

DesertSTAR uses 7 independent single ended mixers, each mounted together with a HDPE lens, isolator and amplifier in a modular rocket, which is cooled by the JT refrigerator via a cold finger. The simple, single ended waveguide design uses a diagonal feedhorn to couple the telescope beam through a multi section impedance transformer to half height waveguide. The waveguide backshort is fixed and there is no E-plane tuner. The cross-guide probe uses the proven suspended stripline design of Blundell & Tong (Blundell et al. 1995). The Nb SIS junctions were designed with an on-chip tuning structure for low return loss across the atmospheric window, permitting a fixed backshort. The optimum backshort position was determined via HFSS modeling. The diagonal horn was chosen because it could be readily made with the UMass micro milling machine. While their coupling to the fundamental gaussian mode is less than a scalar corrugated horn, diagonal feedhorns still provide adequate broadband performance at a fraction of the cost (Johansson et al. 1992). The beam pattern is gaussian, but the diagonal horn has about 14% crosspolarization, lowering its efficiency when used in combination with a linearly polarized input signal. A 4-wire bias tee is mounted in the mixer block, and monitors junction voltage and current

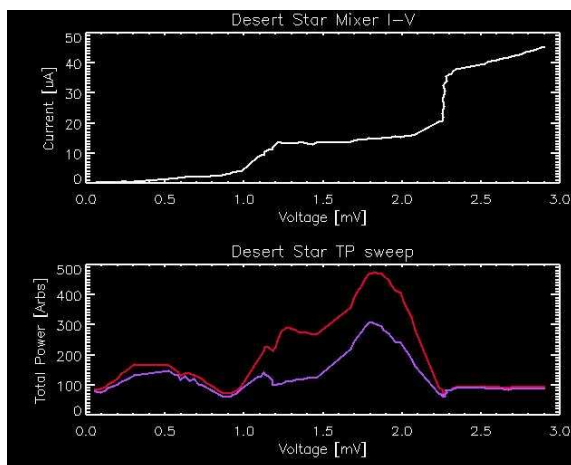


Figure 9: Representative IV and hot/cold total power curves.

with a precision current-sense resistor. Return loss is better than -20 dB from 4-6 GHz and leakage is less than -40 dB. Insertion loss is ~0.1 dB. The mixer produces a 4-6 GHz IF, and is connected via a Pamtech cryogenic ferrite isolator to a Miteq 4-6 GHz cryogenic low noise amplifier (LNA). Losses of the bias tee and isolator are less than 1.5dB from 4-6 GHz, as measured via vector network analyzer. The Miteq amplifiers have 27 dB gain, less than 1 dB passband ripple, 30 mW power dissipation and a measured noise temperature of 7K at 4K operating temperature. The amplifiers require only a single, unipolar 0.6V bias, greatly simplifying the wiring and bias supplies. A simple superconducting coil electromagnet provides the necessary magnetic flux to minimize Josephson noise with soft iron field concentrators embedded in the mixer block. Figure 8 shows the mixer array inside the cryostat with 3 mixers installed.

Backends

The HHT is currently upgrading the telescope control system and back-end electronics for all receivers. As a part of this effort, a modern, flexible fiberbank spectrometer with a 2x1 GHz bandwidth and 1 MHz resolution is being constructed. The IF processor for this backend can process 8x256 MHz IF sub-bands for use with DesertSTAR. This bandwidth and velocity resolution is adequate for a large variety galactic astronomy projects. The fiberbank should provide extremely high stability without the platforming problems often associated with hybrid correlators. During the fall, 2003 season, we will operate the receiver in three pixel mode using the existing facility acousto-optical spectrometers and chirp transform spectrometers.

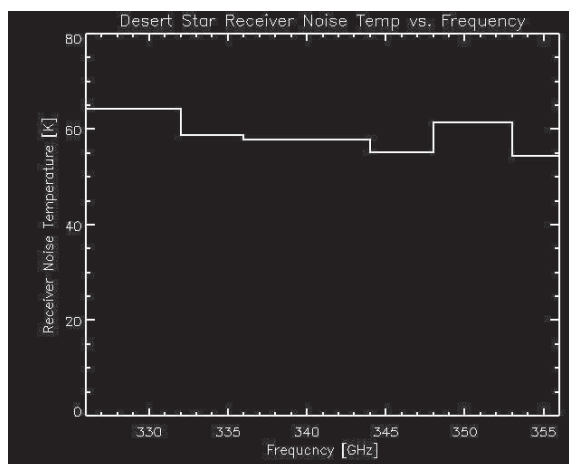


Figure 10: Receiver noise temperature (Mixer 1) as a function of LO frequency.

Noise temperature is relatively flat from 326-356 GHz, as expected from simulation.

Preliminary Results

Initial tests of a single array mixer/IF chain have been conducted in an IR Laboratories LN₂/⁴He cryostat. The test system uses a 0.5 mil Mylar LO diplexer, a 1.0 mil Mylar cryostat vacuum window, and a single layer of Zitex A for IR filtering. The first prototype mixer has a very long backshort channel, that is then shortened to the proper length with aluminum shim stock. This allows some adjustability of the backshort position. All other mixers were fabricated with a machined, non-adjustable backshort. A room temperature total power box and a Hewlett-Packard power detector were used for the Y-factor mea-

surements. The bias control system interrogates the output of this meter to allow total power vs. bias voltage sweeps. Before mounting a device in the mixer block, we tested ~ 20 devices using a dipstick inserted into a liquid helium storage dewar. Of the ~ 20 devices tested, only 3 were nonfunctional, and the remaining devices appeared to be virtually identical. The device mounted in the test block was randomly selected from the good devices.

Test Receiver Performance

Figure 9 shows a pumped I-V curve of the test mixer, along with hot and cold total power curves. The bias system uses the slope of the supercurrent at 0V to measure the contact resistance, and then remove it from the I-V curve. We measured $R_n \sim 48.5 \Omega$, a leakage current of $\sim 3 \mu\text{A}$ and a transition voltage of $\sim 2.3 \text{ mV}$. Optimum bias voltage for the highest Y-factor was $\sim 1.6 \text{ mV}$. Uncorrected receiver noise temperatures as a function of LO frequency are plotted in Figure 10. We expect T_{rx} to remain fairly constant from $\sim 300 \text{ GHz}$ to $\sim 390 \text{ GHz}$. Preliminary measurements indicate receiver temperatures between $\sim 55\text{K}$ and $\sim 65\text{K}$ across the available band, with fairly constant response, as shown in Figure 20. These are uncorrected noise temperatures, and include the losses of the LO diplexer, window and unmatched lens, along with noise from the IF chain. The LO source used in the test was unable to tune below 326 GHz or above 356 GHz , so we could not measure the receiver temperature over the full band of the waveguide probe.

Instrument Performance Characterization

After characterizing the performance of a single mixer in the test system, we installed the prototype mixer, and two additional mixers with extended, machined backshorts into the JT cryostat. We repeated the same tests done in the test setup, and found that the mixers behaved identically, but with receiver noise temperatures of $60\text{-}70\text{K}$. It is not uncommon for the noise of a mixer in an array dewar to be slightly higher than in a highly optimized single pixel test system. We believed that losses in the cryostat window material and IF losses in the long runs of semi-rigid coaxial cable were responsible for the increase in noise temperature. We measured the loss of the window material by inserting a slab of

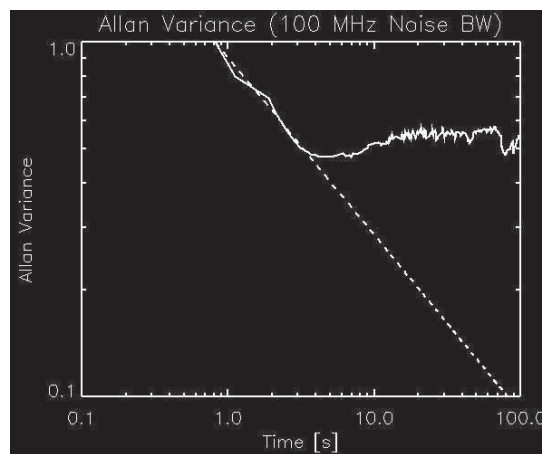


Figure 11: An Allan variance plot from 160 minutes of total power data taken every 50 ms.

This result has been scaled to 100 MHz post-detection bandwidth from the measured data taken with a 2 GHz post-detection bandwidth. The dotted line represents a $t^{1/2}$ decrease in noise with time as theoretically expected.

ZoteFoam in the beam and observing the change in Y-factor. We found the ZoteFoam contributed ~5K to the receiver noise temperature.

Stability Analysis

We performed an Allan variance stability analysis of the receiver to determine if microphonics from the large Balzers cryo-head would negatively effect receiver stability. We used a Hewlett-Packard power meter, sampled every 50 ms with a data acquisition card in the computer control system. Data was taken for ~1.5 hours, and folded every 5 minutes to lower the noise due to the short integration time. We measured the total power over the entire 4-6 GHz IF for this test, and then scale the result to a 100 MHz post-detection bandwidth, since we did not have a narrow-band 5 GHz center frequency filter on hand. The data were analyzed following Kooi et al. (2000), with the help of an algorithm from Narayanan (2003). We assume a power law noise spectrum proportional to t^2 . Then the Allan time scales like $BW^{1/2}$. The results in Figure 11 show an Allen variance time of ~3s for a 100 MHz bandwidth. This translates to an Allan variance time of ~30s with a 1 MHz post detection bandwidth. This stability time is adequate for all observing modes at the HHT.

Beam Pattern Measurement

Using a computer controlled XY stage system, we measured E and H plane cuts of the receiver beam pattern. The source was a liquid nitrogen cold load behind a sheet of room temperature absorber. A small hole in the absorber created a strong, negative source which could be detected using a lock-in amplifier and room temperature chopper wheel. The 3cm source size allowed adequate sampling of the receiver beam, and provided sufficient signal. Several scans were co-added and then fit with a 5 component gaussian. Results showed the beam to be gaussian in shape, but the beam was more broad and elliptical than expected. We found that the original paper on diagonal horns has an error in the formula for the expected beam waist of the horn. The lenses were designed from the results of this paper, but our later HFSS simulations show the actual horn beam to be wider (Johansson et al. 1992). The over illumination of the lens results in a emergent beam 15% too broad. We are currently redesigning the lens mounts to compensate for this effect.

Telescope Performance and Initial Results

In early June, 2003 DesertStar was taken to the HHT for a 6 day engineering run. The goal was to identify areas of difficulty in using the receiver on the telescope, and to perform as many performance tests and verifications of the central mixer as possible. Overall, the results were good with some minor disappointments. Initial installation and cooldown were trouble free, but the receiver's mount proved to be inadequate. The weight of the receiver caused the mount to deform under load, and it was obvious that the mount was not rigid enough to prevent the receiver oscillating due to the cold-head cycle. The mount was

reinforced as a stop-gap measure, and we continued to align the receiver to the telescope. Within two days, we had the central beam of the array on the sky, and had easily achieved receiver noise temperatures of $\sim 90\text{K}$. Measurements with a laser level proved the cryostat was indeed oscillating with a peak to peak amplitude of more than 40." This oscillation prevented us from making the pointing or focus measurements. We used spectra and maps from extended regions to coarsely point the telescope. On centrally concentrated sources, peak line temperature was diluted since the receiver beam was not on-source for all the integration time. Spectra were obtained from a variety of sources including IRAS16293, IRC+10216, DR21, CepA and S140. These data were used to verify the proper operation of the receiver system. A representative spectrum is shown in Figure 12.

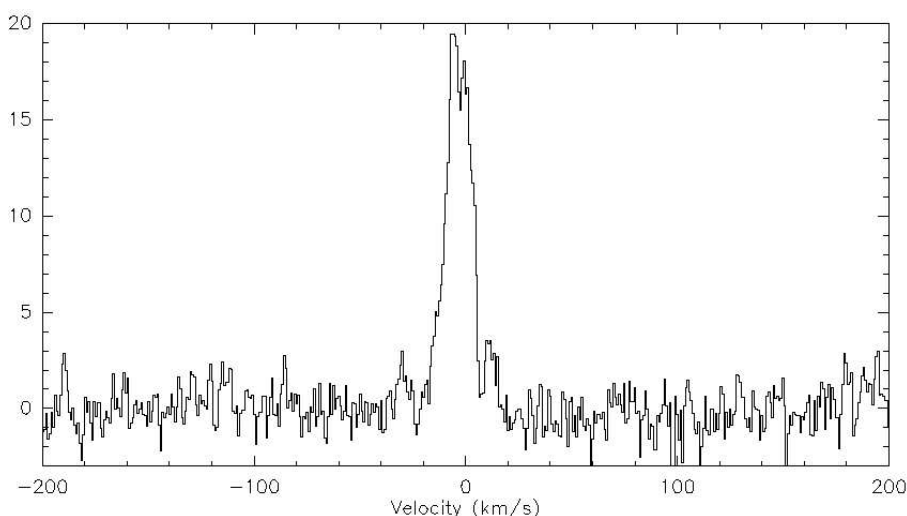


Figure 12: ^{12}CO (3-2) Spectrum from the central position of a map of the high mass star forming region DR21.

This observation was made in position switched mode with an off position of $30'$ in azimuth. A linear baseline has been fit and subtracted.

Summary

We have constructed a 2×2 , 810 GHz array receiver for the AST/RO telescope. The array utilizes a common set of re-imaging optics, an efficient 4-way quasi-optical LO power splitter, a solid-state LO, low noise mixers, a flexible computer controlled bias system, and an array AOS. A state-of-the-art planar, tunerless LO chain with W-band power amplifiers can easily pump all the mixers with only a 0.5 mil Mylar LO diplexer. Upgrades and repairs have reduced the receiver noise temperatures to between 625K and 640K per mixer, making the system ~ 15 times faster for mapping than the previous 810 GHz system on the AST/RO telescope. We have completed the first phase of constructing and testing a 345 GHz heterodyne array receiver for use on the Heinrich Hertz Telescope on Mt. Graham in Arizona. The instrument uses fixed backshort, suspended stripline SIS mixers with 2 GHz IF bandwidth. Cooling is provided by a high capacity closed cycle refrigerator in a

large, expandable cryostat. We have demonstrated proper operation of the cryogenic system and computer controlled bias system. Preliminary measurements indicate the prototype array mixer can provide uncorrected receiver noise temperatures of ~60K-70K from 326-356 GHz. Performance has been verified in the JT cryostat with 3 mixers, and the instrument has had an engineering run on the HHT, where it successfully collected data. The instrument will go into regular operation on the HHT in October 2003 with 3 pixels. The remaining 4 mixers will be added to the system in the summer of 2004, bringing the array up to its full complement of 7 pixels. DesertStar is the first operational 345 GHz array receiver.

REFERENCES

- Baars, J. W. M., Martin, R.N., Mangum, J.G., McMullin, J.P., Peters, W.L., PASP, 111, 759, 1999.
- Blundell, R., Tong, C-Y.E., Papa, D.C., Leombruno, R.L., Zhang, X., Paine, S., Stern, J.A., LeDuc, H.G. & Bumble, B. IEEE MTT Symp. on Space Terahertz Technology, Vol. 43, 1995.
- Dent, W.R.F. Imaging at Radio Through Submillimeter Wavelengths, ASP Conference Proceedings Series, Vol. CS-217, 2000.
- Dotson, J.L., Novak, G., Renbarger, T., Pernic, D., & Sundwall, J.L. Proc. SPIE Vol. 3357, 1998.
- Graf, U. U., Haas, S., Honingh, C. E., Jacobs, K., Schieder, R., Stutzki, J., Proc. SPIE Vol. 3357, 1998.
- Groppi, C.E. et al. Imaging at Radio Through Submillimeter Wavelengths, ASP Conference Proceedings Series, Vol. CS-217, 2000.
- Gusten, R. Imaging at Radio Through Submillimeter Wavelengths, ASP Conference Proceedings Series, Vol. CS-217, 2000.
- Heyminck, S. & Graf, U.U. Proc. SPIE Vol. 4014, 1998.
- Jewell, P.R. & Mangum, J.G. ALMA Memo 170, 1997.
- Johansson, J.F., & Whyborn, N.D. IEEE MTT, Vol. 40, No. 5, 1992.
- Kooi, J.W. CSO Memo, 1998.
- Kooi, J.W., Chattopadhyay, G., Thielman, M., Phillips, T.G., & Schieder, R. Int J. IR and MM Waves, Vol. 21, No. 5, May, 2000.
- Kuo, C.L. et al. American Astronomical Society Meeting 200, #06.03, 2002.
- Lamb, J.W. ALMA Memo 301, 2001.
- Martin, D. H., El-Atawy, S., Duncan, W. D., Puplett, E. F., Fonti, S. Societa Astronomica Italiana, Memorie, vol. 49, 1978.
- Mehdi, I., Schlecht, E., Chattopadhyay, G., Siegel, P.H. Proc. SPIE Vol. 4855, 2003.
- Mueller, E., 2001, DeMaria ElectroOptics Systems, Inc., 1280 Blue Hills Ave., Bloomfield, CT 06002.
- Narayanan, G. Private Communication, 2003.
- Schieder, R.T. et al. Proc. SPIE Vol. 4855, 2003.
- Schuster, K., Blondel, J., Carter, M., Fouilleux, B., Lazareff, B., Mattiocco, M., Pollet, J. Imaging at Radio Through Submillimeter Wavelengths, ASP Conference Proceedings Series, Vol. CS-217, 2000.
- Stark, A. et al. PASP, Volume 113, Issue 783, 2001.
- Sunada, K., Yamaguchi, C., Kuno, N. & Ukita, N. Imaging at Radio Through Submillimeter Wavelengths, ASP Conference Proceedings Series, Vol. CS-217, 2000.
- Thompson, A.R., & Kerr, A.R. ALMA Memo 168, 1997.

TELIS – development of a new balloon borne THz/submm heterodyne limb sounder

P.L. Yagoubov, R.W.M. Hoogeveen, A.M. Maurellis
National Institute for Space Research (SRON), The Netherlands

U. Mair, M. Krocka, G. Wagner, M. Birk
Remote Sensing Technology Institute, DLR, Germany

H.-W. Hübers, H. Richter, A. Semenov
Institute for Space Sensor Technology and Planetary Exploration, DLR, Germany

G. Gol'tsman, B. Voronov
Moscow State Pedagogical University, Russia

V. Koshelets, S. Shitov
Institute of Radio Engineering and Electronics (IREE), Russia

B. Ellison, B. Kerridge, D. Matheson, B. Alderman, M. Harman, R. Siddans, J. Reburn
Rutherford Appleton Laboratory (RAL), United Kingdom

Abstract

We present a design concept for a new state-of-the-art balloon borne atmospheric monitor that will allow enhanced limb sounding of the Earth's atmosphere within the submillimeter and far-infrared wavelength spectral range: TELIS, TeraHertz and submm Limb Sounder. The instrument is being developed by a consortium of major European institutes that includes the Space Research Organisation of the Netherlands (SRON), the Rutherford Appleton Laboratory (RAL) in the United Kingdom and the Deutschen Zentrum für Luft- und Raumfahrt (DLR) in Germany (lead institute). TELIS will utilise state-of-the-art superconducting heterodyne technology and is designed to be a compact, lightweight instrument capable of providing broad spectral coverage, high spectral resolution and long flight duration (~24 hours duration during a single flight campaign). The combination of high sensitivity and extensive flight duration will allow evaluation of the diurnal variation of key atmospheric constituents such as OH, HO₂, ClO, BrO together with longer lived constituents such as O₃, HCL and N₂O. Furthermore, TELIS will share a common balloon platform to that of the MIPAS-B Fourier Transform Spectrometer, developed by the Institute of Meteorology and Climate research of the University of Karlsruhe, Germany. MIPAS-B will provide simultaneous and complementary spectral measurements over an extended spectral range. The combination of the TELIS and MIPAS instruments will provide atmospheric scientists with a very powerful observational tool. TELIS will serve as a testbed for new cryogenic heterodyne detection techniques, and as such it will act as a prelude to future spaceborne instruments planned by the European Space Agency (ESA).

Introduction

A recent ESA study of observational requirements for future atmospheric chemistry missions concluded that improved observations from space of ClO, BrO and other trace gases would be required to understand how stratospheric ozone will respond to changing chlorine and bromine loadings and changing climate beyond 2008 [1]. A sub-millimeter wave limb-sounder with superconducting (SIS) receivers cooled to 4K could meet these requirements. It also concluded that the sensitivity of a hot electron bolometer (HEB) receiver cooled to 4K would be required to observe OH in the lower stratosphere (i.e. <20km) and stratospheric HBr for the first time. These observations by 4K sub-mm and terahertz limb-sounders would be unique within the proposed timeframe as well as improving substantially on preceding satellite missions.

The history of heterodyne detection of species of the Earth atmosphere is rather brief. The Microwave Limb Sounder on board the US Upper Atmosphere Research Satellite (MLS/UARS) was the first mission [2] to measure stratospheric ozone, ClO, water vapor and pressure and temperature using heterodyne detection at 63, 183 and 205 GHz. It was active between 1991 and 1994, and employed room temperature Schottky diodes. Its highly improved successor on board the EOS-Aura satellite will be launched early 2004 [2]. Although the frequency range has been extended up to 2500 GHz, it still employs uncooled Schottky diodes, and a double gas laser to pump the 2.5 THz mixer. The Sub Millimeter Radiometer (SMR) on board the Swedish Odin satellite, launched in February 2002, measures up to 580 GHz with Schottky diodes operating at 100 K, thereby gaining significantly in noise performance. Instead of filterbanks, 2 digital auto correlators and one Acousto-Optic Spectrometer are used as back-end [3]. Only the planned Japanese Superconducting Submillimeter-wave Limb Emission Sounder on board the Japanese Experimental Module (JEM/SMILES) [4] of the International Space Station features two low-noise cryogenic superconducting mixers.

Extrapolating the current trends towards the future we foresee Earth limb sounding from satellite platform with superconducting receivers operating at sub millimeter and Terahertz frequencies. Instead of gas lasers only solid state local oscillators are to be employed to reduce system complexity. As back end the most likely candidates are complete spectrometers such as Acousto-Optic Spectrometers or Digital Auto Correlators.

Anticipating such future space borne atmospheric sounding missions and in support of the above scientific rationale, funding has been secured by three European national institutes (DLR, SRON and RAL) to develop a high sensitivity, balloon borne atmospheric sounder that will allow simultaneous measurement of key molecular constituents within the stratosphere. The instrument is called TELIS (TErahertz and submm LImb Sounder) and will provide measurement of atmospheric constituents including OH, HO₂, O₃, N₂O, CO, HCl, HOCl, ClO, and BrO that are associated with the depletion of atmospheric ozone and climate change. In addition, TELIS will serve as a testbed for a number of novel technologies in the field of low-noise cryogenic heterodyne detection.

The balloon platform on which TELIS will fly also contains a Fourier transform spectrometer (MIPAS-B developed by the Institute of Meteorology and Climate research of the University of Karlsruhe, Germany). MIPAS will simultaneously measure within the range 680 to 2400cm^{-1} . The combination of the TELIS and MIPAS instruments is unusual and although there is no interdependency between the two, simultaneous operation will provide a wealth of scientific data as both a stand alone chemistry mission and in complement to existing spaceborne instruments, e.g., ODIN and Envisat.

The ambitious spectral coverage of the TELIS instrument is accomplished by use of three independent frequency channels: 500 GHz, 650 GHz and 1.8 THz. All channels will use a state-of-the-art superconducting SIS and HEB mixer technology. The 500 GHz channel is being developed by the RAL and is based on a highly successful instrument previously used for airborne measurements of the lower stratosphere [5]. It is a highly compact unit consisting of a fixed-tuned waveguide SIS mixer, cryogenic solid-state local oscillator (LO) chain and a low-noise intermediate-frequency (IF) chain. Single sideband operation is a prerequisite for this channel and is achieved through use of a miniature cryogenic dichroic filter that provides a 4K image termination and image band rejection of $>25\text{dB}$. The 650 GHz channel is being developed in cooperation between IREE and SRON and is based on a single-chip Superconducting Integrated Receiver (SIR) that comprises on one substrate a low-noise SIS mixer with quasi-optical antenna and a superconducting Flux Flow Oscillator (FFO) acting as LO [6]. Tunability of the FFO shall allow for a wideband operation of this channel, with a goal to obtain 100 GHz instantaneous rf bandwidth or even more. The 1.8 THz channel is based on a phonon-cooled NbN HEB mixer technology, similar to that under development for SOFIA by MSPU and DLR [7]. It will utilise a cryogenic solid-state LO coupled to the mixer via an optical interferometer (Martin Puplett type). The channel is designed to allow future upgrade to 2.5 THz.

Instrument design concept

The general design concept of TELIS is shown schematically in Fig. 1. TELIS has a common optical front end for all three channels. A dual offset cassegrain design is used for pointing. In order to reduce size and weight an anamorphic design is applied. After the telescope a warm 300 K blackbody source can be switched in for radiometric calibration. As a calibration cold load a deep space view will be used by pointing the telescope up by about 50 degrees. Further quasi-optical elements allow beam shaping and channel separation: The 500 GHz channel is separated from the two other channels by a polarizer and the remaining submm and the FIR channel are separated by a dichroic filter. The three heterodyne receivers are located inside a custom-made 4K Helium cooled dewar with each channel having a separate optimised vacuum window. The down-converted signals are preamplified and further down-converted in three separate intermediate frequency chains. Digital autocorrelator spectrometers are utilised for spectral analysis. All three channels will be operated simultaneously. From the operational point this requires good coordination in the observation plans. From technical point of view it requires very careful electronic design avoiding both emissions and pick-up of spurious signals.

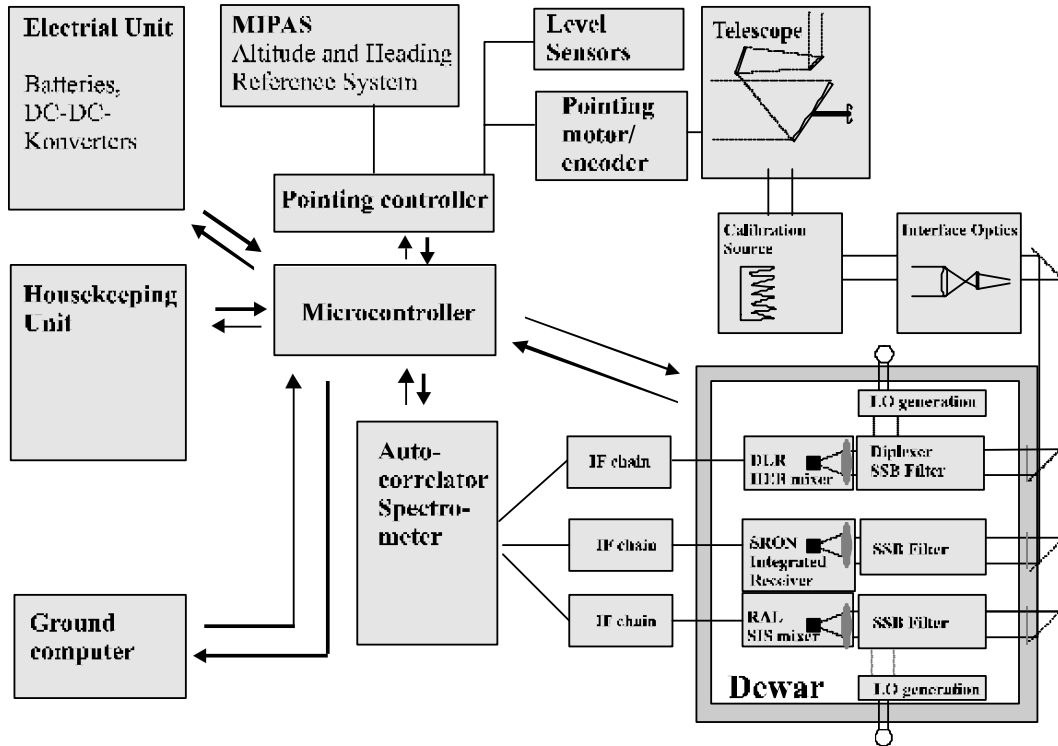


Figure 1. Schematic block diagram of the TELIS instrument.

A PC board together with specially designed microcontroller units are used for control and readout of all instrument components, for data storage and for telemetry. A real time pointing controller will allow accurately pointing to different tangent heights. The attitude information is taken from the MIPAS altitude and heading reference system. Level sensors will determine the relative angles between the TELIS and MIPAS frame.

The raw data is transmitted from the microcontroller to a ground computer system where several users can access the data and higher data products are formed.

The 500 GHz Receiver

The 500 GHz channel will target a range of atmospheric molecular species, but a primary goal is the evaluation of ClO, BrO and N₂O in the lower stratosphere. A calculated example of the spectral range to be observed is shown in Fig. 2 for a tangent of 20 km. In addition to encompassing the ClO, BrO and N₂O emissions, the spectral range also allows observation of O₃, which is essential to allow precise atmospheric retrievals of the more minor species.

The spectral range to be observed places technical demands on both the 500 GHz channel and the overall TELIS instrument concept. For example, an instantaneous bandwidth of 4 GHz is necessary to encompass the primary target range (shown by the dotted lines in Fig. 2). This necessitates multiplexing of the IF and spectrometer chain and also the use of a broad-band low-noise amplifier. Furthermore, it is essential that

spectral contamination from the image sideband of the mixer is reduced to an extremely low value and a goal of 25 dB image band rejection has been set. Achieving this goal requires the introduction of a quasi-optical filtering element into the signal path and the use of a high IF centre frequency.

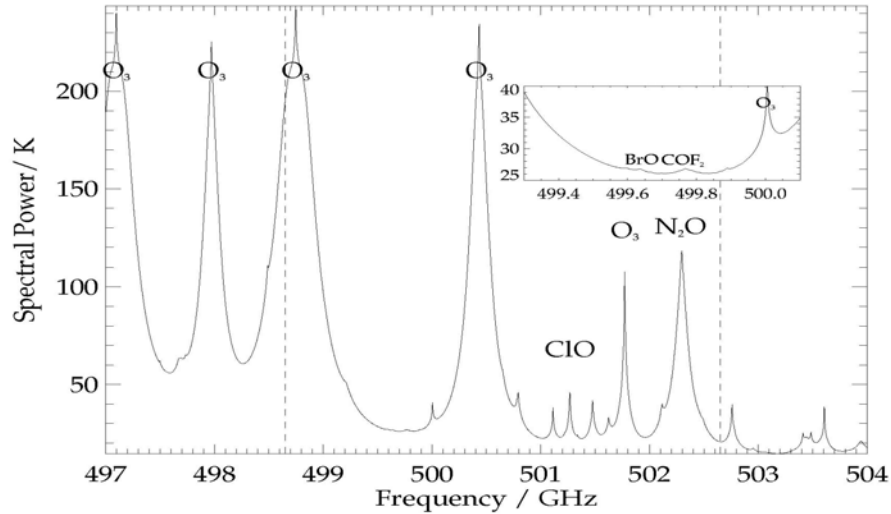


Figure 2. Calculated spectral emission features encompassed by the TELIS 500 GHz.

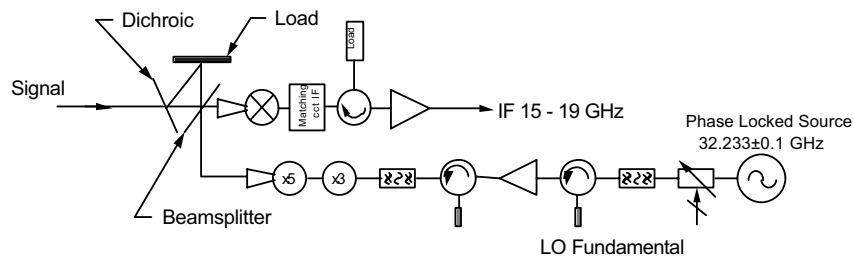


Figure 3. RAL 500 GHz compact SIS receiver channel.

The conceptual design of the 500 GHz channel shown in Fig. 3. Within this concept a dichroic plate filter (DCP) is used to separate the mixer signal and image sidebands prior to direction of the signal band into a reduced height, fixed tuned, single mode SIS waveguide mixer. The image band is directed towards and terminated by a cold (~ 4 K) load that ensures contaminating spectra are rejected and noise contribution from the image sideband is minimised. The use of the DCP filter necessitates the use of an IF centred at ~ 17 GHz which is both a demanding and unusual requirement for an SIS mixer.

The LO chain is formed from a $x3x5$ varactor multiplier combination that up-converts a fundamental frequency of ~ 32.3 GHz (derived from a phase-locked dielectric-tuned resonator) to a nominal LO centre frequency of ~ 484 GHz. With the exception of the fundamental frequency source, the LO chain is placed inside the receiver cryogenic

vessel and cooled to ~ 15 K. The available power from the LO is injected into the SIS mixer through a simple dielectric membrane beamsplitter with typically a 1% coupling factor. It is possible to tune the LO over a narrow range ± 1.7 GHz in order to increase the instrument spectral coverage to a nominal 7 GHz. The total spectral coverage of the 500 GHz channel, limited by the frequency response of the DCP, extends from 497 to 504 GHz with a goal for the system single-sideband noise temperature of 600 K.

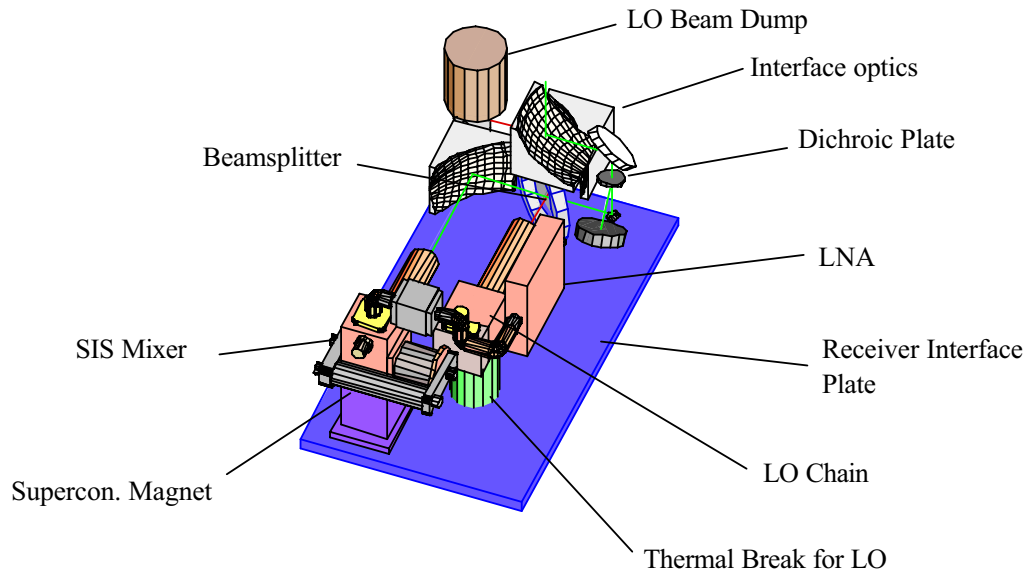


Figure 4. Three-dimensional concept of the RAL 500GHz compact TELIS channel.

Although similar in concept to a previously developed airborne instrument [5], the new TELIS 500 GHz radiometer reflects the requirements associated with a balloon borne environment and remote operation: that is, it must be simple, lightweight and reliable. In fulfilment of these aims we have developed a novel design concept that integrates the majority of receiver components, including the optical interface, SIS mixer, LNA, DCP, beamsplitter and LO, onto a single mounting plate that can be easily installed into the TELIS cryogenic system. The plate will be cooled to 4 K along with the majority of the components, but a suitable thermal insulator is incorporated between the LO and the plate to avoid excess vaporisation of the cryostat liquid helium reservoir. Fig. 4 shows the proposed concept and indicates the primary receiver components that are encompassed within a volume of $90 \times 95 \times 170$ mm³.

The 650 GHz Superconducting Integrated Receiver

A key element of this SRON-provided channel is Receiver (SIR), that comprises on one chip a low-noise SIS mixer with quasi-optical antenna and a superconducting Flux Flow Oscillator (FFO) acting as LO [6]. The FFO is a long Josephson tunnel junction in which an applied dc magnetic field and a bias current drive a unidirectional flow of

spectral contamination from the image sideband of the mixer is reduced to an extremely low value and a goal of 25 dB image band rejection has been set. Achieving this goal requires the introduction of a quasi-optical filtering element into the signal path and the use of a high IF centre frequency.

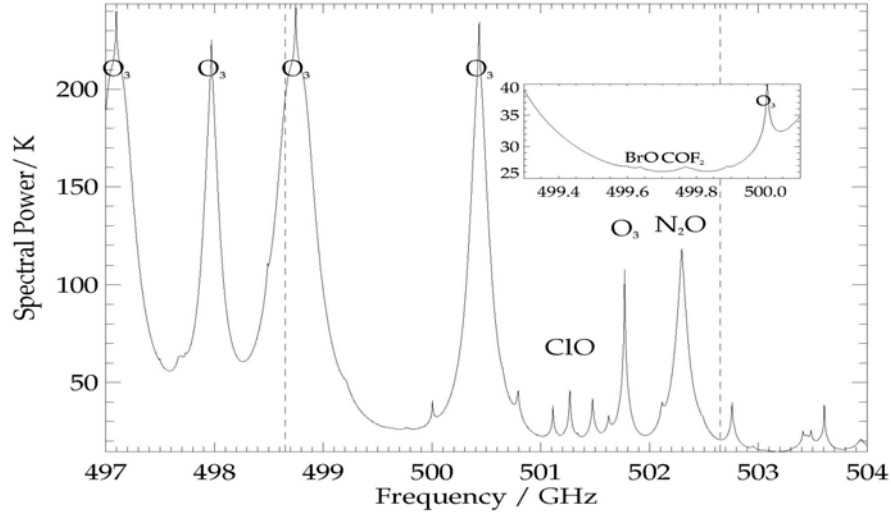


Figure 2. Calculated spectral emission features encompassed by the TELIS 500 GHz.

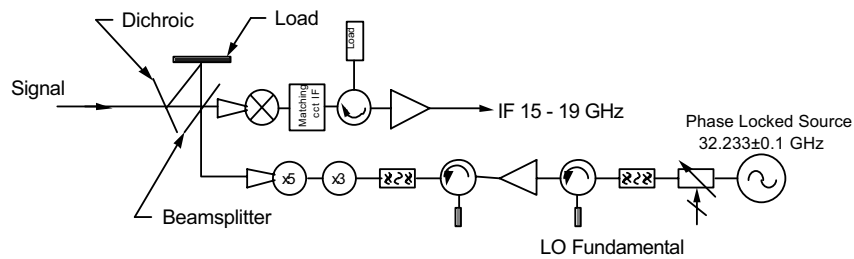


Figure 3. RAL 500 GHz compact SIS receiver channel.

The conceptual design of the 500 GHz channel shown in Fig. 3. Within this concept a dichroic plate filter (DCP) is used to separate the mixer signal and image sidebands prior to direction of the signal band into a reduced height, fixed tuned, single mode SIS waveguide mixer. The image band is directed towards and terminated by a cold (~ 4 K) load that ensures contaminating spectra are rejected and noise contribution from the image sideband is minimised. The use of the DCP filter necessitates the use of an IF centred at ~ 17 GHz which is both a demanding and unusual requirement for an SIS mixer.

The LO chain is formed from a $x3x5$ varactor multiplier combination that up-converts a fundamental frequency of ~ 32.3 GHz (derived from a phase-locked dielectric-tuned resonator) to a nominal LO centre frequency of ~ 484 GHz. With the exception of the fundamental frequency source, the LO chain is placed inside the receiver cryogenic

The concept of SIR looks very attractive for TELIS, foremost due to a wide tuning range of the FFO. Presently, the frequency range of most practical heterodyne receivers is limited by the tunability of the LO. For a solid state multiplier chain the fractional input bandwidth typically does not exceed 10-15 %. In the SIR the bandwidth is basically determined by SIS mixer tuning structure and matching circuitry between SIS and FFO and up to 30-40 % may be achieved with a twin-junction SIS mixer design. In a baseline TELIS concept, the SIR channel will operate from 600 to 650 GHz, eventually aiming at a larger coverage, 500 to 650 GHz, with a single device. The goal single side band receiver noise temperature is 400 K within this band.

A schematic layout of the SIR channel is shown in Fig. 5. The input sky signal is fed through the IR filter and passes through a Single Side-Band (SSB) filter based on Martin-Puplett polarization rotating interferometer. Further, the beam is focused onto the mixer by two mirrors, "M1" and "M2". The unwanted sideband of the mixer is reflected by two wire grids and terminated by a 4 K cold load. The intermediate frequency of the mixer is amplified by a wideband, 4-8 GHz, cryogenic HEMT amplifier ("SIR IF amplifier") with a noise temperature of 5K. In order to reduce external magnetic interference to the sensitive FFO, the mixer block is shielded by two coaxial cans. The external layer is made from cryo-perm and the internal one is copper covered with 100 μm of superconducting lead. The SIR chip is positioned far enough from the opening of the shielding cans, which is the only aperture for entering the signal beam and all electrical connections.

Initially FFO is not a very stable frequency source with an intrinsic linewidth of typically a few MHz, thereby limiting the ultimate spectral resolution of the receiver. However, the FFO is a voltage controlled oscillator and its frequency can be stabilized by locking it to an external reference oscillator using a Phase-Lock Loop (PLL) system. There are currently two concepts of PLL system under investigation and the final choice between those will be made at a later stage. Presently all the components needed to realize either system are envisaged in the design and shown in the schematic layout. In a first approach a submm-wave signal from an external harmonic generator (HG), driven by a 20-22 GHz synthesizer, is focused by mirrors "M3" and "M4" and applied directly to the receiving mixer. A small part of the IF band at 4GHz, is used to monitor the mixing product between the n-th harmonic of the synthesizer signal and the FFO signal. This down-converted signal, after narrow-band filtering, controls the phase-locking loop (PLL) system while the rest of the IF band is used to analyze the downconverted sky signal. In a second approach the chip receiver contains an additional harmonic SIS mixer which is used to mix a part of the FFO signal with the n-th harmonic of the synthesizer. In this case one more IF amplifier ("PLL IF amplifier") is used, but the "HG" and mirrors "M3" and "M4" can be omitted from the design.

All receiver components depicted in the Fig. 5 will be mounted on a single 4 K plate. The complete receiver with a size 240x180x80 mm³ will be pre-aligned and fully tested before mounting into a TELIS system.

The 1.8 THz Receiver

Measurements with the 1.8 THz receiver will focus on the OH triplet at 1.8 THz. However, within a range of 80 GHz a variety of species of particular interest for atmospheric chemistry can be observed (e.g. HO₂, HOCl, NO, NO₂). Therefore the goal is to design the receiver for the frequency band from 1.76 THz to 1.84 THz. At DLR a 2.5 THz airborne heterodyne receiver for the detection of OH is in operation. This receiver is based on a gas laser LO and a room temperature Schottky diode mixer [8]. An example of an OH emission detected with this receiver is shown in Fig. 6. Although the OH emission at 1.8 THz is about a factor of four weaker than at 2.5 THz, the former one was chosen for TELIS because of risks associated with the development of a 2.5 THz solid state LO. In addition, the weaker emission at 1.8 THz is partly compensated by the higher sensitivity of the mixer at 1.8 THz.

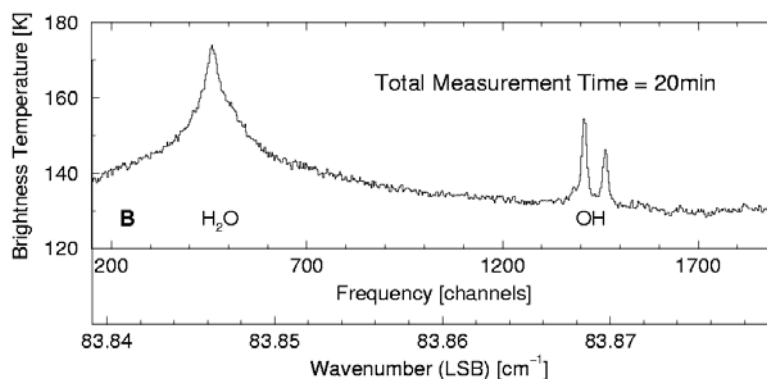


Figure 6. OH and H₂O measured with the DLR 2.5 THz airborne heterodyne receiver.

The preliminary cryogenic design is shown in Fig. 7. An SSB filter will be used to suppress the unwanted sideband. Coupling of LO and signal radiation is done by a polarizing diplexer. Three beam shaping mirrors, one for the LO and two for the mixer, are used. All optical components, the mixer and the IF system up to the first amplifier are mounted at the 4 K stage of the dewar. The multiplier chain of the LO is mechanically connected to the same plate but thermally well isolated. The size of the front-end is about 220 mm × 260 mm.

The mixer is a phonon cooled hot-electron bolometer developed by Moscow State Pedagogical University and similar to the one described in [7]. The HEB is incorporated in a quasi-optical hybrid antenna with a planar double-slot feed antenna and a 6 mm diameter lens. The lens is coated with a Parylene antireflection (AR) coating optimized for 1.8 THz [9]. It has been shown that the response of a HEB with a logarithmic-spiral antenna is linear to at least 400 K [9]. With the more narrow-band design of the TELIS HEB mixer we expect even higher dynamic range. The IF band is from 4 GHz to 6 GHz. A total bandwidth of 2 GHz is necessary in order to have sufficient baseline for the retrieval of the OH line. The IF band was chosen as a compromise between the IF bandwidth of the HEB mixer which is expected to be about 7 GHz (-3 dB DSB noise bandwidth), and the bandwidth of the SSB filter and LO diplexer. The baseline SSB noise temperature in the IF band is 4,000 K to 6,000 K.

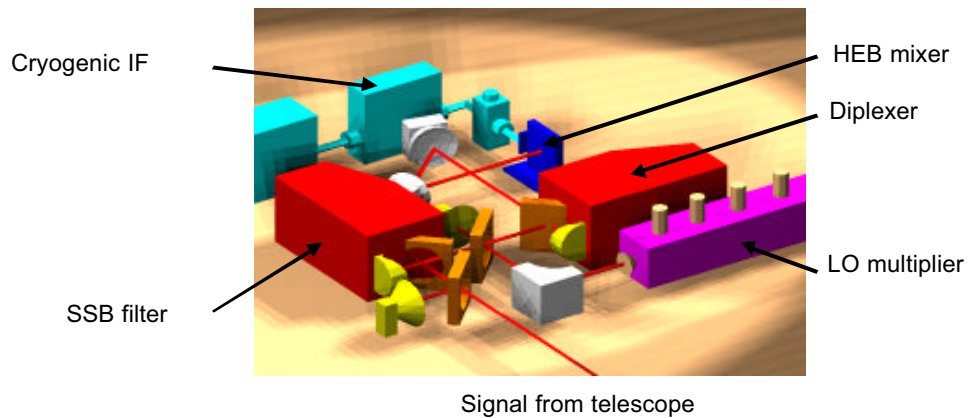


Figure 7. Preliminary design of the 1.8 THz front-end.

The 1.8 THz LO will be a PLL-stabilized synthesizer multiplied and amplified to ~100 GHz. Three additional multiplication stages are necessary to yield 1.8 THz. Since the efficiency of these multipliers increases with decreasing operation temperature they will be mounted inside the dewar and cooled to about 80 K. The power required by the HEB mixer for optimum operation is about 100 nW [10]. However, this power is determined by a method known as isothermal method. It is an estimate of the power, which is absorbed inside the superconducting bridge. Taking coupling losses into account the output power (goal) of the multipliers should be at least $2 \mu\text{W}$ between 1.76 THz and 1.84 THz.

Conclusions

Within the framework of the TELIS project three European institutes are building a balloon borne cryogenic heterodyne instrument. Three receivers will operate at 500 GHz (RAL channel), at 600-650GHz (SRON channel) and at 1.8 THz (DLR channel). The combination of the MIPAS and TELIS instruments will provide a unique balloon platform for atmospheric sounding. TELIS itself will be a testbed for new cryogenic heterodyne detection techniques. To name a few innovations of TELIS: The compactness of the 500 GHz channel, with its challenging high intermediate frequency of 15-19 GHz; the first field demonstration of the Superconducting Integrated Receiver; the 1.8 THz HEB mixer with its solid state Local Oscillator; the cryogenic low-noise IF amplifiers and the application of 2 GHz and 4 GHz digital auto correlators as back end spectrometers.

TELIS is presently in the phase of detailed design and early production. The three individual channels will be designed, assembled and tested after which system integration and test will start in 2004. A test flight is foreseen in 2005.

References

1. ESA report: "Definition of Mission Objectives and Observational Requirements for an Atmospheric Chemistry Explorer Mission", ESA Contract # 13048/98/NL/GD, report date June 2000.
2. Microwave Limb Sounder home page, <http://mls.jpl.nasa.gov/>
3. F. von Schéele, "The Swedish Odin Satellite to Eye Heaven and Earth", <http://www.ssc.se/ssd/papers/odeye/odeye.html>
4. JEM/SMILES home page <http://smiles.tks.nasa.gov/>, or "JEM/SMILES mission plan", http://www2.crl.go.jp/dk/c214/smiles/Mission_Plan/
5. Ellison, B.N., Moyna, B.P., Matheson, D.N., Jones, A., Claude, S.M.X, Mann, C., Kerridge, B.J., Siddans, R., Munro, R., and Reburn, W.J., "Development of a high sensitivity airborne SIS receiver to detect ClO and BrO", Proceedings of 2nd ESA Workshop on Millimetre Wave Technology and Applications, Espoo, Finland, May 1998
6. V. P. Koshelets and S. V. Shitov "Topical review: Integrated superconducting receivers", *Supercond. Sci. Technol.*, **13**, R53–R69, 2000 ; S.V. Shitov, V.P. Koshelets, P.A. Yagoubov, L.V. Filippenko, P.N. Dmitriev, O.V. Koryukin, An.B. Ermakov and R.W.M. Hoogeveen, "SIR Chip for TELIS", 14th International Symposium on Space Terahertz Technology.
7. A. D. Semenov, H.-W. Hübers, J. Schubert, G. N. Gol'tsman, A. I. Elantiev, B. M. Voronov, E. M. Gershenson, "Design and Performance of the Lattice-Cooled Hot-Electron Terahertz Mixer", *J. Appl. Phys.* **88**, 6758-6767, 2000
8. C. R. Englert, B. Schimpf, M. Birk, F. Schreier, M. Krocka, R. Nitsche, R. Titz, M. Summers, "The 2.5 THz heterodyne spectrometer THOMAS: measurement of OH in the middle atmosphere and comparison with photochemical model results", *J. Geophys. Res. D* 105, 22211-22223, 2000
9. H.-W. Hübers, J. Schubert, A. Krabbe, M. Birk, G. Wagner, A. Semenov, G. Gol'tsman, B. Voronov, G. Gershenson, Parylene Anti-reflection Coating of a Quasi-Optical Hot-Electron Bolometric Mixer at Terahertz Frequency, *Infrared Phys. and Technol.* 42, 41-47, 2001
10. S. Cherednichenko, M. Kroug, H. Merkel, P. Khosropanah, A. Adam, E. Kollberg, D. Loudkov, G. Gol'tsman, B. Voronov, H. Richter, H.-W. Hübers, "1.6 THz Heterodyne Receiver for the Far Infrared Space Telescope", Proc. of the European Conf. on Appl. Superconductivity, Copenhagen, September 2001

Heterodyne Instrumentation Development for the Caltech Submillimeter Observatory

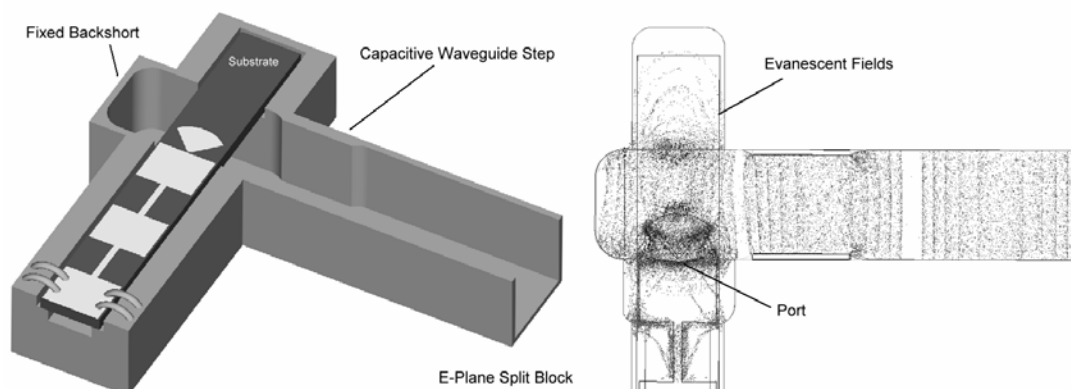
Jacob W. Kooi, Attila Kovacs, T.G. Phillips, and J. Zmuidzinas

Under development at the Caltech Submillimeter Observatory is a dual polarization, continuous comparison (correlation) receiver. The instrument has two beams on the sky; a reference and a signal beam. Using only cooled reflecting optics, two polarizing grids, and a quadrature hybrid coupler, the sky beams are coupled to four tunerless SIS mixers (both polarizations). The 4-8 GHz mixer IF outputs are, after amplification, correlated against each other. In principle, this technique results in flat baselines with very low RMS noise and is especially well suited for high red shift Galaxy work.

At the same time an upgrade is planned to the existing facility heterodyne instrumentation. Dual frequency mode receivers have been development for the 230/460 GHz and 345/660 GHz atmospheric windows. The higher frequency receivers are implemented in a balanced configuration, which reduces both the LO power requirement and noise. Each mixer has 4 GHz of IF bandwidth and can be controlled remotely.

Not only do these changes greatly enhance the spectroscopic capabilities of the CSO, they also enable the observatory to be integrated into the Harvard-Smithsonian Submillimeter Array (SMA) as an additional baseline. Installation is expected to commence in the Fall/2003.

Keywords: Radial probe, full-height waveguide to thin-film microstrip transition, split-block, superconducting-insulating-superconducting (SIS) tunnel junction, broad bandwidth quadrature waveguide hybrid, DC-break, IF match.



CO(9-8) in Orion

Simon J. E. Radford (NRAO), Ray Blundell, Scott Paine, Hugh Gibson,
Dan Marrone, et al. (SAO)

In 2002 November and December, we made 1035 GHz, CO(9-8) observations of Orion from 5500 m altitude on Cerro Sairecabur, Chile. This is about 40 km north and 500 m above the ALMA site near Cerro Chajnantor. We used an 80 cm telescope and a hot electron bolometer mixer receiver built and installed by the SAO receiver lab. In November, we obtained the first 806 GHz and 1035 GHz spectra with the system and in December, we made a small map 1035 GHz of Orion. During the map, the DSB receiver temperature was about 1000 K and the 1035 GHz zenith transmission varied from 14% to 10%. As far as we know, the only previous ground based observations at 1035 GHz was a single spectrum of Orion made with the same receiver at Mt. Graham a couple of years ago under much worse conditions (zenith transparency of 3%). These observations demonstrate the excellent observing conditions available near the ALMA site in the high Andes of northern Chile. Further observations are planned in 2003.

Quasi-Optics for 640 GHz SIS Receiver of International-Space-Station-Borne Limb-Emission Sounder SMILES

Masumichi Seta¹⁾, Axel Murk²⁾, Takeshi Manabe¹⁾, Junji Inatani³⁾,
Richard Wylde⁴⁾, Takeshi Miura³⁾, Toshiyuki Nishibori³⁾,
and SMILES Mission Team

¹⁾Communications Research Laboratory, Koganei, Tokyo 184-8795, Japan.
(E-mail : seta@crl.go.jp)

²⁾Institute of Applied Physics, University of Bern, Silderstrasse 5, 3012 Bern, Switzerland

³⁾National Space Development Agency, Tsukuba, Ibaraki 305-8505, Japan

⁴⁾Thomas Keating Ltd., Station Mills, Billingshurst, West Sussex RH14 9SH,UK

Abstract

We are developing quasi-optics for a 640 GHz limb emission sounder SMILES to be based on the International Space Station (ISS). SMILES is a heterodyne spectrometer and will use SIS mixers first time in space to detect trace molecules in the stratosphere. The engineering model of the optics has already been manufactured. We have demonstrated key functions such as an image-band rejection better than 20 dB, feeding Gaussian like beam pattern to antenna from back-to-back horn, supplying balanced LO power to the two SIS mixers, and radiation-shielding capability of 40 dB against external interference radiation below 26.5 GHz. We also demonstrated that these optical performances could be maintained over the vibration during launch and temperature variation on orbit. These performances almost satisfy specifications. The optics will be assembled into the engineering model of 640 GHz receiver system in 2003.

1. Introduction

We are developing a quasi-optics for a 640 GHz heterodyne receiver for SMILES. SMILES is a limb emission sounder to observe thermal emission from stratospheric molecules related to ozone depletion from the International Space Station (ISS). It is equipped with SIS mixers first time in space. The SIS mixer is known as the lowest noise device for heterodyne detection in 640 GHz band and it makes possible to detect extremely trace molecules (e.g., BrO) as well as precise global mapping for distribution of

trace molecules (e.g., O₃, ClO, and HCl). The ISS presents a number of engineering challenges. The receiver must cope with vibration during launch, large temperature variation while in space, and electrical interference from telecommunications signals on the ISS. The sensitivity of the receiver is determined by the noises of mixer plus amplifiers as well as the losses in the input optics. The sensitivity may also be limited by spurious noise due to interference radiation and standing waves. The receiver optics for SMILES is designed to minimize

these problems while maintaining the input loss as low as possible.

In this paper we describe the design of the receiver optics and show some experimental results of its key functions.

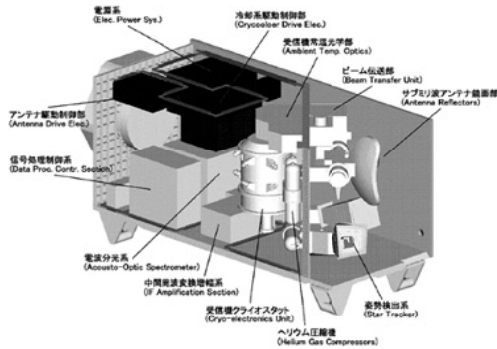


Fig. 1 Schematic view of SMILES as a payload of the Exposed Facility of Japanese Experiment Module of the ISS.

2. Overview of Optics for SMILES

2.1 640 GHz SIS Receiver for SMILES

The SMILES is a payload of the Exposed Facility of the Japanese Experiment Module (JEM) on the ISS. It is packed in a box with a dimension of 1.9 m x 1.0 m x 0.5 m and a mass of 500 kg as shown in Figure 1.

We show block diagram of the 640 GHz receiver of the SMILES in Figure 2. A mechanically scanning a 40 cm x 20 cm offset Cassegrain antenna receives emission from the stratosphere. The receiver optics is composed of an ambient temperature optics (AOPT) and a 4K-cooled optics (COPT). The receiver optics provides quasi-optical coupling between antenna optics and SIS mixers, and has a function to supply local oscillator (LO) signal to two SIS mixers operating in single sideband (SSB) [1], and to

shield the receiver against external interference radiation [2].

The mixer output of the first intermediate-frequency (IF) signal (11-13GHz) is amplified by a chain of 20K-cooled and 100K-cooled amplifiers [3]. A mechanical 4K refrigerator cools down the cryo-electronics (CRE)[4]. The IF signal is further amplified and down-converted into the second IF frequency band of 1.55-2.75 GHz by an ambient temperature amplifier (AAMP) and an IF amplification section (IFA) followed by two acousto-optic spectrometers [5].

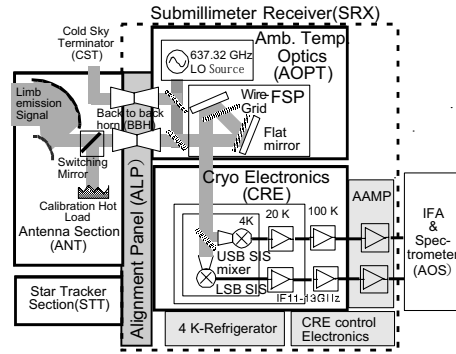


Fig.2 Block diagram of 640 GHz receiver for SMILES.

2.2 Back-to-Back Horn

The receiver optics is connected to the antenna (ANT) optics via two back-to back horns (BBHs) [6]. Figure 3 shows the picture of two BBHs on engineering model of AOPT. The BBH for SMILES is an overmoded waveguide with corrugated wall whose apertures on both ends are designed to match input and output beams. The BBH has two outstanding functions in the optics.

One function is electromagnetic shielding capability. The narrow inner diameter of the waveguide of the BBH works as a cut-off

filter, while keeping small loss because the BBH acts as a oversized corrugated waveguide at frequencies around 640 GHz. Electromagnetic interference radiations within the SMILES IF band (11-13 GHz) might cause spurious signals in observed spectra. We protect the SIS mixers and cooled amplifiers against the interference radiation of 2 V/m below 26.5 GHz expected on the ISS. We require radiation shielding more than 54 dB for the SIS mixer and the amplifiers to suppress the spurious signal below 1.5 K. The main-frame structure of the SMILES payload provides a 14 dB radiation shielding, so the shielding requirement for the cryostat placed within the frame is relaxed to 40 dB. The cryostat is designed to provide >40 dB shielding when it is connected to the AOPT by metallic bellow around it. Thus the frame of the AOPT is required to have shielding capability of more than 40 dB. The shielding requirements for the BBH is 54 dB that is larger than the requirement for the frame since the BBH is opened to outer space of the main frame for the SMILES though the alignment panel.

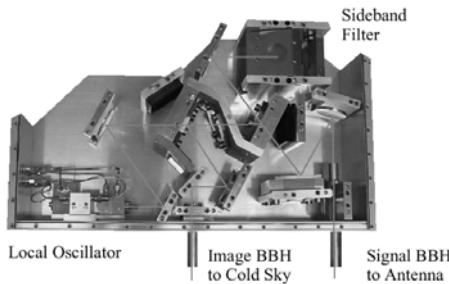


Fig. 3 Picture of engineering model of AOPT.

Second function of the BBH is to separate the basic design of optics at each side of the BBH aperture. The AOPT and antenna optics is placed on opposite side of the

alignment panel that is a reference plane for all the optical components. Thus we can specify the position of the BBH and the beam parameters at the aperture of the BBH as interface conditions for basic design of the optics. The separation in design is useful for fabrication of a big system where different groups develop several components.

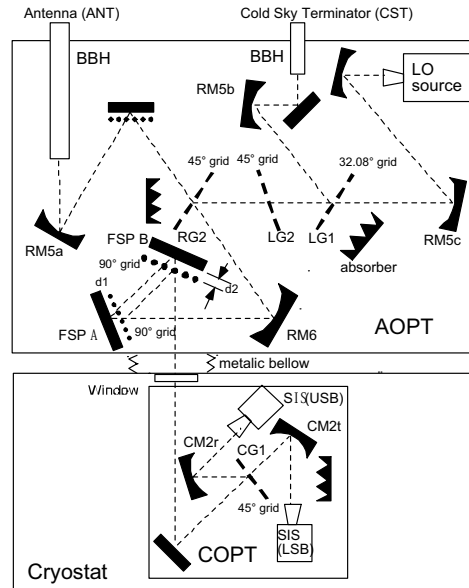


Fig. 4. Schematic diagram of the optics.

3. Single Sideband Filtering and Local Oscillator Signal Diplexing

3.1 SSB Filtering

We show the schematic diagram of the receiver optics in Figure 4. One feature of the optics of the SMILES is operation of two SIS mixers simultaneously in SSB mode for the upper sideband (USB), 649.12-650.32 GHz, and lower sideband (LSB), 624.12-625.52 GHz. An image rejection ratio larger than 15 dB is required for the SSB filter. We developed a new type of SSB filter consisting

of Frequency Selective Polarizers (FSP). The FSP is composed of a flat mirror and a wire grid. The FSP-type SSB filter has two advantages over the conventional Martin-Puplett interferometer (MPI) in that it is almost free from undesired residual return reflection which causes harmful standing waves, and it can be made thermally stable for fixed tuned applications [7,8].

The new SSB filter is composed of two FSPs, a polarizing grid (RG1) in AOPT, and an analyzing grid (CG1) in COPT (Figure. 4). It is a four ports device for lineally polarized beams. It is an interferometer working in the same operational principle for the conventional MPI [8]. The orientation of a the grid of FSP A should be parallel to that of the grid of FSP B, and be 45° tilted that respect to the orientation of the grids of RG1 and CG1 in the projected plane perpendicular to the direction of propagation. The $+45^\circ$ and -45° polarized beam ports are assigned to the SIS mixers for LSB and USB, respectively. The grid RG1 in AOPT selects a $+45^\circ$ polarized beam as the signal from stratospheric emissions via BBH for ANT. The -45° polarized beam in the AOPT is assigned for cold sky termination (CST) signal plus LO signal. The cold sky port is terminated to cosmic back ground radiation via BBH for CTS. The grid-mirror spacing (d_1 and d_2 of Figure 4) of the FSPs determines the power coupling characteristics between these ports. We chose the spacing so that one of the SIS (USB) mixers couples to the signal port in USB while it couples to the CST port in LSB. The other SIS mixer was tuned for detection of the signal in LSB automatically by the choice of the separation.

3.2 Diplexing of the LO Signal

The AOPT also serves as a diplexer for LO signal. There are several quasi-optical diplexing methods. The dielectric thin film coupling is the simplest diplexer. However loss at the film cannot be ignored for the sensitive detector for SMILES. An additional MPI could be used for diplexing without introducing additional loss. However it requires additional optical components that may increase possibility of troubles in space.

We use a freestanding wire grid as a diplexer. The 637.32 GHz LO source on the AOPT is composed of 106.22 GHz fixed tuned Gundiode followed by doubler and tripler. The wire grid LG1 combines signal from the LO source and signals from the image terminating CST (Figure 4). The power coupling ratio of LO source to the signal is determined by the orientation of the grid wire of LG1 relative to that of RG1. The coupling ratio should be minimized as far as enough power is supplied for the SIS mixers, since a large coupling ratio increases the effective temperature of the image terminator and increases standing waves between the SIS mixer and the LO source. We designed to couple 5% of the output power of the LO source to the signal path. Absorber for grid RG1 terminates the remaining 95% power of the LO signal.

The LO signal coupling balance to the SIS mixer is determined by the bandpass characteristics of the SSB filter. We supply the power of LO signal equally to the two SIS mixers. Two SIS mixers for USB and LSB are designed identically, so the same amount of LO signal power is required for operation. The cross polarization leakage of

the grid RG1 is a possible source of the frequency shift of the SSB filter. Thus we inserted a cross polarization clearance grid LG2 in front of the grid RG1. The cross polarization could be reduce by the tandem of wire grids set to the same projected angle.

3.3 Measurements of Bandpass Characteristics

We measured the bandpass characteristics of the engineering model of AOPT [9]. Bandpass and image rejection characteristics between the antenna-side BBH input and the COPT-side output port were measured for the LSB or USB port of the COPT by selecting proper linear polarization. Figure 5 shows measured bandpass and image rejection characteristics around the LSB and USB. In this figure, image rejection ratios better than 20 dB are achieved over the LSB and USB simultaneously. The internal reflections within the AOPT are also measured [9]. The reflection at the FSP was found to be below detection limit of -60 dB. This confirms the low reflectivity of the FSP. We conclude that the new SSB filter based on the FSPs satisfies the requirements for SSB filtering for SMILES.

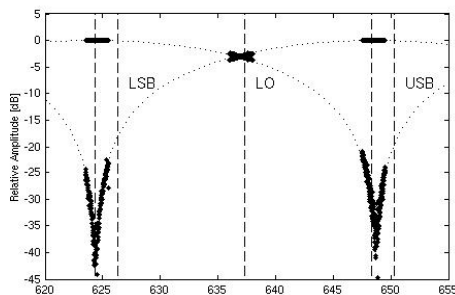


Fig. 5 Measured bandpass characteristics of AOPT.

The measured cross-over characteristics

around the LO signal frequency of 637.32 GHz are shown in detail in figure 6. It shows balanced coupling of the LO signal with imbalance of 0.6 dB. This good balance was realized by good machining of mirror-grid distance and reduction of cross polarization leakage in polarizing grid (RG1 plus LG2 in Figure 4) of the FSP based SSB filter. We checked that removal of cross polarization cleaning grid LG2 increased the coupling imbalance from 0.6 dB to 6dB. We also measured 5% coupling efficiency of the LO source to the COPT by using a submillimeter wave power meter. The power meter received $25\mu\text{W}$ of LO signal at the COPT window of the AOPT when the LO source was operating in the AOPT. It corresponds to the 5% of the LO signal output power of 0.5 mW that is measured for engineering model of the LO source. We consider that the 5% LO signal power coupling to the SIS mixer with imbalance of 0.6 dB satisfies the requirements of the diplexer for SMILES.

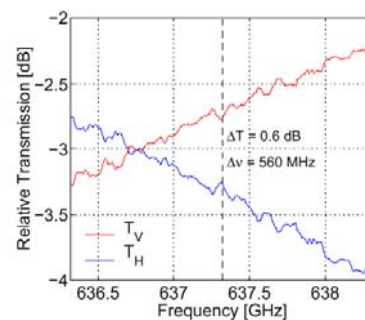


Fig.6 Measured band pass characteristics around the LO frequency.

4. Transformation of Beam

4.1 Design of the Beam Transformation

The loss in the input optics is specified as below 1.7 dB for SMILES to realize an SSB

receiver noise temperature below 500 K. We use focusing mirrors and horns for quasi optical beam transformation elements that are superior to other beam propagation method in 640 GHz. Several attentions were paid for further reduction of the losses in quasi-optical design such as employment of large aperture mirrors to keep beam truncation level below -40 dB in terms of the fundamental Gaussian mode, and small off axis angle for suppressing generation of cross polarization.

There are three requirements for the design of the beam transformation for SMILES. We designed the optical parameters based on the analyses of the fundamental Gaussian mode. One restriction is size of the window of the cryostat. The smaller one is better for the cryogenics. The cryostat and refrigerator is designed to allow the cryostat window size not more than 25 mm in diameter. Second restriction is the size of diameter of the BBH. The diameter of the BBH should be smaller than 6.4 mm so as to work as a cutoff filter against radiations below 26.5 GHz. Final requirement is production of image of the mixer horn at the aperture of the BBH. It is known that Gaussian beam parameters become frequency independent at two image planes. The frequency independent beam reduces losses due to miss coupling of the beam at the apertures of the horns. It also reduces the reflection there.

Name	Distance	Focal length
Mixer horn	0	
CM2	50.00 mm	48.65 mm
RM6	530.669 mm	134.29 mm
RM5	825.669 mm	48.92 mm
BBH	893.859 mm	

Table 1 Position and focal lengths of focusing mirrors.

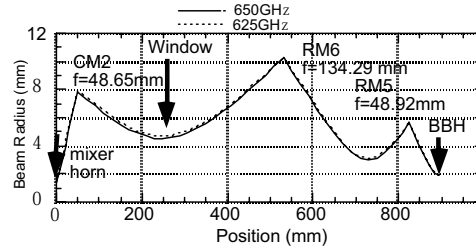


Fig.7 Propagation of quasi-optical beam from mixer horn to BBH. The radius shows 1/e amplitude radius of the Gaussian beam.

We optimized positions and lengths of the three focusing mirrors to realize these requirements as summarized in Table1. We show beam transformation along the optical path from the mixer horn to the BBH for 625 GHz and 650 GHz that are representative for LSB and USB in Figure 7. The two lines are almost overlapping. We confirmed that the Gaussian beam parameter of radius of curvature R and beam radius W is identical for over the frequency range between 624.12 and 650.32 GHz at the apertures of the BBH ($W=1.9$ mm, $1/R=0$) and the mixer horn ($W=1.45$ mm, $R=16$ mm). The beam waist is placed around the window of the cryostat, although there is negligible small difference for the position and size of the beam waist between the two beams. The beam transformation is designed identical for signal path (SIS-FSP-BBH for ANT) and cold sky path (SIS-FPS-BBH for CST). The frequency independent beam condition is relaxed for LO path (SIS-FSP-LO) since LO signal frequency is fixed at 637.32 GHz.

4.2 Beam Pattern Measurements

We evaluated the design of beam

transformation by the output beam pattern from the BBH. We measured the phase and amplitude of the beam from the BBH by AB mm vector network analyzer [9-11]. We placed the detector with a focusing mirror and wire grid at the COPT port of the AOPT that simulates the COPT. We radiated the BBHs by test signal from another horn and scanned it.

We show a beam pattern for a BBH for ANT measured at 649.32 GHz in Figure 8 and Figure 9. There is a good agreement between the theoretical calculations and measured one down to -20 dB. The theoretical pattern simulates the beam from an ideal corrugated horn by CORRUG. This good agreement suggests that our optical design and manufacturing process are good. There is small distortion below -20 dB levels. The distortion in -20 dB levels is close to the boundary of a level above which the antenna beam efficiency was degraded by 1%. We consider that the measured pattern is acceptable for feeding the antenna.

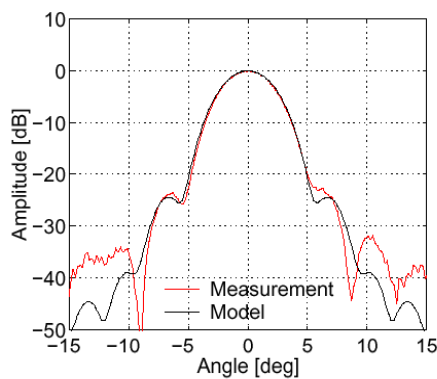


Fig. 8 Measured beam pattern of amplitude from a BBH.

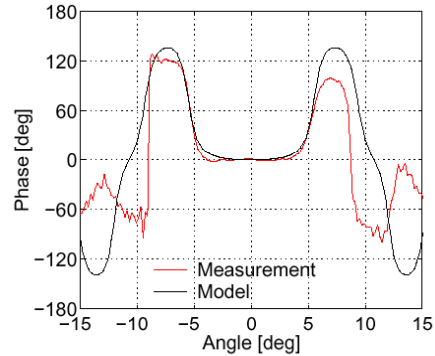


Fig. 9 Measured beam pattern of phase from a BBH.

5. Shielding of Interference Radiation

5.1 Shielding of the Frame Box of Optics

The frame box of AOPT is required to have shielding capability more than 40 dB below 26.5 GHz. The basic structure of frame box of AOPT is aluminum plates (Figure 3). We inserted a conductive rubber tube when we stuck the plates together to improve the shielding. There are six feedthroughs in the frame of the AOPT for biasing cables for LO source. We put Indium for mounting of the feedthroughs. These shielding techniques should be good enough for the 40 dB requirement of the frame box of the AOPT.

5.2 Measurement of Radiation Shielding

We evaluated the radiation shielding capability of the engineering model of the AOPT alone. The COPT-side window was shielded by an aluminum plate to simulate the shielding provided by the cryostat and the bellow. The basic procedure of the shielding evaluation is to measure the shield level inside the AOPT when it is irradiated from outside. We used a level as reference one when we exposed the emitting probe of the

test radiation to the detector. The received power should decrease when we put the probe in the AOPT. We define a shielding capability as the amount of the decreased power. We swept the frequency of the test radiation from 2 GHz to 20 GHz with a frequency step of 0.1 GHz.

We show measured results of the shielding of the AOPT for three different orientations in Figure 10. It shows the AOPT has shielding capability more than 40 dB for the measured frequency range of 1 to 20 GHz. This shielding level is good enough for our requirement of >40 dB.

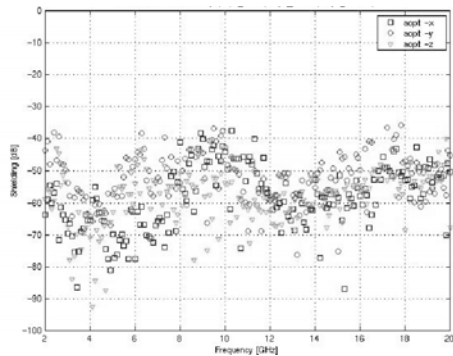


Fig. 10 Measured shielding capability of AOPT.

6. Environmental Conditions as a Space Instrument

The optics of the SMILES is designed to survive the vibration during launch and temperature variation on orbit. SMILES will be transported to the ISS by Japanese HII Transfer Vehicle launched by the HII rocket. The AOPT is placed on the alignment panel of the payload of the SMILES (Figure 1). The AOPT is required to survive 15 Grms level vibration for qualification test on ground. The test vibration level of the COPT is 26 Grms that is higher than the test level for the AOPT because there is some

amplification of the vibration in the supporting mechanism of the 4Kstage for COPT. The AOPT is also required to survive temperature variation between -40 degC to +60 degC. The circulating coolant supplied by JEM controls the temperature of the AOPT between 15 degC to 40 degC on normal operation. We tested the variation of the optical performances before and after the vibration and thermal cycling test.

The null position of the bandpass characteristics is good probe for examining the change in optical performance since it is sensitive to the small change in configurations such as grid-wire distance and orientation of optical elements. We show how the null position changes over the test in Figure 11. There is small change in the frequency. The 200 MHz shift is close to the measurement error. The value of frequency shift is acceptable for SMILES in the senses that this shift will not degrade achieved image rejection ratio better than 15 dB and balanced LO signal coupling to the SIS mixers. We conclude that the optics for SMILE passed the vibration and thermal cycling test.

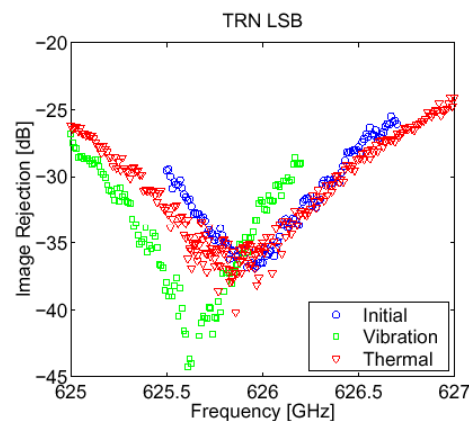


Fig. 11 Variation of null position of the band pass characteristics over the environmental test.

7. Conclusion

We have fabricated engineering model of the receiver optics for International Space station (ISS)-borne limb emission sounder SMILES. We showed that antenna feeding beam pattern agreed with theoretical calculation down to -20 dB. We showed image rejection of 20 dB at the USB and LSB using a pair of Frequency Selective Polarizer (FSP) as a SSB filter. We showed the balanced LO injection to the two SIS mixers. The internal reflection within the optics is very low < -50 dB for the signal path. We showed that shielding capability of the frame box of the optics is better than 40 dB that is large enough to protect SIS mixer and cooled amplifiers from interference radiation expected on the ISS. We showed that the optical performance would not be affected by vibration during launch and temperature variation on orbit. These performances satisfy the specifications imposed on the optics for SMILES. The optics will be integrated into the engineering 640 GHz receiver in 2003. It will show low SSB noise of less than 500 K. The receiver will be refurbished in 2004 for flight model. The launch date of SMILES is postponed from the original schedule due to some reasons for development of the ISS. We expect to operate the SMILES from 2007 for at least one year.

References

- [1] J. Inatani et al., "Single Sideband Mixing at Submillimeter Wavelength," *9th International Symposium on Space Terahertz Technology*, Pasadena, March 1998.
- [2] M. Seta et al., "Development of a Highly Sensitive Submillimeter SIS Receiver for International-Space-Station-Borne Limb-Emission Sounder JEM/SMILES," *23rd International Symposium on Space Technology and Science*, Matsue, Japan, May 26-June 2, 2002.
- [3] Y. Fuji, et al., "Space-borne 640 GHz SIS Receiver Based on 4K Mechanical Cooler," *Proceedings of SPIE*, Vol.4013, pp. 90-99, 2000.
- [4] J. Inatani, K. Narasaki, S. Tsunematsu, M. Kyoya, T. Manabe, M. Seta, T. Iida, and R. Satoh, "Mechanical Cooler and Cryostat for Submillimeter SIS Mixer Receiver in Space," *8th International Symposium on Remote Sensing*, Toulouse, Sep., 2001.
- [5] H. Ozeki et al., "Submillimeter wave spectroscopic performance of JEM/SMILES," *Proc. SPIE*, 4152, 255, 2000.
- [6] B. Maffei, et al., "Shaped corrugated horns for cosmic microwave background anisotropy measurement", *Int. J. IR MM Waves*, 21, 2003, 2000.
- [7] J. Inatani et al., "A New Configuration of the Martin-Puplett interferometer with Low-Reflection," *IEEE 7th International Conference on Terahertz Electronics*, 260, 1999.
- [8] T. Manabe et al., "A new configuration of polarization-rotating dual beam interferometer for space use," *IEEE Trans. Microwave Theory Tech.*, Vol. 8, no. 6, pp. 1696-1704, June 2003.
- [9] A. Murk, N. Kaempfer, R. Wylde, T. Manabe, M. Seta, and J. inatani "Characterization of the Ambient Temperature Optics of the Submillimeter Limb-Sounder SMILES," *27th IEEE International Conference on Infrared and Millimeter Waves*, San Diego, September 2002.
- [10] A. Murk, N. Kaempfer, R. Wylde, T. Manabe, M. Seta, and J. Inatani "Characterization of Various Quasi-Optical Components for the Submillimeter Limb-Sounder SMILES," *12th International Symposium on Space Terahertz Technology*, San Diego, February 2001.
- [11] A. Murk, N. Kaempfer, R. Wylde, T. manabe,

M. Seta, and J. Inatani, "Beam pattern measurements of the Submillimeter Limb-Sounder SMILES Ambient Temperature Optics," *3rd ESA workshop on Millimeter Wave Technology*, Espoo, Finland, May, 2003.

Meeting the Optical Requirements of Large Focal-Plane Arrays

Antony A. Stark
Smithsonian Astrophysical Observatory

ABSTRACT

Technological advances will allow the placement of many Terahertz detectors at the focal plane of a single telescope. For a telescope of a given diameter and wavelength of operation, there is a limit to the number of usable detectors imposed by diffraction and optical aberrations. These effects can be ameliorated through an optical design where the magnification of the telescope's secondary mirror is small and the detector package is therefore located near the secondary mirror. A field mirror can be used to flatten the image, and the focal reducer which matches the detector to the telescope can also provide an image of the aperture for placement of filters and stops. A design concept is presented for the South Pole Telescope which comprises a 10 meter diameter off-axis paraboloidal primary mirror, a Gregorian secondary mirror, a tertiary chopper, dewar window, Lyot stops, band-pass filter, and space behind the focal plane for cryogenics. The telescope is bilaterally symmetric, and all apertures are unblocked. The field of view is one degree in diameter, so this telescope can feed an array of several $\times 10^4$ detectors at Terahertz frequencies.

I. Introduction

The South Pole Telescope (SPT) is a 10 m diameter millimeter- and submillimeter-wave telescope which has been approved for construction at Amundsen-Scott South Pole Station. It is funded by the National Science Foundation Office of Polar Programs, and the participating institutions are the University of Chicago, the Smithsonian Astrophysical Observatory, the University of California at Berkeley, Case Western Reserve University and the University of Illinois. Work on the telescope design is in progress. Construction is expected to begin by the end of 2003.

The initial project planned for this telescope is a large-scale survey covering many thousands of square degrees of sky, searching for the Sunyaev-Zel'dovich effect from clusters of galaxies at all redshifts. This search will be done with a focal-plane array

of bolometers operating at 2 mm wavelength. The diffraction-limited beamsizes at that wavelength (with conservative illumination of the primary mirror) will be about an arcminute, an angular size chosen to be comparable to the size of clusters at cosmological distances. The focal plane array will have about 1000 detectors; making an array of this size is thought to be possible using current bolometer technology (Gildemeister, Lee, & Richards 2000). Such a large number of independent beams of arcminute size requires a field of view about a degree in diameter. This paper describes a design for the telescope optics which will feed 1000 beams at $\lambda = 2\text{mm}$. The significance of this work for Terahertz technology is the serendipitously good quality to which this design can be optimized: the optics are sufficiently well-corrected that they will work at $\lambda = 200\mu\text{m}$ and feed an array containing more than 30,000 detectors.

II. Optical Design Considerations

Submillimeter-wave telescopes have different design constraints than optical telescopes. This is fortunate, because 10 meter class visual-wavelength telescopes have fields of view less than 0.2 degree in diameter, much smaller than the design requirement of the SPT. Since diffraction is more important at submillimeter wavelengths, the allowable size of optical aberrations is larger, and if the aberrations are balanced across the field of view, that field of view can be large (Stark 2000, Stark et al. 1998).

The SPT design is driven by its intended use as a cosmic microwave background instrument. It must have the lowest possible thermal emission from the telescope, the lowest possible variations in the residual thermal emission that remain, and the smallest possible spillover of the beam onto the ground and surrounding structures. This means that the optical path should have

- no aperture blockage anywhere in the system;
- conservatively illuminated optics;
- no warm lenses.

The optical train must therefore consist almost entirely of off-axis mirrors, with the possible exception of a lens or lenses which are inside the cryogenic dewar and cooled to low temperatures. Fortunately, machined aluminum mirrors are near-perfect at millimeter and submillimeter wavelengths; the addition of a mirror to the optical train does not cause significant degradation of the system and many mirrors can be used. Furthermore, it is possible to fabricate mirrors of arbitrary shape.

The cryogenic dewar brings its own set of optical requirements:

- the dewar window must be small enough that it can be constructed from low-loss materials and not implode;
- there should be a Lyot stop—an image of the primary mirror inside the dewar—for placement of a cold aperture which prevents the detectors from seeing beyond the edges of the optical elements;
- there must be a low-pass filter near the dewar window to block infrared radiation;
- the filter diameters must be small enough to be constructible—also, filters do not work at large angles of incidence.

It is best that the dewar not be too large, since the weight of the dewar increases and the ease of handling decreases as the enclosed volume goes up. The Lyot stop should therefore be close to the detector, since both must be kept cold. Mirrors can be warm and need not be inside the dewar. The detectors also impose their own requirements:

- there must be a band-pass filter to determine the wavelength of operation;
- the ratio f/D should be a uniform, fixed value (1.3 in this case) for each point in the image;
- the chief ray at each detector should be perpendicular to the surface of best images; that surface should be flat;
- all detectors should be identically illuminated.

III. The Problem of the Lagrange Invariant

The design difficulties inherent in a wide-field system can be appreciated by consideration of the Lagrange invariant. One way of expressing this quantity is $Inv = \frac{4}{\pi}(A\Omega)^{1/2}$, where at a plane intersecting the optical path, A is the area illuminated by the envelope of all rays through the system, and Ω is the solid angle subtended by the frustum of those rays. This quantity is conserved along the optical path. Evaluating at the aperture of the SPT telescope, $Inv = 10\text{m} \cdot 1^\circ = 10 \text{ meter} - \text{degrees}$. If the beam passes through a small aperture some place in the optical chain, for example at a 200 mm diameter dewar window, then the beam there must converge at a fast 50° angle. It is impossible to pass the beam through a 50 mm diameter aperture, because the included angle of the beam would need to be 200° . The optical path will necessarily

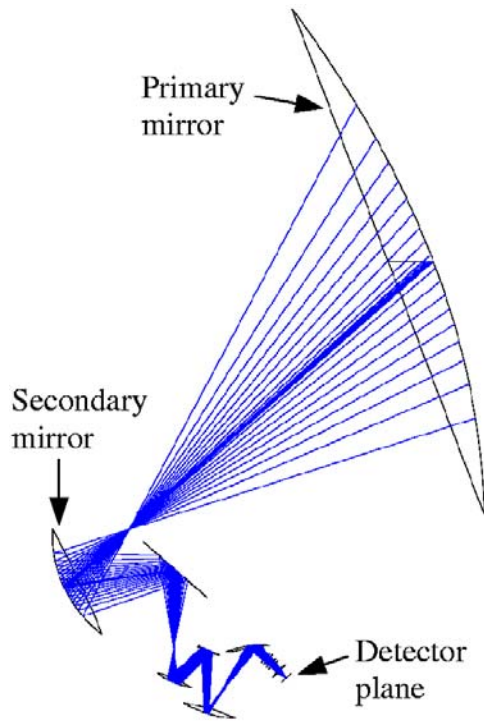


Fig. 1: **Side view of SPST214**
Only rays from the central point
in the field are shown.

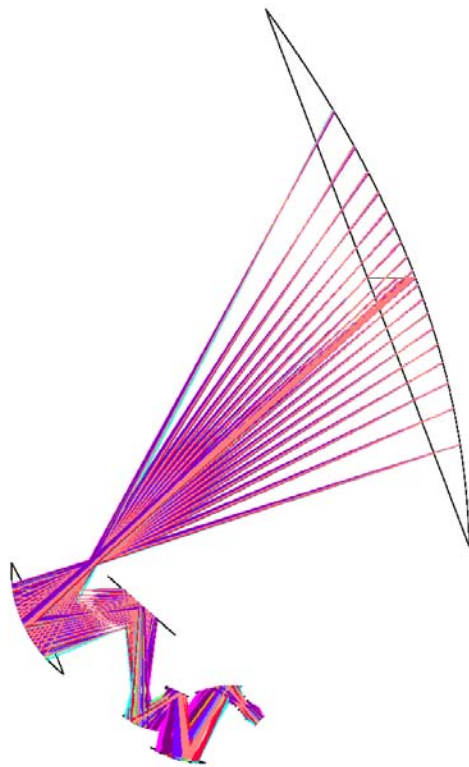


Fig. 2: **Side view of SPST214**
Rays from twelve points in the
field of view are shown. This
fills out the volume occupied by
the optical beams, showing that
the fourth through seventh mir-
rors are neither blocked nor over-
illuminated, even in this design
with a large Lagrange invariant.

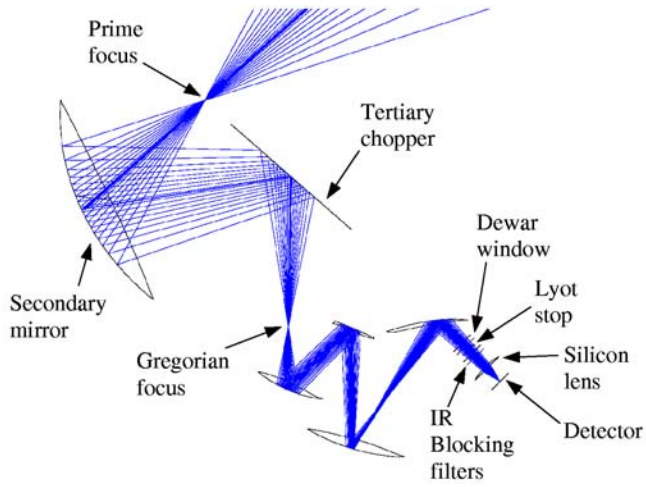


Fig. 3: **Detail view of Figure 1.** Only rays from the central point in the field are shown.

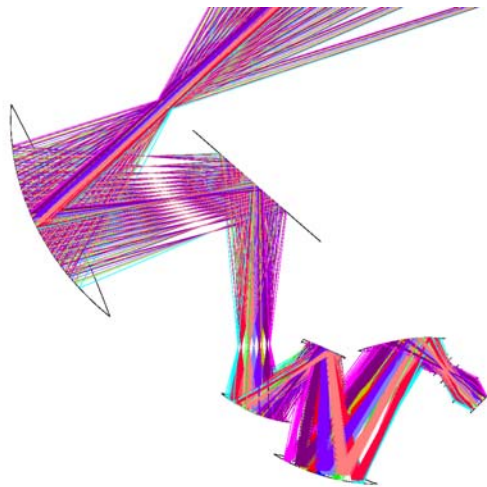


Fig. 4: **Detail view of Figure 2.** Rays from twelve points in the field are shown. Note that rays from different points in the field cross each other at an image of the aperture located between the secondary and tertiary mirrors.

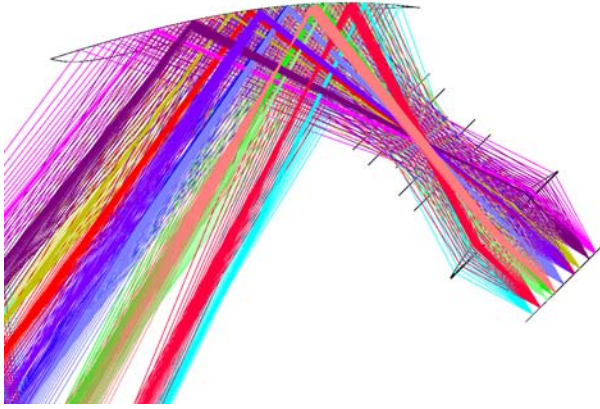


Fig. 5: **Detail view of Figure 4.** The last mirror and dewar optics are shown. Note that the surface of best focus is flat, that the chief ray from each point in the field is perpendicular to the image plane, and that each of the points in the field uniformly illuminate a Lyot stop near the dewar window. The two lines in front of the Lyot stop, representing the approximate position of the dewar window, and the two lines behind the Lyot stop, representing the position of the IR blocking filters, are 250 mm long and spaced 50 mm apart.

consist of large optical elements, of order a meter in diameter, and the beam will spread rapidly between elements, requiring that the separation between optical elements is comparable to their size.

Accommodating a large Lagrange invariant is awkward in conventional Cassegrain or Gregorian telescope designs, because the small size of the secondary mirror and the large distance between it and its focus make the subsequent optics gigantic. The magnification of a telescope's secondary mirror, m , is the distance from the mirror center to the far focus divided by the distance from the mirror center to the near focus. (By definition, the sign of m is negative for Gregorians and positive for Cassegrains.) The secondary mirror magnification in on-axis Cassegrain or Gregorian telescopes is typically $|m| \sim 25$. Let f_1 is the focal length of the primary mirror. In a 10 meter class telescope, $f_1 \sim 7$ m. The size of the image at the Cassegrain focus is $m \cdot f_1 \cdot \tan(FOV)$ where FOV is the field-of-view. If $FOV = 1^\circ$, $m \cdot f_1 \cdot \tan(FOV) \sim 3$ m, so that any tertiary mirror in the vicinity of the the Cassegrain or Gregorian focus must be about 3 meters across—an awkwardly large size. The way around this is to make $|m|$ small, closer to 3 than 25.

If $|m|$ is small, the Cassegrain or Gregorian focus is not far from the secondary mirror, and the subsequent optics and the detector will necessarily be located between the secondary and the primary. Such a position can easily be accommodated in an off-axis telescope design, where the detector dewar and its ancillary optics can be placed in the secondary mirror support structure, out of the way of the primary beam. The National Radio Astronomy Observatory's Green Bank Telescope is configured this way.

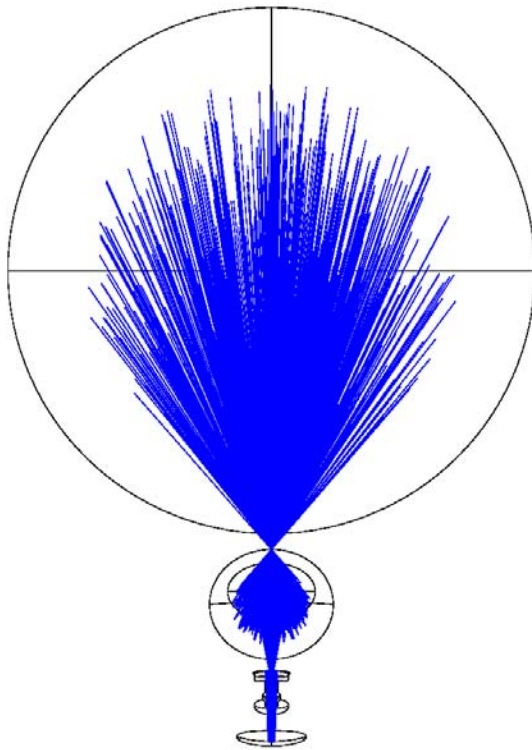


Fig. 6: **Star's view of SPST214** A randomly-chosen but edge-tapered set of rays from the central point in the field of view are shown. Note that the optics are bilaterally symmetric to ensure that horizontal chopping is balanced.

IV. A Specific Design

In optical design, it is difficult to prove that something cannot be done—there are many clever tricks available to the optical designer, and much room for the exercise of ingenuity. It is, however, possible to show that something can be done through an example. What follows is a particular optical design that meets the criteria for the Sunyaev-Zel'dovich effect survey with the South Pole Telescope. This is one possible design out of many. It is not fully optimized and the South Pole Telescope will not be built exactly this way, but it is presented as a demonstration that a wide-field submillimeter-wave telescope is possible. Other designs can be found at <http://www.tonystark.org>. The important point for the development of Terahertz technology is the serendipitous result that this design exceeds the requirements for millimeter-wave work and is sufficiently well-corrected that it will work at Terahertz frequencies.

The figures show various aspects of a ZEMAX* computer model of an optical

*ZEMAX is a trademark of ZEMAX Development Corporation of San Diego, CA

design called SPST214. In this design, the primary mirror is a 10 m diameter section of a paraboloid with a 7 m focal length. The secondary is an off-axis piece of a prolate ellipsoid. Figure 1 is a view from the side, showing seven mirror surfaces, one lens, and the detector plane. Also shown are some rays from a source at the center of the field of view: note that all these rays come together at the prime focus, at the Gregorian focus, and at the detector. Figure 2 is the same view, but shows rays from twelve sources distributed over the one-degree-diameter field of view. Figures 3, 4 and 5 are details of Figures 1 and 2. Figure 6 shows the view from the front, as seen from the source being observed. Note that the secondary mirror is well out of the main beam from the primary mirror. The secondary mirror is 2330 mm wide by 1970 mm high. The tertiary mirror is flat, and will be used as a chopper. Note in Figure 4 that it is located near an image of the primary mirror. The surfaces of mirrors four through seven have arbitrary shapes—their only constraint is that they are bi-laterally symmetric about a vertical plane. From the dewar window to the detector, the optical elements are cylindrically symmetric about the chief ray of the center of the field of view.

As seen in Figure 5, the dewar window is 250 mm diameter and will likely be made of expanded plastic foam. The Lyot stop is an aperture 164 mm in diameter in the 4 K shield of the dewar. Infrared blocking filters are located behind the Lyot stop. The diameter of these filters can be as small as the Lyot stop, or, if they can be made larger, they could be located several centimeters behind it, which would allow the Lyot stop to block some of the photons scattered by the filter.

Silicon is an excellent material for a cold lens at millimeter wavelengths. The lens in this design is 350 mm in diameter and about 25 mm thick. A lens blank this size made of fairly high purity Silicon is readily obtained from several sources. The index of refraction of Silicon at 1.5 K is 3.38 (Loewenstein, Smith, & Morgan 1973), and the loss through a lens this thick is a few percent or less, depending on the purity of the material. The lens is constrained to be plano-convex in order to facilitate anti-reflection coating. A more “bent” lens would work a little better in this application, but the anti-reflection coating might delaminate from a concave surface. The lens is slightly aspheric.

In the 150 GHz detector array to be used in the Sunyaev-Zel’dovich survey, the converging cones of rays will be intercepted by 1027 conical feedhorns drilled into an aluminum plate which is 200 mm in diameter and about 8 mm thick. There will be a short length of waveguide between each feedhorn and each bolometer detector, and that waveguide will incorporate a bandpass filter which will determine the bandwidth of the observations. The bolometers will be the “spiderweb” voltage-biased superconducting transition-edge sensor type (Gildemeister, Lee, & Richards 1999, 2000).

Figure 7 shows a spot diagram, where rays from twelve stars in a one degree diameter field of view are propagated to the detector, and the intersection of each ray with the detector plane is marked with a “+”. The important point for Terahertz

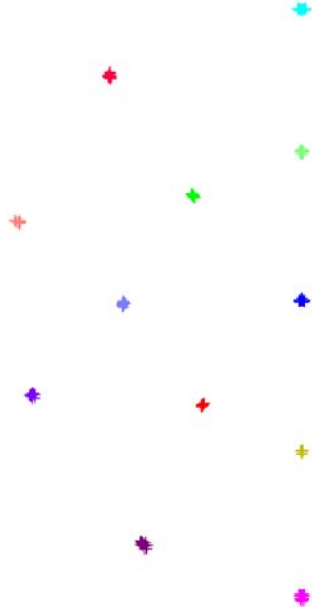


Fig. 7: **Spot diagram for SPST214** This diagram shows the locations where various rays from various stars in the field of view intersect the image plane at the detector. Only the left half of the image plane is shown, because the telescope is symmetric. Each point of intersection is shown with a cross. Note that the rays from a given star fall in a tight cluster. The stars are distributed over a one degree diameter field of view, which maps to a 200 mm diameter circle at the image.

technology is that the quality of the image at the detector plane is good enough to be used at Terahertz frequencies. The root-mean-square wavefront error at the detectors in this design is typically $50\mu\text{m}$. This error could be reduced a factor of ~ 2 by relaxing the quality of the image of the aperture at the Lyot stop, which in this design meets stringent requirements imposed by its use as a microwave background anisotropy instrument. A wavefront error of $50\mu\text{m}$ is totally unsuitable for use at visual wavelengths, which is why wide-field visual wavelength telescopes are not designed this way, but the design begins to be usable at $\lambda = 200\mu\text{m}$ and would work well at $\lambda = 350\mu\text{m}$. Providing it could be made, an appropriate Terahertz array could simply be substituted for the 150 GHz array currently being developed, and the optical system would work. At Terahertz frequencies, the 200 mm diameter image plane could accommodate tens of thousands of detectors.

V. Conclusion

The South Pole Telescope, which is nearing the end of its design phase, will have an optical configuration capable of feeding several $\times 10^4$ detectors at Terahertz frequencies. Such a detector array would be enormously powerful. Consider, for example, the problem of surveying an area of sky to find dusty protogalaxies. These are objects about

one second of arc across, with an areal density of several hundred per square degree at a brightness of a few mJy at $\lambda 350 \mu\text{m}$. The speed at which such objects can be found is proportional to

$$\frac{nAB}{T_{sys}^*{}^2},$$

where n is the total number of detectors (bolometer or heterodyne) in the telescope, A is the total effective collecting area (regardless of whether it is arranged in one dish or many), B is the pre-detection bandwidth, and T_{sys}^* is the effective system temperature adjusted for losses, atmospheric absorption and emission (Stark 2000).

Table 1: Estimated Survey Speed at $\lambda 350 \mu\text{m}$

<i>Telescope</i>	<i>n</i>	<i>A</i>	<i>B</i>	<i>T_{sys}[*]</i>	<i>Relative Speed</i>
SPT	20000	50 m ²	150 GHz	200 K	3750
ALMA	160	6400 m ²	4 GHz	300 K	46

Table 1 estimates the value of this figure of merit for the South Pole Telescope and for the Atacama Large Millimeter Array (ALMA), and shows that the SPT with a large bolometer array would be about 80 times faster than the ALMA at detecting objects in survey fields. Of course the ALMA has much higher angular and frequency resolution, and therefore shows a detailed picture. The SPT will be to the ALMA what a Schmidt camera is to a large visual-wavelength telescope—the means of detecting the objects to be studied. All that is needed is the technological development of large detector arrays.

I thank Nils Halverson, Adrian Lee, and William Holtzapfel for suggesting the use of a Silicon lens in the design. This material is based upon work supported by the National Science Foundation under Grant No. OPP-0130612.

VI. References

- Gildemeister, J., Lee, A., & Richards, P. 1999, *Appl. Phys. Lett.*, 74, 868
- . 2000, *Appl. Phys. Lett.*, 77, 4040
- Loewenstein, E. V., Smith, D. R., & Morgan, R. L. 1973, *Appl. Opt.*, 12, 398
- Stark, A. A. 2000, in *Proceedings of SPIE*, Vol. 4015, *Radio Telescopes*, ed. H. R. Butcher, 434
- Stark, A. A., Carlstrom, J. E., Israel, F. P., Menten, K. M., Peterson, J. B., Phillips, T. G., Sironi, G., & Walker, C. K. 1998, in *Advanced Technology MMW, Radio and Terahertz Telescopes*, Vol. 3357 (*Proceedings of SPIE*), 495–506, astro-ph/9802326

Influence of Temperature Variations on the Stability of a Submm Wave Receiver

A. Baryshev¹, R. Hesper¹, G. Gerlofsma¹, M. Kroug², W. Wild³

¹ NOVA/SRON/RuG

² DIMES/TuD

³ SRON / RuG

Abstract

Radio astronomy requires SIS mixers and receivers with very high stability. The goal for the total power stability of the ALMA receivers is 1×10^{-4} over 1 second. The SIS mixer is one of the most critical components in the receiver signal chain determining stability. Most changes in mixer noise and gain are due to variations of its operating conditions.

In this paper we present accurate measurements of SIS mixer noise and gain variations with respect to physical temperature, operating point and local oscillator power changes. We use an ALMA band 9 prototype waveguide mixer – developed at NOVA-SRON – working in the 600-720 GHz frequency range. Intermediate frequency coverage of this mixer is 4-11 GHz. A 4-12 GHz isolator was used between the mixer and IF amplifier. The physical temperature of the mixer was varied from 2.5 K to 6 K in steps of 0.05 K and the mixer parameters were measured. Based on our measurement data we provide an estimate (derivatives) of the influence of mixer operating temperature on gain and noise temperature for different LO frequencies.

Introduction

Normal mode of operation of a radioastronomical receiver is improving signal to noise ratio by integrating the output signal for a given time (integration time). If the noise sources in the receiver and in front of receiver are uncorrelated (white noise) the relative fluctuations of the receiver output scales with integration time and receiver bandwidth according to well known radiometer equation:

$$\frac{dP}{P} = \frac{1}{\sqrt{Bt}} \quad (1),$$

where B is detection bandwidth and t is integration time. Provisions are usually made to make receiver system as wide band as possible and allow for as long integration time as possible in order to be able to observe weak astronomical signals. For instance ALMA receivers will have at least 8 GHz Intermediate Frequency (IF) bandwidth. With such a bandwidth a relative stability of order of 10^{-5} can be achieved in theory by integrating only for one second.

A receiver output power is determined not only by receiver input signal, gain and noise but it is also determined by a receiver operating conditions. For SIS receiver such conditions are: bias point, Local Oscillator (LO) input power, magnetic field strength and

receiver physical temperature. Variation of receiver output power due to change in operating conditions may exceed variations due to noise signals given by equation (1) for a certain integration time. If that is the case further increasing of integration time will not lead to a signal to noise ratio improvement. More sophisticated techniques like correlation receiver or chopper calibrator are required for further improvement of quality of observations. These techniques allow to calibrate receiver parameters faster than change of a receiver environment and take this change into account. Receiver gain and noise temperature can have different sensitivity for change of different receiver operating conditions. It is instrumental to know this dependence in order to be able to design a receiver that could reach a required stability specification.

One of important operating condition of an SIS receiver is physical temperature. Since SIS technology is based on superconductivity one can intuitively expect that SIS mixer should be quite sensitive to temperature variations. One can also expect temperature variations of mixer block in modern cryogenic systems based on closed cycle refrigerators. By the nature of operation these systems produce a temperature variations on the same scale of several Hertz. In this work we investigate experimentally how gain and noise of SIS receiver change with respect to small variations of the mixer block temperature. For doing this, mixer parameters were measured while mixer temperature was varied with small steps of 0.05 K from 2.6 K to 6.4 K in our laboratory system. This allows us to determine differential sensitivity of output power P , dP/dT for any given operating temperature T with high accuracy. Measurements were done for Nb-AlO_x-Nb type SIS mixer in the frequency range of 600-720 GHz.

Experimental setup and mixer block

A photograph of an experimental setup used in experiment is shown in figure 1. An

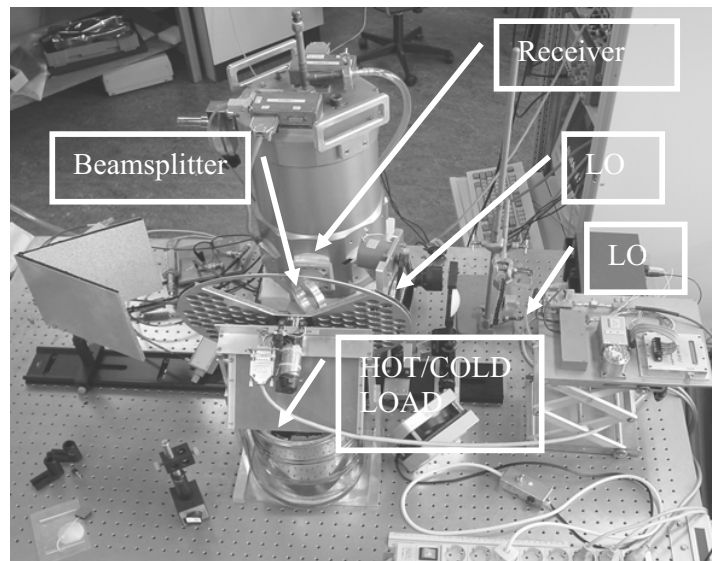


Figure 1. Photograph of experimental setup.

ALMA prototype local oscillator was used to pump an SIS mixer. This LO includes: several high frequency amplifier and multiplier components which result in approx 50 micro watts output power in 600-680 GHz frequency range with total multiplication of 45. A Rohde & Schwartz SR20 synthesizer in the range of 13-15 GHz was used at the input of this LO chain. LO power level was regulated by means of changing the angle of rotation of a wire grid inserted into LO beam. Grid was rotated under angle of 30 degrees to avoid standing waves in LO path. The position of the grid with respect to an LO polarization vector was controlled by an encoder allowing for automatic adjustment of SIS mixer pumping level.

LO power was coupled into receiver signal path by means of 12 micron thick Mylar film beam splitter. It provides about -10 dB LO power coupling to a mixer.

A two level: liquid nitrogen cold load (80 K) and 300 K warm loads were used in the signal path for measuring receiver gain and noise. These loads can be switched also by means of computer allowing fully automated operation.

A standard Infrared Laboratories liquid helium cryostat was used to provide a cryogenic environment. Since liquid helium was used as cryogen the temperature stability of this cryostat was expected to be much better than stability of close cycle refrigerator.

An SIS mixer block (see figure 2) was mounted on 4 K plate of cryostat. Stainless steel washers were used between dewar bottom and mixer block to increase heat resistance to allow temperature regulation. In addition stainless steel bolts were used to attach mixer to a cold stage. A 500 Ohm resistive heater was mounted close to the bottom of the mixer block to be able to heat mixer block up. A semiconductor diode thermometer from Lake

Shore was mounted on top of the mixer block for accurate temperature measurement. A temperature constant of order of 2 seconds was observed when mixer was heated and then cooled by switching voltage through heater resistor. Temperature of the dewar cold plate can be decreased by pumping on He bath. The typical end pressure of helium vapour was about 20 mBar. Lake Shore temperature controller type 330 was used for temperature read out and stabilization. Note that this PID type controller allows for high temperature stability. The temperature resolution of this controller is 0.01 K. It was possible to reach any temperature in the range of 2.5..20 K under conditions of this experiment.

An NRAO 4-12 GHz three stage HEMT amplifier [1] in combination with 4-12 GHz Pamtech isolator [2] was used in this measurement as an IF chain. Amplifier and isolator were firmly connected to the dewar cold plate keeping the temperature constant

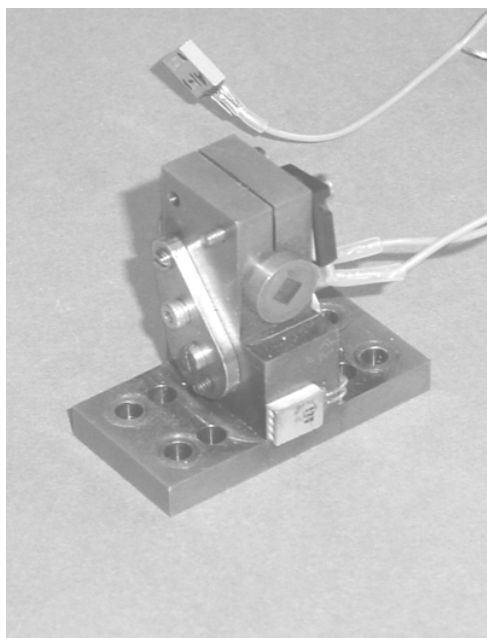


Figure 2, Photograph of SIS mixer block

throughout whole experiment. Outside of the dewar this chain was followed by two MITEQ wide band amplifiers followed by an electronically tunable YIG filter (50 MHz band pass). The central frequency of that filter was also controlled by a computer.

An ALMA band 9 mixer prototype was used in this experiment. This is a waveguide type mixer based on standard Nb-AlO_x-Nb tunnel junction technology. Junctions were produced at DIMES laboratories in TU Delft. RnA product for this junction is about 35 and normal state resistance is about 36 Ohm. Junctions quality factor is about 20 and depends on physical temperature. An integrated microstripline tuner was used to compensate junction's capacitance at the frequency of operation and match it to an input waveguide. Nb was used as conduction material and SiO₂ was used as insulator. Note that gap frequency of Nb (~690 GHz) is close to the frequency of operation of the receiver. Since this frequency scales with gap energy of Nb which depends on the temperature we expect that mixer can be more sensitive for physical temperature variations at higher part of the band. Details of the mixer design can be found in [3-4].

Measurement results and discussions

Measurements were performed for several LO frequencies in 600-720 GHz range. For each LO frequency optimum parameters of receiver were determined giving the best noise temperature. These parameters are: bias point, LO power and intermediate frequency. The Josephson current noise was suppressed for the lowest temperature of operation if 2.6 K. After optimization the temperature of mixer block was varied with the steps of 0.05 K while keeping LO power level and magnetic field current and intermediate frequency constant. A mixer current/voltage and mixer output power/voltage dependences were recorded for both ambient (300 K) and liquid nitrogen (80 K) loads. This was automatically repeated for each temperature steps till 6.5 K temperature was reached.

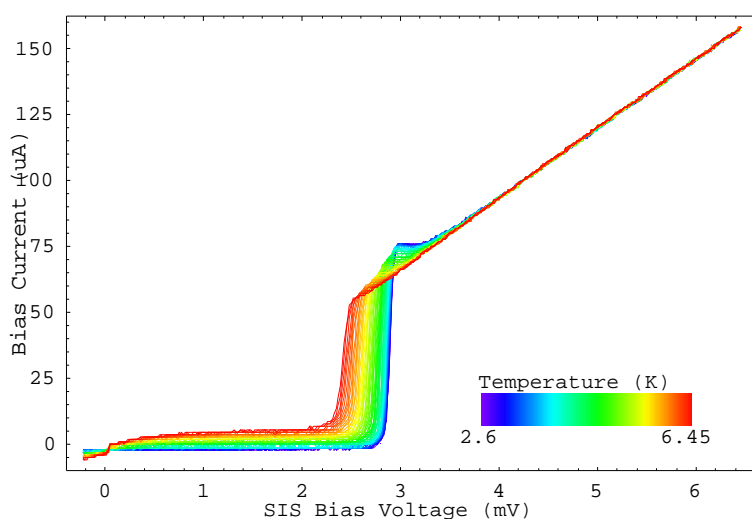


Figure 3, Measured unpumped SIS junction I-V characteristics for different mixer block temperatures

In addition, an “unpumped” I-V characteristics were measured for each temperature as well. Measured “unpumped” I-V characteristics are shown in figure 3 for different ambient temperatures. One can see that both junction's gap voltage and quality factor decreases when temperature increase. One can expect from mixer theory that mixer gain will decrease and mixer noise will

increase when ambient temperature is higher. One can also observe significant increase of leakage current. The junctions critical current, that was suppressed to zero at 2.6 K, becomes visible for higher temperatures. In contrast, the normal resistance of the junction stays independent on temperature for a given temperature range.

The typical data set for LO frequency of 630 GHz is shown in figure 4 for 300 K input and in figure 5 for 80 K receiver input respectively. As expected the receiver output

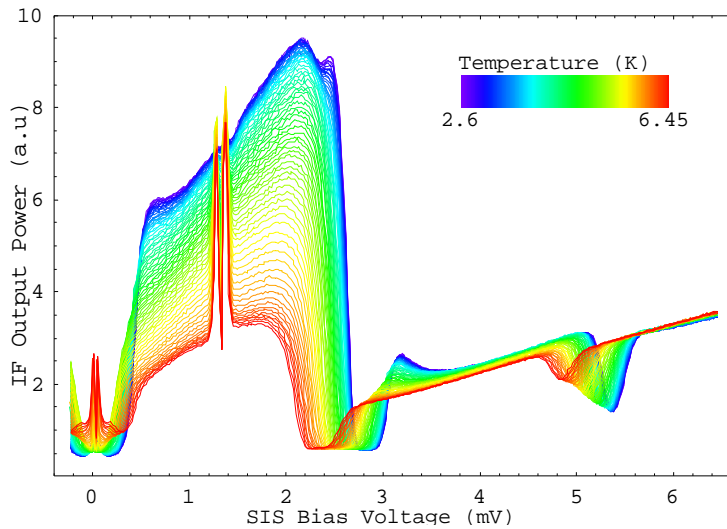


Figure 4, Measured Pumped SIS junction IF output powers for different mixer block temperatures. LO Frequency is 630 GHz. Innut signal is 300 K

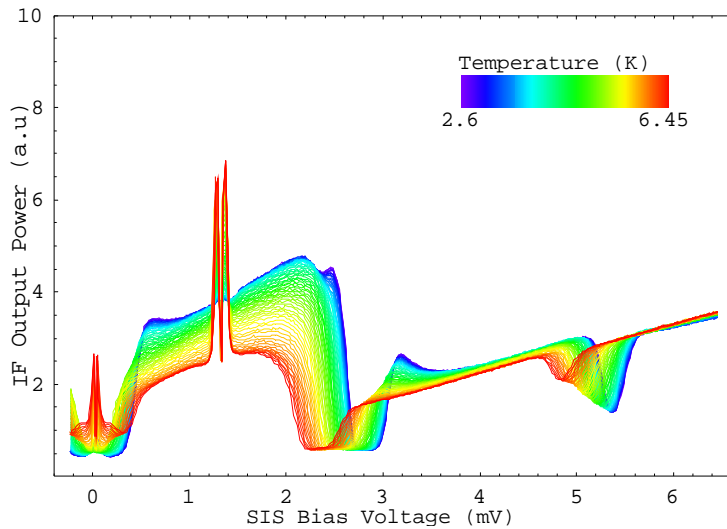


Figure 5, Measured Pumped SIS junction IF output powers for different mixer block temperatures. LO Frequency is 630 GHz. Innut signal is 80 K

power decreases when temperature increases.

A strong dependence of Josephson noise peak at approximately 1.15 mV bias voltage is observed. Despite of the good suppression at lower temperature one can observe a strong Shapiro step at higher temperatures. This creates additional temperature instability of receiver parameters in vicinity of Josephson steps.

Mixer gain can be obtained from the data in figure 4,5 by subtracting curves corresponding to the same physical temperature. The receiver noise temperature can be calculated from the same data by using Y-factor method. Resulting graphs are presented in figure 6,7 for receiver gain and noise temperatures respectively.

The observed mixer gain variation is quite strong especially in the range 5..6 K operating

temperatures. The same is true for receiver noise temperatures. By fixing a certain bias voltage we can obtain dependences of receiver gain and noise temperatures from physical temperature at different bias conditions. This data is presented in figure 8 a),b). Note that at 4 K physical temperature (ALMA receiver operating point) the bias point of 2.4 mV is the most unstable point both for gain and for noise temperature. However, at the same bias point receiver has the best noise temperature. We can conclude that for the most stable operation of receiver we can not choose bias points close to the gap voltage of SIS junction due to strong temperature dependence. For real operation a compromise should

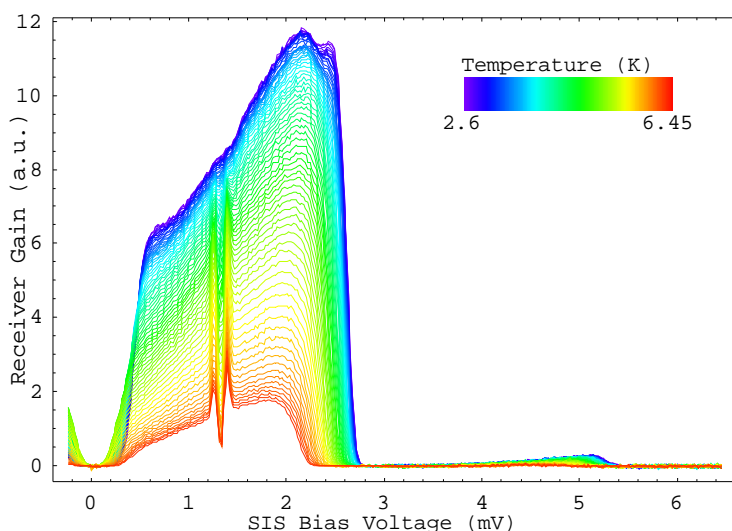


Figure 6, Measured SIS receiver gain for different mixer block temperatures. LO Frequency is 630 GHz

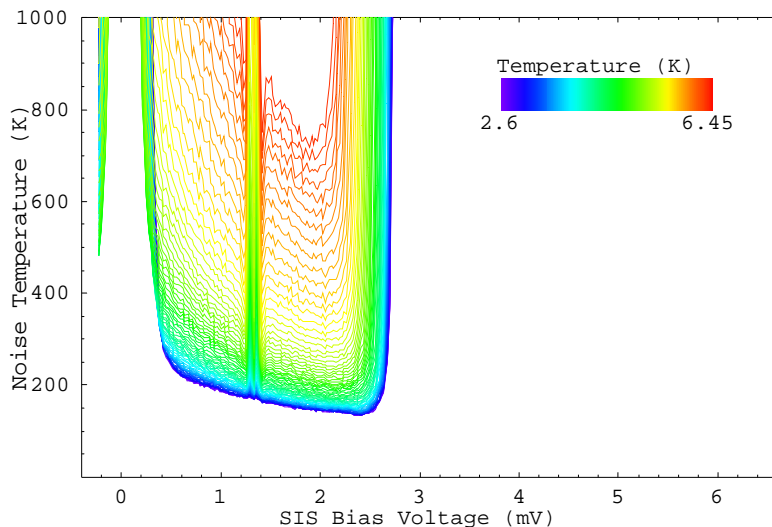


Figure 7, Measured SIS receiver noise temperature for different mixer block temperatures. LO Frequency is 630 GHz

be made between receiver noise temperature and receiver stability.

The most interesting parameter for receiver operation is total power stability. It can be given by following equation:

$$P = (T_s + T_i) \cdot G \quad (2)$$

where T_s is system noise temperature, T_i is receiver input signal and G is receiver gain. We assume further that typical value of input signal $T_i = 80$ K corresponds to an approximate value of atmospheric noise for a 600 - 720 GHz atmospheric window at ALMA site. We also assume that T_i does not depend on receiver temperature when taking derivatives.

Total output power dependencies are presented in figure 8 c). It demonstrates the same principle behavior as noise temperature and gain curves.

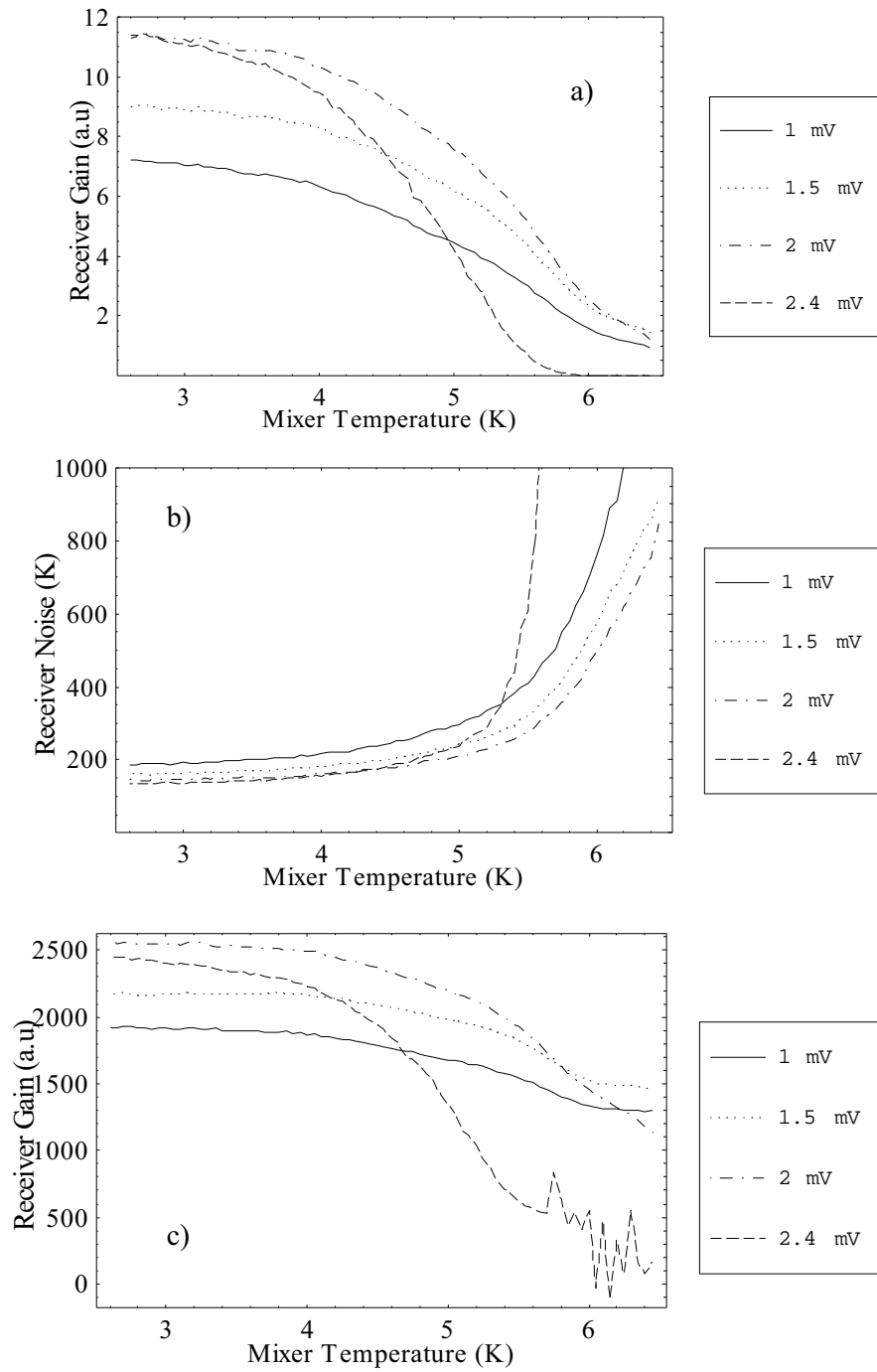


Figure 8, Receiver gain a), receiver noise temperature b) and total output power c) dependence for different bias voltages. LO frequency is 630 GHz. Input signal 80 K.

In order to represent how relative total power stability $\Delta P/P$ relates with the mixer's physical temperature stability ΔT we calculate the following quantity $S(T_i, T) = \frac{dP}{dT} / P$.

The relative receiver stability that we can expect for physical temperature stability ΔT can be expressed as: $\Delta P/P = S(T_i, T) \Delta T$. Graphs for parameter S calculated assuming different bias voltages and input signal $T_i = 80$ K are presented in figure 9. Using this graph we can estimate, that, for reaching relative stability of 10^{-4} over 1 second, absolute temperature stabilities of 2 mK and 0.5 mK are required for bias points of 2 mV and 2.4 mV respectively (mixer temperature is 4 K).

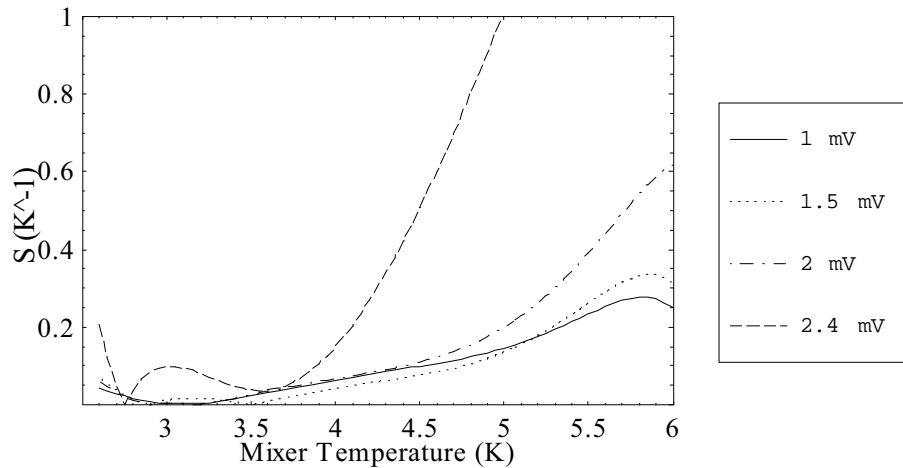


Figure 9. Parameter $S(T_i, T) = \frac{dP}{dT} / P$ calculated for different bias voltages assuming $T_i = 80$ K. LO frequency 630 GHz.

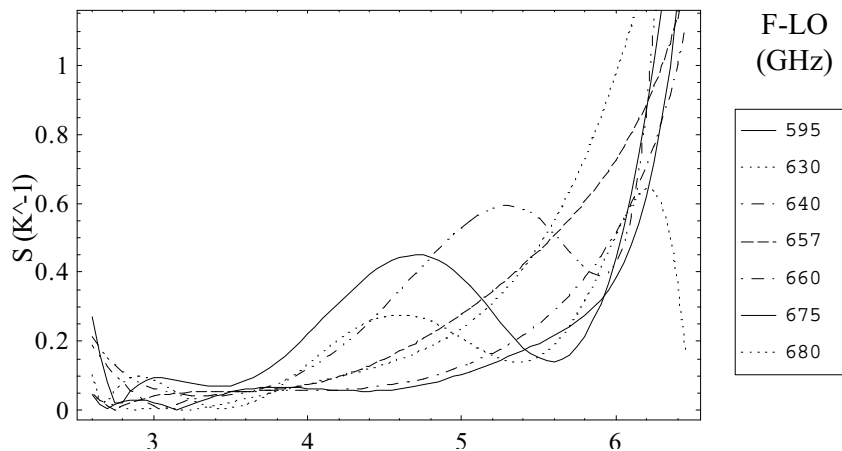


Figure 10. Parameter $S(T_i, T) = \frac{dP}{dT} / P$ calculated for bias voltage of 2.1 mV, assuming $T_i = 80$ K. for different LO frequencies.

The same general trends in receiver stability were observed at different LO frequencies as data was taken. To summarize these measurements, we present parameter S calculated for bias voltage 2.1 mV for different LO frequencies in figure 10. Mixer sensitivity to temperature variations increases as the LO frequency approaches Nb gap frequency (for temperatures 4-5 K).

Conclusion

We have performed detailed measurements of receiver noise and gain with respect to SIS mixer physical temperature for several LO frequencies in ALMA band 9 (600-720 GHz). It was found experimentally that bias point, corresponding the best noise temperature, is about 4 times less stable assuming the same mixer physical temperature variations. A parameter $S(T_i, T) = \frac{dP}{dT} / P$ was estimated from measurements. This parameter allows to connect relative total power stability with absolute temperature stability by following formula: $\Delta P/P = S(T_i, T) \Delta T$. It was found, that, for reaching relative stability of 10^{-4} over 1 second, absolute temperature stabilities of 2 mK ... 0.5 mK are required for bias points 2.1 mV for different LO frequencies at physical temperature of 4 K.

Acknowledgement

Authors would like to thank E. Lauria from NRAO for support. This work is carried out as part of ALMA band 9 development and European Union program FP6 "Radionet".

References

- [1] Lauria, E.F., *et al.*, "A 200-300 GHz SIS Mixer-Preamplifier with 8 GHz IF Bandwidth," ALMA memo #378, <http://www.alma.nrao.edu/memos/html-memos/alma378/memo378.pdf>
- [2] PamTec, Passive Microwave Technology Inc, 4053 Calle Tesoro, Suite A, Camarillo, CA 93012
- [3] Baryshev *et al.*, "Development of a 0.6 THz SIS Receiver for ALMA", Proc of 12th Int. Symp. on Space Terahertz Technology, pp. 581-591, 2001
- [4] Baryshev *et al.*, "Fixed-tuned waveguide 0.6 THz SIS Mixer with Wide band IF", Proc of 13th Int. Symp. on Space Terahertz Technology, pp. 1-9, 2002

Quasiparticle mixing and Josephson electrodynamics in non-uniform parallel junction arrays

F. Boussaha, M.Salez, Y.Delorme, F. Dauplay, A. Feret, K. Westerberg, B. Lecomte

LERMA, Observatoire de Paris, 77 avenue Denfert-Rochereau, 75014 PARIS

Multijunction arrays represent an attractive alternative to single junction SIS mixer devices to provide wideband heterodyne mixers, without the complication of high current density. We have designed such 5-junction arrays to operate in the 460-650 GHz bandwidth.. Our FTS (Fourier Transform Spectroscopic) and heterodyne measurements performed on arrays of 1- μm^2 junctions with current densities ranging from 4 to 13 kA/cm², confirm the bandwidth improvement brought by the multijunction arrays combined with a high mixer sensitivity. We also investigated the static and dynamical states of the Josephson tunnel current in these arrays. The presence in I - V curves of resonant zero-field steps (ZFS), usually observed in long Josephson junctions (LJJ), indicates the occurrence of fluxon motion, and allows to foresee new applications for these devices, not only as mixers but as submillimeter-wave LO sources.

Investigation of the performance of a 700 GHz nline mixer

P. Grimes^a, P. Kittara^a, G. Yassin^a, S. Withington^a and K. Jacobs^b

^aCavendish Laboratory, Madingley Road, Cambridge, UK.
Email:p.grimes@mrao.cam.ac.uk

^bKOSMA, I Physikalisches Institut, University of Cologne, Cologne, Germany

Abstract

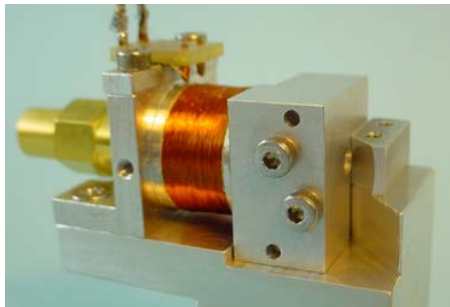
We report the successful operation of an SIS nline mixer at frequencies above and below the superconducting gap of Nb. The mixer is fed by an antipodal nline taper deposited on a quartz substrate in one piece with the Nb-AlO_x-Nb tunnel junction and Nb tuning circuitry. RF power is coupled to the waveguide mounted nline mixer chip via a Pickett-Potter horn-re-ector antenna and the mixer is tuned by a novel three-stage Chebyshev lter and radial stub tuner. We describe the design and testing of the mixer between 640 and 710 GHz, paying particular attention to the evaluation of conduction losses in the nline chip, and the prediction of the conversion gain of the mixer. Our results show that nline mixers can have good performance both above and below the superconducting energy gap.

Introduction

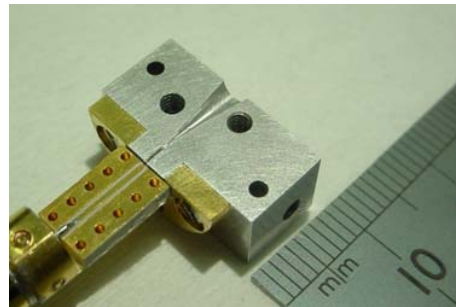
We have previously reported the successful operation of nline based mixers at 230 GHz[1] and 350 GHz[2], and the preliminary testing of a nline based mixer at 700 GHz[3]. We have achieved mixer performance comparable to that of conventional waveguide mixers at low frequencies, but our previous 700 GHz mixer's performance suffered from poor conversion gain, mainly because the particular device tested was tuned above the band of our LO source.

The nline design offers a number of bene ts over more conventional designs, including:

- High performance, wide bandwidth mixer feed



(a) Mixer block assembly, with reflector and mouth of horn on right side.



(b) One half of the mixer block, showing Potter horn and IF CPW.

Figure 1: The aluminium split mixer block.

- Simplified mixer block design, as no backshort is required
- Easier handling of the large mixer chip

the latter two of which are particularly pronounced for high frequency designs. In fact, once the RF signal is connected to the microstrip, the mixer is unaffected by changes in, or removal of the surrounding mixer block. The large chip and lack of mechanical tuning also allows the fabrication of devices with integrated RF circuitry such as on-chip image separation circuits[4] and also back-to-back nlines for interferometric operation and on-chip LO coupling, a design we are already testing at 350 GHz[5].

The nline mixer design necessarily includes a length of superconducting transmission line between the mixer feed and the SIS tunnel junction. At frequencies above the superconducting gap, conduction losses in this line will degrade the performance of the mixer. A nline mixer fabricated from a single superconducting material will only work well above the superconducting gap if these losses are small. Although the losses in many transmission lines can be rigorously calculated, most of this transmission line is part of the nline taper, the losses of which cannot easily be analysed by any one rigorous technique. Conventional waveguide probe mixers are also degraded by conduction losses in their superconducting transmission lines and tuning circuits, but it is not clear whether an all-Nb nline mixer can achieve similar or better performance than an all-Nb waveguide probe design above 700 GHz.

Mixer Design

The 700 GHz mixer described here is fed by a Pickett-Potter horn-receptor antenna, a design which ensures a low side-lobe level and high directivity beam, while simplifying mixer block machining[6, 7]. The mixer chip itself comprises an antipodal nline taper, superconducting microstrip, an SIS Nb-AlO_x-Nb tunnel junction and a three-stage, Chebyshev section tuning circuit. The mixer chip is held within slots machined into the sides of the split aluminium mixer block waveguide so that the tip of the nline taper protrudes into the throat of the horn. The mixer chip also has niobium corrugations deposited as part of the nline structure to prevent RF power leaking into the slots holding the chip.

The mixer's IF output is taken from bonding pads on the chip by 50 μ m bond wires connected to a ground-backed co-planar waveguide, leading to an SMA connector. The IF signal is then passed through an isolator before being amplified by a cryogenic amplifier, with a noise temperature of 6 – 8K across a 4 GHz band centred at 4 GHz.

PPHR Antenna

The mixer described in this paper is fed by a Pickett-Potter horn-receptor (PPHR) antenna, a design chosen to avoid the complexity of machining the large number of deep, narrow grooves required for a corrugated horn at 700 GHz. The Pickett-Potter horn is a dual mode feed employing a single step discontinuity at the throat of a conical horn to excite a small fraction of the TM_{11} mode, in combination with the dominant TE_{11} mode. The horn length and the radii at the step are chosen such that the aperture fields become plane-polarised, similar to the field of a corrugated horn at the design frequency. The circular waveguide feed of the PPHR is gradually transformed to the 320 μ m \times 160 μ m rectangular waveguide holding the mixer chip.

We have previously shown[3], using modal matching simulations and experiment, that this design gives similar performance to a corrugated horn-receptor antenna over at least a 15% band (corresponding to a 100 GHz band for a 700 GHz centred feed). In particular, we have used a previous nline mixer chip within the mixer block as an SIS direct detector to make direct measurements of the mixer's beam pattern and cross polarisation levels.

Inline Taper

Radiation from the PPHR antenna is coupled to the mixer chip via an antipodal nline taper, embedded in the waveguide at the throat of the horn. The ns form the base and wiring layers of the tunnel junction and are fabricated from 310nm and 400nm thick Nb respectively, separated in the region of overlap by 400nm of SiO. The whole of the mixer chip structure is deposited on a 60 μ m quartz substrate, which has a point extending along the waveguide to provide a smooth transition from empty waveguide to waveguide with

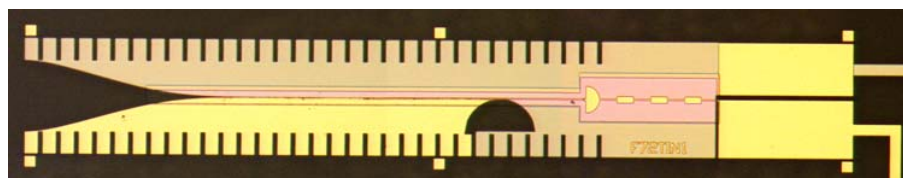


Figure 2: A 700 GHz nline mixer chip. RF signal enters the chip from the left and IF and Bias connections are on the right.

a dielectric across the centre. At the throat of the horn, the nline acts as a unilateral nline, with an impedance of several hundred Ohms. As the ns converge, the impedance is gradually reduced to approximately 50Ω at the point where the ns overlap. Beyond this point, the width of overlap is gradually increased, and when the width is large enough that the fringing effect can be ignored, a transition to 20Ω , $3\mu m$ microstrip takes place. Once the ns begin to overlap, the elds are con ned to the planar structure, and so are insensitive to the waveguide geometry. The only accurate machining required in the mixer block, apart from the horn, is the slot which holds the substrate within the waveguide. We have previously reported theoretical methods for the synthesis of nline tapers, and have successfully used these to design feeds for 230 GHz and 350 GHz mixers[1, 2].

Tuning Structure

Good mixer performance requires ef cient tuning of the junction capacitance over design bandwidth of the mixer. In our previous designs, at lower frequencies, we have employed single $\lambda/4$ end-loaded stubs for this purpose. At higher frequencies this design is less attractive as the stub length becomes comparable to the junction dimensions, and may also be strongly affected by fabrication tolerances. Consequently we have investigated an alternative tuning mechanism based on a three-stage Chebyshev section and a half moon radial stub RF choke.

Initial design was carried out in a lumped element model using Agilent Design Studio to optimise the length and characteristic impedances of the four microstrip elements of the tuner to give the maximum return loss. However, veri cation of the resulting design using Sonnet Software Inc.'s "em Suite" software gave signi cantly different tuning to the lumped element model. This is to be expected as two of the three microstrip sections are substantially wider than they are long, and so the two dimensional nature of the currents in the step regions must be considered. The closeness of these steps in microstrip width also make it dif cult to obtain the low impedance required for the middle section, thus limiting the bandwidth of the mixer. Further design work was carried out wholly within Sonnet.

The last section of the tuning structure (nearest to the junction) is only $7\mu m$ long. The

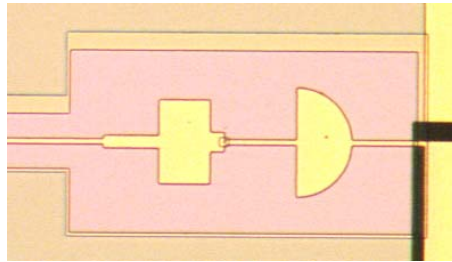


Figure 3: The microstrip tuning structure used on this mixer. RF signal enters down the left hand microstrip and IF signal leaves from the right.

effective length of this section may therefore be altered by fabrication tolerances. Tests in Sonnet with the junction misplaced by up to $0.5\mu m$ have shown significant changes in tuning. However, fabrication tolerances on the junction's characteristic impedance give even greater shifts in tuning.

Device Fabrication

The mixer chip was manufactured by KOSMA, University of Cologne on $200\mu m$ Infrasil quartz. The chip was fabricated in five steps:

- Sputtering of Nb-AlO_x-Nb trilayer ($200nm$, $10nm$ and $100nm$ thickness respectively), and lift-off to form the lower line and ground plane for the tuning circuit
- Junction definition lithography and reactive ion etching of upper Nb layer of trilayer
- Evaporation of first $200nm$ SiO insulation layer
- Evaporation of second $200nm$ SiO insulation layer
- Sputtering of $400nm$ Nb wiring layer and upper line, with $30nm$ Au protection layer

Two insulation layers are used to allow reliable contact to the junction while achieving the low impedances necessary for the three stage tuning structure. Before mounting in the mixer block the chip is diced to size, the point is diced on the substrate at the mouth of the line, and the chip is thinned from $200\mu m$ to $60\mu m$.

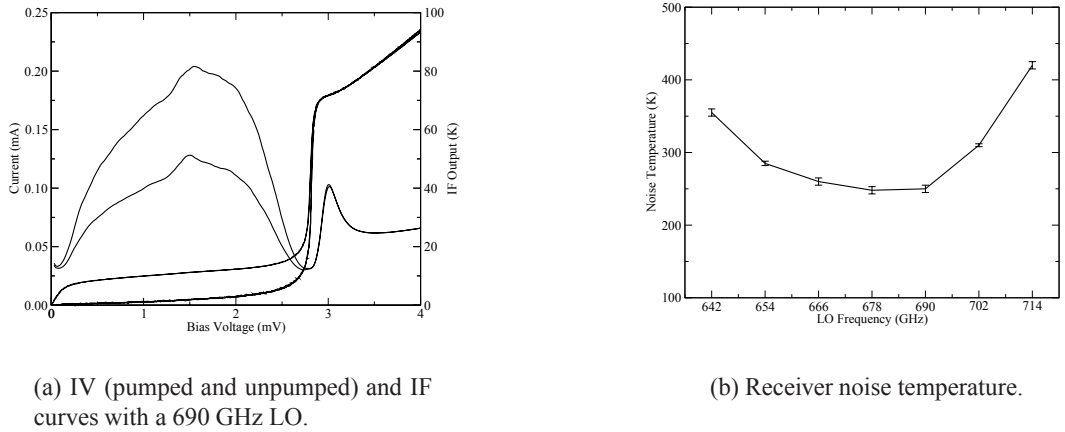


Figure 4: Hot-Cold load mixer test results at 2.5 K.

Results

The particular chip used for these mixer tests was selected on the basis of the Fiske resonance shown by the device during initial dipstick testing, and relatively low leakage current. The voltage biased I-V curve obtained during these tests showed a Fiske resonance at 1.43 ± 0.02 mV, equivalent to 690 ± 10 GHz, with a gap voltage of 2.78 mV, equivalent to 672 GHz.

Mixer tests were carried out at a physical temperature of 2.5 K, achieved by pumping He vapour out of the dewar to reduce the vapour pressure to ~ 200 mBar. Lower temperatures can be achieved with this system, but the performance of the IF amplifier was found to degrade on reducing the temperature to ~ 2.2 K. At 2.5 K the gap voltage of the device was increased to 2.82 mV, equivalent to 682 GHz.

The mixer was tested with a Gunn diode LO using a doubler-tripler multiplier chain, with LO power injected by way of an $8.5\mu\text{m}$ mylar beamsplitter. This LO scheme provided sufficient power to pump the mixer between 642 GHz and 714 GHz. In fig. 4(a), we show the DC response of the mixer, both with and without LO power at 690 GHz, as well as the hot and cold load IF output powers. DSB receiver noise temperatures (fig. 4(b)) were measured by the Y-factor method giving a best receiver noise temperature of 250 K, and the mixer conversion gain was calculated (fig. 5(a)), after calibrating the IF output power using the method of Woody.

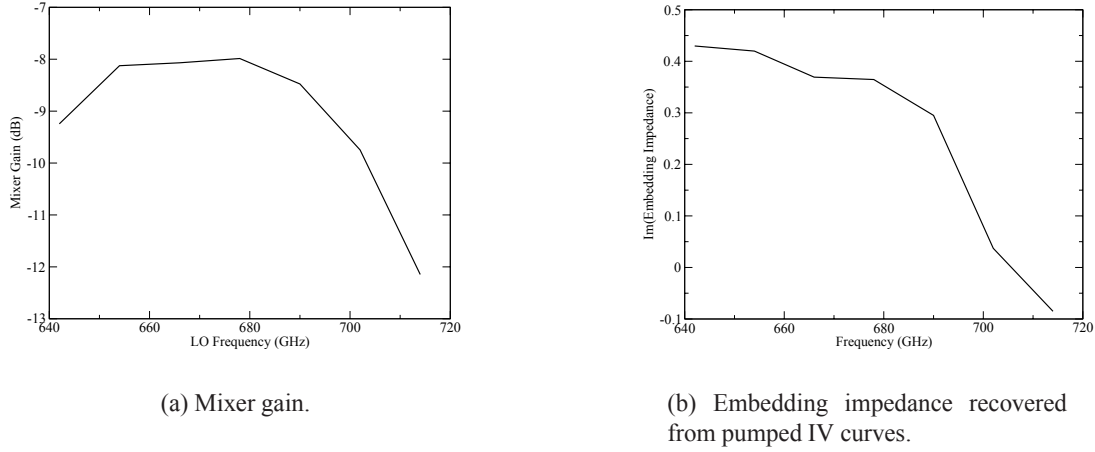


Figure 5: Mixer conversion gain and junction embedding impedance calculated from mixer test results.

Device Tuning

The embedding impedance seen by the tunnel junction greatly affects the gain of a SIS mixer, and is responsible for the tuning of the mixer. In order to accurately simulate the gain and tuning of the mixer we have attempted to recover the embedding impedances and LO pump levels by matching the pumped IV curve calculated from the unpumped IV curve to the measured pumped IV curve[7]. The calculation of the pumped IV curve is based on our recently reported nonlinear mixer theory[9], with the embedding impedance and LO pump power being varied by a downhill simplex algorithm, until the best match to the measured pumped IV curve is found.

The recovered imaginary part of the embedding impedance is shown in g. 5(b), and indicates that the mixer is tuned just above 702 GHz. This agrees well with the position of the Fiske resonance.

Simulations

The nonlinear mixer theory, mentioned above, can be used with the embedding impedance results and the measured unpumped IV curve to simulate the gain of the mixer. In order to get results that are comparable with the experimental results we must take into account the losses in the receiver optics and RF circuitry. For frequencies above the superconducting gap (682 GHz) we expect considerable conduction losses from the large amount of Nb transmission line between the mixer feed and the tunnel junction. This is in addition to effective losses due to re ection from the tuning structure at frequencies where there is an

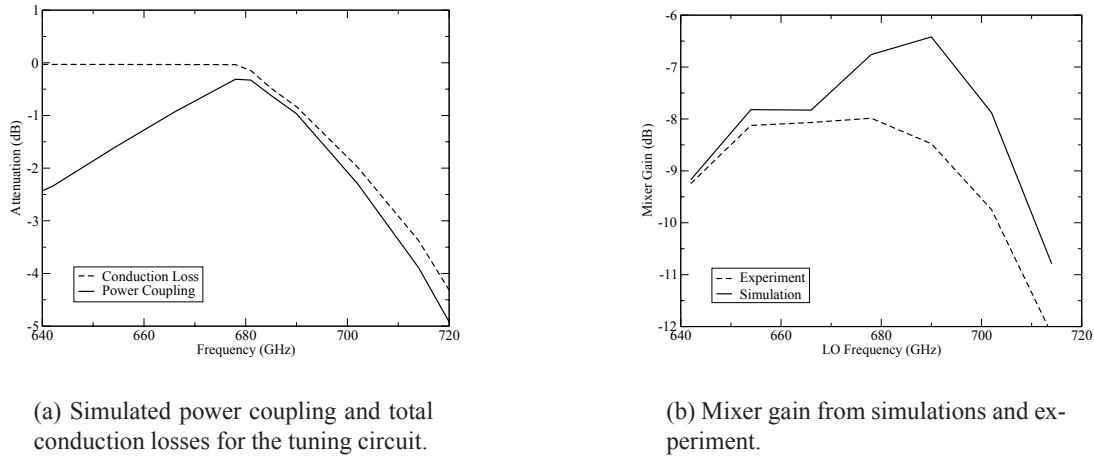


Figure 6: Results of simulations of the tuning circuit and mixer gain simulations.

impedance mismatch.

In order to obtain values for both of these contributions to the RF losses, we have simulated the tuning circuit using “em Suite”, a method of moments planar circuit simulator. The simulated circuit included the tuning structure, RF choke and $300\mu m$ of microstrip that connects the nline taper to the tuner, as well as an extra $250\mu m$ of $3\mu m$ microstrip to account for the loss of the nline taper. The surface impedance and conductivity of the niobium used in the circuit was calculated from Mattis-Bardeen theory[10], and an effective junction capacitance of 85 fF was used.

The results from “em” show that the best power coupling to the junction is achieved at 680 GHz, with a loss of -0.3 dB, which increases rapidly on either side of this point, due to poor impedance match on at lower frequencies, and increasing conduction losses at higher frequencies. The portion of the *available* power (after conduction losses) coupled to the tunnel junction is greatest at 690-702 GHz, in agreement with the embedding impedance results above.

The losses in the beamsplitter and $650\mu m$ polythene dewar window were calculated as 0.2-0.4 dB across the LO band using the methods of Goldsmith[11] and subtracted from the simulated gain. An IR lter is also present in the optical path which will give some losses, as will any re ections from the horn and nline taper, although these should be small at 700 GHz, the design frequency of the mixer feed.

The simulated values of the gain agree well with the experimental results at frequencies below the gap, while there is a difference of 1-2 dB above the gap. This difference is probably attributable to an underestimation of the conduction losses in the circuitry. Well below the gap, the conversion gain is fairly low, mainly as a consequence of the narrow

tuning of the mixer.

Conclusions

We have designed and tested an all Nb nline SIS mixer over the frequency range 640-710 GHz, fed by a Pickett-Potter horn re flector antenna.

We have been able to recover the embedding impedance and LO power levels of the mixer from experimental data using a fully nonlinear mixer theory, and then used this theory to accurately the conversion gain of the mixer. The predicted and measured gains, which have a typical value of -8 dB, agree very well below the superconducting gap, and within 1-2 dB above the gap. The ability to predict the gain is a key factor in improving the performance of future mixers.

The best measured receiver noise temperature of ~ 250 K was obtained just above the superconducting gap, and is comparable to results published in the literature for more conventional all-Nb waveguide probe mixers[12].

The performance of this mixer con rms that nline mixers perform well at frequencies around the superconducting gap. In combination with the excellent results we have recently obtained using a 350 GHz back-to-back nline receiver as both an interferometer and a mixer where the LO and signal are combined on the chip after being fed by separate nlines, we believe that it should be feasible to make complicated integrated receivers, such as side-band separating mixers, at frequencies at least as high as 700 GHz. As part of our development of nline mixers we are testing devices with the niobium ns replaced by aluminium, in order to understand the losses better. This work will also allow the use of alternative, higher gap superconducting materials while still using Nb-AlO_x-Nb junctions. In combination with the simpli ed fabrication of the Pickett-Potter horn and nline mixer blocks over corrugated horns and waveguide probe mixer blocks, this work should allow complex nline mixers to be designed at frequencies above the superconducting gap.

References

- [1] G. Yassin, R. Padman, S. Withington, K. Jacobs and S. Wulff, "A broad band 230 GHz nline mixer for astronomical imaging arrays", *Electron. Lett.* Vol. 33, pp. 498-500, 1997.
- [2] G. Yassin, S. Withington, K. Jacobs and S. Wulff, "A 350 GHz SIS antipodal nline mixer", *IEEE Trans. Microwave Theory Tech.*, Vol. 48, pp. 662-669, April 2003
- [3] G. Yassin, P. Kittara, P. Grimes, S. Withington, K. Jacobs, "A 700 GHz Finline Mixer with Three Stage Stub Tuning", *SPIE Conference on Astronomical Telescopes and Instrumentation*, SPIE, 2002.

- [4] A.R. Kerr and S-K. Pan, "Design of planar image separating and balanced SIS mixers", in Proc. 7th Int. Symp. Space Terahertz Tech. (Charlottesville, USA). pp. 207-219, March 1996.
- [5] S. Withington, E. Campbell, G. Yassin, C. Y. Tham, S. Wulff and K. Jacobs. "Beam-combining superconducting detector for submillimetre-wave astronomical interferometry", *Electron. Lett.*, Vol. 39, pp.605-606, April 2003.
- [6] P. Kittara, G. Yassin, S. Withington and H. Smith, "A Pickett-Potter horn-re ector antenna for submillimetre-wave applications", *Proc. 11th Int. Symp. Space Terahertz Tech. (Michigan, USA)*, pp. 598-606, May 2002.
- [7] P. Kittara, "The development of a 700 GHz SIS mixer with Nb nline devices: non-linear mixer theory, design techniques and experimental investigation", Thesis. Cambridge University, 2002.
- [8] D. Woody, R. E. Miller and M. J. Wengler, "85-115 GHz receivers for radio astronomy", *IEEE Trans. Microwave Theory Tech.*, Vol. 33, pp. 90-95, Feb 1985.
- [9] S. Withington, P. Kittara, G. Yassin, "Multitone quantum simulations of saturating tunnel junction mixers", *J. Appl. Phys.*, in press.
- [10] D. Mattis and J. Bardeen, "Theory of the anomalous skin effect in normal and superconducting metals", *Physical Review*, Vol. 111(2), pp. 412-417, 1958.
- [11] Paul F. Goldsmith, "Quasi-optical Systems: Gaussian Beam Quasi-optical Propagation and Applications" *IEEE Press, MTTTS*, 1998.
- [12] J. Kooi, C. Walker, H. LeDuc, P. Schaffer, T. Hunter, D. Benford and T. Phillips, "A low noise 665 GHz SIS quasi-particle waveguide receiver", *Int'l J. IR and MM Waves*, Vol. 15(3), pp. 477, 1994.

MEASUREMENT OF GAIN COMPRESSION IN SIS MIXER RECEIVERS

A. R. Kerr¹, J. Effland¹, S.-K. Pan¹, G. Lauria¹,
A. W. Lichtenberger² and R. Groves¹

¹National Radio Astronomy Observatory*
Charlottesville, VA 22903

²University of Virginia
Charlottesville, VA 22904

ABSTRACT

When an SIS mixer is partially saturated by broadband noise, it continues to exhibit a linear response to a small CW test signal, with the small-signal gain depending on the level of the saturating noise. This allows the CW test signal to be used as an indicator of the receiver gain in the presence of high-level noise. If not taken into account, gain compression can be a significant factor limiting the accuracy of high precision radio astronomy instruments.

Keywords: Superconductor-Insulator-Superconductor mixers, saturation, gain compression, dynamic range

INTRODUCTION

The Atacama Large Millimeter Array (ALMA) is striving to achieve an absolute flux measurement accuracy of 1%. Plambeck [1] has pointed out that gain compression (saturation) in SIS mixer receivers is likely to be a significant factor limiting the measurement accuracy. In this paper, we report measurements of the saturation of an SIS receiver in the 230 GHz band and show that in this band the thermal noise from a room temperature black body source is sufficient to produce ~ 1% gain compression in a mixer with four junctions in series.

At the 2002 Space Terahertz Technology Symposium we described a method for calculating the gain compression in an SIS mixer with a broadband noise input [2]. It was noted that, even when partially saturated by a high-level noise signal, the response of an SIS mixer to a small CW test signal is linear, the small-signal gain depending on the level of the saturating noise signal. This allows the CW test signal to be used as an indicator of the receiver gain in the presence of high-level signals.

*The National Radio Astronomy Observatory is a facility of the National Science Foundation operated under cooperative agreement by Associated Universities, Inc.

MEASUREMENT PROCEDURE

The gain compression measurements described here were made on a mixer-preamplifier for ALMA Band 6 (211-275 GHz) [3] with an intermediate frequency of 4-12 GHz. The measurement setup is shown in Fig. 1. A small CW test signal is introduced through the LO waveguide while the receiver input is switched between liquid nitrogen and room temperature sources using the chopper wheel. (The 20 dB cold pad between the mixer-preamp and the IF switch allows similar signal levels to be maintained throughout the IF system when measuring the mixer-preamplifier and when measuring the gain and noise temperature of the IF system using the hot and cold IF loads in the Dewar.)

The RF test signal is adjusted to give an IF power output power P_{HS} 10-20 dB above the output noise power P_H with only the hot load at the receiver input. With the cold load at the input, the IF power levels with the test signal on and off are P_{CS} and P_C . The output power due to the test signal alone is $(P_{HS} - P_H)$ with the hot load at the input and $(P_{CS} - P_C)$ with the cold load. If it is assumed that the receiver is not significantly saturated when connected to the cold load, it follows that the percentage gain compression due to the hot load is given by

$$C = 100 \times \left(1 - \frac{P_{HS} - P_H}{P_{CS} - P_C} \right) \text{ percent.} \quad (1)$$

The mixer-preamp may not be the only contributor to saturation; in fact, it is likely that the IF amplifier chain will have some degree of gain compression. This can be particularly important when the full IF bandwidth is large compared with the bandwidth of the final filter before the power meter. If the percentage gain compression of the mixer-preamp is C_1 and that of the rest of the IF chain is C_2 , then the percentage gain compression for the whole

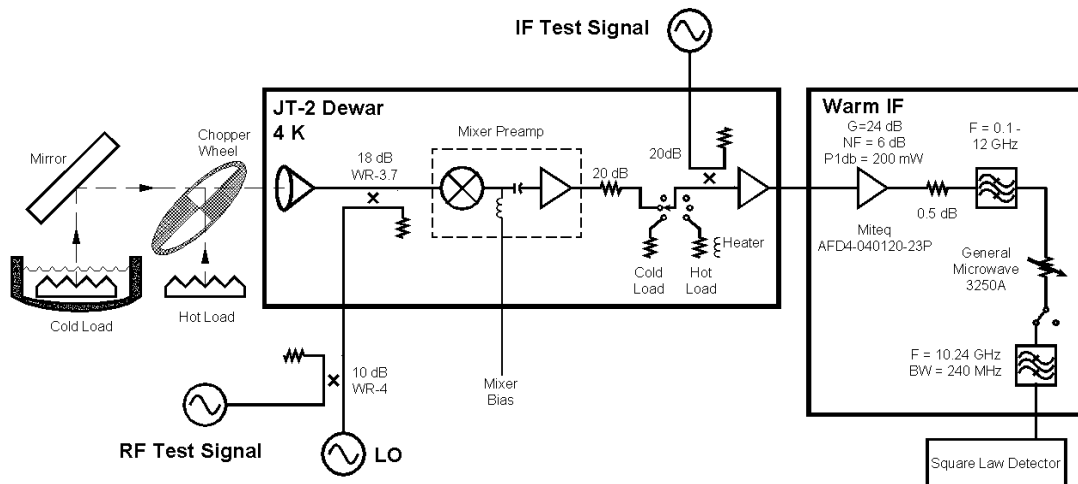


Fig. 1. Setup for measuring gain compression.

receiver is, to first order, $C = (C_1 + C_2)$. To measure the gain compression of the amplifier stages following the mixer-preamp under test, a small IF test signal can be introduced through the directional coupler following the IF switch in Fig. 1. In measuring C_2 , it is important not only to ensure that the IF input (noise) power is the same as when C is measured for the whole receiver, but also that the input noise spectrum has the same shape.

MEASUREMENTS

Figure 2 shows the data from a typical saturation measurement. The SIS mixer has four junctions in series and the LO frequency is 230 GHz. The percentage saturation is seen to vary almost sinusoidally with a period of ~ 8 minutes. When liquid nitrogen was added to the cold load, a change of phase was observed in the ripple, indicating that it is caused by the reflection of the test signal at the surface of the LN_2 . LO power emerging from the receiver is also reflected at the LN_2 surface, but the magnitude of the LO reflection, indicated by the modulation of the DC mixer current, is insufficient to contribute significantly to the measured gain variation. To check that the CW test signal does not itself cause significant saturation, its level was changed by ~ 4 dB during each measurement and no significant change was observed in the results.

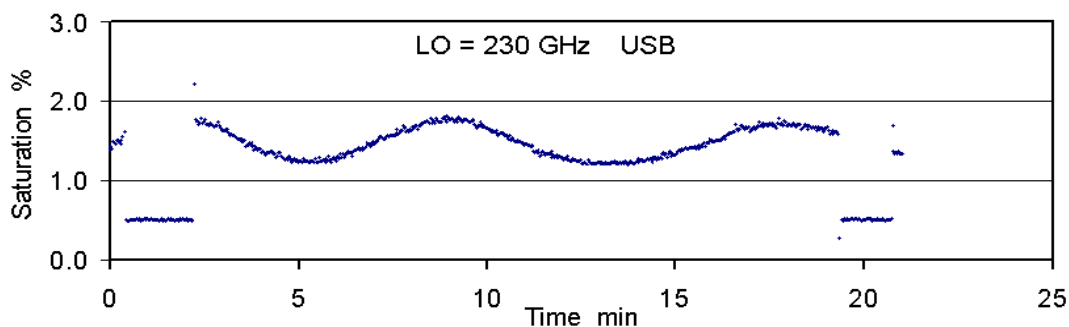


Fig. 2. Gain compression (saturation) data as a function of time, measured on a four-junction SIS mixer-preamp with the LO at 230 GHz and the small test signal in the upper sideband. The sinusoidal ripple is caused by reflection of the test signal at the surface of the LN_2 in the cold load as it boils away. The horizontal end segments at 0.5% indicate the degree of gain compression in the IF stages following the mixer-preamp.

Saturation in the IF amplifiers following the mixer-preamp was measured with exactly the same setup used to measure the overall receiver saturation, except that the test signal is now injected at the IF through the 20 dB coupler in the Dewar, shown in Fig. 1. The RF hot and cold loads are connected at the receiver input as before, thus ensuring that the IF amplifiers see the same noise power and spectral characteristics as in the overall saturation measurement. The results of this measurement are shown in the end segments of the data in Fig. 2 and indicate that $\sim 0.5\%$ saturation is due to the IF amplifiers following the mixer-preamp.

DISCUSSION

Large-Signal Gain Compression and Incremental Gain Compression

Fig. 3 shows the output power of a receiver with gain compression at higher input powers, as a function of the receiver input power. With zero input power, the output power from the receiver is $G_0 P_{Rx}$, where G_0 is the receiver gain at low input power and P_{Rx} is the equivalent input noise power of the receiver. P_H represents the input power from a hot noise source sufficient to cause some degree of gain compression and produce an output power $G_{LS}(P_H + P_{Rx})$, which is lower than the output power $G_0(P_H + P_{Rx})$ which would be produced in the absence of any gain compression. $G_{LS}(P_{in})$ is the large-signal gain of the receiver. The incremental gain $G_{inc}(P_{in})$ is the slope dP_{out}/dP_{in} of the gain curve. At low input powers, $G_{LS} = G_{inc} = G_0$. The incremental and large-signal gains are related by

$$G_{inc} = \frac{dP_{out}}{dP_{in}} = \frac{d(G_{LS} P_{in})}{dP_{in}} \quad (2)$$

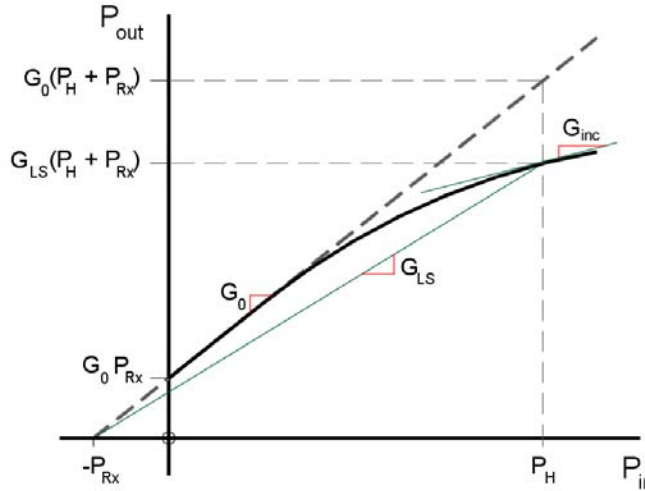


Fig. 3. Receiver gain curve, P_{out} vs P_{in} , showing large signal gain G_{LS} and the incremental gain $G_{inc} = dP_{out}/dP_{in}$. The quantity P_{Rx} is the equivalent input noise power of the receiver.

Our earlier analysis [3] of gain compression was concerned with the large-signal gain compression, which is difficult to measure at low levels. In the present work, we have described a simple method for measuring the incremental gain compression. The large-signal gain compression can be related to the incremental gain compression using equation (13) of [2] which gives the large signal gain as a function of the normalized RMS noise input voltage S_{in} :

$$G_{LS} = G_0 \frac{1}{\sqrt{2\pi} C_3^2 S_m^3} \int_{-\infty}^{\infty} \arctan^2(C_3 V_{in}) \exp\left(-\frac{V_{in}^2}{2S_m^2}\right) dV_{in}, \quad (3)$$

where $S_m^2 = \left(\frac{e}{Nh\nu}\right)^2 G_0 P_{sig} R_L$, $C_3 = 3.3$ is a constant for all SIS mixers, P_{sig} is the signal input noise power, and R_L is the IF load resistance seen by the SIS mixer. From this, the incremental gain is determined using (2).

Figure 4 shows the large-signal and incremental gain compression plotted together as functions of S_m^2 . Using Fig. 4, it is possible to deduce the large-signal gain compression from the (measured) incremental gain compression, and thereby to apply an appropriate correction to a receiver gain calibration made using hot and cold loads. Referring to Fig. 3, the output power measured with the hot load in front of the receiver $G_{LS}(P_H + P_{Rx})$ can be corrected to give the output power $G_0(P_H + P_{Rx})$ which would be measured if the receiver had no gain compression. For the mixer-preamplifier gain compression measurement shown in Fig. 2, the incremental gain compression is 1% (after correcting for the 0.5% compression in the following IF amplifiers). From Fig. 4, the corresponding value of S^2 is 0.00025, and the large-signal gain compression is 0.5%.

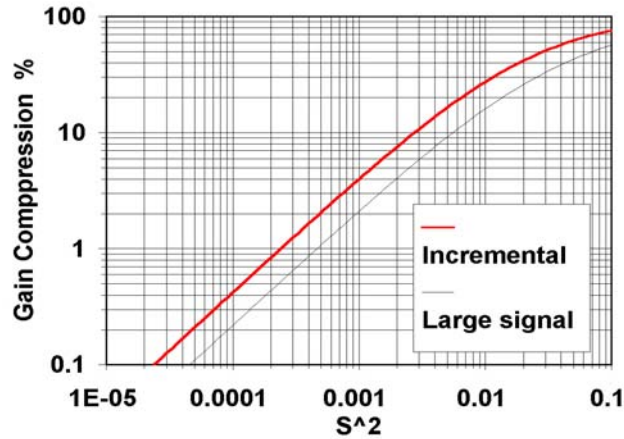


Fig. 4. Incremental and large-signal gain compression as functions of the normalized signal input noise power S^2 . These universal curves apply to all SIS mixers.

Agreement with Earlier Work

Figure 4 can also be used to deduce the incremental gain compression of a mixer whose large-signal gain compression has been estimated as described in [2]. Fig. 5 (from [2]) shows the large-signal gain compression produced, in a 230 GHz SIS mixer with N junctions in series, by a room temperature source, as a function of the single-sideband mixer gain,

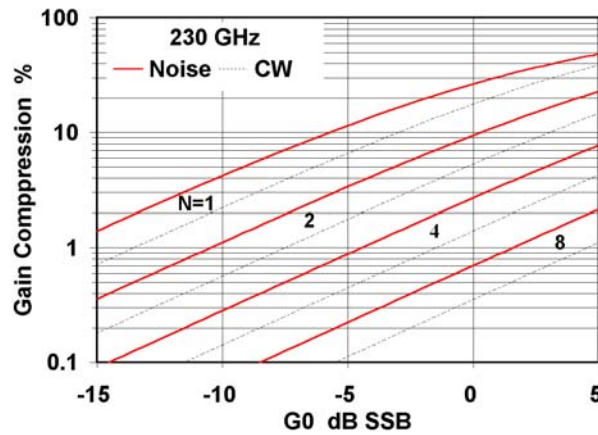


Fig. 5. Gain compression produced by noise from a room temperature source in an SIS mixer with N junctions in series, under the assumptions listed in the text. (From [2].)

under the following assumptions: (i) the input noise bandwidth B_1 in each sideband is equal to 20% of the LO frequency, (ii) the IF load impedance is 50 ohms over the extended IF band $0 < f_{IF} < B_1$, and (iii) the small-signal gain is constant over $0.8 f_{LO} < f_{sig} < 1.2 f_{LO}$. We were not able to measure the gain of the mixer used in these measurements because it was integrated with the preamplifier but, based on experience with similar mixers without integrated preamplifiers, we estimate the (SSB) mixer gain to be in the range -3 to -7 dB. Under the above assumptions, Fig. 5 indicates a large-signal gain compression of 0.6% to 1.5% when the receiver is connected to a room temperature source. This is slightly higher than the 0.5% large-signal gain compression deduced using Fig. 4 from the measured incremental gain compression — a discrepancy not surprising given the uncertainty of assumptions (i) - (iii) used in the theoretical calculation.

Post-Mixer Noise Contribution

In the present discussion, it has been assumed that all the noise power at the receiver output originates in or before the mixer, and thereby contributes to the saturation of the mixer. In fact, noise originating in the IF preamplifier and subsequent amplifiers does not appear at the output of the mixer and therefore does not contribute to saturation of the mixer. In most practical cases this will cause little error in the gain compression analysis — the noise contribution of the IF amplifier being far less than that required to cause significant gain compression (*e.g.*, a room temperature source). However, in a few unusual cases, *e.g.*, if the mixer saturates at a very low input power, or the IF preamplifier is very noisy, it could be necessary to separate the noise of the IF stages from that of the mixer and source in analyzing the saturation.

Square-Law Detector vs Power Meter

Our initial measurements of saturation were made using an IF power meter with the RF chopper wheel running slowly (several seconds in each position), but gain drift in the room temperature IF amplifiers made consistent measurements difficult to obtain. The power sensor was replaced by a tunnel diode detector and the chopper run at ~ 10 revolutions per second (~ 20 Hz chopping rate); then the drift was much less significant.

Square-Law Detector vs Spectrum Analyzer

If a spectrum analyzer is used instead of a square-law detector (or power meter), caution may be necessary in estimating the quantities $(P_{HS} - P_H)$ and $(P_{CS} - P_C)$. This is because most modern spectrum analyzers use an envelope detector as opposed to a square-law detector, and the indicated signal power in the presence of noise is not simply the sum of the signal and noise powers. If envelope detection is used with the usual log display, the correction factor is $-10.42 \times 10^{-0.333(H(\text{dB}))}$ dB, where H is the indicated signal-to-noise ratio [4]. This is shown in the upper curve of Fig. 6.

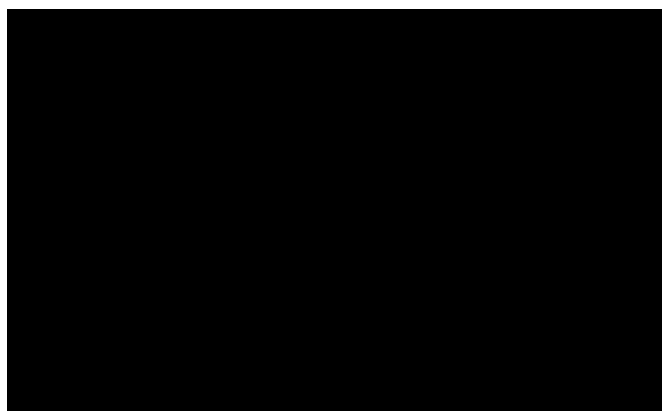


Fig. 6. Correction for system noise when measuring a CW test signal. The correction factor is plotted as a function of the indicated signal-to-noise ratio H . The upper curve applies to measurements using a spectrum analyzer with an envelope detector (usual in modern spectrum analyzers) and a log (dB) display. The lower curve is for measurements using a power meter with a square-law detector. From [5].

Source Mismatch

A possible source of error in measuring gain compression occurs if LO reflections from the hot and cold loads are sufficient to modulate the mixer gain at the chopper frequency. The mixer bias current is a good indication of the LO level at the mixer. Separate measurements can be made of the receiver gain and mixer current as functions of LO power, and the resulting gain vs mixer current curve allows the degree of gain modulation due to

chopper modulation of the LO power to be estimated. This was not significant in the present measurements.

REFERENCES

- [1] R. L. Plambeck, "Receiver amplitude calibration for ALMA," ALMA Memo 321, August 27, 2000. (<http://www.alma.nrao.edu/memos/>)
- [2] A. R. Kerr, "Saturation by noise and CW signals in SIS mixers," *Proc. 13th Int. Symp. on Space Terahertz Tech.*, Harvard Univ., pp. 11-22, 26-28 March 2002. (<http://www.alma.nrao.edu/memos/>)
- [3] E. F. Lauria, A. R. Kerr, M. W. Pospieszalski, S.-K. Pan, J. E. Effland, A. W. Lichtenberger, "A 200-300 GHz SIS mixer-preamplifier with 8 GHz IF bandwidth," *2001 IEEE International Microwave Symposium Digest*, pp. 1645-1648, May 2001. (<http://www.alma.nrao.edu/memos/>)
- [4] A. A. Moulthrop and M. S. Muha, "Accurate measurement of signals close to the noise floor on a spectrum analyzer," *IEEE Trans. Microwave Theory Tech.*, vol. 39, no. 11, pp.1182-1885, November 1991.
- [5] A. R. Kerr, S.-K. Pan and J. E. Effland, "Sideband calibration of millimeter-wave receivers," ALMA Memo 357, 27 March 2001. (<http://www.alma.nrao.edu/memos/>)

Investigations into the effect of reflections at the RF and LO ports of an SIS mixer

Nicholas D. Whyborn
(N.D.Whyborn@sron.rug.nl)

National Institute for Space Research (SRON), Groningen, the Netherlands

Abstract:

The effect of reflections at the signal and local oscillator (LO) ports of an SIS mixer has been calculated using the Tucker mixer theory. As expected, it is found that the reflections affect both the mixer conversion gain and mixer effective input noise temperature with the magnitude of these effects depending on the details of the mixer matching circuit. For a well optimised single sideband SIS mixer working below the gap frequency it is found that a -40dB source reflection coefficient can give 2% peak-to-peak IF ripple. For a double sideband mixer, the input reflection also modulates the sideband ratio and a peak-to-peak variation of 4% is found for a -40 dB source reflection coefficient.

The results are discussed in the context of mm & sub-mm wavelength radio astronomy systems where potentially important sources of reflections include the telescope and the LO source. By considering the sensitivity of the mixer to input reflections, upper limits to the allowed input reflection coefficient and the dimensional stability of the round trip path-length are derived.

Development of NbN Terahertz HEB Mixer Devices and Films*

Eyal Gerecht and Ashok Bhupathiraju

National Institute of Standards and Technology
Boulder, CO 80305

**John Nicholson, Dazhen Gu, Yan Zhuang, Fernando Rodriguez Morales, Xin Zhao,
Richard Zannoni, and Sigfrid Yngvesson**

Department of Electrical and Computer Engineering, University of Massachusetts
Amherst, MA 01003

ABSTRACT - Until recently, the thin-film NbN samples used by most research groups studying phonon-cooled hot electron (PHEB) devices across the world have been produced in Moscow (MSPU). We have developed a process for fabricating NbN thin films at the National Institute of Standards and Technology (NIST) in Boulder, CO. A two-fold approach has been taken. One approach is to maximize the critical temperature, but at the expense of IF bandwidth and noise temperature. With this approach, we can hope to develop NbN HEB receivers that will operate at 6-10 K using alternative, less costly, coolers. The other approach focuses on minimizing the receiver noise temperature and maximizing the IF bandwidth, while operating at 4 K. We have developed a film-deposition process that utilizes our DC reactive magnetron sputtering chamber. The films were deposited on MgO substrates that were heated to about 800 °C during deposition. A typical critical temperature (T_c) is about 10-11 K, and the transition width is very small (0.5 K). The films were then evaluated by measuring their superconducting characteristics as well as their thickness and surface roughness by use of AFM analysis.

PHEB devices were fabricated on the films in order to study their performance as THz HEB mixers. The device fabrication process performed at both NIST and UMass/Amherst involved lift-off lithography of the antenna (gold), and reactive-ion etching (RIE) or wet etching of the NbN. Receiver noise temperatures and receiver noise bandwidths were then measured at UMass/Amherst with a laser local oscillator (LO) that allows testing at a number of different frequencies. The latest results are described and discussed in this paper. A new antenna design and a new generation of monolithic microwave integrated circuit (MMIC) amplifiers to be incorporated with HEBs are also described.

* *Publication of the National Institute of Standards and Technology, not subject to copyright.*

I. INTRODUCTION

Heterodyne detection is the most sensitive spectroscopic technique over a broad frequency range that produces high spectral resolution in the terahertz region. In astronomical applications, observations of spectral lines have played a major role in expanding our understanding of the interstellar medium and planetary atmospheres. In order to achieve the required sensitivity for astronomical, remote sensing, and plasma diagnostics applications, we need to develop receivers operating at sensitivities near quantum noise limits and focal plane arrays with multiple mixer elements. Until recently GaAs Schottky barrier diodes (SBD) were used almost exclusively for heterodyne receivers in the terahertz region. Below 1 THz, SIS (Superconductor/Insulator/Superconductor) mixer receivers have excellent noise temperature (only a few times the quantum noise limit). This performance is limited to frequencies below or about equal to the superconducting bandgap frequency. Hot electron bolometric (HEB) mixers, which use nonlinear heating effects in superconductors near their transition temperature [1], have become an excellent alternative for applications requiring low noise temperatures at frequencies from 1 THz to 5 THz. There are two types of superconducting HEB devices, the diffusion-cooled (DHEB) version [2][3] and the phonon-cooled (PHEB) version [4]. The two versions differ according to the cooling mechanism of the hot electrons. NbN PHEB detectors have demonstrated an order of magnitude increase in sensitivity and a three orders of magnitude decrease in LO power requirement in the last few years. FIG.1 shows a survey of the noise temperature as a function of frequency for different types of detectors operating in the terahertz regime.

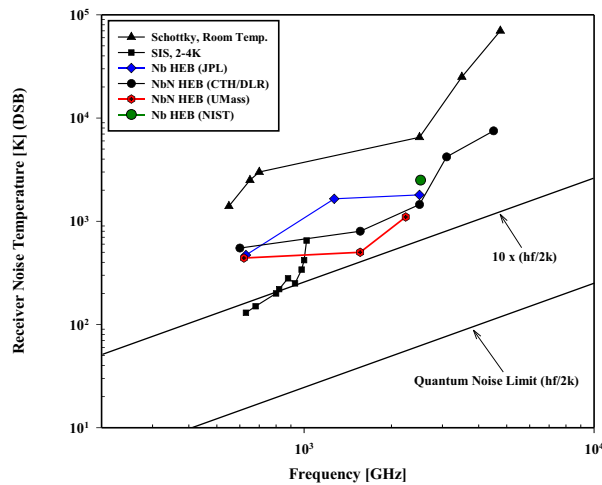


FIG. 1. Noise temperatures vs. frequency for receivers in the terahertz regime [1]-[7].

A two-fold approach can be taken in developing HEB technology. One approach focuses on minimizing receiver noise temperature and maximizing IF bandwidth at the expense of operational temperature (4 K). The NbN superconducting films have lower critical temperature (T_c). The other approach focuses on maximizing the operational temperature (6-10 K) at the expense of possibly higher noise temperature and narrower bandwidth, allowing the use of newly developed crycoolers. Here, we have concentrated on maximizing the critical temperature at the expense of bandwidth. We have developed an NbN film-deposition process utilizing our dc reactive magnetron sputtering chamber. After characterizing the superconducting films, we fabricated phonon-cooled HEB devices and studied their performance.

II. FILM DEPOSITION

NbN thin films were deposited using dc reactive sputtering from a Nb target in an atmosphere of nitrogen and argon. The deposition chamber was cryopumped down to a base pressure of 1.5×10^{-5} Pa. The total pressure is controlled with a variable throttle valve on the cryopump and is measured with a capacitance manometer. Ultra high purity (UHP) grade argon and zero-grade nitrogen were introduced into the chamber and their flow was controlled by needle valves. The partial pressure of nitrogen was determined simply by subtracting the initial Ar pressure from the total pressure of the mixture. The Nb sputtering target of 75 mm diameter was specified to have a purity of 99.95 %. The sample-to-target distance in our system is 10 cm. Crystalline MgO substrates, with (100) orientation, were cleaned in ambient temperature HF solution, followed by rinsing in organic solvents with ultrasonic agitation. The substrate was glued to a vacuum compatible heater block with silver paint and baked under a radiant heater for an hour prior to mounting in the deposition chamber.

The deposition sequence starts with cleaning of the target by sputtering Nb typically for five minutes onto a dummy sample in an atmosphere of pure Ar. In the next step nitrogen is added and pre-sputtering continues for another five minutes, while equilibrium is reached with regard to the nitrogen content at the target surface.

As discussed at length in the literature [8], a feedback mechanism exists in the magnetron plasma during reactive sputtering of NbN. When the plasma is voltage or power biased, the feedback is positive, leading the target surface to be either completely covered with nitride or completely free of nitride. The plasma current-voltage (I-V) characteristic in this condition is hysteretic, and control of the stoichiometry of sputtered films is problematic.

The resulting films are either nitrogen or niobium-rich, depending on the state of the target surface. However, under current bias the feedback is negative and the plasma I-V curve is single-valued, although it includes a region of negative differential resistance. Therefore, all NbN films described in this paper were grown with the plasma current-biased. FIG.2 shows the I-V curves for different pressures and gas compositions for our sputtering chamber. We have noticed a drift in the I-V characteristics over time, which was remedied by readjusting the deposition parameters.

During pre-sputtering, the MgO substrate was heated to 800 °C and actively stabilized at that temperature. Substrate temperature was monitored using a thermocouple embedded in the body of the heater block. Experience with identical heater blocks used for high-temperature laser ablation of YBCO films indicates that a significant temperature gradient (probably 20 to 50 °C) exists between the thermocouple and the surface of the substrate. Once the films were deposited, the sample was cooled to ambient temperature in nitrogen at 1atmosphere background pressure.

Our highest critical temperature samples ($T_c=11.2$ K, $\Delta T_c=0.2$ K) were obtained in a mixture of 15 % N₂, 85 % Ar, at 1.33 Pa total pressure, an applied current of 1.2 A, and resulting voltage of about 275 V. Film thickness was measured using a commercial atomic force

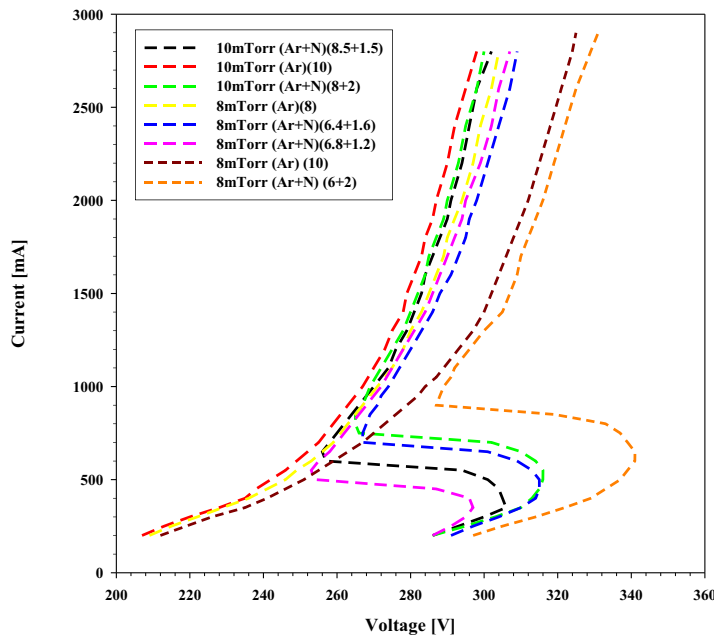


FIG. 2. I-V characteristics of the sputtering plasma.

microscope (AFM). Typical deposition rates are around 0.25 nm/s. For the series of samples described here, a uniform film thickness of 5 nm was desired. The deposition time for each film was adjusted based on the assumption that the deposition rate is proportional to power, which in turn depends on the plasma current.

III. DEVICE FABRICATION

Our next step was to evaluate the films by fabricating phonon-cooled HEB mixer devices, and to measure the noise temperature and IF bandwidth of these devices. A quasi-optical coupling design was used to couple the terahertz radiation into the device. We fabricated devices at the terminals of a twin-slot antenna design and at the terminals of a much broader design utilizing the toothed self-complementary log-periodic antenna. The antennas were photo-etched in a 200 nm gold layer that had been e-beam evaporated over the NbN film. After the gold layer was lifted off, the NbN film was wet-etched or dry-etched to define a HEB device with length of 1 μm and width of 4 μm . The twin-slot antenna response is centered at 1.5 THz, with a bandwidth of 1 THz to 1.9 THz. FIG.3 shows a photograph of the HEB device at the terminals of the twin-slot antenna. Lastly, an elliptical Si lens was affixed to the backside of the substrate. The lens was positioned using lines that had been accurately scribed on the lens side of the substrate and then affixed with purified bee's wax.

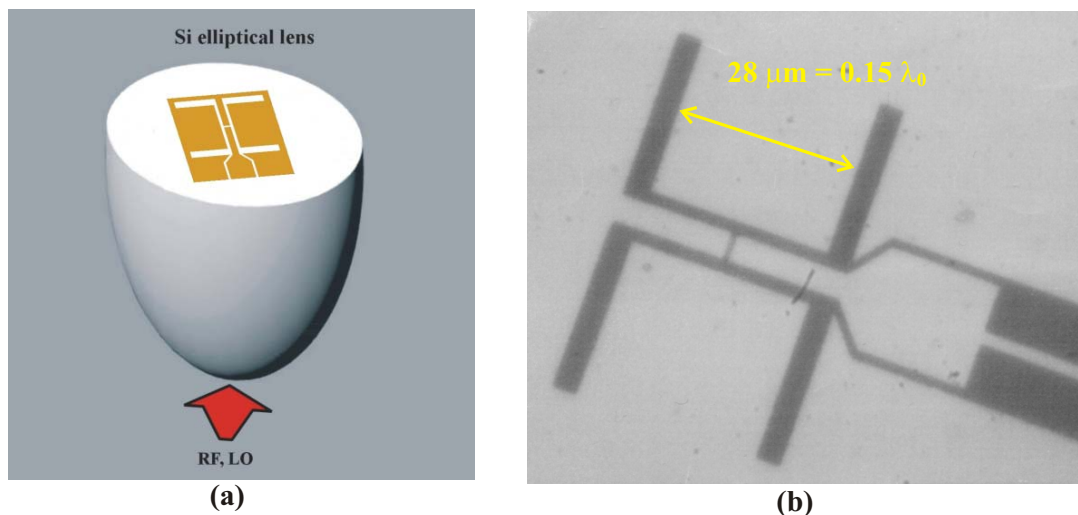


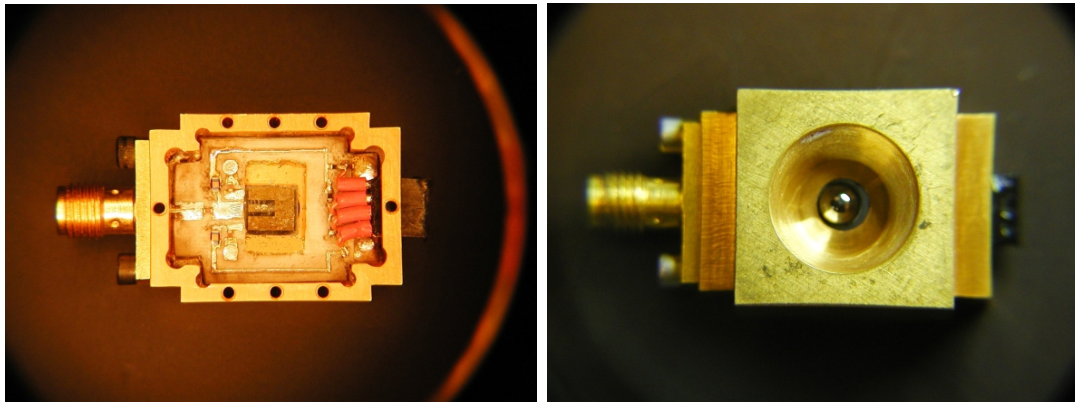
FIG.3. (a) a quasi-optical design illustration; (b) a photograph of the twin-slot antenna. The PHEB device in the center is too small to be seen.

IV. EXPERIMENTAL SETUP

The lens/substrate assembly was inserted into a mixer block, which also served as a bias tee. The mixer block (shown in FIG.4) was attached to a copper post, which was thermally anchored at its other end to the liquid helium reservoir of a commercial dewar. A heater controls the temperature of the mixer block. A cooled HEMT amplifier with a gain of 20 dB is used inside the dewar. This IF amplifier has a pass band from 1000 to 1800 MHz with a noise temperature of about 5 K. The contribution of the IF chain to the total double sideband receiver noise temperature is given by

$$T_{DSB,R} = \frac{Lc}{2} (T_{Device,out} + T_{IF}). \quad (1)$$

The receiver noise temperature was measured with a CO₂ laser pumped far infrared (FIR) gas laser as the LO source. Mylar beam splitters with a thickness of 6 μm act as diplexer between the LO and a chopped hot/cold noise source. The LO radiation is focused by an off-axis paraboloid (OAP) mirror. FIG.5. shows an illustration of the experimental setup for noise temperature measurements.



(a)

(b)

FIG.4. Photographs of the mixer block (a) front view; (b) back view.

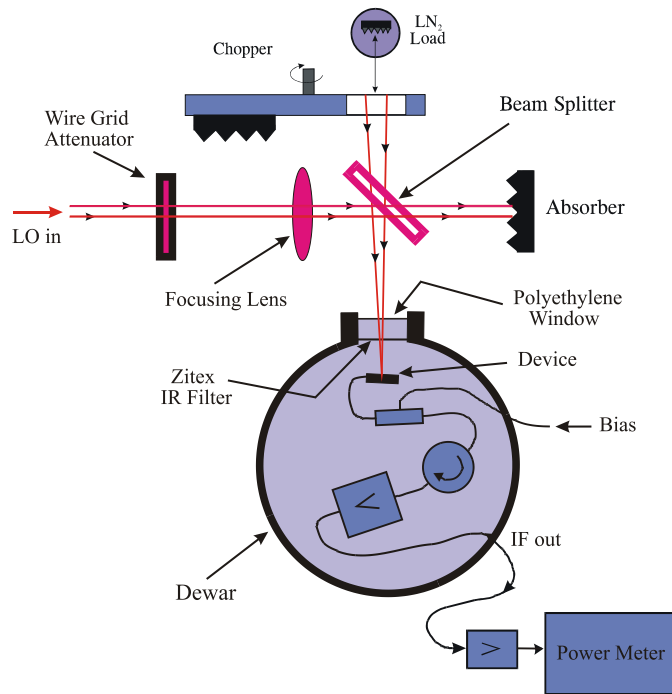


FIG.5. A diagram of the experimental setup for noise temperature measurements.

V. RESULTS AND DISCUSSION

The measured I-V curves for the devices resemble those of the best devices fabricated [4]. The LO power coupled to the devices here is an order of magnitude larger than for the best devices. The coupling losses are evidently more substantial for the devices produced here. The mismatch between the MgO substrate and the silicon lens and some optical misalignments are probably responsible for the higher LO power requirement and subsequently for the degraded noise temperature results. The best double-sideband receiver noise temperature measured at a wavelength of 184 μm (1.63 THz) is 3700 K. We also studied the dependence of noise temperature and IF bandwidth on the ambient temperature. FIG.6(a) shows the LO pumped I-V curves for one of the devices at two ambient temperatures (4 K and 7 K). The optimum pumped curves are identical for different temperatures and the LO power decreased by 1.3 dB for the elevated ambient temperature of 7 K. This results was expected from the principle of electrical substitution. The noise temperature performance was degraded slightly for the elevated ambient temperature (see FIG.6(b)). The noise tempera-

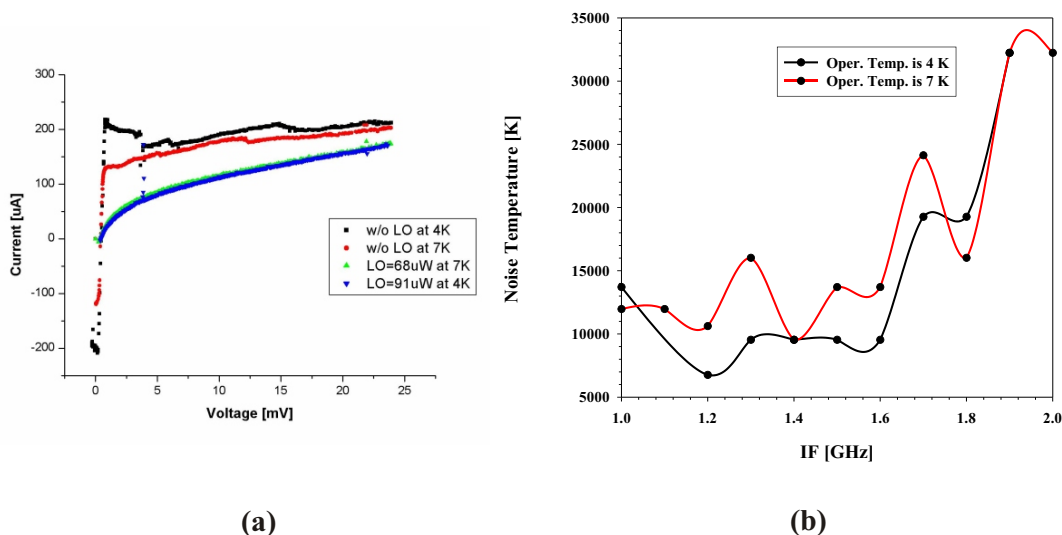


FIG.6. (a) I-V characteristics of the device at two ambient temperatures; (b) noise temperature vs. IF at the two ambient temperatures.

ture results for this device are not the best; nevertheless, the behavior of the HEB at two different temperatures shows that the receiver noise temperature change is quite small. Since receiver noise temperatures of a few (10-20) times the quantum noise limit have been demonstrated for many devices operating at 4 K, our results show that the same performance should eventually also be possible at elevated temperatures. The IF bandwidth at 7 K with a 5 nm thick NbN film deposited on an MgO substrate is at least 2 GHz. These preliminary results are very encouraging.

In order to improve the power coupling to the PHEB device, we are experimenting with a different type of antenna. An illustration of the slot-ring antenna design currently under development is shown in FIG.7. Slot-ring antennas are well suited for use with terahertz PHEBs. A CPW stub filter, which presents an open circuit at the slot-ring, is used. The CPW will be fabricated with air bridges (well-known in MMIC technology at lower frequencies) in order to ensure that only the main CPW mode propagates. Although slot-ring antennas have been used successfully at much lower frequencies, they present a challenge at terahertz frequencies.

We also develop an InP HEMT MMIC cryogenic low-noise amplifier technology to be integrated with HEB receivers. An IF bandwidth of 1 to 10 GHz, together with a noise temperature less than 10 K, are now within reach. FIG.8 shows photographs of an MMIC design

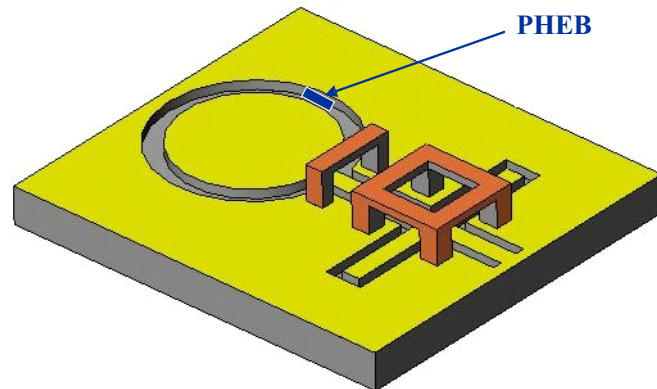


FIG.7. An illustration of a slot-ring antenna design with PHEB device.

under development at UMass. The MMIC chip was obtained courtesy of Dr. Sander Weinreb from JPL/CalTech. The amplifier noise temperature shown in FIG.8 includes contributions from the second stage (1.5 K-1.8 K approx.) and about 0.8-0.9 K from the isolator.

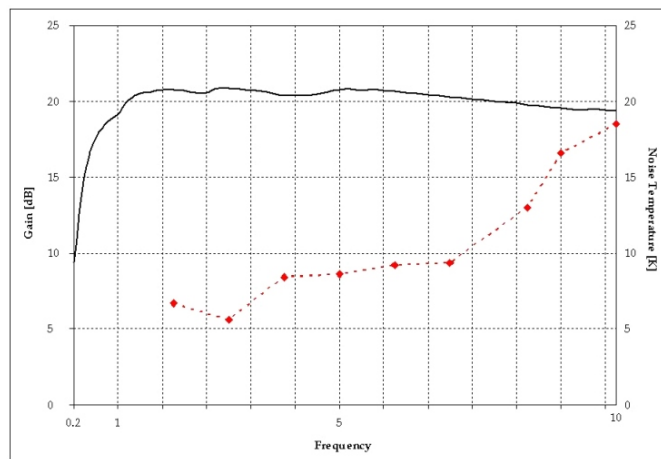
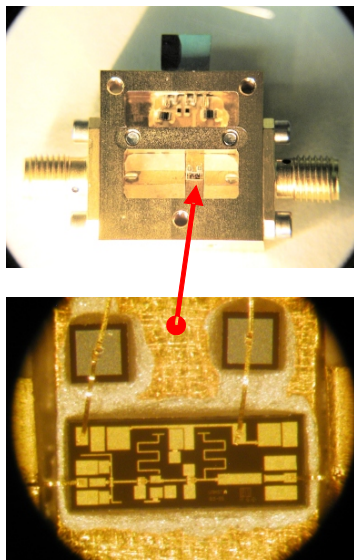


FIG.8. An InP HEMT MMIC cryogenic low-noise amplifier.

ACKNOWLEDGMENTS

This work was supported by NASA through grant NRA-00-01-SARA-012 to NIST and UMass/Amherst, and contract NAS1-01058 to UMass/Amherst.

REFERENCES

1. E. M. Gershenzon, G. N. Gol'tsman, I. G. Gogidze, Y. P. Gousev, A. I. Elant'ev, B. S. Karasik, and A.D. Semenov, "Millimeter and Submillimeter Range Mixer Based on Electronic Heating of Superconducting Films in the Resistive State", *Soviet Physics: Supercon.*, **3**, 1582, 1990.
2. D.E. Prober, "Superconducting Terahertz Mixer Using a Transition-Edge Microbolometer," *Appl.Phys.Lett.*, **62**, 2119, 1993.
3. R.Wyss, B.Karasik, W.R. McGrath, B. Bumble, and H. LeDuc, "Noise and Bandwidth Measurements of Diffusion-Cooled Nb HEB Mixers at Frequencies Above the Superconductive Energy Gap," *Proc. Tenth Intern. Space THz Technol. Symp.*, U.Virginia, March 1999, p. 214.
4. E. Gerecht, C.F. Musante, Y. Zhuang, M. Ji, K.S. Yngvesson, T. Goyette, and J. Waldman, "Development of Focal Plane Arrays Utilizing NbN Hot Electron Bolometric Mixers for the THz Regime," *Proc. Eleventh Intern. Space THz Technol. Symp.*, U. Michigan, May 2000.
5. A.L. Betz and R.T. Boreiko, "A Practical Schottky Mixer for 5 THz (Part II)," *Proc. Seventh Intern. Space THz Technol. Symp.*, pp. 503-510, Charlottesville, VA, March 1996.
6. P. H. Siegel, "Terahertz Technology", *IEEE Trans. on Microw. Theo.and Techn.*, 50/3, 910-928, March 2002.
7. E. Gerecht, C. D. Reintsema, E. N. Grossman, A. L. Betz, and R. T. Boreiko, "Noise Temperature For Nb DHEB Mixer Arrays for Far-Infrared Spectroscopy," *Proc. Thirteenth Intern. Space THz Technol. Symp.*, Harvard Univ., March 2002.
8. P. Yagoubov et al., "The Bandwidth of HEB Mixers Employing Ultrathin NbN Films on Sapphire Substrate," *Proc. Seventh Intern. Space THz Technol. Symp.*, Charlottesville, VA, March 1996.

GAIN BANDWIDTH AND NOISE TEMPERATURE OF NbTiN HEB MIXER

Matvey Finkel, Yuriy Vachtomin, Sergey Antipov, Vladimir Drakinski,
Natalia Kaurova, Boris Voronov, and Gregory Goltsman
Moscow State Pedagogical University, Moscow 119992, Russia

Abstract

We have determined that the gain bandwidth of phonon-cooled HEB mixer employing NbTiN films deposited on MgO layer over Si substrate is limited by the escape of phonons to the substrate. The cut-off frequencies of 1 μm long devices operating at $T \cong T_c$ based on 3.5 nm, 4 nm and 10 nm thick films amount to 400 MHz, 300 MHz, and 100 MHz, respectively. The gain bandwidth of 0.13 μm long devices fabricated from 3.5 nm thick film is larger and amounts to 0.8 GHz at the optimal operating point and to 1.5 GHz at larger bias. The increase of the gain bandwidth from 400 MHz up to 1.5 GHz with the change of bridge length is attributed to diffusion cooling. A double sideband noise temperature of 4000 K was obtained for heterodyne receiver utilizing pilot NbTiN HEB mixer (not optimized for normal state resistance) operating at the local oscillator frequency of 2.5 THz.

Introduction

Recently superconducting NbTiN thin films have aroused much interest as a promising basis for HEB mixer technology. The sensitivity and the required local oscillator power of HEB mixers employing this material [1] are rapidly approaching the level of NbN phonon-cooled HEB mixer, which is the best candidate now for heterodyne receivers operating at frequencies well above 1 THz. The gain bandwidth of HEBs based on NbTiN is still well below the value needed to fit the requirements of currently developed projects [2]. In this work, we have studied gain bandwidth of the devices based on NbTiN thin films at 0.14 and 0.9 THz local oscillator (LO) frequencies and noise temperature of the heterodyne receiver employing NbTiN HEB mixer operating at 2.5 THz LO frequency. As a result of these measurements, we have determined the main physical process which limits the gain bandwidth of our devices. We have also compared the sensitivity of pilot NbTiN HEB mixer with the sensitivity of NbN HEBs at that high LO frequency.

In practical operation, the electron subsystem of the device is heated up to the optimal operating point by applying DC and LO power, while the physical temperature of the device stays low. Under these conditions, the HEB mixer shows the best noise performance, but the physics of its operation is complex, most of all due to the non-uniform distribution of the electron temperature along the bridge. The cut-off frequency of the device in this regime is determined not only by phonon cooling, but also by electro-thermal feedback, Andreev reflections, diffusion of hot electrons, spatial variations of critical current along the bridge, and so on. It is difficult to estimate the influence of each factor separately. In the case of uniform electron temperature distribution along the bridge, the physics of the device operation can be described by simpler equations, and the mixer's cut-off frequency is completely determined by several characteristic times [3]. The values of these characteristic times can be obtained from the dependence of gain bandwidth on temperature and film thickness. Practically, the distribution of electron temperature is uniform along the bridge if LO and DC powers are small and electron effective temperature is equal to T_c and, in its turn, to the physical temperature of the device.

The operating point can be reached either by increasing the temperature up to the transition value, or by applying magnetic field that would decrease T_c to the physical temperature. There are two main processes determining the gain bandwidth of phonon-cooled HEB mixer for this regime. First, the energy is transmitted from hot electrons to the lattice via inelastic scattering of electrons with phonons. Thermal equilibrium between electron and phonon subsystems is established during phonon-electron interaction time $\tau_{ph-e} = \tau_{e-ph}c_e/c_{ph}$. Here c_e and c_{ph} are, respectively, electron and phonon specific heats, τ_{e-ph} is electron-phonon interaction time which depends on temperature as $\tau_{e-ph} = \alpha T^{-\beta}$, where α and β are certain constants determined by the film material. The specific heat of the phonons at temperatures close to typical value of T_c has the same order of magnitude as the electron specific heat, and therefore the escape of non-equilibrium phonons to substrate influences the energy relaxation process. The escape of non-equilibrium phonons to the substrate can also be described by the characteristic time τ_{esc} . In the case of uniform heating, the cut-off frequency of HEB mixer is mostly influenced by the largest of these time constants [3] if the bridge length is greater than thermal healing length $L_{e-ph} = (D\tau_{ph})^{1/2}$ [4]. In this equation, τ_{ph} is the hot electron bolometer's time constant if the diffusion cooling is neglected, D is the diffusivity of electrons in the superconducting bridge.

When the bridge length is about L_{e-ph} or smaller, the diffusion cooling contributes to the cut-off frequency of the device. The gain bandwidth of HEB mixer with bridge length that is much shorter than L_{e-ph} is determined only by diffusion cooling. For intermediate bridge lengths, both the diffusion cooling and the phonon cooling should be considered.

In this work, we have studied several NbTiN HEB mixers. The analysis of the dependence of 1 μm long mixer's cut-off frequency on temperature and film thickness at $T = T_c$ allows us to determine the physical process which limits the phonon-cooling rate. It is the escape of non-equilibrium phonons from the film to the substrate. The gain bandwidth of 0.13 μm long devices operating at a low temperature is larger than for the 1 μm long ones. This could be explained if the diffusion cooling is considered. In order to verify this assumption, the diffusivity of electrons in NbTiN films has been measured. The noise performance of practical NbTiN HEB mixers has been tested in a 2.5 THz heterodyne receiver.

Device design and fabrication

The HEB mixers are manufactured from superconducting NbTiN film on silicon substrate with 200 nm thick MgO buffer layer deposited by e-beam evaporation. The 3-4 nm and 10 nm thick NbTiN films are deposited by DC reactive magnetron sputtering of NbTi composite target in Ar and N_2 mixture. The Ar partial pressure is 3.2×10^{-3} torr, and the N_2 partial pressure is 1.2×10^{-4} torr. With discharge current and voltage amounting to 1 A and 300 V respectively, a sputtering rate of 0.5 nm/s is obtained. During the deposition the substrate is heated up to 600 $^{\circ}\text{C}$. The typical film transition temperature T_c is 11 K for 3-4 nm thick films and 13 K for 10 nm thick NbTiN film. Transition width amounts to 0.3-0.5 K for NbTiN films of both thicknesses. The film transition temperature decreases during the device fabrication.

The films are patterned using e-beam and photolithography to form 2.4 μm wide and 0.13 μm long structures for investigation of noise temperature of heterodyne receiver employing NbTiN HEB mixer, and 10 μm wide and 1 μm long structures for studying mixer's gain bandwidth at a physical temperature close to T_c . Devices made for noise

measurements are fabricated from 3.5 nm thick NbTiN films on MgO buffer layer over Si substrate by lift-off electron-beam lithography and lift-off photolithography. The 0.13 μm long mixer element is formed by lift-off e-beam lithography across two overlaid Ti-Au-Ti (Ti \sim 3 nm, Au \sim 30 nm, Ti \sim 10 nm) small contact pads, and the 2.4 μm width is formed by using a SiO mask made by e-beam lithography as well. The central part of the self-complementary spiral antenna is formed using lift-off e-beam lithography based on Cr-Au metallization (Cr \sim 3 nm, Au \sim 200 nm). Next, the outer part of the mixer is made by lift-off photolithography based on Ti-Au-Ti metallization (Ti \sim 5 nm, Au \sim 200 nm, Ti \sim 20 nm). The normal resistance of the typical device is 20 Ω . Contact resistance also contributes to this value, and the resistance of the bridge itself is slightly less than 20 Ω .

The devices developed for investigation of phonon cooling in NbTiN HEBs at $T \cong T_c$ are much larger in-plane (10 μm wide and 1 μm long) than the previous ones, and are fabricated from 3.5, 4.2 and 10 nm thick NbTiN films on MgO buffer layer over Si substrate. This design allows us not to use e-beam lithography for fabrication process, and the spiral antenna is formed using direct photolithography. Physically, this design increases the volume of superconducting bridge, which, in turn, increases the dynamic range of the device. The device noise temperature increases with an increase of physical temperature. At temperatures close to T_c , the sensitivity of HEB mixer is rather low. This fact along with small dynamic range of practical device makes it impossible to perform heterodyne measurements at $T = T_c$ for 2.4 μm wide by 0.13 μm long devices.

The last process for both designs is the removal of the NbTiN layer by ion milling in Ar atmosphere from the whole substrate surface except the central part of spiral antenna which was protected by SiO or resist masks.

Experimental setup

The noise temperature of quasioptical heterodyne receiver employing NbTiN mixer at 2.5 THz LO frequency was measured at the Institute of Space Sensor Technology and Planetary Exploration, DLR, in collaboration with Alexei Semenov and Heinz-Wilhelm Hubers. The experimental setup is described in [5].

The experimental setup for measurements of the output power versus IF at 0.9 THz LO frequency is presented on Fig. 1. Radiation from two backward wave oscillators (BWOs) operating within the frequency range of 0.87–1 THz is superimposed by Maylar beam splitter and arrive into liquid He-cooled vacuum cryostat through a Teflon window. Terahertz radiation is coupled to the mixer via a hybrid antenna, an extended hemispherical Si lens along with a planar spiral antenna integrated into the device. The device under test is glued to the flat side of the lens. A bias tee is used to feed bias to the device and to pass the output signal at an intermediate frequency to the room temperature amplifier chain. The amplifier chain has a gain of approximately 70 dB and operates within frequency ranges of 0.1-2 GHz, 0.7-4 GHz, and 3.5-8 GHz. The value of the intermediate frequency is monitored using spectrum analyzer inserted in the chain via a -20 dB directional coupler. The output power is measured using power meter.

The mixer's output power as a function of intermediate frequency is measured at the 140 GHz LO frequency. The radiation from two BWOs is superimposed by Maylar beam splitter and arrives into dipstick with vacuum chamber through a Teflon window. It passes the oversized waveguide and is coupled to the device via a horn antenna. To the end of horn antenna a massive copper plate is soldered, to provide enough space for attached thermometer and for framing an appropriate coupling

between a device and the IF chain. The temperature is kept near the transition point value of the device under test by applying DC power to the heater. The heater is mounted on the horn antenna far from the device to provide an almost uniform temperature along copper plate. Output signal passes through a 50 Ohm coaxial cable to a room temperature bias tee used for applying bias voltage to a device. Then the output signal is amplified using a room temperature amplifier chain and is monitored by a power meter. One of the BWOs is tuned to change intermediate frequency and its power is maintained at a constant level by a grid attenuator. The power of both BWOs is kept at low level to ensure that the effective electron temperature stays close to the physical temperature of the device. Thus, a chopper is inserted into the path of the tuned BWO, and the RF power is observed by recording the direct response voltage of the bolometer using a selective nanovoltmeter.

Experimental results

The double sideband (DSB) receiver noise temperature of a heterodyne receiver employing NbTiN HEB mixer is measured by Y-factor method. The receiver shows 4000 K noise temperature at LO frequency of 2.5 THz. The best noise performance of the mixer is obtained at the operating point marked on Fig. 2 as point 1. At much larger bias voltage the noise performance is worse but the gain bandwidth is larger. One of such operating points is marked on Fig. 2 as point 2.

The gain bandwidth of a 0.13 μm long device is measured at 0.9 THz LO frequency at two different operating points mentioned above. The device shows the gain bandwidth of 0.8 GHz and 1.5 GHz at operating points 1 and 2 respectively. Obtained dependencies of output power versus IF are presented on Fig. 3

The cut-off frequencies for the devices based on 3.5, 4.2 and 10 nm thick NbTiN films deposited on MgO buffer layer over Si substrate are measured using the experimental setup with BWOs operating in 127-142 GHz frequency range. This frequency range is used because the 10 μm wide and 1 μm long bridge requires a large central part of spiral antenna, while the size of that central part limits the high frequency response of the antenna. The curves of output power versus IF for the devices operating at transition temperatures T_c are presented on Fig 4. The experimental data are marked as triangles for the 10 nm thick device, squares for the 4.2 nm one, and circles for the 3.5 nm one, and are best fitted by the cut-off frequency of 100 MHz, 300 MHz, and 400 MHz, respectively.

In order to measure the gain bandwidth at physical temperatures well below T_c and to provide uniform electron temperature distribution, it is necessary to apply a high enough magnetic field and to keep DC and LO powers low. The magnetic field lowers the device T_c , and the operating point can be achieved at a low physical temperature and low bias current and LO power. The superconducting solenoid provides a magnetic field of up to 4 T perpendicular to the device surface. This field is enough to perform measurements at temperatures approximately 2 K lower than the transition temperature of the device. No change in the gain bandwidth is observed in this temperature range.

The diffusivity of the superconducting film can be derived from the dependence of critical magnetic field H_{c2} on temperature according to [6]:

$$D = 1.086 [(-dH_{c2}/dT)_{T=T_c}]^{-1}$$

The dependence of the critical magnetic field H_{c2} on temperature is measured using the same superconducting solenoid providing a 4 T magnetic field. The obtained H_{c2} versus T for 4 nm thick NbTiN film deposited on Si substrate with an

MgO buffer layer is presented on Fig. 5. The corresponding value of the diffusivity is $D = 1.13 \text{ cm}^2/\text{s}$.

Discussion

For a device operating at $T=T_c$, when the distribution of effective electron temperature is uniform along the bridge, the hot electron bolometer's time constant τ_{ph} depends only on τ_{eph} and τ_{esc} . The gain bandwidth of phonon-cooled device depends on temperature via electron-phonon interaction time and on film thickness via phonon escape time. As can be seen from Fig. 6, the IF bandwidth of the studied $1 \mu\text{m}$ long NbTiN mixers is inversely proportional to the thickness of the superconducting film. Taking into account that gain bandwidth does not noticeably change with temperature, we can assume that τ_{eph} in the case of 3.5 nm or thicker NbTiN films deposited on MgO layer over Si substrate is much shorter than τ_{esc} and does not influence the gain bandwidth. The gain bandwidth of those devices is limited only by the escape of non-equilibrium phonons to the substrate, and the bolometer time constant is equal to τ_{esc} , which depends on film thickness as follows [3]:

$$\tau_{\text{esc}} = 4d/\alpha u,$$

where α is the acoustic mismatch between the superconducting film and the MgO layer, u is the speed of sound in NbTiN.

The gain bandwidth obtained at low physical temperatures under optimal pumping by LO power depends on bias voltage due to electro-thermal feedback. The influence of this effect decreases with the increase of bias voltage. Hence, the results obtained at a larger bias (operating point 2) should be closer to the results obtained under uniform distribution conditions than those obtained at the optimal operating point.

The increase in gain bandwidth of the devices based on 3.5 nm thick NbTiN film from 0.4 GHz to 1.5 GHz with the change of the bridge length from $1 \mu\text{m}$ to $0.13 \mu\text{m}$ can be explained if the diffusion cooling mechanism is considered. The bolometer's time constant τ_{Θ} approximately depends on phonon relaxation time and on diffusion relaxation time as follows:

$$1/\tau_{\Theta} = 1/\tau_{\text{ph}} + 1/\tau_{\text{diff}},$$

where τ_{ph} is the bolometer's time constant neglecting diffusion cooling and τ_{diff} is the time constant of the bolometer as if the phonon cooling did not take place. The analysis of diffusion cooling predicts the following dependence on the bridge length L for τ_{diff} [4]:

$$\tau_{\text{diff}} = \pi^2 L^2 / D,$$

where D is an electron diffusion constant in the superconducting material of the HEB mixer. The gain bandwidth of a device with fixed film thickness depends on the bridge length according to the following equation:

$$f_{\text{cut-off}} = (\pi^2 \tau_{\text{ph}} D + L^2) / 2\pi \tau_{\text{ph}} L^2.$$

This dependence is represented in Fig. 7 along with our experimental data for the gain bandwidth. The theoretical predictions do not fit the experimental data completely, and for shorter bridge lengths the cut-off frequency is much lower than it is provided by the experimentally obtained diffusivity. This effect was not systematically studied, and we can only make a guess that it is due to a finite area under contact pads, in which electrons out-diffuse from the superconducting film into cold metal pads.

The noise temperature of the heterodyne receiver operating at the 2.5 THz LO frequency employing NbTiN mixer is higher than that reported in [7] for NbN HEB mixer. This result is not yet conclusive, because the normal state resistance of the superconducting bridge is less than 20 Ohm and causes noticeable mismatches with both RF circuit (antenna impedance is approximately 75 Ω) and IF chain (isolator input impedance is 50 Ω). We believe that a device with appropriate normal state resistance will be able to demonstrate improved noise performance.

Acknowledgment

This work was supported by the INTAS-ESA grant 99-0569, as well as grants of Ministry of Science and Technology of Russian Federation (Contract No. 40.031.1.1.1187 and 40.012.1.1.1355). We wish to thank A. Semenov and H.-W. Hubers for having provided us the opportunity to do 2.5 THz heterodyne measurements at the Institute of Space Sensor Technology and Planetary Exploration, DLR. Special thanks are due to D. Meledin for fruitful discussions.

References

1. C. Edward Tong, Jeffrey Stern, Krikor Megerian, Henry LeDuc, T. K. Sridharan, Hugh Gibson, Raymond Blundell, "A Low-noise NbTiN Hot Electron Bolometer Mixer", 12th Int. Symp. on Space THz Techn., 2001
2. <http://astro.estec.esa.nl/SA-general/Projects/FIRST/first.html>
<http://sofia.arc.nasa.gov/>
<http://telis.af.op.dlr.de/>
3. E. M. Gershenson, M. E. Gershenson, G. N. Goltsman, A. M. Lyul'kin, A. D. Semenov, and A. V. Sergeev, "Electron-phonon interaction in ultrathin Nb films", Sov. Phys. JETP, vol. 70 (3), 1990
4. P. J. Burke, R. J. Schoelkopf, D. E. Prober, A. Skalare, W. R. McGrath, B. Bumble, and H. G. LeDuc, "Length scaling of bandwidth and noise in hot-electron superconducting mixers", Appl. Phys. Lett. 68 (23), 3344 1996
5. K.V. Smirnov, Yu.B. Vachtomin, S.V. Antipov, S.N. Maslennikov, N.S. Kaurova, V.N. Drakinsky, B.M. Voronov, G.N. Gol'tsman, A.S.Semenov, H.-W.Hubers, H.Richter, "Noise and Gain Performance of spiral antenna coupled HEB Mixers at 0.7 THz and 2.5 THz.", *this issue*
6. M. Tinkham, "Introduction to Superconductivity", McGraw-Hill, 2nd edition, 1995
7. S. Cherednichenko, M. Kroug, P. Khosropanah, A. Adam, H. Merkel, E. Kollberg, D. Loudkov, B. Voronov, G. Goltsman, H. Richter, H.-W. Hubers, "A Broadband Terahertz Heterodyne Receiver with an NbN HEB Mixer", 13th Int. Symp. on Space THz Techn., 2002

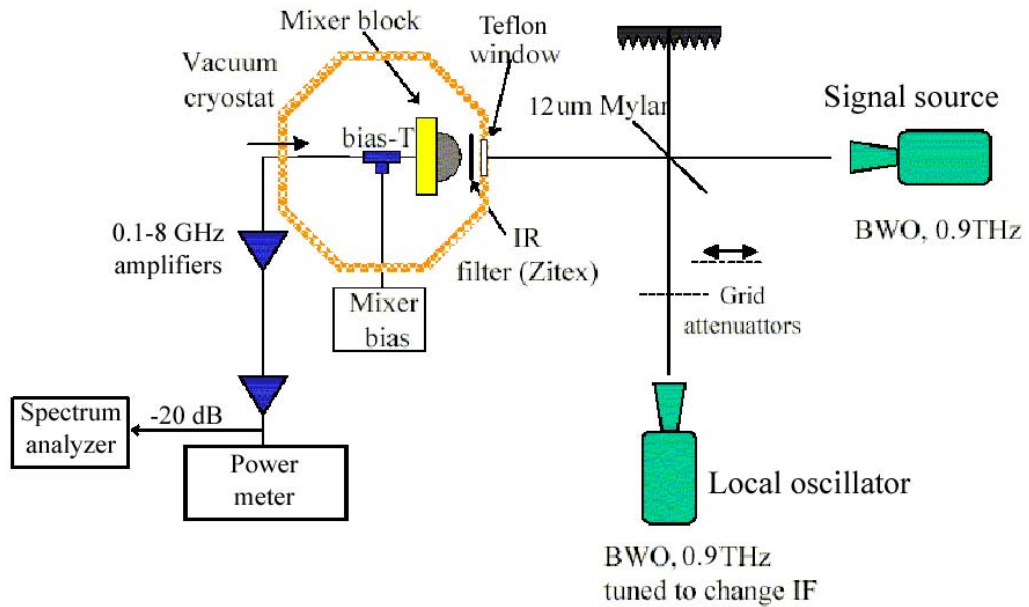


Fig. 1 Experimental setup for heterodyne measurements at 0.9 THz frequency

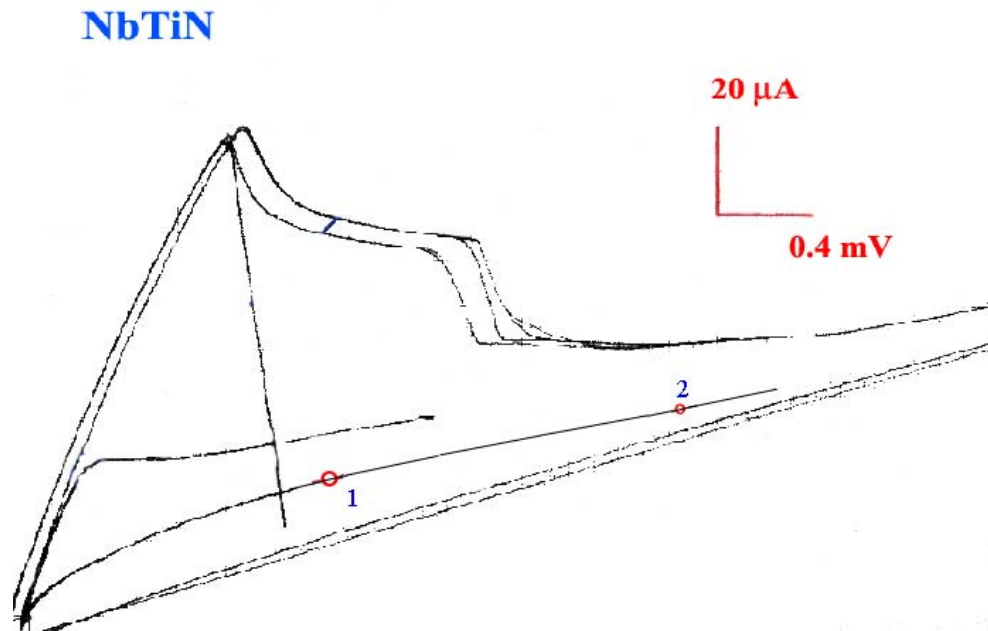


Fig. 2 Family of IV-curves for different pumping RF power

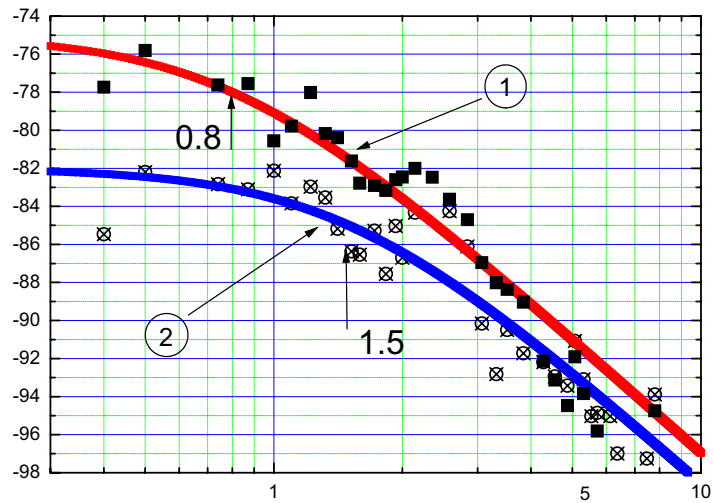


Fig. 3 Output power as a function of IF for 0.13 μm long device based on 3.5 nm thick film. Experimental data are marked by squares (for optimal operating point) and crossed circles (for larger bias voltage).

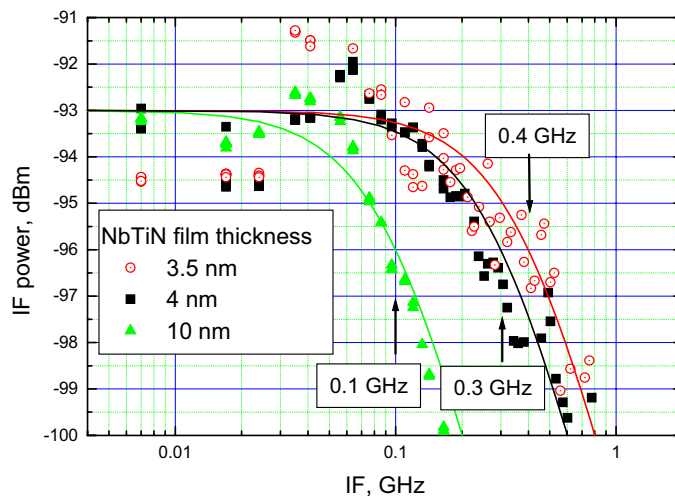


Fig. 4 Output power as a function of IF for 1 μm long devices with different NbTiN film thickness

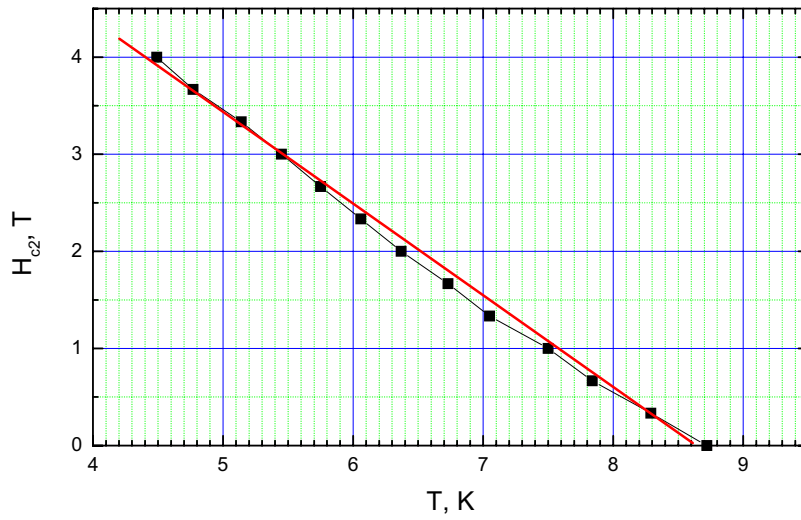


Fig. 5 Critical magnetic field as a function of temperature for 4 nm thick NbTiN film deposited on MgO layer over Si substrate

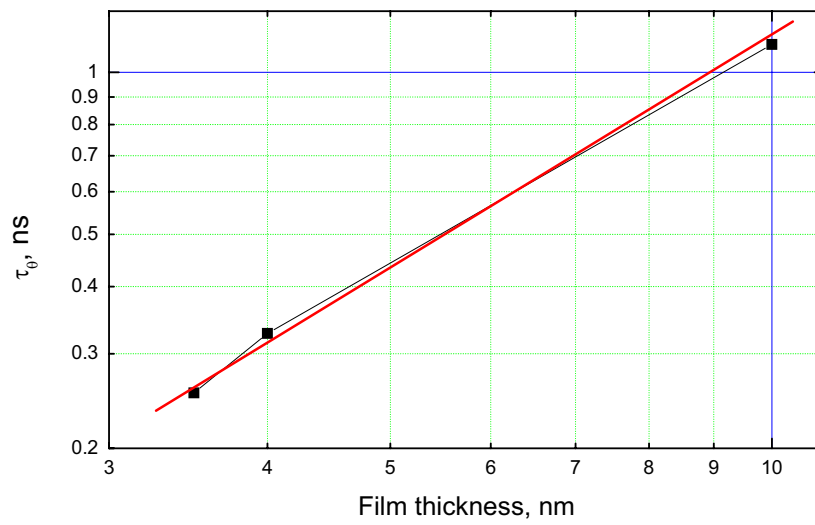


Fig. 6 The cut-off frequency as a function of film thickness

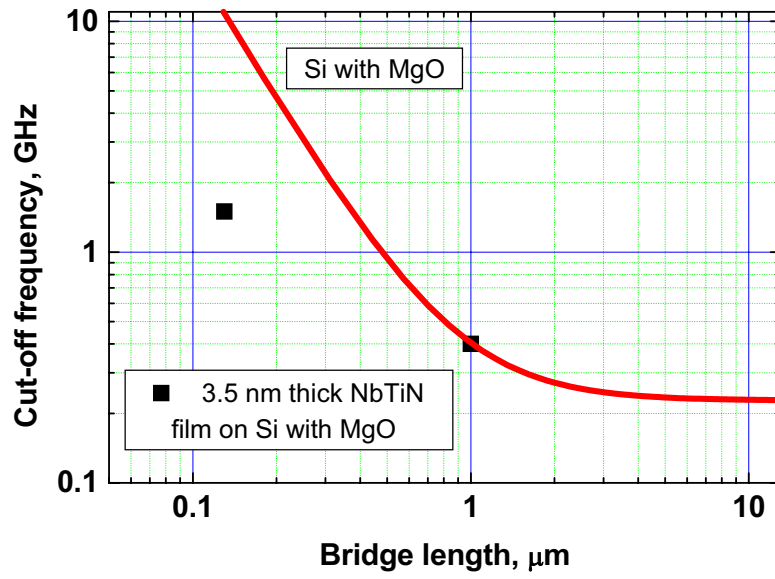


Fig. 7 The cut-off frequency as a function of bridge length

A 1.5 THz hot-electron bolometer mixer operated by a planar diode-based local oscillator

C.-Y. Edward Tong, Denis Meledin and Raymond Blundell
Harvard-Smithsonian Center for Astrophysics, 60 Garden St., Cambridge, MA 02138

Neal Erickson
Department of Astronomy, University of Massachusetts, Amherst, MA 01002

Jonathan Kawamura and Imran Mehdi
Jet Propulsion Laboratory, California Institute of Technology, Pasadena, CA 91109

Gregory Gol'tsman
Physics Department, Moscow State Pedagogical University, Moscow, 119435, Russia

We describe a 1.5 THz heterodyne receiver based on a superconducting hot-electron bolometer mixer, which is pumped by an all-solid-state local oscillator chain. The bolometer is fabricated from a 3.5 nm-thick niobium nitride film deposited on a quartz substrate with a 200 nm-thick magnesium oxide buffer layer. The bolometer measures 0.15 μm in width and 1.5 μm in length. The chip consisting of the bolometer and mixer circuitry is incorporated in a fixed-tuned waveguide mixer block with a corrugated feed horn. The local oscillator unit comprises of a cascade of four planar doublers following a MMIC-based W-band power amplifier. The local oscillator is coupled to the mixer using a Martin-Puplett interferometer. The local oscillator output power needed for optimal receiver performance is approximately 1 to 2 μW , and the chain is able to provide this power at a number of frequency points between 1.45 and 1.56 THz. By terminating the rf input with room temperature and 77 K loads, a Y -factor of 1.11 (DSB) has been measured at a local oscillator frequency of 1.476 THz at 3 GHz intermediate frequency.

Broadband Millimeter-Wave Bolometric Mixers Based on Ballistic Cooling in a Two-Dimensional Electron Gas

Mark Lee, L. N. Pfeiffer, and K. W. West

Bell Laboratories, Lucent Technologies, 600 Mountain Ave., Murray Hill, NJ 07974

The intermediate frequency (IF) bandwidth of “hot” electron bolometric mixers is determined by the energy relaxation time for the electron system to dissipate energy absorbed from the electromagnetic fields into a heat sink. For devices of small enough length scale L , the energy relaxation time is set by the transit time τ_{tr} for hot electrons to cross a channel and deposit excess energy into the leads, which act as the thermal reservoir. This transit-time limited cooling principal has been implemented successfully to construct low-power, wideband bolometric mixers using thin superconducting metal films.^{1,2} In these mixers hot electrons diffuse elastically across the channel, so that momentum but not energy is relaxed in the channel. The constraint on IF bandwidth in metal films is the small diffusion constant $D \sim 1$ to $10 \text{ cm}^2\text{s}^{-1}$, which necessitates fabricating devices with $L \sim 0.1 \text{ }\mu\text{m}$ in order to obtain several GHz of IF bandwidth. It has been suggested³ and shown⁴ that this same diffusion-cooling principal applies to a high mobility two-dimensional electron gas (2DEG) of the type formed at the interface of a GaAs-AlGaAs semiconductor heterostructure. Because the 2DEG can have D be two orders of magnitude larger than in metal films, IF bandwidths exceeding 10 GHz can be obtained in a 2DEG at much larger channel lengths $L \sim 5 \text{ }\mu\text{m}$ at 77 K.

We have examined the fundamental physical speed limits on bolometric mixing bandwidth using the transit-time cooling principal. When the transit mechanism is elastic diffusion, τ_{tr} is the elastic diffusion time $\tau_D = L^2/\pi^2 D$, so that the -3 dB IF bandwidth $f_{3\text{dB}} \propto L^{-2}$. This bandwidth-length scaling is the signature of the diffusion-cooling process. However, it is clear that this diffusive scaling cannot persist to arbitrarily small L because it makes no physical sense for τ_D to be smaller than L/v_F , which is the time it takes electrons near the Fermi velocity v_F to cross a channel in the absence of any elastic scattering. More specifically, the diffusion-cooling mechanism should fail when $L < \ell_{el}$, the elastic mean free path, since there is then on average no momentum nor energy relaxation in the channel. The hot electron outflow is then expected to be

¹A. Skalare, *et al.*, Appl. Phys. Lett. **68**, 1558 (1996)

²I. Siddiqi, *et al.*, IEEE Trans. Appl. Supercond. **11**, 958 (2001)

³K. S. Yngvesson, Appl. Phys. Lett. **76**, 777 (2000)

⁴M. Lee, *et al.*, Appl. Phys. Lett. **78**, 2888 (2001)

ballistic rather than diffusive, changing the bandwidth-length scaling to $f_{3\text{dB}} \propto L^{-1}$. Ballistic-cooling establishes the fundamental speed limit on IF bandwidth for a given bolometric mixer size and bias condition.

While the condition $L < \ell_{\text{el}}$ is unreachable in metal films, in sufficiently high quality 2DEGs ℓ_{el} can exceed 3 μm at 77 K and 50 μm near 1 K. To test whether a ballistic-cooling mechanism is observable, we performed millimeter-wave mixing experiments using a GaAs-AlGaAs 2DEG with mobility $\mu = 3.1 \times 10^5 \text{ cm}^2\text{V}^{-1}\text{s}^{-1}$ at 77 K and $7.5 \times 10^6 \text{ cm}^2\text{V}^{-1}\text{s}^{-1}$ at 1.5 K. The mixers had channel lengths L ranging from 1.3 μm to 10 μm . Heterodyne mixing was done using a fixed 105 GHz source as the *rf* signal and a tunable 105 to 145 GHz source as the local oscillator (LO). The IF bandwidth of the system was 40 GHz, limited by the IF low-noise amplifier.

At 77 K, a clear crossover in the bandwidth-length scaling from $f_{3\text{dB}} \propto L^{-2}$ for $L > 4 \mu\text{m}$ to $f_{3\text{dB}} \propto L^{-1}$ for $L < 3 \mu\text{m}$ was observed. For the smallest device, $L = 1.3 \mu\text{m}$, an IF bandwidth $f_{3\text{dB}} = 38 \text{ GHz}$ was measured. At 1.5 K, $f_{3\text{dB}} \propto L^{-1}$ across the entire range of L , consistent with a complete transition to ballistic rather than diffusive cooling. Further evidence for ballistic dynamics comes from measurements of the average transit velocity $v_{\text{av}} = 2\pi f_{3\text{dB}} L$ as a function of DC bias voltage V . Data for all channel lengths can be collapsed onto one common curve described completely by semiclassical Bloch acceleration. There is also a signature of kinetic inductance in the mixer load impedance when in the ballistic-cooling regime.

The change in LO power requirement and noise temperature of these mixers will be compared between diffusion-cooled and ballistic-cooled states. We find preliminary evidence that the both the optimal LO power and the noise temperature decrease by about an order-of-magnitude upon crossing into the ballistic-cooling regime.

BISTABILITY IN NbN HEB MIXER DEVICES

Yan Zhuang, Dazhen Gu and Sigfrid Yngvesson

Department of Electrical and Computer Engineering
University of Massachusetts, Amherst, MA 01003

ABSTRACT-All researchers working on THz HEB mixer devices are aware of the fact that the device is unstable in one part of its IV-curve. We have earlier reported that in this unstable region we observe relaxation oscillations at about 5 MHz for a number of devices in both the voltage and the current [1]. In this paper, we will present a quantitative model which describes the relaxation oscillations as well as some new transient measurements, which we will also report. As an HEB device is brought from the superconducting state through the critical current, it will enter a *bistable* state, which has been described for superconducting films in earlier papers and was reviewed in [2]. The bistable state means that two different states can potentially occur; a normal “hotspot” or “electrothermal domain”, and the superconducting state. The theory in [2] predicts how the domain, once formed, may either expand, contract, or be in steady state, depending on the device current. The velocity with which the wall of the hotspot moves is also predicted. We propose a modification to the original bistability theory [2], taking into account the Andreev Reflection effect and the phonon specific heat. The relaxation oscillation frequency and the velocity of the hotspot boundary, for the conditions during the new measurements presented here, has been calculated according to the modified theory and the calculated results are within a satisfactory range in comparison with the measured data. Complete understanding of the role played by the movement of the hotspot boundary under various bias conditions (with and without LO power) for HEBs will require further measurements and theoretical work.

I. INTRODUCTION

We have reported in [1] measurements of an HEB device DC biased in the unstable region of its IV-characteristic. The measurement setup is shown in Figure 1. The devices were identical to devices which were used in our HEB mixer development program, with length $1\mu\text{m}$ and width $4\mu\text{m}$. They were placed in a shielded box at the end of a “dipstick”, which was inserted in a liquid helium storage dewar. We consistently recorded a repetitive waveform, in which we could distinguish two different frequencies. The device basically switched back and forth between a state in which it had a resistance, and

its superconducting state, at a frequency in the range of several hundred kHz, which we will call the repetition frequency. Its value changed with the external circuit conditions such as the bias voltage or the external reactance. When the device was in the resistive state, we recorded a much faster oscillation with decaying amplitude, which we will call the relaxation oscillation frequency. The latter frequency was around 5 MHz. We found that the relaxation frequency was essentially the same for all devices we have measured, and insensitive to large changes in the external circuit. For example, low-pass filters with different cut-off frequencies were inserted in series with the DC bias supply. Thus we hypothesize that the relaxation oscillations are related to physical phenomena inside the device itself. Figure 2 shows the waveforms of both voltage and current of a $1\mu\text{m}$ long device. Observing the waveforms carefully we found that the maximum voltage across the device corresponds to the product of the average current and the normal resistance of the entire device. This implies that at the time when the peak voltage was recorded, the normal hotspot region covers the total length of the device. Thus we have reason to believe that the relaxation oscillation is due to the fact that the hotspot in the device changes its size periodically. If we assume that the resistivity inside the hotspot is equal to the resistivity of the NbN in its normal state, then the resistance of the device will vary periodically, and consequently the voltage across the device as well. We later found that in longer devices (5 and $10\mu\text{m}$) the hotspot may not cover the entire length of the device. Its maximum size is proportional to the ratio of the peak voltage and the average current. The relaxation frequency of the longer device is somewhat lower than that of the short device because the hotspot travels longer in this case. A remarkable feature of these measurements is that the relaxation oscillations occur at a frequency (about 5 MHz) which is much lower than the frequency at which the device responds during mixing (in the low GHz range). Since movements of the hotspot boundary are likely to be important for modeling the device behavior in all of its possible states, we have continued to explore and measure the dynamic behavior of hotspots in NbN HEB devices.

In order to observe the hotspot boundary movement more directly, we performed a new set of pulsed measurements. Two pulse generators were inserted parallel to the DC bias supply in Figure 1. We investigated three ways of initiating the movement of the hotspot boundary by using the pulsed sources: 1) the device makes a transition from the superconducting state to the normal state (“fly-out”), 2) the device makes a transition from the normal state to the superconducting state (“fly-back”), 3) the size of the hotspot changes within the stable hotspot region. We concentrate on the fly back condition in this paper, and will only comment briefly on the other two cases, as well as the relaxation oscillations, at the end of the paper. The devices being used in this experiment are again phonon cooled NbN HEB devices similar to our mixer devices. The thickness of the film is 4nm, the width of the devices is $5\mu\text{m}$, and the length of the devices is $1\mu\text{m}$ and $5\mu\text{m}$, respectively. In the experiment, after we have applied two positive pulses the device is in

the normal state; it is then transferred from the normal state to the superconducting (SC) state under a constant bias current. We find, in accordance with the theory which will be discussed in a later section, that the current has to be less than the minimum propagation current I_p , for the device to make this transition back to the SC state. We are able to calculate the propagation velocity of the hotspot boundary by analyzing the transient voltage and current waveforms. We reported an order of magnitude discrepancy between the theory and measured data on relaxation oscillations in [1]. Further details about the earlier measurements and the theory can be found in [3]. In this paper we propose that the original bistability theory needs to be modified by taking in account the Andreev Reflection and the phonon specific heat. The agreement between the modified theory and the measured data has been significantly improved.

II. EXPERIMENTS AND RESULTS

The experimental setup is similar to that in [1] except that we are using a current source instead of a voltage source. The device is first biased in the superconducting state. Then two positive current pulses are applied; the first one lasts about 75ns with an amplitude of 1.5mA, which generates a hotspot in the device; the second current pulse lasts about 2 μ s. Its amplitude is above the minimum propagation current I_p when combined with the bias current. The duration of the second pulse should be long enough so that the hotspot can expand and cover the entire device. After the second pulse ends, the device is biased only through the DC power supply, which is set to a value below I_p . The hotspot begins to shrink under this condition and finally disappears, and the device goes back to the superconducting state. The transient response of the voltage and the current of the device are recorded by a fast digital oscilloscope. Figure 3 shows the voltage and the current responses during this process. The voltage gradually decreases with time until it reaches zero, while the current stays at an intermediate value until the time when the voltage goes to zero, when it returns to the value set by the bias supply after a brief positive transient. We will try to explain this behavior in the next section. The same procedure was repeated for several different DC bias currents below I_p . The hot spot boundary velocity was calculated for the time period when the voltage changed linearly with time and the current was essentially constant, as marked in Figure 3. The velocity of the hotspot boundary can be calculated from the measured transient voltage and current waveforms as:

$$v = \frac{L}{2R_N} \frac{dV}{dt} [I(t)]^{-1} \quad (1)$$

where L is the maximum length of the hotspot, and R_N is the normal resistance of the entire device. The factor of 1/2 is used because there are two hotspot boundaries involved.

We find that the larger the difference between I_p and the measured average current is, the shorter time it takes for the device to go back to the superconducting state. Figure 4 shows the measured results (filled triangles) for the $1\mu\text{m}$ long device. We measured both $1\mu\text{m}$ and $5\mu\text{m}$ long devices and got similar results.

III. DISCUSSION

As shown in [1] and [2], when the bias current is less than the minimum propagation current (I_p) there is only one interception point between the curves of Joule heating (Q) and heat transport (W) as a function of temperature. This means that there is only one stable state in this case: the device will eventually go back to the superconducting state. The time needed for the device to go back to the superconducting state depends on the difference between Q and W . The device operating under a lower bias current will take a shorter time. As the voltage across the device decreases gradually, the current stays at an intermediate constant level, which is independent of the voltage, until the device becomes superconducting. Figure 5 shows the usual IV curve of the device, as well as the current when the voltage decreases from the stable hotspot region, based on our fly back measurement data. Note that this behavior is very similar to the hysteresis effect, which happens when decreasing the bias voltage in the IV curve from the left-most point in the stable hotspot region. The difference is that the device is still in the stable hotspot state when decreasing the bias voltage, and the current through the device at this time is the minimum propagation current I_p ; during the fly back measurement, the device is instead in the transition state from the normal state to the superconducting state, and the current through the device must be less than I_p because the hotspot is shrinking. The current stabilizes at a new value slightly lower than I_p , but greater than the current imposed by the bias supply. In other words, the hotspot seems capable of self regulating the current, even in the dynamic state. We may designate this current I_p^{dyn} . The value of this current also depends on the current imposed by the bias supply, I_B . The lower I_B is, the lower is also I_p^{dyn} .

In order to fit the measured results to the bistability theory we need to calculate the normalized velocity with normalizing factor v_h , which is called the thermal velocity and is expressed as [1],[2]:

$$v_h = \frac{1}{C_e} \sqrt{\frac{2\lambda_e h}{kt}} \quad (2)$$

where C_e is the specific heat of the electron system; λ_e is the lateral thermal conductivity of the NbN film; h is the heat transfer coefficient to the substrate; k is a constant, and t is the thickness of the film. The normalized velocity can now be calculated as in [1] and [2]. We find the measured velocity to be drastically lower than the theory based on the bulk

thermal conductivity for NbN. We believe that the reason for this large discrepancy is that the value of v_h calculated in equation (2) is too high. In order to reduce v_h we propose that the theory needs to be modified by taking into account two effects: phonon specific heat and Andreev Reflection. Firstly, in the case of NbN films it is well known that the energy given off by the hot electrons to the phonons is not immediately transported to the substrate (the phonons effectively make a few “bounces” in the film before they can escape through the film/substrate interface). As the hotspot shrinks, and the film cools down from being normal at just above T_c (10 K) to being superconducting at 4.2K, energy must be released from the phonons as well as from the electrons. The evidence from the bandwidth studies [4] suggests that essentially the entire value of the phonon specific heat, C_p , should be added to C_e in equation (2). Secondly, Andreev Reflection must be considered when a current passes through a normal to superconducting interface. Figure 6 illustrates the process of Andreev Reflection. Assume that the Fermi energy is zero, and that the superconducting energy gap of the NbN film is 2Δ . An electron in the normal hotspot with energy less than Δ will be reflected back as a hole by the superconducting-normal boundary, while two electrons are transferred across the interface to form a Cooper pair, which adds to the superconducting Cooper pair condensate. Note that the Andreev Reflection preserves the current continuity. However, only charge is transferred, and no heat is transported across the interface. Thus the superconducting-normal interface acts as a perfect thermal isolator. Only the electrons with energy higher than Δ can transfer the heat. To obtain a first-order estimate¹ of the thermal conductivity across the interfaces, we assume that it is proportional to the fraction α_{th} of the incident electrons that can transport heat across the interface. This fraction can be calculated by multiplying the Fermi-Dirac distribution function, and a constant density of states (justified by the very small energy range), to find the electron density in the normal hotspot, $n_E(E)$, and then integrating over the appropriate energy intervals [5]:

$$\alpha_{th} = \frac{\int_{\Delta}^{\infty} n_E(E) dE}{\int_{-\infty}^{\infty} n_E(E) dE} = \frac{kT \ln \left(1 + e^{-\frac{\Delta(T)}{kT}} \right)}{kT \ln 2} \quad (3a)$$

$$\Delta(T) = \Delta_0 \left(1 - \frac{T}{T_c} \right)^{\gamma} \quad (3b)$$

The exponent γ in (3b) is the same as in the expression for the temperature-dependence of

¹ A more accurate calculation would weight the electron density to yield the actual energy flow across the interface [6].

the critical current:

$$I_C(T, x) = I_C(0) \left[1 - \frac{T(x)}{T_C} \right]^\gamma \quad (4)$$

Here γ is chosen to be 1.0 to achieve the best fit with measured data for NbN devices on MgO substrates. As we apply a bias current to a device, the critical temperature of the film is partially suppressed by the current. We can use (4) to calculate an effective critical temperature, which we then use when performing the integral in (3a). Finally, after taking into account the phonon specific heat and the Andreev Reflection effect, the thermal velocity in equation (2) changes to:

$$v_h = \frac{1}{C_e + C_p} \sqrt{\frac{2\alpha_{th}\lambda_e h}{kt}} \quad (5)$$

Figure 4 shows the measured normalized hotspot boundary velocity vs. current, compared with calculations based on the modified theory (Eq. (5)). We adjusted the value of α_{th} to obtain a best fit between the measured data and theory. If we calculate α_{th} from (3a) we find a value which is about twice as large, as summarized in Table 1. Note that the latter calculation uses only measured parameters. Given the uncertainties in several parameters, and the error bars in the measurements, we believe that the agreement between theory and experiment is satisfactory. For example, a small adjustment of the parameter γ from 1.0 to 0.8 will produce much better agreement, as also noted in Table 1. We note that a similar measurement to the one reported here was performed by Freytag and Huebener [7]. These researchers measured Sn films and obtained agreement between theory and experiment without invoking Andreev reflection. The AR would have a much smaller effect in the case of Sn due to its smaller bandgap.

IV. CONCLUSION

In this paper the movement of the hotspot boundary when the HEB device makes transitions from the normal state to the superconducting state has been successfully measured. The measurement results fit the theory quite well after taking into account the phonon specific heat and Andreev Reflection effect. It is quite clear that under the conditions of this particular measurement the hotspot boundaries move very slowly, compared with the thermal response time of the device as a mixer. We also found an additional interesting phenomenon: the device is able to stabilize the current during the dynamic transient response. We want to briefly comment on the results of other experiments which we have done so far. When we triggered the device with a pulse to make a transition from the superconducting state to the normal state, we found an even slower velocity than measured here (for a given value of $I-I_P$). It is possible that during

this transition, during which the device is in a strong negative resistance state, further nonlinearities play a role. Measured pulse response when the device moves from one stable hotspot state to another (either with or without applied LO power) appears faster than the process described in this paper, based on preliminary measurements. However, we must improve the detection speed of our measurement system in order to confirm this. The relaxation oscillation frequency is predicted very well (within a factor of two) based on our modified model. In order to fully understand the mechanism of the hotspot boundary propagation more experiments clearly need to be performed and interpreted under different conditions.

V. ACKNOWLEDGEMENTS

We would like to acknowledge stimulating discussions with Drs. Harald Merkel and Erik Kollberg of Chalmers University of Technology. We would also like to acknowledge support from NASA Contract NAS1-01058 from NASA Langley Research Center, and from the NSF program for Advanced Technologies and Instrumentation (ATI), Division of Astronomical Sciences, NSF award # AST 9987319.

REFERENCES

- [1] Y. Zhuang and S. Yngvesson, "Detection and Interpretation of Bistability Effects in NbN HEB devices", 13th Intern. Symp. Space THz Tech., pp.463-472 (2002).
- [2] A.V.I. Gurevich and R.G. Mints, "Self-Heating in Normal Metals and Superconductors," Rev. Mod. Physics, **59**, pp. 94-999 (1987).
- [3] Y. Zhuang, "Linear and Nonlinear Characteristics of NbN Hot Electron Bolometer Devices," Ph.D. Thesis, Dept. of Electrical and Computer Engineering, University of Massachusetts at Amherst, Sept. 2002.
- [4] S. Cherednichenko, P. Yagoubov, K. Il'in, G. Gol'tsman, and E. Gershenzon, "Large Bandwidth of NbN Phonon-Cooled Hot-Electron Bolometer Mixers on Sapphire Substrates", 8th Intern. Symp. Space THz Tech., pp. 245-257 (1997).
- [5] H. Merkel, "A Hot Spot Model for HEB Mixers Including Andreev Reflection", 13th Intern. Symp. Space THz Tech., pp. 53-64 (2002).
- [6] H. Merkel, priv. comm..
- [7] L. Freytag and R.P. Huebener, "Temperature Structures in a Superconductor as a Nonequilibrium Phase Transition," J. Low Temp. Physics, **60**, 377 (1985).

Table 1: Comparison of the AR factor α_{th} between the measurement and the calculation

Length (μm)	1	5
α_{th} (Measure)	0.08	0.12
α_{th} (Calculate) for $\gamma=1$	0.18	0.21
α_{th} (Calculate) for $\gamma=0.8$	0.10	0.11

FIGURES

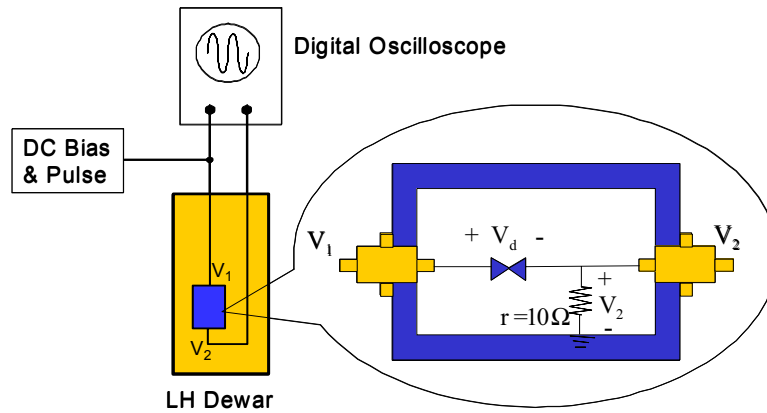


Figure 1: Experimental setup for the bistability measurement

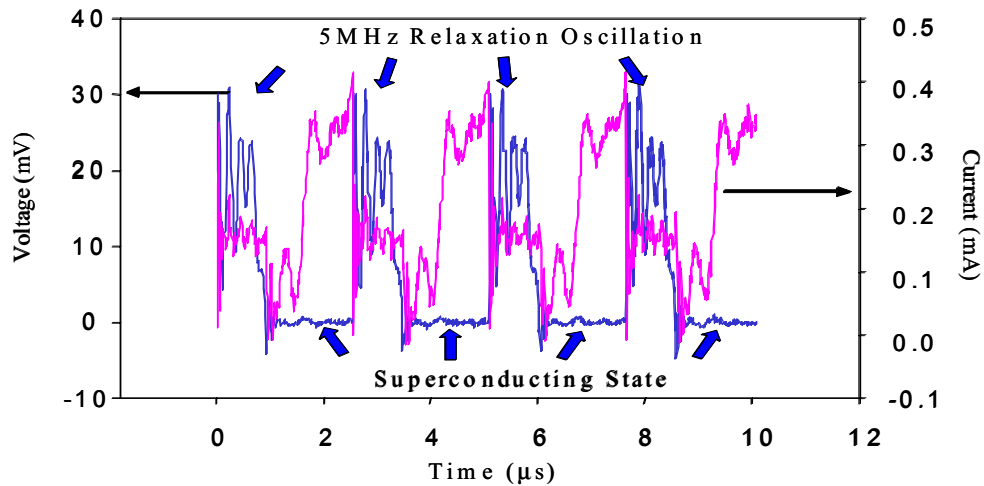


Figure 2: Voltage and current waveform in the bistability region of the HEB device

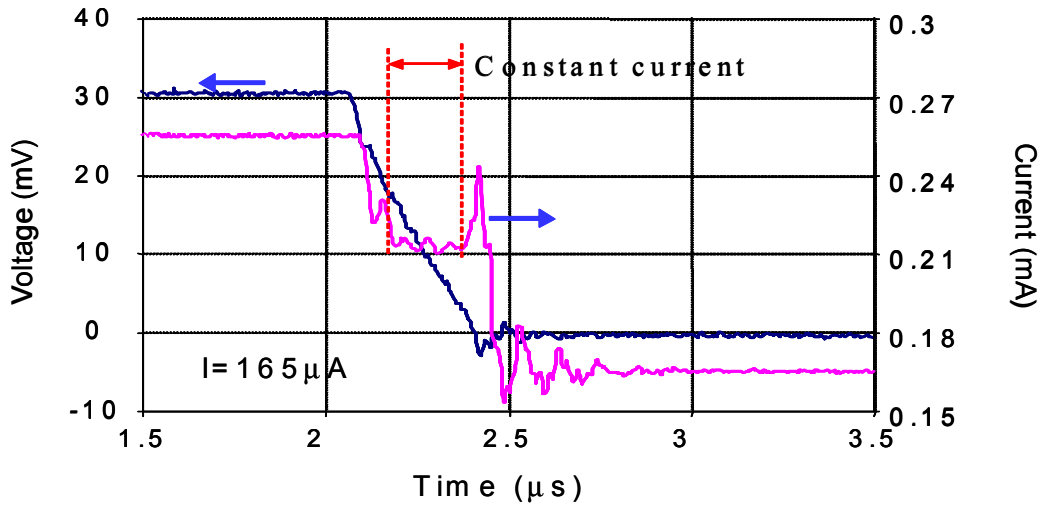


Figure 3: Voltage and Current waveform in the fly back measurement with bias current $I=165\mu\text{A}$

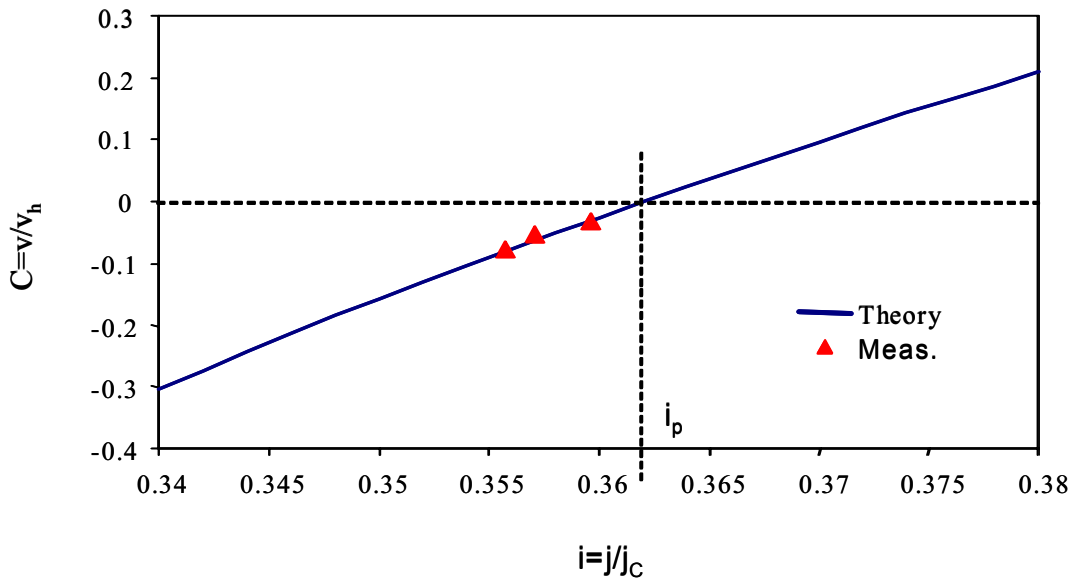


Figure 4: Comparison of normalized propagation velocity of the hotspot boundary between the measurement and the modified bistability theory

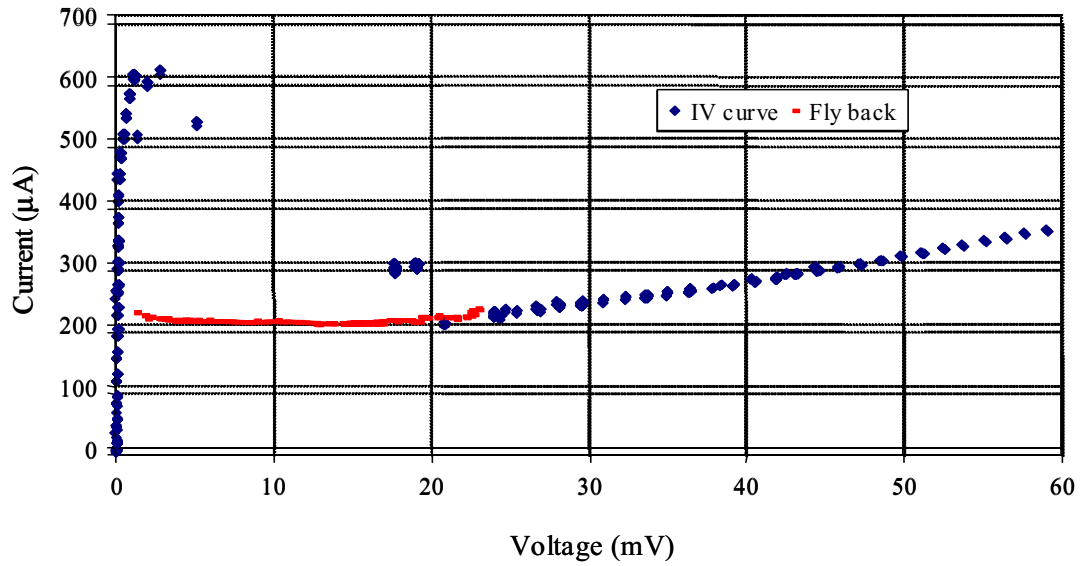


Figure 5: IV curve from DC bias supply and IV relation from fly back measurement

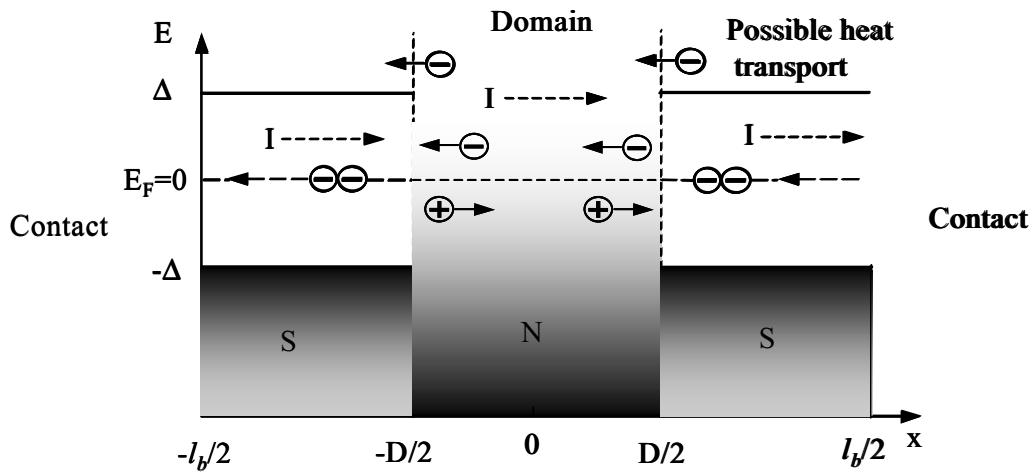


Figure 6: Andreev reflection and possible heat transport in an HEB device

Heterostructure Barrier Varactor Frequency Triplers to 220 – 325 GHz

Yiwei Duan, Qun Xiao, Jeffrey L. Hesler, and Thomas W. Crowe
Department of Electrical and Computer Engineering
University of Virginia, Charlottesville, VA 22903 USA

Abstract --- HBV frequency triplers to the WR-3 waveguide band have been designed, fabricated and tested. The epitaxial materials used were from the InGaAs/InAlAs material system. The initial batch of discrete planar HBVs was designed and fabricated based on a three-barrier epitaxial wafer. Individual chips were fabricated and flip-chip mounted on existing quartz circuits designed for a Schottky diode tripler. Test results showed that these six-barrier planar HBVs could not be fully pumped with available input power of about 100mW. To achieve better performance in terms of efficiency and output power, a two-barrier epitaxial wafer with lower doping in the modulation layers was designed and purchased. With the same mask set as for the previous run a batch of discrete planar HBV was fabricated with this new wafer and tested.

Next, integration of the HBV diodes directly on the quartz circuit was considered and determined to reduce parasitic capacitance, ease assembly and improve reliability. Therefore our semiconductor-on-quartz integration process was modified to allow the formation of InGaAs mesas and an integrated version of the HBV circuit was designed and fabricated. This batch of integrated HBV triplers showed dramatically improved performance. Output power of 3.87 mW and efficiency of 4.5% at 300 GHz were measured with an Erickson PM1B power meter (about 6mW was measured with an Anritsu WR-3 meter). Issues concerning the epitaxial wafer design, device fabrication and tripler testing will be presented in this paper.

I. INTRODUCTION

People are becoming more and more interested in millimeter and submillimeter-wave technology for such applications as radio astronomy, chemical spectroscopy and atmospheric studies [1, 2, 3]. However, this frequency range is technologically very challenging, and amplifiers are not available. Therefore, heterodyne receivers are used in this research field to convert, by frequency mixing, the high frequency spectrum to a low frequency range where it can be amplified and analyzed. In this application, millimeter and submillimeter-wave local oscillators with sufficient output power are needed. Because fundamental oscillators and amplifiers do not work well above about 150 GHz, frequency multipliers, i.e. nonlinear harmonic generators, are widely used. In principle, any nonlinear impedance can be used to generate frequency harmonics. However, variable capacitance, or varactor, diodes have better efficiency and power handling capabilities than variable resistance, or varistor, diodes for this application.

HBV's, which were proposed by Kollberg in 1989 [4], have excellent characteristics for frequency tripling. Primarily, this is because HBV diodes have a symmetric C-V

characteristic. Thus, for triplers using HBV's, the second harmonic idler circuitry is not necessary because only odd harmonics are produced. Furthermore, DC bias is not needed because the capacitance modulation region is centered at zero-bias. Therefore, the circuit design is much simpler than that required for a standard Schottky varactor. Also, due to the stackable barrier structure of HBVs, large power handling ability can be achieved by stacking more barrier layers vertically instead of putting more diodes in series as is done with Schottky diode frequency multipliers. HBV triplers have recently been demonstrated to have good performance to WR-3 band frequencies by this research and others [5, 6].

II. DEVICE FABRICATION

To make an HBV frequency tripler with greater efficiency, lower leakage current through the barrier is preferred. Therefore materials with higher barrier height are preferred. So InGaAs/InAlAs/InGaAs materials were chosen in our research instead of GaAs/AlGaAs/GaAs.

The MBE grown 3-inch diameter epitaxial wafers were purchased from Global Communication Semiconductors, Inc. <<http://www.gcsincorp.com/>>. The first structure is shown in Table 1. Strained thin layers of AlAs are added to improve the barrier height [7]. The InAs capping layer was added to make non-alloyed ohmic contacts [8].

	Layer Thickness	Layer Doping	Material	Repeat
n ⁺⁺ Contact Layer	10nm	n ⁺⁺	InAs	
	40nm	n ⁺⁺	In _x Ga _{1-x} As x=0.53 to 1	
	100nm	n ⁺⁺	In _{0.53} Ga _{0.47} As	
Modulation	300nm	1.7X10 ¹⁷ cm ⁻³	In _{0.53} Ga _{0.47} As	
Spacer	20nm	u-d	In _{0.53} Ga _{0.47} As	X 3
Barrier	5nm	u-d	In _{0.52} Al _{0.48} As	
	3nm	u-d	AlAs	
	5nm	u-d	In _{0.52} Al _{0.48} As	
Spacer	20nm	u-d	In _{0.53} Ga _{0.47} As	
Modulation	300nm	1.7X10 ¹⁷ cm ⁻³	In _{0.53} Ga _{0.47} As	
n ⁺⁺ Buffer Layer	3μm	n ⁺⁺	In _{0.53} Ga _{0.47} As	
Substrate	650μm	SI	InP	

Table 1: Lattice matched InGaAs/InAlAs/InGaAs on InP substrate for 6-barrier HBV.

To evaluate the quality of the epitaxial material, whisker contacted HBV's with large mesas (diameter of 70μm) were made on a 0.2 by 0.2 inch square wafer and tested. Then discrete planar HBV's were made on a 0.4 by 0.5 inch wafer. The fabrication processing includes the following steps, 1. modulation mesa etch, 2. ohmic contact metals evaporation and lift-off, 3. ohmic contact thermal treatment (around 330 C° to 340 C°), 4. planarization and ohmic contact area reopening, 5. seed layer gold sputtering, 6. finger and contact pad patterning and gold plating, 7. photoresist and seed layer gold removal, 8. surface channel isolation etch, 9. substrate thinning and device separation. Several

variations of HBV's with different mesa sizes were fabricated. An SEM picture of a discrete planar HBV before separation is shown in Fig. 1.

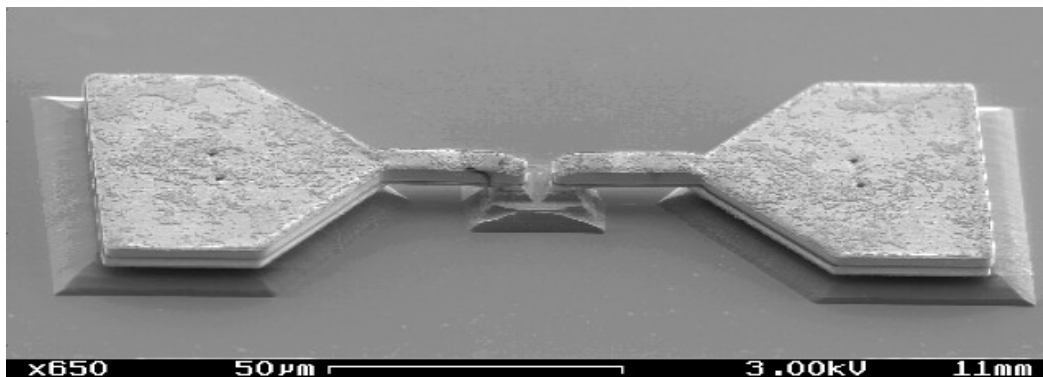


Fig. 1: SEM of a discrete planar HBV before separation.

Flip-chip mounting of the discrete HBV diode onto a quartz circuit is always a hard task to fulfill. Integration of the HBV diodes with the quartz circuit during the device fabrication process makes the tripler block assembly much easier. It also provides perfect alignment of the diode to the circuit and reduces shunt capacitance. Therefore, integration should improve tripler performance, repeatability and reliability.

The integrated HBV circuits were made on a 0.4 by 0.5 inch wafer. The fabrication processing includes the following steps, 1. wafer bonding on quartz, 2. modulation mesa etch, 3. non-alloy ohmic contact metals evaporation (Ti 1000Å / Au 2000Å) and lift-off, 4. n^{++} mesa etch, 5. planarization and ohmic contact area reopening, 6. seed layer Ti and Au evaporation and Au sputtering, 7. finger and circuit patterning and gold plating, 8. photoresist and seed layer metals removing, 9. substrate thinning and device separation. An SEM image of an integrated HBV circuit before separation is shown in Fig. 2.

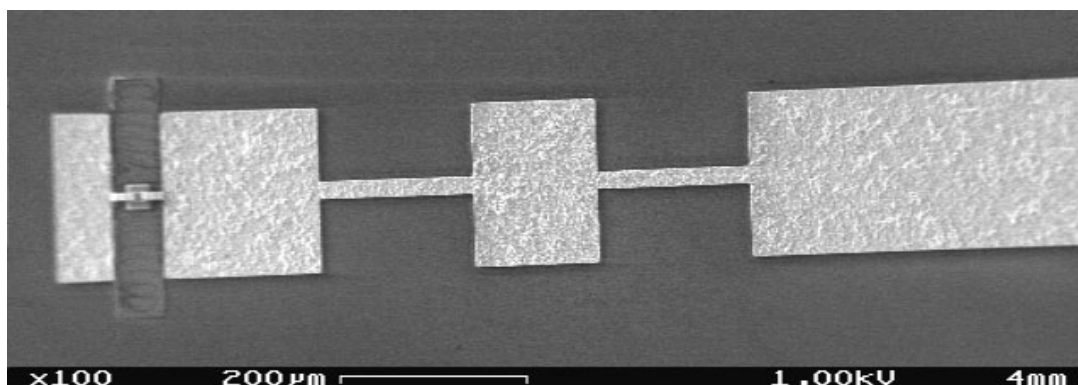


Fig. 2: An SEM view of an integrated HBV circuit before separation. The dark areas are the quartz substrate, the light areas are the deposited metal circuitry and the small InGaAs mesa is shown near the left end and is contacted by two air-bridged fingers.

III. DC AND RF MEASUREMENTS

A. Whisker Contacted HBV

The C-V and I-V characteristic of the 6-barrier whisker contact HBV were measured, and they showed good symmetry and anti-symmetry, respectively. However, the measured value of capacitance at zero bias (1.6pF, see Fig. 3) is significantly larger than calculated (1.1pF). The calculation is based on [9], in which the spacer layers are modeled as part of the barrier when calculating junction capacitance. If the effect of the spacer layers is excluded, the calculated capacitance at zero bias is 2.2pF. Therefore, we believe that a significant number of electrons from the modulation layers have diffused into the spacer layers and thereby increased the zero bias junction capacitance.

B. Six-Barrier-Discrete-HBV Frequency Triplers

After testing at DC bias, a discrete 6-barrier HBV was flip-chip mounted onto a quartz circuit and assembled into a tripler block. The RF testing result is shown in Fig. 4. This data indicates that the efficiency has not saturated at the maximum available input power. Thus, the 6-barrier HBV frequency tripler could have even higher efficiency with higher input power. In other words, these HBV diodes are not optimized at the maximum available input power. Therefore, we decided to fabricate another batch of HBVs with only four barriers to reduce the amount of power required for optimum efficiency.

C. Four-Barrier-Discrete-HBV Frequency Triplers

The epitaxial structure for 4-barrier HBVs is shown in Table 2. Compared to the 6-barrier design, this wafer has fewer barriers (reduced from 3 to 2), lower modulation layer doping (reduced from $1.7 \times 10^{17} \text{ cm}^{-3}$ to $1.0 \times 10^{17} \text{ cm}^{-3}$) and thinner spacer layers (reduced from 20nm to 5nm). The first two modifications were made to increase efficiency at the available input power. The spacer layers are used to prevent dopant diffusion and electron wave function penetration [7]. However, we concluded that five nanometers thick spacer layers are sufficient. The thinner spacer layers also make the $C_{\text{max}}/C_{\text{min}}$ ration larger, thereby yielding higher cut-off frequency and better efficiency [9, 10].

The RF testing result of one tripler is shown in Fig. 5. Because the mask set for previous 6-barrier HBV was used to fabricate this batch of 4-barrier HBV diodes, the junction capacitance of this batch is 50% larger. Therefore, the cutoff frequency is lower and testing was performed at 81/243 GHz.

Several sample diodes were sent to Dr. Chris Mann at the Rutherford Appleton Laboratory (UK). Their tripler block has both input and output tuning back shorts to optimize coupling, while our block has only an input E-H tuner attached externally to the block. The RAL results, shown in Fig. 6, are excellent and demonstrate the quality of this batch of HBV diodes.

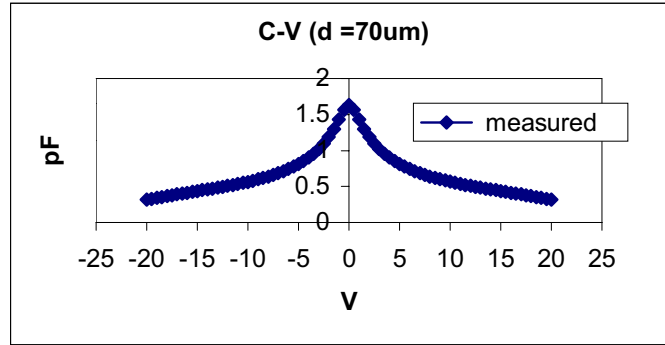


Fig. 3: C-V curve of a six-barrier whisker contacted HBV.

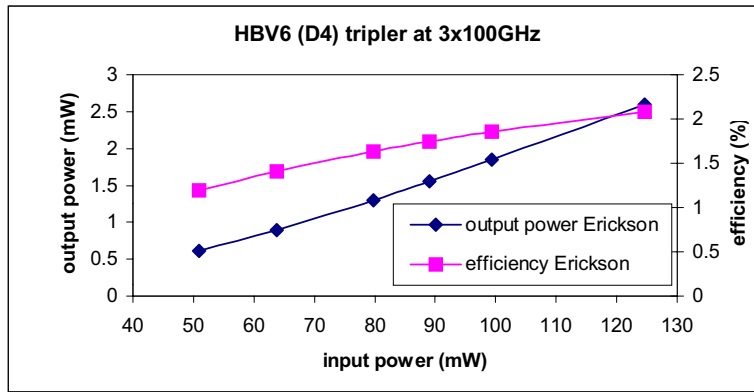


Fig. 4: Output power and efficiency of a 100/300GHz frequency tripler with a 6-barrier discrete HBV.

	Layer Thickness	Layer Doping	Material	Repeat
n ⁺⁺ Contact Layer	10nm	n ⁺⁺	InAs	
	40nm	n ⁺⁺	In _x Ga _{1-x} As x=0.53 to 1	
	100nm	n ⁺⁺	In _{0.53} Ga _{0.47} As	
Modulation	300nm	1.0X10 ¹⁷ cm ⁻³	In _{0.53} Ga _{0.47} As	
Spacer	5nm	u-d	In _{0.53} Ga _{0.47} As	X 2
Barrier	5nm	u-d	In _{0.52} Al _{0.48} As	
	3nm	u-d	AlAs	
	5nm	u-d	In _{0.52} Al _{0.48} As	
Spacer	5nm	u-d	In _{0.53} Ga _{0.47} As	
Modulation	300nm	1.0X10 ¹⁷ cm ⁻³	In _{0.53} Ga _{0.47} As	
n ⁺⁺ Buffer Layer	3μm	n ⁺⁺	In _{0.53} Ga _{0.47} As	
Substrate	600μm	SI	InP	

Table 2: Lattice matched InGaAs/InAlAs/InGaAs on InP substrate for 4-barrier HBV.

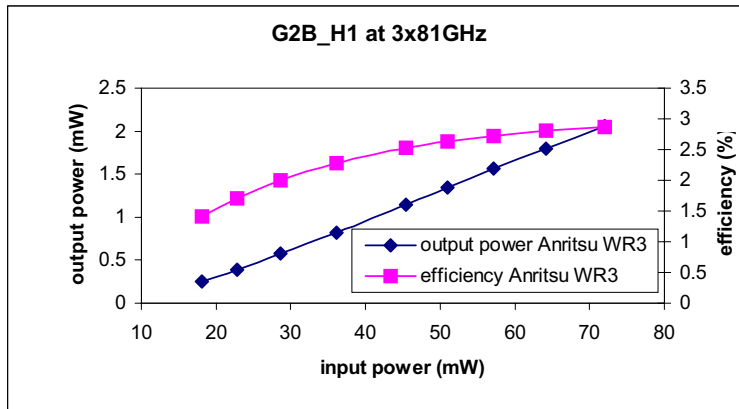


Fig. 5: Output power and efficiency of an 81/243GHz frequency tripler with a 4-barrier discrete planar HBV.

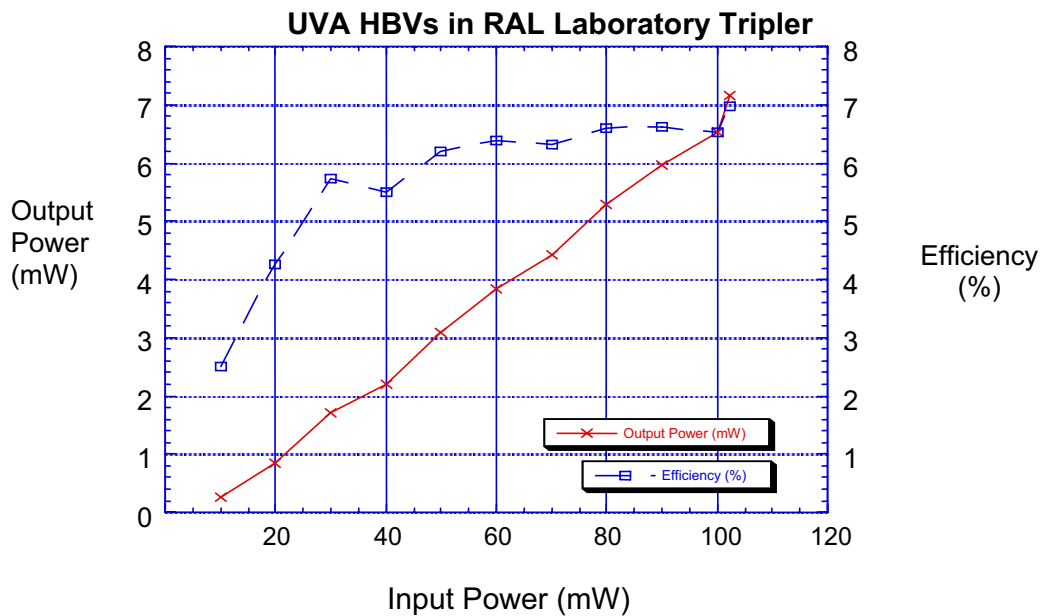


Fig. 6: Output power and efficiency of an 82/246GHz frequency tripler of RAL lab using UVa 4-barrier discrete planar HBV.

D. Four-Barrier-Integrated-HBV Frequency Triplers

In the previous batch of discrete 4-barrier HBV frequency triplers, the design with the smallest modulation mesa size had the best efficiency and the efficiency was still not saturated at the maximum input power. In the integrated version, several variations were included with smaller modulation mesa sizes.

A frequency tripler was very easily assembled by bonding an integrated HBV circuit into the channel of the block with glue. The RF test data is shown in Fig. 7. This result is on par with the best reported HBV frequency tripler at the same frequency [6].

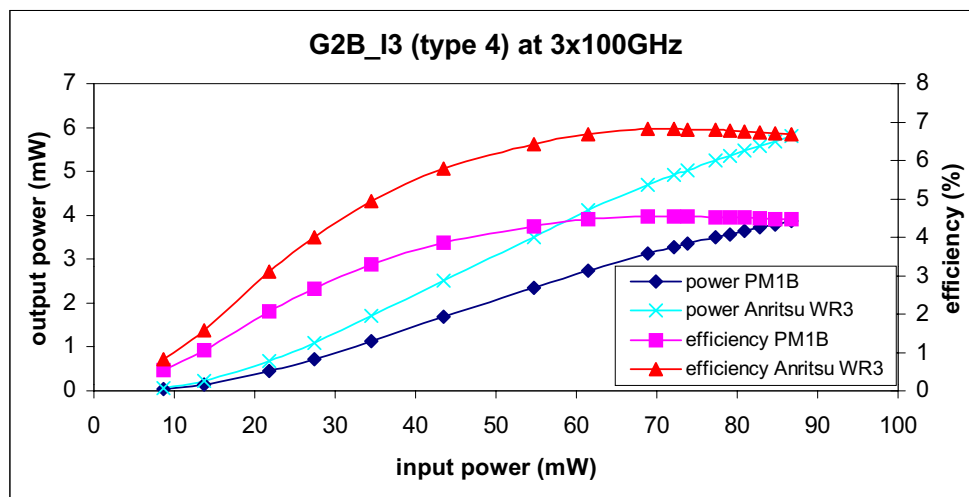


Fig. 7: Output power and efficiency of a 100/300GHz integrated 4-barrier HBV frequency tripler.

E. Output Fix-Tuned Integrated HBV Frequency Triplers

Encouraged by the results from the previous run of integrated HBV frequency triplers, we attempted to improve the performance further by adding a tuning circuit in the output matching network of the quartz circuitry. To make sure that we achieve the right impedance target, many variations of tuning circuits were designed. Also, modulation mesas have just one size which is a little larger than the best performer from previous integrated batch. However, the RF test results were only improved marginally. We believe the reason is that the output matching for previous untuned integrated version may be already good enough.

IV. CONCLUSION

Discrete and integrated HBV frequency triplers to WR-3 waveguide were designed, fabricated and tested. Integration significantly improved the tripler performance and reliability because of the better alignment, lower parasitic capacitance and easier assembly. Output power of 3.87 mW and efficiency of 4.5% at 300 GHz were measured with an Erickson PM1B power meter (about 6mW on with an Anritsu WR-3 meter). This tripler can be a good LO source for a heterodyne receiver or a good input source for another multiplier to higher frequencies.

ACKNOWLEDGEMENT

This research was supported by the following contracts, Army Research Office (MURI) grant DAAD19-01-1-0622, NASA grant NAG5-8663, and the Army National Ground Intelligence Center grant DASC01-01-C-0009. Mr. Bill Bishop (UVa) gave a lot of advice about the fabrication process. Dr. Chris Mann (RAL) built a HBV tripler using our discrete HBV and supplied the data shown in Fig. 6. Dr. Jan Stake (Chalmers University) provided some initial material and lots of advice on material design and processing.

REFERENCES

- [1] R. Blundell and C.-Y.E. Tong, "Submillimeter Receivers for Radio Astronomy," *Proc. of IEEE*, Vol. 80, No. 11, pp. 1702-1720, Nov. 1992.
- [2] G. A. Blake, K. B. Laughlin, R. C. Cohen, K. L. Busarow, D-H. Gwo, C. A. Schmuttenmaer, D. W. Steyert, and R. J. Saykally, "Tunable far infrared laser spectrometers," *Rev. Sci. Instrum.* Vol. 62, No. 7, pp.1693-1700, July 1991.
- [3] J.W. Waters, L. Froidevaux, W.G. Read, G.L. Manney, L.S. Elson, D.A. Flower, R.F. Jarnot and R.S. Harwood, "Stratospheric ClO and Ozone from the Microwave Limb Sounder on the Upper Atmosphere Research Satellite," *Nature*, Vol. 362, pp. 597-602, April 15, 1993.
- [4] E. Kollberg and A. Rydberg, "Quantum-Barrier-Varactor diodes for high-efficiency millimeter-wave multipliers," *Electronics Letters*, Vol. 25, No. 25, pp. 1696-1698, Dec. 1989.
- [5] X. Melique, A. Maestrini, R. Farre, P. Mounaix, M. Favreau, O. Vanbesien, J. Goutoule, F. Mollet, G. Beaudin, T. Nahri and D. Lippens, "Fabrication and Performance of InP-Based Heterostructure Barrier Varactors in 250-GHz Waveguide Tripler," *IEEE Transactions on Microwave Theory and Techniques*, Vol. 48, No. 6, pp.1000-1006, June 2000.
- [6] T. David, S. Arscott, J.-M. Munier, T. Akalin, P. Mounaix, G. Beaudin, and D. Lippens, "Monolithic Integrated Circuits Incorporating InP-Based Heterostructure Barrier Varactors," *IEEE Microwave and Wireless Components Letters*, Vol. 12, No. 8, pp.281-283, August 2002.
- [7] Y. Fu, J. Stake, L. Dillner, M. Willander, E. L. Kollberg, "AlGaAs/GaAs and InAlAs/InGaAs heterostructure barrier varactors," *J. Appl. Phys.* 82 (11), 5568-5572, 1 December 1997.
- [8] J. M. Woodall, J. L. Freeout, G. D. Pettit, T. Jackson, and P. Kirchner, "Ohmic contacts to n-GaAs using graded band gap layers of Ga_{1-x}In_xAs grown by molecule beam epitaxy," *J. Vac. Sci. Technol.*, 19 (3), 626-627, Sept./Oct. 1981.
- [9] J. Stake, S. Jones, L. Dillner, S. Hollung and E. Kollberg, "Heterostructure-Barrier-Varactors Design," *IEEE Transactions on Microwave Theory and Techniques*, Vol. 48, No. 4, pp.677-682, April 2000.
- [10] P. Penfield and R. P. Rafuse, *Varactor Applications*. Cambridge, MA: MIT Press, 1962.

THz Range Unipolar Ballistic Tunnel-Emission Transit Time Oscillators

N.Z.Vagidov¹, J.East², V.V.Mitin¹ and G.I.Haddad²

¹Department of ECE, Wayne State University, Detroit, MI

²Department of EECS, University of Michigan, Ann Arbor, MI

Abstract

This paper describes THz ballistic transit-time oscillators using a unipolar tunnel injection of electrons from a cathode into a drift region. This new injector design has several advantages over more conventional TUNNETT structures. First, the injection of carriers is by tunneling through a thin barrier, rather than a tunneling p^+n^+ reverse biased junction. The heterobarrier will be easier to fabricate since very high doping and abrupt doping changes will not be required and only n type doping is needed. The p type contact required in a conventional device is not needed, reducing the contact resistance. The barrier current can be tailored to the drift region requirements by proper injector design and the transport in the drift region can be optimized to improve performance. Conventional TUNNETT devices have a high field drift region. The proposed device can have an injector electric field that produces a drift region field similar to a conventional saturated velocity device or a much lower field that will allow ballistic transport. Ballistic transport in the drift region will allow a higher operating frequency.

I. Introduction

Local oscillators are a critical component in all submillimeter and Thz systems. Solid state sources are particularly useful, since they are compact, light, able to withstand vibrations and have modest power requirements. Fundamental solid state oscillators operate to several hundred GHz with harmonic operation further extending the frequency range. However the physics of these devices limits their operation at higher frequencies. Varactor based solid state multipliers can produce nearly a milliwatt at frequencies approaching one Thz, but they require a series of complex circuits to reach this frequency. We will describe a new solid state device fundamental oscillator that overcomes some of the physical limitations of existing solid state

sources and the complexity of multiplier chains. The next section of the paper will describe some of the limitations of existing solid state oscillators. Section III will describe the operation of the proposed new device. Section IV is a brief summary.

II. Limitations of Existing Solid State Oscillators

Existing solid state sources such as Gunn oscillators and transit time devices operate up to several hundred GHz. However their operation at higher frequencies is limited by device and semiconductor physics. Gunn oscillators require an increase in the effective mass of carriers with increasing electric field. Low electron mass central valley electrons transfer to higher mass satellite valleys when they obtain enough energy from the electric field. The valley transfer is fast because of the larger electron density of states in the upper valley. However the operation also requires a decrease in effective mass as the field is reduced from high values. Problems occur at submillimeter frequencies. The difference in densities of state in the two valleys that favors rapid transfer to the upper valley slows the return to the central valley as the field is reduced. This valley transfer delay limits the fundamental operation of Gunn devices to several hundred GHz.

Transit time devices are limited by device design requirements. A transit time device consists of an injection region to introduce carriers into the structure and a transit region to provide the phase delay needed to produce negative resistance. At frequencies below 100 GHz carriers can be injected by avalanche multiplication. Avalanche multiplication also has the advantage of providing additional time delay that improves the phase angle of the carriers being injected. However the avalanche injector is limited for devices designed for high frequencies. The time delay associated with the avalanche, an advantage at lower frequencies, must be scaled to shorter times. The avalanche region width must also be reduced. Both require higher doping and electric fields in the avalanche region. At frequencies above 100 GHz the fields in the avalanche region become large enough that band to band tunneling can occur. A mixed tunneling and avalanche operation and finally a mainly tunneling operation occurs with increasing frequency. The tunneling injection is very fast but the material structure requirements become very precise at submillimeter frequencies. The goal of the device described in this paper is

to overcome the transport limitations associated with the Gunn device and the injector limitations associated with conventional transit time devices to realize a THz frequency solid state oscillator. The design and operation of this new device will be described in the next section.

III. Unipolar Ballistic Transit Time Devices

The structure of the proposed device is shown in Fig. 1. It consists of a cathode and an anode, a heterstructure tunnel barrier and a transit or drift region. Typical materials would be InAs cathode and anode ohmic contacts, an InAlAs barrier and an InGaAs transit region all grown lattice matched on an InP substrate. This structure has several advantages over conventional transit time devices. It has only n type doping, allowing low ohmic contact resistances. The barrier width depends on MBE growth rather than the doping profile of a pn junction. It is much easier to grow a material step than to abruptly change from n to p doping in a junction. The grown barrier width can be less than the depletion layer width associated with even a very heavily doped p^+n^+ junction. The barrier height in a conventional junction depends on the material bandgap. Here the barrier depends on the conduction band offset of the barrier with respect to the cathode. The barrier can be varied by adjusting the barrier material composition, using combinations of InGaAlAs for example.

We can also take advantage of ballistic transport in III-V materials to increase the carrier velocity and the transit time frequency for the same length transit region compared with a conventional device design. This requires careful consideration of the drift region width and voltage drop to obtain the desired overshoot velocities. A small signal model can be used to investigate the operation of ballistic structures. Gildeen and Hines¹ published an analytic expression for the small signal admittance of an avalanche transit time device based on a separation of the device into an avalanche injection region and a saturated velocity drift region. This model can be modified to have a tunnel injector and a ballistic drift region. The drift region characteristics will depend on the carrier dynamics of the ballistic carriers and the injection region characteristics will depend on the properties of the tunnel junction.

¹M. Gildeen and M.F. Hines, "Electronic Tuning Effects in the Read Microwave Avalanche Diode, IEEE Trans. On Electron Devices, Volume ED-13, page 169, 1969.

The proposed device exploits ballistic transport in order to produce very short transit times and THz operation. An analytic analysis can be used to predict ideal operation. However we need a more detailed model to better predict realistic device operation. A Monte Carlo transport model based on a two valley constant effective mass approximation has been used to study transient motion in transit regions for different materials. Typical results are shown in Fig. 2 for an applied electric field of 50 KV/cm. The figure shows several characteristics of nearly ballistic transport. For ballistic motion in a constant electric field the acceleration depends inversely on the electron effective mass. The constant acceleration should give a straight line velocity vs. time up to a peak velocity. This is nearly true for the InGaAs with additional energy loss in the InP due to polar optical phonon scattering. We can plot the velocity information vs. distance instead of time. This is shown in Fig. 3. This figure shows the distance dependence of the ballistic motion. The satellite valley energy is smaller in GaAs so electrons in GaAs travel a shorter distance in the constant electric field before obtaining the energy required for valley transfer. InGaAs electrons travel a larger distance with a higher velocity because of the larger valley separation. The net result is that ballistic electrons can have velocities an order of magnitude larger than the saturated velocities in the same material, but only for distances on the order of a fraction a μ and for times of a fraction of a ps.

The properties of the tunneling barrier are also important. The barrier conductance and capacitance are needed for the small signal injector. An analytic expression for the tunnel current through a barrier between 2 metal contacts with the barrier width, height and material properties such as effective mass as parameters is given by Simmons.² However our proposed device will have semiconducting rather than metal contacts. Properly accounting for the band bending in the semiconductor contact will give a bias dependent barrier with a conductance superior to a similar barrier with metal contacts. A conduction band diagram for a metal and semiconductor contact barrier is shown in Fig. 4. The unbiased structure on the left has a heavily doped semiconductor or metal contact and an undoped barrier. The conduction band is flat. The center structure is a biased barrier with metal contacts. This is the typical structure described by a Fowler-Nordheim expression for

²J. Simmons, "Generalized Formula for the Electric Tunnel Effect between Similar Electrodes Separated by a Thin Insulating Film", Journal of Applied Physics, Volume 34, Number 6, pp 1793-1803, June 1963.

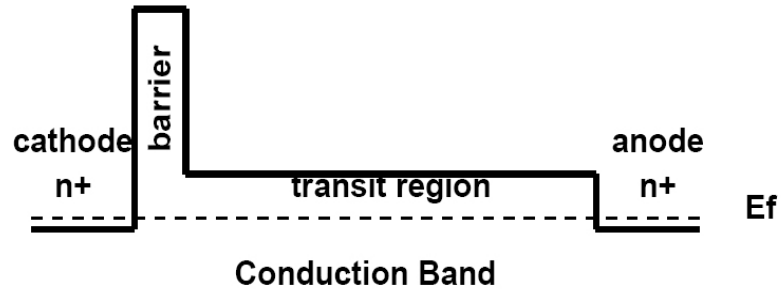


Figure 1: Proposed Unipolar Ballistic Device Structure

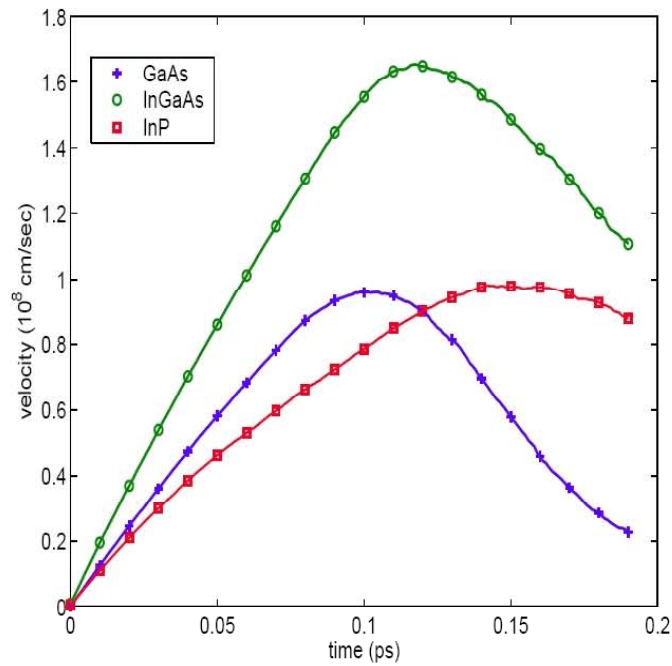


Figure 2: Electron Velocity vs. Time for Various Materials

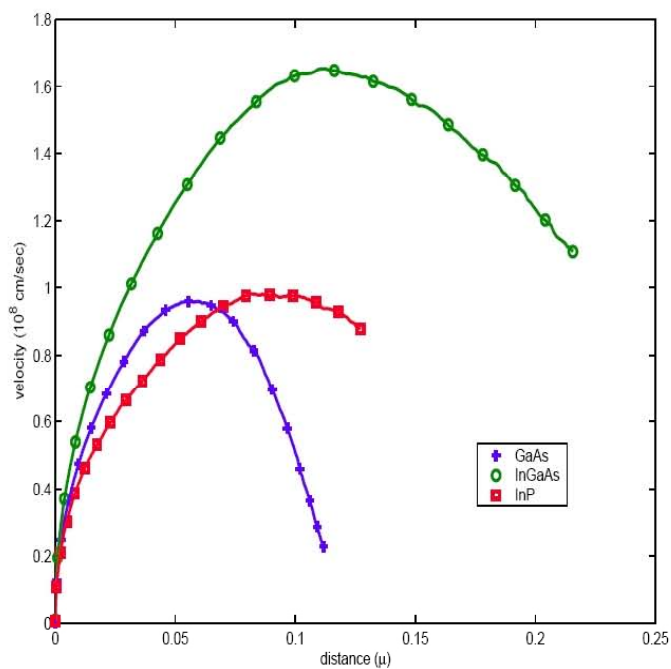


Figure 3: Electron Velocity vs. Distance for Various Materials

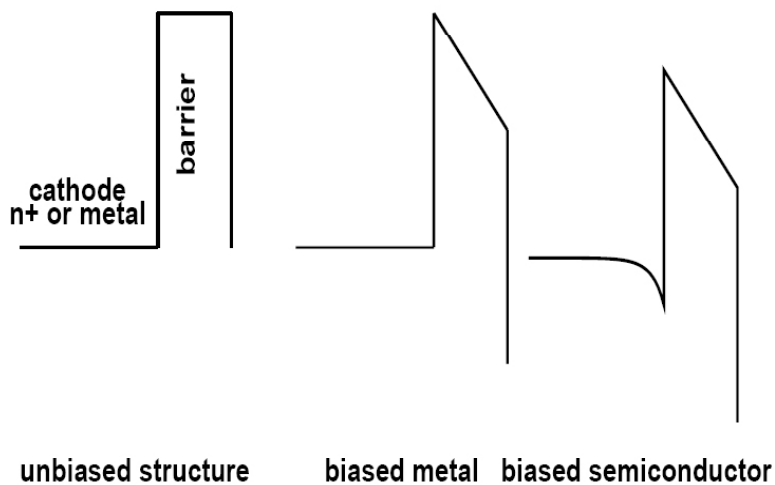


Figure 4: Band Structure for Different Barrier Structures

the tunnel current. All of the applied voltage appears across the barrier. The ballistic structure has the band structure shown on the right. The voltage drop across the barrier is the same as the voltage drop across the center metal structure, but there is additional voltage due to band bending in the semiconductor. The total voltage across the structure is larger for the same barrier voltage drop. However, due to the band bending the "effective barrier height" is lower by the amount of band bending in the semiconductor. The capacitance of the metal contact barrier will be $C_{metal} = \epsilon/w_b$ and will not depend on the bias. The capacitance of the semiconductor contact barrier will be the series combination of the barrier and semiconductor capacitances. The barrier capacitance will be the same as the metal value and the semiconductor capacitance will be the inversion layer capacitance. Except for small differences in the dielectric constants in the barrier and contact materials the electric field will be continuous across the contact barrier interface. A more detailed analysis would include image force lowering at the interface. A simple model based on a Fermi-Dirac solution for the conduction band bending was used with the Fowler-Nordheim current expression for the tunnel current. The barrier height in the tunneling expression will then depend on the semiconductor conditions. This model can be used to investigate the properties of semiconductor barrier structures. The capacitance is on the order of a $\mu F/cm^2$ for a contact doping of $10^{18}/cm^3$. A typical barrier would have an undoped spacer to improve the interface, but this has little effect on the capacitance. If we use an "effective width" for the inversion region based on $C_{inversion} = \epsilon/w_{effective}$, then the inversion layer is 40 to 60 Å wide. We will see in the next paragraph that the barriers are on the order of 20 to 50 Å thick, so the effective capacitance of the barrier in the small signal model will be approximately 1/2 the value estimated for the barrier alone.

The next step is to investigate the tunnel current characteristics. The current vs. voltage characteristics of a 30 Å thick, 300 meV high barrier with a $10^{18}/cm^3$ contact doping are shown in Fig. 5. The curves correspond to the characteristics of the barrier alone and the barrier with the band bending and the voltage drop in the contact included. The curves have a change in slope due to the nature of the barrier approximation. The barriers shown in Fig. 4 are approximately rectangular with a constant width with varying voltage and a triangular top portion. When the potential drop across the barrier is equal to the barrier height the conduction band at the right edge will equal the conduction band in the contact on the left side and the barrier will become

triangular. Further increasing the voltage across the barrier will reduce the barrier thickness. The inflection point in the current characteristics occurs at the changeover from a rectangular to triangular barrier. The current curves in Fig. 5 show the effect of the semiconductor contact on the tunneling current. The barrier only curve is a conventional Fowler-Nordheim tunnel characteristic. The barrier plus contact curve includes the barrier reduction due to band bending in the contact. The terminal voltage is split between the contact but the barrier height is reduced by the contact potential drop. The band bending produces nearly a two order of magnitude increase in current density for a given terminal voltage.

The Monte Carlo transport information can be combined with the injector results to obtain initial small signal device predictions. The important parameters in the device design are the voltage drop in the transit region and the injection properties of the unipolar injector. If we assume an InGaAs transit region the carriers can have nearly ballistic transport for voltage drops less than 0.6 volts, a field can be used with each length to give this maximum voltage drop. Five example structures with different drift region lengths are shown in Table I.

length (nm)	Field (KV/cm)	Frequency(THz)	Q
80	75	7.4	-12.9
100	60	5.8	-9.6
120	50	4.6	-7.5
140	43	3.8	-6
160	37.5	3.2	-5

Table I Initial Ballistic Structure Results

We would like to operate in the THz frequency range. Devices shorter than 80 nm begin to operate in the range above 10 THz with poor performance due to the susceptance of the structure. The longer devices have a lower operating frequency and better performance, but the electric fields needed to keep the drift region voltage lower than the 0.6 electron volt valley separation become small. The small signal admittance of the five structures were simulated using a constant injector conductance of $1.2e7 \Omega^{-1}cm^{-2}$ and an injector width of 50\AA . Other choices of injector conditions will give different results. Fig. 6

shows the small signal admittance for the devices in Table I for frequencies between 2.2 and 8 THz. The markers on the curves are 400 GHz apart. This performance is similar to the behavior of conventional saturated velocity device except the carriers are moving at higher velocities and the frequencies are higher. The peak negative conductance frequency depends on the velocity and the length. This is shown in column 3 of the table for the 5 structures. The device susceptance depends on the operating frequency and the length. Since the optimal negative conductance frequency is $\propto 1/\text{length}$ the optimal susceptance is $\propto f^2$. The negative conductance depends on the properties of the induced current waveform. The ballistic device will have an induced current that increases with time or distance through the structure. This triangular waveform will be superior to the constant velocity version with the same injection angle. The negative conductance will have a modest increase with reduced transit region length. The device $-Q$, the ratio of the susceptance to the conductance is an important parameter for device operation. The power available from the device depends on its negative resistance, area and the RF voltage along with the parasitic losses. The small signal $-Q$ is a useful measure of the device performance and the device area required to match the device to a given load impedance. These results show that the ballistic structure has the potential for useful operation at THz frequencies.

IV. Summary and Conclusions

This paper described the properties of a new ballistic transit time device with a unipolar tunnel barrier injector. The unipolar injector has both performance and fabrication advantages over conventional p^+n^+ TUNNETT structures. The proposed ballistic transport reduces the transit time compared to a conventional saturated velocity device for the same transit region length and thus increases the operating frequency. However the requirements of ballistic transport limit the device design. Low voltages and electric fields are required for proper operation. The device operation also depends on the unipolar tunnel injector. The results show that the effects of band bending in the semiconductor contact reduce the barrier height under bias and improve the barrier conductance. The small signal results show that these devices can have excellent properties at THz frequencies.

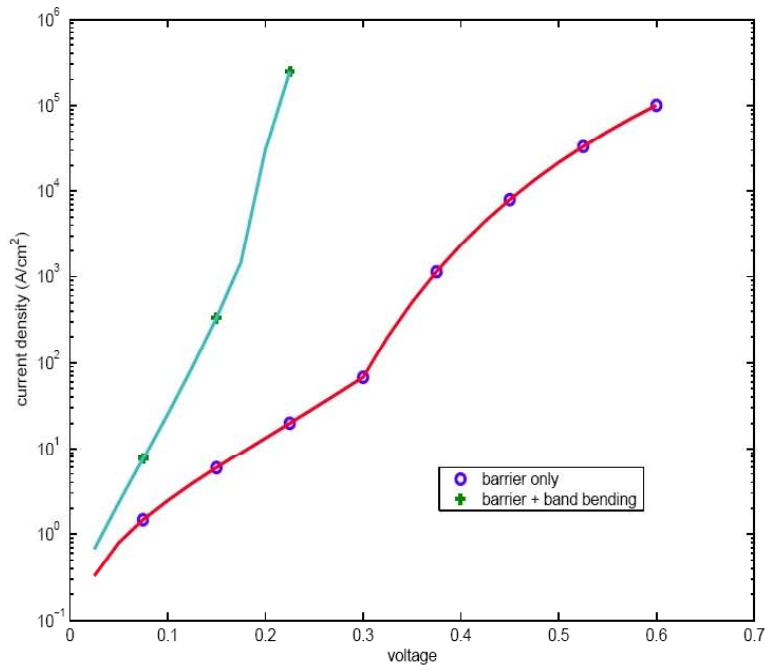


Figure 5: Current vs. Voltage Characteristics for Tunnel Barrier

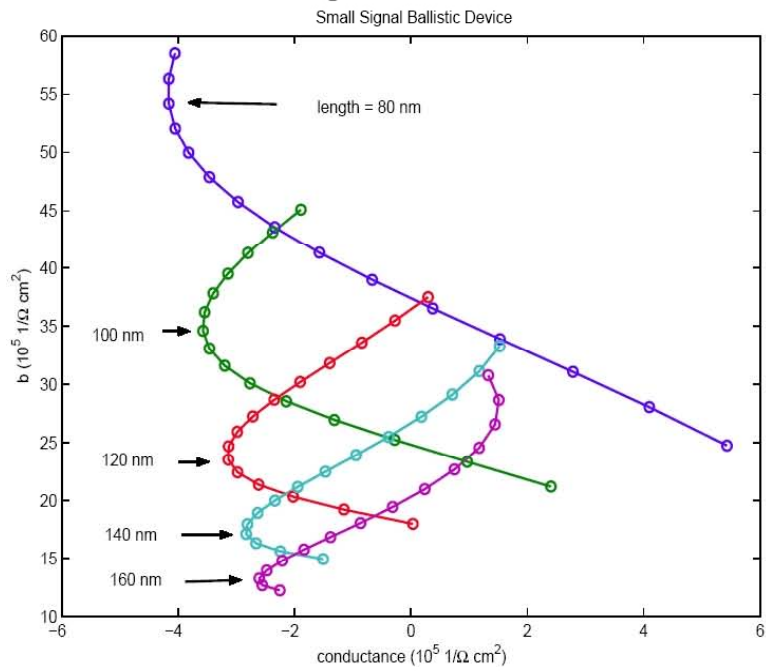


Figure 6: Small Signal Ballistic Operation Between 2.2 and 8 THz

This work was partially supported by The ARO MURI program on The Science and Technology of Chemical and Biological Sensing at THz Frequencies, contract DAAD-01-0622 and the AFOSR MURI program on Phonon Enhancement of Electronic and Optoelectronic Devices, contract F 49620-00-1-0328.

F-Band (90-140 GHz) Uni-Traveling-Carrier Photodiode Module for a Photonic Local Oscillator

Hiroshi Ito, Tsuyoshi Ito, Yoshifumi Muramoto, Tomofumi Furuta, and *Tadao Ishibashi

NTT Photonics Laboratories, NTT Corporation
3-1 Morinosato Wakamiya, Atsugi-shi, Kanagawa 243-0198, Japan
*NTT Electronics Corporation
1841-1 Tsuruma, Machida-shi, Tokyo 194-0004, Japan

Abstract

A compact uni-traveling-carrier photodiode (UTC-PD) module with a WR-8 rectangular waveguide output port for operation in the F-band (90 - 140 GHz) has been developed. A resonating matching circuit integrated with a UTC-PD and a microstrip-line-to-rectangular-waveguide transformer are designed to realize high output powers with a wide bandwidth covering the F-band. The module size and configuration are equivalent to those of conventional optoelectronic devices, which enables the use of standard assembly technology. The fabricated module exhibits a record millimeter-wave output-power of 17 mW at 120 GHz for a bias voltage of -3 V. The 3-dB down bandwidth is as wide as 55 GHz, which fully covers the F-band. An optical input stress test at a photocurrent of 10 mA performed to confirm the long-term stability of the module showed that the dark current stays below 1 μ A for more than 3000 hours.

Introduction

Photonic generation of millimeter (mm) and sub-mm wave signals is a promising technique for a local oscillator system in radio telescopes [1] because it provides an extremely wide bandwidth and can use low-loss fibers for transmission of very-high-frequency signals. For example, in one of the options proposed for the Atacama Large Millimeter/sub-millimeter Array (ALMA) [2], signals in a very wide frequency range from about 80 to 160 GHz have to be distributed to 64 antennas within an area of ~ 10 km². In addition, the use of a high-output-power O/E conversion device can eliminate the costly post amplification circuit and thus simplify the system configuration. Thus, the photonic local oscillator system requires a photodiode that has a high-output-power as well as superior high-frequency characteristics. The uni-traveling-carrier photodiode (UTC-PD) [3] is one of the best solutions, because it provides a high 3-dB down bandwidth (f_{3dB}) and a high-saturation-output power simultaneously. To date, excellent performance, an f_{3dB} of 310 GHz [4] and an output power of over 20 mW at 100 GHz [5], has been demonstrated. These features come from the unique operation mode of the UTC-PD in which only electrons are the active carriers traveling through the junction depletion region [3]. For practical use, especially in the frequency range above 100 GHz, the device should be in a module with a rectangular waveguide (WG) output port, because the useful frequency range of the coaxial connector is limited to below ~ 100 GHz. Although photodiode modules with a waveguide output port have been reported [6, 7], they are generally bulky and incompatible with standard optoelectronic (O/E) device assembly technology. Recently, we have developed a compact waveguide output UTC-PD module for operation

in the W-band (75 - 110 GHz) [8]. This module exhibits a very high mm-wave output power of 11 mW at 100 GHz, which is about two orders of magnitude larger than that obtained by a pin-PD module at the same frequency [6]. Despite these promising results, it is still necessary to develop photodiode modules operating at higher frequencies to fulfill the requirements for a much simpler local oscillator system [2].

In the present work, we have developed a WR-8 waveguide output UTC-PD module for operation in the F-band (90 - 140 GHz), which is suitable for use in a photonic local oscillator system. Its size and configuration are equivalent to those of conventional semiconductor optoelectronic (O/E) devices, so that it is compatible with standard assembly/testing equipment for O/E device modules. The module was designed to generate high output power in the F-band, and the output power characteristics as well as the stability for long-term operation were evaluated.

Design and Fabrication

A. Photodiode

At frequencies above 100 GHz, it is important to implement methods for improving output power because the influence of the CR time constant of the PD becomes significant in a conventional wide-band design. A resonating matching circuit is a promising technique to improve the O/E conversion efficiency, which it achieves by compensating the imaginary part of the internal impedance in the UTC-PD at a designed frequency. The matching allows us to use a relatively large area (large junction capacitance) device to increase saturation photocurrent level and reduce self-heating of the PD. This matching circuit simultaneously acts as an integrated bias circuit, which eliminates hybrid integration of a fine-structure bias-line in the waveguide-output module. Thus, we fabricated a UTC-PD integrated with a short-stub matching circuit [5, 9] (Fig. 1). The stub length was optimized to be 70 μm to make the output power peak at around 120 GHz.

The UTC-PD epi-layers were grown by MOCVD. The absorption layer consists of p-InGaAs ($p = 4 \times 10^{17} / \text{cm}^3$, 122 nm), p-InGaAs ($p = 1 \times 10^{18} / \text{cm}^3$, 10 nm) and undoped InGaAs (8 nm), and the collection layer consists of undoped InGaAsP (16 nm), undoped InP (6 nm), n-InP ($n = 1 \times 10^{18} / \text{cm}^3$, 7 nm) and n-InP ($n = 2 \times 10^{16} / \text{cm}^3$, 201 nm). The rest of the structure is similar to ones reported previously [3,10]. Hexagonally shaped double-mesa edge-illuminated refracting-facet UTC-PDs with an absorption area (S) of 74 μm^2 were fabricated by wet chemical etching and metal-lift-off processes. This relatively large absorption area for increasing the maximum output power is possible because the matching circuit effectively compensates the imaginary part of the internal impedance of the UTC-PD. Each device was integrated with 50- Ω CPWs (one for the output, one for the short-stub) on the InP substrate. These passive elements were monolithically integrated without employing an additional process step in the standard UTC-PD process. The MIM capacitor has a capacitance of 2 pF. Then, the refracting facet structure [11] was fabricated on the side of the PD by using the spontaneous etch-stop nature of InP on the (111)A facet. The side of the device was then anti-reflection coated and the wafer was cleaved into chips. The chip size is 300 $\mu\text{m} \times 450 \mu\text{m}$, and all elements are integrated within this small area. The responsivity measured in a broad-area device at $\lambda = 1.55 \mu\text{m}$ was 0.4 A/W.

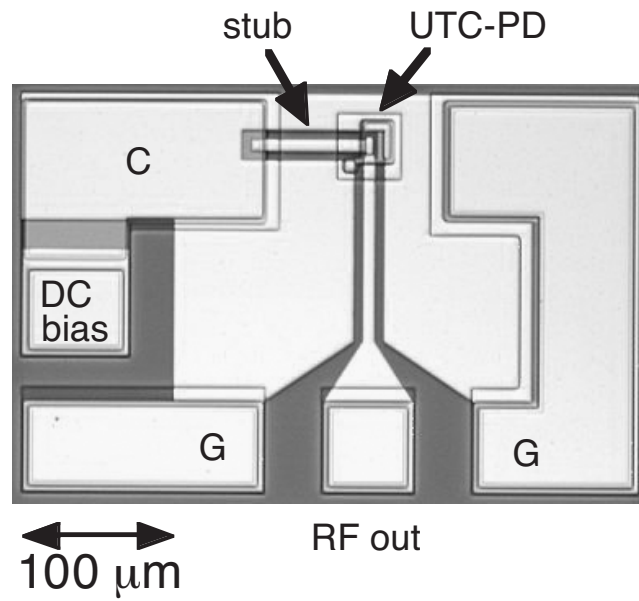


Fig. 1. Micrographs of the fabricated UTC-PD chip with an integrated matching circuit.

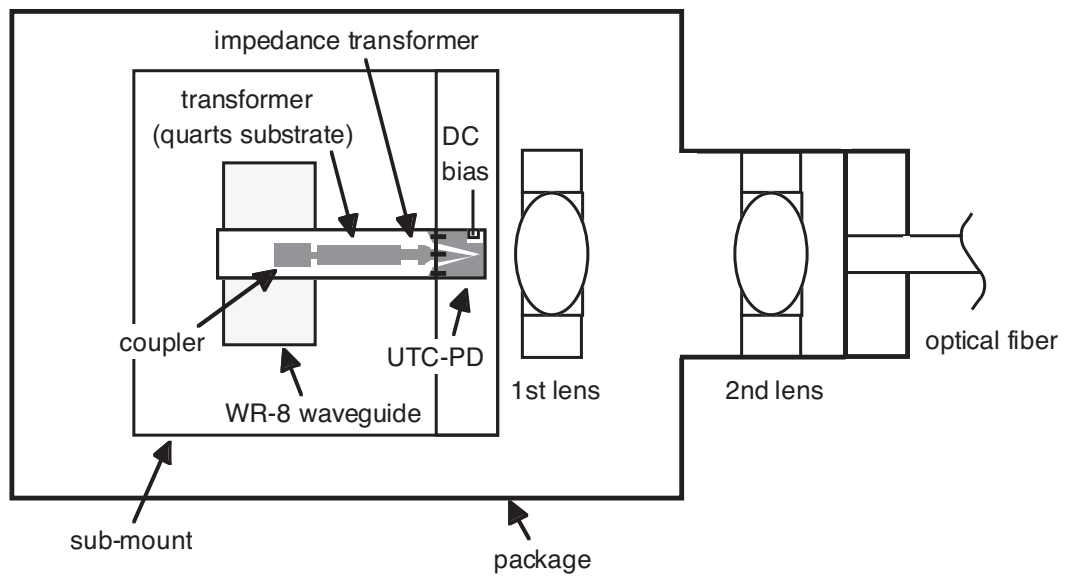


Fig. 2. Schematic drawing of the module configuration.

B. Module

To maintain good fabrication yield and performance reproducibility, the module should be compatible with standard electrical/optical assembly technology. We therefore developed a waveguide output UTC-PD module whose size and configuration are equivalent to those of the conventional butterfly-type O/E device module. Figure 2 is a schematic drawing of the module configuration. MSL based transformer was designed and fabricated on a quartz substrate (thickness: 150 μm) to electrically connect the PD to the rectangular waveguide output port with low loss and less frequency dependence. It has an impedance transform circuit (from 50 Ω to 75 Ω) on the PD side, and an MSL-to-rectangular-WG coupler on the other side. Figure 3 shows the return loss of the transformer against frequency calculated by using a three-dimensional numerical simulator (High Frequency Structure Simulator; HFSS). Here, the size of the coupler and the back-short depth were chosen to be 390 μm \times 220 μm and 640 μm , respectively, as optimum values. As seen in this figure, the return loss is successfully suppressed to less than -10 dB in the entire frequency range in the F-Band, and the transmittance of this transformer has nearly flat frequency dependence and is larger than -0.5 dB in the F-Band. The transformer connecting the UTC-PD and the WR-8 waveguide was placed in a trench (width \times height = 0.6 \times 0.5 mm) on a sub-mount, and the UTC-PD chip was electrically connected to the quartz transformer using gold ribbons. A DC bias pad was also electrically connected to the DC-bias port on the side of the package through a series resistor (50 Ω) and a parallel capacitor (2.2 nF) to protect the PD from external electrical surges. Then, a fixed back-short, which eliminates mechanical tuning, was placed on the sub-mount. Thus, the output signal goes to the bottom side of the sub-mount shown in Fig. 2. Finally, the photodiode was optically coupled to the optical fiber using a two-lens system, and these optical parts were welded onto the package using an automated YAG laser welder. This assembly technique provides highly stable optical alignment between the photodiode and optical fiber. The entire fabrication sequence is quite similar to that of the conventional O/E device module, so that standard assembly/testing equipment can be used. The optical beam was slightly defocused on the device, so that the effective responsivity became about 0.35 A/W.

Figure 4 is a photograph of the fabricated module connected to the WR-8 waveguide. The module size is 12.7 mm \times 30 mm \times 10 mm, excluding the optical fiber. The rectangular waveguide output port is located on the bottom side of the module and connected to a standard F-3922/67B-008 flange using a miniaturized waveguide extension. A miniature SMC connector was used as the DC bias port.

C. Characterization

The mm-wave output characteristics of the fabricated module were measured using a power meter (DORADO, DS-28-6A). For the output power characterization, pulse trains from an actively mode-locked laser diode operating at 60 GHz were optically multiplexed by using an arrayed waveguide grating [12] to prepare quasi-sinusoidal 120-GHz mm-wave light signal ($\lambda = 1.55$ μm , FWHM: 1.5 ps). For the measurement of frequency characteristics, the optical sinusoidal signal was prepared by two-mode beating using two wavelength-tunable laser-diodes ($\lambda \approx 1.55$ μm) so that the mm-wave frequency could be changed in a very wide range. The optical modulation index of this signal was close to unity.

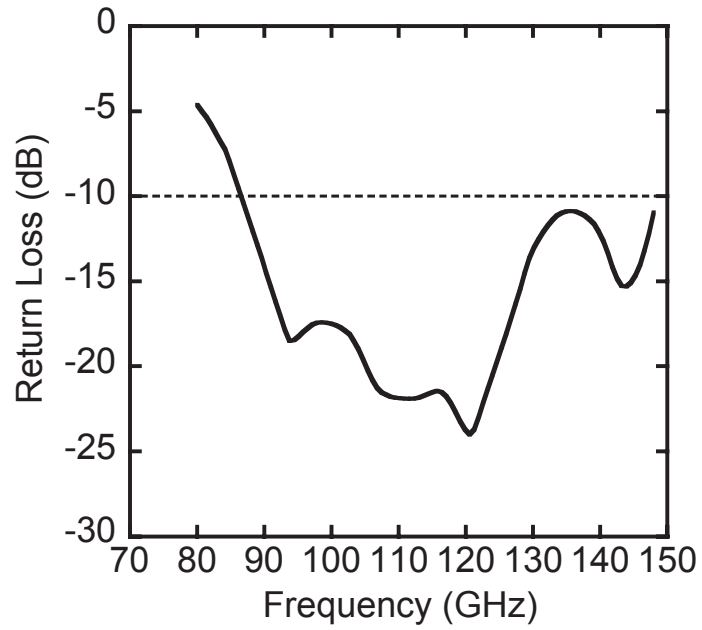


Fig. 3. Calculated return loss of the transformer.

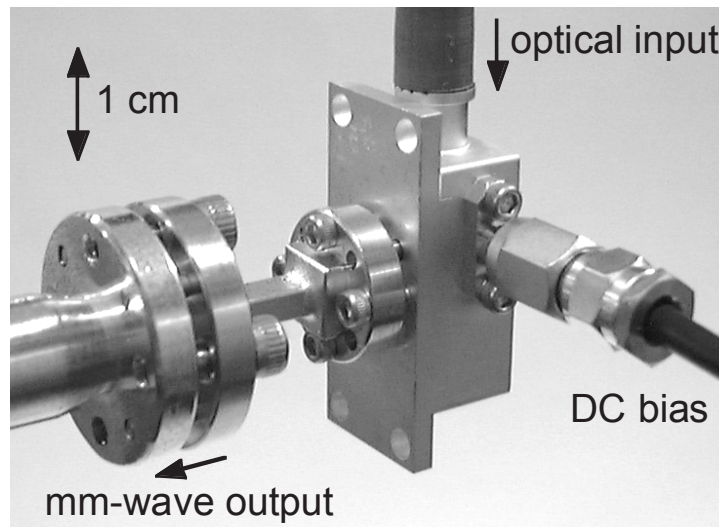


Fig. 4. Photograph of the waveguide-output URC-PD connected to the WR-8 waveguide port.

Experimental Results

Figure 5 shows the relationship between measured mm-wave output power and diode photocurrent for the fabricated module at a frequency of 120 GHz. Here, the input optical power was changed. A wide linearity is maintained up to a very high mm-wave output power of over 10 mW. The saturation point of the output power increased with increasing bias voltage, and the maximum output power of 17 mW (at a photocurrent of 25 mA) was obtained at a bias voltage of -3 V. To our knowledge, this is the highest mm-wave output power directly generated from a PD module in the F-band. The variation of the maximum output power against bias voltage is attributed to both the shift in the operating voltage along the load line and the space-charge effect in the collection layer [5].

Figure 6 shows the relative output power against frequency for a photocurrent of 10 mA. The output 3-dB down bandwidth was about 55 GHz, which fully covers the F-band. The solid curve in the figure is a fitting calculation based on an analytical model of the matching circuit. The experimental result agrees well with the calculation, indicating that most of the frequency variation is that of the integrated matching circuit, and thus the frequency variation of the transformer is considered to be reasonably flat in the measured range. In addition, the steep decrease of the output power at the low-frequency side is due to the cut-off characteristics of the WR-8 waveguide (at 73.8 GHz), which were not included in the calculation. In the high-frequency region, on the other hand, the output power does not decrease steeply with increasing frequency. This is because higher-order-mode output is possible in the frequency region above 147.6 GHz. Thus, the fabricated module can cover the required frequency range for ALMA (from about 80 to 160 GHz [2]) by itself.

Figure 7 summarizes the reported maximum RF output powers against the operation frequency for UTC-PDs [7,8,13-16] and conventional pin-PDs [6,17-19]. The difference between the two types of devices becomes larger as the frequency increases, and the output power of the UTC-PDs becomes about two orders of magnitude larger at around 120 GHz, reflecting their much higher saturation current level. These results clearly demonstrate that the UTC-PD is a promising device for generating high-power mm-wave signals without electrical power amplifiers. Moreover, the output power from the UTC-PD module in this study is comparable to those obtained by the UTC-PD chips. This implies that the transformer connecting the UTC-PD to the rectangular waveguide has a low transmission loss.

For the practical use, long-term stability is also an important issue. Although bias-temperature and optical-input stress tests have confirmed that UTC-PDs designed for 40 Gbit/s optical communication systems have excellent reliability [20], we also measured the variation of dark current in the fabricated waveguide-output module under optical input stresses at room temperature (Fig. 8). Here, the module designed for the operation in the W-band [8] was used. The internal configuration of this module is identical to the one for the F-band. The module was biased at -2 V with an optical input corresponding to a photocurrent of 10 mA (responsivity is about 0.35 A/W). Except for the initial increase, the dark current stays at a very low level for more than 3000 hours. These values are considerably lower than the generally required level for high-speed PDs of 1 μ A. This indicates that the fabricated UTC-PD chip is reasonably reliable. The changes in responsivity and mm-wave output power at the same photocurrent were also confirmed to

be very small after this long-term stability test. These results indicate that the optical alignment by YAG laser welding as well as the device parameters, such as series resistance and junction capacitance, are quite stable.

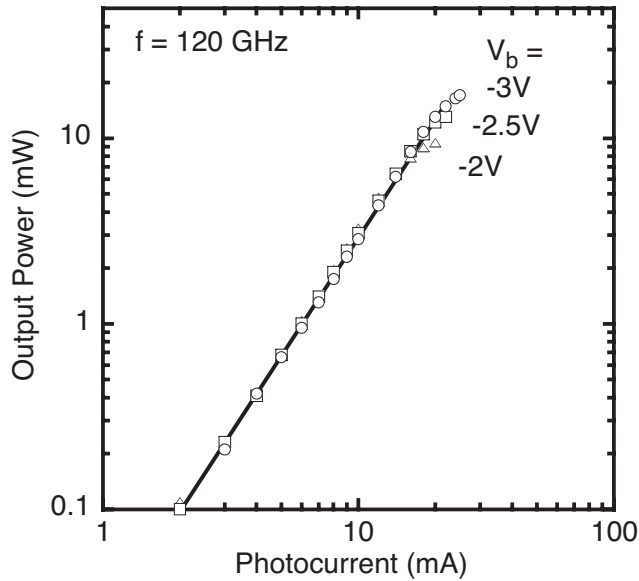


Fig. 5. Relationships between the measured mm-wave output power and diode photocurrent at 120 GHz for several bias voltages.

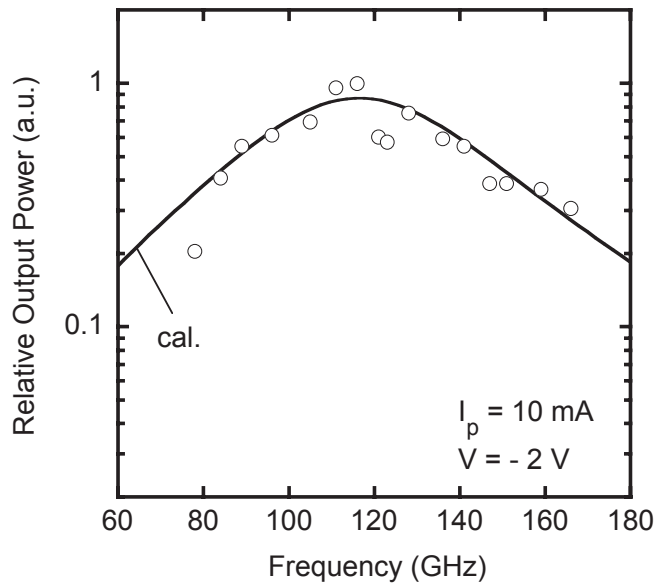


Fig. 6. Relative output powers from the module against frequency. The solid curve in the figure is a calculation based on an analytical model.

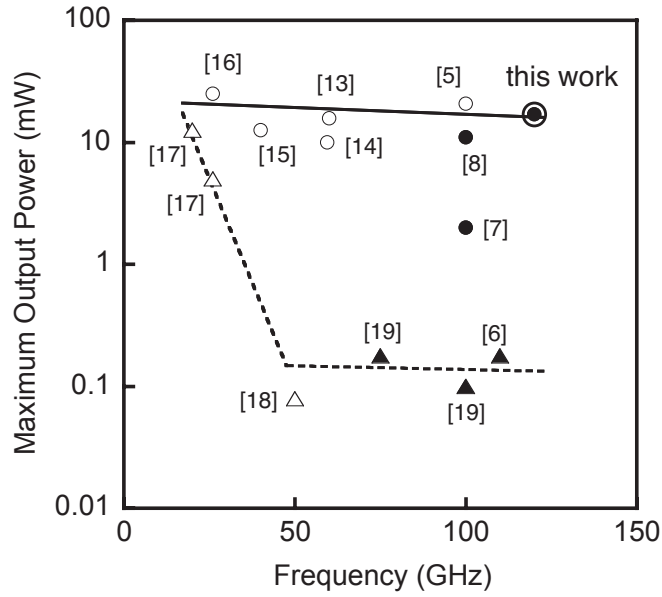


Fig. 7. Comparison of reported mm-wave output power against the operation frequency for UTC-PDs and pin-PDs. Circles are for UTC-PDs and triangles for pin-PDs. Open marks are for chips, and closed ones for modules. Numbers in the figure correspond to the references.

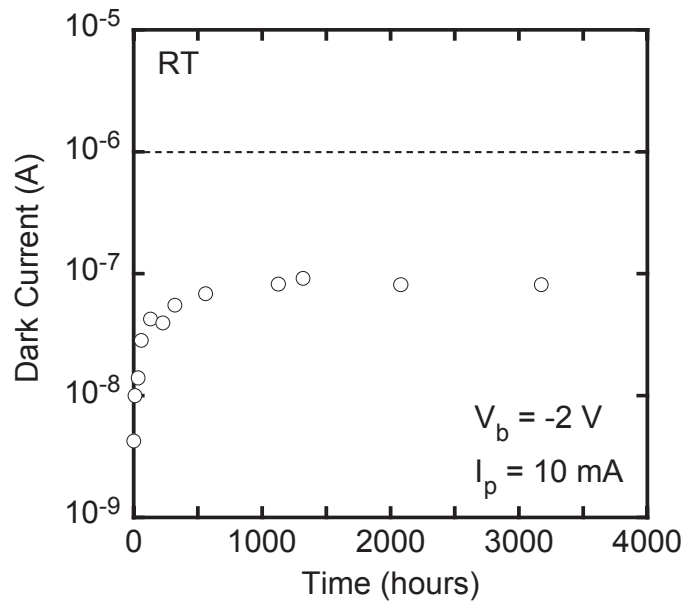


Fig. 8. Variation of the dark current against time under optical input and reverse bias stresses.

Summary

We have designed and fabricated a uni-traveling-carrier photodiode module having a rectangular waveguide output port for operation in the F-band. The module is designed to be compatible with standard assembly technology. It exhibits a record maximum saturation output-power of 17 mW at 120 GHz, and a 3-dB bandwidth as wide as 55 GHz, which fully covers the F-band. The stability of the module was also characterized under an optical input stress (photocurrent = 10 mA). It was found that the dark current stays at a sufficiently low level for more than 3000 hours, and the mm-wave output power does not change during that time. These results clearly demonstrate that the waveguide-output UTC-PD module is highly promising for use as a high-power photonic mm-wave generator in a photonic local oscillator system in radio telescopes, such as ALMA.

Acknowledgement

The authors thank T. Nagatsuma, and A. Hirata for their valuable discussions on the measurements, J. Yumoto for his continuous encouragement, and Prof. M. Ishiguro of National Astronomical Observatory of Japan for his stimulating discussions on photonic mm-wave sources.

References

- [1] J. Payne, B. Shillue, and A. Vaccari, "Photonic techniques for use on the Atacama large millimeter array," Tech. Dig. Int. Topical Meeting on Microwave Photonics, pp. 105-108, 1999.
- [2] M. Ishiguro, Y. Sekimoto, A. Ueda, S. Iguchi, T. Noguchi, J. M. Payne, L. R. D'Addario, and W. Shillue, "A hybrid option for the first LOs using direct photonic LO driver," ALMA Memo #435, <http://www.cv.nrao.edu/alma/almaweb/www/memos/>, pp. 1-16, 2002.
- [3] T. Ishibashi, N. Shimizu, S. Kodama, H. Ito, T. Nagatsuma, and T. Furuta, "Uni-traveling-carrier photodiodes," Tech. Dig. Ultrafast Electronics and Optoelectronics, pp. 83-87, 1997.
- [4] H. Ito, T. Furuta, S. Kodama, and T. Ishibashi, "InP/InGaAs uni-travelling-carrier photodiode with 310 GHz bandwidth," Electron. Lett., vol. 36, pp. 1809-1810, 2000.
- [5] H. Ito, T. Nagatsuma, A. Hirata, T. Minotani, A. Sasaki, Y. Hirota, and T. Ishibashi, "High-power photonic millimetre-wave generation at 100 GHz using matching-circuit-integrated uni-travelling-carrier photodiodes," IEE Proc. Optoelectron., vol. 150, in press, 2003.
- [6] P. G. Huggard, B. N. Ellison, P. Shen, N. J. Gomes, P. A. Davis, W. P. Shillue, A. Vaccari, and J. M. Payne, "Generation of millimetre and sub-millimetre waves by photomixing in 1.55 μm wavelength photodiode," Electron. Lett., vol. 38, pp. 327-328, 2002.
- [7] T. Noguchi, A. Ueda, H. Iwashita, Y. Sekimoto, M. Ishiguro, T. Ishibashi, H. Ito and T. Nagatsuma, "A Photonic Local Oscillator for SIS Mixer in the 100 GHz Band," Abstract of 13th International Symposium on Space Terahertz Technology, 6.1, 2002.
- [8] H. Ito, T. Furuta, T. Ito, Y. Muramoto, K. Tsuzuki, K. Yoshino, and T. Ishibashi, "W-Band Uni-Travelling-Carrier Photodiode Module for High-Power Photonic Millimetre-Wave Generation," Electron. Lett., vol. 38, pp.1376-1377, 2002.

- [9] H. Ito, Y. Hirota, A. Hirata, T. Nagatsuma and T. Ishibashi, "11 dBm photonic millimeter-wave generation at 100 GHz using uni-travelling-carrier photodiode," *Electron. Lett.*, vol. 37, pp. 1225-1226, 2001.
- [10] T. Ishibashi, T. Furuta, H. Fushimi, S. Kodama, H. Ito, T. Nagatsuma, N. Shimizu, and Y. Miyamoto, "InP/InGaAs uni-traveling-carrier photodiodes," *IEICE Trans. Electron.*, vol. E83-C, pp. 938-949, 2000.
- [11] H. Fukano, Y. Muramoto, K. Takahata, and Y. Matsuoka, "High-efficiency edge-illuminated uni-traveling-carrier-structure refracting-facet photodiode," *Electron. Lett.*, vol. 35, pp. 1664-1665, 1999.
- [12] A. Hirata, M. Harada, and T. Nagatsuma, "3-Gb/s wireless data transmission using a millimeter-wave photonic techniques," *Tech. Dig. 3rd Japan-Korea Joint Workshop on Microwave and Millimeter-Wave Photonics*, pp. 95-98, 2002.
- [13] T. Nagatsuma, N. Sahri, M. Yaita, T. Ishibashi, N. Shimizu, and K. Sato, "All optoelectronic generation and detection of millimeter-wave signals," *Tech. Dig. Int. Topical Meeting on Microwave Photonics*, pp. 5-8, 1998.
- [14] H. Ito, T. Ohno, H. Fushimi, T. Furuta, S. Kodama, and T. Ishibashi, "60 GHz high output power uni-travelling-carrier photodiodes with integrated bias circuit," *Electron. Lett.*, vol. 36, pp. 747-748, 2000.
- [15] N. Shimizu, Y. Miyamoto, A. Hirano, K. Sato, and T. Ishibashi, "RF saturation mechanism of InP/InGaAs uni-travelling-carrier photodiode," *Electron. Lett.*, vol. 36, pp. 750-751, 2000.
- [16] H. Ito, H. Fushimi, Y. Muramoto, T. Furuta and T. Ishibashi, "High-power photonic microwave generation at K- and Ka-Bands using a uni-traveling-carrier photodiode," *IEEE J. Lightwave Technol.*, vol. 20, pp. 1500-1505, 2002.
- [17] K. J. Williams, R. D. Esmen, and M. Dagenais, "Nonlinearities in p-i-n microwave photodetectors," *IEEE J. Lightwave Technol.*, vol. 14, pp. 84-96, 1996.
- [18] G. Unterborsch, D. Trommer, A. Umbach, and G. G. Mekonnen, "High-bandwidth 1.55 μm waveguide integrated photodetector," *Proc. 8th International Conference on Indium Phosphide and Related Materials*, pp. 203-206, 1996.
- [19] P. G. Huggard, B. N. Ellison, P. Shen, N. J. Gomes, P. A. Davis, W. P. Shillue, A. Vaccari, and J. M. Payne, "Efficient generation of guided millimeter-wave power by photomixing," *IEEE Photonics Technol. Lett.*, vol. 14, pp. 197-199, 2002.
- [20] T. Furuta, H. Fushimi, T. Yasui, Y. Muramoto, H. Kamioka, H. Mawatari, H. Fukano, T. Ishibashi, and H. Ito, "Reliability study on uni-traveling-carrier photodiode for a 40 Gbit/s optical transmission systems," *Electron. Lett.*, vol. 38, pp. 332-334, 2002.

Optical Far-IR wave Generation - An ESA review study

B. Leone¹, V. Krozer², M. Feiginov³, H. Roskos⁴, H. Quast⁴, T. Löffler⁴,
G. Loata⁴, G. Döhler⁵, P. Kiesel⁵, M. Eckardt⁵, A. Schwanhäußer⁵,
T. O. Klaassen⁶, P. Lugli⁷

¹ ESA Directorate of Technical and Operational Support, ESTEC, Noordwijk, The Netherlands

² Denmark Technical University, Lyngby, Denmark

³ Technical University of Darmstadt, Darmstadt, Germany

⁴ University of Frankfurt, Frankfurt, Germany

⁵ University of Erlangen, Erlangen, Germany

⁶ Delft University of Technology, Delft, The Netherlands

⁷ University of Rome "Tor Vergata", Rome, Italy

Abstract

A study initiated by the European Space Agency was recently concluded, which aimed at identifying the most promising technologies to significantly improve on the generation of coherent electromagnetic radiation in the THz regime for space applications. The desired improvements include, amongst others, higher output powers and efficiencies at increasingly higher frequencies, wider tunability and, possibly, miniaturization.

As the title of the paper suggests, the baseline technologies considered from the start in this study revolved around optical schemes, such as photomixing, compared to all electronic techniques. However, emphasis was put on conducting a perusal of any scheme found in the literature and performing an overall comparison with a fixed set of criteria. To this end, a number of universities and research institutes were involved to allow for a sufficient coverage of all relevant technical and research areas and, thus, ensure a review of both current and emerging technologies in this field that would be as thorough and complete as possible.

The review study combined published results and mathematical modelling in order to determine the theoretical performance limitations of a given technology and/or scheme. The basic requirements to help crystallize selection criteria were, broadly speaking: power performance, linewidth, tunability and space worthiness in the frequency range ~1 to 3 THz.

Some of the most significant findings will be presented together with the two technologies selected for medium to short term development. These are a scheme using advanced p-i-n photomixer superlattice structures and, reflecting recent results, THz Quantum Cascade Laser technology.

Introduction

Several Terahertz heterodyne technology development activities have been initiated and funded in the past years by the European Space Agency (ESA) mainly in response to the technological needs of the Herschel Observatory mission. Several of these activities are still ongoing and were well represented at this conference [1–8].

These include:

- Superconducting mixer development [1–4]
- Multipixel heterodyne HEB receiver [6]
- Far-IR optics design and verification tools [5]
- Optical Far-IR wave generation

This paper deals with the last activity, which is complementary to the mixer development activities. In particular, any multipixel heterodyne receiver requires considerable LO power if the same source is used for several pixels. Presently, there exists no compact THz source to do this. Therefore, the development of compact, Spaceworthy, high power sources is considered by ESA as an enabling technology for instruments incorporating THz mixer arrays. The title of the development activity pointed from the outset that this should be achieved by optical means. Indeed, this was also a conclusion of the study.

Study Rationale

The optical Far-IR wave generation activity was split into two phases. In the first phase, current technologies were reviewed from available scientific literature and their potential analysed in turn using modelling and first principle calculations. In the second phase the most promising technologies will be developed.

The first phase was articulated according to a set of tasks summarized as follows:

- Establish the theoretical limit for the maximum output power from multipliers at the frequencies under consideration,
- Survey and assess the various novel techniques for the generation of THz power,
- Demonstrate the experimentally achievable capabilities of photo-mixer devices based on LT GaAs, p-i-n diodes, and of lasers for THz power generation,
- Survey and assess the measurement, characterisation and system techniques and requirements for optical far-infrared power generation, and
- Outline the technological development plan and a detailed technological road-map for the most promising technology.

In this phase two competing research consortia were contracted to perform the review in parallel. One consortium is represented by the co-authors of this paper; the Rutherford Appleton Laboratory led the other consortium. At the end of this first phase, only one of the two consortia would be selected to continue the actual technology development on grounds of the novelty of the selected optical THz technology or scheme. This way, the quality of the review was ensured through competitiveness.

Here, only the results of the winning consortium will be presented. This will not affect the completeness of the results since most conclusions regarding existing technologies were similar for both consortia and only the conclusions on the implementation of the technology roadmap differ.

The second phase is currently ongoing and focuses on development of the most promising technologies selected in the first phase according to a development roadmap.

Summary of Results

The selection criteria used in the review reflected both the desired characteristics of an ideal THz source for space applications as well as the actual technologies considered in the study. Without loss of generality, however, one can summarize the following list of criteria:

- Maximum output power
- Conversion (optical) efficiency
- Electrical efficiency
- Maximum output frequency
- Frequency stability
- Linewidth
- Spectral purity
- Tunability
- Operating conditions (temperature, current, voltage, magnetic field, vacuum, etc...)
- Coupling issues
- Miniaturization
- Space qualifiability

The current state-of-the-art THz source technology for space is represented by solid-state frequency multiplication. Therefore, the theoretical limit of multiplier circuits with Schottky varactor diodes were established in this study by simulation and the simulated results were subsequently used for comparison with experimental results from photomixing and laser experiments. Although impressive results have been demonstrated up to almost 2 THz [9–10], the resulting efficiencies and output powers are really only sufficient to drive single pixel mixers rather than mixer arrays. Furthermore, efficiency plummets at higher frequencies such that is believed to be difficult to push these results above 2.5 THz. This is due to the fact that the doping concentrations for the Schottky varactor devices employed in these multipliers ought to be well above $1 \cdot 10^{17} / \text{cm}^3$. At these doping levels the contribution of the parasitic tunneling current becomes large and the $C_{\text{max}}/C_{\text{min}}$ ratio is lowered. Consequently, the efficiency rapidly deteriorates.

Furthermore, a large number of other known and published techniques for the generation of THz power, with special emphasis on their CW THz power capabilities have also been considered in the study but have been rejected from the technology development roadmap, at least for the time being, on the basis of their shortcomings with respect to selec-

tion criteria listed above. In the following sections these results will not be presented for brevity's sake.

In summary, the technologies selected for the development roadmap are optical photomixing and direct THz laser generation. The state-of-the-art in the area of photomixing is currently set by two device concepts, namely the LTGaAs MSM structures and the p-i-n diode structures. Both device concepts have already demonstrated the working principle but are still far from the requirements in output power for receiver applications at THz frequencies. These techniques and the other published in the literature will be considered in this study report.

Direct generation of THz power with either Quantum Cascade Laser structures or p-Ge lasers was also thought to be very promising. In particular THz QCLs have been introduced only recently and their potential in performance, especially for operation in the higher end of the THz frequency range, is of great interest in the preparation of new applications.

Introduction to Photomixers

The generation of high frequency radiation by photomixing is based on generating periodically charge carriers in a semiconductor by two lasers emitting at nearly the same photon frequencies ν_0 , detuned by the beat frequency ν_{THz} . If these photo-generated carriers are subjected to a DC electric field F_0 applied between two contacts connected to an antenna, a THz current $I_{\text{THz}}(t)$ is induced by the photo-generated carriers, which, depending on the load represented by the antenna, leads also to an AC voltage $U_{\text{THz}}(t)$ at the contacts. If the beat frequency is low compared to the inverse carrier transport time $1/\tau$, the AC current and voltage will follow the carrier generation fully in phase with the beat frequency and with an amplitude,

$$I^0 = e (dN/dt) = e \eta_{\text{ph}} (P_L/h\nu_0) \quad (1)$$

Here, e stands for the elementary charge, dN/dt is the electron-hole pair generation rate, which is equal to the average photon absorption rate $\eta_{\text{ph}} P_L/h\nu_0$; P_L is the laser power, $h\nu_0$ the lasers photon energy and η_{ph} the fraction of incident photons absorbed in the active part of the mixer. The “carrier transport time” can be either the transit time between the contacts or the recombination lifetime. Assuming reasonable values for the high-field drift velocities v_{dr} of electrons and holes of the order of 10^7 cm/s and contact separations L of the order of a μm , we expect transit times $\tau_{\text{tr}} = L/v_{\text{dr}}$ of the order of 10 ps, i.e. the condition for maximum AC photocurrent is fulfilled only if the beat frequency is $\ll 1/10\text{ps} = 100$ GHz. In general, when this condition is not fulfilled it can be shown that the following relation relates the AC current to the average current:

$$I_{\text{THz}}(t) = I^0 (1+2\pi i \nu_{\text{THz}} \tau_{\text{tr}})^{-1} \cos(2\pi \nu_{\text{THz}} t) = e \eta_{\text{ph}} (P_L/h\nu_0) (1+2\pi i \nu_{\text{THz}} \tau_{\text{tr}})^{-1} \cos(2\pi \nu_{\text{THz}} t) \quad (2)$$

Thus, at THz-frequencies the amplitude of the THz-current I_{THz}^0 is much smaller than I^0 . At first glance, the situation would *seem* to improve drastically, if the carrier transport time were to become much smaller than the transit time. This happens if transit times are limited due to the recombination lifetime $\tau_{\text{rec}} \ll \tau_{\text{tr}}$, so that τ_{rec} replaces τ_{tr} in Equ. (2). However, in this case each photo-generated carrier no longer contributes the same amount to I^0 , as its drift length $l_{\text{dr}} = v_{\text{dr}}\tau_{\text{rec}}$ is now only the fraction l_{dr}/L , i.e., the photoconductive “gain” $g = l_{\text{dr}}/L = (\tau_{\text{rec}}/\tau_{\text{tr}})$ becomes $\ll 1$. Now, by replacing the expression for I^0 given in Equ. (1) by the following,

$$I^0 = e (dN/dt) (v\tau/L) = e \eta_{\text{ph}} (P_L/h\nu_0) (\tau_{\text{rec}}/\tau_{\text{tr}}) \quad (3)$$

into Equ. (2), one finds that

$$I_{\text{THz}}(t) = I^0 (1+2\pi i v_{\text{THz}}\tau_{\text{rec}})^{-1} \cos(2\pi v_{\text{THz}}t) = e \eta_{\text{ph}} (P_L/h\nu_0) (\tau_{\text{rec}}/\tau_{\text{tr}}) (1+2\pi i v_{\text{THz}}\tau_{\text{rec}})^{-1} \cos(2\pi v_{\text{THz}}t) \quad (4)$$

We see that for $\tau_{\text{rec}} \ll \tau_{\text{tr}}$: (i) the 3dB-frequency becomes much larger, i.e. $v_{3\text{dB}} = 1/2\pi\tau_{\text{rec}}$, instead of $v_{3\text{dB}} = 1/2\pi\tau_{\text{tr}}$, (ii) the amplitude of the AC current for $v_{\text{THz}} \gg v_{3\text{dB}}$ given by $I_{\text{THz}}^0 = e \eta_{\text{ph}} (P_L/h\nu_0) (2\pi v_{\text{THz}}\tau_{\text{tr}})^{-1}$ is unchanged, whereas (iii) the DC current I^0 is strongly reduced by $g = l_{\text{dr}}/L = (\tau_{\text{rec}}/\tau_{\text{tr}})$.

For arbitrary v_{THz} the emitted THz power can be estimated by,

$$P_{\text{THz}} = \frac{1}{2} (I_{\text{THz}}^0)^2 R_a = \frac{1}{2} \{e \eta_{\text{ph}} (P_L/h\nu_0)\}^2 (\tau_{\text{rec}}/\tau_{\text{tr}})^2 [1+(2\pi v_{\text{THz}}\tau_{\text{rec}})^2]^{-1} R_a = P_{\text{THz}}^{\text{id}} (\tau_{\text{rec}}/\tau_{\text{tr}})^2 / [1+(2\pi v_{\text{THz}}\tau_{\text{rec}})^2] \quad (5)$$

where,

$$P_{\text{THz}}^{\text{id}} = \frac{1}{2} \{e \eta_{\text{ph}} (P_L/h\nu_0)\}^2 R_a \quad (6)$$

corresponds to the THz-power emitted by an ideal photomixer, assuming $\eta_{\text{ph}} = 1$. R_a is the radiative resistance of the antenna, which is typically in the order of 50 to 100 Ω . For an ideal GaAs photomixer (with $h\nu_0 = 1.43 \text{ eV} \approx E_g$) the following values are expected: $R_a = 70 \Omega$ and $P_L = 10 \text{ mW}$ value of $P_{\text{THz}}^{\text{id}} = 1.7 \text{ mW}$, corresponding to a conversion efficiency $\eta_{\text{THz}} = P_{\text{THz}}/P_L = 17 \%$.

Assessment of Photoconductors

LT-GaAs is used in *photoconductive* photomixers because of the short electron and hole capturing and recombination lifetime. Minimum values of $\tau_{\text{rec}} = 130 \text{ fs}$ have been reported, corresponding to a 3dB frequency of 1.2 THz. In optimized LT-GaAs-photomixers the photoconductive area consists of an LT-GaAs-layer with a thickness of the order of 1 μm and an interdigitated contact structure with contact separations of $L =$

1.8 μm , covering a quadratic area of $8 \times 8 \mu\text{m}^2$. Using again $v_{\text{dr}} = 10^7 \text{ cm/s}$ we obtain $\tau_{\text{tr}} = 18 \text{ ps}$. The maximum laser power is typically about $P_{\text{L}} = 100 \text{ mW}$. With these values Equ. (5) yields, at 1 THz, a value of $P_{\text{THz}}^{\text{th}} = 170 \text{ mW} (0.130 \text{ ps}/18 \text{ ps})^2 / (1+0.67) = 5 \mu\text{W}$, or an optical conversion efficiency of $\eta_{\text{THz}}^{\text{th}} = 5 \times 10^{-5}$. These values are rather close to the best-reported experimental values of $P_{\text{THz}}^{\text{exp}} = 2 \mu\text{W}$ and $\eta_{\text{THz}}^{\text{exp}} = 2 \times 10^{-5}$, respectively [11]. It should be noted that, although in this case v_{THz} is slightly smaller than $v_{3\text{dB}}$, the low efficiency at this frequency does not result primarily from the short recombination lifetime, but rather from the long transit time. For $\tau_{\text{rec}} \gg 130 \text{ fs}$, Equ. (5) yields only a slightly higher value of $P_{\text{THz}} = P_{\text{THz}}^{\text{id}} (1/2\pi v_{\text{THz}} \tau_{\text{tr}})^2 = 13 \mu\text{W}$.

In fact, the real advantage of the short recombination lifetime is the reduction of the steady-state carrier density at such high laser power. A simple estimate yields an average photo-induced carrier density in the LT-GaAs layer of about 10^{15} cm^{-3} for the present example. Although seemingly small this carrier density tends to screen the electric fields between the contacts, thus lowering the photocurrent, provided that the drift velocities of electrons and holes are not equal. Even if the steady state carrier density were determined by an ideal carrier transit time of about 20 ps, the photo-induced carrier density would be larger than 10^{17} cm^{-3} . In this case, even extremely high external voltages would be nearly completely screened by space charge building up near the contacts.

Inspection of Equ. (5) suggests that the most promising approach for improving on the performance of photomixers might be a reduction of the transit time by reducing the contact separation L . Unfortunately, a reduction of L , while keeping the active area constant, results in an increase of the capacitance approximately proportional to L^{-2} . Taking into account that the present example represents already the design where the RC-3dB frequency $\nu_{\text{RC}} = 1/2\pi R_{\text{a}} C_{\text{LT}} \approx 1 \text{ THz}$ (C_{LT} is the capacitance of the LT-GaAs layer with the interdigitated contacts) this implies a superlinear roll-off of the AC current I_{THz} with decreasing L which overcompensates the expected linear increase.

These simple theoretical design considerations are supported by the empirical observation that in spite of significant efforts no fundamental improvement of performance has been achieved in the field of LT-GaAs photomixers during the past years. In principle, the RC-roll-off problem can be overcome by taking advantage of the traveling wave concept. At suitably chosen angle of incidence of the photomixing lasers the interference pattern and, thus, the phase of maximum photocurrent generation can propagate with the same speed as the THz mixing signal in an active transmission line with LT-GaAs in between [12–15].

Assessment of Photodiodes

Similar considerations as outlined above can be applied also to p-i-n photomixers. One obtains the ideal value for the emitted THz power, according to Equ. (6) if the amplitude of the AC current, I_{THz}^0 , is affected neither by the RC nor by the transit time roll-off, pro-

vided that $\eta_{ph}=1$. In the general case the product of the corresponding roll-off factors reduces the emitted power:

$$P_{THz} = \frac{1}{2} (I_{THz}^0)^2 R_a [1+(v_{THz}/v_{RC})^2]^{-1} = P_{THz}^{id} [1+(v_{THz}/v_{RC})^2]^{-1} [1+(v_{THz}/v_{tr})^2]^{-1} \quad (7)$$

The RC-3dB frequency $v_{RC} = 1/(2\pi\tau_{RC}) = 1/(2\pi R_a C_{pin})$ (with $C_{pin} = \epsilon L_x L_y / 4\pi L_z$ and $\epsilon =$ dielectric constant) scales linearly with the i-layer thickness L_z and inversely with the sample cross section. Thus *large* L_z and small cross section appear attractive. On the other hand, the transit time 3dB-frequency $v_{tr} \approx 1/2\tau_{tr}$ increases with the transit times becoming short. Thus, *small* values of L_z appear attractive. An optimum value of L_z for a pin photomixer can be determined from the condition $v_{RC} = v_{tr}$. The transit time is (conventionally) determined by $\tau_{tr} = L_z/v_{dr}$, where for typical fields $v_{dr} = v_{sat} = 10^7$ cm/s is taken for electrons in GaAs, as the electrons are traveling at the (nearly field independent) saturation velocity v_{sat} , whereas $v_{dr} = \mu_h F$ is taken for the holes. Taking $v_{dr} = 10^7$ cm/s for electrons and holes and assuming a reasonable minimum value of the cross section ($L_x = L_y = 5 \mu\text{m}$) we obtain $L_z^{opt} = 0.33 \mu\text{m}$ and $v^{opt} = 150$ GHz. According to Equ. (7) the emitted THz power is then expected to be a factor of 4 less than P_{THz}^{id} . At 1 THz the emitted THz power should be still about 0.05 % of the ideal value. A major limitation of pin-photomixers is due to field screening effects. As the photo-generated electrons and holes drift towards the n- and the p-layers, respectively, with transit times in the ps range, a stationary space charge distribution – changing from positive sign near the p-layer to negative sign towards the n-layer – builds up in the i-layer. In order to maintain a sufficiently high field for the fast transport throughout the whole i-layer an increasingly large reverse bias is required if the laser power increases. In our case about 10 V reverse bias are necessary for $P_L = 100$ mW. With a photocurrent of 70 mA a dissipated electrical power of 700 mW (!) would result. With $R_a = 70 \Omega$, e.g., a value of $P_{THz} = 75 \mu\text{W}$, would be obtained, which would represent a drastic improvement by 1 to 1 1/2 orders of magnitude compared to the theoretical or the best experimental LT-photomixer results, respectively.

There are only a few reports on pin photomixers found in the literature. The best results reported are 2mW @ 100 GHz and 100 nW @ 0.625 THz achieved with 100 mW laser power [16–17]. More recently, 17 mW @ 120GHz was obtained [18].

Novel n-i-pn-i-p Superlattice Photodiode Concept

As the current in photomixers is uni-directional, the transport time ideally should be less

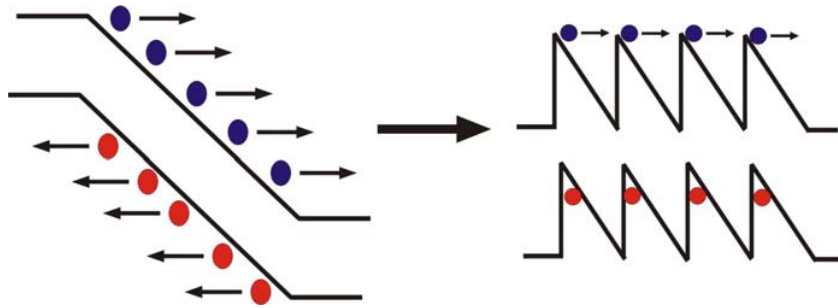


Figure 1: In order to reduce the drift length but keeping the capacitance of the whole structure constant, the pin-diode is subdivided into N nano - pin-diodes.

than about one half of the THz period, i.e. $\tau_{tr} < T_{THz}/2$. As these times are in the fs range, this implies that for the time of interest the transport can be ballistic. During this time electrons acquire a velocity strongly exceeding the high-field drift velocity and, consequently, contribute a much larger amount to the current and propagate over a longer distance. As transport for times $> T_{THz}/2$ is counterproductive it is advantageous if the electrons are stopped after a time of about $T_{THz}/2$. As (ballistic) holes are much slower, it is desirable that transport is mainly carried by the electrons. To a good approximation ballistic electron transport in the uniform electric field of a pin diode can be described by a velocity linearly increasing in time until the minimum energy for scattering into higher side valleys, $\Delta E_{\Gamma L} \approx 250$ meV in the case of GaAs, is reached. The average velocity is $v_{bal} = v_{max}/2 = 5 \times 10^7$ cm/s with v_{max} determined from $m_c v_{max}^2/2 = \Delta E_{\Gamma L}$ (where m_c stands for the effective conduction electron mass in the Γ -valley). As v_{bal} is by a factor of 5 higher as v_{sat} , for a given flight time of $T_{THz}/2$ the electrons travel over correspondingly larger distances $l_z = v_{bal} T_{THz}/2 = v_{bal}/(2\nu_{THz})$. For $\nu_{THz} = 1$ THz, e.g., we obtain $l_z = 250$ nm. In order to avoid that the capacitance becomes too high and, hence, the RC-3dB frequency too low, we keep L_z sufficiently large to assure that $v_{3dBt} \geq \nu_{THz}$ by subdividing L_z into a superlattice consisting of N nano – p-i-n diodes of length l_z , i.e. $L_z = N l_z$, as shown schematically in Fig. 1. As the photo-generated carriers are now distributed over N superlattice periods the AC current amplitude I_{THz}^0 is reduced by a factor of N . Hence,

$$P_{THz} = P_{THz}^{id} N^{-2} [1 + (\nu_{THz}/\nu_{RC})^2]^{-1} [1 + (\nu_{THz}/\nu_{tr})^2]^{-1}. \quad (8)$$

For a given THz-frequency, ν_{THz} , the optimized number of superlattice periods, N^{opt} , is obtained from the conditions $\nu_{RC} = \nu_{THz}$ and $\nu_{tr} = \nu_{THz}$. For a superlattice of N periods ν_{RC} is given by $\nu_{3dB} = 1/(2\pi R_a C_{tot})$ with

$$C_{tot} = \epsilon L_x L_y / (4\pi N l_z) = \nu_{THz} \epsilon L_x L_y / (2\pi N v_{bal}), \quad (9)$$

which yields, together with $\nu_{tr} = 1/2\tau_{tr} = v_{bal}/2l_z$

$$N^{opt} = (\nu_{THz})^2 R_a \epsilon L_x L_y / v_{bal} \quad (10)$$

and

$$P_{THz}^{opt} = \frac{1}{2} (e \eta_{ph} P_L / h\nu_0)^2 R_a / (2N^{opt})^{-2} = \frac{1}{2} (e \eta_{ph} P_L / h\nu_0)^2 v_{bal}^2 / [4R_a (\nu_{THz}^2 \epsilon L_x L_y)^2] \quad (11)$$

Equ. (11) suggests that the THz power increases quadratically with the laser power and decreases with the 4-th power of the THz frequency and quadratically with the cross section of the mixer. For sufficiently high values of ν_{THz} the emitted THz power is, in fact, limited only by the maximum laser power, which can be dissipated by the mixer and the minimum device dimensions L_x and L_y that can be achieved. In the range of 1 THz, however, the minimum cross section at a given laser power is limited by the maximum tolerable field changes in the i-layer, where the ballistic transport takes place. This field change is proportional to the laser power and inversely proportional to the THz fre-

quency, the number of periods and the capacitance. Using Equ.s (9) and (10) for C_{tot} and N^{opt} we see that ultimately the field changes are proportional to $P_L(L_x L_y)^{-2} v_{\text{THz}}^{-4}$. For our estimates we take $P_L=100$ mW (as typically used in the LT-GaAs photomixing experiments; the n-i-pn-i-p photomixer can most probably tolerate even higher power, as no external voltage is to be applied to these devices, in contrast to the LT-GaAs photomixers, where the high voltage at the Schottky contacts is the origin of thermal failure near P_L exceeding 100 mW). At $v_{\text{THz}} = 1$ THz one finds $l_z^{\text{opt}} = 250$ nm. The condition that periodic field changes should be less than ± 25 % yields $L_x = L_y = 9$ μm and $N^{\text{opt}} = 10$. According to Equ. (11) one finds $P_{\text{THz}} = 425$ μW . For $v_{\text{THz}} = 3$ THz one finds $l_z = 93$ nm. At this frequency the periodic field changes turn out to be far below the critical values, even if the dimensions are reduced to $L_x = L_y = 5$ μm (the smallest values which can be achieved “easily”). In this case one finds $N^{\text{opt}} = 28$ and $P_{\text{THz}} = 54$ μW .

For the realization of the concept one has to bear in mind:

- 1) The transport should predominantly be carried by the (light, and therefore fast) electrons
- 2) The potential drop between the starting and arrival point of the electrons should be of the order of the energy difference $\Delta_{\Gamma\text{L}}$ between Γ - and L-valley (in case of GaAs).
- 3) Although after arrival the velocity of the carriers is zero the electrons at the minimum of the conduction band have to recombine fast enough with the holes at the valence band maximum in the neighboring n-i-p-diode (See Fig.1) in order to avoid too much carrier accumulation.
- 4) Although we discuss here only the example of GaAs-based photomixers other compound semiconductors (like InGaAs) have even more favorable properties regarding v_{bal} and the critical energies for scattering into side valleys $\Delta_{\Gamma\text{L}}$ or $\Delta_{\Gamma\text{X}}$.

In Fig. 2 one period of the proposed “n-i-pn-i-p superlattice” structure, designed to meet these requirements is shown. The individual “n-i-p-electron – transport diodes” which are designed to have the optimum length l_e for the ballistic electron transport and a short

transport length l_h for the holes for the chosen THz-frequency are connected to each

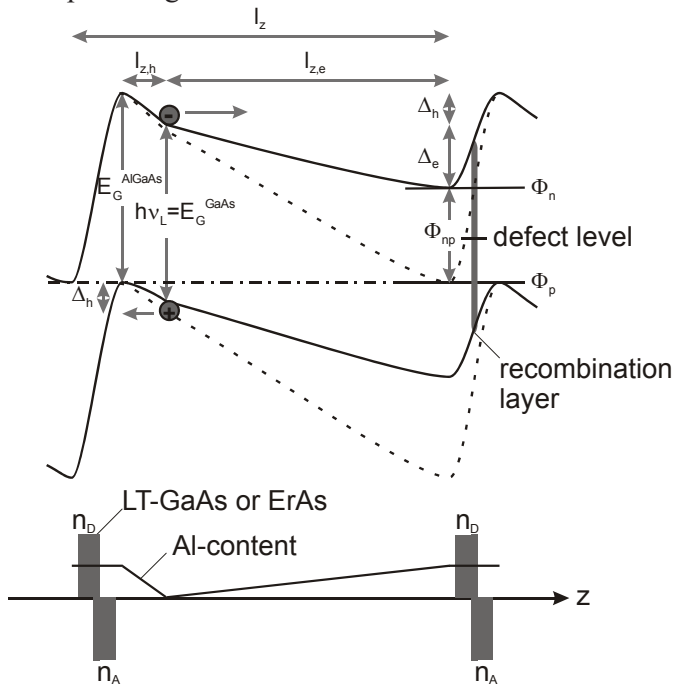


Figure 2: Band diagram, Al-content and doping profile of one period of the n-i-pn-i-p-superlattice

other by “recombination pn-junctions”. These junctions are highly doped and contain a thin electron-hole recombination layer composed of either LT-GaAs or ErAs [19] and will be discussed in more detail below. The Al-content is asymmetrically graded in the i-layers (see Fig.2). Because of the varying band gap in the i-layer the electron generation takes mainly place near the point of minimum band gap as indicated in Fig.2, if the laser photon energy is suitably chosen. In Fig. 2 the band diagrams are shown for both the ground state and the excited state at illumination with high excitation energy. The ground state (dotted lines) is characterized by a common Fermi level in the n- and the p-layers. The sheet electron and hole density in the ground state is $n_0^{(2)}$ and $p_0^{(2)}$, respectively. As the photo-generated electrons and holes do not recombine instantaneously an additional sheet electron and hole density $\Delta n^{(2)} = \Delta p^{(2)}$ builds up under illumination. This space charge partially screens the built-in potential. This results in a splitting of the quasi-Fermi levels for the electrons in the n-layers and the holes in the p-layers $\phi_{np} = \phi_n - \phi_p$ (full lines in Fig. 2). Under photomixing conditions the average photocurrent generated per period of the n-i-pn-i-p superlattice, I^0/N , is flowing through the recombination diode as a (nearly constant) recombination current. The value of ϕ_{np} and thus also the potential drop within the “n-i-p electron – transport diodes” and the “np recombination diodes” corresponds to eU_{np} , where U_{np} stands for the forward bias at which just this current I^0/N is flowing in the “pn recombination diode”. Under ideal operation conditions

the average value of $\phi_{np} = eU_{np}$ should be somewhat larger than $E_g - \Delta_{\Gamma L}$ and the amplitude of the (THz)-periodic variation of ϕ_{np} should be significantly smaller than ϕ_{np} , as discussed in the paragraph following Equ. (11).

Simple estimates show that depending on the laser power and the number of periods the current density in our devices will be in the order of $j_{av} = 1$ to 100 kA/cm^2 because of the small cross sectional area $L_x L_y$, required according to Equ.s (9) to (11). As these values are required for a photo-induced Fermi level splitting of $\phi_{np} = eU_{np} \approx 1 \text{ eV}$ these values turn out to be by many orders of magnitude larger than in standard pn-junctions. Therefore, special “pn recombination diodes” have to be used, as shown in Fig. 2. In Fig. 3 the measured current density vs voltage curves for strongly doped p-n diodes with a 1.2 monolayer thick ErAs recombination layer at the interface and $n_D = 5 * 10^{18} \text{ cm}^{-3}$ and $n_A = 2 * 10^{19} \text{ cm}^{-3}$ are compared with reference diodes with the same doping densities, but without ErAs recombination layer. We see, that using this trick, the required high current densities are, in fact, accessible at the required excitation level.

In order to support our simple estimates from Section 4 we show in Fig. 4 the results of Monte Carlo calculations for the transient high-field transport in bulk material. From this figure it can be seen, that our estimates regarding the average ballistic velocity v_{bal} , the transport time and distance, τ_{tr} and l_z , respectively are quite realistic. In particular, we see that the position of the electrons after a given time of flight does not depend too critically on the actual field.

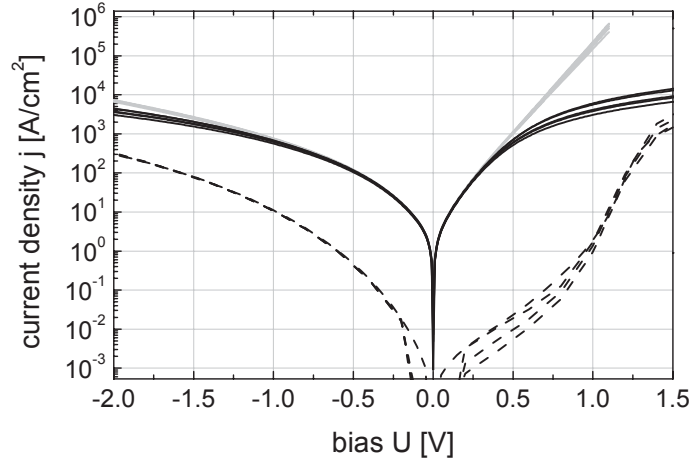


Figure 3. current density vs. voltage curves of highly doped pn-junctions without (dashed) and with ErAs recombination layer. Recombination diode (with ErAs-layer): black lines = measured, grey lines = corrected for contact layer series resistance; reference diode (without ErAs-layer): dashed line.

The distance reached after 0.5 ps, e.g., is nearly the same, if the field changes between 10 and 20 kV/cm. Recent fs- studies of the transient transport in similar nanostructures have quantitatively confirmed our Monte Carlo simulations [20–21].

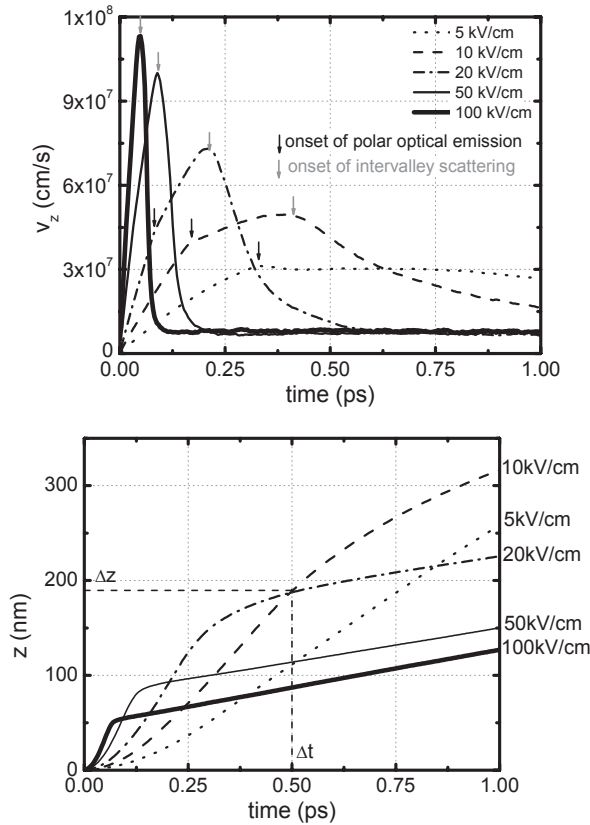


Figure 4: Monte Carlo results velocity and position vs time.

We conclude that the main drawbacks of conventional LT-GaAs based photomixers as THz-sources result from the low photoconductive gain. Our approach based on ballistic transport in a n-i-pn-i-p superlattice, in contrast, yields optimized THz-currents and THz-voltages. Impedance matching to the antenna can be achieved by suitable choice of the number of periods N of the superlattice. Moreover, this approach overcomes the usual problem of the frequency limitation due to the carrier lifetime in LT-GaAs. Therefore, particularly interesting results are expected at frequencies up to about 3 THz.

Quantum Cascade Lasers

Quantum cascade lasers are unipolar lasers that exploit the radiative transitions between two subbands of a multi quantum well system [22] or two minibands of a superlattice [23]. The basic cell is composed of an injector and an active region. The injector, usually doped, provides electrons to the upper level of the active region. Under sufficiently high electric fields, a population inversion builds up between such upper level and the lower one, which in turn depletes itself via non-radiative transitions with the level(s) of the ac-

tive region sitting at even lower energy. The basic cell is repeated for 30 to 40 periods in order to enhance the output power.

Quantum cascade lasers have been built on the InGaAs/InAlAs systems (lattice matched to InP) and GaAs/AlGaAs one (lattice matched to GaAs) [24–27]. They are usually n-type and operate in the range 5-20 μm , with output power of the order of few mW, under CW conditions (at least of to 200 K) or under pulsed condition up to room temperature and higher. Weak electro luminescence in the THz regime (above 5 THz) has been reported in [28–30]. Recently, two Monte Carlo simulations have indicated that it is possible to achieve population inversion and lasing action in this regime. One of the analyses [31] was based on a conventional QCL with a 2-well active region.

Population inversion is achieved up to 77 K with an electric field of about 35 kV/cm.

The second considered a SL GaAs/AlGaAs QCL [32], with well width of 22 nm. An experimental verification of the THz QCLs was announced [33] recently. The laser works at 4.4 THz with an output power of 2 mW up to a temperature of 45 K.

More recently progress in the field has been rapid with experimental results achieved at 3.4 and 2.3 THz [34,35].

Stressed p-Ge Lasers

A candidate for tunable THz generation would have been the cryogenic p-Ge “hot hole” laser that emits broadband THz radiation resulting from transitions between the light- and heavy hole bands [39]. However, the large excitation power needed to obtain “streaming motion” of holes under crossed magnetic and electric fields prevents CW operation. More recently, it has been observed that for p-Ge under large uni-axial external pressure, laser action occurs at moderate excitation powers, without the need of a magnetic field [36]. The proposed population inversion mechanism is illustrated in fig.a [40, 37]. Under uni-axial pressure the light- and heavy hole sub-bands split up and, for $P > 2.5$ kbar // [100] and $P > 4$ kbar // [111], the acceptor ground state connected with the heavy hole band enters the continuum of the light hole sub-band and becomes a so-called resonant state. Under impact ionisation conditions, the scattering of the holes at this resonant state results in a trapping of the holes near this state, leading to a maximum of the non-equilibrium hole distribution function near this energy [42].

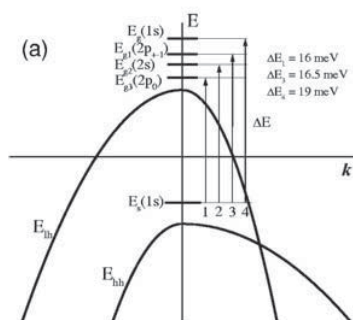


Fig.5. Energy level scheme showing the heavy hole 1s resonant state in the light hole con-

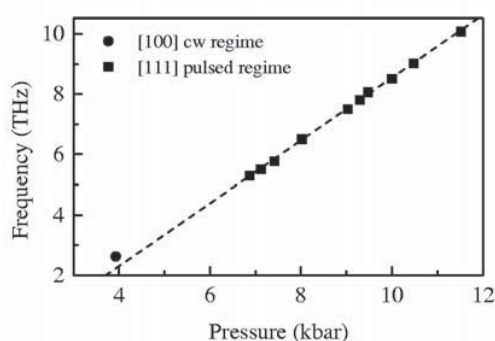


Fig. 6. Pressure dependence of the frequency of the main emission peak in stressed p-Ge [40]

tinuum + possible laser transitions [40]

Lasing action occurs between this resonant state and the bound ground- and excited states of the acceptor connected to the light hole sub-band, as shown in fig. 5.[40]. Frequency tuning between from 2.5–10 THz is possible by changing the pressure (fig. 6). The low excitation voltage needed to reach laser action proves that in this case, contrary to the p-Ge hot hole laser, no streaming motion of the holes is necessary to create a population inversion. Due to heating, for bias voltages above 10V/cm only pulsed operation is possible at a mW power level. For lower voltages CW operation at the microwatt level has been observed at 2.5 THz with a lasing threshold excitation power of only 10 mW [38, 41].

Conclusions and Further Work

The novel photomixing scheme presented in this paper is believed to be the only way forward in improving THz performance of photomixers, as a result of this study. In order to introduce the advantages of this scheme a detailed, and lengthy, explanation of photomixer physics and state-of-the-art performance was hardly avoidable. The other two technologies presented, THz QCLs and p-Ge lasers, are thought to be equally promising and their development is ongoing without this study. Presently, the second phase of this ESA study has begun for some time and has focused on the realisation of the superlattice photodiode as well as the duplication of the THz QCL and p-Ge results reported in the literature. Emphasis is also put on QCL modelling in order to better understand the ultimate theoretical limitations, in terms of lower frequency and operating temperatures.

References

- [1] J.J.A. Baselmans, M. Hajenius, J.R. Gao, P.A.J. de Korte, T.M. Klapwijk, B. Voronov, G. Gol'tsman, "Noise Performance of NbN Hot Electron Bolometer Mixers at 2.5 THz and its Dependence on the Contact Resistance", Published in these Proceedings.
- [2] P. Khosropanah, S. Bedorf, S. Cherednichenko, K. Jacobs, H.F. Merkel, E. Kollberg, "Fabrication and Noise Measurement of NbTiN Hot Electron Bolometer Heterodyne Mixers at THz Frequencies", Published in these Proceedings.
- [3] H.F. Merkel, P. Khosropanah, S. Cherednichenko, E. Kollberg, "Comparison of the Noise Performance of NbTiN and NbN Hot Electron Bolometer Heterodyne Mixers at THz Frequencies", Published in these Proceedings.
- [4] R. Teipen, M. Justen, T. Tils, S. Glenz, C. E. Honingh, K. Jacobs, B.D. Jackson, T. Zijlstra, M. Kroug, "Influence of Junction Quality and Current Density on HIFI Band 2 Mixer Performance", Published in these Proceedings.
- [5] W. Jellema, P. Wesselius, S. Withington, G. Yassin, J.A. Murphy, C. O'Sullivan, N. Trappe, T. Peacocke, B. Leone, "Experimental Verification of Electromagnetic Simulations of a HIFI Mixer Sub-Assembly", Published in these Proceedings.
- [6] J. Baubert, M. Salez, P. Khosropanah, S. Cherednichenko, H.F. Merkel, "A Hot-Spot Model for Membrane-Based HEB", Published as Poster in these Proceedings.

- [7] M. Hajenius, J.J.A. Baselmans, J.R. Gao, T.M. Klapwijk, P.A.J. de Korte, “Current-Voltage and Resistance-Temperature characteristics of Nb(Ti)N Phonon Cooled HEB Mixers With and Without Contact Resistance”, Published as Poster in these Proceedings.
- [8] H.F. Merkel, “NbAu Bilayer Diffusion Cooled HEB – Model versus Experiment, Published as Poster in these Proceedings.
- [9] N. Erickson, R. Grosslein, J. Wielgus, V. Fath, “An All Solid State Source for 1.7 THz”, Published in these Proceedings.
- [10] J. Ward, F. Maiwald, A. Maestrini, G. Chattopadhyay, E. Schlecht, J. Gill, I. Mehdi, “1400–1900 GHz Local Oscillators for the Herschel Space Observatory”, Published in these Proceedings.
- [11] E.R. Brown, et al., APL 66, 4903 (1995).
- [12] S. Matsuura et al., “A travelling-wave THz photomixer based on angle-tuned phase matching”, Appl. Phys. Lett. **74**, 2872 (1999).
- [13] S. Matsuura et al., “Design and characterization of optical-THz phase-matched travelling wave photomixers”, Proceedings of SPIE 3795, 484 (1999).
- [14] E.K. Duerr et al., “Distributed photomixers”, Proceedings of CLEO, CWU6 (2000).
- [15] E.K. Duerr, “Distributed photomixers”, PhD Thesis, Massachusetts Institute of Technology, September 2002.
- [16] N. Shimizu, et al., Jpn. J. Appl. Phys. **37**, 1424 (1998).
- [17] N. Shimizu, et al., Jpn. J. Appl. Phys. **38**, 2573 (1999).
- [18] H. Ito, T. Ito, Y. Muramoto, T. Furuta, T. Ishibashi, “F-Band (90-140 GHz) Uni-Traveling-Carrier Photodiode Module for a Photonic Local Oscillator”, Published in these Proceedings.
- [19] C. Kadow, et al., Physica E **7**, 97 (2000).
- [20] M. Eckardt, et al., Proceedings of HCIS12 (2001), Physica **B 314**, 154 (2002).
- [21] A. Schwanhäußer, et al., Proceedings of HCIS12 (2001), Physica **B 314**, 273 (2002).
- [22] J. Faist, F. Capasso, D. L. Sivco, C. Sirtori, A. L. Hutchinson, and A. Y. Cho, Science, **264**, 553 (1994).
- [23] G. Scamarcio, F. Capasso, C. Sirtori, J. Faist, A.L. . Hutchinson, D. L. Sivco, and A. Y. Cho, Science, **276**, 773 (1997).
- [24] F. Capasso, C. Gmachl, R. Paiella, A. Tredicucci, A. L. Hutchinson, D. L. Sivco, J. N. Baillargeon, A. Y. Cho, and H. C. Liu, IEEE J. Sel. Top. Quantum Electron. **6**, 931 (2000).
- [25] D. Hofstaetter, M. Beck, T. Aellen, J. Faist, U. Oesterle, M. Illegems, E. Gini, and H. Melchior, Appl. Phys. Lett. **78**, 1964 (2001).
- [26] J. Faist, F. Capasso, D. L. Sivco, S. N. G. Chu, and A. Y. Cho, Appl. Phys. Lett. **72**, 680 (1998).
- [27] A. Tredicucci, C. Gmachl, F. Capasso, D. L. Sivco, A. L. Hutchinson, and A. Y. Cho, Appl. Phys. Lett. **74**, 638 (1999).
- [28] M. Rochat, J. Faist, M. Beck, U. Oesterle, and M. Ilegems, Appl. Phys. Lett. **73**, 3724 (1998).
- [29] B. S. Williams, B. Xu, Q. Hu, and M. R. Melloch, Appl. Phys. Lett. **75**, 2927 (1999).

- [30] J. Ulrich, R. Zobl, K. Unterrainer, G. Strasser, and E. Gornik, *Appl. Phys. Lett.* **76**, 19 (2000).
- [31] R. Köhler, R.C. Iotti, A. Tredicucci, and F. Rossi, *Appl. Phys. Lett.* **79**, 3920 (2001).
- [32] F. Compagnone, M. Manenti, and P. Lugli, Submitted for publication.
- [33] R. Köhler, A. Tredicucci, F. Beltram, H.E. Beere, E.H. Linfield, A.G. Davies, D.A. Ritchie, R.C. Iotti, F. Rossi, *Nature* **417**, 156 (2002).
- [34] B.S. Williams, H. Callebaut, S. Kumar, H. Qing, J.L. Reno, "TeraHertz Quantum Cascade Laser Based on LO-Phonon-Scattering Assisted Depopulation", Published in these Proceedings.
- [35] G. Scalfari. Private communication.
- [36] I.V. Altukhov, E.G. Chorkova, M.S. Kagan, K.A. Korelev, V.P. Sinis, F.A. Smirnov, *Sov. Phys. JETP* **74**(1992)404.
- [37] "Resonant acceptor states and terahertz stimulated emission of uniaxially strained germanium", I.V. Altukhov, M.S. Kagan, K.A. Korelev, V.P. Sinis, E.G. Chorkova, *JETP* **88**(1999)51
- [38] "Continuous stimulated THz emission due to intra-centre population inversion in uniaxially strained germanium", I.V. Altukhov, M.S. Kagan, , Yu. P. Gousev,, I.V. Altukhov, *Physica B* **272**(1999)458
- [39] *Opt. Quantum Electron.* Vol. 23, Special Issue on Far-Infrared Semiconductor Lasers, edited by E. Gornik and A.A. Andronov (Chapman and Hall, London 1991)
- [40] "Widely tunable continuous-wave THz laser", Yu. P. Gousev, I.V. Altukhov, K.A. Korelev, V.P. Sinis, M.S. Kagan, E.E. Haller, M.A. Odnoblyudov, I.N. Yasseievich, K-A. Chao, *Appl. Phys. Lett.* **75**(1999)757
- [41] "Resonant acceptor states and stimulated THz emission in semiconductors and semiconductor structures", M.S. Kagan, I.N. Yasseievich, *Proceedings of the 11th International Symposium on Ultrafast Phenomena in Semiconductors*, Vilnius, 2001.
- [42] "Population inversion induced by resonant states in semiconductors", M.A. Odnoblyudov, I.N. Yasseievich, M.S. Kagan, Yu. M. Galperin, K.A. Chao, *Phys. Rev. Lett.* **83**(1999)644.

Amplitude Noise in a Photomixer Using a UTC-PD in the 100 GHz Band

T. Noguchi, A. Ueda, H. Iwashita, S. Takano, Y. Sekimoto, M. Ishiguro,
T. Ishibashi^{†,1}, H. Ito[†], and T. Nagatsuma^{††}

Nobeyama Radio Observatory

[†]*NTT Photonics Laboratories, NTT Corporation*

^{††}*NTT Microsystem Integration Laboratories, NTT Corporation*

Abstract

We have developed a waveguide-mounted photomixer in the 75-115 GHz band with a uni-traveling-carrier photodiode which is optically-pumped by two 1.55- μm lasers. We have successfully demonstrated to produce an output power of ~ 2 mW at 100 GHz with an input laser power of ~ 100 mW. An SIS (Superconductor-Insulator-Superconductor) mixer has been pumped by the photomixer as a local oscillator (LO). We have made similar experiment using a Gunn-diode LO source and carefully compared the receiver noise temperature of the SIS mixer with those pumped by the photomixer. It is found that the receiver noise temperatures of the SIS mixer pumped by the photomixer is as low as those pumped by the Gunn oscillator. The photomixer was employed as an LO in an SIS receiver used in the 45-m telescope at Nobeyama Radio Observatory and we have successfully observed an interstellar molecular spectral line with the receiver for the first time.

1. Introduction

It has been recently shown that photomixers using a uni-traveling-carrier photodiode (UTC-PD) have a great potential for generation of millimeter-wave radiation [1]. Based on a simple analysis, it is expected that a 3-dB falloff bandwidth of the UTC-PD determined by carrier traveling time can be in a THz range [2]. The UTC-PD photomixer has emerged as one of the promising candidates to generate the millimeter- and submillimeter-wave radiation.

We have designed a new photomixer using the UTC-PD and successfully demonstrated to generate output power of ~ 1 mW at 100 GHz by the photomixer. Although the output power of the photomixer is thought to be enough to pump SIS mixers as an LO of the usual receivers in this frequency band, noise characteristics of the photomixer have not been fully understood yet. At present, it is especially important to know the noise level of the photomixer when it is used to pump a low-noise SIS mixer as an LO. We have systematically measured noise temperature of an SIS mixer pumped by the photomixer as well as a Gunn diode as an LO. The measured noise temperature of those two cases are carefully compared to estimate the noise level of the photomixer in reference to that of Gunn diode.

¹Present affiliation: NTT Electronics Corporation

In this paper, performance of the photomixer using the UTC-PD in the W band is briefly described. Then an experimental setup and results of measurement on noise temperature of SIS mixers using the photomixer as well as the Gunn diode as an LO are presented. Finally, we present preliminary results of radio astronomical observation of an interstellar molecular spectral line of a carbon monoxide (CS) at 97.98 GHz with an SIS receiver in which the photomixer is used as an LO.

2. Photomixer Performance

We have made a waveguide photomixer in the W-band using the UTC-PD. Detailed design of the UTC-PD and photomixer is described in Ref.[3]. Schematic diagram of the photomixer oscillator at the W band is shown in Fig. 1. Millimeter-wave output power from the photomixer measured by a Schottky-diode detector is plotted as a function of photocurrent of the UTC-PD in Fig. 2. It is noted here that the photocurrent of the UTC-PD induced by lasers is approximately proportional to the amount of laser power coupled to the diode in the previous experiment at lower frequency [4]. It is clear that the output power increases approximately in proportion to the photocurrent (or the input laser power) at lower photocurrent. The output power reaches ~ 2 mW at the photocurrent of 20 mA where laser power of ~ 100 mW each is applied to the photomixer [5, 6]. It is noted that as far as we know, the power achieved in this experiment is one or two orders of magnitude higher than those generated by photomixers in this frequency band [7].

A typical spectrum of photomixer output near 100 GHz is shown in Fig. 3. Frequency width of the output spectrum of the photomixer is less than 10 MHz, which is mainly governed by fluctuation of frequencies of the lasers, since freely-running lasers are used in the experiment. It should be noted that no serious spurious peaks are not found in this frequency range. Frequency dependence of output power of the photomixer is plotted in Fig. 4. It is found that relative variation of the photomixer output power is less than 3 dB over the entire range of W-band (75 – 115 GHz) without any mechanical tuning mechanisms usually used in Gunn-diode oscillators.

3. Photomixer LO for SIS Mixers

The photomixer was used as an LO source for SIS mixers in the 100 GHz band. The photomixer output as an LO and an RF signal are combined by a cross-guide coupler with a coupling efficiency of < -20 dB placed on a 4-K stage in a dewar and then coupled into the SIS mixer. It is noted here that this LO coupling scheme is popularly used in low-noise receivers at millimeter wavelengths. Schematic diagram of a low-noise receiver employing SIS mixer associated with an LO source of the photomixer is shown in Fig. 5.

In order to compare noise of the photomixer with that of Gunn-diode oscillator, we have carried out similar experiment using a Gunn-diode LO source. Then, we carefully compared receiver noise temperature of the SIS mixer pumped by the photomixer with those pumped by the Gunn-diode oscillator. Pumped and unpumped I-V curves of an SIS mixer by the Gunn-diode oscillator and photomixer at 100 GHz are shown in Fig. 6(a) and

(b), respectively. Total IF power response to hot (295 K) and cold (80 K) loads are also shown in those figures. We have found that the photomixer is able to provide sufficient LO power required to pump the SIS mixer in the frequency band from 85 GHz, which approximately corresponds to a cut-off frequency of the waveguide in the cross-guide coupler and mixer block, to 120 GHz. The frequency dependence of the measured receiver noise temperature for the Gunn-diode LO as well as the photomixer LO are shown in Fig. 7. No significant difference between the noise temperatures of the SIS mixer pumped with the Gunn diode and photomixer was found in this experiment.

The estimated noise in the photomixer output from the measured receiver noise temperature is as high as ~ 10 K/ μ W, which is much smaller than that expected by Shillue including relative intensity noise (RIN) of lasers [8], if the noise in the Gunn diode output of 1 K/ μ W is assumed. It is demonstrated by this experiment that the noise in the photomixer is sufficiently low and that the photomixer is quite adequate for supplying the LO to SIS mixers in the 100 GHz band.

Radioastronomical Observation Using Photomixer LO

As a next step, the photomixer was applied to an LO source of an SIS receiver used in the 45-m telescope at Nobeyama Radio Observatory and we carried out actual radioastronomical observations using the SIS receiver with the photomixer LO [9]. The laser system employed here generates an optical comb, which enables stable and precise production of the beat signal from the photomixer [10]. A block diagram of the laser system is shown in the left side of Fig. 8. The output of a laser at about $1.55 \mu\text{m}$ is amplitude-modulated by a radio frequency (RF) and consequently the optical comb is generated. Two appropriate emission lines of this comb are selected with tunable optical filters and amplified, and then transmitted to the photomixer with an optical fiber.

We have used two nearly identical SIS receivers simultaneously. One (called S80) is pumped by a conventional Gunn-diode LO system, while the other (called S100) is pumped by the photomixer LO as schematically shown in Fig. 8. The radio signal was divided into two by a polarization grid placed in front of the receivers and they are coupled to the respective SIS receivers. In order to make a direct comparison, data were simultaneously obtained by the two SIS receivers. The intermediate frequency (IF) of 1.375 GHz was used in those two receivers. As the performance of the SIS receiver strongly depends on the LO power applied to the SIS mixer, output of power of the photomixer was carefully optimized by adjusting gain of optical amplifier and by adjusting an RF attenuator. Acousto-optic spectrometer (AOS), with a bandwidth of 40 MHz and frequency resolution of 37 kHz, were used as radio spectrometer.

The observed spectral line was the $J = 2 - 1$ rotational transition of a CS at 97.98 GHz, which is one of strong observable lines near 100 GHz in many kinds of astronomical sources. The observed source was W51, which is a famous high-mass star-forming region in our galaxy. The CS $J = 2 - 1$ spectra simultaneously observed with the receiver pumped by the photomixer LO and with that pumped by the conventional Gunn-diode LO

are shown at the top and middle in Fig. 9, respectively. The integration time on source was 260 seconds. At the bottom in Fig. 9, a difference between those two spectra is shown for comparison. It is clear that both spectra are approximately identical. This result indicates that useful spectral data for radioastronomical research can be obtained by using the photomixer LO.

We carried out a small mapping observation toward the central region of W51 using the receiver with photomixer LO for further demonstration. The CS $J = 2 - 1$ line was mapped at 9 positions with a 3×3 grid as shown in Fig. 10. The integration time of each spectrum on source was 140–160 seconds. The variation of the CS intensity is clearly found, which is consistent with the result reported previously using receivers with the conventional Gunn-diode LO.

Summary

We have exploited a photomixer for generation of millimeter wave at W band using a UTC-PD and successfully demonstrated to generate millimeter-wave radiation with a power as high as 2 mW in the 100 GHz band. As far as we know, this is the highest output power ever generated by any kind of photomixers in this frequency band. An SIS mixer was pumped by the photomixer as an LO and we found that the photomixer can provide a sufficient power to drive the SIS mixer. It is found that the noise added to the SIS mixer by the photomixer is as low as that by a Gunn oscillator. The photomixer was employed as an LO in an SIS receiver used in a telescope and we have successfully observed an interstellar molecular spectral line with the receiver for the first time.

Acknowledgment

The authors would like to thank S. Matsuura of Institute of Space and Astronautical Sciences (ISAS) for stimulative discussion. This work was supported by a Grant-in-Aid for Scientific Research from the Ministry of Education, Culture, Sports, Science and Technology.

References

- [1] H. Ito, T. Furuta, S. Kodama and T. Ishibashi, "InP/InGaAs Uni-Traveling-Carrier Photodiode with 310 GHz Bandwidth", *Electron. Lett.*, **36**, 1809-1810, 2000.
- [2] T. Ishibashi, H. Fushimi, T. Furuta, and H. Ito, "Uni-Traveling-Carrier Photodiodes for Electromagnetic Wave Generation", *Proc. IEEE 7th Int. Conference on Terahertz Electron.*, pp. 36–39, Nara, Japan, Nov. 1999.
- [3] T. Noguchi, A. Ueda, H. Iwashita, S. Takano, Y. Sekimoto, M. Ishiguro, T. Ishibashi, H. Ito, and T. Nagatsuma, "Millimeter Wave Generation Using a Uni-Traveling-Carrier Photodiode", *Proc. 12th Int. Symp. Space Terahertz Technology*, pp. 73–80, San Diego, CA, USA, 2001.
- [4] H. Ito, T. Ohno, H. Fushimi, T. Furuta, S. Kodama, and T. Ishibashi, "60 GHz high output power uni-traveling-carrier photodiodes with integrated bias circuit", *Electron. Lett.*, **36**, 747–748, 2000.

- [5] T. Noguchi, A. Ueda, H. Iwashita, Y. Sekimoto, M. Ishiguro, T. Ishibashi, H. Ito, and T. Nagatsuma, "A photonic Local Oscillator for an SIS Mixer in the 1001 GHz Band", *Proc. 13th Int. Symp. Space Terahertz Technology*, pp. 205–212, Boston, MA, USA, 2002.
- [6] A. Ueda, T. Noguchi, H. Iwashita, Y. Sekimoto, M. Ishiguro, S. Takano, T. Nagatsuma, H. Ito, A. Hirata, and T. Ishibashi, "W-band waveguide photomixer using a uni-traveling-carrier photodiode with 2mW output", to appear in *IEEE Trans. Microwave Theory Tech.*, **51**, 2003.
- [7] P. G. Huggard, B. N. Ellison, P. Shen, N. J. Gomes, P. A. Davies, W. P. Shillue, A. Vaccari, W. Grammer, and J. M. Payne, "A Photonic MM-Wave Reference and Local Oscillator Source", *ALMA Memo #396*, <http://www.alma.nrao.edu/memos/>.
- [8] B. Shillue, "Photonic Local Oscillators for Radio Astronomy: Signal-to-Noise Issues", *ALMA memo #319*, <http://www.alma.nrao.edu/memos/>.
- [9] S. Takano, A. Ueda, T. Yamamoto, S. Asayama, Y. Sekimoto, T. Noguchi, M. Ishiguro, H. Takara, S. Kawanishi, H. Ito, A. Hirata and T. Nagatsuma, "The First Radioastronomical Observation with Photonic Local Oscillator", To appear in *Publ. Astron. Soc. Japan*, **55**, 2003.
- [10] T. Yamamoto, H. Takara and S. Kawanishi, "270-360 GHz tunable beat signal light generator for photonic local oscillator", *Electron. Lett.*, **38**, 795–797, 2002.

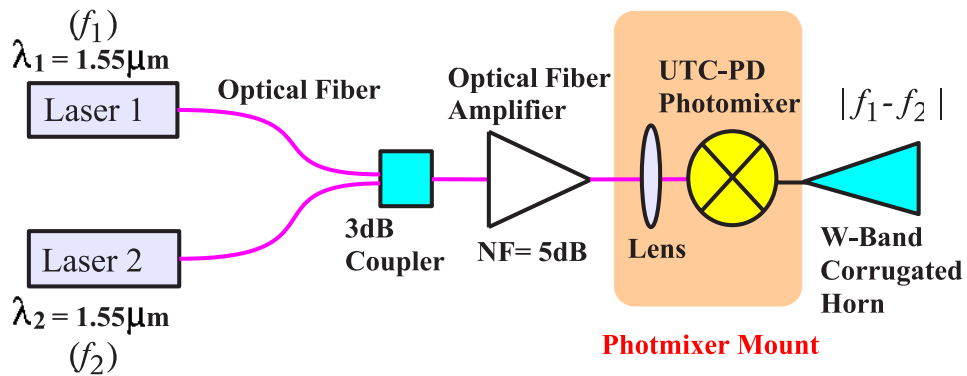


Fig. 1 Schematic diagram of a photomixer.

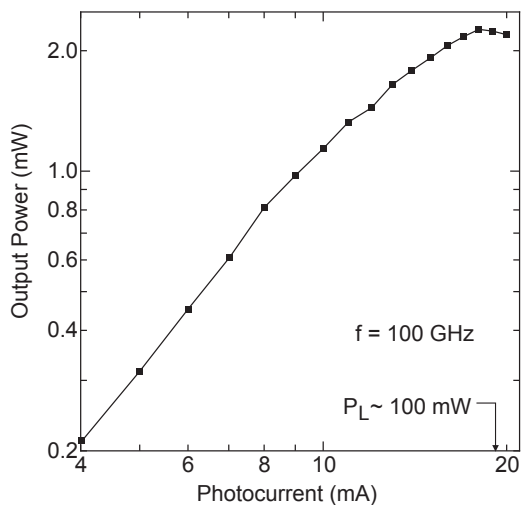


Fig. 2 Output power of the photomixer as a function of photocurrent.

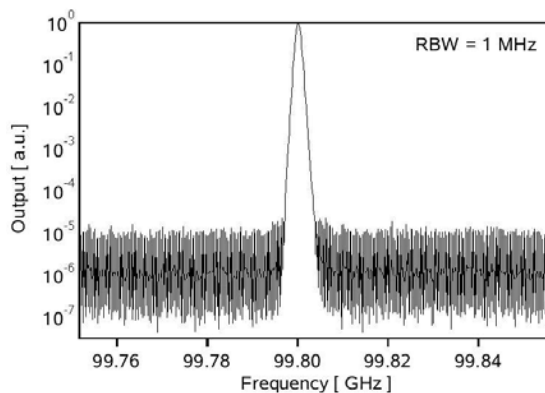


Fig. 3 Typical spectrum of photomixer output.

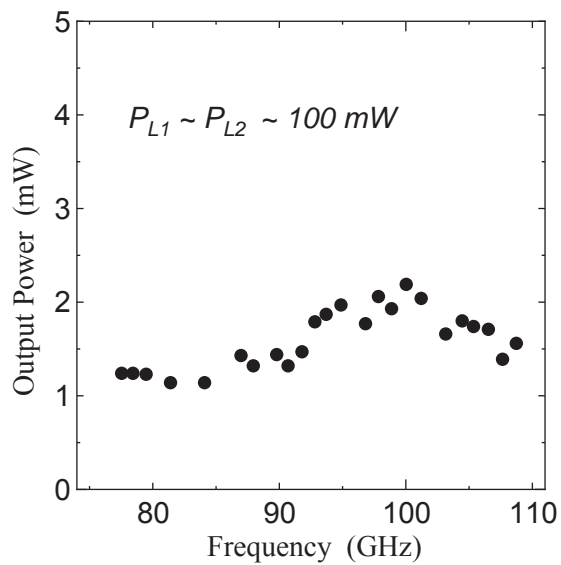


Fig. 4 Output power of the photomixer as a function of frequency.

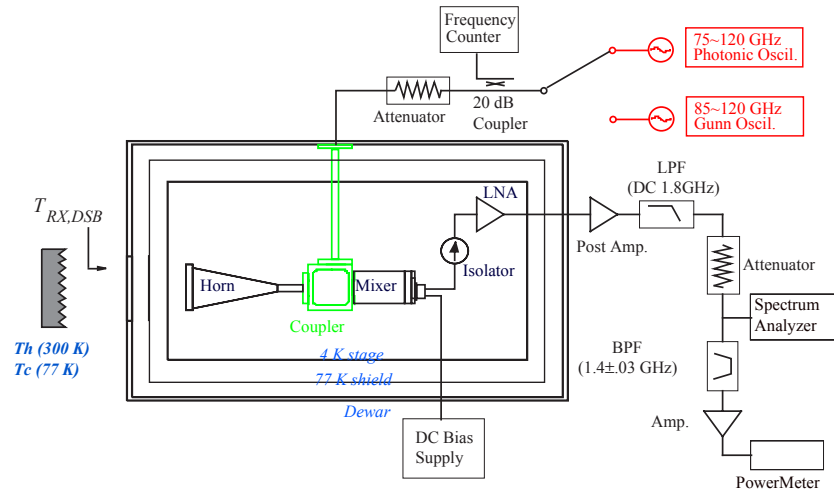


Fig. 5 Measurement setup of photomixer LO experiment using a low-noise SIS mixer.

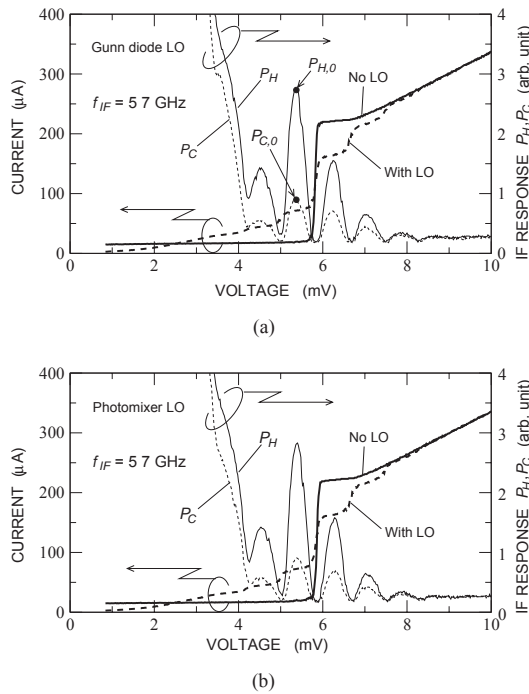


Fig. 6 dc I-V curves and IF response pumped by (a) Gunn-diode and (b) photomixer LO.

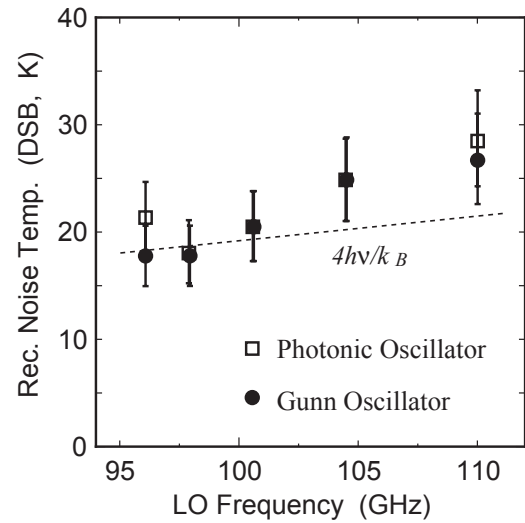


Fig. 7 Receiver noise temperature of SIS mixers pumped by the photomixer and Gunn-diode LO.

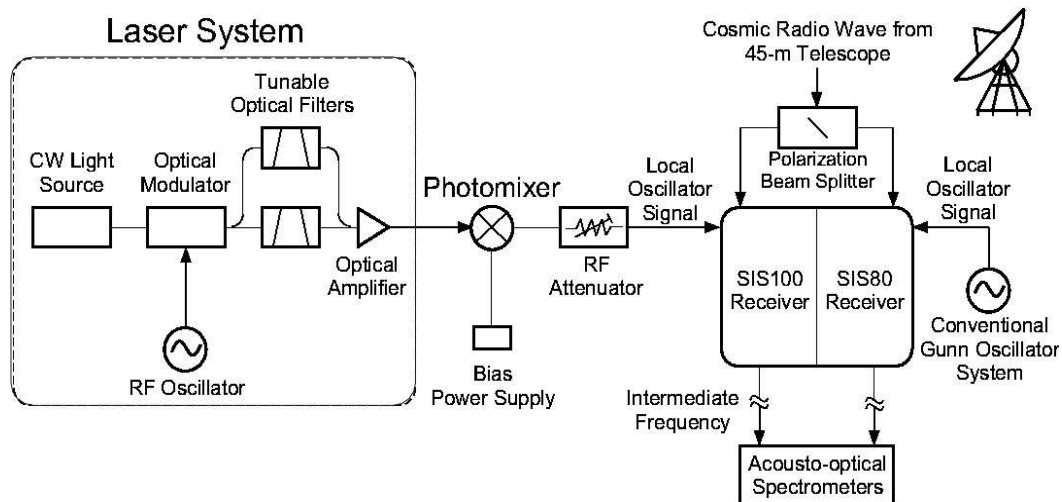


Fig. 8 Block diagram of the laser system, the photomixer and the SIS receivers used for radio-astronomical test observations.

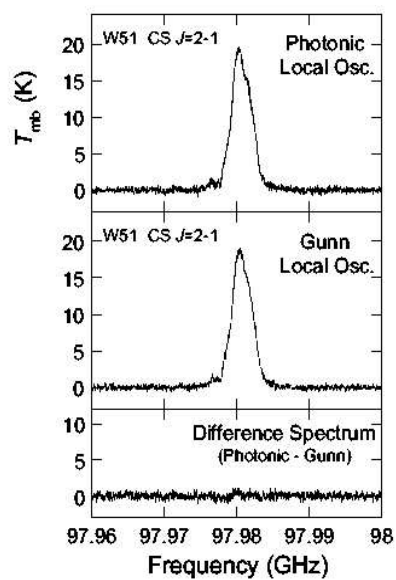


Fig. 9 CS ($J = 2 - 1$) spectra obtained with the Gunn-diode LO (top) and the photomixer LO (middle). A difference between both spectra (bottom) is also shown.

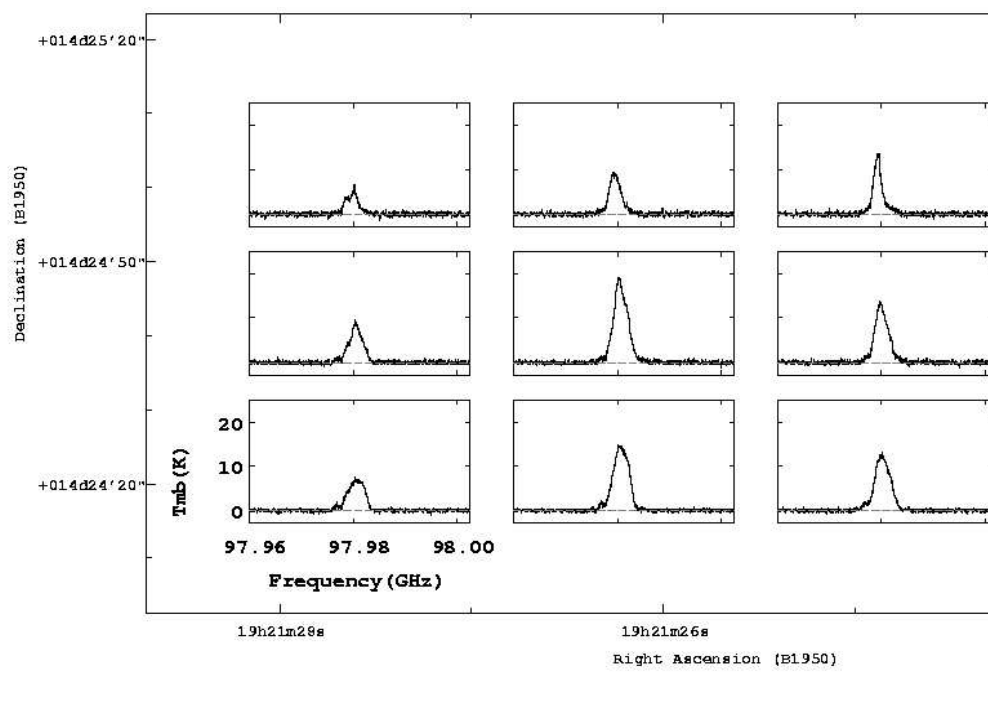


Fig. 10 Spatial map of CS ($J=2-1$) spectrum.

Propagating Partially Coherent THz Fields Using Non-Orthogonal Over-Complete Basis Sets

R.H.Berry, S. Withington, M.P. Hobson, G. Yassin

Cavendish Laboratory, University of Cambridge, Madingley Road, Cambridge, UK.

April 30, 2003

Abstract

We discuss a general theoretical framework for representing and propagating coherent and partially coherent submillimetre-wave fields by means of mathematically over-complete sampled basis functions. One such basis set, Gabor modes, consists of overlapping translated and modulated Gaussian beams. In the paper, we present some extraordinary results from modal field reconstructions and propagations, including simple models of bolometer arrays. Our new formalism is currently being used to study other interesting schemes such as spatially compressed, and therefore non-orthogonal, Gaussian-Hermite polynomials.

1 Introduction

The THz region of the electromagnetic spectrum (100GHz-10THz, 3mm-30 μ m) offers numerous scientific and technical opportunities in areas as diverse as astronomy, atmospheric physics, medical imaging, gas phase spectroscopy, antiquities, and industrial process control. A major difficulty when designing instruments for these wavelengths is how to model, in an accurate and efficient manner, the behaviour of complicated coherent and partially coherent optical systems.

Two problems are encountered when attempting to model THz optical systems. First, the field of interest may be in a complicated state of coherence. For example, in the case of astronomical imaging arrays, the total field is comprised of the fields of the individual pixels, and depending on the type of system, these can be individually coherent or incoherent, and mutually coherent or incoherent. Second, when propagating and scattering a THz field, diffraction is important, and therefore ray tracing cannot be used, but conversely, full electromagnetic simulations are slow as multiple finely-sampled diffraction integrals are needed.

A partially coherent field may be regarded as an incoherent linear superposition of a set of fully coherent fields—the natural modes—and therefore the propagation and scattering of a partially coherent field can be regarded as the propagation and scattering of a number of coherent fields. Clearly, it will not be possible to analyse the behaviour of partially coherent systems unless the behaviour of fully coherent systems can be analysed efficiently. Gabor decompositions may offer a way out of this difficulty. It is known that Gabor decompositions can sample the real and Fourier spaces of space- and band-limited functions in a compact and elegant manner. In addition, a Gaussian field propagates in a modal fashion, and complex ray tracing can be used to trace the evolution of a Gaussian beam through a complex system of optical components. If Gabor decomposition can be extended to partially coherent fields, then partially coherent optical systems could be analysed easily, and many practical and theoretical developments would follow.

Previously we have analysed [1, 2, 3], partially coherent fields using a finite number of Gaussian-Hermite and Gaussian-Laguerre modes, basis sets in which the modes are mutually orthogonal but not complete, since an infinite number of such modes are needed to form a complete set. Such simulations have been very successful because the natural modes of a finite throughput Gaussian beam telescope are prolate spheroidal functions, closely related to such Gaussian based modes. In this paper we present a framework to quantify the degrees of freedom in a field a basis can support and we explicitly consider the numerical sampling of bases for optimal results. By these means we present an opportunity for the optimisation of sampling within modal analysis, ensuring that computational operations are reduced to a minimum.

We also demonstrate the feasibility of modelling the behaviour of partially coherent THz optical systems through the use of Gabor modes. In actual fact, the core of our analysis is not restricted to Gabor decompositions, but can be applied to any set of functions that form a non-orthogonal and *complete* or *over-complete* basis set. By complete we mean that the basis set supports all the degrees of freedom over a field's span without linear dependence between the basis functions, whereas for over-complete basis there are additional basis functions relative to the complete case and hence linear dependence in the basis set. In addition, we do not work with infinite-dimensional function spaces, but work with the practical reality of sampled, space-limited functions, which are spanned by finite dimensional vector spaces. Not only do we explore the behaviour of the basic mathematical structures involved, but we also provide an efficient numerical algorithm for decomposing partially coherent fields. The algorithm is demonstrated by propagating various fields through a simple two-dimensional Gaussian beam telescope. These models reproduce all of the well known classical behaviour, and achieve exceptional levels of numerical performance. Although in this paper we restrict ourselves to three-dimensional, scalar, paraxial propagation, the extension to vectorial paraxial propagation is straightforward essentially because paraxial vector fields separate in Cartesian coordinate systems. We also believe that it is straightforward to extend the basic technique to wide-angle, three-dimensional vector fields. Extended techniques to couple the power between fields and calculate the entropy associated with a field are presented in another of our forthcoming papers[4]. For the purpose of demonstrating the basic technique, we only propagate fields between Fourier planes, but in later work we will use complex ray tracing to calculate the field across intermediate surfaces.

2 Handling basis sets that are non-orthogonal and have varying degrees of completeness, including over-complete

We have previously shown[2] that partially coherent optical fields decomposed in orthogonal *complete* basis sets (modes) can be handled within the coherence matrix formalism. Now we shall present the analogous formalism for non-orthogonal *over-complete* basis sets. We decomposed optical fields into orthogonal complete bases by using continuous integral equations, but when such a method is implemented numerically the functions must be sampled at discrete points, and the sampling determines the number of degrees of freedom that must, potentially, be represented. The use of discrete representations is closely related to the way in which optical fields are measured experimentally. In order to deal with the degrees of freedom explicitly, therefore, we shall now work with discretely sampled fields. More specifically, we represent a one-dimensional optical field by a column vector \mathbf{x} of length N . Throughout the paper, the notation $\mathbf{x}(i)$ is used to denote the i^{th} element of the vector, \mathbf{x} . Consider an arbitrary over-complete and non-orthogonal basis set $\{\mathbf{e}_k\}$ where $k \in \{1, 2, \dots, M\}$. In other words, we sample the field at N points, and we wish to use M basis functions to represent the field. Loosely speaking, over-determined implies $M > N$, uniquely-determined implies $M = N$, and under-determined $M < N$. That is to say, we certainly require enough degrees of freedom to describe all of the points in the original field. We wish to represent the field vector \mathbf{x} in the form

$$\mathbf{x} = \sum_k a_k \mathbf{e}_k, \quad (1)$$

which is analogous to the continuous representation. We define the 'frame' matrix, \mathbf{S} , as the sum of the matrices formed by taking the outer product of each basis function with its own conjugate transpose,

$$\mathbf{S} = \sum_k \mathbf{e}_k \mathbf{e}_k^\dagger, \quad (2)$$

where $(\cdot)^\dagger$ indicates the conjugate transpose. At this point the physical and theoretical meaning of \mathbf{S} and the associated operator are put aside, although it is beneficial to notice that for an orthonormal set $\mathbf{S} = \mathbf{I}$, indicating completeness, as would be true for an infinite set, $k \rightarrow \infty$, of discretely sampled Gaussian-Hermite modes. Equivalently, we can define a new $N \times M$ matrix \mathbf{E} by collecting together the column vectors that represent the basis functions:

$$\mathbf{E} = [e_1 \cdots e_k \cdots e_M]. \quad (3)$$

The frame matrix then simply becomes

$$\mathbf{S} = \mathbf{E}\mathbf{E}^\dagger. \quad (4)$$

We see that whereas the $N \times N$ matrix $\mathbf{S} = \mathbf{E}\mathbf{E}^\dagger$ is associated with completeness, the $M \times M$ matrix $\mathbf{R} = \mathbf{E}^\dagger\mathbf{E}$ is associated with orthogonality. Consider operating on \mathbf{x} with \mathbf{S} thus:

$$\mathbf{S}\mathbf{x} = \sum_k (e_k^\dagger \mathbf{x}) e_k, \quad (5)$$

where we use parentheses throughout the paper to emphasise when the enclosed quantity is an inner product, and therefore can be moved easily to a different position within an equation. Now assume that \mathbf{S} is invertible in that there is some matrix \mathbf{S}^{-1} such that,

$$\mathbf{S}^{-1}\mathbf{S} = \mathbf{I}. \quad (6)$$

The formal proof that \mathbf{S} is invertible for a complete or over-complete set is presented in our theoretical paper [4]. It follows applying \mathbf{S}^{-1} to (5) that

$$\mathbf{S}^{-1}\mathbf{S}\mathbf{x} = \mathbf{x} = \sum_k (e_k^\dagger \mathbf{x}) \mathbf{S}^{-1} e_k. \quad (7)$$

Now we identify a dual basis set $\{\tilde{e}_k\}$. Each element is not a conventional dual vector, in the sense that because of over-completeness, the orthogonality condition,

$$e_k^\dagger \tilde{e}_l = \delta_{kl}, \quad (8)$$

is not satisfied. Rather, the dual basis functions are such that,

$$\tilde{e}_k = \mathbf{S}^{-1} e_k. \quad (9)$$

The dual function obtained through the use of \mathbf{S}^{-1} is the canonical dual, the dual of lowest energy. Clearly in the case of a complete orthogonal set, $\mathbf{S} = \mathbf{I}$, and the dual vectors are the same as the basis vectors. According to (9), (7) becomes

$$\mathbf{x} = \sum_k (e_k^\dagger \mathbf{x}) \tilde{e}_k. \quad (10)$$

It is convenient to define a set of coefficients $b_k = e_k^\dagger \mathbf{x}$, in which case the field expansion becomes

$$\mathbf{x} = \sum_k b_k \tilde{e}_k. \quad (11)$$

We can now go through the same procedure again, but starting with the assumption that the inverse of \mathbf{S} exists such that,

$$\mathbf{S}\mathbf{S}^{-1} = \mathbf{I}. \quad (12)$$

Hence,

$$\mathbf{S}\mathbf{S}^{-1}\mathbf{x} = \mathbf{x} = \sum_k \mathbf{e}_k \mathbf{e}_k^\dagger \mathbf{S}^{-1}\mathbf{x}. \quad (13)$$

It can be shown that because \mathbf{S} is Hermitian, its inverse must be Hermitian:

$$(\mathbf{S}^{-1})^\dagger = \mathbf{S}^{-1}, \quad (14)$$

and by using (9) we find

$$\tilde{\mathbf{e}}_k^\dagger = \mathbf{e}_k^\dagger \mathbf{S}^{-1}. \quad (15)$$

Substituting (15) into (13),

$$\mathbf{x} = \sum_k (\tilde{\mathbf{e}}_k^\dagger \mathbf{x}) \mathbf{e}_k. \quad (16)$$

Finally, we define the coefficients a_k according to $a_k = \tilde{\mathbf{e}}_k^\dagger \mathbf{x}$ and obtain

$$\mathbf{x} = \sum_k a_k \mathbf{e}_k, \quad (17)$$

which on comparing with (1) is the form required. In summary, the set $\{\tilde{\mathbf{e}}_k\}$ forms an over-complete basis with the coefficients b_k , and the set $\{\mathbf{e}_k\}$ also forms an over-complete basis with coefficients a_k and we have shown that a field can be decomposed into either of these bases.

3 Handling partially coherent fields

Using the expansions described in the previous section, we can now represent partially coherent fields using over-complete basis sets. Throughout this paper we assume, in accordance with the theory of analytic signals, that the complex sampled field components $\mathbf{x}(i)$ have small fractional bandwidth, $\delta f/f \ll 1$, and the spatial correlations of interest are characterised by second-order ensemble averages. Defining the space domain coherence matrix (SCM), \mathbf{W} , as the ensemble average, $\langle \cdot \rangle$, of the outer product of the optical field vector \mathbf{x} with its own conjugate:

$$\mathbf{W} = \langle \mathbf{x}\mathbf{x}^\dagger \rangle. \quad (18)$$

Each element of \mathbf{W} is a measure of the complex spatial coherence between the field at two points. In this sense the SCM is the coherence matrix obtained when a set of delta functions, positioned at the sample points, is used as the basis set. The SCM contains sampled information that is the discrete analogy of the cross spectral density function. Using the results of the previous section, we can expand the SCM as follows. Substituting (11) and (17) into (18), we find

$$\begin{aligned} \mathbf{W} &= \langle \mathbf{x}\mathbf{x}^\dagger \rangle \\ &= \sum_k \sum_h \langle b_k a_h^* \rangle \tilde{\mathbf{e}}_k \mathbf{e}_h^\dagger \\ &= \sum_k \sum_h C_{kh} \tilde{\mathbf{e}}_k \mathbf{e}_h^\dagger, \end{aligned} \quad (19)$$

where the complex coefficients C_{kh} constitute the coherence matrix elements in this representation. Substituting the definitions of the basis-function coefficients we find

$$\begin{aligned} C_{kh} &= \langle b_k a_h^* \rangle \\ &= \mathbf{e}_k^\dagger \mathbf{W} \tilde{\mathbf{e}}_h. \end{aligned} \quad (20)$$

The elements of the coherence matrix can therefore be calculated easily once the SCM, and the dual basis vectors are known. Here we have expressed the coherence matrix in terms of the correlations between the coefficients of the Gabor functions and the coefficients of the associated dual basis. Later we will discuss the alternative representation using correlations between the Gabor functions and themselves. First we will examine why the representation in (20) has a number of attractions. It can be seen from (20) that the overall structure reduces to simple and well-known forms in all of the various limits that can be imagined. For example, suppose that the source comprises a fully-incoherent surface with uniform intensity. In this case $\mathbf{W} = \mathbf{I}$, and according to (20) the coherence matrix elements become

$$C_{kh} = e_k^\dagger \tilde{e}_h. \quad (21)$$

For an *over-complete* set, the basis functions and the associated dual functions are not orthogonal; however for a *complete* non-orthogonal set, the basis functions and the dual functions are mutually orthogonal, and in this case,

$$C_{kh} = \delta_{kh}, \quad (22)$$

and the conventional dual condition (8) holds. (22) is important as it shows that, for a non-orthogonal and complete set, a completely spatially incoherent source excites all basis functions incoherently and equally, as is the case for orthonormal sets. In the case of an over-complete basis set, a fully-incoherent source leads to correlations between the basis vectors, due to their linear dependence, as would be expected on physical grounds.

The expansion described by (19) has many convenient qualities, but it is inconvenient from an optical point of view, as we would like to propagate partially coherent fields by propagating the basis functions only. If we use (19) it would be necessary to propagate the dual functions as well as the basis functions. Suppose, therefore, that we use the form

$$\begin{aligned} \mathbf{W} &= \langle \mathbf{x} \mathbf{x}^\dagger \rangle \\ &= \sum_k \sum_h \langle a_k a_h^* \rangle e_k e_h^\dagger \\ &= \sum_k \sum_h C_{kh} e_k e_h^\dagger, \end{aligned} \quad (23)$$

where the matrix coefficients are given by

$$C_{kh} = \tilde{e}_k^\dagger \mathbf{W} \tilde{e}_h. \quad (24)$$

This decomposition has the advantage that it is only necessary to propagate basis functions, but has the disadvantage that even for non-orthogonal complete sets, the coherence matrices do not take on simple forms for fully incoherent fields. It does, however, lead to an insight into the meaning of the frame matrix \mathbf{S} . Suppose that we excite all of the basis functions incoherently and equally, which we cannot do in practice for an over-complete set because of linear dependence. In this case, the coherence matrix becomes $\mathbf{C} = \mathbf{I}$, which can be substituted into (23) to yield the implied spatial correlations, this substitution gives,

$$\begin{aligned} \mathbf{W} &= \sum_k \sum_h \delta_{kh} e_k e_h^\dagger \\ &= \sum_k e_k e_k^\dagger, \end{aligned} \quad (25)$$

which is the frame matrix \mathbf{S} . This result is not surprising when one remembers that $e_k e_k^\dagger$ gives the spatial correlations for each basis vector, and if two mutually incoherent fields are added, regardless of the state of coherence of each, the overall coherence matrix is simply the sum of the two individual coherence matrices. Hence, the frame matrix is simply the coherence matrix of a sum of individually fully coherent, but mutually incoherent basis fields. In short, the frame matrix contains information about the spatial correlations, due to linear dependence, associated with all of the basis vectors.

The explicit use of the SCM to calculate the coherence matrix elements provides a method for represent-

ing coherent, fully incoherent and partially coherent fields using over-complete bases. A major advantage of the scheme is that SCM can be calculated for a variety of different fields, and complicated forms assembled. For a fully coherent field described by vector \mathbf{x} , the coherence matrix is trivially $\mathbf{W} = \mathbf{x}\mathbf{x}^\dagger$. For a fully incoherent uniform field $\mathbf{W} = \mathbf{I}$, whereas for a fully incoherent field, with some spatially varying intensity distribution, the SCM is simply diagonal, with the diagonal elements scaled according to the intensity.

By noticing that we can add mutually incoherent fields by adding coherence matrices, we can set up the fields associated with numerous practical situations. For example, we can model a noisy aperture by adding to the scattered field, the field associated with the blackbody radiation of the aperture.

4 Properties of the frame matrix

The invertibility of \mathbf{S} to form the \mathbf{S}^{-1} matrix is vital to the existence and formation of the dual frame. It can be demonstrated using elegant linear algebra that \mathbf{S} is invertible for critically or over sampled frames [4]. The invertibility of \mathbf{S} appears in a different form in Daubechies'[5] definition of an associated frame operator for continuous frames and use of Bessel's inequality. Here we give explicit consideration to the singular value decomposition (SVD) of the frame matrix leading us to the same conclusion. We shall now consider two hermitian matrices formed from matrix \mathbf{E} (3),

$$\mathbf{S} = \mathbf{E}\mathbf{E}^\dagger, \quad (26)$$

and

$$\mathbf{R} = \mathbf{E}^\dagger\mathbf{E}, \quad (27)$$

Several important properties of the basis can be investigated by considering the SVD of these matrices and the matrix, \mathbf{E} . \mathbf{E} can be expressed in the form of a singular value decomposition as described in numerical recipes[6] such that

$$\mathbf{E} = \mathbf{U}\mathbf{\Sigma}\mathbf{V}^\dagger, \quad (28)$$

where both matrices \mathbf{U} and \mathbf{V} are unitary, \mathbf{U} having dimensions $N \times N$ and \mathbf{V} having dimensions $M \times M$ and $\mathbf{\Sigma}$ is a matrix $N \times M$. The columns of \mathbf{U} contains the left singular values of \mathbf{E} , the vectors that span the range of \mathbf{E} . \mathbf{V} contains the right singular vectors of \mathbf{E} . $\mathbf{\Sigma}$ is diagonal with the i^{th} diagonal element, σ_i . The elements of $\mathbf{\Sigma}$ are ordered in descending size and the first $\min(M, N)$ diagonal elements are non-zero with the i^{th} element corresponding to the i^{th} column of \mathbf{U} , \mathbf{u}_i , is the corresponding vector that spans the range of \mathbf{E} . The condition of the vector space spanned by \mathbf{E} is defined as the ratio of the smallest and largest values, we have considered an ill conditioned situation to arise when this ratio $< 10^{-5}$. The values of $\mathbf{\Sigma}$ where σ_i is zero (or as good as numerically) correspond to the i^{th} column of \mathbf{V} , \mathbf{v}_i , the column of \mathbf{V} that gives a vector that span the null space of \mathbf{E} .

Using the unitary properties of \mathbf{U} and \mathbf{V} it follows that,

$$\begin{aligned} \mathbf{S} &= \mathbf{E}\mathbf{E}^\dagger \\ &= \mathbf{U}\mathbf{\Sigma}\mathbf{V}^\dagger\mathbf{V}\mathbf{\Sigma}^\dagger\mathbf{U}^\dagger \\ &= \mathbf{U}\mathbf{\Sigma}\mathbf{\Sigma}^\dagger\mathbf{U}^\dagger, \end{aligned} \quad (29)$$

and

$$\begin{aligned} \mathbf{R} &= \mathbf{E}^\dagger\mathbf{E} \\ &= \mathbf{V}\mathbf{\Sigma}\mathbf{U}^\dagger\mathbf{U}\mathbf{\Sigma}^\dagger\mathbf{V}^\dagger \\ &= \mathbf{V}\mathbf{\Sigma}\mathbf{\Sigma}^\dagger\mathbf{V}^\dagger. \end{aligned} \quad (30)$$

Given $\mathbf{\Sigma}$ is diagonal the first $\min(M, N)$ diagonal elements of both $\mathbf{\Sigma}\mathbf{\Sigma}^\dagger$ and $\mathbf{\Sigma}^\dagger\mathbf{\Sigma}$ are identical with an i^{th} diagonal element of σ_i^2 . So the smaller matrix of $\mathbf{\Sigma}\mathbf{\Sigma}^\dagger$ and $\mathbf{\Sigma}^\dagger\mathbf{\Sigma}$ has eigenvalues satisfying σ_i^2 and the larger matrix has the same first $\min(M, N)$ eigenvalues with the rest numerically equivalent to zero.

From equation(29)

$$\begin{aligned} \mathbf{U}^{-1}\mathbf{S}\mathbf{U} &= \mathbf{U}^{-1}\mathbf{E}\mathbf{E}^\dagger\mathbf{U} \\ &= \mathbf{U}^{-1}\mathbf{U}\mathbf{\Sigma}\mathbf{\Sigma}^\dagger\mathbf{U}^\dagger\mathbf{U} \\ &= \mathbf{\Sigma}\mathbf{\Sigma}^\dagger, \end{aligned} \quad (31)$$

and likewise,

$$\begin{aligned} \mathbf{V}^{-1}\mathbf{R}\mathbf{V} &= \mathbf{V}^{-1}\mathbf{E}^\dagger\mathbf{E}\mathbf{V} \\ &= \mathbf{V}^{-1}\mathbf{V}\mathbf{\Sigma}\mathbf{U}^\dagger\mathbf{U}\mathbf{\Sigma}^\dagger\mathbf{V}^\dagger\mathbf{V} \\ &= \mathbf{\Sigma}\mathbf{\Sigma}^\dagger. \end{aligned} \quad (32)$$

Since both \mathbf{S} and \mathbf{R} are hermitian the columns of \mathbf{V} are the normalised eigenvectors of \mathbf{R} , \mathbf{v}_i , $i = 1...M$; and the columns of \mathbf{U} are the normalised eigenvectors of \mathbf{S} , \mathbf{u}_i , $i = 1...N$. The matrix \mathbf{S} measures the completeness of the basis set, whereby if the number of non-zero eigenvalues of \mathbf{S} equals N then the basis is complete or over-complete and can represent all the degrees of freedom in the signal. The matrix \mathbf{R} measures the orthogonality of the basis set.

5 Gabor Basis Sets

An over-complete non-orthogonal basis can be formed by a subset of frames known as the Gabor frames. Indeed much of the development of the formulation to handle frames was done with consideration to this particular set of bases. In Gabor bases the basis set modes are generated from a single mother function or *atom*(\mathbf{g}), translated and modulated. Now we shall describe the modulation operator and translation operator which together generate the frame from the mother atom. We are again considering the 1-D field sampled by a vector of length N , our mother atom and consequently basis modes are therefore also described by vectors of length N . To form a frame, a translation spacing(a) and a modulation spacing(b) are chosen. To avoid boundary artifacts arising from assumed periodicity in the field signal and basis both a and b are chosen to be integer factors of N . Two other integers representing the number of modes arising from the operators on field vector are defined, $\tilde{a} = \frac{N}{a}$ and $\tilde{b} = \frac{N}{b}$. The expression $(p \bmod q)$ represents the modulo operation associated with integer division, giving the integer remainder when p is divided by q . The translation operator T is,

$$\mathbf{T}_{va}\mathbf{g}(j) = \mathbf{g}((j - va) \bmod N) \quad v \in Z, \quad (33)$$

and the modulation function M operates such that

$$\mathbf{M}_{vb}\mathbf{g}(j) = e^{-\frac{2\pi i \cdot j \cdot ((v+v_0) \bmod N)b}{N}} \mathbf{g}(j) \quad v \in Z, \quad (34)$$

where v_0 is an phase offset introduced to ensure that the phase differences between modes are zero on the input plane for at a defined optical axis, this method for assigning an optical axis can only be used when the optical axis is chosen to lie on a sampling point and not between them. To define an optical axis at a half-integer point we use $(v_0 = 0)$ and multiply every element in \mathbf{g} by a complex phase factor, this is slightly more costly computationally so to maximise the size of the largest system that can be realistically examined it is advisable to chose the sampling such that the optical axis lies at a sampling point, giving an integer value of v_0 . Using the Gabor basis functions the frame matrix elements can again be calculated as the outer product of the basis functions as in equation(4) giving,

$$\mathbf{S}_{jk} = \sum_{n=0}^{\tilde{a}-1} \sum_{m=0}^{\tilde{b}-1} \mathbf{M}_{mb}\mathbf{T}_{na}\mathbf{g}(j)(\mathbf{M}_{mb}\mathbf{T}_{na}\mathbf{g}(k))^\dagger \quad (35)$$

As yet no information about the functional form \mathbf{g} is assumed other than it must have suitable support for a complete basis to be formed. Given our definitions above of \mathbf{T}_{na} and \mathbf{M}_{mb} , for Gabor frames, \mathbf{S} will clearly have a sparse banded form, this structure can be exploited as many optimised matrix manipulation

algorithms exist for such matrices. Additionally and importantly the Gabor frame operator, associated with the frame matrix, commutes with both the modulation and the translation operator such that when \mathbf{S}^{-1} exists (i.e. for complete and over-complete frames) we see,

$$\begin{aligned}\tilde{\mathbf{g}}_{mn} &= \mathbf{S}^{-1}\mathbf{g}_{mn} \\ &= \mathbf{S}^{-1}\mathbf{T}_{na}\mathbf{M}_{mb}\mathbf{g} \\ &= \mathbf{T}_{na}\mathbf{M}_{mb}\mathbf{S}^{-1}\mathbf{g} \\ &= \mathbf{T}_{na}\mathbf{M}_{mb}\tilde{\mathbf{g}}.\end{aligned}\tag{36}$$

Consequently only the mother dual associated with the mother function need be calculated and the entire basis set can be generated using the same operators. Gabor originally presented a Gaussian mother function atom as suitable with the form,

$$\mathbf{g}(x) = A_0 \exp(-\pi \frac{x^2}{2a^2}),\tag{37}$$

where A_0 is a scaling factor and a is again the translation spacing of the basis as described above. Gabor modes have been used for coherent signal coefficient decomposition and image analysis and such applications and implementations of frames are discussed in papers such as Feichtinger's papers[7, 8].

6 Implementation

The inversion of the frame matrix was not performed directly but a conjugate gradient method (CGM), as described in Numerical Recipes [6], was used to minimise the residue,

$$\epsilon = \|\mathbf{S}\tilde{\mathbf{g}} - \mathbf{g}\|,\tag{38}$$

and hence determine the mother dual for a 1-D system. The choice of the norm operator $\|\cdot\|$ in (38) determines the form of the dual and whether null space vectors of \mathbf{S} are added to the canonical dual. This method avoids any direct intermediate calculation of the inverse of \mathbf{S} and was found to converge very rapidly. The success of this process of minimisation is directly related to the results of the SVD of \mathbf{E} and the invertibility of \mathbf{S} . Additionally this method was able to find an approximate solution when \mathbf{S} is not invertible, i.e. for under-complete frames, when an approximate form for the dual is found through the use of the analogous form of (36). Having obtained the mother dual and consequently the dual basis set, successful decompositions and reconstructions of fields were performed using the coherence matrix form given in (23). This is the form of the coherence matrix which contains the coherence elements associated with the Gabor basis functions themselves and was used because, as described next, these basis functions were then propagated.

6.1 Propagating the Gabor basis functions

The Gabor basis functions are Gaussian in intensity and of particular interest as many techniques for propagating Gaussian beams exist in this field. Propagation is especially simple for paraxial quasi-optical systems. Complex ray tracing of Gaussian beams is also extremely useful. An important subset of frames is that of critically sampled frame where $N = M$ (and hence $N = ab$) and additionally the Gabor mother function takes the form of (37). An oversampled frame has $N < M$ (and hence $N > ab$). The mathematical continuous form of a critically sampled frame was shown to be complete in Gabor's original paper of 1946 proposing such a basis set [9], however the duals were not deduced until 1980 by Baastians [10]. Propagation between Fourier planes is trivial for these frames if condition (37) is satisfied because the frame at the input plane propagates to another Gabor frame at the Fourier plane formed at the focal plane of a lens. The propagation was perform by coherence matrix element swapping, as each modulation function in the original basis set propagates to a translation function in the Fourier frame and vice-versa. This method of Fourier transform elegantly leads to the same information sampling across both the input and transform plane and is extremely fast. Fourier analysis can of course only be applied to paraxial quasi-optical systems, however such systems are of considerable interest and worth considering. We analysed

several 1-dimensional systems using such frames including systems where the Fourier plane was limited. Additionally we then analysed some 2-dimensional systems through the use of 1-dimensional operations described, the justification and method to do this is now given.

6.2 Two Dimensional Fields

An important subset of two dimensional fields $\mathbf{F}(x, y)$ is where the field is separable in that the two components, $\mathbf{X}(x)$ and $\mathbf{Y}(y)$ are independent. Such a two dimensional field is simply the product of one dimensional fields, $\mathbf{F}(x, y) = \mathbf{X}(x)\mathbf{Y}(y)$, and can naturally be analysed using the product of two one dimensional basis function sets. Any components and the propagation process itself must not affect the separability of the field. Non-separable basis functions can be analysed within the mathematical framework; however, the numerical cost involved in any practical implementation calculating the coherence matrices in such a basis set is high and for a realistic number of sampling points often prohibitively so. Considering a two dimensional system as the product of two one dimensional systems creates a problem of the order $2 \times N^2$ whereas to consider the initial field as non-separable is a problem of the order N^4 , when double inner products are necessary within the analysis the high cost of this is very apparent. Components such as circular apertures and Zernike phase screens are non-separable in such an analysis. Fortunately we can analyse such components within the separable framework through explicit consideration of the discrete sampling used. For any field sampled in Cartesian coordinates (pixellated) a non-separable field can be expressed as a sum of separable sampled fields. This trivially follows from the pixel basis being the outer product of the x and y co-ordinate systems. Likewise, discrete sampling of components such as circular apertures allows them to be analysed in the same way. As a pixellated system tends from separable into two 1-D functions to only separable on a pixel scale the cost of the computation tends to the higher N^4 limit. Each of the separable fields within the total field can be analysed separately and the coherence matrix elements of constituent fields summed at the appropriate output plane. To determine the separable form of any continuous field we can consider another SVD performed on the matrix \mathbf{F} where the elements of \mathbf{F} are $F_{ij} = \mathbf{F}(x_i, y_j)$. If the SVD is performed, using the same notation as before for the SVD, such that $\mathbf{F} = \mathbf{U}\mathbf{\Sigma}\mathbf{V}^\dagger$, then the pixellated form of the function sampled by an $H \times H$ matrix is given by,

$$\mathbf{F}(x, y) = \sum_{n=1}^H \sigma_n \mathbf{u}_n(x) \mathbf{v}_n(y)^\dagger. \quad (39)$$

For many fields the field or a good approximation to it can be given by,

$$\mathbf{F}(x, y) = \sum_{n=1}^J \sigma_n \mathbf{u}_n(x) \mathbf{v}_n(y)^\dagger, \quad (40)$$

where $J < H$, reducing the complexity and increasing the computational limits of the problem. Some simple 2-dimensional fields formed as the outer product of two 1-dimensional fields were investigated.

7 Results

7.1 The form of the dual

The form of some of the dual mother atoms for a fixed value of N but with varying values of a and b , forming critically or over-complete frames, are shown in Fig.1. The form of the duals can be seen to differ dramatically. Many of the duals can be seen to contain discontinuities especially in critically sampled frames and careful consideration of these is necessary within numerical simulations. Additionally it can be seen that increasingly over-sampled systems have smoother dual functions.

7.2 Investigating the completeness of the basis set

The eigenvalues of $\mathbf{\Sigma}\mathbf{\Sigma}^\dagger$ and $\mathbf{\Sigma}^\dagger\mathbf{\Sigma}$ were found using SVD and the highest and lowest eigenvalues of both \mathbf{S} and \mathbf{R} plotted for a variety of frames with a fixed number of samples in a field. The results for two frames

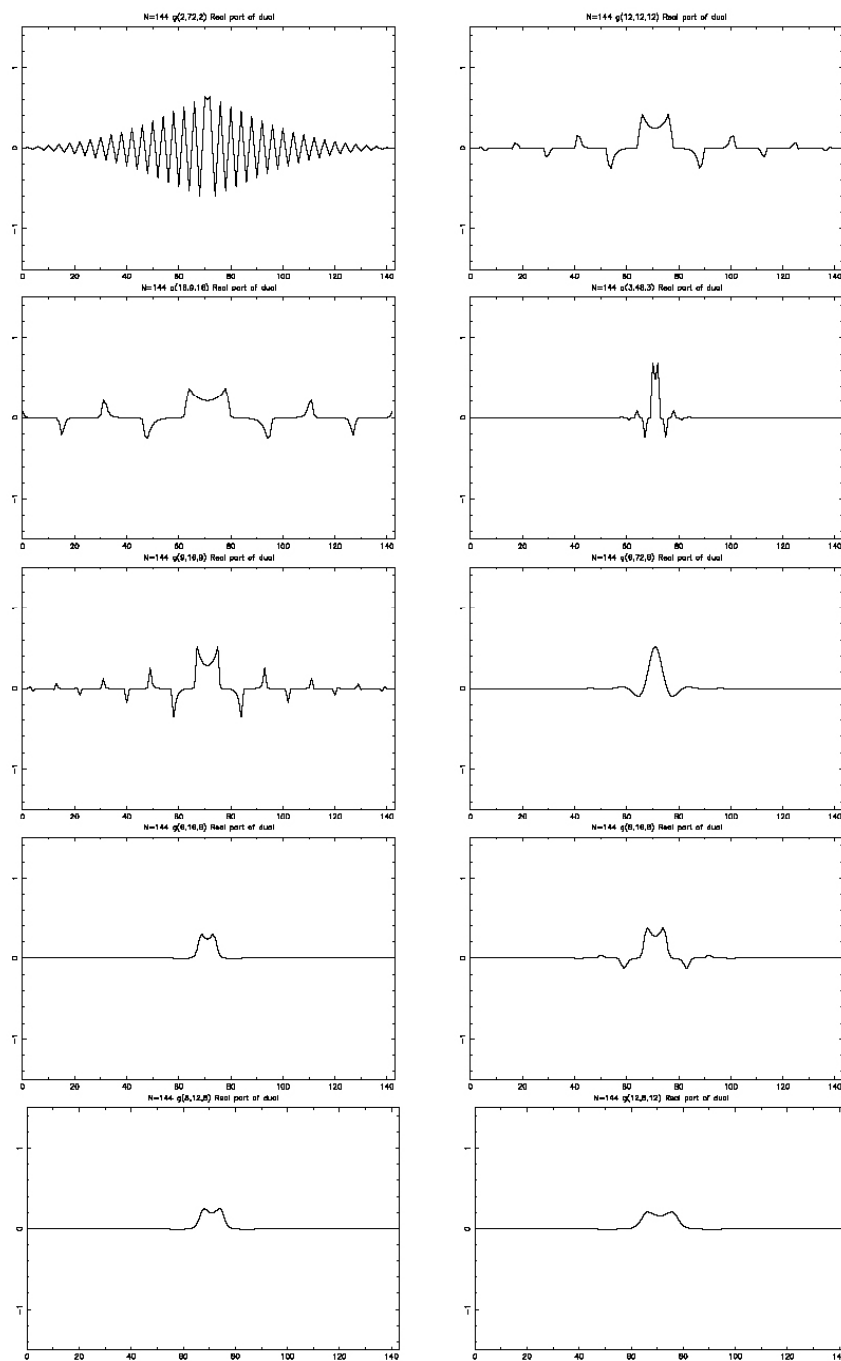


Figure 1: From top to bottom and left to right the frames are defined with a mother atom of the form given in 37 and the values of (N, a, b) are given to define the frames as $(144,2,72)$, $(144,12,12)$, $(144,9,16)$, $(144,6,72)$, $(144,16,9)$, $(144,3,48)$, $(144,6,16)$, $(144, 8, 16)$, $(144,8,12)$, $(144,12,8)$

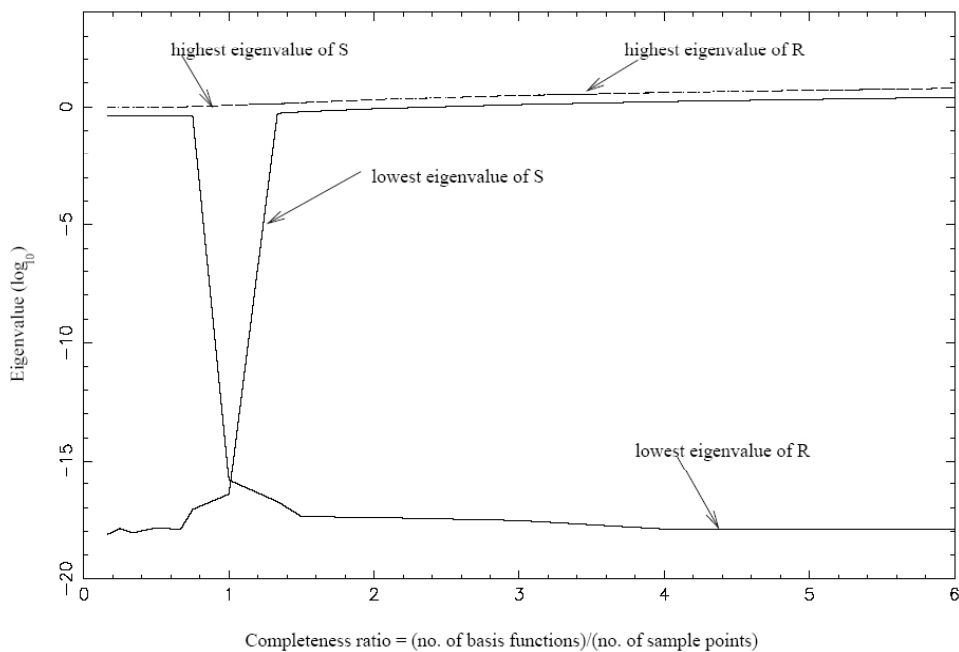


Figure 2: The highest and lowest eigenvalues of both \mathbf{S} and \mathbf{R} . $N = 144$, $a = 12$, $b \in \{2, 3, 4, 6, 8, 9, 12, 16, 18, 36, 72\}$ waists satisfying (37). The critically sampled frame is not complete.

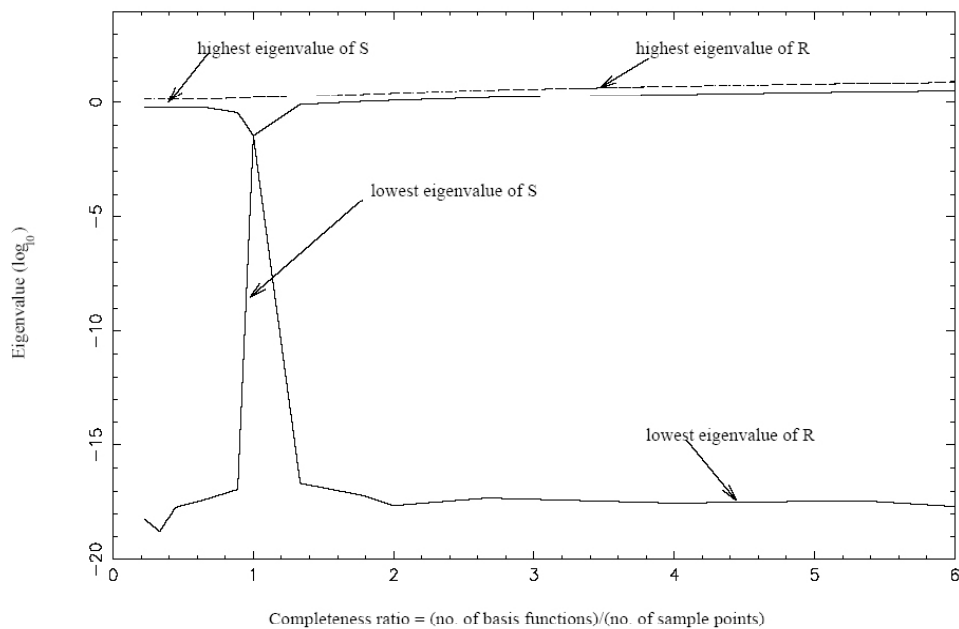


Figure 3: The highest and lowest eigenvalues of both \mathbf{S} and \mathbf{R} . $N = 144$, $a = 9$, $b \in \{2, 3, 4, 6, 8, 9, 12, 16, 18, 36, 72\}$ waists satisfying (37). The critically sampled frame is complete.

with $N = 144$ are considered here. The first frame with $a = 12$ and $b \in \{2, 3, 4, 6, 8, 9, 12, 16, 18, 36, 72\}$ is shown in Fig.2, a second frame with $a = 9$ and $b \in \{2, 3, 4, 6, 8, 9, 12, 16, 18, 36, 72\}$ is shown in Fig.3. The waist for every frame was taken to satisfy (37). In these investigations we fixed the number of translational modes and changed the completeness of the frame by varying the number of modulations used.

7.3 Quantifying the degree of completeness of a frame

The information that can be supported was investigated for under determined, critically sampled and over determined frames. The number of samples of the basis functions was fixed. The ratio of the number of non-singular eigenvalues from the SVD to samples of the basis function was plotted against the translation spacing a for various values of modulation spacing b . By the assumed periodicity of our method we are restricted to certain values of a and b , however other frames with different numbers of samples can provide other values. Data for the parameters $N = 144$, $a \in \{2, 3, 4, 6, 8, 9, 12, 16, 18, 36, 72\}$ and $b \in \{6, 8, 9, 12, 16, 18, 36, 72\}$ was calculated, the waist for every frame was taken to again satisfy (37). The results are shown in Fig.(4).

7.4 Analysing the results investigating the completeness of the frame

An interesting feature arises in our results; when investigating critically sampled Gabor frames we expect \mathbf{S} to be invertible and to support N degrees of freedom. However the results of Fig.2 show that the SVD results in a zero lowest eigenvalue, on closer investigation it was found that only this eigenvalue was zero and thus a single degree of freedom is not represented. However the frame investigated in Fig.3 was found to be complete and support all degrees of freedom in the signal. The continuous form of the traditional Gabor mother atom has been shown to form a frame that spans the space and the discontinuities seen in the duals of critically sampled frames in Fig.1 can be described mathematically in a continuous analysis[10]. However this missing degree of freedom anomaly arises from a discretely sampled implementation of such discontinuous duals. Critically sampled frames can be said to be *unstable* due to this behaviour. Clearly as critical sampling is approached there is a change in behaviour of the frames in Fig.2 and Fig.3, where by the lowest eigenvalue dips relative to the trend. It is simply the size of this effect that determines whether \mathbf{S} is invertible and the frame spans the space. For our paraxial propagation investigations we investigated critically sampled frames, ensuring that the frames were complete or that there was no power in any missing degree of freedom. Ideally in the future we wish to quantify the conditions under which critically sampled frames are also complete frames. However it should be emphasised that this is a minor consideration as we have found and used complete, critically sampled frames with great success.

7.5 A 1-D illustration of the Van-Cittert Zernike Theorem

Fig.5 shows the simulations of two systems. The top left plot shows the reconstruction of two fully self and mutually coherent Gaussians, the intensity is shown by the solid line and lies concurrently with a dashed line showing the coherence function. The reconstruction of the field of length $N = 81$ was performed in a Gabor basis set with $a = 9$ and $b = 9$, i.e. using a basis set consisting of Gaussians of a different size to those in the field. The field was then propagated to the Fourier plane and the results of the reconstruction are shown in the top right plot. The bottom left plot shows the reconstruction of two fully self and mutually incoherent Gaussians, and two dashed lines are plotted plotting the coherence function relative to the centre of each Gaussian. The intensities of the Gaussians were identical to the coherent case as was the basis set used for the decomposition. This field was propagated to the Fourier plane and the results are shown in the bottom right plot. It should be emphasised that the input fields shown are not simply the input field but the basis function coherence matrix decomposition and reconstruction of this field.

There are several outstandingly successful features to notice in these results. The decompositions successfully retain all the degrees of freedom in the field, including the representation of the delta functions associated with the coherence function of the incoherent Gaussians. The coherent Fourier plane results show the fringes as expected from regular Fourier theory. Although the fringes in Fig.5 are extremely sharp, they are *not* under sampled but simply only contain the original information from the field, without artificial smoothing from oversampling. By only representing the degrees of freedom in the original field

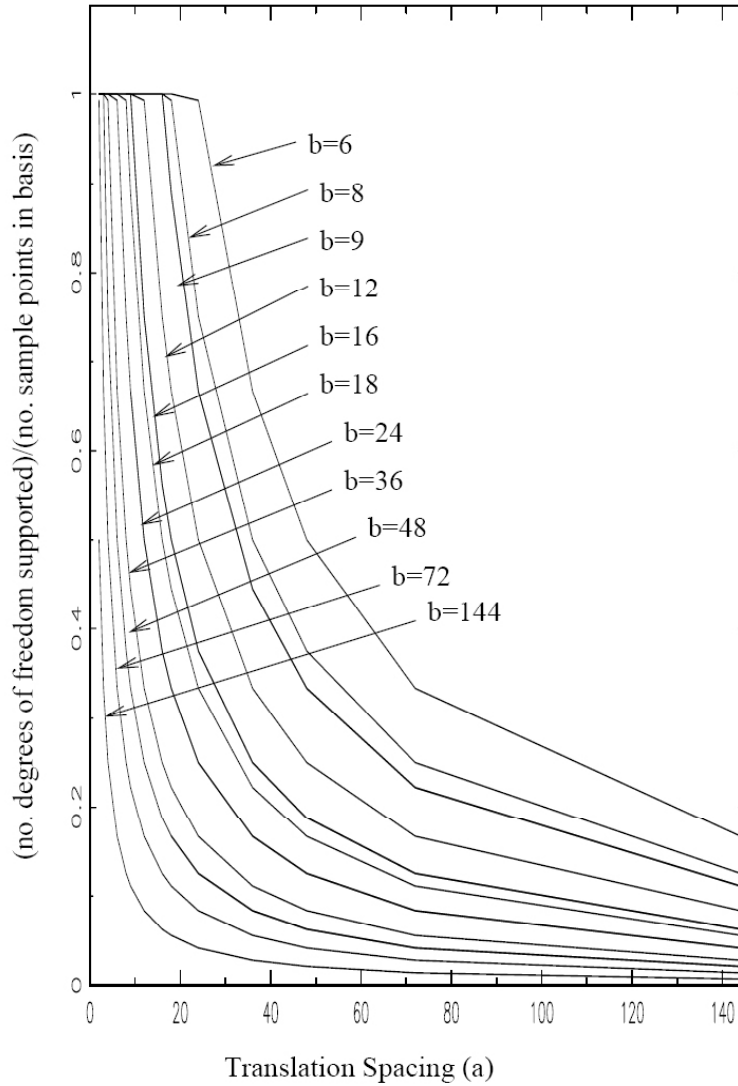


Figure 4: The degrees of freedom a frame with the parameters $N = 144$, $a \in \{2, 3, 4, 6, 8, 9, 12, 16, 18, 36, 72\}$ and $b \in \{6, 8, 9, 12, 16, 18, 36, 72\}$ is shown, the waist for every frame was taken to again satisfy (37). An important feature of this plot is the region where the plots tend to a value of 1 on the vertical axis; it can be seen some critically sampled frames are complete whereas others have a single missing degree of freedom.

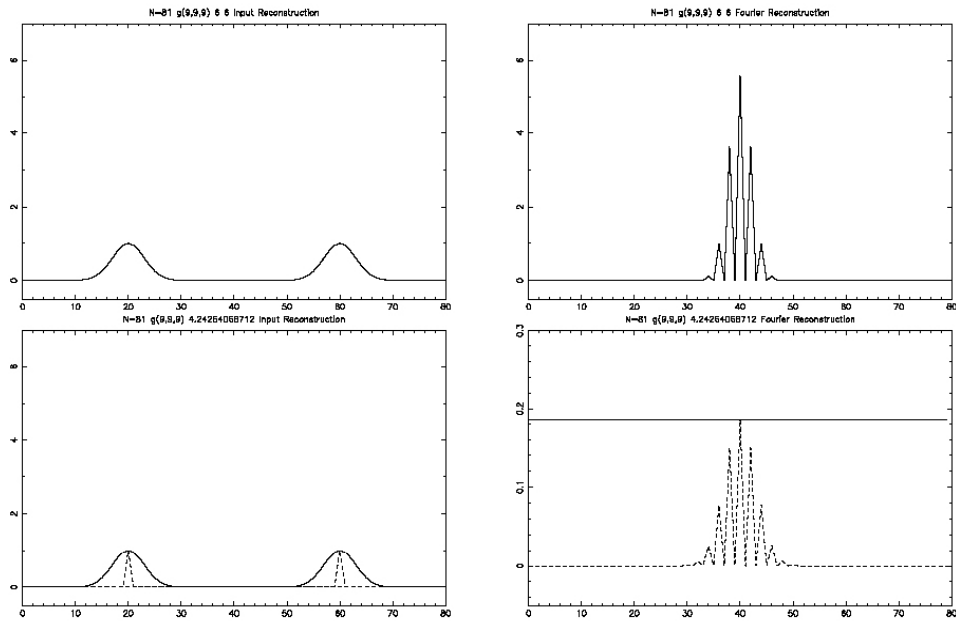


Figure 5: Top Left: Two coherent Gaussian sources, reconstructed in a basis set of Gabor functions consisting of Gaussians of a *different* width to the sources, at input plane. Top Right: The coherent Gaussian sources at the image (Fourier) plane. Bottom Left: Two mutually and self incoherent Gaussian sources, reconstructed in a basis set of Gabor functions consisting of Gaussians of a *different* width to the sources, at the input plane. Bottom Right: The incoherent Gaussian sources at the image (Fourier) plane. The solid line in all plots shows the intensity of the function and the dotted line the coherence function. At the input plane for the coherent Gaussians the coherence function and the intensity line are concurrent. At the input plane, for the incoherent sources, two coherence functions are plotted relative to the centre of each of the Gaussians.

we are not supporting redundant information and are dramatically increasing the power and efficiency of the simulations. There are equally interesting results from the incoherent system's Fourier plane, as expected from a fully incoherent field the Fourier intensity is uniform and contains no spatial features. Additionally the form of the fringes in the Fourier coherence function can be seen to be the same as those in the coherent Fourier intensity; illustrating the well known results from the Van-Cittert Zernike theorem whereby the forms of the coherence and the intensity are swapped at the Fourier plane.

7.6 Diffraction Limited 1-D System

A simple finite throughput quasi-optical system was simulated. A fully coherent top hat function was decomposed and propagated to the Fourier plane, where an aperture was placed to limit the throughput. The limited field was then propagated to the image plane and reconstructed. The results for varying size of apertures are shown in Fig.6. It should be noted that all the fields shown have resulted from reconstructions, where the coefficients associated with the basis Gabor functions have been calculated and the basis functions propagated. The top left hand plot is the reconstruction where an infinite aperture has been used at the Fourier plane and hence the original field has been reconstructed at the subsequent image plane.

Again all degrees of freedom in the original field have been preserved in the decomposition and remarkably the stepped edges of the top hat function have been perfectly reproduced. Even using a large number of Gaussian-Hermite modes the edges are not reproduced and Gibbs oscillations are seen.

7.7 2-D separable systems, including simple bolometer and horn array models

We modelled a simple bolometer system and transformed the field to the Fourier plane. The intensity and coherence function of the original field represented in a frame basis and the corresponding results in the Fourier plane are shown in Fig.7. A simple horn array was then modelled with the same intensity function as the bolometer array modelled in Fig.7. The horn array results are shown in Fig.8.

8 Conclusions

We conclude that the mathematical framework, presented in this paper, provides a method for:

- Explicitly handling sampling within modal decompositions ensuring no redundancy in the field information is propagated. By optimising the sampling to the field we avoid unnecessary calculations that are computationally expensive while still maintaining the accuracy of our simulations.
- Simulating fully coherent, fully incoherent and partially coherent field
- Elegantly handling new basis sets, previously avoided because of the difficulties handling non-orthogonal over-complete basis sets.
- Quantifying the range of basis sets and quantifying improvements to basis sets by measuring ratio of the degrees of freedom in the field to those supported by the basis.

The simulations presented demonstrate the success of this framework by:

- Producing field reconstructions which retain all the degrees of freedom present in the initial field.
- Reconstructing delta functions and sharp edges in fields, field features that a finite set of Gaussian-Hermite basis modes can not support.

Additionally our work in this area has derived relations for the power coupled between two partially coherent fields and the entropy of a partially coherent field within the framework of over-complete basis sets. To be published [4].

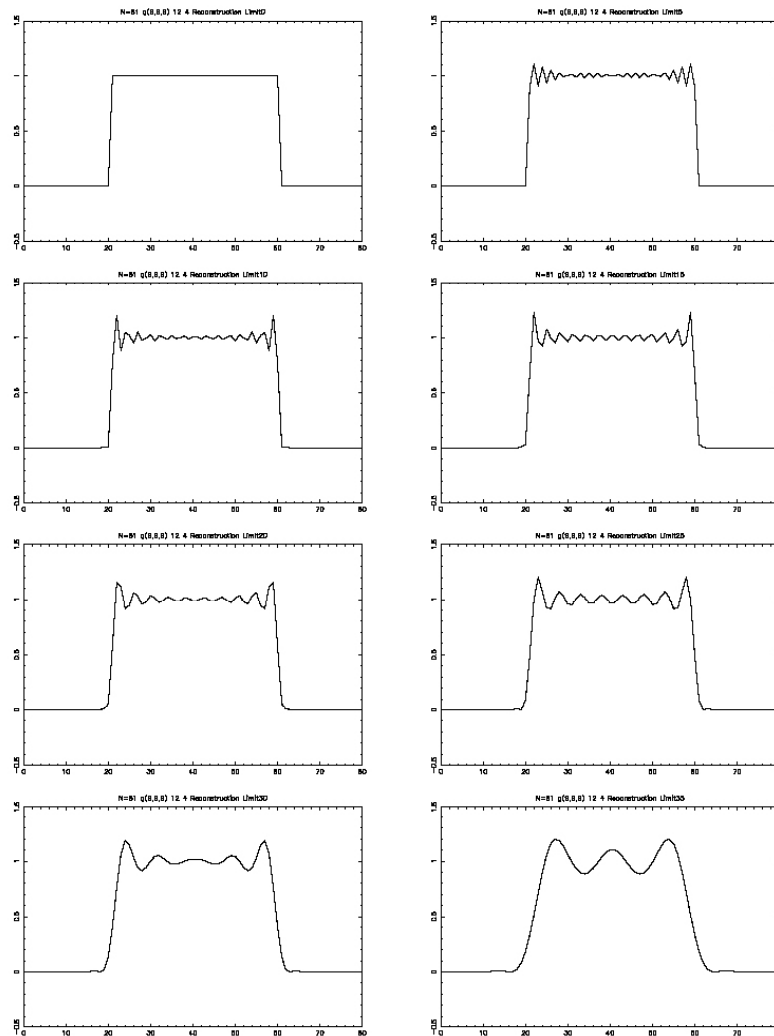


Figure 6: A top hat of was propagated to the Fourier plane where decreasingly small apertures were simulated. Propagation of the limited field was then performed to the next Fourier plane. Each plot is titled with an index Limit# where # gives the number of samples set to zero, to simulate the aperture, from each side of the signal. Qualitatively the throughput of the system decreases from top to bottom and left to right.

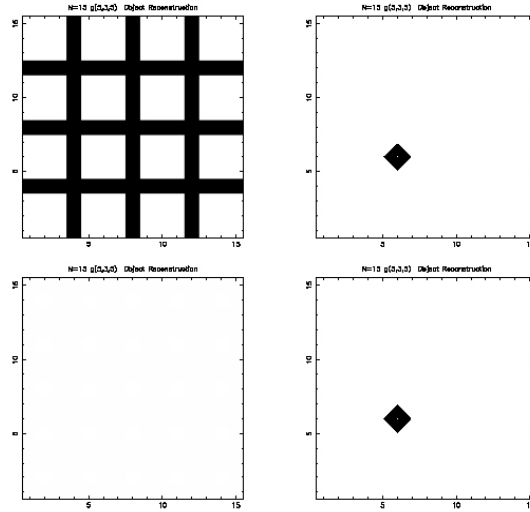


Figure 7: The top left image shows the basis function reconstruction of the intensity at the input plane and the top right image shows a contour map of the coherence function of the array at the same plane centred on a single pixel. Each bolometer element is made up of 9 mutually incoherent pixels and each element is also mutually incoherent. The bottom left plot shows the intensity at the Fourier plane and the bottom right the coherence function at the same plane centred on a single pixel.

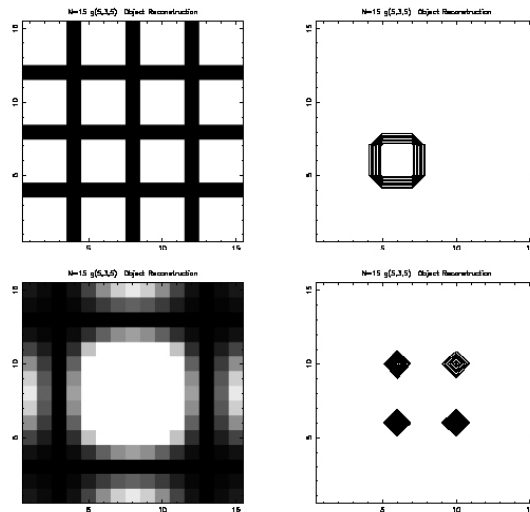


Figure 8: The top left image shows the basis function reconstruction of the intensity at the input plane and the top right image shows a contour map of the coherence function of the array at the same plane centred on a single pixel. Each horn element is made up of 9 mutually coherent pixels (i.e. each element self coherent) but each element is mutually incoherent. The bottom left plot shows the intensity at the Fourier plane and the bottom right the coherence function at the same plane centred on a single pixel.

References

- [1] S. Withington and G. Yassin. Power coupled between partially coherent vector fields in different states of coherence. *Optical Society of America Journal*, 18:3061–3071, December 2001.
- [2] S. Withington and J.A. Murphy. Modal Analysis of Partially-Coherent Submillimetre-Wave Quasioptical Systems. In *Eighth International Symposium on Space Terahertz Technology*, pages 446–+, 1997.
- [3] S. Withington, J. A. Murphy, and G. Yassin. Gaussian-beam-mode analysis of multibeam quasioptical systems. *IEEE Trans. Antennas and Propagation*, AP:49, 2000.
- [4] S. Withington, M.P. Hobson, and R.H. Berry. *To be published*, May 2003.
- [5] I. Daubechies. The wavelet transform, time-frequency localization and signal analysis. *IEEE Transactions on Information Theory*, 36:961–1005, September 1990.
- [6] H.P. William, A.T. Saul, T.V. William, and P.F. Brian. *Numerical Recipes in C*. Cambridge University Press, 2 edition, 1992.
- [7] S. Qiu and H.G. Feichtinger. Structure of the Gabor matrix and efficient numerical algorithms for discrete Gabor expansions. In *Proc. SPIE Vol. 2308, p. 1146-1157, Visual Communications and Image Processing '94, Aggelos K. Katsaggelos; Ed.*, volume 2308, pages 1146–1157, September 1994.
- [8] H.G. Feichtinger, N. Kaiblinger, and P. Prinz. POCS approach to Gabor analysis. In *Proc. SPIE Vol. 3346, p. 18-29, Sixth International Workshop on Digital Image Processing and Computer Graphics: Applications in Humanities and Natural Sciences, Emanuel Wenger; Leonid I. Dimitrov; Eds.*, volume 3346, pages 18–29, January 1998.
- [9] D. Gabor. Theory of communication. *J. IEE (London)*, 93:429–457, 1946.
- [10] M.J. Bastiaans. Gabor's signal expansion and degrees of freedom of a signal. *Proc. IEEE*, 68:538–539, April 1980.

Experimental Verification of Electromagnetic Simulations of a HIFI Mixer Sub-Assembly

W. Jellema¹, P. R. Wesselius¹, S. Withington², G. Yassin², J. A. Murphy³,
C. O'Sullivan³, N. Trappe³, T. Peacocke⁴ and B. Leone⁵

¹National Institute for Space Research (SRON), Groningen, the Netherlands

²Cavendish Laboratory, Cambridge, UK

³National University of Ireland Maynooth (NUIM), Co. Kildare, Ireland

⁴UK Astronomy Technology Centre (UKATC), Edinburgh, UK

⁵European Space Agency (ESA/ESTEC), Noordwijk, the Netherlands

Abstract: In Phase II of the study "Far-Infrared Optics Design & Verification", commissioned by the European Space Agency (ESA), we investigate the ability of several commercial software packages (GRASP, CODEV, GLAD and ASAP) to predict the performance of a representative example of a submillimeter-wave optical system. In this paper, we use the software packages to predict the behaviour of a Mixer Sub-Assembly (MSA) of HIFI, and we compare the simulations with near-field measurements at 480 GHz. In order to be able to distinguish between the predictions of the packages, we move the corrugated horn of the MSA through its nominal focus position. A unique feature of the experimental arrangement is that the measured position of every field point is known absolutely to within fractions of a wavelength. In this paper we present the results of this through-focus experiment, which give a good first-order indication of the agreement between measured and simulated behaviour of a typical submillimeter-wave optical system.

Keywords: ESA-TRP, far-infrared, submillimeter, optics, verification, HIFI

1. INTRODUCTION

The accurate modelling of optical systems in the far-infrared and submillimeter-wave bands is complicated because of the long wavelength character and in many applications necessity for a compact optical layout. The associated diffraction effects inevitably become important and can no longer be ignored. The unique nature of optical systems in this wavelength band and the lack of dedicated simulation software has lead to the non-ideal use of software packages designed and intended for other wavelengths and based on a variety of underlying physical principles. The adapted use of these software tools for the far-infrared is not

reported comprehensively in literature and much uncertainty surrounds the accuracy of these optical simulations.

In order to verify the ability of these commercial packages (GRASP, CODEV, GLAD and ASAP) to predict the performance of submillimeter-wave optical systems, the European Space Agency (ESA) has commissioned the study “Far-Infrared Optics Design & Verification”. In Phase I of the study we carefully selected test cases to reveal strengths and weaknesses of the packages in typical submillimeter-wave applications on the basis of the underlying physical principles [1, 2]. In the end of Phase I we carried out first-order simulations of a typical real system case represented by a Mixer Sub-Assembly for HIFI [3, 4]. We observed that the simulated differences in a focussed system were too small to be observed experimentally. In order to distinguish between the packages we therefore proposed a through-focus test revealing differences at a relatively high intensity level relaxing the need for high dynamic range. In Phase II we constructed a near-field facility capable of measuring both amplitude and phase at 480 GHz. The main objective of this work is to address the question to what extent measured and simulated performance of a typical example of a submillimeter-wave system may be expected to agree.

2. SUMMARY OF SIMULATION PACKAGE CAPABILITIES

We have compared the beam predictions of the four different software packages summarized below: **GRASP8**, **ASAP (v7.1)**, **GLAD (v4.5)** and **CODE V (v9.0 and v9.2)**. The strengths and weaknesses of each package were reported in detail during Phase I of the project [1, 2]

GRASP is a general antenna analysis program package marketed by TICRA. Its theoretical analysis is based on Physical Optics (PO) and the Geometrical Theory of Diffraction (GTD). Physical Optics is based on calculating the induced currents on the reflector surfaces without taking the edge effects into account. This clearly degrades the accuracy of the method predictions at wide angles. In GRASP8 the PO method is supplemented with GTD in order to improve the accuracy of the equivalent current calculation near the edges. GTD approximates the non-uniform current at the reflector edge to the induced current at the edge of a canonical scatterer that conforms to the shape of the reflector in the locality of the edge points. Multiple reflector systems are analyzed in GRASP by calculating the induced current on one reflector and using it as a source illuminating the next reflector. Although not investigated here, cross-polar predictions are also available from GRASP. The model system could be set up in GRASP exactly as it

is described in section 3. Throughout Phase I and II of this project we have taken GRASP to be our benchmark software.

ASAP is a package for the analysis of visible / near-IR optical systems. It was originally designed for the analysis of stray light, but was extended for the analysis of diffraction. It is essentially a non-sequential ray tracing package but has an additional diffraction analysis capability. For this it uses a technique called Gaussian beam decomposition. Rays representing a set of Gabor-Gaussian modes are traced through the optical system. These modes can be recombined at any point in the system to calculate the field. ASAP has three forms of decomposition algorithm. In the first, a straightforward spatial sampling is performed. The Gaussian beams have equal sizes, but are spaced out across a grid. In the second algorithm, an angular decomposition is performed. Each Gaussian beam is equal in size but has a different propagation direction, so that the beams are equally spaced in angle in the far field. The third method is a combined spatial / angular decomposition. This last method has only recently been added. The description of the MSA optical system within ASAP was straightforward and very precise.

GLAD was developed to model laser and optical systems where diffraction is expected to play an important role. A beam is represented by its complex amplitude distribution, which need not be a simple function. The primary propagation algorithms in GLAD are based on a plane-wave decomposition with no special symmetry assumed. Light is treated as being strictly monochromatic and therefore perfectly polarized. Optical systems are modelled to the accuracy of small-angle, scalar Fresnel diffraction theory. Conic mirrors can be modelled using exact ray-tracing to compute aberrations. This facility is to be extended to lenses, apertures and obscurations in future versions of GLAD. (In fact tilted apertures have been introduced into the version of GLAD released towards the end of this project. This version has not been used in any of the work presented here.) The mirrors of the model system are set up in GLAD by considering them as sections of larger paraboloids and ellipsoids. Edges cannot be defined for the mirrors themselves, and are therefore approximated by placing apertures in front. This was the only approximation that was made when setting up the system as drawn in Fig. 1. of the next section.

CODE V is an optical analysis and design package for visible / near-IR optical systems. Like ASAP it is primarily a geometrical ray-tracing package, but offers in addition some diffraction analysis capability. CODE V uses a plane wave expansion of fields in its diffraction calculations and allows mirrors and apertures to be de-centered and tilted. In this case, the MSA mirror edges were modelled as tilted elliptical apertures. The field mirror, MAM2 (Fig. 1.) was modelled as a

toroid. The greater control of sampling in the latest version of CODE V (v9.2) allowed a technique to be developed to overcome the problems reported throughout the first stages of the project [1].

A more detailed account of setting up the model system in each of the packages is included as Appendix B in the final report of Phase II [5].

3. MODEL SYSTEM DESCRIPTION

In Phase II of the project one of the Mixer Sub-Assemblies of HIFI represents a typical submillimeter-wave optical system. The optics of the selected MSA are designed to operate in the 480-640 GHz frequency range (HIFI band 1). In this paper however, we only consider the lower frequency end of the band, i.e. we only present results in the long-wavelength limit at 480 GHz where diffraction effects are most pronounced.

In Fig. 1. a simplified layout of the optics is shown. The reduced MSA (as shown in Fig. 2.) comprises a conical corrugated horn and three off-axis mirrors. Because of this off-axis geometry we refer to the plane of drawing as the asymmetric plane. When the horn is in its nominal focus position the three mirrors form an image of the horn aperture in the output plane, which is located at 66.25 mm from the parabolic mirror MAM1. At actual wavelengths a frequency independent beam waist is located in this plane with a waist radius of 3.55 mm. The corrugated horn has a slant length of 15.4 mm and an aperture radius of 2.5 mm. The polarisation direction of the corrugated horn is perpendicular to the plane of drawing. We only consider this component of the electric field in the output plane.

Also indicated in Fig. 1. is a set of through-focus positions for the corrugated horn. Apart from the nominal focus position (solid line), the horn can be moved towards the elliptical mirror MAM3 by 5 mm, and away in two steps of 5 mm. Through-focus measurements were simulated for each of these four configurations. As mentioned in the introduction the through-focus test offers a means to systematically study the differences between simulations and experiment by introducing different levels of aberration. The advantage of this model system is that differences which would normally be present at relatively low intensity levels in the far-field, will now show up as main beam distortions in the near-field. We therefore expect that this experimental arrangement will illustrate the differences between the package predictions.

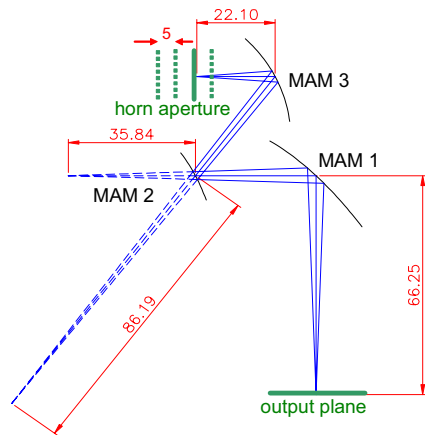


Fig. 1. Layout of model system

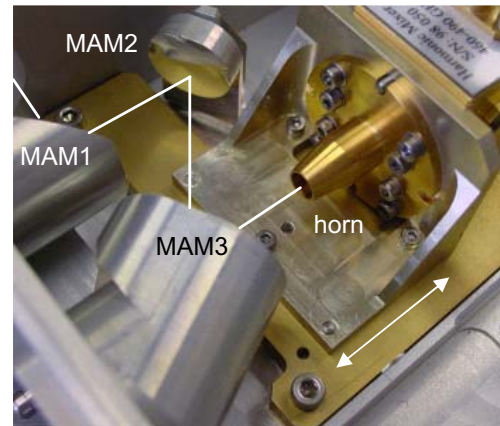


Fig. 2. HIFI Mixer Sub-Assembly.

4. SOFTWARE PACKAGES SIMULATIONS

Initial simulations were done by assuming a Gaussian distribution at the aperture plane of the horn. This aperture field distribution was propagated through the optics to the output plane. These first-order simulations proved to be a useful starting point to define the criteria to be met by the measurement system. Given the differences in the through-focus simulations we found that an experimental system that could detect differences of 3-4 dB at the level of -20 dB would be sufficient to distinguish between the aberrations predicted by the packages. We furthermore found that ASAP had serious difficulties in modelling this compact system with a horn aperture of only eight wavelengths in diameter. We decided to exclude ASAP from the final comparison since we found that its predictions were not sufficiently close to expected behaviour. The intrinsic problem in our particular case appeared to be the decomposition of the source field for which we could not find an independent and consistent procedure for all through-focus positions simultaneously.

We subsequently improved the horn field approximation by assuming an ideal hybrid feed that can be described by a truncated Bessel function with a spherical phase error [6]. Although it is common practise in submillimeter design to substitute the real source field of a corrugated horn by a fundamental mode Gaussian beam, we found that differences might not be negligible. We found that using a Gaussian beam to approximate the horn field did not predict either the sidelobe level or the amount of main-beam distortion. An example that illustrates this point is shown in Fig. 3. which shows the GRASP prediction (dotted) assuming a Gaussian approximation in comparison to the GRASP and GLAD predictions (solid) assuming an ideal hybrid feed for -5 mm defocus (away from

the first mirror). It is clear that the Gaussian approximation fails to predict the main beam distortion leading to significant errors already at the -10 dB level. The differences in phase predictions were also significant and measurable given the demonstrated measurement performance at this stage. The narrowest spatial features in the predictions could be resolved by the measurement system and based on this set of simulation results we were able to define the final test criteria.

Finally the field from the actual corrugated horn was calculated using the mode-matching technique and this was taken as the input to the model system. For these last simulations the new CODE V version was available and its results were a significant improvement on those reported earlier [1]. In order to compare the differences between an ideal and real horn field, we used GRASP to predict the output beam when the horn is moved 10 mm away from the first mirror. The result is shown in Fig. 4. It can clearly be seen that the two patterns are indistinguishable. The remarkable similarity between the two patterns results from a good horn design in which the ideal and real field distributions are almost identical in the upper 30 dB, and due to the finite throughput of the optical system (spatial filtering).

The final set of simulation results is partly shown in section 6 together with the experimental results. The full set of simulation and measurement results can be found in the final report of Phase II of this project [5].

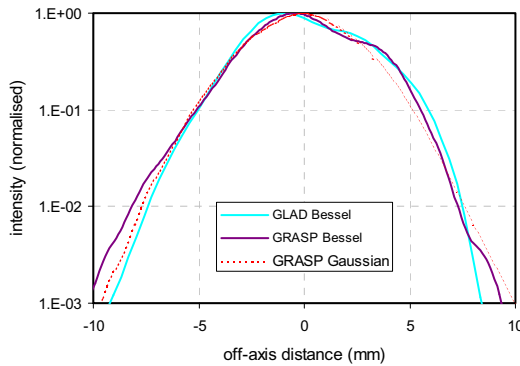


Fig 3. Asymmetric cut for an ideal and real horn field for a -5 mm defocus.

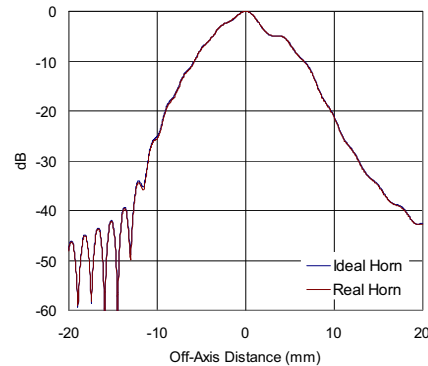


Fig. 4. GRASP simulation comparing ideal and real horn fields.

5. EXPERIMENTAL SETUP AND RESULTS

A substantial task in Phase II of the project was the development of a near-field facility capable of measuring both amplitude and phase at 480 GHz. In this paper

we only briefly summarize some characteristics of the facility which is fully described in the final report [5].

The schematic diagram of the detection system is shown in Fig. 5 and is quite similar to other systems reported in literature [7, 8, 9]. In the upper-left corner of the diagram the Phase-Lock Loop (PLL) is shown. An InP Gunn oscillator is phase-locked at 80 GHz. A second directional coupler and waveguide harmonic mixer provide an independent reference signal. Because this signal is taken before multiplication to 480 GHz, the Intermediate Frequency (IF) of the waveguide harmonic mixer is multiplied by a factor of six, i.e. $N = 6$ in the diagram. The actual detector in the MSA is a subharmonically pumped Schottky mixer pumped by the same Local Oscillator (LO) as the reference mixer. We use a compensating pair of mixers to remove any correlated phase variations present in both the reference and detected signal. This allows a very narrow-band detection increasing system sensitivity. We finally use a Vector Network Analyzer (VNA) in the S21 mode to detect the relative field coupling between the test source and the detector. A signal-to-noise calculation shows that the dynamic range can be as high as 60 dB when detecting in a 100 Hz IF bandwidth and integrating in 10 ms. More details on performance can be found in [10].

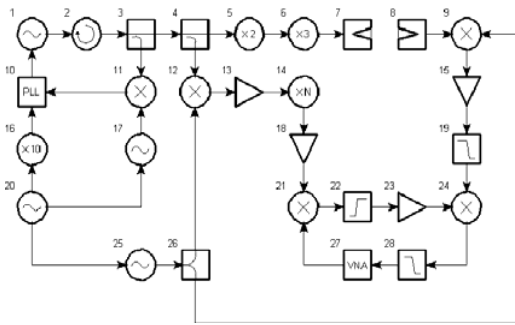


Fig. 5. Detection system diagram

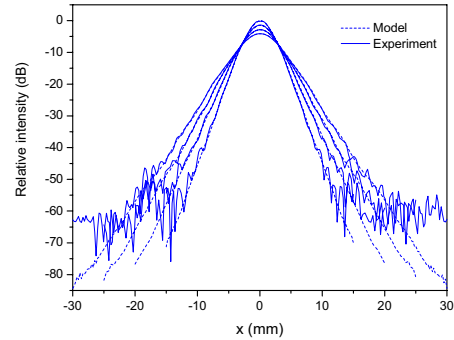


Fig. 6. Near-field horn measurements

In addition to the detection system several other system components were designed. We designed and modelled a modified version of the HIFI corrugated horn to shift the centre frequency to 480 GHz. In order to resolve the spatial structures present in the simulated beam patterns a flared-waveguide probe was designed that could resolve spatial frequencies of $\frac{1}{2} \text{ mm}^{-1}$. Special mechanical flanges for the horn and probe were designed to fix the horn axis and aperture position with tight mechanical tolerances.

A three-dimensional scanner system was used to scan the test source with probe in the output plane of the MSA. A special support frame for the source and MSA was designed that also contained alignment devices. In the frame of the source we mounted two alignment windows with well-established relations to the probe coordinate system. We placed two alignment mirrors on the MSA support frame. Using an optical theodolite we were able to accurately align the scanner system with respect to the MSA. We achieved a lateral alignment accuracy of 25 - 50 μm , an axial accuracy of 0.1 - 0.2 mm, a tilt accuracy of a few arcmin and a polarisation alignment of 0.5 deg. A unique feature of the facility is therefore that the absolute coordinates of the measured fields points are known within fractions of a wavelength.

A detailed performance characterisation and error analysis was performed in which we identified and quantified the sources of error [5, 10]. We furthermore developed first-order error correction methods to reduce errors due to multiple reflections and long-term drift [5, 10]. To verify the performance, near-field measurements of the corrugated horn were taken at distances of 15, 20, 25 and 30 mm respectively at 480 GHz. The results and simulations are shown in Fig. 6. Both the level of agreement and the observed sensitivity clearly illustrate that we realised an accurate near-field system with known, and well understood, errors.

We finally mounted the corrugated horn and harmonic mixer in the MSA (Fig. 2.) and took co-polar measurements at 480 GHz in the output plane in both the asymmetric as well as the symmetric direction for each of the through-focus positions. The individual amplitude and phase plots can be found in chapter 5 of the final report [5] and some of the results will be presented in the next section of this paper.

6. COMPARISON SIMULATIONS AND EXPERIMENTAL RESULTS

Before we start comparing the simulations and experimental results, we would like to note that the comparison of one particular field component, and in particular its phase, is not straightforward at all. Apart from GRASP, the packages produce a scalar quantity that represents the field, i.e. the vector-nature of the field is completely ignored. A comparison is therefore only reasonable in the limit that the cross-polar component is very small. Using GRASP we found that the cross-polar level is indeed sufficiently low. The comparison between GRASP and experiment is however sound, since the detection system is sensitive to only one field component (polarised probe).

In general we observed good agreement in amplitude between the predictions and experiment in the main beam. In particular, GRASP and CODE V agreed exceptionally well (see Fig. 7.). Below the -40 dB level there were only small differences which could be easily attributed to sampling and systematic errors of the facility. It is not clear whether experiment or simulations get wrong at this level. More experimental and simulation work is therefore required to draw firm conclusions below the -40 dB level. In several cases GLAD failed to agree with experimental results. In particular in the asymmetric cases where the horn was moved 5 mm towards respectively 10 mm away from the mirror, GLAD failed to predict the sidelobe structure and distortion (see Fig. 8.). Considering that GLAD integrates over a projected aperture rather than over the physical mirror aperture, we indeed expect the sidelobe level for the asymmetric patterns to be inaccurate.

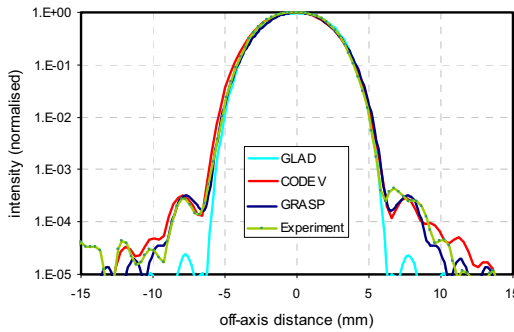


Fig. 7. Measured and simulated amplitude at nominal focus (symmetric cut).

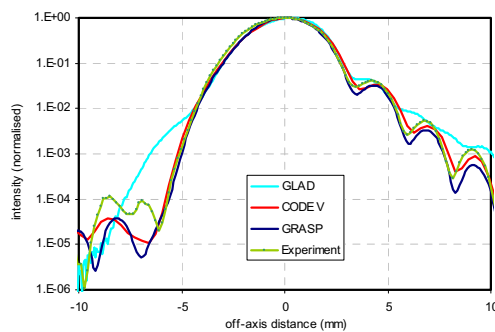


Fig. 8. Asymmetric cut at +5 mm defocus (towards mirror MAM3).

Regarding the phase simulations and measurement we found that phase information indeed provided additional useful information in assessing the performance of the packages. It is remarkable that GLAD, which predicted amplitude relatively well in many test cases, failed completely to predict phases correctly. In Fig. 9. for example the phase predicted by GLAD is in complete disagreement even in the symmetric plane. In the asymmetric cuts we observed substantial differences with experiment especially for positive off-axis distances (Fig. 10.). This again might be due to integrating over a projected aperture rather than the physical one. CODE V showed in general good agreement with the experimental results. The agreement is however best in the main beam region and starts to deviate at lower intensity levels. The GRASP simulations showed best agreement with the measured curves and predicted the observed phase structure most accurately. An example of an asymmetric pattern is given in Fig. 10. Although the differences might appear significant one should realize that the absolute deviations in phase between GRASP, CODE V and experiment are all below $\lambda / 20$ at 480 GHz once again illustrating the accuracy of our work.

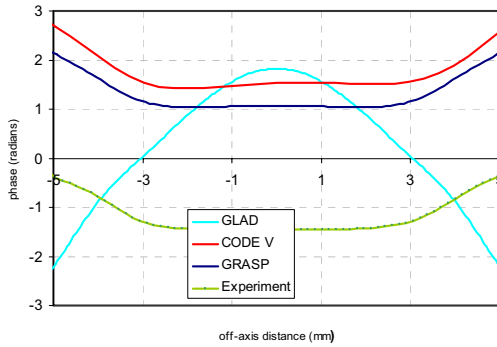


Fig. 9. Phase distributions (symmetric cut) for +5 mm defocus (towards mirror).

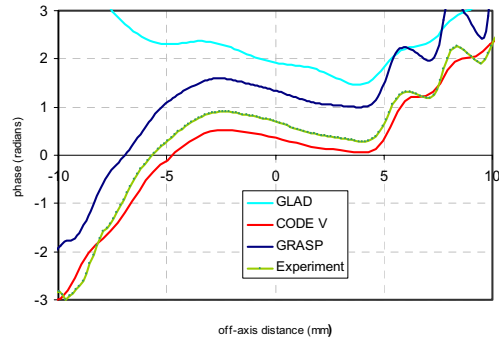


Fig. 10. Phase distributions at nominal focus position (asymmetric cut).

7. SUMMARY AND CONCLUSIONS

In Phase II of the study "Far-Infrared Optics Design & Verification" we investigated the ability of several commercial software packages (GRASP, CODEV and GLAD) to predict the performance of a representative example of a submillimeter-wave optical system. We did not attempt to compare the different packages in a competitive way. We were only interested in assessing the ability of each package to carry out a predetermined task. In this part of the study a modified version of one of the Mixer Sub-Assemblies for HIFI was taken as a model system. The optical layout is believed to be typical of a high performance submillimeter-wave system. The key question we beared in mind is to what extent simulated and measured performance may be expected to agree. To address this question we selected a strategy of through-focus near-field phase and amplitude measurements revealing the differences between the packages. In this through-focus test the differences were shifted from the far-out sidelobes into the main beam relaxing dynamic range requirements for the measurement system. We developed a near-field facility and demonstrated a dynamic range of at least 50 dB. A unique feature of the experimental system is that geometry is controlled within fractions of a wavelength. Therefore the theoretically derived and experimentally measured field patterns were determined by reference to one single absolute position and overlaid without any adjustment. We finally constructed a full error model of the measurement system and experimentally verified the system on a corrugated horn. Both the level of agreement and the observed sensitivity clearly illustrated that we realised an accurate near-field system with known, and well understood, errors.

After initial investigations we excluded the simulation results of ASAP as we found that its predictions were not sufficiently close to expected behaviour in this particular case. In contrary to what we found in early stages, CODE V now showed good performance whereas we initially had severe problems in getting meaningful results. Based on the out-of-focus measurements we conclude that GLAD is only accurate above the -20 dB level. Phase measurements furthermore revealed that GLAD can make substantial errors when simulating phase. The principle limitation seems to originate from the definition of the rim of mirrors which are represented as projected apertures perpendicular to the chief ray. This limitation has been addressed however in the version that has become available since. Both GRASP and CODE V simulation results agree very well with experiment down to -40 dB. GRASP was even capable of tracing the sidelobe structure down to -45 dB. Below this level it is not clear whether simulations or measurements become inaccurate. Finally we observed that the phase distributions predicted by GRASP and CODE V are generally in agreement with measurement. In particular the agreement between GRASP and experiment was excellent with the exception of one single case. In general the overall agreement between simulation and experimental results is best for GRASP. The advantages of its full electromagnetic approach are evident. For design purposes however the awkwardness of setting up models might limit the flexibility to explore different layouts. We therefore feel that an excellent approach would be to combine GRASP with a first-order pre-processing and design package before verifying an optical system using rigorous electromagnetic calculations.

8. ACKNOWLEDGEMENTS

The authors would like to acknowledge Peter de Maagt and Maurice Paquay from ESA / ESTEC for their useful comments. The authors are grateful for design support by Edward Tong from Harvard-Smithsonian, Matt Carter from IRAM and Andrey Baryshev from SRON / RuG. We finally acknowledge Lenze Meinsma and Geert Keizer from SRON as well as Jan Idserda from ASTRON for their mechanical design efforts. This work was carried out in Phase II of the ESA TRP Study "Far-Infrared Optics Design and Verification Tools", ESTEC/Contract No. 13043/98/NL/PB.

9. REFERENCES

- [1] Atad-Ettinger E., Duncan W., Henry D., Jellema W., Murphy J. A., Trappe N., van de Stadt H., Withington S. and Yassin G., "Far-IR Optics Design and Verification Tools", *Final Report Phase I ESA TRP Study 13043/98/NL/NB*, December 2000, ESA.

- [2] O'Sullivan C., Atad-Ettdgui E., Duncan W., Henry D., Jellema W., Murphy J.A., Trappe N., van de Stadt H., Withington S. and Yassin G., "Far-IR Optics Design and Verification", *International Journal of Infrared & Millimeter Waves*, pp. 1029-1045, Vol. 23, No. 7, July 2002.
- [3] T. de Graauw, F. P. Helmich, "Herschel-HIFI: The Heterodyne Instrument for the Far-Infrared", in *The Promise of the Herschel Space Observatory*, edited by G. L. Pilbratt et al., ESA SP-460, pp. 45-51, 2001.
- [4] B. D. Jackson, K. J. Wildeman, N. D. Whyborn on behalf of the HIFI Focal Plane Consortium, "The HIFI Focal Plane Unit", *Proc. 13th International Symposium on Space Terahertz Technology*, pp. 339-348, 26-28 March 2002, Harvard University, Cambridge, Massachusetts, USA.
- [5] P. R. Wesselius et al, "Far-Infrared Optics Design and Verification Tools", *Final Report Phase II ESA TRP Study 13043/98/NL/PB*, March 2003, to be made available by ESA.
- [6] P. F. Goldsmith, *Quasioptical Systems: Gaussian Beam Quasioptical Propagation and Applications*, IEEE Press: New York, Chapter 4 and 7, 1997.
- [7] P. Goy, M. Gross, "Vector Transceiver for mmWave Antennas", *Proc. 20th ESTEC Antenna Workshop on Millimetre Wave Antenna Technology and Antenna Measurement*, pp. 289-294, 18-20 June 1997, ESTEC, Noordwijk, The Netherlands.
- [8] N. Erickson, V. Tolls, "Near-Field Measurements of the Submillimeter Wave Astronomy Satellite Antenna", *Proc. 20th ESTEC Antenna Workshop on Millimetre Wave Antenna Technology and Antenna Measurement*, pp. 313-319, 18-20 June 1997, ESTEC, Noordwijk, The Netherlands.
- [9] C. E. Tong, S. Paine, R. Blundell, "Near-Field Characterization of 2-D Beam Patterns of Submillimeter Superconducting Receivers", *Proc. 5th International Symposium on Space Terahertz Technology*, pp. 660-673, 1994.
- [10] W. Jellema, S. J. Wijnholds, P. R. Wesselius, S. Withington, G. Yassin, J. A. Murphy, C. O'Sullivan, N. Trappe, T. Peacocke, B. Leone, "Performance Characterisation and Measurement Results of a Submillimeter-Wave Near-Field Facility for the Heterodyne Instrument for the Far-Infrared", *Proc. 3rd ESA Workshop on Millimeter-Wave Technology and Applications*, Millilab, Espoo, Finland, May 2003.

A Novel Procedure for Designing Band-pass Filters Using FSS Structures

Ge Wu, Volkert Hansen

Chair of Electromagnetic Theory, University Wuppertal
Rainer-Gruenter-Str. 21, D-42119 Wuppertal, Germany

Ernst Kreysa, Hans-Peter Gemuend

Max Planck Institute for Radioastronomy, Bonn, Germany

1 Abstract

In this paper, a novel design procedure for band-pass filters using frequency selective surfaces is presented. The connection to the classical filter theory makes it possible to develop a design method for the specification and the performance of FSS filters with a sharp filter slope and a good attenuation in the stop band.

2 Introduction

The frequency selective surfaces (FSS) embedded in layered media are applied as high frequency filters for astronomical investigations. The so-called capacitive grids, which are composed of infinite periodic array of patches on a dielectric support (polypropylene), are used as basis elements. The filters will be operated in the submillimetre wave range. They shall, on the one hand, exhibit a selectivity as high as possible; on the other hand, a broad stop band - a good attenuation is necessary particularly at higher frequencies because of the thermal radiation rising with f^2 .

The design procedure consists of two main steps. It starts with a strict synthesis procedure of the classical filter theory for the development of filters with certain characteristics and their realization on the basis of lumped elements and transmission-lines, the equivalent circuits. For the second step a connection is established between the equivalent circuits and their realization as FSSs, in other words, the FSS filters, which consist of multi-layered patch structures of different patterns, are specified in such a way that their filter characteristics correspond to those of the equivalent circuits.

3 Realization of the band-pass filters from the capacitive grids

For the proposed astronomical experiments band-pass filters are required, which can be realized with inductive grids [1, 2]. However, for technological reasons only capacitive grids can be applied, which possess the characteristics of band-stops (Fig. 1).

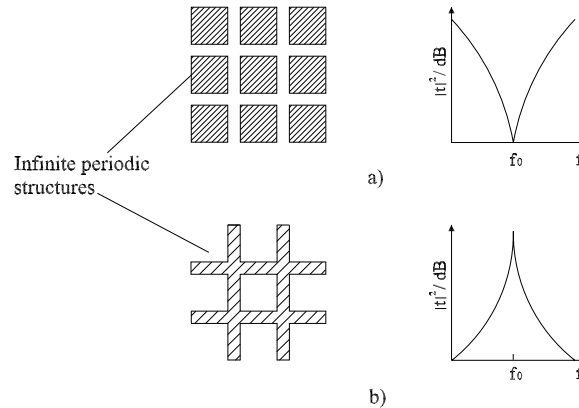


Fig. 1. Filter characteristics of a) capacitive b) inductive grid

A solution is found by first developing a band-stop filter from capacitive grids and then connecting it to a high-pass. The resulting filter exhibits the characteristics of a band-pass in the frequency range up to the onset of diffraction. This combination is indicated in Fig. 2, schematically.

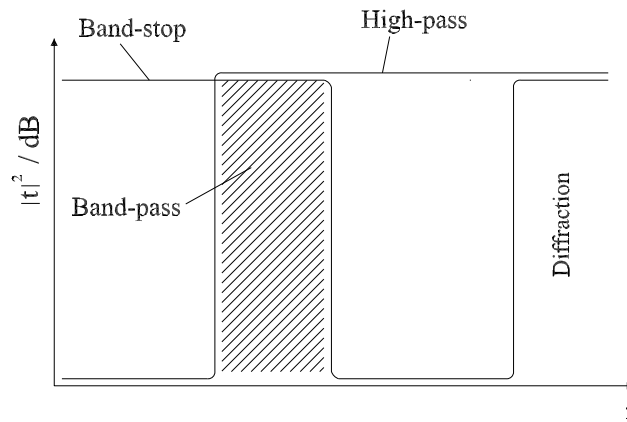


Fig. 2. Cascading of a high-pass and a band-stop

For the high-pass filter a circular waveguide is used. Because it is easy to design a circular waveguide, the entire problem is reduced to the task of developing the band-stop filters using capacitive grids.

4 Synthesis procedure of the classical filter theory

The approximation and synthesis of filter functions is one of the well-established problems in the communication technology ([3, 4, 5, 6]), i.e., the classical filter theory. The

design of band-stop filters on the basis of lumped elements and transmission-lines is generally divided into the following steps:

It starts with a filter synthesis carried out in the so-called equivalent low-pass range. The filter slope and the attenuation can be entered as input data. The circuit obtained, the so-called Chebyshev low-pass, is composed of series inductors and shunt capacitors, i.e. an LC-network. The main parameters for specification are the degree of the filter, i.e. the number of the lumped elements, and the filter coefficients, which are obtained from tables given in the handbooks of filter design. The filter tables by Saal ([5]) are applied in this study. In Fig. 3, such a reference low-pass is indicated. It possesses the filter degree of 7 and the appropriate filter coefficients $g_1 \sim g_7$.

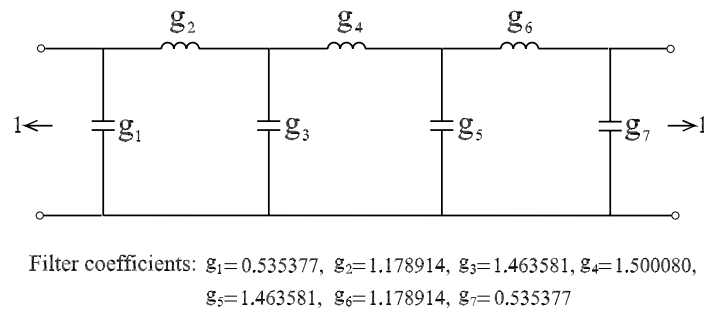


Fig. 3. Equivalent low-pass of 7th degree with the filter coefficients

Fig. 4 shows the function of the so-called impedance inverter, which transforms a series inductor into a shunt capacitor.

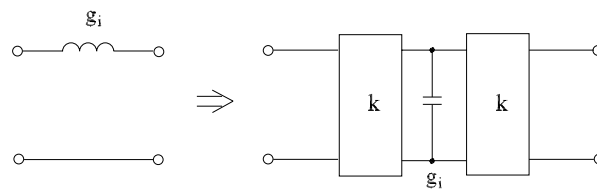


Fig. 4. Circuit transformation by the impedance inverter. k is the coupling factor

In the next step, the LC network we got in the first step, is transformed with the help of such impedance inverters into a circuit, which only contains shunt capacitors and impedance inverters (see Fig. 5).

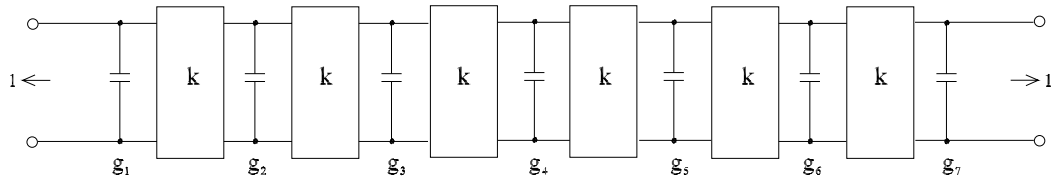


Fig. 5. Network with shunt capacitors and impedance inverters

In the third step, the low-pass is transformed into a band-stop using the low-pass / band-stop transformation (see Fig. 6a)).

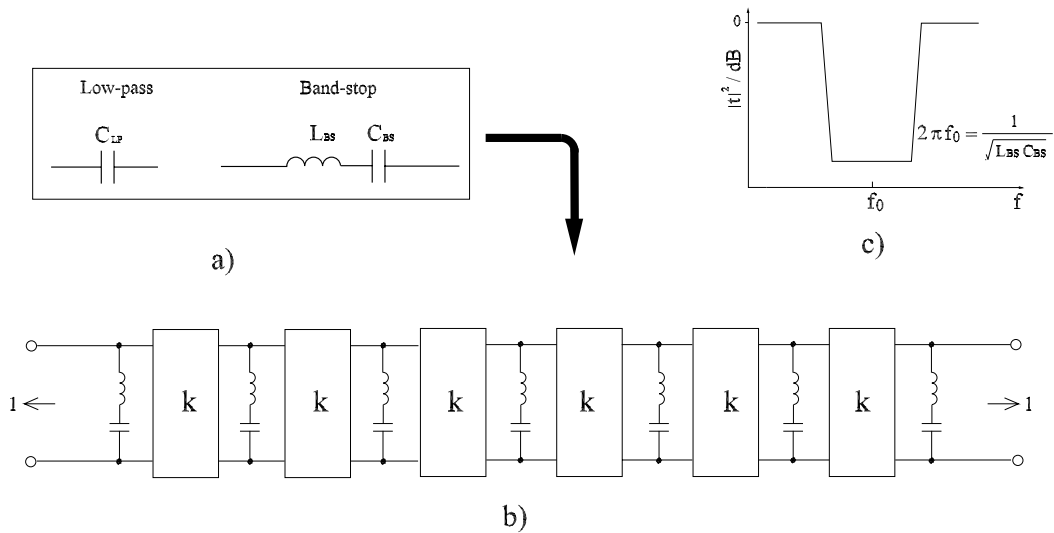


Fig. 6. a) Low-pass / band-stop transformation b) Network obtained after the Low-pass / band-stop transformation c) Filter characteristic of the band-stop

Now a band-stop filter is obtained, which is made up of the impedance inverters and series-resonant circuits in parallel (see Fig. 6b)). Fig. 6c) displays schematically the transmission character of the band-stop obtained, with the center frequency f_0 .

Finally, as illustrated in Fig. 7, the impedance inverters are replaced by $\lambda/4$ -transmission-lines, acting as impedance inverters. Thus we get a network, which contains series-resonant circuits connected by $\lambda/4$ -transmission-lines.

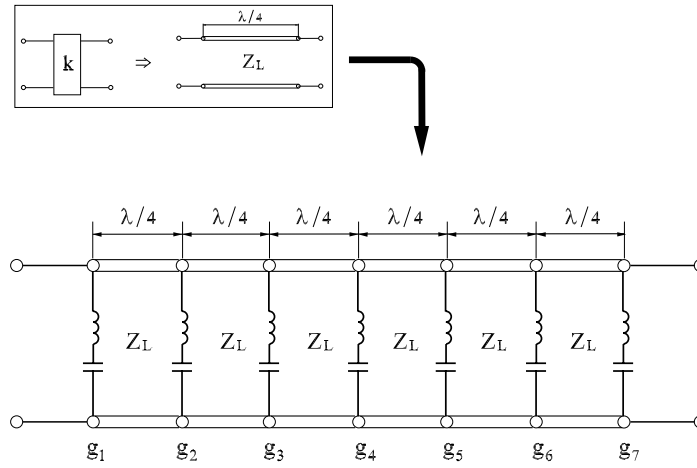


Fig. 7. Band-stop from series-resonant circuits connected by the $\lambda/4$ -transmission-lines

5 Realization of the FSS filter

The transformation of the filter developed so far into an FSS structure starts with some well-known approximations ([7, 8, 9, 10]). As illustrated in Fig. 8, the $\lambda/4$ -transmission-lines are first substituted by $\lambda/4$ dielectric layers. Then two additional layers of thickness $\lambda/2$ are attached above and below the FSS filter to provide a mechanical protection of the outer grids.

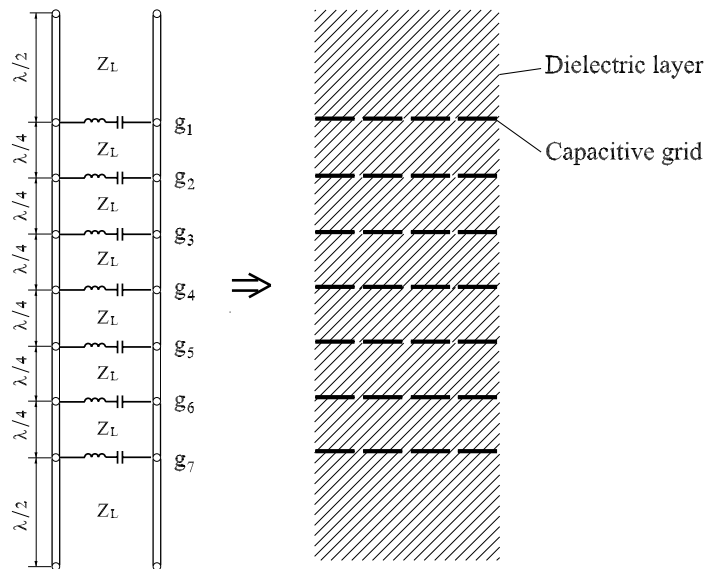


Fig. 8. Equivalent circuit model and the realization as FSS filter

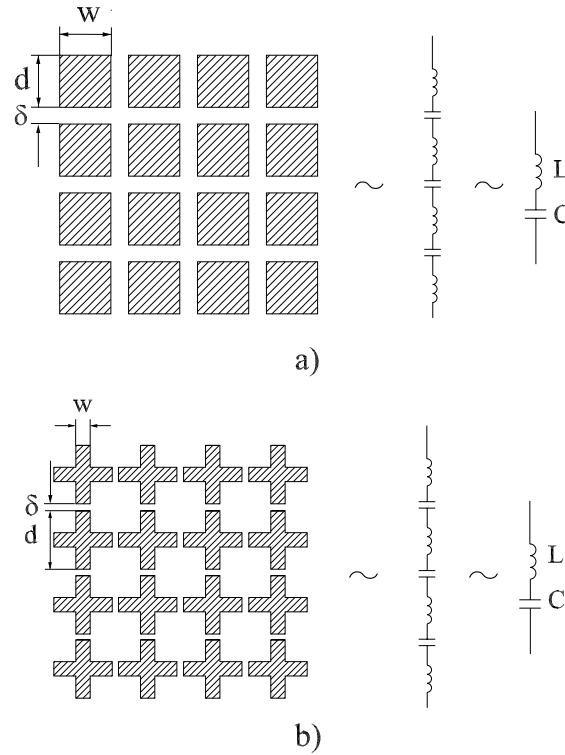


Fig. 9. Capacitive grid of a) square patch structure and b) cross dipole structure and their equivalent circuits as lumped elements

For the filters presented in this paper metallic square patches and crossed dipoles are applied as resonant structures. The geometries of these capacitive grids and their equivalent circuit as lumped elements are given in Fig. 9. Approximate design formulas available from literature are supplied as a starting point for the realization of the series-resonant circuits. For closely neighboring patches ($\delta/d \leq 0.2$), the formulations in [7]

$$L = \frac{A_L}{d\sqrt{w}} Z_0 \text{ [nH]} \quad (1)$$

and

$$C = A_C d^3 \sqrt{w} / Z_0 \text{ [nF]}, \quad A_L, A_C = \text{constant}, \quad (2)$$

are applied to derive the following proportionality

$$\frac{C_i}{C_j} \sim \frac{L_j}{L_i} \sim \frac{g_i}{g_j} \sim \sqrt{\frac{w_i}{w_j}}, \quad (3)$$

which is used for the specification of different FSS grids (here i and j) with the help of the existing filter coefficients (g_i and g_j).

Fig. 10 shows the structure of the FSS filter developed on the basis of the equivalent circuit model in Fig. 7.

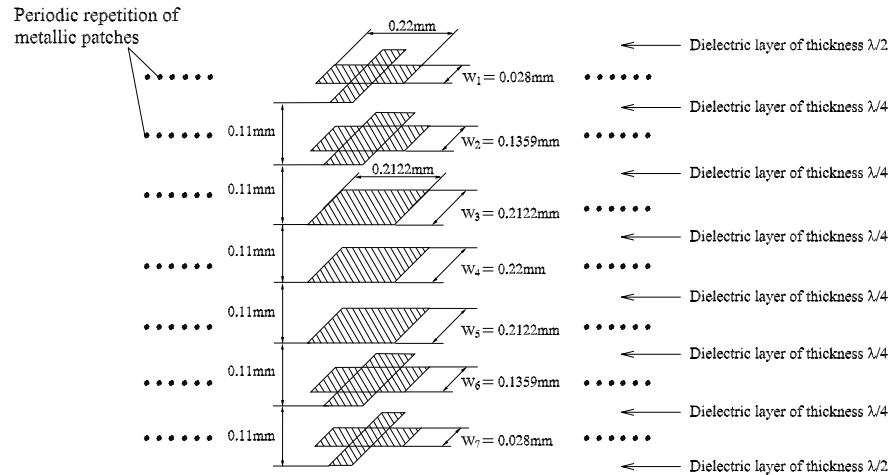


Fig. 10. Structure of an FSS filter of 7th degree from square patches and cross dipoles

The FSS structure obtained by this procedure is then analyzed with the below-mentioned numerical code. The performance of this first design is further improved by systematic variation of all design parameters.

6 Cascading of two or several filters

In order to further improve the band-stop character of the resulting filter, the diffraction will be suppressed or moved further to higher frequencies, respectively. This aim is partly achieved by the cascading of two or several band-stop filters, which corresponds to a shift of the diffraction range. Thus, a broader band-width of the resulting filter is provided.

7 Computation of the transmission factors

The transmission characteristics of the equivalent circuits are computed recursively starting from the end of the circuit with the help of the well-known transmission-line theory.

The computation of the FSS filters uses a spectral domain analysis based on an integral equation formulation applying the appropriate Green's function of layered media. The integral equation is solved by the method of moments combined with the Floquet theorem. A computer program on the basis of this theory has been developed. A lot of FSS structures have been calculated and a large number of measurements have been made, yielding a rather good agreement between the measured and the calculated values [11, 12].

8 Numerical results

In this section, some numerical results are presented, which first demonstrate the design steps according to the classical filter theory, and then show the correspondence between the equivalent circuits and the FSS filters. Fig. 11 shows the transmission factor of the filters of 7th degree, which work at the center frequency of 500GHz. For the filter slope the FSS filter and the circuit model are fairly in agreement. Further we get the result, that the FSS filter possesses a broader band-width and a greater attenuation in the stop band. This is because of the grating lobes phenomenon and the electromagnetic coupling within the structure. The curves of the filters of 11th degree with the center frequency of 500GHz are given in Fig. 12. These filters have a broader band-width and a larger attenuation compared with the filters of 7th degree. In Fig. 13, we demonstrate the cascading of 2 filters of 7th degree, which work at the center frequencies of 500GHz and 700GHz, respectively. The resulting filter possesses a much broader band-width in comparison with each single filter (see also Fig. 11).

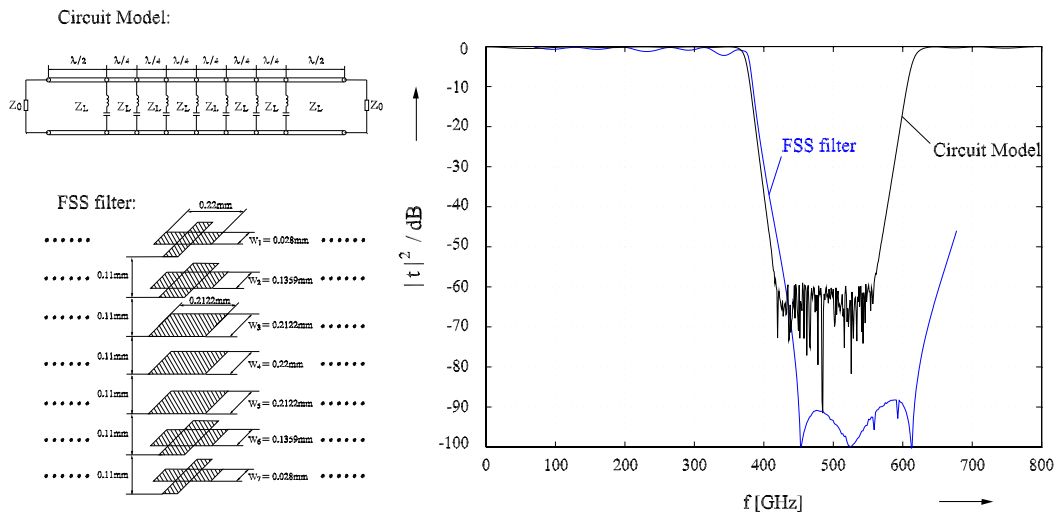


Fig. 11. Transmission characteristics of the circuit model and the FSS filter of 7th degree

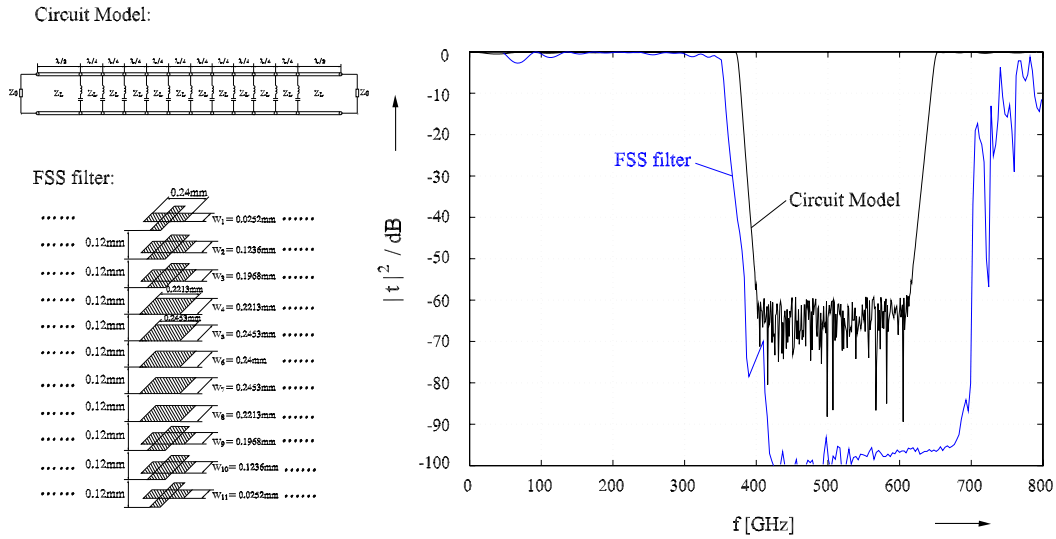


Fig. 12. Transmission characteristics of the circuit model and the FSS filter of 11th degree

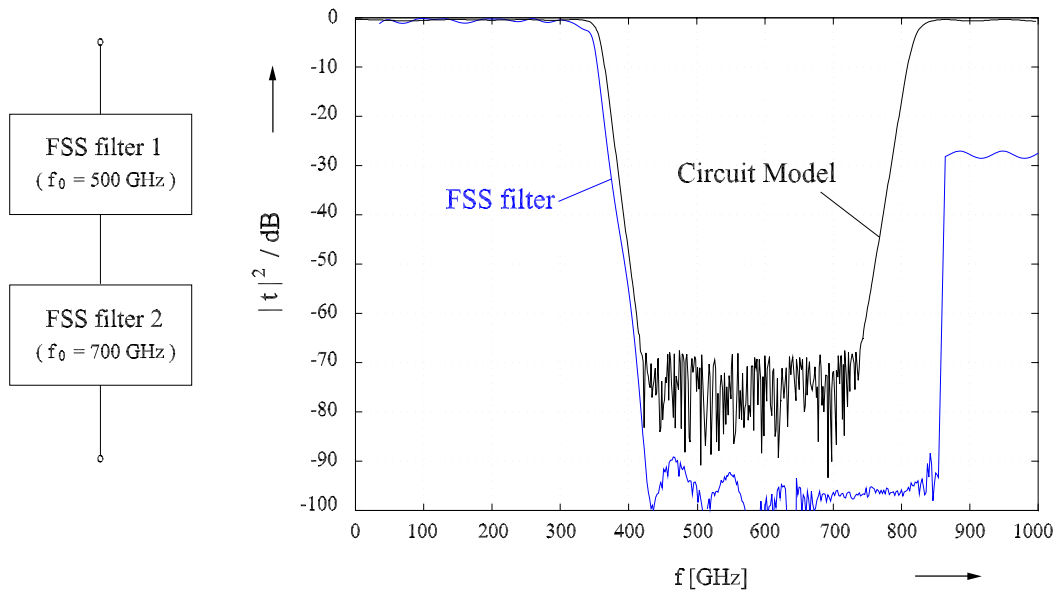


Fig. 13. Cascading of 2 FSS filters of 7th degree

9 Conclusion

With the help of the developed synthesis procedure it is possible to specify FSS filters consisting of a large number of layers. Therefore, the procedure is suitable for designing extremely complex filter structures in order to meet some special requirements. Up to now, filters with some ten layers have been investigated.

References

- [1] Munk, B.A. Frequency Selective Surfaces, Theory and Design, *John Wiley & Sons, Canada* 2000.
- [2] Wu, T.K. Frequency Selective Surfaces and grid array, *John Wiley & Sons, Canada* 1995.
- [3] Matthaei, G., Young, L., Jones, E.M.T. Microwave filters, impedance-matching networks, and coupling structures, *Artech House Books, Dedham, MA*, 1964.
- [4] Mildenerger, O., Entwurf analoger und digitaler Filter, *Friedr. Vieweg & Sohn Verlagsgesellschaft mbH, Braunschweig und Wiesbaden*, 1992.
- [5] Saal, R. Handbook of Filter Design, *AEG-Telefunken, Berlin und Frankfurt am Main*, 1979.
- [6] Pfitzenmaier, G. Tabellenbuch Tiefpässe, *Siemens Aktiengesellschaft, Berlin und München*, 1971.
- [7] Erdemli, Y.E. Multilayer frequency selective surfaces as artificial substrates for broadband conformal arrays, *Dissertation, University of Michigan*, 2002.
- [8] Lee, C.K., Langley R.J. Equivalent-circuit models for frequency-selective surfaces at oblique angles of incidence, *IEE Proceedings, Vol. 132, Pt. H, No. 6*, 1985.
- [9] Marcuvitz, N. Waveguide Handbook, *Peter Peregrinus Ltd, London*, 1986.
- [10] Ulrich, R. Far-infrared properties of metallic mesh and its complementary structure, *Infrared Physics, Vol. 7, pp.37-55*, 1967.
- [11] Aroudaki, Spektralbereichsanalyse von mehrlagigen planaren Schaltungen mit dreidimensionalen Diskontinuitäten, *Dissertation, Universität Wuppertal* 1996.
- [12] Aroudaki, H., Hansen, V., Gemünd, H., Kreysa, E. Analysis of low-pass filters consisting of multiple stacked FSS's of different periodicities with applications in the submillimeter radioastronomy, *IEEE Trans. Antennas Propagat., vol. 43, pp. 1486 - 1491*, December 1995.

A hot-spot model for membrane-based HEB mixer

J.Baubert^{1,2}, H. Merkel², M.Salez¹, P.Khosropanah²

¹LERMA, Observatoire de Paris, 77, av. Denfert-Rochereau, 75014 Paris France

²MC2, Chalmers University, Gothenburg, Sweden

ABSTRACT

Membrane-based hot electron bolometric mixers (HEB) are of specific interest for applications above 2.7 THz. There the absence of a dielectric close to the antenna reduces losses and enlarges the antenna structure. This allows the usage of large volume devices at higher RF frequencies. All these effects are beneficial to reduce the mixer noise temperature. A reduction in IF bandwidth due to the reduced cooling is by far outweighed by these effects. Here a device model for membrane-based HEB mixers is presented that takes the interaction between electrons and phonons of the film and membrane phonons as well as the phonon diffusion along the membrane into account. The model is based on a numerical solution of two nonlinear coupled heat balance equations on the superconducting strip: One relation is set up for the electron temperature and another for the phonon temperature resulting in I-V curves. The mixer conversion gain and the receiver noise temperature are obtained by applying a small signal model. The model allows comparing the performance of thick substrate-based HEB and membrane-based HEB: membrane-based HEB exhibit a conversion gain lower than in substrate-based HEB for a given LO power. However the maximum conversion gain (obtained when the hot spot is as short as possible to ensure a stable operating point) is comparable. It is clearly shown that, for the same conversion gain the LO power is expected to be reduced by a factor of 20% in the membrane-based case. Moreover, using the membrane-based HEB in a quasi-optical receiver together with a matched back-short offers the possibility to improve the LO and RF coupling efficiency.

INTRODUCTION

The submillimeter band, which may be defined as the wavelength region between 1 mm and 100 μm is of great importance to astronomy, atmospheric study, and more generally molecular spectroscopy. Hot bolometric mixers (HEB) have been accepted as the best devices for those receivers [1-3], when one seeks to detect molecular lines at wavelengths smaller than 300 μm , and when cryogeny is available. Describing and modeling the physics and the behavior of this device is critical to optimize the HEB performances. In contrast with earlier models [4], the "hot-spot model" [5] has been accepted within the last few years as the most accurate and powerful one. In this model, the mixing in a HEB is described by a time-varying normal conducting hot spot governed by a system of one-dimensional heat transport equation. For phonon-cooled bolometers, a coupled heat balance for electrons and phonons must be considered. Two major model assumptions have to be made for the large signal model: Assuming the phonon diffusion to be negligible compared to phonon escape to the substrate, leading to the localized cooling assumption, the phonon heat balance relation is reduced to an analytic equation allowing eliminating the phonon temperature from the electron heat balance. So far, all models simulated the behavior of the phonon-cooled bolometer based on a cold substrate. If we investigate the case where the substrate would be shortened from 250 micron (typical of Si wafer) to 1 micron (typical of the membrane we use [7]), the heat removal capability of the substrate will then be considerably attenuated. On top of that, as the membrane is very thin, it will be taken into account the phonon diffusion. In the usual substrate-based hot spot model, the equations are set up without the phonon diffusion effect. This paper present the comparison of the behavior of a bolometer, mounted on a thick substrate and on a thin membrane. The differences are due to the phonon-diffusion effect in the membrane, along the strip. Moreover, at the transition between the superconductor and the normal resistive metal (hot-spot), the andreev reflexion occurs. This will be expressed in the equation, by adding a factor in the electron diffusion process.

ANDREEV REFLECTION

At the border between the hot spot and the superconducting parts of the HEB bridge, electrons from the hot spot may only cross into the superconductor when there is a “partner” with suitable impulse to form a Cooper pair. This partner is provided by a formation of an electron-hole pair with appropriate impulse resulting in the transition of the initial electron plus the reflection of a hole. Only those electrons are allowed to pass into the superconductor that has an energy larger than the bandgap. This process is called Andreev reflection. Most of the electrons in the normal conductor have an energy lower than the bandgap. Therefore Andreev reflection provides a good thermal insulation of the hot spot. Recent hot spot model takes into account the Andreev reflection [6]. The bandgap is assumed temperature independent. The Andreev reflection has to be recalculating with the normal-supraconductor interface and the temperature dependency bandgap shape is summarized in Figure 1:

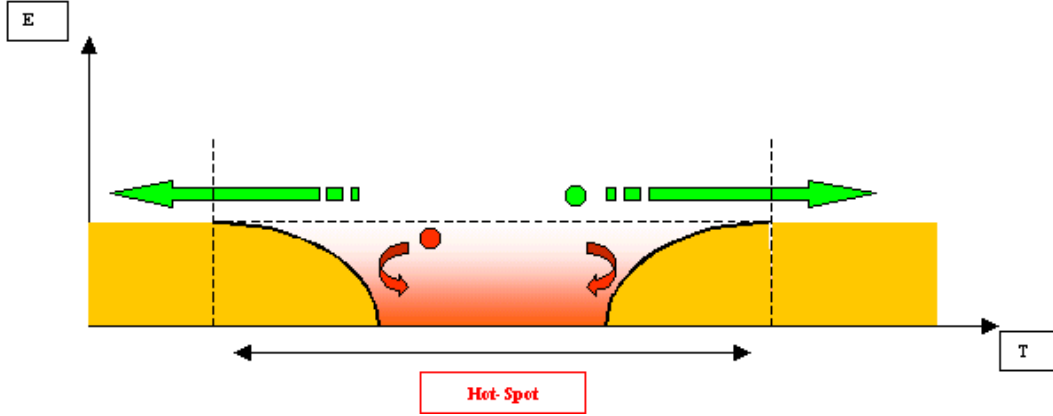


Figure 1: Schematic of a HEB bridge. The whole bridge is heated by RF, the bias heating acts only on the hot spot where superconductivity is suppressed. The electrons are cooled by phonon escape to the substrate and by outdiffusion to the pads. Outdiffusion is reduced by Andreev reflection at the hot spot boundary. We can consider the heat Andreev transmission coefficient as:

$$\alpha = \frac{\int_0^{\infty} \sqrt{E} f(E) n_E(E) dE}{\int_0^{\infty} \sqrt{E} f(E) n_E(E) dE} \quad (1)$$

with :

$$\Delta(T) = \Delta_0 \left[1 - \frac{T}{T_c} \right] ; n_E(E) = n(0) \cdot \frac{E}{\sqrt{E^2 - \Delta^2}} ; f(E) = \frac{1}{1 + e^{E/kT}}$$

As the bandgap energy is temperature dependant, we then have to integrate equation (1) over the temperature, in order to find the Andreev reflexion:

$$\beta = \frac{\int_0^{T_c \Delta(T+\delta T)} \int_{\Delta(T)}^{\infty} \sqrt{E} f(E) n_E(E) dE . dT}{\int_0^{\infty} \sqrt{E} f(E) n_E(E) dE}$$

It is numerically found an Andreev reflexion of 12 %. This Term will be taken into account for the electron diffusion in the film, in the equation (8), by a factor 0.12.

HOT-SPOT MODEL

A hot electron bolometer is a submicronic, ultra-thin (2-3 nm) superconducting micro-bridge, in which the resistive state can be modulated by photon irradiation. The total radiation power, which causes resistance change, can be written as:

$$P(t) = P_{LO} + 2\sqrt{P_{LO}P_S} \cos(\omega_{IF}t)$$

The resistivity depends on the electron temperature. In traditional resistive phonon-cooled bolometers, incident radiation is absorbed by electrons which strongly interact with the lattice atoms. The absorbed energy is therefore quickly transformed into lattice vibrations (phonons). Then, the whole bolometer medium (film and substrate) is being heated up. As illustrated in Fig. 2, there are basically two ways for the heat to be removed from electrons : electron diffusion into the normal-metal electrodes via the film layer ("diffusion-cooling")[3], or scattering via phonons in the substrate layer ("phonon-cooling") [1-2].

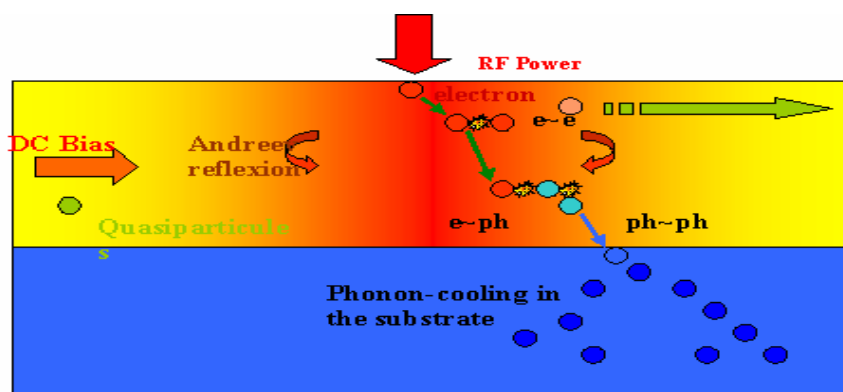


Figure 2: Hot Electron Bolometer is a radiation sensor. Energy absorbed is distributed in the electron subsystems. Heated electrons exchange energy via electron diffusion or via phonon scattering.

The energy removal mechanism can be described in an energy exchange system between electrons of the film, electrons and phonons in the film and between film and substrate phonons. In the substrate-based HEB mixer case, the substrate acts as a heat reservoir. Fig. 3 explains the energy transfer mechanism between the subsystems. The RF power heats up electrons in the film. Those electrons can diffuse in the film, and interact with phonons in the films. The phonons in the film can then interact with phonons of the substrate and remove heat. By describing the energy exchange between the 3 subsystems « electrons », « film phonons » and « substrate phonons », we can derive the heat-balance equation for a bolometer (7).

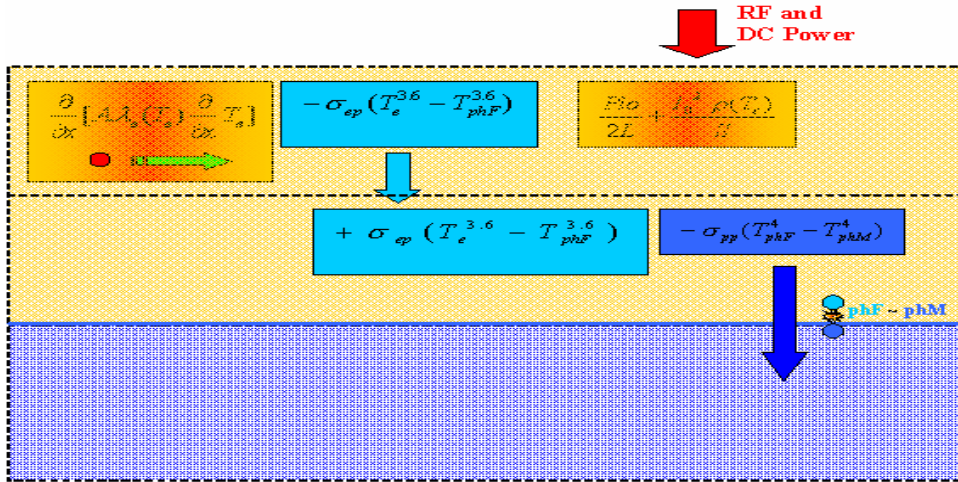


Figure 3: The power exchange subsystems.

λ_e and λ_p are called electron and phonon thermal conductance and g_{ep} is called electron-phonon coupling efficiency.

$$\frac{\partial}{\partial x} \left[\lambda_e(T_e) \frac{\partial}{\partial x} T_e \right] - \sigma_e(T_e^{3.6} - T_p^{3.6}) + \frac{P_{LO}}{2L} + \frac{I_0^2 \rho(T_e)}{S} = 0 \quad (7)$$

$$\sigma_e(T_e^{3.6} - T_{p_{substrate}}^{3.6}) = \sigma_p(T_p^4 - T_{substrate}^4)$$

Solving these equations for electron temperature T_e , assuming a certain electron temperature dependence of the resistivity, gives the I-V curves, mixer gain, and noise temperature curves for substrate-based HEB mixers.

HOT-SPOT MODEL ON MEMBRANE

The HEB is built on a substrate with a thin membrane on it (this will allow us to investigate new quasi-optical injection techniques and designs, for instance to construct compact HEB heterodyne 2D arrays at higher frequencies [8]). The substrate is then removed and only the membrane remains, as seen on Fig.4:

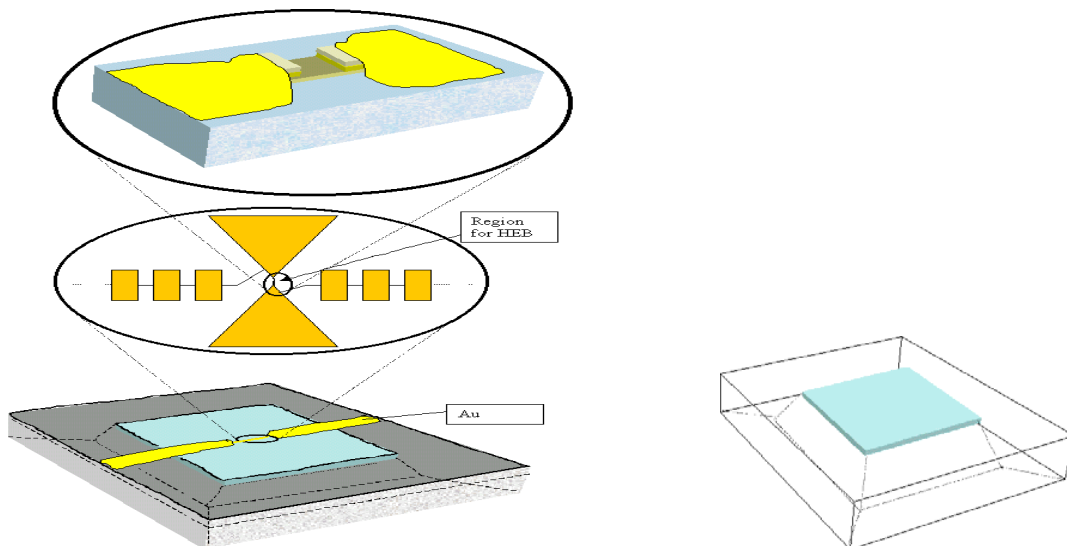
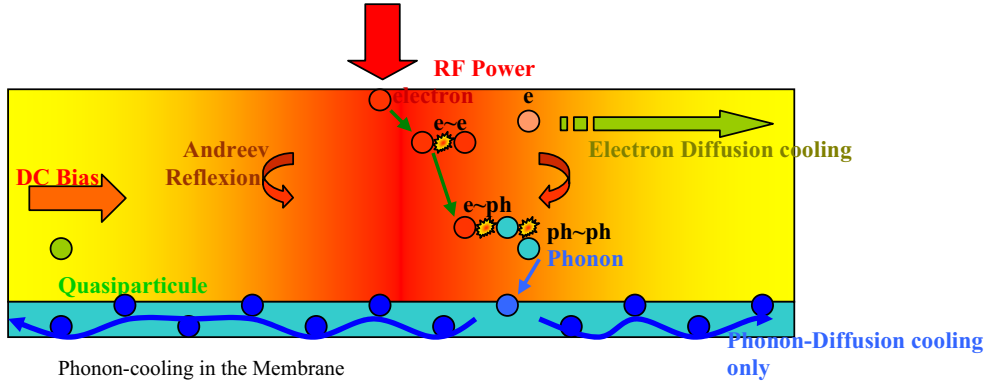
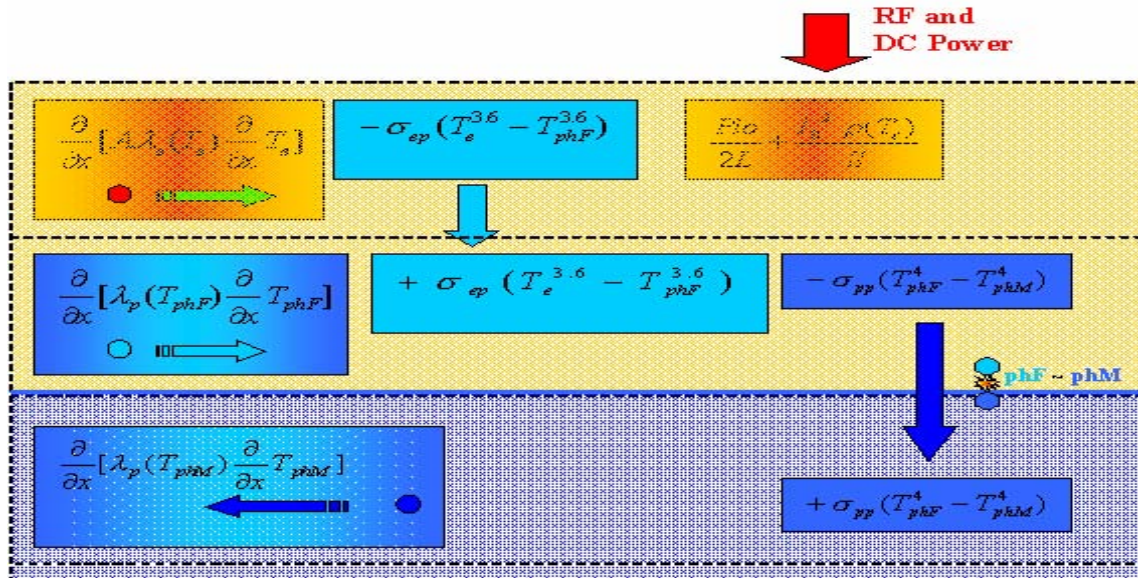


Figure 4 : membrane-based HEB configuration

In the membrane-based HEB device, the substrate has been considerably thinned from 250 micrometers to 1 micrometer. The result can be intuitively seen immediately: the heat reservoir provided by a thick substrate is suppressed and the heat will be mainly removed in the membrane by phonon diffusion along the membrane. The phonons temperature in the membrane will then increase and heat up back the phonons in the film. This effect will increase the electron temperature and then the resistance and the mixer properties.



Equation 7 will then be considerably changed, since it will be taken into account the disappearance of the energy removal by the substrate reservoir and the effect of the phonon diffusion along the membrane, which leads to the subsystems and to equation 8:



$$\left\{ \begin{array}{l} \frac{\partial}{\partial x} \left[A \lambda_e(T_e) \frac{\partial}{\partial x} T_e \right] - \sigma_{ep} (T_e^{3.6} - T_{phF}^{3.6}) + \frac{P_{LO}}{2L} + \frac{I_0^2 \rho(T_e)}{S} = 0 \\ \frac{\partial}{\partial x} \left[\lambda_{phF}(T_{phF}) \frac{\partial}{\partial x} T_{phF} \right] + \sigma_{ep} (T_e^{3.6} - T_{phF}^{3.6}) - \sigma_{pp} (T_{phF}^4 - T_{phM}^4) = 0 \\ \frac{\partial}{\partial x} \left[\lambda_{phM}(T_{phM}) \frac{\partial}{\partial x} T_{phM} \right] + \sigma_{pp} (T_{phF}^4 - T_{phM}^4) = 0 \end{array} \right. \quad (8)$$

Assuming λ proportional to d/L , d being the thickness of the material in which the phonon is diffusing, and L the nanobridge length, we obtain:

$$\frac{\lambda_{phF}}{\lambda_{phM}} = \frac{F}{M}$$

F being the film thickness and M the membrane thickness.

Taking $\lambda_{ph} = \lambda_e/10$, λ_{phF} and λ_{phM} x independent, and assuming T_{phM} and T_{phF} of approximately the same shape and magnitudes:

$$\lambda_{eff} = \frac{\lambda_e}{10} (1 + M/F)$$

Then equations (8) become:

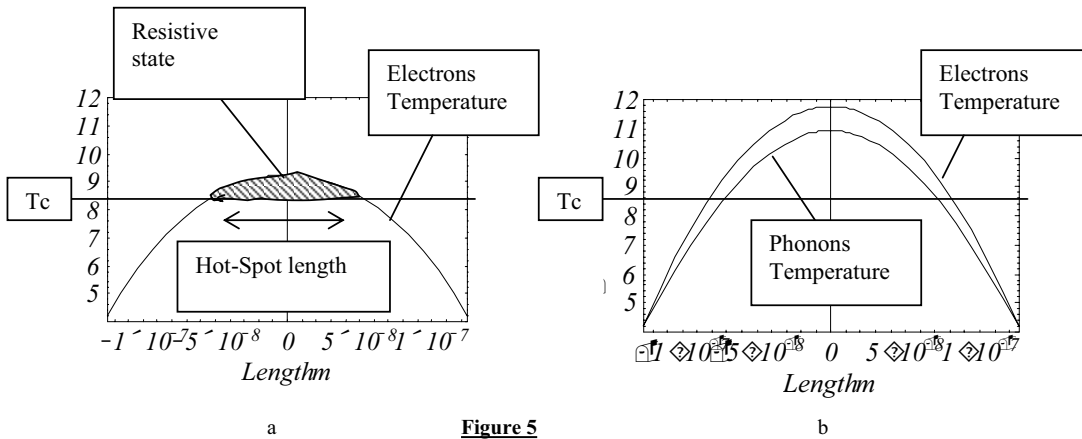
$$\left\{ \begin{array}{l} \frac{\partial}{\partial x} \left[\lambda_e(T_e) \frac{\partial}{\partial x} T_e \right] - \sigma_{ep} (T_e^{3.6} - T_{phF}^{3.6}) + \frac{P_{LO}}{2L} + \frac{I_0^2 \rho(T_e)}{S} = 0 \\ \frac{\partial}{\partial x} \left[\lambda_{p,eff}(T_{phM}) \frac{\partial}{\partial x} T_{phM} \right] - \sigma_{ep} (T_e^{3.6} - T_{phM}^{3.6}) = 0 \end{array} \right. \quad (9)$$

In order to compare the results with the same model and to see the effect of the phonons diffusion along the membrane, we will see the substrate as a very thick membrane of 300 μm . The thickness of the membrane will be taken as 1 μm , and other parameters as follow:

Parameter	$\lambda_e(T_e)$	σ_{ep}	Rn	δT
Value	$6.10^{-18} \cdot T_e^3$	$5.6.10^{-4}$	50	0.1
Dimension	Wm/K	W/(mK ^{3.6})	Ω	K

Membrane effect

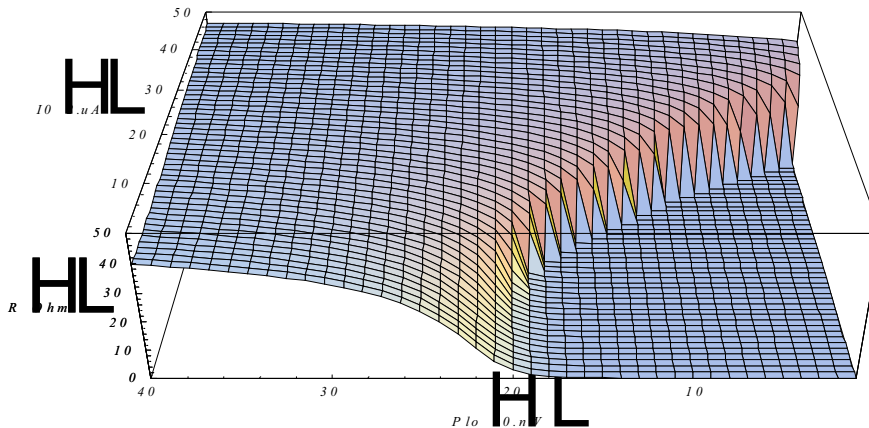
Solving the two nonlinear coupled heat balance equations (9) derived for the membrane-based HEB case, we obtain on Fig. 5 the film electron temperature profile (a) and the film phonon temperature profile (b). The part of the superconducting film, which becomes normal due to heated electrons, is called the "hot spot".



It is clearly shown in fig.5 that the minimization of the substrate, which usually acts as an energy acceptance reservoir, now increase the electron temperature profile of the film. In clear, the phonon will heat up the electron in the film. Indeed, the superconducting nanobridge will need less microwave power irradiation to be driven into the resistive state. Then, the sensitivity of the membrane-based HEB mixer should be higher.

Hot-spot length comparison

As we've just seen, less irradiation power is needed in case of a membrane. We plotted on Fig.6 the Hot-spot length versus P_{lo} and P_{dc}



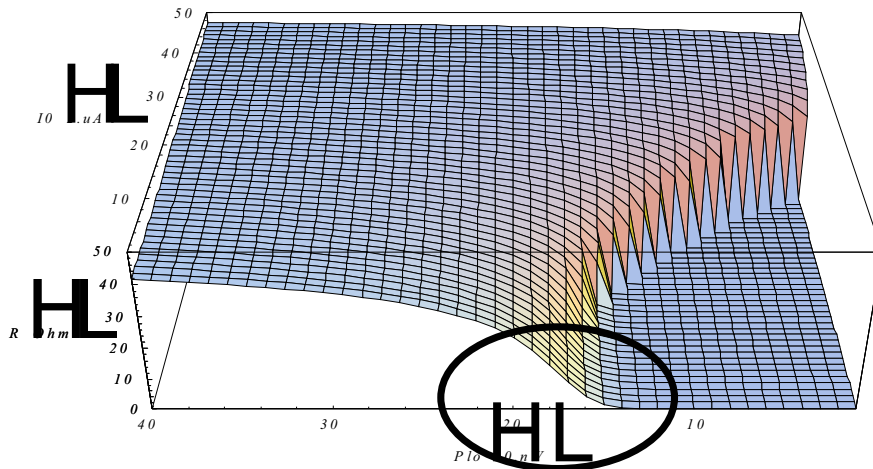


Figure 6: comparison of Hot-spot length, with respect to substrate or membrane cases.

Here is shown that the hot-spot start to be formed at less P_{10} and P_{dc} , as we expected. While the HEB built on substrate show a hot-spot start at around 220 nW, the membrane-based HEB show it at 170 nW.

I-V curves comparison

The results presented show the model works well with the addition of the phonons diffusion term. I-V curves are obtained in both the thick substrate and membrane (see Fig. 7 and 8). As expected, since the hot-spot will be formed “earlier” with the membrane, less LO power (P_{10}) will be needed at fixed DC power (P_{dc}), in the membrane-based HEB case, to produce the same pumped I-V curve.

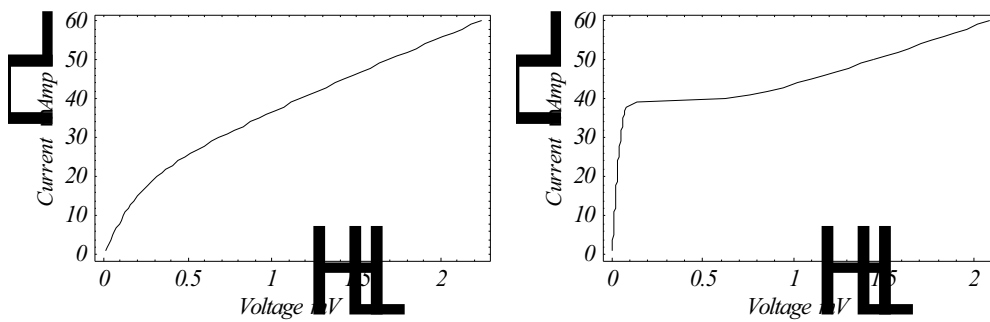


Figure 7: a) IV, 220 nW P_{10} , thick substrate

b) I-V, 190 nW P_{10} , thick substrate

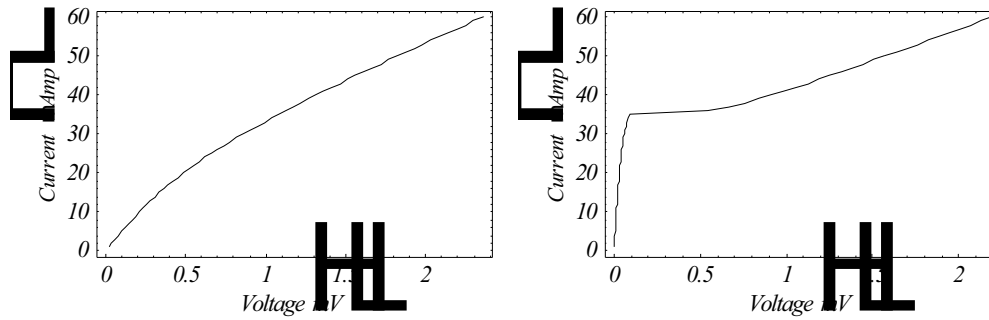


Figure 8: a) I-V, 190 nW P_{lo} , membrane

b) I-V, 150 nW P_{lo} , membrane

Then, theoretically, less LO power will be needed to pump the I-V curve for the HEB on membrane and reach the optimum curve.

Gain curves comparison

The Gain(V) curves depend as well on the Hot-spot formation. Gain curves have been plotted in Fig.9, for both the thick substrate and the membrane cases.

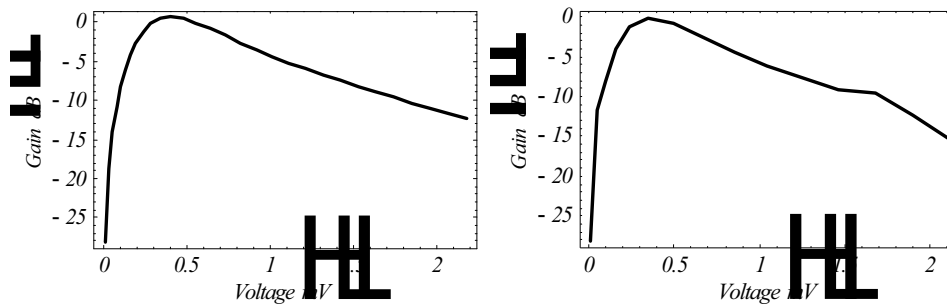


Figure 9: a) substrate, 220 nW P_{lo}

b) membrane, 173 nW P_{lo}

It is shown again that similar curves are obtained for different LO powers, due to the membrane effect. Indeed the hot spots are approximately identical but are formed at different power irradiations, hence giving identical results for different LO powers.

Simulation of the behavior of the gain curves while increasing the irradiation power is described in Fig. 10.

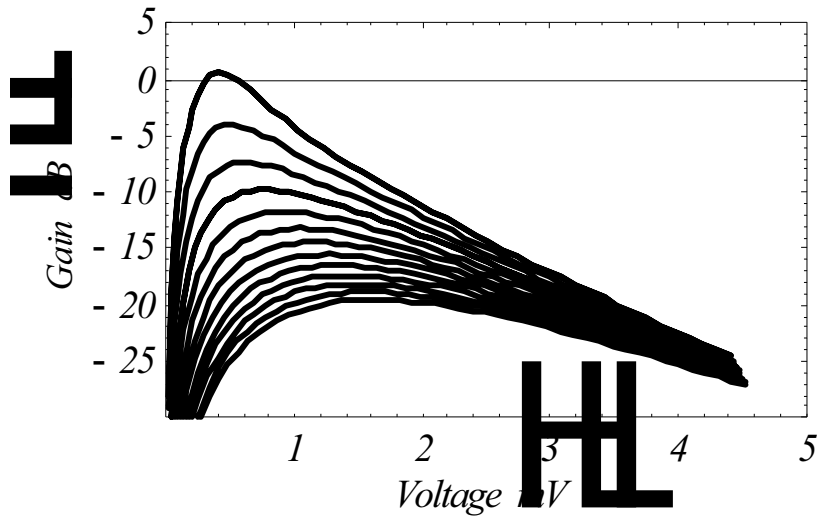


Figure 10: Gain curves for increased LO power

As we can see, the maximum of the gain curve decrease as we increase the LO power. We can see this effect on Fig. 11 for the membrane on the thick substrate and then are able to compare the two curves.

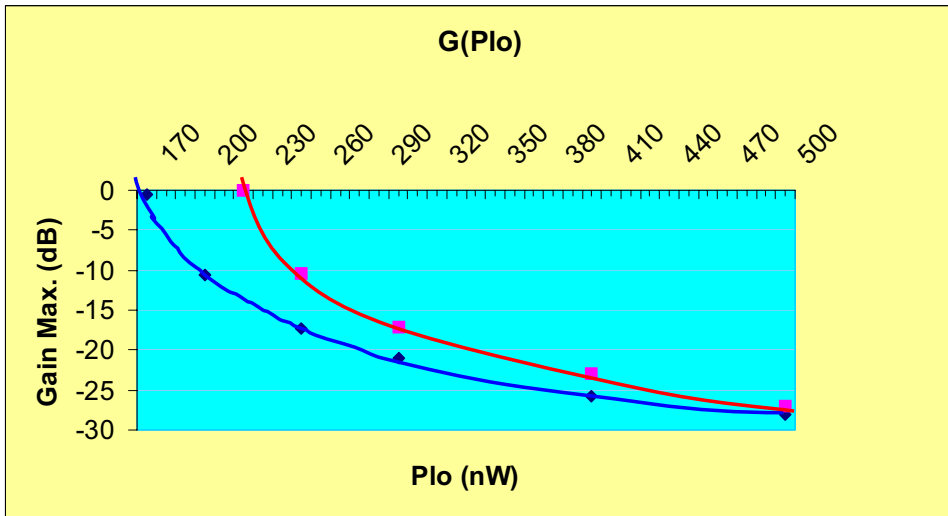


Figure 11: maximum gain Vs Plo for membrane, maximum gain Vs Plo for substrate

The two curves present approximately the same behavior, again due to the fact that all those curves are mainly hot-spot length dependant. Nevertheless, they converge for high Plo.

For a fixed gain, less power will be needed in the membrane case. It means that the substrate cools too much the film, below 220 nW of Plo, to see a hot-spot to form. But, as the phonons in the membrane, due to the diffusion along the membrane, heat up the electrons in the films, the hot-spot will be able to form at 170 nW, showing as well a gain at this irradiation power.

From the curves of fig. 11, we can calculate the difference of Plo needed to obtain the same maximum gain, with respect to different membrane thicknesses. (we find for instance a difference of Plo of 4% between a membrane of 1 μm and a substrate of 250 μm)

Further calculation are depicted in Fig. 12.

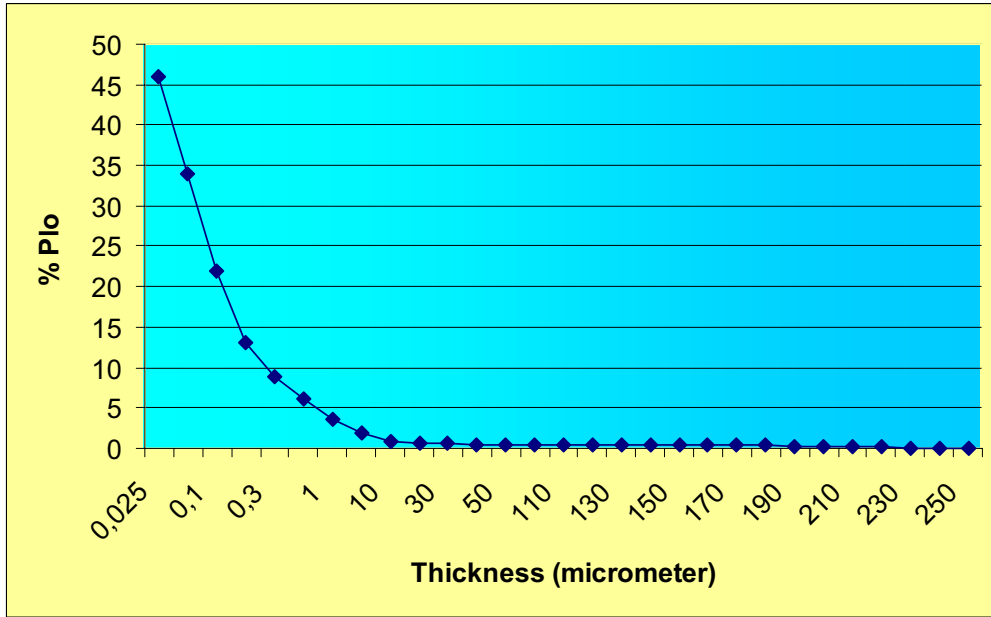


Figure 12: %Plo gained between substrate and membrane

A percentage of 20 % could be achieved with a membrane thickness of 0.25 μm , which seems to be processable. To summarize, irradiation power can be gained by reducing the membrane thickness below 1 μm . As the cooling mechanism will be less efficient, the IF bandwidth should be affected (since the time taken by the substrate to remove the heat from the film will be shorter). Above this limit, a phonon-cooled HEB should work as well as on a normal substrate.

Noise Temperature curves comparison

We want here to check the model behavior by simulating the noise temperature curves for both cases. We expect to find same curve for different Plo. Indeed, that result is similar that finding the noise temperature higher in the membrane case for a fixed Plo .

Those assumptions are verified on Fig.13.

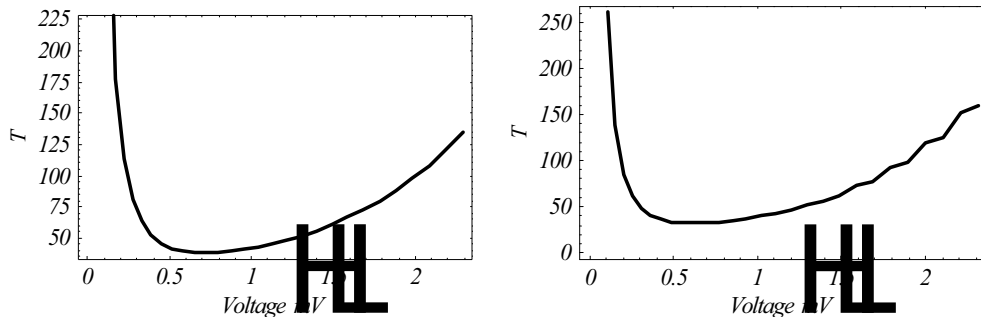


Figure 13: a) 250 nW, thick substrate

b) Membrane, 195 nW

CONCLUSION

On the basis of our simulations, we can foresee a normal behavior for a phonon-cooled HEB based on a thin membrane, provided that the membrane thickness is not smaller than 1 μm . For those thicknesses, even the IF bandwidth shouldn't been affected, since the membrane still removes the heat as fast as would a thick substrate. Below 1 μm , however, the IF bandwidth might be affected. Nevertheless, mixer sensitivity will then improve and less LO irradiation power will be needed to reach the same gain and noise temperature, compared to the thick substrate case. This is a worthy consideration since LO power generation remains a technological challenge at the very high (above 1 THz) frequencies where HEB mixers are to be used increasingly. Moreover, the absence of dielectric close to the antenna permits to avoid the use of a lens and to investigate new quasi-optical injection techniques and designs, such as planar diffractive optics or focusing mirrors, for instance to construct compact HEB heterodyne 2D arrays at higher frequencies. Smaller optics loss is also beneficial with respect to improving the overall HEB receiver noise temperature.

REFERENCES

- [1] E.M Gershenson, G.N Gol'tsman, IG Gogidze, Y.P Gusev, A.I Elant'ev, B.S Karasik, A.D Semenov, *Millimeter and submillimeter range mixer based electronic heating of superconducting films in the resistive state*, superconductivity 3(10), (1990), p1582.
- [2] B.Karasik, G.N Gol'tsman, B.M Voronov, S.I Svechnikov, E.M Gershenson, H. Ekstrom, S. Jacobsson, E. Kollberg, K.S Yngvesson, *hot electron quasioptical NbN superconducting mixer*, IEEE Trans. Appl. Supercond. 5(2), (1995), p2232.
- [3] D.E Prober, *superconducting terahertz mixer using a transition-edge microbolometer*, Appl. Phys. Letter 62(17), (1997), p2119.
- [4] Hans Ekström, Boris Karasik, Erik Kollberg, "Conversion Gain and Noise of Niobium Superconducting Hot Electron Mixers", IEEE Trans. Microwave Tech. Vol.45 #4 ,(April 1995) pp.938-946
- [5] Harald F. Merkel, Erik L. Kollberg, K. Sigfrid Yngvesson, "A Large Signal Model for Phonon-Cooled Hot Electron Bolometric Mixers for THz Frequency Applications", Proceedings of the 9.th Space Terahertz Symposium, Pasadena, CA (March 1998),pp 81-97
- [6] Harald F. Merkel, « A hot spot model for HEB mixers including Andreev reflexion », Proceedings of the 13.th Space Terahertz Symposium, Cambridge, Massachusetts (March 2002), p 53-64.
- [7] P.Pons, K.Grenier, L.Rabbia, T.Parra, R.Plana, P.Gaudriller, P.Combes, O.Pascal, H.Aubert, A.Takacs, M.Salez, G.Goltsman, *Membrane Supported Circuits for Millimetric and Sub-millimetric Wavelength*, 26th International Conference on Infrared and Millimeter Waves (IRMMW'2001), 10-14 September, Toulouse, France
- [8] J.Baubert, M.Salez, Y. Delorme, P.Pons, G.Goltsman, H. Merkel, B. Lecomte, *Membrane-based HEB mixer for THz applications*, Proceedings of the SPIE international symposium on microtechnologies for the new millennium 2003, gran canaria, Spain..

Noise and Gain Performance of spiral antenna coupled HEB Mixers at 0.7 THz and 2.5 THz.

K.V. Smirnov, Yu.B. Vachtomin, S.V. Antipov, S.N. Maslennikov,
N.S. Kaurova, V.N. Drakinsky, B.M. Voronov, G.N. Gol'tsman
Physics Department, Moscow State Pedagogical University, Moscow 119992,
Russia.

A.D.Semenov, H.Richter, H.-W.Hübers.
DLR Institute of Space Sensor Technology, D-12489 Berlin, Germany

Abstract

Noise and gain performance of hot electron bolometer (HEB) mixers based on ultrathin superconducting NbN films integrated with a spiral antenna was studied. The noise temperature measurements for two samples with different active area of $3 \mu\text{m} \times 0.24 \mu\text{m}$ and $1.3 \mu\text{m} \times 0.12 \mu\text{m}$ were performed at frequencies 0.7 THz and 2.5 THz. The best receiver noise temperatures 370 K and 1600 K, respectively, have been found at these frequencies. The influence of contact resistance between the superconductor and the antenna terminals on the noise temperature of HEB is discussed. The noise and gain bandwidth of 5GHz and 4.2 GHz, respectively, are demonstrated for similar HEB mixer at 0.75 THz.

Introduction

The radioastronomic observations require heterodyne receivers that are able to register weak emission lines associated with rotation and vibration transitions in the molecules of the far galaxies. Available local oscillators (LO) at frequencies above 1 THz are not tunable enough and have low output power. Therefore, a heterodyne detector designed for these frequencies should have wide intermediate frequency (IF) band and should require small LO power. The most suitable receiver for the frequencies above 1 THz is the receiver based on NbN phonon cooled HEB mixer. The IF gain bandwidth of such a mixer achieves 5 GHz [1,2]. At the 2.5 THz LO frequency, the best measured value of the double side band (DSB) noise temperature is 1100 K at $T=2$ K and 1400 K at $T=4.2$ K [2]. Authors of the Ref. 2 used 3.5 nm thick NbN films deposited on MgO substrate. This material is not stable enough for radioastronomic applications. The purpose of this paper is to measure the noise and gain characteristics within one batch of mixers based on superconducting 3.5 nm thick NbN films grown on Si substrate with MgO buffer layer. Such films show much better superconducting properties than NbN films grown on either Si or MgO substrates. In this paper we present the results of the noise temperature and gain bandwidth measurements of NbN HEB mixer at the LO frequencies 0.7 THz and 2.5 THz.. We also discuss the effect of the mixer dimensions on its noise temperature.

Device design and fabrication.

The HEB mixers were manufactured from superconducting NbN film on Si substrates with MgO buffer layer. MgO buffer layer 200 nm thick was deposited by

e-beam evaporation from MgO pellet. The substrate temperature during the MgO deposition process was about 400 °C.

Ultrathin NbN films have been deposited by reactive dc magnetron sputtering in the Ar + N₂ gas mixture. The maximum values of the critical film parameters (T_c and j_c) are reached at the Ar partial pressure of 5×10^{-3} mbar, the N₂ partial pressure of 9×10^{-5} mbar, the discharge current value of 300 mA, the discharge voltage of 300 V and the substrate temperature 800 °C. The deposition rate was 0.5 nm/s. It was defined as ratio of the film thickness, measured with a Talystep profilometer-profilograph, and its deposition time. The film thickness was 3.5 nm and determined by deposition rate. The quasioptical mixer was made by lift-off e-beam lithography and photolithography. The 0.12 μm and 0.24 μm long bolometers were formed by lift-off e-beam lithography across the gap between two Ti-Au (Ti ~ 3 nm, Au ~ 30 nm) small contact pads. The width of bolometers, 1.3 μm and 3.0 μm, respectively, was formed by SiO mask (SiO ~ 70 nm) made by one more e-beam lift-off process. The central part of self-complementary spiral antenna was formed using lift-off e-beam lithography based on Cr-Au metallization (Cr ~ 5 nm, Au ~ 70 nm). SEM images of the central part of the devices are shown in Fig. 1. The next process was the fabrication of the outer part of the mixer by lift-off photolithography based on Ti-Au metallization (Ti ~ 5 nm, Au ~ 200 nm). The last process was the removing of the NbN layer by ion milling in Ar atmosphere from the whole surface of the substrate except the central part of spiral antenna which was protected by SiO mask.

Typically, mixers based on 3.5 nm thick NbN films on silicon substrates with MgO buffer layer have a superconducting transition temperature between 10 K and 11 K.

Experimental setup

Experimental setup for noise temperature measurements at 0.7 THz and 2.5 THz is presented in Fig. 2. The hyper-hemispherical lens fabricated from high-resistivity silicon with a HEB positioned on the flat side of the lens were mounted on a copper holder which in its turn was tightly bolted to the 4.2 K cold plate of an Infrared Labs HD-3 LHe cryostat. The cryostat has a wedged 1.5 mm thick TPX pressure window. A 1.2 mm thick quartz window with an antireflection coating was mounted on the 77 K shield. This filter has a cut-off frequency exceeding 6 THz. The intermediate frequency (IF) signal was guided out of the HEB via a 50 Ω coplanar line, which was soldered to SMA connector. A bias tee followed by an isolator was used to feed the bias to the mixer and to transmit the IF signal to a low noise (<3 K) 1.2-1.8 GHz HEMT amplifier (36 dB gain at 1.5 GHz). The bias tee, the isolator and the amplifier were also mounted on the cold plate of the cryostat. The output of the amplifier was filtered at 1.5 GHz with a bandwidth of 75 MHz, further amplified and finally rectified with a crystal detector. The measurements at 0.7 THz and 2.5 THz were performed using an optically pumped FIR ring laser [3]. The ring laser design prevents back-reflection of CO₂ pump radiation from the FIR cavity into the CO₂ laser cavity resulting in a stable output power of the FIR laser. Out-coupling of FIR radiation was performed through a 3 mm diameter hole in one of laser mirrors.

The LO radiation was focused onto the HEB mixer by two high-density polyethylene lenses. In order to monitor the LO output power a wire grid in the LO

beam path reflected a minor fraction of the LO radiation into a pyroelectric detector. A second, rotating wire grid served for attenuation of the LO power delivered to the HEB. The signal and the LO beam were superimposed by a 6 μm thick Mylar beamsplitter.

DSB receiver noise temperatures were determined by the Y-factor method. Ecosorb was used as the hot and cold load. The temperature of the hot and cold load was 293K and 77K, respectively. The stability of the laser systems was good enough to measure the noise temperature by putting alternately the hot load and the cold load in the signal path behind the beamsplitter. The optical path from the load to the pressure window of the cryostat was about 25 cm long. The hot and cold reading was averaged by a computer and the Y-factor as well as the noise temperature were calculated. The noise temperature was also measured by chopping (frequency 15 Hz) between the hot and cold load using lock-in technique. It was verified at the other frequencies that the direct technique and chopping technique yield the same result.

For bandwidth measurements we used an The gain and noise temperature bandwidths were measured by experimental setup similar to the one shown in Fig. 2. A backward wave oscillator OB-39 served as a local oscillator at 0.75 THz. LO radiation was focussed by Teflon lens, near infrared background radiation was filtered by 350 μm thick Zitex foil. In the IF bands 1.3 - 1.7 GHz and 4.4 – 5.2 GHz, IF signal can be amplified by two HEMT amplifiers did not noticeably contribute in the receiver noise temperature. Outside these bands, the measured receiver noise temperature was corrected for amplifier noise.

Experimental results and discussion

Below we discuss results obtained for two devices. The mixer L310(#5) had the planar dimensions (length x width) 0.24 μm x 3 μm wide and showed the best noise temperatures of 370 K and 1600 K at LO frequencies of 0.7 and 2.5 THz, respectively. The device L391(#23) with the dimensions 0.12 μm x 1.3 μm had the noise temperature 2200 K at 2.5 THz. We should admit that the noise temperature of the device L310(#5) - 370 K at 0.7 THz - was measured with the silicon lens whose antireflection coating was optimized for 2.5 THz. Thus, the noise temperature can be further decreased using the antireflection coating with appropriate thickness. We should admit that the improvement of the noise temperature with the increase of the bolometer width was found for all batches of mixers that we have studied. The essential difference between the noise temperature values can be understood taking into account additional to the bolometer itself contact resistance contributed by contact areas between the gold antenna and the thin NbN bolometer (Fig.3). Contact resistance between NbN film and metallization is most likely due to residue of photolack used in the lift-off process and/or to oxidization of the NbN film between film and contact deposition. In order to clean the surface of the NbN film right before the contact deposition, we use plasma etching in O_2 . Among other cleaning methods, this one results in the lowest contact resistance. of the structure. However, this process can increase oxidization depth of the NbN film.

In comparison to gold metallization, the 3.5 nm thick NbN is a bad conductor for high-frequency (RF) current. Therefore, when gold is present on the top of the NbN film, RF current flows mostly through gold. This current enters the bolometer within contact areas having the length d (see Fig. 3). The dimensions of this contact

areas determine the magnitude of the additional resistance. Both the contact resistance itself and the resistance of two additional portions of the NbN film forming the contact area dissipate part of the RF current and thus decrease radiation coupling. This impacts the noise temperature.

Our results show that the additional resistance contributed by the contact areas decreases when the width of the bolometer increases. Such tendency was found by analyzing several batches of devices with different width. In order to keep the bolometer impedance and the IF match unchanged it is also necessary to increase the bolometer length. Thus, the noise temperature of a HEB mixer can be improved by increasing the size of the bolometer size. However, the increase of the mixer dimensions cause the increase of the required LO power. Since output power of multiplied solid-state radiation sources drops with frequency, it may be not sufficient to optimally pump a large device. That is why the general way to improve the noise performance of the mixer is to decrease the contact resistance between the metal antenna and the bolometer without increasing its dimensions. The most prospective process of ohmic contact formation is in situ gold deposition. However, there are difficulties in removing gold from the bolometer. We consider that the difference of the mixer noise temperature over the batch is first of all determined by the spread in values of additional resistance. Moreover, because of film non-uniformities at the submicron scale, submicron bolometers that nominally have the same dimensions may not have the same resistance. This also causes spread in the noise characteristics within the batch.

We also measured the noise and gain bandwidths of the mixer L310(#7) at the LO frequency of 0.75 THz. The mixer showed the noise temperature of 840 K at the intermediate frequency about 1 GHz. To measure the noise temperature of this mixer we used two HEMT amplifiers that brought the negligible contribution to the noise characteristics of the receiver in the IF ranges of 1.3-1.7 GHz and 4.4-5.2 GHz. Outside these bands the noise of the receiver was effected by amplifier noise. To obtain complete IF frequency dependence of the mixer noise temperature we carried out the measurements in a wider frequency range and corrected the result for frequency dependent noise temperature of the amplifier and their effect on the system noise temperature. The corrected mixer noise temperature dependence is shown in Fig. 4. The noise temperature bandwidth of the mixer was about 5 GHz. The gain bandwidth of the mixer (Fig. 5) was about 4.2 GHz that was the typical value for the mixers based on the 3.5 nm thick NbN film.

Conclusion

The contact resistance appearing at the boundary between the superconducting bolometer film and contact metallization impacts the noise temperature of HEB mixers. One possibility to decrease the contact resistance and improve noise performance of the receiver is an enlargement of the mixer working area that is the bolometer itself. The enlargement of the working area from $1.5 \times 0.12 \mu\text{m}^2$ up to $3 \times 0.24 \mu\text{m}^2$ cause a decrease of the noise temperature from 2200 to 1600 K at LO frequency of 2.5 THz. However the required LO power is also increased along with enlargement of the mixer working area, that is unacceptable for wide range of the applications because available power from multiplied solid state sources decreases at the terahertz frequencies. At frequencies above 2 THz, antenna geometry also limits

dimensions of the bolometer. Further improvement of HEB mixers is connected with development of the technology which would allow us to decrease the impact of contact resistance between the superconductor and contact metallization.

Acknowledgment

This work was supported by INTAS-ESA grant 99-0569 and INTAS-YSF grant 2002-408, as well as grants of Ministry of science and technology of Russian Federation (contracts numbers are 40.031.1.1.1187 and 40.012.1.1.1355).

References

1. S. Cherednichenko, M. Kroug, P. Khosropanah, A. Adam, H. Merkel, E. Kollberg, D. Loudkov, B. Voronov, G. Goltsman, H. Richter, H.-W. Hubers, "A Broadband Terahertz Heterodyne Receiver with an NbN HEB Mixer", 13th Int. Symp. on Space THz Techn., 2002
2. Y.B. Vachtomin, M.I. Finkel, S.V. Antipov, B.M. Voronov, K.V. Smirnov, N.S. Kaurova, V.N. Drakinski, G.N. Gol'tsman "Gain bandwidth of Phonon-Cooled HEB Mixer made of NbN Thin Film with MgO Buffer Layers on Si", In 13th Intl. Sym. On Space Terahertz Technology, pp. 259-270, Cambridge, MA, 2002.
3. H.-W. Huebers, G.W. Schwaab, H.P. Roser Proc. 30th ESLAB Symp. "Submillimetre and Far-Infrared Space Instrumentation", ESA SP-388, p. 159(1996).

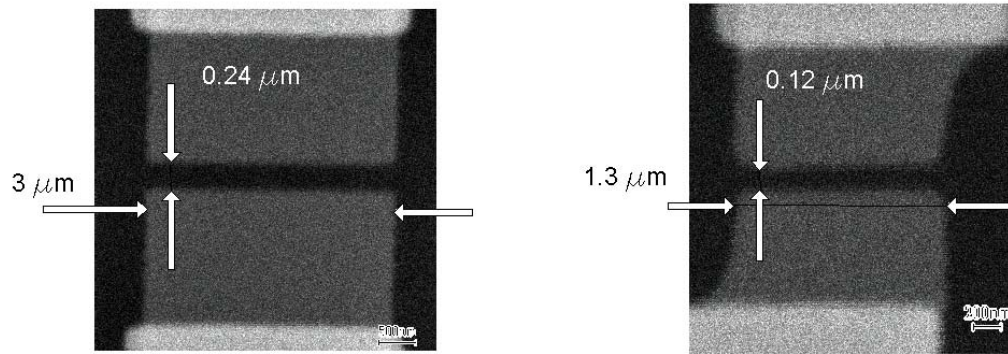


Fig. 1 SEM image of the central part of the spiral antenna.

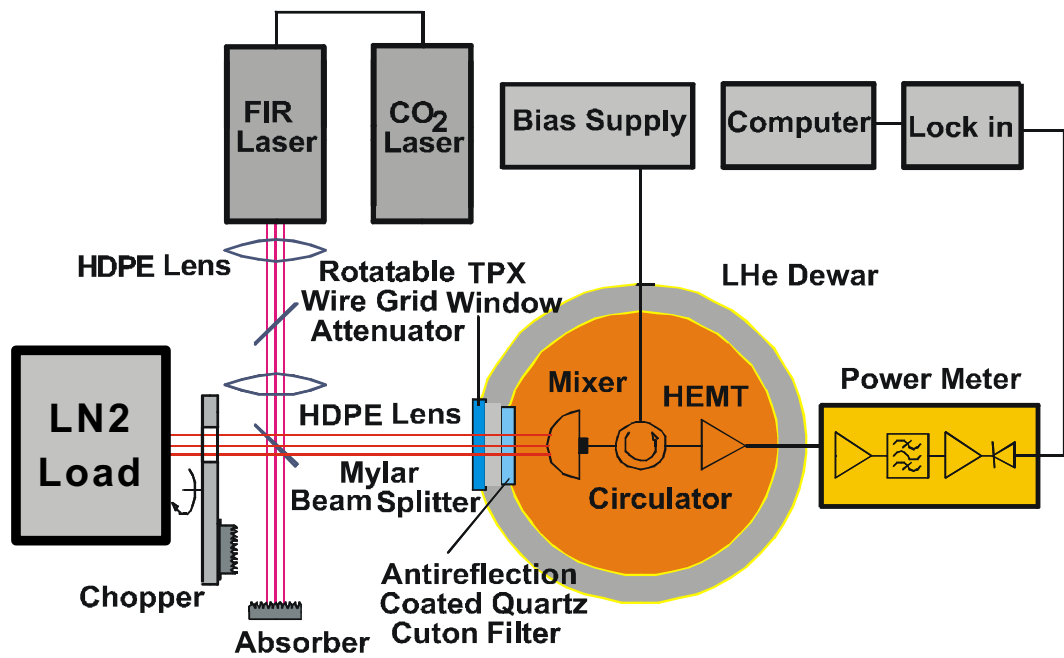


Fig. 2 Schematics of the experimental setup used for noise temperature measurements.

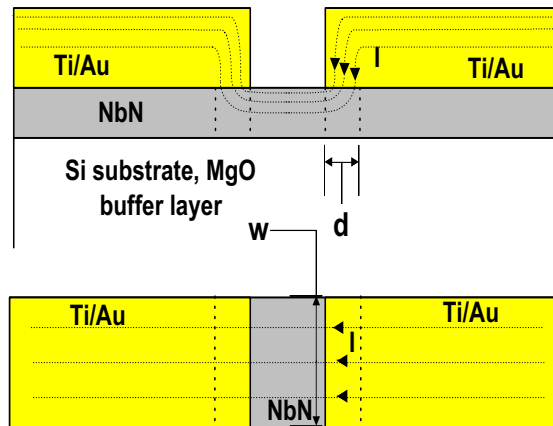


Fig. 3 Location of contact areas between the bolometer and antenna terminals. Shown is the current redistribution resulting in the excess contact resistance.

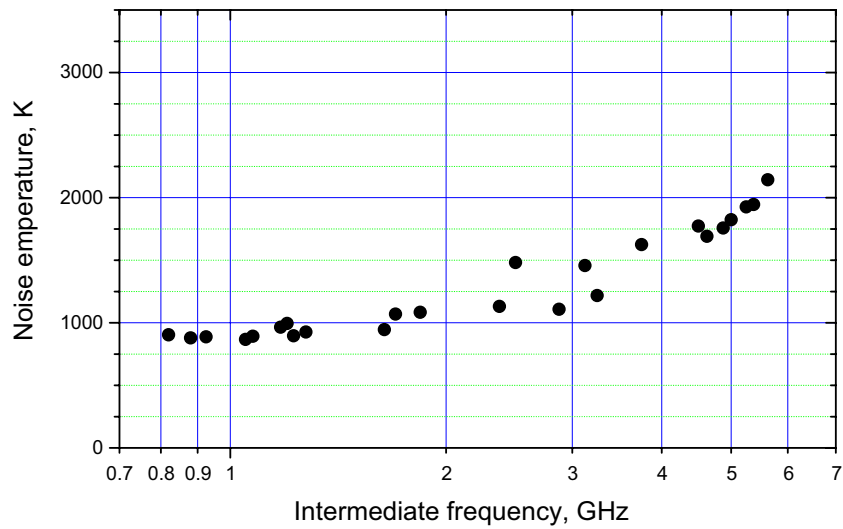


Fig. 4 Noise temperature vs. intermediate frequency for device L310(#7).

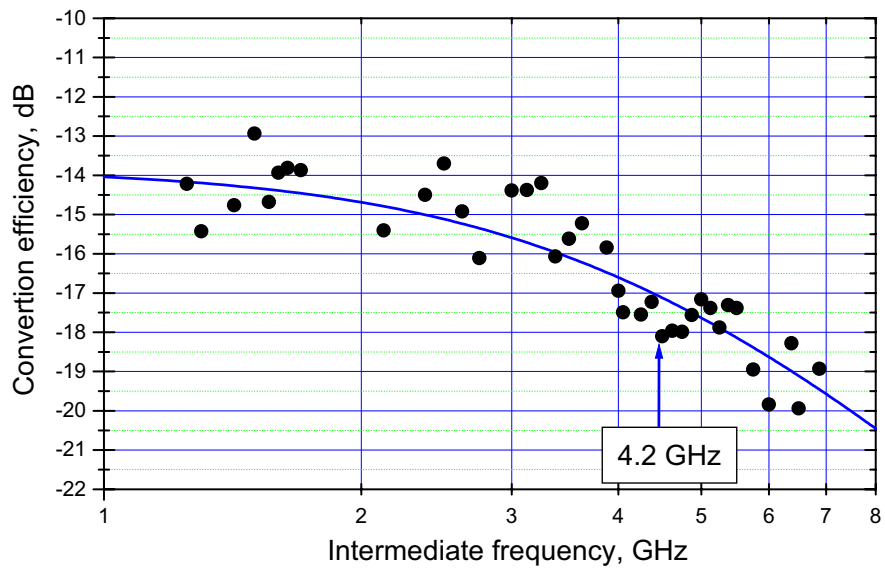


Fig. 5 Gain vs. intermediate frequency for device L310(#7).

Improved NbN Phonon Cooled Hot Electron Bolometer Mixers

M.Hajenius^{1,2}, J.J.A. Baselmans², J.R. Gao^{1,2}, T.M. Klapwijk¹, P.A.J. de Korte², B. Voronov³
and G. Gol'tsman³

¹Department of Nanoscience, Delft University of Technology, Lorentzweg 1, 2628 CJ Delft, The Netherlands.

²Space Research Organisation Netherlands, Sorbonnelaan 2, 3584 CA Utrecht, The Netherlands

³Moscow State Pedagogical University, Moscow 119435, Russia.

Abstract

NbN phonon-cooled hot electron bolometer mixers (HEBs) have been realized with negligible contact resistance to Au pads. By adding either a 5 nm Nb or a 10 nm NbTiN layer between the Au and NbN, to preserve superconductivity in the NbN under the Au contact pad, superior noise temperatures have been obtained. Using DC I,V curves and resistive transitions in combination with process parameters we analyze the nature of these improved devices and determine interface transparencies.

1. Introduction

Currently, for frequencies beyond 1 THz, superconducting hot electron bolometers (HEB's) appear to be the only option for low noise heterodyne mixing elements. Phonon-cooled HEB's, based on thin superconducting NbN with a fast electron-phonon cooling time, are particularly promising because they combine a high sensitivity with a reasonably large intermediate frequency (IF) roll-off [1-6]. However, these detectors have not yet reached the ultimate sensitivity limit set by quantum noise: $\hbar\omega/k_b$, in which \hbar is Plank's constant, ω the angular frequency, and k_b is Boltzman's constant. Further progress, both theoretically and experimentally, is critically dependent on a proper understanding of the device-operation. Originally it was proposed that these devices would exploit the strong temperature dependence of the resistive transition. However, it has become clear that both diffusion-cooled and phonon-cooled devices are based on an electronic hot spot, formed because they are biased with a relatively high DC current. This resistive electronic hot spot of variable length has been identified as the source of the mixing process.

In a HEB the active superconducting material is in direct contact with an antenna structure, which also serves as electrodes for the dc bias. To minimize losses at the high frequencies a high conductivity normal metal, such as gold, is used. In a series of experiments we have recently learnt that improved mixing-performance can be realized by focusing on improved contacts between the NbN, optimized for phonon-cooling, and the Au electrodes. If an intermediate layer of Nb or NbTiN is inserted between the active NbN and the Au significantly better noise temperatures are reached. To date best receiver noise temperatures of *1000 K @ 2.5 THz* have been obtained with a device with a NbTiN intermediate layer. Details of the RF measurements can be found elsewhere [8].

In this paper we describe the various contacts we have developed and studied based on the DC I,V curves and resistive transitions. To understand the critical temperature of the different multi-layers appearing in the different contact structures we use a proximity-effect model for bi-layers [9].

2. Devices with different contacts

The NbN HEBs are based on a 3.5 nm thick NbN film on a Si substrate, produced at Moscow State Pedagogical University. These films, optimized for phonon-cooling, have a sheet resistance of 635 Ω , measured at 300 K, and after subsequent fabrication steps a T_c of ~ 9.9 K. The layout of a mixer together with a cross section of the contact structure is shown in Fig. 1. A spiral antenna of 120 nm thick Au (layer 1 in Fig. 1) is used to couple the RF and DC signal into the superconducting bridge. The connection between the bolometer itself (3) and the antenna is made by the contact structure, consisting of a gold layer (“2”) and an intermediate layer (“4”) on top of the NbN film. The intermediate layer consists of either a normal metal (Ti) as an adhesion layer or a superconductor (Nb or NbTiN). The latter is to avoid a proximity-effect induced destruction of the superconductivity in the NbN under the Au. Typical dimensions of the bridge are 4 μm in wide and 0.4 μm in length, measured between the contact-pads, the part of the NbN uncovered by any contact layer.

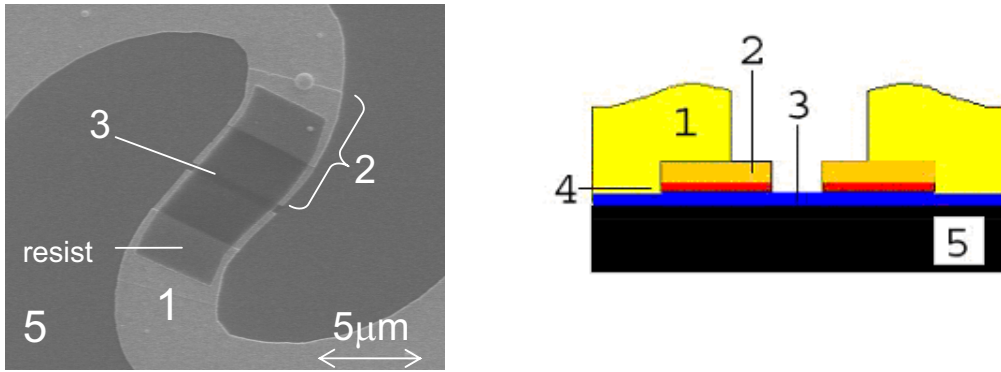


Figure 1. Spiral antenna coupled NbN HEB devices. On the left a SEM picture of the top view of a device and on the right a cross section of the device. “1” indicates the Au spiral antenna structure which is ~ 150 nm thick; “2” the Au layer on the contact pads; “3” the superconducting NbN film, which extends underneath the contact layer/antenna; “4” the intermediate layer between the Au and the NbN film; “5” the Si substrate.

The thin optimized NbN films have to become part of the antenna-structure. It was found [10] that they suffer from irreproducible contact resistances due to a native oxide or other surface contaminants on the NbN film. A short Ar^+ physical etching step is applied to remove such a contamination layer. To find an optimal recipe for the best contacts various experiments have been executed using the more readily available NbTiN layers. Fig. 2 shows the results of an Ar^+ etch calibration curve using a freshly made NbTiN thin film. The devices have been artificially contaminated by applying an O_2 plasma for 15 sec. Fig. 2 clearly shows, that an Ar^+ etch during more than 10 sec helps to reduce the contact resistance. These data are not yet conclusive because we could not deposit the subsequent the Ti/Au layer in the same vacuum system, where the Ar sputter etch is performed. Hence, the remaining resistance could be due to the brief exposure of the freshly cleaned film to ambient pressure. We should also point out that applied to a NbN film an Ar etch of 5 seconds already leads to a reduction of T_c by 0.5 K.

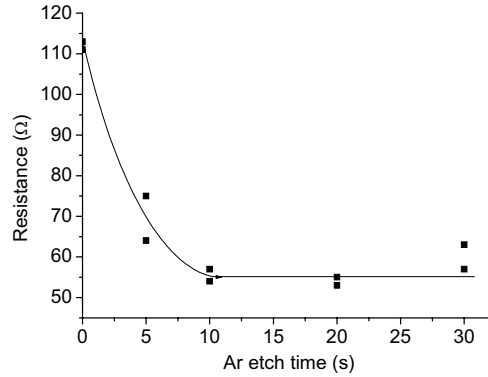


Fig. 2. Resistance of a HEB-like devices measured at a temperature above T_c plotted as a function of Ar^+ etch duration. Before Ar^+ etching, the NbTiN has been artificially contaminated by an O_2 plasma for 15 sec. We note that for a plain NbN film, the effect of 5 s Ar^+ etching is a decrease in T_c of ~ 0.5 K.

Minimizing a contact resistance between Au and NbN is attractive to reduce the losses and to avoid a voltage-drop in the device at a point where it cannot be an active part of the mixing process. However, a reduced contact resistance between the thick Au and the thin NbN means also an enhanced transparency for electronic exchange, or a maximally effective proximity-effect, which will lead to a destruction of the superconductivity in the NbN underneath the Au. To make sure that the uncovered NbN (Fig.1) would be the weakest link we also developed devices with a superconducting film inserted between the NbN and the Au to maintain superconductivity in the covered NbN.

We developed and studied four different types of contact structures. For clarity we first define our terminology. We will use the term *contact layer* for the composite layer of Au (“2”) and the intermediate layer (“4”) in Fig. 1, which is deposited on top of the NbN. We will use the term *contact pad* for the triple-stack layer of the NbN and the contact layer (“4”+“2”). This triple-stack sets the boundary conditions for the signal fed to the active NbN layer and also for hot-spot formation. All device geometries are identical except for the contact layer and the treatment of the NbN surface prior to the deposition of the intermediate layer. All devices are made on a single wafer. Details of the four different types of contacts are listed below:

Type A: The contact layer is 5 nm Ti layer, introduced to improve Au adhesion, and 70 nm thick Au on top. The interface to NbN is cleaned by a low power and low pressure O_2 plasma for 6 seconds, meant to remove resist-residues. The contact-layer (“4”+“2”) is evaporated *ex situ* afterwards.

Type D: The contact layer is 5 nm Ti and 70 nm Au. The interface to the NbN is prepared by cleaning first the residual e-beam resist using the same O_2 plasma cleaning as type A. Then an Ar^+ physical etch cleaning (15 seconds) is performed. The metals are evaporated *ex-situ* afterwards.

Type H: The contact layer is 5 nm Nb and 45 nm Au on top. The interface to the NbN is made by cleaning first the residual e-beam resist using the same O_2 plasma, followed by an Ar^+ physical etch cleaning (15 seconds). The metals (of layers “4”+“2”) are sputtered *in-situ* afterwards. Although we did not monitor the T_c of this Nb layer, from experience we expect it to be superconducting at a T_c of about 6 K.

Type G: The contact layer is 10 nm NbTiN and 40 nm Au on top. The interface to the NbN is prepared identically to the method used for type H. From previous measurements, we expect the intrinsic T_c of the NbTiN layer to be $\sim 8\text{ K}$.

Note that the O_2 plasma cleaning step is critical. If the duration is too short, not all residual e-beam resist is removed. But if too long, the O_2 plasma starts to oxidize the surface of the NbN [11]. To illustrate this point we present resistance versus temperature measurements (Fig.3) from a testbatch of HEB like devices using NbTiN as the active film. All devices have the same bridge dimensions, but with different O_2 plasma etch duration for the contacts. Starting with 4 seconds the device resistance first decreases, which we attribute to resist-residue removal. For etch times longer than 6 seconds the device resistance increases and the T_c drops. This combination of observations indicates a deterioration of the NbTiN film. We have subsequently used 6 sec as a value for optimized O_2 cleaning.

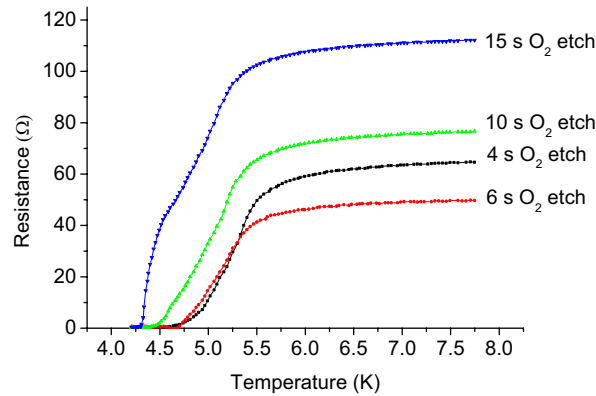


Fig.3. Resistance versus temperature measurements of HEB-like devices with various O_2 plasma cleaning duration before the metal contact pad is evaporated (*ex-situ*). In this case, a thin 4.5 nm NbTiN film with a lower T_c than the NbN is used. A clear reduction in T_c is observed for O_2 plasma etch durations longer than 10 s as well as an increase in resistance.

3. Resistance versus Temperature Measurements

We first compare the $R(T)$ curves of type A and type D devices, which only differ with respect to interface cleaning (Fig. 4). In the normal state type A devices show a resistance of $170\ \Omega$, which cannot be accounted for by the bridge resistance alone, using the known resistivity of the film. (Similar anomalously high resistance values for HEB's were reported before [10]). The resistance of type D devices is $\sim 80\ \Omega$ and approaches the expected resistance of the bridge. Because the devices are identical except for the cleaning of the NbN film we associate the additional $120\ \Omega$ with the contact resistance between the active NbN bolometer and the contact layer. Obviously, the physical interface cleaning reduces the contact resistance significantly.

Upon cooling the devices we find that type A devices have only one superconducting transition temperature around 9.3 K . The type D devices show two transitions, one at 7 K (T_{c2}) and one at 9.9 K (T_{c1}). Since the measurements are two-point measurements on an effectively NSN one would not expect a full zero-voltage state. However, the resistive contribution of the Au is negligible on the scale of Fig.4 and all resistance must be due to the highly resistive NbN (apart from the contribution due to the interface). The lower transition

temperature T_{c2} observed for type D devices is attributed to the NbN underneath the contact layer. The highest transition temperature T_{c1} is assumed to be due to the bridge itself. The lower value of T_{c2} may be partly due to 15 sec Ar^+ etching and partly due to the superconducting proximity effect. Although not analyzed in detail it is reasonable to assume that the resistance “tail” between 7 and 9.5 K is due to the conversion of quasi-particle current to supercurrent and the associated resistance [14,15].

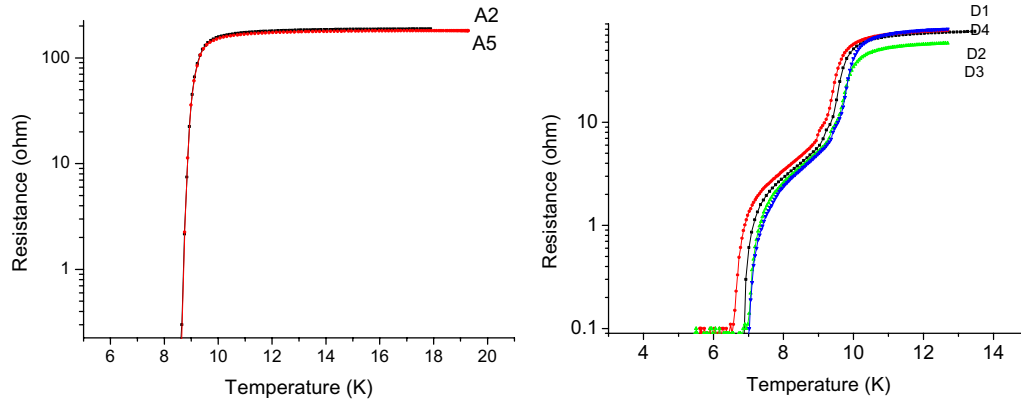


Figure 4: Resistance versus temperature curves of type A (left) and type D (right) devices. (All devices have similar lengths, except for device D3, which is shorter). Note that T_{c2} (lower value) is identical for devices with the same contact. This indicates good process control of the interface.

For devices of type A we only observe one transition temperature, indicating that the critical temperature of the pads is identical to the one of the bolometer. This is consistent with our understanding that there is a contact resistance in between the layers.

Fig. 5 shows $R(T)$ curves measured for several devices with an intermediate superconducting layer contact, which might suppress the reduction of T_c of the pads by the proximity-effect (with Nb, type H (left), and with NbTiN, type G (right)). These devices show normal state resistance values ranging from 56 to 78 Ω , depending on bridge length. In addition the overall shape of the resistive transition is quite comparable to those of type D devices.

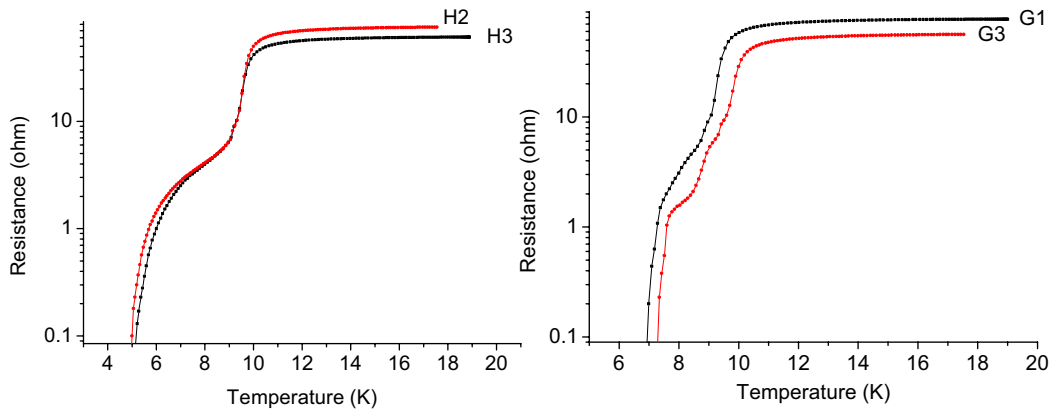


Fig.5 $R(T)$ curves of devices with superconducting intermediate layers (type H with Nb (left) and type G with NbTiN (right)). H3 and G3 are shorter. Note that the T_{c2} values are identical for the devices with same contact types.

All data have been summarized in Table 1. A small difference remains between measured resistance values and calculated ones (between brackets). Whether this is due an uncertainty in the value for the sheet resistance or reflects a remnant contact resistance is not known. Note that devices of type D, G and H have similar T_{c1} 's (9.9 K) but different values of T_{c2} . The latter value is interpreted as reflecting the critical temperature of the contact pads.

Table 1, Summary of measured DC parameters of devices of batch M2S, containing devices with four different types of contacts. R_{11K} and R_{300K} are the resistance measured at 11K and at the room temperature. The expected values for R_{11K} are estimated from the bridge size and the sheet resistance of the NbN film. RRR is the ratio between R_{300K}/R_{11K} . T_{c1} is the critical temperature of the bridge and T_{c2} the contact pads, determined from the RT curve. I_{c1} is the maximum critical current measured manually in the current-bias mode.

Device	R_{11K} (expected)	R_{300K}	RRR	T_{c1}	T_{c2}	I_{c1}
A1	147 Ω	98 Ω	0.67	*	9.5 K	311 mA
A3	218 Ω	116 Ω	0.53	*	9.3 K	345 mA
A4	236 Ω	135 Ω	0.59	*	9.3 K	348 mA
D1	79 Ω	67 Ω	0.83	9.7 K	6.7 K	367 mA
D2	86 Ω	70 Ω	0.83	9.8 K	7.0 K	451 mA
D3	59(52) Ω	53 Ω	0.91	9.9 K	7.1 K	478 mA
D4	80 Ω	72 Ω	0.91	9.9 K	7.1 K	499 mA
H2	78(60) Ω	65 Ω	0.83	9.8 K	5.3 K	436 mA
H3	62(52) Ω	53 Ω	0.83	9.7 K	5.3 K	400 mA
G1	78 Ω	65 Ω	0.83	9.5 K	7.0 K	456 mA
G3	56(52) Ω	50 Ω	0.91	9.9 K	7.2 K	515 mA

4. Transition Temperatures of Bi-layers

For a quantitative understanding of the possible T_c variations in stacks of contact layers we study a few typical bilayers using the proximity-effect model developed by Golubov et al. [9]. The model contains the intrinsic T_c 's, the resistivities and the thicknesses of the different layers as well as the interface transparency. Even for a chemically clean interface the transmissivity will still differ from unity because of Fermi velocity mismatch. Fig. 6 shows the reduced transition temperatures t (T/T_c) for three different cases: NbN (3.5 nm)/Au (70 nm), Nb (5 nm)/Au (45 nm), and NbTiN (10 nm)/Au (40 nm), as a function of interface transparency.

For NbN/Au the reduction of T_c has a strong dependence on the transparency, because the NbN is extremely thin. A transparency of 0.05 is already enough to push the T_c to below 4 K ($T_c = 9.9$ K for NbN). Since type A devices show a minor reduction in T_c , the interface transparency must be smaller than 0.005. For type D devices we find experimentally a reduced temperature of 0.7-0.8, which would be consistent with a transparency between 0.01-0.02. This value is considerably smaller than the value of ~ 0.2 , which we expect from the Fermi velocity mismatch based on $v_f = 1.39 \times 10^6$ m/s for Au [16] and $v_f = 5.7 \times 10^4$ m/s for a NbN film [17].

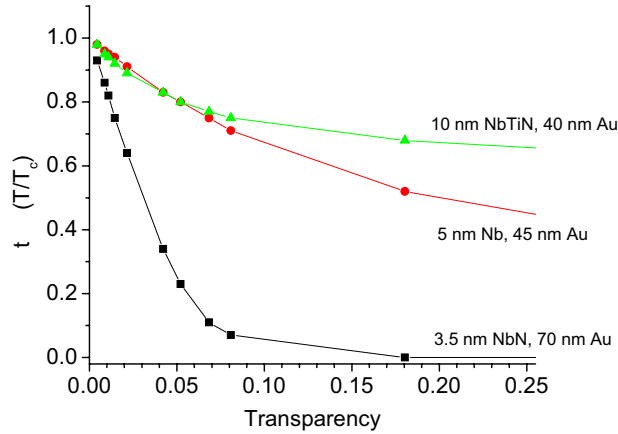


Fig. 6. Reduced critical temperature (T/T_c) as a function of interface transparency calculated for three different bilayers, NbN/Au, Nb/Au and NbTiN/Au.

We also use the results of Fig.6 to determine an expected value for the T_c of the bilayers involved. For the Nb/Au interface we assume a transparency of 0.5, which is calculated using $v_f = 2.77 \times 10^5$ m/s for Nb [18]. Using a T_c of 6 K for the Nb film, we expect a T_c for the contact bilayer of 1.8 K. For temperatures far above 1.8 K, we can treat this contact layer as a single normal metal layer. Unfortunately we have no data for the Fermi-velocity of NbTiN film. To proceed we assume the transparency of the NbTiN/Au interface to be the same as for Nb N/Au (~ 0.2). Using this we find an expected T_c of the NbTiN/Au layer of ~ 5 -6 K, using a T_c of 8 K for the NbTiN film.

Type H contacts show a T_{c2} of 5 K, i.e. a reduced critical temperature of 0.5-0.6. Assuming that we can indeed treat the Nb/Au bilayer as a fully normal layer, more specifically as a single Au layer we can apply the calculated curve for NbN/Au of Fig. 6. From this we find a relatively small interface transparency of 0.02-0.03 in Type H devices between NbN and the contact layer.

Type G devices have an identical interface between the NbN and the intermediate layer because the interface was made in the same way. If we use the transparency value of Type H contact for Type G as well we find a consistent value for T_{c2} (7.1 K).

We conclude by emphasizing that the transparency for Type H and G contacts is still relatively low, $T \sim 0.02$ -0.03, compared to the expected maximum value of $T = 0.2$. However, it is better than for Type D ($T \sim 0.01$ -0.02), probably because of the in-situ deposition. It certainly indicates that the deviation between the expected and measured resistances as listed in Table 1 may be partly due to the interface resistance.

5. Current versus Voltage measurements

The $R(T)$ measurements and the evaluation of the proximity-effect model build a coherent picture, suggesting that the successful device-types G and H consist of NS'SS'N devices with N representing the Au antenna wiring, S' the contact pads and S the active superconducting layer. S' has a slightly lower T_c than S if measured with a low bias current. In actual use HEB's are cooled down to a bath temperature of 4.2 K or lower, and then biased by a DC voltage, which establishes a working point for the mixer by the formation of the electronic hot spot. The evolution towards this working point can in principle be followed in the current-voltage characteristics. In interpreting the I,V curves one extra element has to be kept in mind. The variation in thickness (or cross-section) causes the local current density to be highest in the active NbN material. And a variation in current-density might cause a variation in local power-density when normal. However, the variation in thickness as well as the nature of the materials should also be dealt with in establishing the heat out-flow conditions. Therefore I,V curves are not easily interpretable.

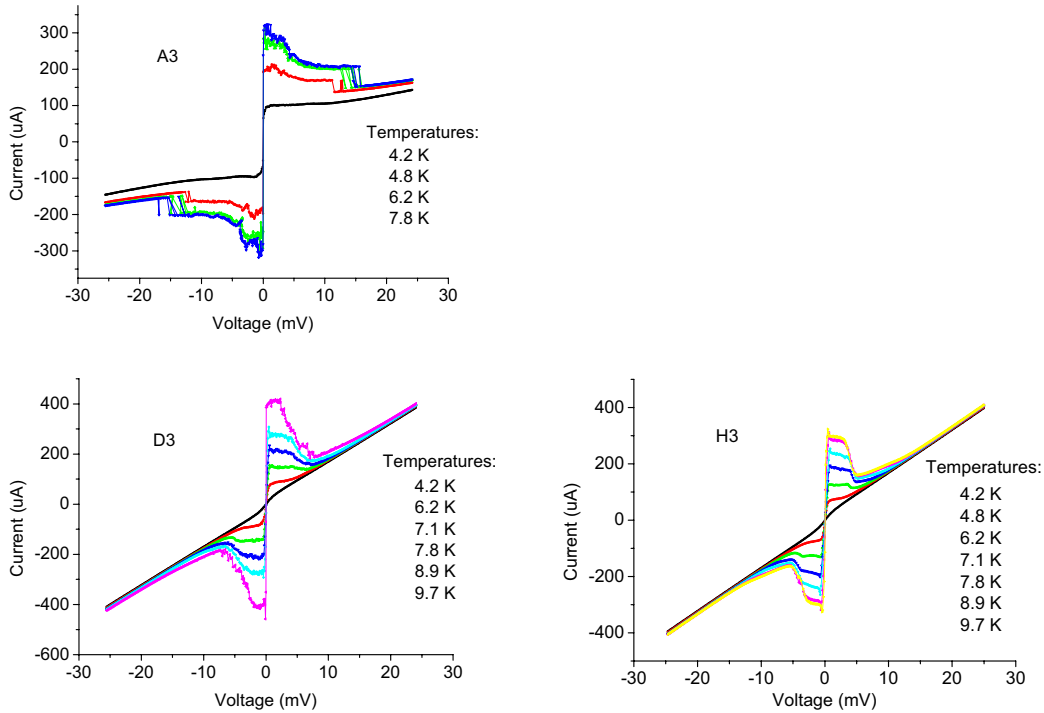


Figure 7, I,V curves of devices with contact type A, D and H, measured at different temperatures. The curve for type G is not shown since at this voltage range it is very similar to the curve of type H.

Fig. 7 shows I,V curves of typical devices of type A, D, and H, measured using a voltage bias for various bath temperatures from 4.2 K to about 10 K. For Type A devices a rather broad feature is visible at low voltages ending around ± 15 mV. Beyond 15 mV, the I,V curves do not overlap for different temperatures. Similar features have been reported for devices fabricated in similar way [2,3]. As argued before these devices have a rather large contribution to the resistance due to the NbN/Au interface, which will contribute as local source of dissipation, which will influence the formation of a usable hot spot. Since this broad feature appears only

for type A devices we believe that this contact resistance plays a role. Note that it appears directly after the critical current is exceeded at the lowest voltages. It is known that in this regime a negative resistance region appears causing time-dependent relaxation–oscillations. So the actual shape might be a time-averaged result and not necessarily informative about the DC I,V curve.

I,V curves of type D and H contacts do not show these broad shoulder-like structures. Instead we observe a much narrower features at low voltages followed by a smooth transitions of the IV curves to a regime with positive resistance. This transition takes place within a bias voltage ± 10 mV for type D and ± 5 mV for type H. The change of IV curves from low temperatures to T_c behaves very similar to what one expects from the electronic hotspot model [12,13]. All the IV curves at high bias overlap for different bath temperatures, indicating that a normal resistive hot spot is established and that the resistance of the contact pads does not play a role.

The dissipative state characteristic of a fully established hot spot is reached by starting with a nearly zero-resistance state. For increased current a critical value is reached after which the normal state is approached through some intermediate state. Therefore, we also checked the critical current of various types of devices at 4.2 K. The results are also included in Table 1. These reported values are measured manually using the current-bias mode. Slightly lower values are found from the I,V curves recorded in the voltage-bias mode. For Type A devices the maximum critical current, defined as I_{c1} , varies substantially. However, it is clear that Type A devices have the lowest critical current, while the type G devices the highest value.

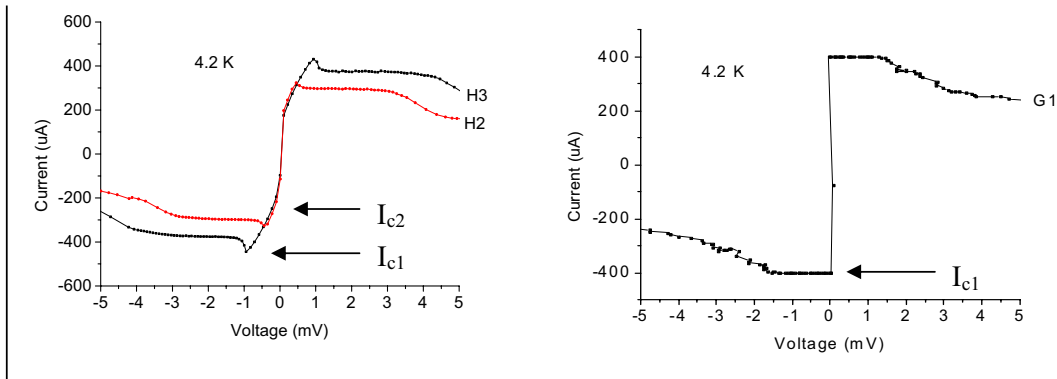


Figure 8. On the left side: the IV plots of device type H; on the right side, the IV plots of type G. All curves are taken around the zero bias voltage and at 4.2 K.

In Fig. 8 the I,V curves for Type H and G devices are shown on an expanded voltage scale. In Type H devices (Nb intermediate layer) we observe at low voltages two critical currents. The slope of the IV curve above the kink corresponds to a dynamic resistance of $\sim 3.5 \Omega$. I_{c1} is defined as the highest critical current where the voltage rapidly increases and the hot spot is formed. The lower critical current I_{c2} signals the onset of a resistive state with a value much lower than can be attributed to a fraction of the bridge being normal. It is reminiscent of features observed in superconducting microbridges and might also reflect flux-flow or phase-slip behaviour. This lower critical current, I_{c2} , decreases with increasing temperature and disappears completely when the temperature reaches T_{c2} for the pads. We therefore believe that I_{c2} is related to the contact pads, which implies that the small dynamic resistance signals

the resistance associated with the conversion of the currents from N' (S' in the normal state) and S the active superconducting layer.

These two critical currents are strikingly absent in devices of Type G (NbTiN intermediate layer). This suggests that the I_{c2} associated with the pads is either equal to or larger than I_{c1} . Such a difference might qualitatively be understood by the differences in T_c . However, the important issue is what conditions are established for the electronic hot spot when operated as a mixer. These remain to be worked out.

6. Conclusions

The crucial importance of the contacts between the Au antenna and the active NbN layer in phonon-cooled hot-electron bolometers has been demonstrated. Best results have been obtained with contacts in which a NbTiN layer is inserted between the Au and the NbN. Devices *without* physical cleaning of the NbN surface have significant contact resistance ($\sim 100 \Omega$). Devices with contact pads *with* physical cleaning of the interface show negligible contact resistances ($<10 \Omega$). It is argued that the interface transparencies are still not close to unity (0.01-0.02 for ex-situ and slightly better (0.02-0.03) for in-situ deposited contact pads). The results suggest that further optimisation of mixer performance is to be found in improving further the transparency and determining the optimal use of the superconducting intermediate layer.

Acknowledgement: We would like to thank Z. Wang and S. Miki from Communication Research Laboratory in Japan for providing high quality thin NbN films, which were used for the development of the process. We are grateful for stimulating discussions with M. Kroug and T. Zijstra at Delft, P. Khosropanah and H. Merkel at Chalmers. This work is supported partly by the European Space Agency (ESA) under Contract No. 11653/95/NL/PB

Corresponding author: *m.hajenius@tnw.tudelft.nl*

References:

1. J. Kawamura, R. Blundell, C-y E. Tong, G. Gol'tsman, E. Gershenzon, B. Voronov, and S. Cherednichenko, "Low noise NbN lattice-cooled superconducting hot-electron bolometric mixers at submillimeter wavelengths" *Appl. Phys. Lett.* **70**, 1619 (1997)
2. P. Yagoubov, M. Kroug, H. Merkel, E. Kollberg, G. Gol'tsman, S. Svechnikov, E. Gershenzon, "Noise temperature and local oscillator power requirement of NbN phonon-cooled hot electron bolometric mixers at terahertz frequencies". *Appl. Phys. Lett.* **73**, 2814 (1998).
3. A.D. Semenov, H.-W. Hübers, J. Schubert, G.N. Gol'tsman, A.I. Elantiev, B.M. Voronov, E.M. Gershenzon, "Design and Performance of the Lattice-Cooled Hot-Electron Terahertz Mixer", *J. Appl. Phys.* **88**, 6758, (2000).
4. S. Miki, Y. Uzawa, A. Kawakami, Z. Wang, "IF Bandwidth and Noise Temperature Measurements of NbN HEB Mixers on MgO Substrates", *IEEE Trans. On Appl. Supercon.* **11** (1), 175, 2001.
5. T. Lehnert, H. Rothermel, and K. H. Gundlach, "Low-noise heterodyne mixing with NbN microbolometers at 800 GHz", *J. Appl. Phys.* **83**, 3892 (1998).
6. E. Gerecht, C.F. Musante, Y. Zhuang, M. Ji, K.S. Yngvesson, T. Goyette, and J. Waldman, Proc. 11th Int. Symposium Space THz Technol, May 1-3, 2000, Ann Arbor, Michigan, pp 209
7. <http://astro.estec.esa.nl/SA-general/Projects/First/first.html>

8. J.J.A. Baselmans, M. Hajenius, J.R. Gao, T.M. Klapwijk, P.A.J. de Korte, B. Voronov, G. Gol'tsman. "Noise Performance of NbN Hot Electron Bolometer mixers at 2.5 THz and its dependence on the contact resistance", *Proc. of 14th Int. Symp. Space THz Technology*, Tucson. USA, March 2003. We note that the noise temperature of 1000 K is determined using the Callen and Welton definition.
9. A.A. Golubov, "Proximity effect in dirty N/S multilayers", *Superconducting Superlattices and Microstructures*, I. Bozovic, ed., SPIE proc. 215 (SPIE, Bellingham, WA, 1994), p353; A.A. Golubov, E.P. Houwman, J.G. Gijsbertsen, V.M. Krasnov, J. Flokstra, H. Rogalla, and M. Yu. Kupriyanov, *Phys. Rev. B* **51**, 1073 (1995).
10. M. Kroug, "NbN Hot Electron Bolometric Mixers for a Quasi-Optical THz Receiver", *Ph.D. Thesis*, Chalmers University, 2001, also P. Yagoubov, M. Kroug, H. Merkel, E. Kollberg, J. Schubert and H-W. Hübers, "NbN hot electron bolometric mixers at frequencies between 0.7 and 3.1 THz", *Supercond. Sci. Technol.* **12**, 989-991, 1999.
11. J.H. Greiner, "Josephson Tunneling Barriers by rf Sputter Etching in an Oxygen Plasma", *J. Appl. Phys.* **42**, 5151, 1971.
12. D. Wilms Floet, E. Miedema, T.M. Klapwijk, and J.R. Gao, "Hotspot Mixing: a Framework for Heterodyne Mixing in Superconducting Hot Electron Bolometers", *Appl. Phys. Lett.* **74**, 433 (1999).
13. H. Merkel, P. Khosropanah, P. Yagoubov, and E. Kollberg, *Proceedings Tenth International Symposium Space Terahertz Technology*, University of Virginia, Charlottesville, March 16-18, 1999. p. 592.
14. D. Wilms Floet, J.J.A. Baselmans, T.M. Klapwijk, and J.R. Gao, "Resistive transition of niobium superconducting hot-electron bolometer mixers", *Appl. Phys. Lett.* **73**, 2826 (1998).
15. A.H. Verbruggen, T.M. Klapwijk, W. Belzig, and J.R. Gao, "The resistive transition of aluminium hot electron bolometer mixers with normal metal cooling banks", *Proc. of 12th Int. Symp. Space THz Technology*, San Diego, USA, Page 42, February 2001.
16. N.W. Ashcroft and N. David Mermin, *Solid State Physics*, W.B. Saunders Company, International Edition, Philadelphia (1976)
17. Derived from measured coherence length ξ_0 in NbN film: A.D. Semenov, G.N. Gol'tsman, A.A. Korneev, "Quantum detection by current carrying superconducting film", *Physica C*, (351), pp. 349-356, 2001
18. H.R. Kerchner, D.K. Christen, S.T. Sekula, "Critical fields H_c and H_{c2} of superconducting niobium" *Phys. Rev. B* **24**, 1200, 1981.
19. M. Hajenius, "The DC Characterisation of a superconducting HEB using a Niobium-Gold bilayer", *Grad. Report TU Delft*, April 2002.

NbAu Bilayer Hot Electron Bolometer

H. Merkel, P. Khosropanah, S. Cherednichenko,
T. Ottoson, J. Baubert, E. Kollberg

*Department of Microtechnology & Nanoscience,
Chalmers University of Technology*

Abstract

Hot Electron Bolometer (HEB) mixers based on NbAu bilayers have been reported recently. In this paper, a model is presented to quantitatively explain the device performance. Proximity effect suppresses superconductivity under the antenna pads. In a part of the bolometer bridge, the critical temperature is reduced by this effect. Solving a heat balance relation indicates, that NbAu bilayer HEB have a comparably bad conversion gain (about -20dB compared to -17dB for Nb) since a considerable fraction of heating power is lost in and close to the antenna pads.

1 Introduction

Analyzing point-HEBs, it has been concluded that the receiver noise temperature depends on the square of the critical temperature ([1], [2]). Large efforts have been undertaken to reduce the critical temperature of the HEB material (e.g. Al [3]). Al HEB have failed and Andreev reflection has emerged as a bottleneck for Nb HEB. Recently NbAu bilayers have been proposed to optimize the critical temperature without changing other material properties substantially [4]. NbAu HEB have not yet shown the expected reduction in noise temperature. This is due to strong Andreev reflection and due to the absence of contact resistance. Controlling contact resistance under the antenna pads is crucial to achieve low noise and low power HEB mixers. For in-situ Au top layers the electron transmissivity of the interface is large giving rise to proximity effect. Eventually the critical temperature under the antenna pads becomes lower than the bath temperature. This normal zone extends then into the bridge efficiently reducing conversion gain.

2 Device Modelling

The full details of HEB modelling are found in [5]. There is a fundamental difference between bilayer HEB and other types of HEB found in the presence of contact resistance

effects. Covering a very thin superconducting film with a normal metal suppresses the superconductivity in the film by proximity effect. This effect depends strongly on the quality of the contact - in-situ contacts (as in this case) or excessive cleaning of the superconductor layer prior to film deposition yields very good contacts and therefore a large proximity effect. This reduction of the critical temperature under the pad is partially visible in a region of the bridge close to the pads (at a distance λ_q^* [6]) where the critical temperature of the HEB bridge smoothly changes from its value at the center to the value under the pads. An empirical model for this proximity effect is to perform a polynomial fit of the critical temperature profile. The parameter to be fitted is β in the following template:

$$T_c(x) = \left(T_{c0} + (T_c - T_{c0}) \left(1 - \left(\frac{|x|}{L} \right)^\beta \right) \right) \quad (1)$$

Fit data are obtained using $R(T)$ curves with two transition temperatures - one in the center (allowing to extract T_c) and another under the pad (yields $T_{c,0}$). Values for the exponent β are found by a curve fit. For NbAu one obtains $\beta \approx 7...8$, and for Nb, NbN and NbTiN $\beta \approx 15...25$. This critical temperature profile is used in the heat balance relation instead of a constant critical temperature.

3 Theory versus Experiment

NbAu HEB have been produced at DIMES in Delft (the Netherlands). Results for the proximity effect on these films are found in literature [?]. Devices have been tested at DIMES [4]. In Figure 1, this published material is compared with calculated results.

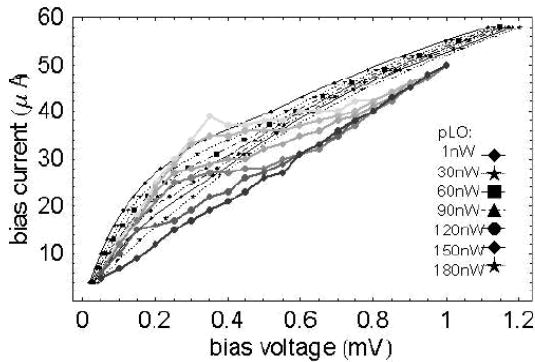


Figure 1: Measured and calculated IV curves.

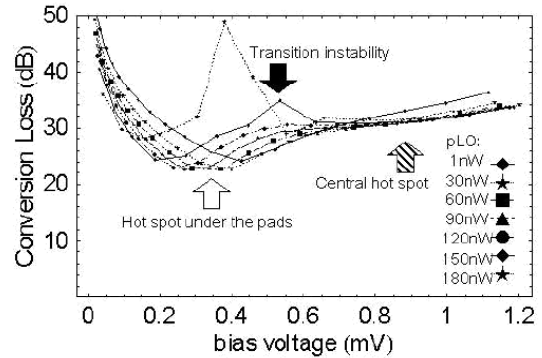


Figure 2: Conversion loss versus bias voltage curves.

In Figure 1, an unpumped and a series of pumped curves for NbAu HEB are compared with model calculations. No measured data on RF properties of these devices is available at this moment. Theoretical results for the conversion loss are shown in Figure 4. Clearly two distinct regimes (without and with a central hot spot) can be seen. Both regions are separated by a transition instability where the hot spot configurations change from one to

another without an change in device resistance. Theoretical results for the noise are shown in Figure 3. For the same bias points the IF bandwidth is shown in Figure ??.

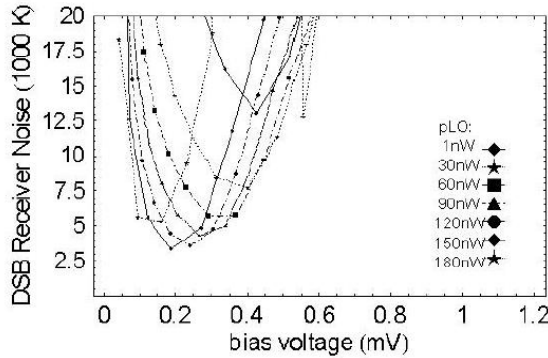


Figure 3: DSB Receiver Noise Temperature versus bias voltage

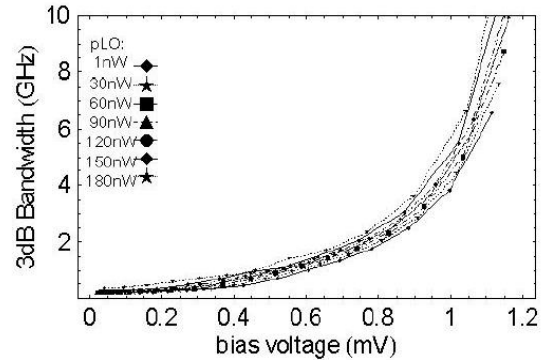


Figure 4: IF bandwidth versus bias voltage curves.

4 Conclusion

NbAu HEB are not very suited as Terahertz mixers. Nevertheless they have proven to be a valuable tool to study the influence of contact resistance on the bolometer performance - too good contacts destroy indeed the HEB noise performance by creating additional parasitic hot spots. Extremely bad contacts result in a large zone where the RF current is squeezed from the Au top layer to the superconductor yielding a large effective bolometer size requiring a lot of LO power to be pumped properly. As a conclusion, contacts under the antenna pads must be controlled bad. Excessive cleaning of the superconducting film prior to adding the top layer is detrimental for the performance.

The authors want to thank M. Hajenius and J.R.Gao (DIMES/Delft) for sharing the measurement data and many fruitful discussions.

References

- [1] H. Ekstrom, B. Karasik, E. Kollberg, and K. Yngvesson, "Conversion gain and noise of niobium superconducting hot-electron mixers," *IEEE Transactions on Microwave Theory and Techniques* **43**, p. 938, 1995.
- [2] B. Karasik, M. Gaidis, W. McGrath, B. Bumble, and H. LeDuc, "A low-noise 2.5 thz superconductive nb hot-electron mixer," *IEEE Transactions on Applied Superconductivity* **7**, p. 3580, 1997.
- [3] I. Siddiqi, A. Verevkin, D. Prober, A. Skalare, B. Karasik, W. McGrath, P. Echternach, and H. LeDuc, "Noise and conversion efficiency of aluminum superconducting hot-electron bolometer mixer," *IEEE Transactions on Applied Superconductivity* **11**, p. 958, 2001.
- [4] X. Lefoul, P. Yagoubov, M. Hajenius, W. Vreeling, W. Ganzevles, J. Gao, P. deKorte, and T. Klapwijk, "Dc and if bandwidth measurements of superconducting diffusion cooled hot electron bolometer mixers based on nbau bilayers," *Proceedings of the 13.th Terahertz Workshop Cambridge MA.*, pp. 369-372, 2002.
- [5] P. Khosropanah, Merkel, S. Cherednichenko, J. Baubert, T. Ottosson, and E. Kollberg, "Nbtin and nbu hot electron bolometer," *Proceedings of the 14.th Terahertz Workshop, Tucson*, 2003.
- [6] D. Wilms-Floet, *Ph.D. Thesis: Hotspot mixing in THz Nb superconducting HEB mixers*, Dept. of Applied Physics, RU Groningen, Groningen, The Netherlands, 2001.

Transition Edge Operation of Tantalum Diffusion-Cooled Hot-Electron Bolometers

Anders Skalare, William R. McGrath, Bruce Bumble, Henry G. Leduc
*Jet Propulsion Laboratory, California Institute of Technology
Pasadena, CA 91109*

Diffusion-cooled hot-electron bolometers (HEB's) differ from the phonon-cooled variety in that the electron temperature distribution inside the device has an approximately parabolic shape, instead of being essentially uniform. As a result, the electron temperature T_e is close to the transition temperature T_c only in a small portion of the device, and it is only that portion that can generate thermal fluctuation (TF) noise and that can contribute to the frequency conversion in a mixer. Heat from the DC current is dissipated in any parts of the device that are in the normal state, while RF heat dissipation (above the gap frequency) is uniform throughout the device. The internal temperature distribution is determined by this heat dissipation and the dominant heat transport mechanism, which is electron diffusion, as described by the Wiedemann-Franz law. The difference in heat conductivity between the superconducting and the normal-conducting regions of the device should also affect the heat transport, as should Andreev reflections at the interface between the regions. For a thorough description of these effects and others, the reader is referred to [1].

In a simple model the electron temperature inside the device is close to T_c only in some limited regions of the device, as marked in Fig. 1. For the bias conditions B and C in Figs. 1 and 2, which can be reached at least theoretically, these regions are quite small. For bias point A the normal conducting part of the device is quite small, and as a result the bias current needs to be higher than at point B in order to dissipate a sufficient amount of heat to support the temperature distribution. This creates the region of negative differential resistance around point A that cannot be easily reached experimentally due to instability.

With a sharply defined transition, the model in Fig.1 reduces to the hot-spot model [2], where mixing is achieved by the expansion and contraction of the central normal region as a response to modulation of the heat dissipation by the signal and local oscillator (LO) voltages. In laboratory measurements a finite transition width is always seen in small devices. The reason may be variations in the actual T_c between different grains in the device film, or possibly that the transition is widened by the thermodynamic energy fluctuations themselves. A small piece of the device (about the size of a few coherence lengths) will have a fluctuating energy content, so that if the electron temperature is close to T_c it could at some times be in the normal state and at other times superconducting. This could at least partially explain the measured transition width, and could also justify the use of a finite transition width in simplified mixer calculations to represent that mixing can occur also in regions that are slightly above or below the nominal T_c . It

would seem that only a small amount of thermal fluctuation noise could be generated and only low conversion efficiency could be achieved at bias points B and C in Figs 1 and 2, since such small parts of the device are close to the T_c . However, this is not necessarily the case when the bias is close to point B, where the dc bias circuit / device combination becomes unstable. Close to that point even small variations in heat content can result in significant voltage shifts, which constitute output noise when those variations are due to thermal fluctuations, and intermediate frequency output power when they are due to the beating between the signal and the LO in a mixer. Since this is in principle caused by a feedback effect, the bandwidth of these parameters will be affected.

Experimentally, the T_c does not seem to be uniform throughout a device, and in short bolometers a “foot” structure appears in the resistance-versus-temperature (R vs. T) curve. This structure, which is present in both tantalum and niobium devices and is even more pronounced in those made from aluminum, appears to be associated with the ends of the microbridge. One explanation for this effect is that the superconducting gap is suppressed at the ends due to proximity to the normal metal pads, or that a charge-imbalance effect at the S-N interface is responsible [3]. The measurable effects include the foot structure and an apparent lowering of the supercurrent at the device ends that creates two breakpoints in the “supercurrent” of the entire bridge when the temperature is not too far below T_c . Also, in many devices high output-noise peaks occur at high DC bias voltages (several mV), that can be attributed to the end effects if these can indeed be regarded as a lowering of T_c . According to this theory, the “ T_e -distribution” can sometimes intersect the “ T_c -distribution” close to tangentially near the device ends, as in Fig.3 (case A). This means that a larger fraction of the device would be close to its “local T_c ” than would be the case at surrounding bias points where the intersection occurs at a larger “non-tangential” angle. As a consequence, a larger amount of noise is generated at the specific bias point indicated in case A in Fig.3 . The height of the noise peak can be quite high even though only a fairly small part of the device is involved, since the dc bias current is high and since the amount of output noise is proportional to the square of that current. The interpretation is supported by the experimental observation that the noise peaks are shifted down to lower bias levels (and lower electron temperatures) if the ambient temperature is closer to the “ T_c ” of the foot structure, cases B and C in Fig.3 . The fact that the noise peaks in Fig.3 can be shifted down, points to a method that can potentially increase the conversion efficiency of a diffusion-cooled HEB mixer. The peaks are not useful for a low-noise mixer application when they occur at high voltages (Fig.3 Case A), since only the end points of the device would be close to T_c . The electron temperature at these endpoints cannot be modulated significantly by the signal and LO, since they are heat sunk directly to the contacts, which are held at a fixed (ambient) temperature. The conversion efficiency would therefore be very low. The situation is different in Case C, since the electron temperature is close to T_c also in regions inside the bridge where the electron temperature can be coherently modulated. This would suggest that an internal “ T_c -distribution” with a parabolic shape would allow the electron temperature to be close to T_c in a larger part of the device. In reality it is not known what shape the effective T_c -distribution has in actual devices. The simplest analysis would be

to represent the distribution by the shape of the R vs. T curve, but whether this is indeed physically justified remains to be determined. The device length would need to be used as a parameter in adjusting the shape of the Tc, and it would depend on how far into the device the end effects do extend. In this model the maximum supercurrent (I_c) should be a local parameter inside the device (similar to the description in [1]) and should depend both on the local electron temperature $T_e(x)$ and the “local transition temperature” $T_c(x)$. A finite dc bias current is required to operate the device as a mixer, and in our model one condition for high conversion efficiency should therefore be that the local $I_c(T_e(x), T_c(x))$ is close to this bias current in much of the device, rather than having direct agreement between $T_e(x)$ and $T_c(x)$. In a way the situation resembles larger phonon-cooled HEB’s that automatically have T_e close to T_c in much of the device. Such phonon-cooled devices sometimes exhibit a “flat” segment in the IV-curve, which does indicate that much of the device has the same I_c . We have observed such a flat segment at 1.22 K in a 100 nm long diffusion-cooled Ta device with a T_c of about 2.5 K, Figs. 4 and 5, which indicates that this situation can indeed also be achieved in a diffusion-cooled device over a narrow ambient temperature range (less than 0.1 K in this case). As seen in Fig.5, the flat part of the IV curve also generates more noise, as expected from the described model.

In brief conclusion, by observing output noise from Ta diffusion-cooled HEB’s we conclude that the suppression of T_c at the ends of a device can be used to achieve a constant I_c in a significant fraction of the device at a specific ambient temperature, if the device length is chosen correctly. If this situation can be achieved in an actual HEB mixer with LO power applied, the conversion efficiency would likely be increased since a larger part of the device could participate in the mixing process.

This research was carried out at the Jet Propulsion Laboratory, California Institute of Technology, under a contract with the National Aeronautics and Space Administration. Reference herein to any specific commercial product, process, or service by trade name, trademark, manufacturer, or otherwise, does not constitute or imply its endorsement by the United States Government or the Jet Propulsion Laboratory, California Institute of Technology.

References

- [1] H. Merkel, “A hot-spot model for HEB mixers including Andreev reflection”, Proc. Thirteenth Int. Symp. on Space Terahertz Tech., Harvard University, Cambridge, MA, 26-18 March 2002, pp.53-64
- [2] D. Wilms-Floet, E. Miedema, T. M. Klapwijk, J. R. Gao, “Hotspot mixing: A framework for heterodyne mixing in superconducting hot-electron bolometers”, Appl. Phys. Lett. **74**, 433 (1999)
- [3] D. Wilms-Floet, J.J.A. Baselmans, T.M. Klapwijk, J.R. Gao, “Resistive transition of niobium superconducting hot-electron bolometer mixers”, Appl. Phys. Lett. **73**, pp. 2826 (1998)

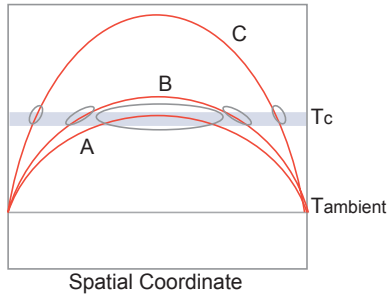


Fig. 1; Internal temperature distributions for three different bias points (Fig.2)

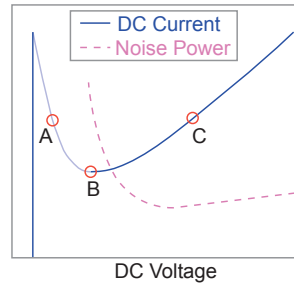


Fig.2; Schematic of an IV curve and of the microwave output noise.

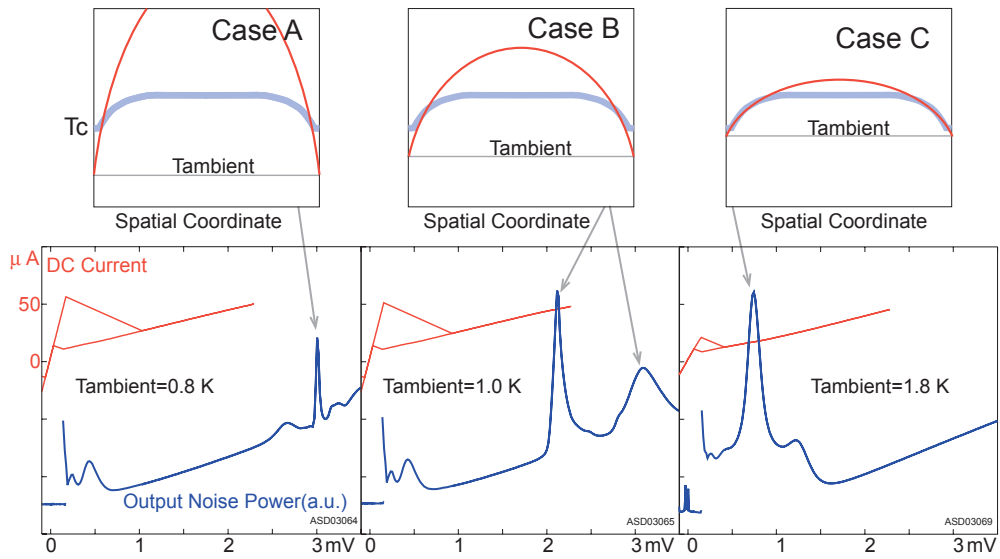


Fig.3; Measured IV curves and output noise at 1.5 GHz, measured with a 0.2 micron long Ta bolometer. The graphs of the internal temperature distributions are schematics only.

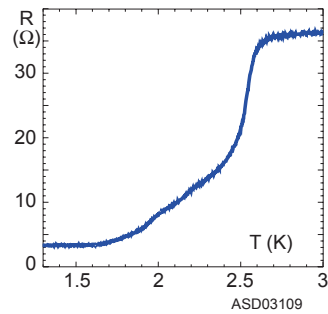


Fig.4; Resistance vs. Temperature curve for a 0.1 micron device.

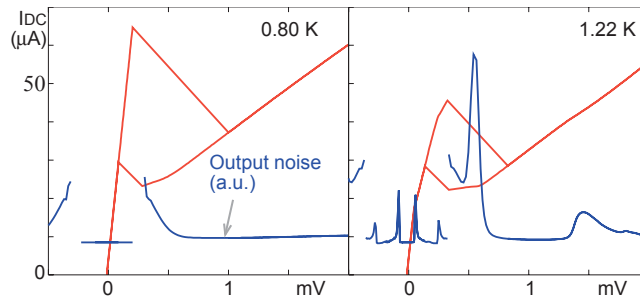


Fig.5; Measured IV curves and output noise at 1.5 GHz for the device in Fig.4 at two different temperatures.

Impedance and Bandwidth Characterization of NbN Hot Electron Bolometric Mixers

F. Rodriguez-Morales and K.S. Yngvesson

Department of Electrical and Computer Engineering
University of Massachusetts, Amherst, MA 01003
yngvesson@ecs.umass.edu

Abstract

We are presenting here our recent results of noise temperature and impedance measurements for NbN Hot Electron Bolometer (HEB) mixers.

The noise temperature measurements were performed over a 1-8 GHz IF band using an LO frequency of about 1.6 THz using quasi-optical coupling and a single low noise HEMT MMIC amplifier.

On the other hand, the impedance measurements were completed with a network analyzer in the presence of LO power and DC bias, over a 2-10 GHz frequency range.

The experimental results of both sets of measurements are used to predict noise and gain bandwidth of our devices and for comparison with those obtained from the standard model.

Introduction

Hot Electron Bolometer (HEB) technology has become mature enough over the past years to allow the development and implementation of observing platforms in the terahertz region such as HIFI [3], TREND [10], GREAT [4] and TELIS [7].

In such receivers, there are two parameters that are particularly important, since they may ultimately determine the threshold for the minimum signal level that can be reliably detected, namely the *IF gain bandwidth*, defined as the IF frequency at which the conversion efficiency of the mixer drops by 3 dB from its low IF value; and the *noise bandwidth*, defined as the frequency at which the mixer noise doubles compared to its zero frequency value [9].

For NbN or Nb based HEB mixers, the noise and gain bandwidth depend upon film properties such as thickness, critical temperature (T_c) and acoustic coupling between film and substrate [6]. In principle, these mixers can reach an IF gain bandwidth of a few gigahertz, whereas their noise bandwidth can be even larger [1].

Here we present experimental results obtained from characterization of two of the main properties of HEB devices that are relevant to their intermediate frequency response, namely the IF small signal impedance, which can be useful to estimate gain bandwidth without requiring a THz tunable source, and the receiver noise temperature as a function of intermediate frequency.

The measurements were performed over a wider frequency range than it has ever been done (1-8 GHz and 2-10 GHz, respectively), with the purpose of evaluating the effectiveness of HEB mixers as low-noise broadband receivers.

Experimental Setup

Two different setups were used to carry out the two sets of measurements.

A pair of mixers were selected from two different batches. The sample used for noise bandwidth quantification was fabricated on silicon substrate with an active NbN area 5 nm thick, 1 μm long and 4 μm wide. A twin-slot antenna was used with this device.

For impedance measurements, though, the device was fabricated on magnesium oxide substrate and the dimensions for the superconducting area were 4 nm thick, 2 μm long and 20 μm wide. No antenna was used in this case.

In both cases, the THz radiation was coupled to the device using a quasi-optical approach, in which a elliptical silicon lens couples both the RF and LO beams into the HEB.

The LO source was a CO_2 -pumped laser running in continuous wave (CW) mode in the THz regime.

A. Noise Bandwidth

Figure 1 shows the apparatus used for noise temperature characterization. The wavelength for the local oscillator was 184 μm , which corresponds to 1.63 THz.

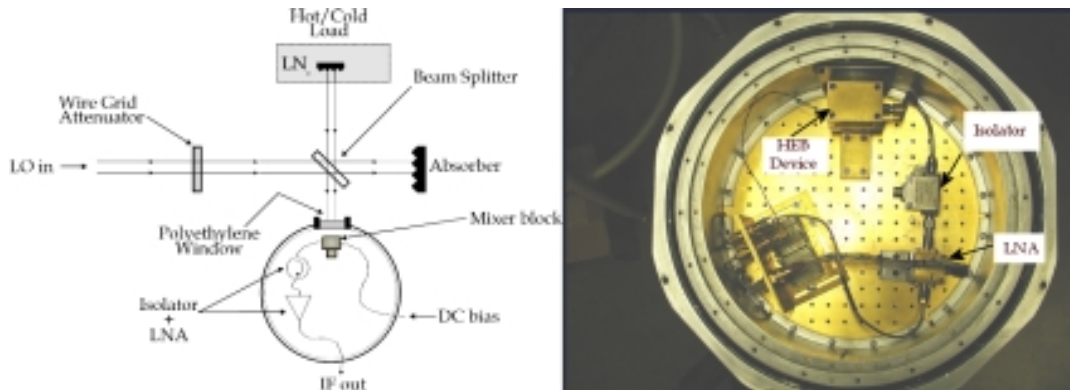


Figure 1: Laboratory setup for measuring HEB noise temperature

A hot/cold blackbody source is inserted into the beam path, and the change in IF power (Y-factor) is registered at the power meter. The noise temperature of the receiver is then computed directly from the Y-factor.

The interior of the liquid helium cryostat used to cool down the specimens is also shown in Figure 1. The bolometer chip was mounted in a mixer block, to provide it with a bias circuit along with a connection to the IF chain achieving a reasonably good match over the desired bandwidth and eliminating the need for an external bias tee.

The wide-band HEMT InP MMIC low noise cryogenic amplifier was designed by Prof. Sander Weinreb at JPL/Caltech. This amplifier has two stages, a gain of 20 dB and an equivalent noise temperature below 10 K throughout its band (1–10 GHz).

In order to minimize standing wave problems and improve stability, a cryogenic isolator was placed at the input of the LNA. Since none of the currently available cryogenic isolators can cover more than an octave, the band of interest was divided into three smaller bands; 1–2 GHz, 2–4 GHz and 4–8 GHz.

B. Impedance and Gain Bandwidth

Figure 2 illustrates the setup used for this part of the experiment.

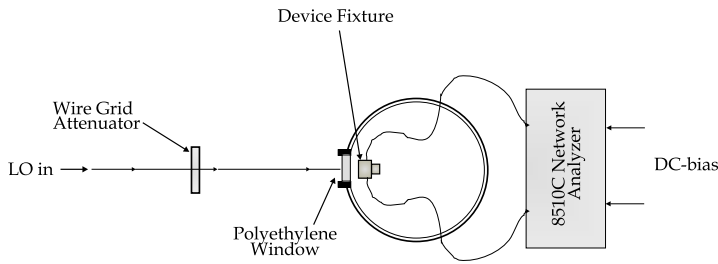


Figure 2: Setup used for IF impedance measurements

A transmission technique similar to that described in [5] was used to determine the impedance of HEB mixers by measuring the scattering parameter S_{21} as a function of frequency.

One may note that all measurements of HEB impedance such as in [5], thus far have been performed without LO power. It is obviously much more important to measure the impedance under more realistic operating conditions and near the optimum point for mixing, as done here ¹.

The impedance characterization took place in the presence of laser illumination at a wavelength of 194 μm (1.55 THz), while DC bias was applied to the sample through the bias tees included in the 8510C Automatic Network Analyzer (ANA). A thru-reflect-line (TRL) calibration technique at 4 K was performed in order to establish the reference planes prior to completing the actual measurements [8].

The device was carefully put in place between the two microstrip launchers using a flip-chip technique (Figure 3A). A silicon lens was used for coupling the THz LO power to the device in a more efficient way (Figure 3B).

In order to prevent saturating the mixer with microwave power from the ANA, both the calibration and the measurement were taken to completion with a microwave power level of -48 dBm, which was found to be convenient for this study, since it was well below the LO power required to suppress the superconducting state in the HEB.

¹One early impedance measurement was performed with LO power applied, but in that case the LO frequency was only 20 GHz [2].

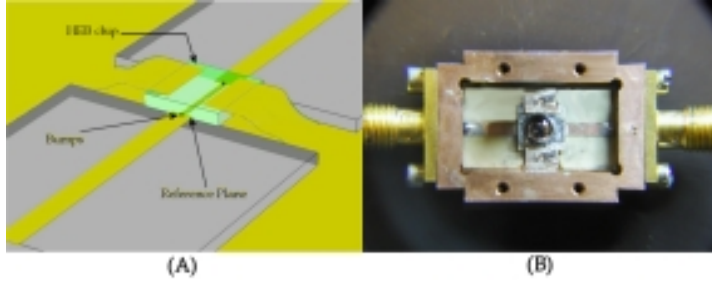


Figure 3: Device fixture used to measure IF small signal impedance

Results and Discussion

A. Noise Bandwidth

The critical current for this device was $420 \mu\text{A}$. The optimum operating point (best Y-factor) was found for $V_0 = 1 \text{ mV}$ and $I_0 = 42 \mu\text{A}$ ($R_0 = 23.8 \Omega$).

The double-sideband receiver noise temperature, $T_{R,DSB}$, was computed from the experimental Y factor and plotted as a function of frequency (Figure 4).

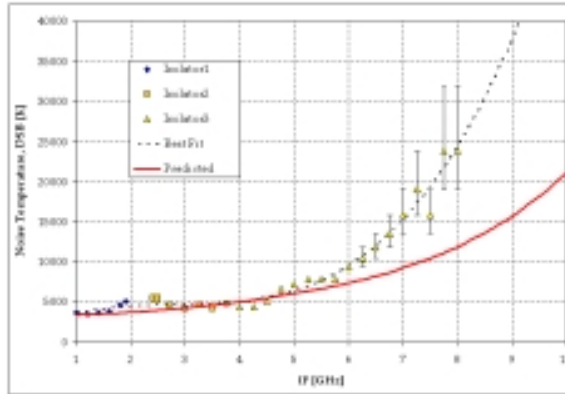


Figure 4: Measured noise temperature vs IF frequency

The dashed line represents the best fit to the experimental data set and the solid line corresponds to the predicted value based on the standard model, which was computed using fitting parameters such as the total conversion loss of the mixer, L_{Ctot} , the self-heating parameter $C = C_0 I_0^2$, the measured thermal fluctuation noise at the lowest IF frequency, T_{fIM} , and the electron thermal relaxation time, τ_θ .

The agreement among the calculated receiver noise temperature and its experimental counterpart is reasonable for frequencies below 6 GHz, after which the actual noise temperature grows more rapidly compared to the theoretical calculation. The discrepancies between predicted and measured values of $T_{R,DSB}$ above 6 GHz are attributed to changes in the frequency response of the mixer block at low temperatures, extra parasitics not considered in the model of its impedance, as well as mismatch between components in the IF

chain.

We can estimate the noise bandwidth from the data plotted in Figure 4, resulting in 5.32 GHz using the standard model formulae and close to 5.25 GHz using the experimental data.

By taking the ratio of the receiver output noise power with the mixer at the optimum operating point (DC and LO power applied), P_{op} , to the output noise power in the superconducting state (no DC or LO power applied), P_{sc} , it was possible to use this value (often called the U-factor, $U = P_{op}/P_{sc}$) to predict the total conversion gain of the mixer, G_C , as well as its output noise, T_{out} , expressly [8]

$$G_C = \frac{U(T_{bath} + T_{IF})}{2T_{cold} + 2T_{R,DSB}} \quad (1)$$

$$T_{out} = \frac{U(T_{IF} + T_{bath})}{T_{cold} + T_{R,DSB}} T_{R,DSB} - T_{IF} \quad (2)$$

where $T_{cold} = 77$ K is the temperature of a broadband blackbody noise source present at the input of the mixer when the U-factor measurement is performed, T_{IF} is the equivalent noise temperature of the IF chain, $T_{bath} = 4.2$ K is the temperature of a 50-ohm load at the matched port of the circulator and $T_{R,DSB}$ is the measured double-sideband noise temperature of the receiver.

The U-factor was recorded for the same set of frequencies as shown in Figure 4, then (1) and (2) were used to compute G_C and T_{out} , respectively (Figure 5). The solid line in these plots corresponds to the predicted value, estimated also from the standard model.

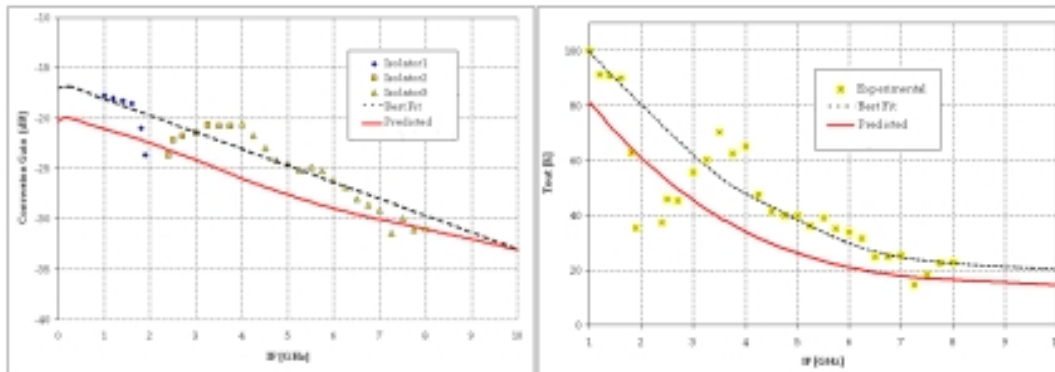


Figure 5: Measured conversion gain and mixer output noise vs IF frequency

There exists qualitative agreement between the best fit to the measured conversion loss and output noise shown in Figure 5; the discrepancy between these quantities is less than 3 dB and less than 20 K throughout the band, respectively. The actual gain bandwidth is close to 2.4 GHz.

One may note that the noise bandwidth is about 2.2 times the gain bandwidth.

B. Impedance and Gain Bandwidth

It can be shown that the gain bandwidth of an HEB can be estimated as [5]

$$B_e = \frac{1}{2\pi\tau_\theta} \left(1 - C \frac{R_L - R_0}{R_L + R_0} \right) \quad (3)$$

The dependence of the conversion gain of the mixer on IF frequency, self-heating parameter C , as well as the electron relaxation time τ_θ , also holds for the IF small signal impedance, i.e.

$$Z(\omega) = R_0 \left(\frac{1+C}{1-C} \right) \left(\frac{1 + j\omega \frac{\tau_\theta}{1+C}}{1 + j\omega \frac{\tau_\theta}{1-C}} \right) \quad (4)$$

Therefore, by measuring the impedance of the mixer, it is possible to fit the experimental data to (4), obtain a suitable value for C and τ_θ , and then predict the gain bandwidth using (3).

Figure 6 shows the real and imaginary part of the impedance of the sample biased at 1.5 mV and 56 μ A ($R_0 = 26$ ohm), after subtracting the effect of the microstrip feed lines and parasitic reactances associated to the contact bumps.

The two different predictions in Figure 6 correspond to different values of C , one obtained by fitting the measured data to (4) and one obtained from the differential slope of the IV curve (dV/dI) at that particular point, $C = \frac{dV/dI - R_0}{dV/dI + R_0}$, as predicted from the standard model [2]. The time-constant τ_θ is 47.98 ps in both cases and was obtained only using the least-square fit of the experimental impedance to (4).

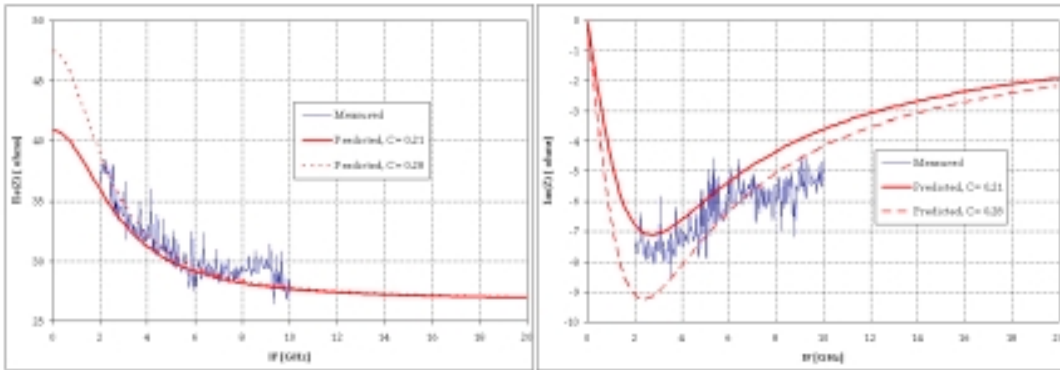


Figure 6: Measured and modelled impedance with device biased at (1.5 mV, 56 μ A)

The impedance of this specimen was measured for some other quiescent points as well. The results for different settings are summarized in Table 1. The gain bandwidth was

Table 1: Predicted gain bandwidth for different operating conditions

V_0 [mV]	I_0 [μ A]	dV/dI [Ω]	Gain BW [GHz]
0.6	14	44.7	3.6
0.6	30	27.6	3.4
1.0	23	66.2	3.3
1.0	42	38.1	3.5
1.5	56	47.5	3.3

estimated using (3) and the appropriate value for C and τ_θ obtained from the impedance measurements.

Though there is previous empirical evidence that suggests that there is a bias dependence of the IF bandwidth with bias voltage [6], our observations indicate only small changes in the bandwidth as V_0 changes. This is because we biased the device close to the optimum point for minimum noise temperature.

The predicted bandwidths exceed that for the device used in the noise bandwidth measurements. It is expected that a device on an MgO substrate should yield larger bandwidth, as observed.

Large values of V_0 would yield higher bandwidths at the expense of poor sensitivity.

Conclusions

A systematic study of the bandwidth properties of hot electron bolometric mixers has been reported in this paper.

The noise temperature of an HEB mixer was measured using a single MMIC low-noise amplifier based on InP HEMT transistors. This measurement allowed us to estimate the noise bandwidth, gain bandwidth and mixer output noise with moderate accuracy. The results are somewhat consistent with those obtained from the standard model.

The impedance of a sample mixer was characterized by means of an Automatic Network Analyzer using a TRL calibration at cryogenic temperatures. By using the impedance data, it was possible to predict the bandwidth of the device under test without having a tunable THz source. The predicted bandwidth agrees with previously reported results for similar devices.

Further experiments will improve the accuracy of the measurements and the data will be useful for improvement of the current models of superconducting HEBs.

Acknowledgements

This work was supported by the National Aeronautics and Space Administration (NASA) and the National Council for Science and Technology in Mexico (CONACyT).

References

- [1] S. Cherednichenko, M. Kroug, H. Merkel, E. Kollberg, K. Yngvesson, B. Voronov, and G. Gol'tsman. IF Bandwidth of Phonon Cooled HEB Mixers Made from NbN Films on MgO Substrates. In *Proceedings: 11th International Symposium on Space Terahertz Technology, Ann Arbor, MI, May 2000*.
- [2] H. Ekstroem, B. Karasik, E. Kollberg, and K. Yngvesson. Conversion Gain and Noise of Niobium Superconducting Hot-Electron Mixers. *IEEE Transactions on Microwave Theory and Techniques*, 43(4):938–947, April 1995.
- [3] T. Graauw and F.P.Helmich. Herschel-HIFI: The Heterodyne Instrument For The Far-Infrared. In *Proc. of 'The Promise of the Herschel Space Observatory' Symposium, December 2000*.
- [4] R. Guesten, P. Hartogh, H.-W. Huebers, U. Graf, K. Jacobs, H.-P. Roeser, F. Schaefer, R. Schieder, R. Stark, and J. Stutzki. GREAT The First-Generation German Heterodyne Receiver For SOFIA. In *Proc. SPIE, 2000*.
- [5] B. Karasik and W. McGrath. Microwave Transmission Technique for Accurate Impedance Characterization of Superconductive Bolometric Mixers. *IEEE Transactions on Applied Superconductivity*, March 1998.
- [6] M. Kroug. *NbN Hot Electron Bolometer Mixers for a Quasi-Optical THz Receiver*. PhD thesis, Chalmers University of Technology, Sweeden, 2001.
- [7] U. Mair, M. Krocka, G. Wagner, M. Birk, H.-W. Huebers, H. Richter, A. Semenov, P. Yagoubov, R. Hoogeveen, T. de Graauw, A. Maurellis, A. Selig, V. Koshelets, S. Shitov, B. Ellison, B. Kerridge, D. Matheson, R. Siddans, and J. Reburn. TELIS Development of a New Balloon Borne THz/Submm Heterodyne Limb Sounder. In *Proceedings: 13th International Symposium on Space Terahertz Technology, Cambridge 2002, December 2002*.
- [8] F. Rodriguez-Morales. Impedance and Bandwidth Characterization of NbN Hot Electron Bolometric Mixers. Master's thesis, University of Massachusetts Amherst, USA, 2003.
- [9] R. Schoelkopf, P. Burke, D. Prober, A. Skalare, B. Karasik, M. Gaidis, W. McGrath, B. Bumble, and H. LeDuc. Noise Bandwidth of Diffusion-Cooled Hot-Electron Bolometers. *IEEE Transactions on Applied Superconductivity*, 7(2):3576–3579, June 1997.
- [10] K. Yngvesson, C. Musante, M. Ji, F. Rodriguez, Y. Zhuang, E. Gerecht, M. Coulombe, J. Dickinson, T. Goyette, , J. Waldman, C. K. Walker, A. Stark, and A. Lane. Terahertz Receiver With NbN HEB Device (Trend) - A Low-Noise Receiver User Instrument for AST/RO at the South Pole. In *Proceedings: 12th International Symposium on Space Terahertz Technology, San Diego CA, Febr 2001*.

Sideband-Separating SIS Mixer at 110GHz for the measurement of atmospheric ozone

Shin'ichiro Asayama⁽¹⁾, Takashi Noguchi⁽²⁾, and Hideo Ogawa⁽¹⁾

⁽¹⁾ Department of Earth and Life Sciences, College of Integrated Arts and Sciences,
Osaka Prefecture University, 1-1 Gakuen-Cho, Sakai-City, Osaka, 599-8531 Japan

⁽²⁾ Nobeyama Radio Observatory, 462-2 Nobeyama, Nagano, 384-1305 Japan

ABSTRACT

We present performance and test observation result of a sideband-separating SIS mixer at 100GHz band. All mixer components are integrated on a split-block waveguide unit. The measured single-sideband (SSB) receiver noise temperatures with L-band IF ($f_c = 1.5$ GHz) are less than 60 K in the LO frequency range of 90-115 GHz, and minimum value of around 35 K is achieved at 100 GHz. The image rejection ratios are more than 11 dB in the frequency range of 90-110 GHz. We have installed the sideband-separating SIS mixer into an atmospheric ozone measuring system and successfully observed an ozone spectrum at 110 GHz in SSB mode.

1. INTRODUCTION

There is a strong interest in the millimeter astronomical and atmospheric community to operate low noise quasi-particle mixers in SSB mode in order to eliminate atmospheric noise in the image band during spectral line observations. SSB observations are more efficient not only for spectroscopic observations in one sideband, but even if spectral lines of interest are present in both sidebands. Therefore, wideband and tuner-less SSB receiver is requested for observations in radio astronomy and atmospheric radiometer. To meet these demands we have been developing a sideband-separating mixer. In this report we have demonstrated performance and test observation result of a sideband-separating SIS mixer at 100GHz band.

2. MIXER DESCRIPTION

Detailed structure of a split-block waveguide unit for our sideband-separating mixer is shown in Fig. 1. We adopted W-Band waveguide (2.54 x 1.27 mm) for our waveguide unit. The basic design of the sideband-separating SIS mixer is similar to that described by Claude *et al.*[1]. The split-block waveguide unit contains an RF quadrature hybrid, two LO directional couplers, a LO power divider, and 4 K cold image terminations. We also integrated two DSB mixers on the split-block waveguide unit through the waveguide taper transformer. Note that no LO power is reflected back into another mixer in the case of ideal quadrature hybrid, since most of LO power reflected at a mixer is transmitted to the 4 K load and the feed horn through the RF quadrature hybrid. The IF signals from the two DSB mixers are combined in a commercial quadrature hybrid (Anaren Microwave, Inc.). For the initial experiment, we have chosen an IF of 1.0-2.0 GHz suitable for the existing atmospheric ozone measuring system at Osaka Prefecture University.

More detailed information is written in ALMA MEMO 453 [2].

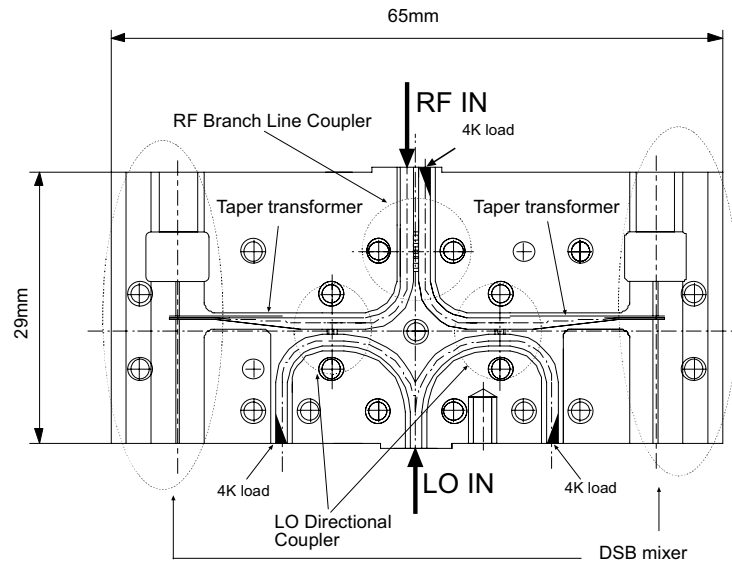


Fig. 1. Configuration of the split-block waveguide unit. The split-block waveguide contains two DSB mixers, an RF quadrature hybrid, two LO directional couplers, a LO power divider, and 4 K cold image terminations.

3. RESULT

3.1. Receiver Performance

The overall receiver noise temperature (SSB) of the receiver (including noise contribution of the vacuum window, feed horn, and IF amplifier chain) is plotted in Fig. 2 (a). The measured SSB receiver noise temperatures are less than 60 K in the LO frequency range of 90-115 GHz, and minimum value of around 35 K is achieved at 100 GHz. The measured sideband rejection ratio is plotted in Fig. 2 (b). The image rejection ratios are more than 11 dB in the frequency range of 90-110 GHz.

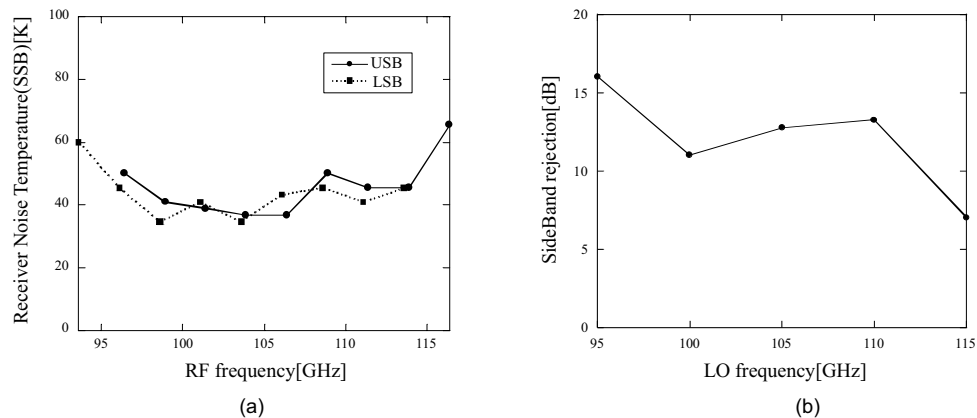


Fig. 2. (a) SSB receiver noise temperatures and (b) sideband-rejections as functions of frequency.

3.2. Observation

We have installed the sideband-separating SIS mixer into the atmospheric ozone measuring system at Osaka Prefecture University. The atmospheric ozone spectra obtained with DSB and SSB (USB) receiver system are shown in Fig. 3. It is noted here that the brightness temperature of the ozone spectrum observed in SSB mode is just twice of that observed in DSB mode as expected.

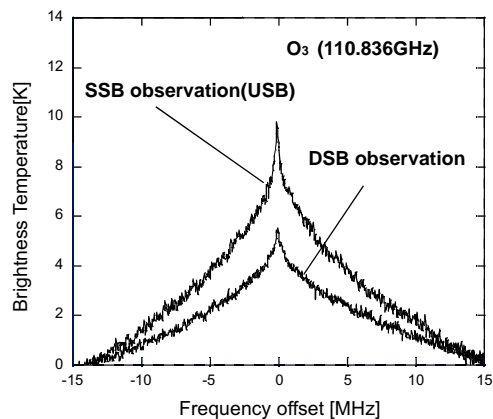


Fig. 3. Atmospheric ozone spectra obtained with DSB and SSB receiver system.

4. CONCLUSION

We have demonstrated performance and test observation result of a sideband-separating SIS mixer at W-band. We integrated all mixer components on the split-block waveguide unit, which contains two DSB SIS mixers, an RF quadrature hybrid, two LO directional couplers, a LO power divider, and 4 K cold image terminations. The measured single-sideband (SSB) receiver noise temperatures with L-band IF ($f_c = 1.5$ GHz) are less than 60 K in the LO frequency range of 90-115 GHz, and minimum value of around 35 K is achieved at 100 GHz. The image rejection ratios are more than 11 dB in the frequency range of 90-110 GHz. We have installed the sideband-separating SIS mixer into an atmospheric ozone measuring system and successfully observed an ozone spectrum at 110 GHz in SSB mode. This experimental result indicates that the sideband separating SIS mixer is very useful for astronomical observation as well as atmospheric observation.

References

- [1] S.M.X. Claude, C.T. Cunningham, A.R. Kerr, S.-K. Pan, "Design of a Sideband-Separating Balanced SIS Mixer Based on Waveguide Hybrids", ALMA Memo 316, <http://www.alma.nrao.edu/memos>
- [2] S. Asayama, H. Ogawa, T. Noguchi, K. Suzuki, H. Andoh, A. Mizuno, "An Integrated Sideband-Separating SIS mixer Based on Waveguide Split Block for 100 GHz Band," ALMA Memo 453, <http://www.alma.nrao.edu/memos>

Repeatability and Reliability of the 640 GHz SIS Mixer for JEM/SMILES

Ken'ichi KIKUCHI¹, Yasunori FUJII^{1,2}, Wen-Lei SHAN³,
and Junji INATANI¹

¹ National Space Development Agency of Japan, Tsukuba, Ibaraki 305-8505, Japan

² Nihon Tsushinki Co., Ltd., Yamato, Kanagawa 242-0018, Japan

³ Communications Research Laboratory, Koganei, Tokyo 184-8795, Japan

I. Introduction

The development of SIS mixers at 640 GHz band is a key issue of JEM/SMILES mission [1], which is an atmospheric observatory to be onboard the International Space Station. Through an early development phase, a good receiver noise performance less than 200 K (DSB) has been achieved with Nb-based Parallel-connected Twin-junction (PCTJ) SIS mixer as a breadboard model [2]. For use in a space experiment, not only to achieve a good noise performance, but also to establish a way to fabricate a reliable SIS mixer is critical. This presentation summarizes a recent investigation to understand and improve the controllability of SIS device parameters in our process. We also briefly reports the result of environmental tests, such as ion irradiation, to confirm the compatibility with the space environment.

II. SIS Device Fabrication

Our Nb/Al-AlO_x/Nb junctions are being fabricated at the Nobeyama Radio Observatory. Typical junction area is $\sim 1 \times 1 \mu\text{m}^2$, and current density is 6–8 kA cm⁻². Considering the space application, we adopted the PCTJ-type device to achieve a broad RF impedance matching without troublesome mechanical tuning.

Fig. 1 shows an example of cross-sectional image of junction portion observed using TEM. Since parameters such as the thickness of layers and the superconductivity of Nb films are directly related to the mixer performance, we should realize their characteristics and improve the controllability in our fabrication process. After several improvements, we attained moderately stable fabrication, and succeeded in increasing the yield of good junctions.

One of difficulties in fabrication is to control the junction size. As shown in Fig. 2, the deviation in size is sometimes up to 10 % even in the same wafer, which corresponding to a ~ 3 % shift in center frequency. Although some problems still remains to be solved, we obtained the SIS devices which show an excellent receiver noise performance with ~ 150 K.

III. Environmental Tests

The space environment is hostile to operating a sensitive measurement system in many ways. We carried out various tests with SIS mixers to confirm their compatibility with the space environments. Following describes some topics:

Cosmic Ray Particles : We performed a proton irradiation test with cooling the SIS device below 4 K. Although some changes in DC characteristics were observed after extremely high fluence irradiation, we confirmed the tolerance of SIS device against the cosmic ray was far higher than the total dose expected in the orbit.

Thermal Cycle : The SIS mixer is expected to experience some thermal -30°C to $+60^{\circ}\text{C}$ cycles in orbit during power-off period of mechanical cooler system. Moreover, baking of cryostat system is scheduled to reduce outgass before launch. In our test, an increase of normal resistance by $\sim 10\%$ (corresponding to $\sim 1\ \Omega$) was observed after one week of 80°C load. It is probably due to the increase of tunnel barrier potential by the reaction of unbound oxygen with Al atoms.

Launch Vibration : The vibration load at 4 K stage of cryostat is estimated to $\sim 40\ G_{\text{rms}}$ for our launcher. We have performed a vibration test on the SIS mixer with the same level. As the result, no change in DC and RF performance was found.

References

[1] SMILES Science Team and SMILES Mission Team, “JEM/SMILES Mission Plan”, Version 2.1, November 2002 (available at <http://smiles.tksk.nasda.go.jp/index.shtml>)
 [2] Y. Fujii, K. Kikuchi, J. Inatani, Y. Irimajiri, M. Seta, S. Ochiai, T. Manabe, H. Masuko, T. Noguchi, K. Narasaki, S. Tsunematsu, and T. Shiota, “Space-borne 640-GHz SIS Receiver Based on 4-K Mechanical Cooler”, *SPIE*, 4013, 90, 2000

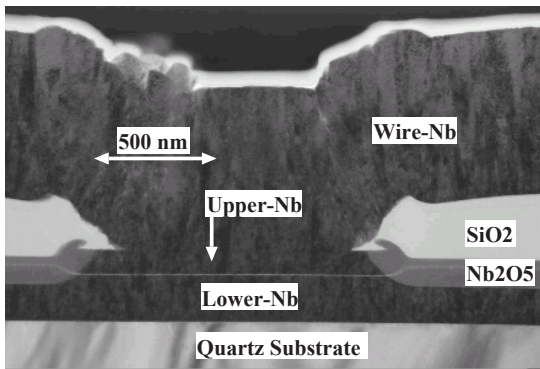


Figure 1: Cross-sectional image of SIS junction.

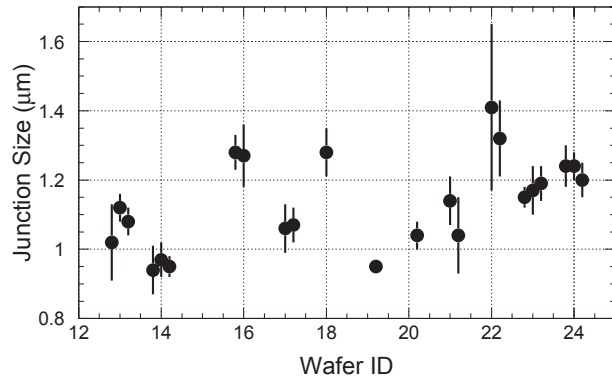


Figure 2: Mean junction size with 1- σ deviation in a wafer.

Observation of an anomalous IF peak at high bias voltage in 660-GHz SIS Mixers

M. J. Wang^(a), W. L. Shan^(b), W. Zhang^(b), H. W. Cheng^(a), T. Noguchi^(c), S. C. Shi^(b), Y. Irimajiri^(d), T. Manabe^(d)

(a) Institute of Astronomy and Astrophysics, Academia Sinica, Nankang, Taipei, Taiwan

(b) Purple Mountain Observatory, Nanjing, China

(c) Nobeyama Radio Observatory, NAOJ, Nobeyama, Nagano 384-13, Japan

(d) Communications Research Laboratory, Nukui-kita-machi, Koganei-shi, Tokyo Japan

Abstract

We have designed and fabricated 660GHz parallel-connected-twin-junction mixer for SMA. The receiver noise temperature, T_{rx} , is around 200K with a wire grid of 80% signal coupling. However, some mixers have poor performance when an anomalous IF peak beyond the junction's gap voltage is observed. In this paper, we will discuss the origin and influence of this IF peak.

Corresponding author: Ming-Jye Wang

Phone : +886-2-3655-2200 :Email : mingjye@asiaa.sinica.edu.tw

We have designed and fabricated parallel-connected-twin-junction 660GHz SIS mixers. Typically the receiver noise of these mixers is near 200K[1]. However, some junctions have poor performance although their junction's parameters are similar. The LO pumping of these mixers are difficult and the receiver noise temperature can be worse than 1000 K. It is important issue to understand the reason causing the poor performance for future design and fabrication.

Since the junction parameters are similar for good and poor performance mixers. Some important effects might be missing in regular measurement. Thus, we measured the junction's I-V curve and mixer's IF response to high bias voltage, up to 17mV, as shown in Figure 1(a). Anomalous IF peaks are observed, an indication of the non-linearity in junction's I-V curve. The peak position shifts to higher voltage as the temperature decreases. Figure 1(b) shows the temperature dependence of corresponding current of IF peak. The data (solid square) can be fitted by a formula of $I_C \sim 1-(T/T_C)^\alpha$, where T_C is 9.2 K and α is 4.6. In addition, not shown here, the IF peak position is modulated by an external magnetic field. Both temperature and magnetic field dependence indicate the existence of unintentional weak-link junctions in series with the SIS junctions.

To understand the origin of this unintentional junction, the cross section structure of junction with good and poor performance is studied by TEM. A regular contact between top and wiring Nb is observed in the junction with good performance, as shown in Figure 2(a). On the contrary, the contact area is small in the junction with poor performance, Figure 2(b). Most area on the top Nb seems filled by the fragments of insulating oxide. The contact area is estimated to be $0.15\mu\text{m}$ in diameter. This small contact behaves as an unintentional weak-link junction. The oxide fragments might fall into the contact hole during the oxide lift-off process.

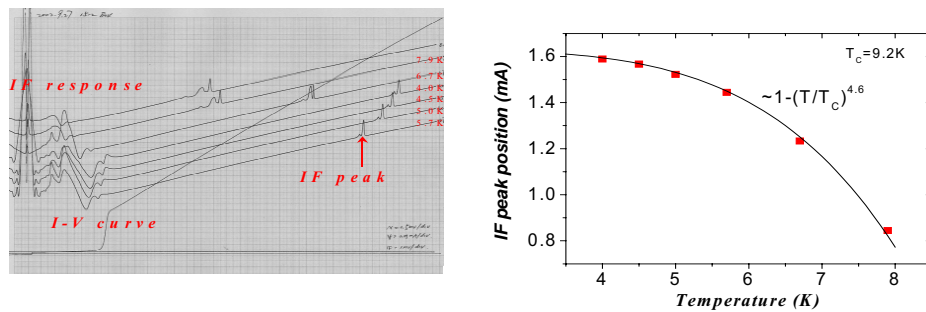


Figure 1 The anomalous IF peak beyond junction's gap voltage, (a) IF peak at different temperature and (b) temperature dependence of corresponding current of IF peak.

We have found that the 660-GHz SIS junctions showing the IF-peak structure are usually difficult to be pumped by LO signals, thereby giving high receiver noise temperature. Obviously, such additional weak-link junctions might absorb a fraction of RF/LO signal power and result in poor mixer matching. As exhibited in Fig. 3(a), the

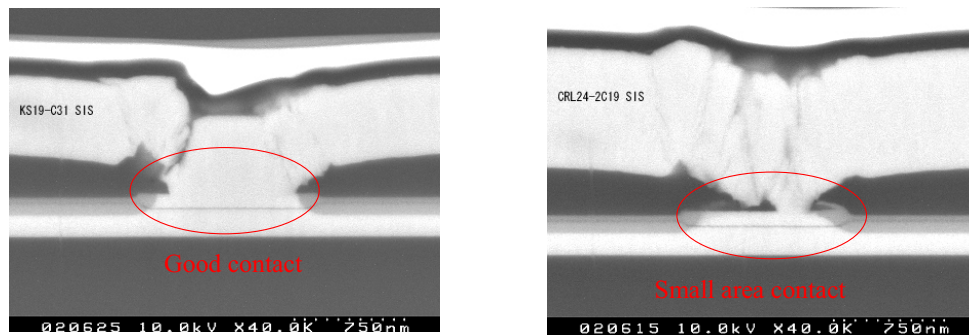


Fig. 2 Cross-sectional views of (a) good contacting junction and (b) poor contacting junctions

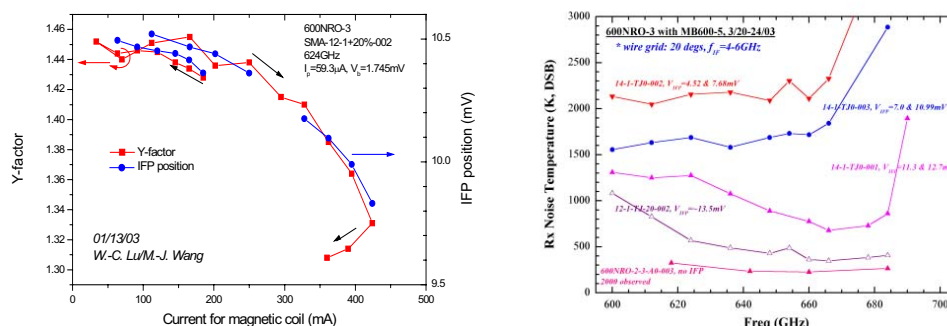


Fig. 3 Measured Y-factor as a function of magnetic field (a) and Measured receiver noise temperature for five different junction samples of different IF peak positions (b).

testing result for a mixer demonstrates that the mixer performance (Y-factor) is dependent upon the magnetic field applied to the SIS junction, which changes the position of the IF peak correspondingly. Fig. 3 shows the receiver noise temperature of five mixer samples, which have different IF peak positions. Obviously, the receiver noise temperature is strongly dependent upon the position of the IF peak, differing from $\sim 200K$ to $>2000K$. The higher voltage the IF peak occurs at, the lower receiver noise temperature the junction demonstrates.

In summary, an anomalous IF peak at high bias voltage region is observed in our 660-GHz SIS mixers when their performance is poor. The cross section structure of junction shows that some insulating oxide fragments might fall on the top Nb layer because of imperfect lift-off process. It reduces the contacting area between top and wiring Nb and an unintentional weak-link junction is formed. The existence of this unintentional weak-link junction will result in (1) the absorption of RF signal, and (2) the change of the mixer RF impedance. We have demonstrated the correlation between junction's IF peak position and mixer's performance. The performance becomes better when the IF peak is observed at higher bias voltage. In practical operation, the mixers with IF peak can be screened by checking the linearity of junction's I-V curve at high bias voltage.

References:

1. C.C. Chin *et al.*, Int. J. of IR & MM Waves, vol.23, pp.731-743, 2002

Development of the HIFI band 3 and 4 mixer units

G. de Lange⁽¹⁾, B.D. Jackson⁽¹⁾, M. Eggen⁽¹⁾, H. Golstein⁽¹⁾, W.M. Laauwen⁽¹⁾, L. de Jong⁽¹⁾, S. Kikken⁽¹⁾, C. Pieters⁽¹⁾, H. Smit⁽¹⁾, D. Van Nguyen⁽¹⁾, M. Kroug⁽²⁾, T. Zijlstra⁽²⁾, T.M. Klapwijk⁽²⁾

⁽¹⁾ *SRON National Institute for Space Research Postbus 800, 9700 AV Groningen, the Netherlands*

⁽²⁾ *Department of Nanoscience, Faculty of Applied Science, Delft University of Technology. Lorentzweg 1, 2628 CJ Delft, The Netherlands*

Abstract

We describe the current status of the HIFI mixer units for Band 3 and Band 4. The mixer units cover the 800-960 GHz and 960-1120 GHz frequency range and have a 4-8 GHz IF frequency band. The major requirements and the performance status are presented.

1. INTRODUCTION

The Herschel Space Observatory (launch date 2007) will fly two cameras/medium resolution spectrometers (PACS and SPIRE) and the heterodyne instrument HIFI [1,2,3]. An international consortium led by the PI institute, SRON, is building HIFI. SRON is also responsible for the development of the mixer units for band 3 (800-960 GHz) and 4 (960-1120 GHz)[4]. Each of these bands contains two tunerless waveguide mixers (to measure both orthogonal polarizations) with a 4-8 GHz IF band. The mixer unit development program is currently in the Qualification Model phase, in which extensive environmental testing will prove the flight worthiness of the units. In this paper we present the current status of the mixer unit design and the performance.

2. REQUIREMENTS

A summary of the design drivers for the mixer units is given in Table 1. The two main requirements for the instrument are reliability and sensitivity. Note that the challenging goal sensitivities of the mixer units given in Table 1 are the sensitivities of the mixer unit only, without noise contributions from the optics and IF.

3 PERFORMANCE STATUS.

The current design of the mixer unit is shown in Fig. 1.

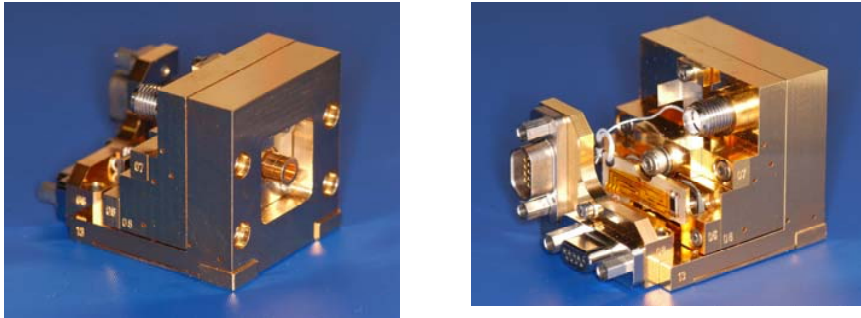


Figure 1 Front and backside view of an assembled mixer unit

The heterodyne elements in the mixer units are Nb/Al₂O₃/Nb SIS twin junctions with Al and NbTiN top and bottom wiring layers, respectively. The devices are fabricated at DIMES [5,6]. For band 4 we currently use NbTiN films grown at the Jet Propulsion Laboratory by J. Stern. Some typical receiver DSB Noise Temperatures versus RF frequency of band 3 and 4 mixer units are shown in Fig. 2. The figure shows noise measurements performed at 2 K with both a thin (14 μm) and thick (55μm) mylar beam splitter, and the expected performance within the HIFI instrument . The noise temperature is measured with the full 4-8 GHz IF-band. The measured receiver noise temperature for the thin beam splitter measurement ranges from 240 to 750 K DSB, but the receiver noise temperature in HIFI will be considerable lower (by approximately 100 K) than in our laboratory receiver, since HIFI will operate with a cold diplexer and LO and without heat filters in the signal path.

T_{mix} DSB	Band 3		Band 4	
Frequency	800 GHz	960 GHz	960GHz	1120 GHz
Baseline	119 K	158 K	158 K	190 K
Goal	99 K	129 K	129 K	151 K

Sensitivities, excluding contributions from IF chain and optics losses

- Withstand shelf life, bake-out, launch and in-orbit operation (9 years)
- Mass < 75 grams
- Envelope 32x32x45 mm
- IF range 4-8 GHz, ripple < 2dB/1 GHz
- De-flux heater operating at current < 20 mA
- Magnet current < 10 mA for second minimum in the Fraunhofer pattern
- Beam quality
- Optical alignment tolerances (goal): x,y: 42 μm, tilt 0.2°
- ESD protection, EMC shielding
- Bias circuit isolation > 30 dB in IF range

Table 1 Summary of the main requirements of the HIFI band 3 and 4 mixer units

5. ACKNOWLEDGEMENT.

We would like to thank Jeff Stern from JPL for providing the NbTiN film in the band 4 mixer unit and Wim Kooi from Caltech for the detailed simulation of the IF and RF design.

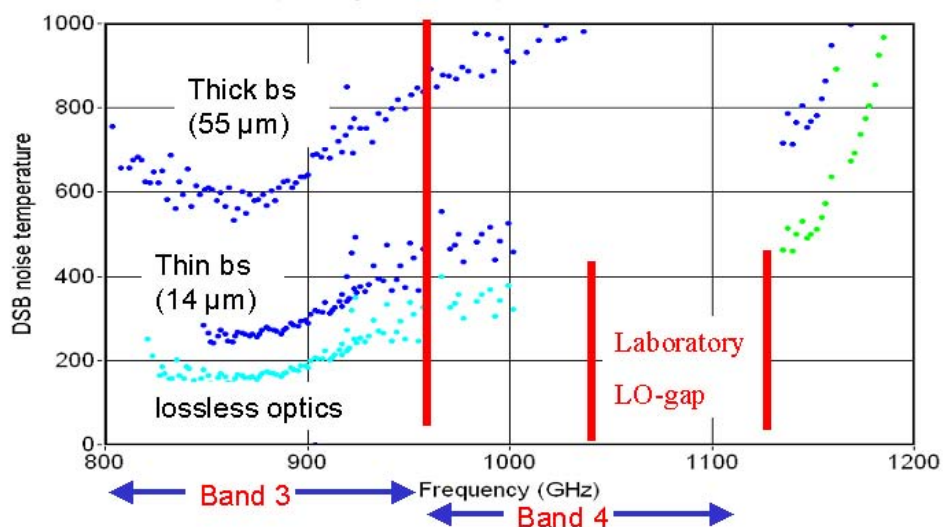


Figure 2 DSB receiver noise temperatures at 2 K measured with a thick (55 μm , upper curve) and thin (14 μm) beamsplitter of band 3 and band 4 mixer units. Data above 922 GHz is measured with the band 4 mixer unit (two different devices). The lower curves indicate the predicted performance for the case of zero optical loss.

6. REFERENCES

- [1] T. de Graauw, F. P. Helmich, "Herschel-HIFI: The Heterodyne Instrument for the Far-Infrared", in *The Promise of the Herschel Space Observatory*, edited by G. L. Pilbratt et al., ESA SP-460, pp. 45-51, 2001.
- [2] Web site at : <http://spdex.t.estec.esa.nl/home/herschel/>
- [3] Web site at: <http://www.sron.nl/divisions/lea/hifi/>
- [4] G. de Lange, B.D. Jackson, M. Eggens, H. Golstein, W.M. Laauwen, L. de Jong, S. Kikken, C. Pieters H. Smit, D. Van Nguyen,, "Development of the HIFI band 3 and 4 mixer units", *Proc. 13th International Symposium on Space Terahertz Technology*, pp. 359-368, 26-28 March 2002, Harvard University, Cambridge, Massachusetts, USA.
- [5] B.D. Jackson, G. de Lange, W.M. Laauwen, L. de Jong, T. Zijlstra, N.N. Iosad, and T.M. Klapwijk, "THz SIS mixer development for HIFI", *Proc. 13th International Symposium on Space Terahertz Technology*, pp. 561-570, 26-28 March 2002, Harvard University, Cambridge, Massachusetts, USA.
- [6] B.D. Jackson, A.M. Baryshev, G. de Lange, S.V. Shitov, J.-R. Gao, N.N. Iosad, and T.M. Klapwijk, "Low-noise 1 THz superconductor-insulator-superconductor mixer incorporating a NbTiN/SiO₂/Al tuning circuit", *Appl. Phys. Lett.*, vol. 79, no. 3, pp. 436-438, 16 July 2001.

Design of 129-174 GHz SSB SIS mixer for Band 2 of New Generation Receiver of IRAM PdB Interferometer

A. Navarrini* and B. Lazareff

IRAM, Grenoble, France

*Present Address: Radio Astronomy Lab, University of California, Berkeley, CA, USA

Abstract

We present the design of a Single Side Band (SSB) SIS mixer covering the band 129-174GHz. A reactive termination is used to reject the image sideband. We discuss the problems posed by the requirements of SSB operation, stability, wide IF band (3.85-7.85 GHz), and the design solutions that were adopted.

Introduction. A stability criterion for an SSB SIS mixer with distinct signal and image termination impedances under typical operating conditions has been derived for the band 129-174 GHz using the standard quantum theory of mixing. One of the most significant design issues is to achieve SSB operation over a wide tuning range, while ensuring stable operation in all cases according with the derived criterion. A series array of $N=2$ SIS junctions has been preferred to a single junction design to increase the saturation power of the mixer, which scales approximately as N^2 .

Waveguide and transition to Suspended Substrate Microstripline (SSL). We use a WR6 full-height waveguide (1.651×0.825 mm²), which is easier to fabricate and has lower loss than a reduced-height waveguide. The wideband transition to SSL (quartz thickness and width 160 μ m and 500 μ m, respectively) is similar to the one adopted in a previous work [1], properly rescaled and further optimized using a numerical EM simulator. This is based on a probe (and quartz substrate) stretching only part way inside the waveguide with the substrate perpendicular to the waveguide axis (see Figs.(1)-(2)).

A choke type noncontacting backshort with rectangular cross-section can be displaced inside the waveguide. It has been optimized to provide a large amplitude of reflection coefficient (above -0.03 dB) over the 129-174 GHz band taking into account of mechanical tolerances. For a given position, it provides a good match to a ~ 75 Ω impedance at the single-ended probe driving point. Image rejection is achieved by adjusting the backshort so that, simultaneously, an optimum match is achieved at the signal frequency, while a reactive termination is presented to the junctions at the image frequency. With a central IF frequency of 5.85 GHz, the required backshort distance from the antenna plane necessary to fulfill such condition is of the order of $l_{BS} \approx 5$ mm. The mixer can also be operated in DSB with a fixed backshort position close to the antenna plane at a distance of $\approx \lambda_g/4 \approx 0.5$ mm.

RF and IF Matching Circuits. Each of the two Nb/Al-AlO_x/Nb junctions has an area of 1.6×1.6 μ m², a critical current density of ≈ 4 kA/cm² ($C_s \approx 58$ fF/ μ m²), and a normal state resistance of $R_n = 25 \Omega$ ($\omega R_n C \approx 3.5$). The top contacts of the tunnel barriers are located inside a short section of an electrically isolated rectangular pad on a Niobium layer 430

nm thick. RF currents from the antenna gets to the junctions flowing from a bottom Niobium strip (120 nm thick) connected to the pad (see bottom of Fig.(2)). The short length (18 μm) of the isolated rectangular pad allows to minimize the series inductance of the array (≈ 6 pH) so that its total RF reactance is still dominated by the total intrinsic capacitance of the junction series $C \approx 75$ fF. A parallel tuning inductor (9 pH), realized as a short section of coplanar waveguide (CPW) terminated into a short circuit through a $16 \times 16 \mu\text{m}^2$ junction via, allows to tune out the reactive part of the series combination of the SIS array with a capacitive stub. Such a stub provides a ground for the RF and a path for the IF output and junction bias through a two sections RF choke connected to it. Each section of the choke is realized as CPW followed by a microstrip capacitor, and is designed to present a high RF impedance to the junction array. The resulting impedance of the tuned SIS series array is matched to the 75Ω antenna using a two section impedance transformer consisting of a short inductive CPW section ($\approx \lambda/20$) followed by a short capacitive microstrip section ($\approx \lambda/40$).

To achieve the required 4 GHz IF band, the intrinsic capacitances and inductances of the chip have been kept to a minimum value. An IF matching circuit external to the chip has been designed to present a real part of the load impedance as seen at the junction port in the range $50\text{-}80 \Omega$ over the $3.85\text{-}7.85$ GHz IF band.

The mixer has been optimized using various electromagnetic simulators.

Mixer block construction. The main mixer block ($25 \times 25 \times 20 \text{ mm}^3$) is split in two parts which will be made of brass to allow easy machining (see Fig.(3)). The rear mixer block houses the mixer chip and the copper-beryllium backshort. The rectangular waveguides will be realized by spark erosion technique, while the other parts require standard micromachining process.

Predicted performances. The final result of simulation for the impedance seen by the junctions when the mixer is operated in SSB mode (ex. LSB 149 GHz, backshort at 5.6 mm from the antenna plane) is shown in Fig.(4). At intervals of $2 \times \nu_{\text{IF}} = 11.70$ GHz, the junction sees alternately an approximate match and a reactive termination which is confined in the derived stability region. The quantum theory of mixing is used to compute the mixer and receiver noise temperatures. The results are shown in Fig.(5) (we have assumed a noise temperature of the IF amplifier of 6 K; input losses are not taken into account). A receiver noise below 15 K (quasi-SSB, image gain less than -14 dB) is estimated over the operating band of the mixer.

Conclusions. A new type of SSB SIS mixer has been designed for the $129\text{-}174$ GHz frequency band of the new generation receiver of IRAM PdBI. The mixer chip includes a series array of two junctions and has been designed with low output capacitance and inductance to cover an IF band of 4 GHz. The mixer can achieve low noise and image band rejection while maintaining stable operation over the whole RF band.

References

- [1] Navarrini, A., Lazareff, B., Billon-Pierron, D., and Peron, I., "Design and characterization of a $225\text{-}370$ GHz DSB and a $250\text{-}360$ GHz SSB full height waveguide

SIS mixers”, Proceedings of the 13th International Symposium on Space Terahertz Technology, Cambridge, MA, USA, March 26-28, 2002, p. 33-40;

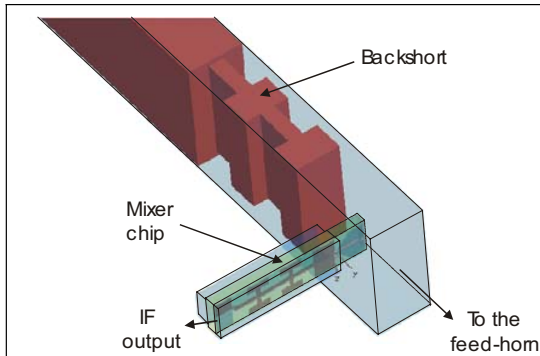


Fig.(1): Inner structure of the SSB mixer.

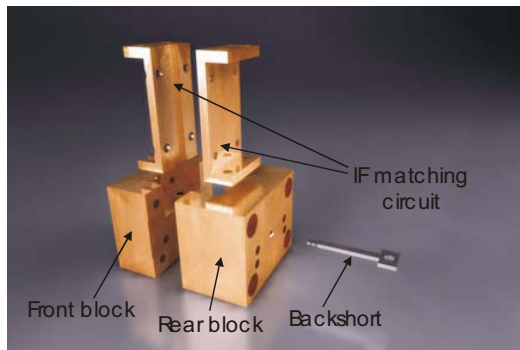


Fig.(3): Overview of the mechanical assembly of the mixer.

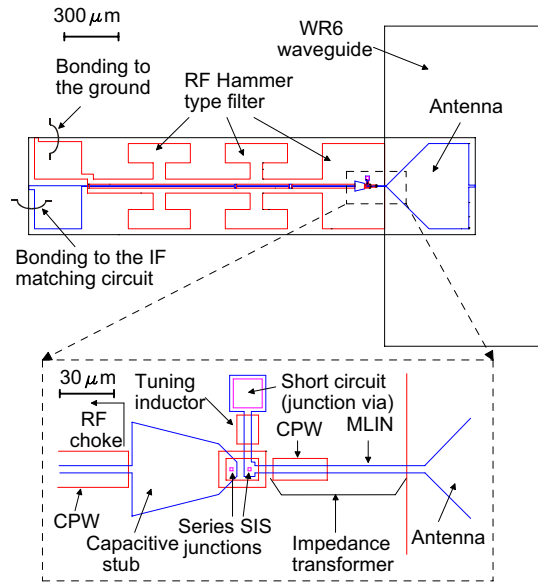


Fig.(2) *Top*): View of the mixer chip showing the antenna, the RF Hammer type filter and the bonding wires to the external ground and IF matching circuit. *Bottom*): Central part of the chip including the array series of two SIS junctions with its RF tuning structure. The mixer chip has dimensions $0.16 \times 0.5 \times 2.37 \text{ mm}^3$.

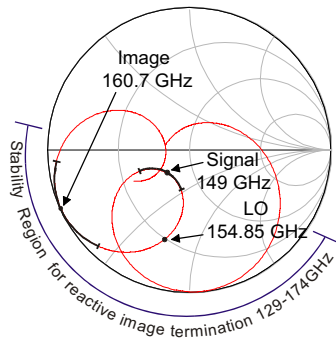


Fig.(4): Embedding impedance seen by the junction, over the design operation band for a SSB tuning in LSB at 149 GHz. The Smith chart is normalized to the small signal RF resistance of the series array $R_{RF}(150\text{GHz}) \approx 24 \Omega$.

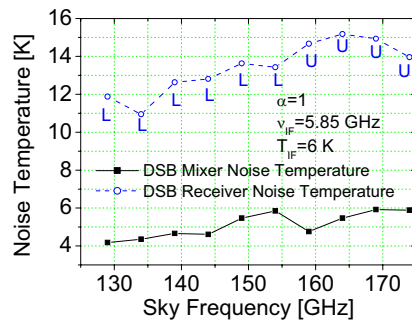


Fig.(5): Predicted DSB mixer and receiver noise temperature of the SSB mixer referred at its input. The letters *L* and *U* over each point indicate whether the corresponding value is obtained in, respectively LSB or USB.

Scaled Model Measurement of the Embedding Impedance of a 660-GHz Waveguide SIS Mixer with a 3-Standard De-embedding Method

W. Zhang¹, C.-Y. Edward Tong² and S.C. Shi¹

1. Purple Mountain Observatory, Chinese Academy of Sciences, China
2. Harvard-Smithsonian Center for Astrophysics, Cambridge, MA 02138, USA

Abstract: In this paper, the embedding impedance of a 660-GHz waveguide SIS (superconductor-insulator-superconductor) mixer is investigated using a 100-times scaled model with a new 3-standard de-embedding technique. The mixer embedding impedance is extracted from the reflection coefficients measured at the waveguide port of the mixer for three different terminations at the SIS junction's feed point. The three standards chosen are open-circuit, short-circuit and resistive load. Measured results are compared with those simulated by HFSS (High Frequency Structure Simulator).

1. Introduction

For the design of fixed-tuned waveguide SIS mixers in the submillimeter regime, it is necessary to have a precise knowledge of the mixer embedding impedance (i.e., the impedance seen at the junction's feed point). Embedding impedances have been determined using scaled-model measurement [1] or numerical methods [2]. The conventional scaled-model method measures the embedding impedance directly via a miniature coaxial connected to the junction's feed point. The accuracy of this method is limited by the model accuracy of the coaxial probe's tip. Numerical methods that derive impedances from the pumped I-V curves of SIS junctions depend largely upon junction parameters. Full-wave electromagnetic solvers, like HFSS, have been used to model a few submillimeter mixers [3]. However, it is important to have experimental confirmation of simulated data.

In this paper, we propose a new scaled-model measurement method, which incorporates a 3-standard de-embedding technique [4]. This technique extracts the scattering parameters of a two-port network from the reflection coefficients measured at one port when the second port is terminated with 3 different impedance standards. Using this new method, we have determined the embedding impedance of a 600-720 GHz waveguide SIS mixer mount [5] with a 100-times scaled model. The measured impedances are then compared with those simulated by HFSS.

2. Measurement method

Fig. 1 shows the fabricated 100-times scaled model. Its operating frequency was 6.0-7.2 GHz scaled down from 600-720 GHz. The crystalline quartz substrate was replaced by a 4-mm thick dielectric slab ($\epsilon_r \sim 3.5$), and the junction's feed point was scaled to a gap (0.2x1 mm). In our measurements, the feed point was connected to 3 different calibration standards:

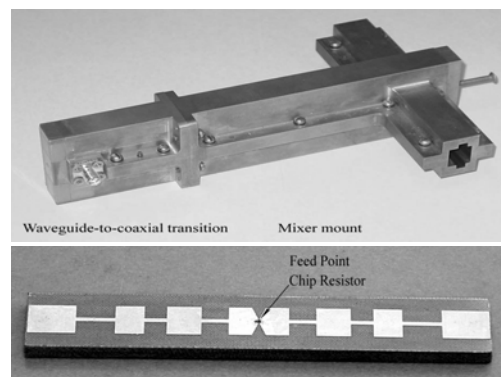


Fig. 1 100-times scaled model for a 660-GHz waveguide SIS mixer mount, (a) overall view of the model, (b) photograph of the dielectric slab used inside the model

open-circuit, short-circuit and resistive load given by chip resistors (0.5x1 mm). A waveguide-to-coaxial transition was included to interface to a microwave network analyzer.

First, we measured the complex reflection coefficients at the coaxial port of the waveguide-to-coaxial transition, while its waveguide port was shorted. Let Γ_m ($m=1, 2, 3$) be the measured reflection coefficients corresponding to 3 different short circuit planes, and $[S']$ the scattering matrix of the transition. The relation between Γ_m and $[S']$ is

$$\Gamma_m = S'_{11} + \left\{ S'_{12} S'_{21} R_m / (1 - S'_{22} R_m) \right\}, \quad (1)$$

where R_m is the complex reflection coefficient of the waveguide short circuit m at the waveguide port. $[S']$ can be easily solved using Equation (1) [4].

Next, we connected the transition to the scaled mixer block and the complex reflection coefficients were measured again at the coaxial port of the transition while the device feed point was terminated by the three calibration standards. Let Γ_i be the measured complex reflection coefficient when the junction's feed point was terminated by calibration standard i , where $i = o$ (open), s (short) or r (resistive). Let Γ_i' be the corresponding reflection coefficient at the mixer's waveguide port when the port was terminated by a matched load instead of the transition. The relation between Γ_i' and Γ_i is

$$\Gamma_i' = (\Gamma_i - S'_{11}) / \left\{ S'_{12} S'_{21} + (\Gamma_i - S'_{11}) S'_{22} \right\} \quad (2)$$

The embedding impedance Z_{emb} at the device feed point can be solved in terms of Γ_i'

$$Z_{emb} = Z_r (\Gamma_o' - \Gamma_r') / (\Gamma_r' - \Gamma_s') \quad (3)$$

where Z_r is the impedance of the chip resistor at the measured frequency.

Equation (3) shows that the derived embedding impedance is directly proportional to Z_r . It is therefore very important to know the accurate value of this impedance. We have measured the actual impedances of these chip resistors in a separate experiment setup.

3. Measurement results

The impedances of three chip resistors, whose nominal resistances are 24, 51, and 100 Ω , were measured with a microstrip fixture (0.5 mm thick and 1.2 mm wide) having a 1-mm gap at its center where the chip resistor was to be soldered. Time-domain gating technique was employed to remove the discontinuity effect due to SMA connectors to microstrip line [6]. The loss and phase shift of the microstrip

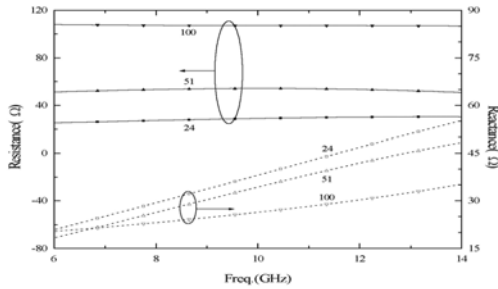


Fig. 2 Measured impedances of three chip resistors.

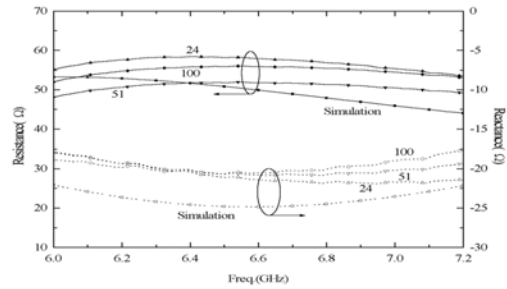


Fig. 3 Measured embedding impedance of the 100-times scaled model for three instances.

line were also compensated. The measured impedances for the three chip resistors are plotted in Fig. 2. Obviously, the chip resistors have resistances close to their nominal values, but all have a considerably large positive reactance in the frequency range of 6-14 GHz. The larger the nominal resistance is, the smaller the measured reactance becomes. In addition, the measured reactance is proportional to frequency, suggesting that there is a series parasitic inductance.

The waveguide-to-coaxial transition had been designed with the aid of HFSS by optimizing its power transmission coefficient in the frequency range of 6.0-7.2 GHz. Using the procedure described above, we have measured the scattering parameters of the transition. It has been found that the measured S_{12}^t values are in good agreement with the simulated ones.

Equations (2) and (3) were then used to determine the embedding impedance of the scaled 660-GHz SIS mixer. Three sets of data were available, one from each chip resistor. The results are plotted in Fig. 3. The embedding impedances, both real and imaginary parts, are in good agreement for the three instances. The dispersion of the 3 data sets is less than 7Ω , averaged across 6.0–7.2 GHz. The embedding impedance simulated for the same structure by HFSS is also displayed in Fig. 3. Clearly, the simulated resistance differs slightly from the measured one and the simulated reactance shows better agreement with the measured one.

4. Summary

A new scaled-model measurement method incorporating the 3-standard de-embedding technique has been employed to characterize the embedding impedance of a 660-GHz waveguide SIS mixer. The impedances of the chip resistors used in our scaled-model measurement were accurately measured using the time-domain gating technique. By comparing the data dispersion between embedding impedances derived from different calibration standards, we infer that the measured impedances are accurate to within 7Ω . These measured embedding impedances also agree with the numerically simulated ones. The new scaled-model method is very useful for the characterization of submillimeter mixer mounts.

References

1. A.V. Raisanen, W.R. McGrath, et al, "Scaled model measurements of embedding impedances for waveguide SIS mixers," *Int. J. of Infrared and Millimeter Waves*, vol. 6, pp. 1169-1189, 1985.
2. Anders Skalare, "Determining embedding circuit parameters from DC measurements on quasiparticle heterodyne mixers," *Int. J. of Infrared and Millimeter Waves*, vol. 10, pp. 1339-1353, 1989.
3. Ansoft High Frequency Structure Simulator, Ansoft Corporation, Four Station Square, #200 Pittsburgh, PA 15219-1119, USA.
4. Simo Ramo, John R. Whinnery and Theodore Van Duzer, *Fields and Waves in Communication Electronics*, 2nd edition, New York, NY: John Wiley & Sons, 1984, p.538.
5. S.C. Shi, C.C. Chin, M.J. Wang, et al, "Development of a 660-GHz SIS Mixer for SMART," in *Proc. 12th Int. Symp. On Space THz Tech.*, San Diego, CA, Feb. 2001, pp. 215-222.
6. Gregor Gronau and Ingo Wolf, "A simple Broad-Band Device De-embedding Method Using an Automatic Network Analyzer with Time-Domain Option," *IEEE Trans. Microwave Theory Tech.*, vol. MTT-37, no. 3, pp. 479-483, 1989.

SUPERCONDUCTING MICROSTRIP LINE MODELS AT MILLIMETER AND SUB-MILLIMETER WAVES AND THEIR COMPARISON

V. Belitsky[†], C. Risacher, M. Pantaleev, V. Vassilev

Group for Advanced Receiver Development
Onsala Space Observatory, Chalmers University of Technology
S 412 96, Gothenburg, Sweden

Abstract

Performance of superconductor – insulator - superconductor (SIS) tunnel junction mixers and their instantaneous input RF bandwidth are mostly depending on the integrated tuning circuit used to resonate out SIS junction capacitance; Nb-based SIS mixers operate in the frequency range of about 80 - 1000 GHz and typically use microstrip-based integrated tuning circuitries. One of the major challenges in designing the tuning circuitry for SIS mixers is accuracy of models for superconducting microstrip line (SML). Modeling gives the only tool to solve the problem of designing SML-based circuits because for such high frequencies *no* direct measurements of a superconducting transmission line can be made with *required* high accuracy. However, creating an accurate model for such a superconducting transmission line is a challenge by itself. In the SML, produced usually by thin-film technology, the magnetic field penetration depth is comparable with the thicknesses of the dielectric and superconductors comprising the line. As a result the electromagnetic wave is propagated not only in the dielectric media but also inside the superconducting strip and ground electrodes constituting the SML. This creates dramatic changes in the transmission line behavior that should be carefully accounted by including the superconducting material properties into the modeling. Nb superconductor, as the most commonly exploited material, was used in this study for modeling of the superconducting microstrip though the same approach would work for any different BCS superconducting material. The purpose of this paper is to introduce a new model for SML and compare it with previously suggested models and results of SML numerical simulation.

Introduction

Superconductor – insulator - superconductor (SIS) tunnel junction mixer is a dominating technology for MM and SubMM super heterodyne receivers for radio astronomy [1-3]. Presence of large intrinsic capacitance makes use of SIS-based mixers at these extremely high frequencies (80-1000 GHz) problematic; employing of an integrated tuning circuitry to resonate out SIS junction capacitance is the most convenient way to achieve ultimate performance and wide operational frequency band. Typical approach for implementing such a tuning circuitry is to integrate it on the substrate and fabricate it in the same processing steps as the SIS junction itself. The resulting tuning structures are typically a microstrip-based circuitry; the microstrip is a natural choice due to its complete compatibility with the SIS fabrication process, low RF loss and flexibility. As a result of this approach the SIS mixer tuning circuitry is being fabricated using thin-film technology and superconductors for the microstrip conductors. Accuracy of modelling for a superconducting microstrip line (SML) introduces one of the major challenges in design of tuning circuitry for the SIS mixers. The purpose of this article is an introduction of a new model for SML and its comparison with previously suggested models [4 - 8] and numerically simulated SML using 3D electromagnetic simulation package. The frequency range

[†] belitsky@oso.chalmers.se

of interest is 80 - 1000 GHz; experimental direct measurements of a superconducting transmission line at this frequency range are extremely challenging technically (the object of measurement is in a cryostat at 4 K ambient temperature) and cannot provide necessary precision required for accurate design. In the SML, produced by thin-film technology, magnetic field penetration depth is comparable with the thicknesses of the dielectric and the conductors of the line and this produces radical changes in the transmission line performance. The energy stored in the layers of the superconducting strip and ground electrodes, where H-field penetrates in, becomes comparable with the energy of the electromagnetic wave propagating in the dielectric and affects performance of the SML. Therefore, besides the geometry, the modelling of the SML should involve accurate simulation of the superconducting material properties and its influence on the SML characteristic impedance and the propagation constant.

Superconducting Microstrip Transmission Line

SML has a conventional microstrip transmission line geometry (depicted in Fig. 1) with both strip and ground conductors made of a superconductor material. RF and DC current conductivity in the superconducting materials is provided by paired electrons, Cooper pairs, and single electrons, quasiparticles, produced by thermal excitations or by breaking the Cooper pairs caused by the propagating RF signal with its corresponding energy of quanta. In this article we will consider the line strip and ground planes made of low- T_c BCS¹ superconducting materials. Nb superconductor is used in the model calculations through the whole paper as a material the most widely used for superconducting thin-film technology.

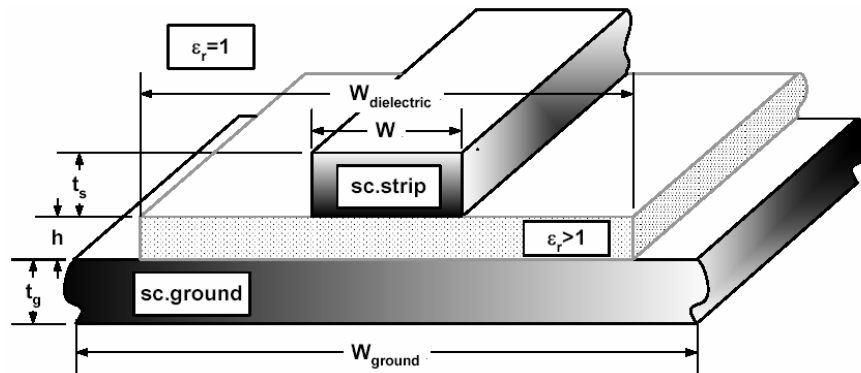


Figure 1. Schematic view of the superconducting microstrip line. The strip conductor thickness, t_s , ground conductor thickness t_g and the dielectric thickness h considered to be comparable with the static penetration depth of magnetic field, λ_o , while the widths are as following $W_{ground} \gg W_{dielectric} \gg W$.

The existing SML models [4 - 8], including the one being suggested in this paper, provide different ways for calculating the characteristic impedance and propagation constant for superconducting microstrip line; close formula equations based on conformal mapping or approach based on transmission line lump element circuit and/or superconductor surface impedance are used in the SML modelling. We are interested in the microstrip lines where the dielectric thickness is *comparable* with magnetic field penetration depth, the London penetration depth, λ_o , as well as with the thicknesses of the strip and ground superconductors forming the line. These particular relations between the strip, ground and dielectric thicknesses reflect typical geometry of the superconducting microstrip line produced by a thin-film technology used

¹ BCS Theory: J. Bardin, L.N. Cooper, J.R. Schrieffer, "Theory of Superconductivity", Phys. Rev. 1957

for, e.g., SIS mixer fabrication [9, 10]. In this article we compare the accuracy of different models for calculations of the line characteristic impedance, propagation constant and its dispersion. Additionally we use a numerical simulation with High Frequency Structure Simulator, HFSS [11], representing the superconducting material conducting properties via its surface impedance as proposed in [12].

RF Conductivity of a Superconductor

In contrast with conventional conductors, the DC and RF currents in superconducting materials are carried mainly by dual-electron carriers, Cooper pairs, without any conducting loss (super-current); a lossy part of the current is carried by quasiparticles (single electrons) generated by thermal excitations and interaction of electromagnetic field and the Cooper pairs. The presence of energy gap in the electron density of states, $\Delta=\Delta(T)$ ($e\Delta \approx 1.5$ mV for Nb material), limits the ability of the Cooper pairs in superconductors to carry the RF current at frequencies closer to the gap frequency, $F_g=2e\Delta/h$, where e is the electron charge, h is the Plank's constant and F_g is the gap frequency; above F_g the conducting properties of the superconductor become close to that of a conventional conductor.

The *magnetic* component of the field penetrates into superconductor within a characteristic depth defined as the static London penetration depth, λ_o , for DC current. Actual magnetic field penetration depth, λ , has noticeable frequency dependence for frequencies even well below the gap frequency and, as the frequency approaches the gap frequency of the superconducting material, λ becomes highly frequency dependent [13 - 15]. The microstrip line with superconducting electrodes becomes material-dispersive, and above the gap frequency the line has increased losses [16, 17] due to breaking of Cooper pairs and an increased appearance of conducting loss in the strip and ground electrodes.

The Mattis – Bardeen theory [18] of the skin anomalous effect describes the behaviour of a superconductor vs. frequency in terms of complex conductivity σ :

$$\sigma = \sigma_1 - j \cdot \sigma_2 \quad (1),$$

where the real and the imaginary components, σ_1 and σ_2 , translate directly into the normal-electron and Cooper-pair currents in a superconductor. The applicability of the Mattis - Bardin theory to specific superconducting materials is discussed in [16, 17]. In integral form the equations for σ_1 and σ_2 are as the follows [16]:

$$\begin{aligned} \frac{\sigma_1}{\sigma_n} = & \frac{2}{\hbar\omega} \int_{\Delta}^{\infty} [f(\varepsilon) - f(\varepsilon + \hbar\omega)] \times \frac{\varepsilon^2 + \Delta^2 + \hbar\omega\varepsilon}{\sqrt{(\varepsilon^2 - \Delta^2)} \cdot [(\varepsilon + \hbar\omega)^2 - \Delta^2]^{1/2}} d\varepsilon + \dots \\ & \dots + \frac{1}{\hbar\omega} \int_{\Delta}^{\hbar\omega - \Delta} [1 - 2f(\hbar\omega - \varepsilon)] \times \frac{\hbar\omega\varepsilon - \Delta^2 - \varepsilon^2}{\sqrt{(\varepsilon^2 - \Delta^2)} \cdot [(\hbar\omega - \varepsilon)^2 - \Delta^2]^{1/2}} d\varepsilon \end{aligned} \quad (2),$$

and

$$\frac{\sigma_2}{\sigma_n} = \frac{1}{\hbar\omega} \int_{\Delta - \hbar\omega, -\Delta}^{\Delta} [1 - 2f(\varepsilon + \hbar\omega)] \times \frac{\varepsilon^2 + \Delta^2 + \hbar\omega\varepsilon}{\sqrt{(\varepsilon^2 - \Delta^2)} \cdot [(\varepsilon + \hbar\omega)^2 - \Delta^2]^{1/2}} d\varepsilon \quad (3),$$

where T is the temperature [K], σ_n is the conductivity of a superconductor just above the critical temperature T_c , $\Delta=\Delta(T)$ is the energy gap parameter [eV], $f(\varepsilon)=1/(1 + \exp(\varepsilon/kT))$ is Fermi

function, $\omega=2\pi f$ is the angular frequency, k is Boltzman's constant and h is the reduced Plank's constant. The first integral of σ_1 represents conduction of thermally excited normal electrons, while the second integral of σ_1 introduces generation of quasiparticles by incoming radiation. The lower limit on the integral for σ_2 becomes $-\Delta$ when the frequency exceeds the gap frequency. To complete the description of a superconductor we need the relation between the physical parameters of a superconducting material [16]:

$$\lambda_o = \sqrt{\frac{h}{\pi\mu_o\sigma_n\Delta}} \quad (4),$$

where μ_o is the permeability of vacuum. The specific surface impedance Z_s per square (unit area) of the superconducting film with thickness d is expressed as follows [16]:

$$Z_s(\omega) = (j\omega\mu_o/\sigma)^{1/2} \coth((j\omega\mu_o\sigma)^{1/2}d) = R + jX \quad (5).$$

For magnetic and electric field penetration depths, λ and δ_r , respectively, we then can write the follow expressions [17]:

$$\lambda = \frac{X}{\omega\mu_o} \quad (6), \quad \delta_r = \frac{R}{\omega\mu_o} \quad (7).$$

The equations (1-6) describe the behaviour of the magnetic field penetration depth vs. frequency and the equations (1-5, 7) give the skin depth vs. frequency dependence.

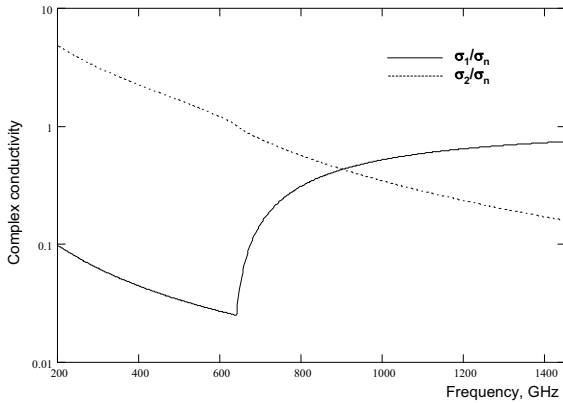


Figure 2. σ_1 (solid line) and σ_2 (dot line) components of Nb superconducting film, calculated based on Mattis-Bardn theory. In the modelling the Nb material parameters were used as follows: $\sigma_n = 1.739 \times 10^7 [\Omega^{-1}m^{-1}]$, $T_c = 8.1 [K]$, $\lambda_o = 8.5 \times 10^{-8} [m]$; the calculation was made for 4 K physical temperature.

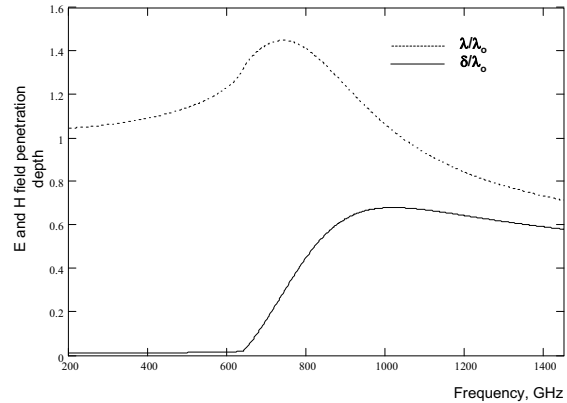


Figure 3. δ (solid line) and λ (dot line) penetration depth of E and H components of the electromagnetic field correspondingly for Nb superconducting film, calculated based on Mattis-Bardn theory (the values are normalized by London penetration depth, λ_o). In the modelling the Nb material parameters were used as above; the calculation was made for 4.2 K physical temperature. Already at 200 GHz, less than 30% of the gap frequency, the magnetic field penetration depth, λ , is about 5% larger than the static London penetration depth, reaching maximum of about $1.47\lambda_o$.

References [13, 19] present approximation for the frequency dependence of the magnetic penetration depth in a close-form equation. Concluding, the dispersion in a superconducting microstrip transmission line has two different contributions, i.e., the modal dispersion as in any conventional microstrip line *and* dispersion due to the frequency dependence of the superconducting material properties.

Microstrip Superconducting Line Models with Uniform EM Field

Swihart [20] analyzed the SML for the case of uniform electromagnetic field across the dielectric, i.e., with $W_{\text{ground}} \gg W \gg h$ (see Fig. 1) and found solution for the Maxwell equations in that case, with the line characteristic impedance and the propagation constant expressed as the follows*:

$$Z_o = \frac{120\pi}{\sqrt{\epsilon_r}} \cdot \frac{h}{W} \cdot \sqrt{1 + \frac{\lambda_o \coth(t_s/\lambda_o) + \lambda_o \coth(t_g/\lambda_o)}{h}} = Z_p \times S_w^{0.5} \quad (8),$$

$$\beta_o = \frac{2\pi}{\Lambda_o} \cdot \sqrt{\epsilon_r} \cdot \sqrt{1 + \frac{\lambda_o \coth(t_s/\lambda_o) + \lambda_o \coth(t_g/\lambda_o)}{h}} = \beta_p \times S_w^{0.5} \quad (9),$$

$$S_w = 1 + \frac{\lambda_o \coth(t_s/\lambda_o) + \lambda_o \coth(t_g/\lambda_o)}{h} \quad (9a),$$

where Λ_o is the free space wavelength, Z_p and β_p are the characteristic impedance and the wave-factor of the line with the same geometry, uniform field distribution and made of a perfect conductor, the rest of the parameters in the equations (8, 9) and (9a) are dimensional parameters of the superconducting microstrip line (Fig. 1).

The equations (8) and (9) have a very simple physical interpretation: the electromagnetic field penetrates in the strip and ground superconducting electrodes of the microstrip transmission line at the effective depth of λ_o , the London penetration depth, extending the thickness where the electromagnetic wave propagates beyond the thickness of dielectric, h , into the both superconductors. Similar approach to a microstrip line made from a normal conductor with the dielectric thickness comparable with the skin depth of the strip and ground conductors is presented in [21]. Swihart solution assumes that the magnetic field penetration depth is the static London penetration depth, λ_o , independent on the frequency of the electromagnetic wave propagating inside the microstrip line.

With the same assumption about the field uniformity in the SML, Kautz [16] has applied the theory of Mattis and Bardeen, taking into account that the behaviour of the superconducting material depends on frequency and, at frequencies close to the superconducting material gap frequency, the conducting properties of the superconductor are described by anomalous skin effect with surface impedance of the superconductor presented via complex conductivity. The SML impedance, the propagation constant and loss were calculated for a wide band of

* Here and through the entire paper we assume that the strip and ground electrodes are made from the same type of superconducting material.

frequencies. However, the both models neglect the fringing component of the electromagnetic field, which contributes substantially giving error up to 30% of the line characteristic impedance and the wave propagation constant in practical SML.

Line Models Including Fringing EM Field and a New SML Model

The behaviour of a superconducting microstrip transmission line taking into account fringing fields was analyzed by a number of authors [4 - 8]. Two approaches are used to obtain characteristics of the superconducting microstrip line. The first approach is, as for a conventional microstrip, a solution of Maxwell equations for given geometry and boundary conditions, using e.g., conformal mapping [7], and, as a result, deriving close form equations for SML impedance and wave-propagation factor. Another approach to obtain the impedance and the wave propagation factor in SML uses surface impedance of the superconductors comprising the line, derived by employing the Mattis-Bardoin theory, and include this impedance in the calculations of the line characteristic impedance and the wave-factor via taking into account geometry factor, i.e., the RF current distributions in the strip and ground electrodes, e.g., in [5, 6, 8]. Interestingly, the result obtained by Swihart, who assumed the uniform field, shows that the superconducting material contribution is factorized in a form of a multiplier for both the characteristic impedance and wave-factor, equation 8, 9 and 9a, compare to a perfect-metal based line; similarly for the SML with negligible loss and the fringing field, taken into account, the factorizing takes place as well, e.g., [8].

In order to introduce a new model for the SML we would like to consider the influence of a superconducting material on the characteristic impedance and the propagation constant of a superconducting transmission line via analyzing a lump model equivalent circuit of transmission line, depicted in Figure 4. Let us assume a microstrip transmission line using a perfect conductor with radiation and dielectric material losses being negligibly small. The line equivalent parameters, L and C , take into account the geometry and the fringing field. Similar circuit can be used for SML, having the same geometry, with additional circuit components describing the superconductors, Fig.4 (2).

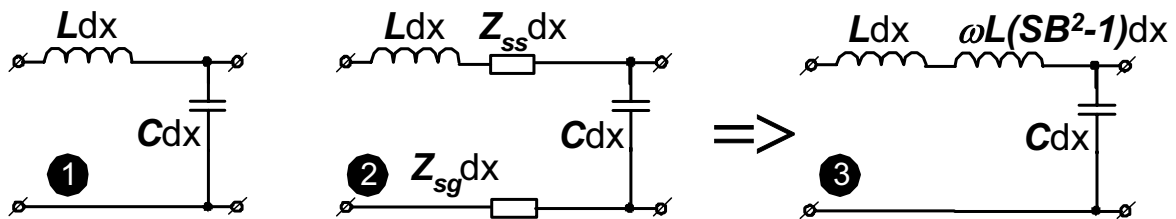


Figure 4. Equivalent circuit of a short piece, dx , of a lossless microstrip transmission line (1) made of a perfect conductor: L is inductance and C is capacitance, per unit of length extracted using, e.g., [22]. Equivalent circuit for dx long superconducting transmission line (2 & 3): L is inductance and C is capacitance (the same as for the perfect conductor line) per unit of length. Z_{ss} and Z_{sg} are impedances of the strip and ground respectively, per unit of length describing contribution of the superconductor.

If the frequency of the electromagnetic wave propagating through the line is well below the gap frequency (about 650 GHz for Nb material used as example here) the RF conducting loss in the superconductor is negligible (Fig. 3), thus the impedances Z_{ss} and Z_{sg} should be pure imaginary and *inductive*. Representing these impedances, Z_{ss} and Z_{sg} , as a product of the specific line inductance impedance, ωL , we can write the follows:

$$Z_{ss}, Z_{sg} \Rightarrow \omega L \times (SB^2 - 1) \quad (10),$$

where SB represent a correction factor for the specific inductance of the perfect conductor line and comprises both geometrical [23] and superconducting material contributions. Calculating the characteristic impedance and the wave factor of the transmission lines represented in Fig. 4 and taking into account that the series impedance and shunt admittance of the transmission line in Figure 4, (1), are $Z=\omega L$ and $Y=\omega C$ and correspondingly $Z= \omega L+(Z_{ss}+Z_{sg})$ and $Y=\omega C$ for SML for the equivalent circuit shown in Figure 4, (2 & 3), we arrive to the following equations:

- for the perfect conductor microstrip line the characteristic impedance Z_P and wave factor β_P are:

$$Z_P = \sqrt{\frac{\omega L}{\omega C}} = \sqrt{\frac{L}{C}} \quad \text{and} \quad \beta_P = \sqrt{\omega^2 LC} = \omega \sqrt{LC} \quad (11);$$

- for the superconducting microstrip line the characteristic impedance Z_S , taking into account equation (10):

$$Z_S = \sqrt{\frac{\omega L + \omega L \times (SB^2 - 1)}{\omega C}} = SB \times \sqrt{\frac{L}{C}} = SB \times Z_P \quad (12),$$

and the wave-factor β_S :

$$\beta_s = \sqrt{(\omega L + \omega L \times (SB^2 - 1)) \times \omega C} = \sqrt{\omega^2 SB^2 \times LC} = SB \times \omega \sqrt{LC} = SB \times \beta_P \quad (13),$$

where L and C are the equivalent inductance and shunt capacitance of the line based on a perfect conductor.

The correction factor **SB** depends, in general, on: **i.** the surface impedance of the strip and ground electrodes constituting the microstrip line, see equations (1 - 5), **ii.** the geometrical factor of the field penetration including the RF current distribution effects and the fringing field.

G. Yassin and S. Withington [7] introduced a penetration factor, χ , that is a parameterized H-field penetration in the superconductors of microstrip line and is a function of the line geometry. The calculations of χ , made in [7] for different geometries of the SML (Fig. 5), show that when the SML strip conductor is relatively thin, $t_s/h \leq 0.1$, and narrow, $W/h \leq 7$, the penetration factor χ is larger than unit, indicating difference in the field penetration compare to the case of the uniform field distribution when $\chi \rightarrow 1$.

Practical considerations and limitations of thin-film technology narrow and constrain the range of attainable SML geometries. In case if *no* planarization process is used for fabrication of SML, e.g., Nb-material based transmission line with SiO or SiO₂ dielectric, we should consider appearance of steps with the height equal to the thickness of the dielectric layer; in order to avoid physical and electrical breaks in the strip conductor the latter should be thicker than the height of the step.

Taking into account RF conducting properties and the H-field penetration depth, the follow empirical formula can be introduced for obtaining the strip thickness, t_s , for a given dielectric thickness h:

$$t_s \geq h + (1.5 \dots 2.0) \times \lambda_o \quad (14).$$

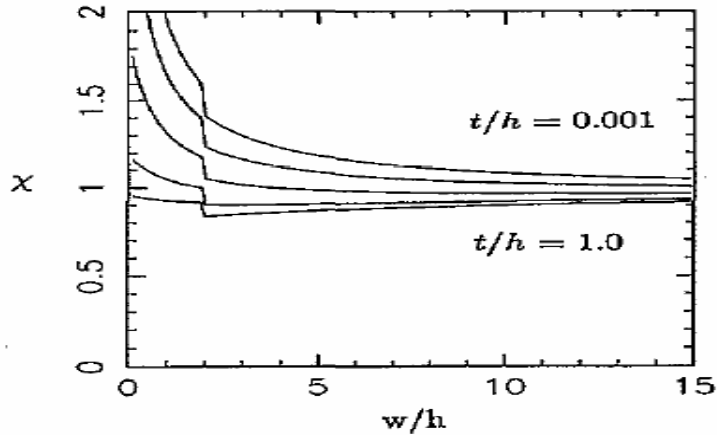


Figure 5 from the ref. [7]. The penetration factor χ is shown as a function of normalized strip width for various strip thicknesses: $t/h = 1.0, 0.5, 0.1, 0.01, 0.001$ and 0.0001 .

Maximum thickness of the dielectric layer is limited typically due to the restrictions of lift-off process allowing of about 350 nm thick SiO and slightly thinner SiO₂; with the aim of achieving a thicker dielectric two consequent depositions can be performed, e.g. [24], giving maximum thickness of about 450 – 650 nm. Taking into account typical impedances we should attain, the thickness of dielectric is to be more than 100 nm. These considerations define a range of the SML dielectric thickness $100 \text{ nm} \leq h \leq 650 \text{ nm}$ and, for Nb film with $\lambda_0 \approx 85 \text{ nm}$, corresponding range of the strip thickness $230 \text{ nm} \leq t_s \leq 780 \text{ nm}$.

Processing, involving optical and E-beam lithography, gives different accuracies in resolving linear dimensions: with E-beam lithography it is possible to achieve the width of strip well below 1 μm and thus reach a higher line impedance for a given thickness of dielectric, while for repeatable results with optical lithography the strip width $W \geq 5 \mu\text{m}$ would be an appropriate choice. Bringing these additional considerations to define the ranges of parameters used to calculate penetration factor χ [7], we find out that the strip normalized thickness is of $1.2 \leq t_s/h \leq 2.3$ and the strip normalized width is of $7.7 \leq W/h \leq 50$ for optical lithography. The latter lead us to the conclusion that the SML line with geometries of interest has the field penetration factor χ , that is *very close to the line with uniform field distribution* ($\chi \cong 1$).

Based on that fact and referring the equations (8, 9), (11, 12) and (9a), we can write a new equation for the correction factor SB:

$$SB = \sqrt{1 + \frac{\lambda(\omega) \cdot \coth\left(\frac{t_s}{\lambda(\omega)}\right) + \lambda(\omega) \cdot \coth\left(\frac{t_g}{\lambda(\omega)}\right)}{h}} \quad \text{and} \quad \lambda(\omega) = \frac{X(\omega)}{\omega\mu_0} \quad (15).$$

In the equation (15) we bear in mind the Swihart solution for static (frequency independent) London penetration depth, λ_0 , as in equation (9a), and use similarity of the equation (8, 9) with the equations (12, 13), suggesting that $SB \propto \sqrt{S_w}$, which should be exact for $W \gg h$. Taking into account that the H-field penetration depth is a *frequency dependent quantity*, as it is clear from the equation (6), and considering that $\lambda(\omega)$ is a slow function of the frequency (Figure 2), we use the frequency dependent $\lambda(\omega)$ in the S_w factor, equation (9a), assuming the Swihart solution to be valid for every single frequency. Summarizing, the proposed new model takes into account the fact that contribution of the superconducting state of the strip and ground conductors to the

microstrip line performance can be represented in the form of the SB multiplier factor, equation (15). The SML characteristic impedance and the propagation factor can be obtained from those of a microstrip line with the same geometry based on ideal conductor via scaling them by the **SB** factor.

The presented model was successfully used for a number of SIS mixer projects [15, 19, 24 - 26] demonstrating its accuracy. However, the accuracy was judged indirectly, via the achieved performances of the SIS mixers. In this paper we would like to evaluate the suggested model further by competitive comparison with the previously proposed SML models and 3-D electromagnetic field numerical simulation.

Numerical Simulation of SML with HFSS

The SML was simulated using 3-D electromagnetic field numerical simulation package, HFSS by Agilent. We used approach suggested by A.R. Kerr [12] where a superconductor of finite thickness T is represented by two infinitely thin conducting planes (Fig. 6 below) with surface impedance calculated based on the transmission line theory, the surface impedance of the actual superconductor and the fact that the two surfaces interact via the penetration of the magnetic field (the thickness T is assumed to be comparable with the magnetic field penetration depth λ). The equation for surface impedance in the HFSS simulation was slightly modified for term β , page 7, reference [12]; the modifications introduced in the equation reflect the fact that the magnetic field penetration is frequency dependent item. Therefore, the surface impedance of the superconductor of the thickness T , having its bulk surface impedance $Z_s(\omega)$, equation (5), is represented as the follows:

$$Z_x(\omega, T) = Z_s(\omega) \times \left[1 - \frac{j\omega\mu_o T}{2 \cdot Z_s(\omega)} + \sqrt{1 + \left(\frac{j\omega\mu_o T}{2 \cdot Z_s(\omega)} \right)^2} \right] \quad (16)$$

Based on the equation [16], the ground plane is represented in HFSS as an infinite conducting plane with the surface impedance $Z_{\text{ground}}(\omega) = Z_x(\omega, t_g)$, Figures 1, 6. Employing the same approach to the strip we should represent it as rectangular structure with conducting planes having the surface impedance of the horizontal planes $Z_{\text{strip}_h}(\omega) = Z_x(\omega, t_s)$ and the vertical plane surface impedance, edges of the strip, $Z_{\text{strip}_v}(\omega) = Z_x(\omega, W)$, as depicted in Figure 6.

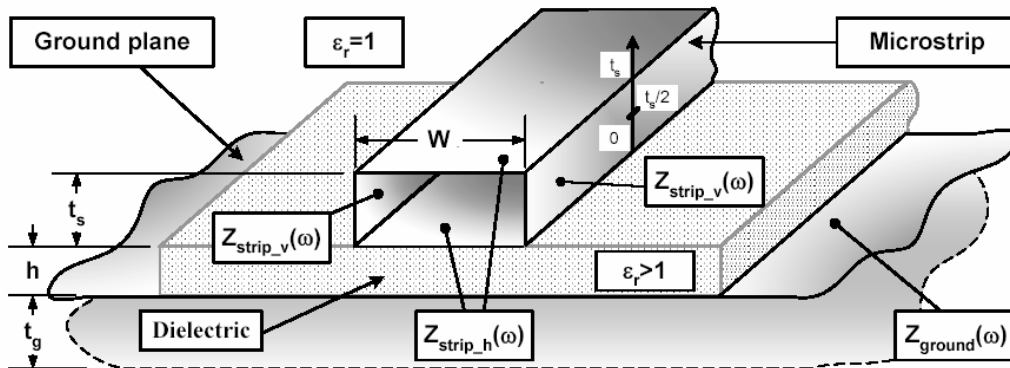


Figure 6. Simulation of the SML in finite-element solver (HFSS). The strip is simulated as a box structure with conducting planes having different surface impedances for vertical and horizontal planes.

SML Model Comparison

In order to establish common reference for the model comparison we used Nb-material based SML with the material properties as follows: the normal state conductivity, $\sigma_n = 1.619 \times 10^7$ [$\Omega^{-1}\text{m}^{-1}$], critical temperature, $T_c = 8.7$ [K], London penetration depth, $\lambda_o = 8.5 \times 10^{-8}$ [m] and ambient temperature $T = 4.2$ K. This combination of the material parameters gives the superconducting gap $\Delta(4.2) = 1.377$ meV at 4.2 K. For modelling we have chosen SiO_2 as the dielectric ($\epsilon_r = 3.74$) with several thicknesses of 150, 250, 450 and 650 nm. The penetration depth, λ_o , is a superconducting material constant of an absolute value for a given material; in order to preserve this fact we used absolute thickness of the dielectric material in the modelling, as above, and the strip width of 2, 4, 6 and 10 μm for each thickness of the dielectric, rather than usual relative ratio of the dielectric thickness, t/h , and the strip width, h/w . With the thicknesses of the dielectric and the widths of the strip as above we go slightly beyond the area of usual SML-based tuning circuitry for SIS mixers as discussed before and therefore could check how the suggested new model is compared to others with the wider range of geometries. In the modelling, the strip and the ground plane were assumed having the same thicknesses calculated according to the equation (14).

The starting point for every presented below modelling results is: the line geometry, as in Figure 1, the superconducting material parameters, as above, and, if required, the surface impedance calculated for every thickness of the Nb material according to the equations (1-7) and for the Nb material parameters listed. The modelling was done using MathCAD [27] program to implement the models from references [4, 7]. In order “to align” W.H. Chang model, [4], and make it more representative in the comparison with more recent ones, we introduced frequency dependence of the H-field penetration depth $\lambda = \lambda(\omega)$ and used it *instead* of λ_o as was in the original model. The SML model used in Caltech [5, 6] was realized in the *SuperMIX* software package [28] and the code was used to model the described above SML configurations. We have chosen to plot slow-wave factor or the wavelength ratio, $\Lambda_{\text{free_space}}/\Lambda_{\text{in_line}}$, in order to characterize the propagation in the SML for different models.

Discussion

The results of the simulations show that more or less all the models converge towards HFSS simulations. The most spread in the modelling results is in the slow-wave factor while the results on the characteristic impedance calculations show more consistency. As expected, introducing the frequency dependent H-field penetration produces drastic changes in the SML impedance and the slow-wave factor, $\Lambda_{\text{free_space}}/\Lambda_{\text{in_line}}$, those become up to 30% higher for thin dielectric (150 nm) around the gap frequency compared to, e.g., @100 GHz.

The new model produces results, which are very close to HFSS simulations and the model presented by G. Yassin & S. Withington for all SML geometries, while require relatively simple calculation procedures as described above especially if one of the approximation functions for $\lambda(f)$ is used. Presence of a noticeable discrepancy between Yassin & Withington model on one side and HFSS on another side for thin dielectric, e.g., Figure 22 and 30, brings us to the conclusion that further adjustments can be made for HFSS approach using more realistic distribution of the surface impedance at the edges of the strip. The discrepancy leaves open the question about a reference model.

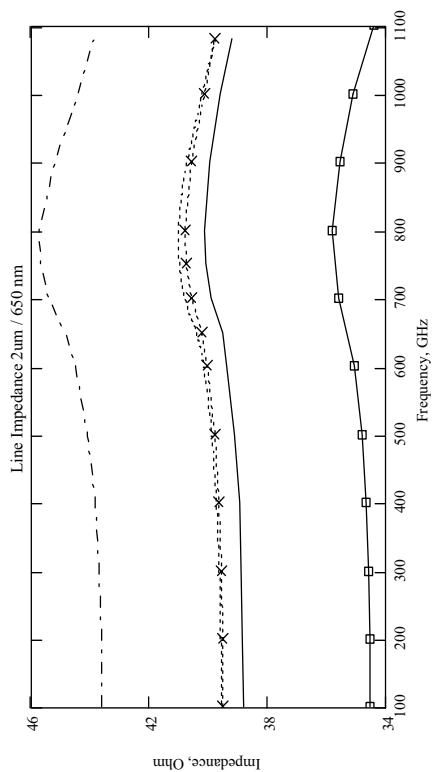


Figure 7. SML impedance for the 2µm wide strip on 650 nm thick SiO₂. Legend: solid line - HFSS, dot line - the new model, dot line with crosses - [7], dash-dot line - SuperMIX, solid line with rectangles - Chang with $\lambda(f)$.

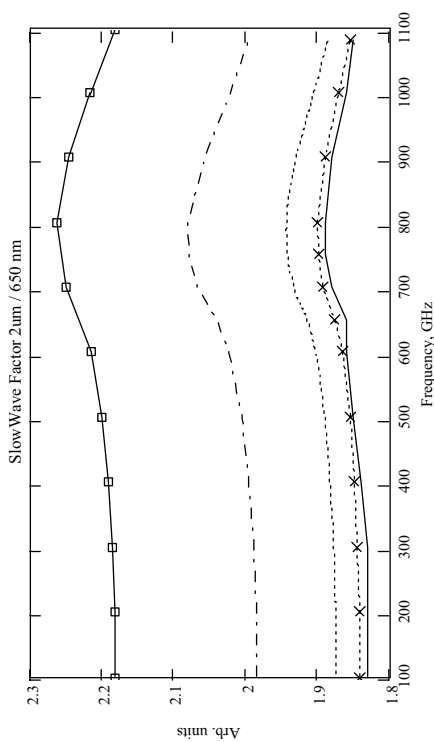


Figure 8. SML slow-wave factor for the 2 µm wide strip on 650 nm thick SiO₂. Legend: solid line - HFSS, dot line - the new model, dot line with crosses - [7], dash-dot line - SuperMIX, solid line with rectangles - Chang with $\lambda(f)$.

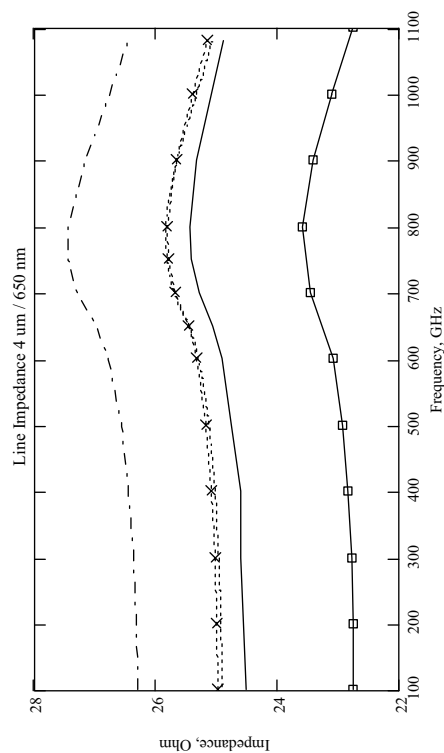


Figure 9. SML impedance for the 4 µm wide strip on 650 nm thick SiO₂. Legend: solid line - HFSS, dot line - the new model, dot line with crosses - [7], dash-dot line - SuperMIX, solid line with rectangles - Chang with $\lambda(f)$.

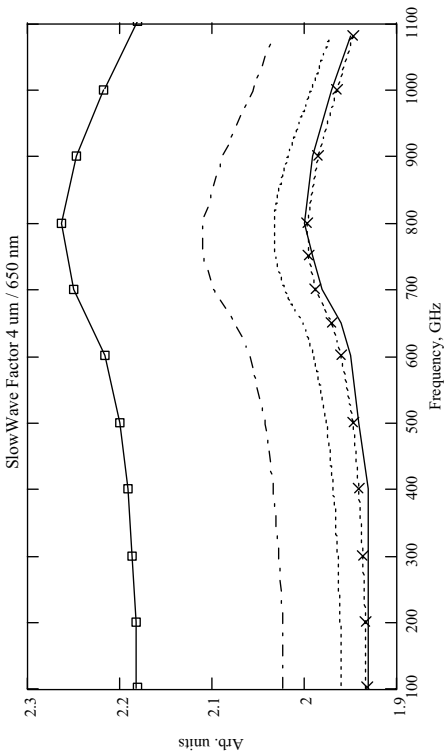


Figure 10. SML slow-wave factor for the 4 µm wide strip on 650 nm thick SiO₂. Legend: solid line - HFSS, dot line - the new model, dot line with crosses - [7], dash-dot line - SuperMIX, solid line with rectangles - Chang with $\lambda(f)$.

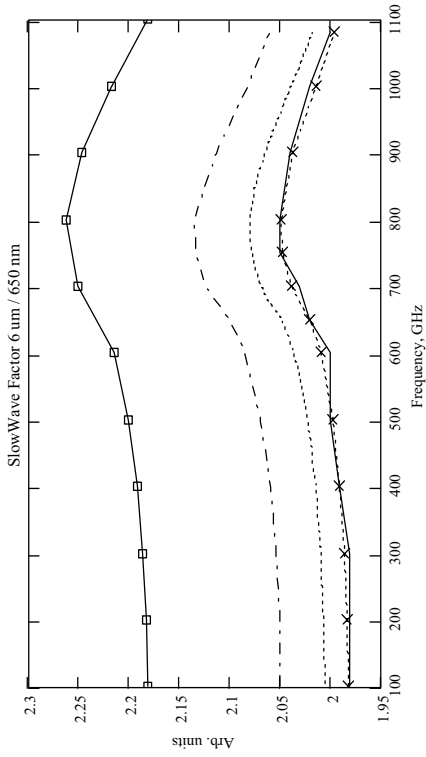


Figure 11. SML impedance for the 6 μm wide strip on 650 nm thick SiO₂. Legend: solid line - HFSS, dot line - the new model, dot line with crosses - [7], dash-dot line - SuperMIX, solid line with rectangles - Chang with $\lambda(f)$.

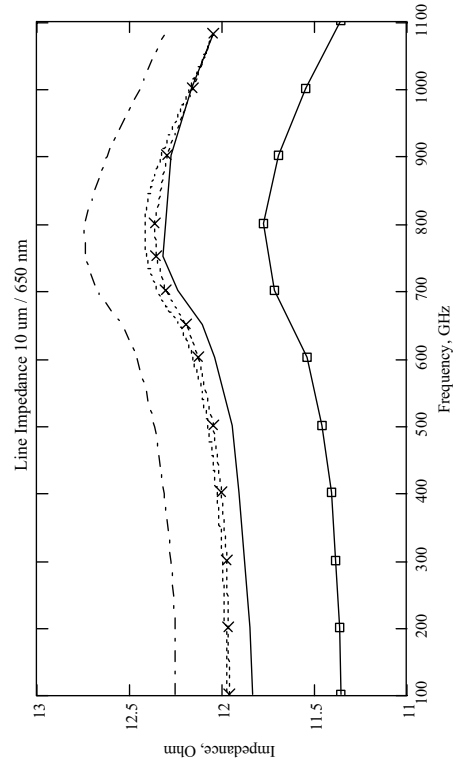


Figure 13. SML impedance for the 10 μm wide strip on 650 nm thick SiO₂. Legend: solid line - HFSS, dot line - the new model, dot line with crosses - [7], dash-dot line - SuperMIX, solid line with rectangles - Chang with $\lambda(f)$.

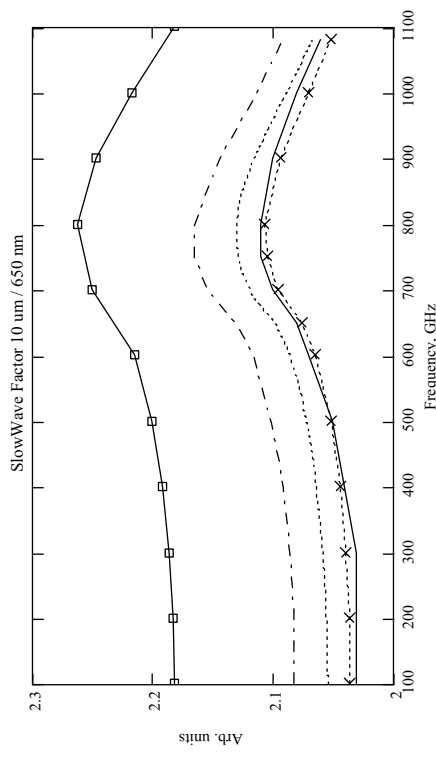


Figure 12. SML slow-wave factor for the 6 μm wide strip on 650 nm thick SiO₂. Legend: solid line - HFSS, dot line - the new model, dot line with crosses - [7], dash-dot line - SuperMIX, solid line with rectangles - Chang with $\lambda(f)$.

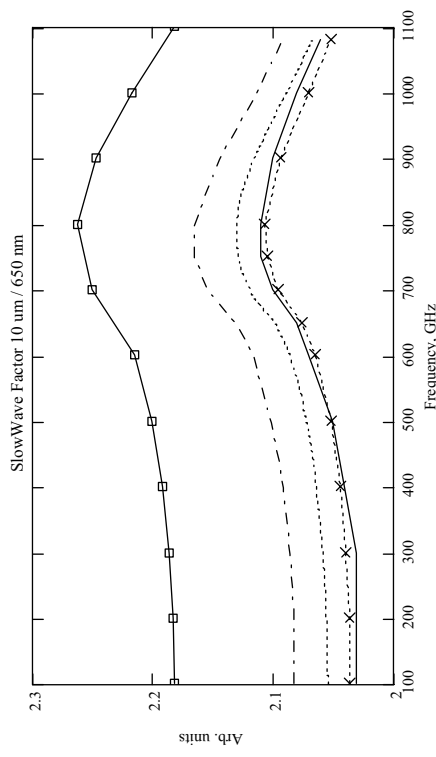


Figure 14. SML slow-wave factor for the 10 μm wide strip on 650 nm thick SiO₂. Legend: solid line - HFSS, dot line - the new model, dot line with crosses - [7], dash-dot line - SuperMIX, solid line with rectangles - Chang with $\lambda(f)$.

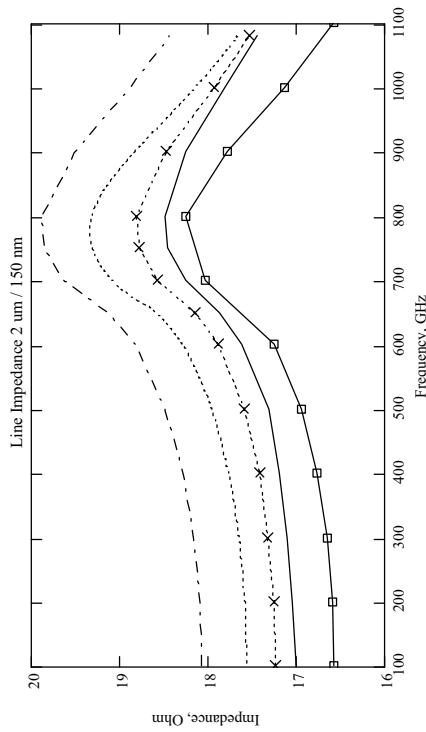


Figure 15. SML impedance for the 2 μm wide strip on 150 nm thick SiO₂. Legend: solid line - HFSS, dot line - the new model, dot line with crosses - [7], dash-dot line - SuperMIX, solid line with rectangles - Chang with λ(f).

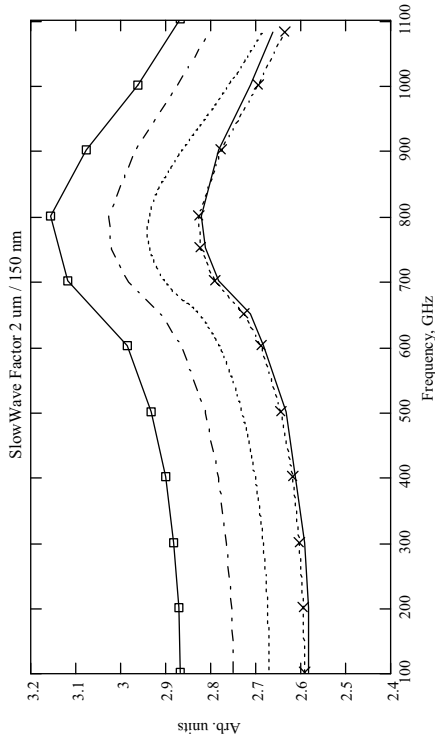


Figure 16. SML slow-wave factor for the 2 μm wide strip on 150 nm thick SiO₂. Legend: solid line - HFSS, dot line - the new model, dot line with crosses - [7], dash-dot line - SuperMIX, solid line with rectangles - Chang with λ(f).

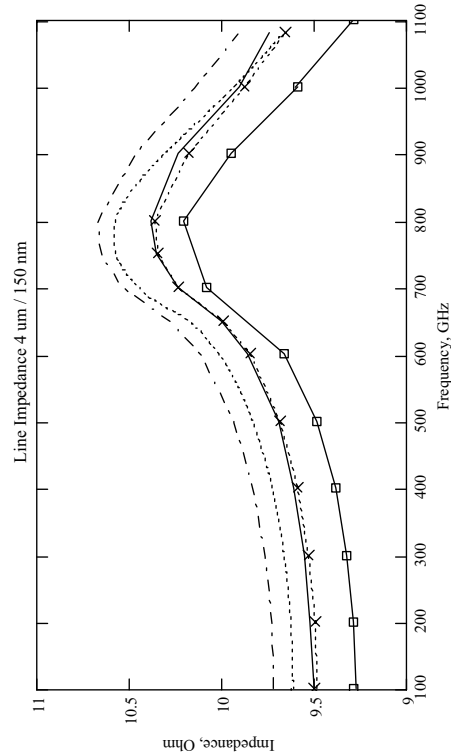


Figure 17. SML impedance for the 4 μm wide strip on 150 nm thick SiO₂. Legend: solid line - HFSS, dot line - the new model, dot line with crosses - [7], dash-dot line - SuperMIX, solid line with rectangles - Chang with λ(f).

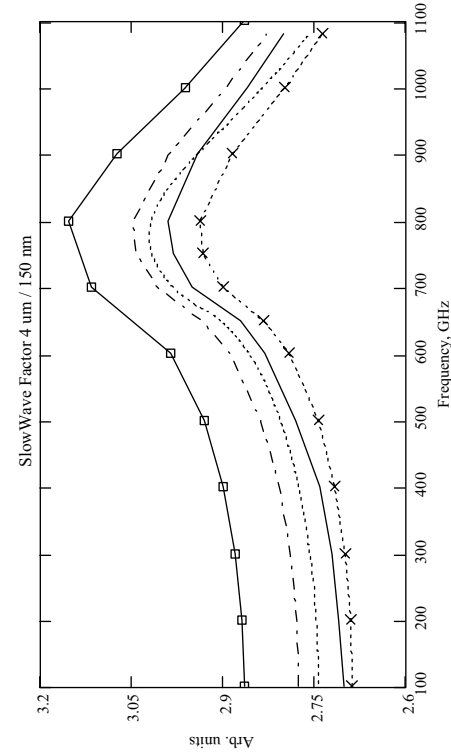


Figure 18. SML slow-wave factor for the 4 μm wide strip on 150 nm thick SiO₂. Legend: solid line - HFSS, dot line - the new model, dot line with crosses - [7], dash-dot line - SuperMIX, solid line with rectangles - Chang with λ(f).

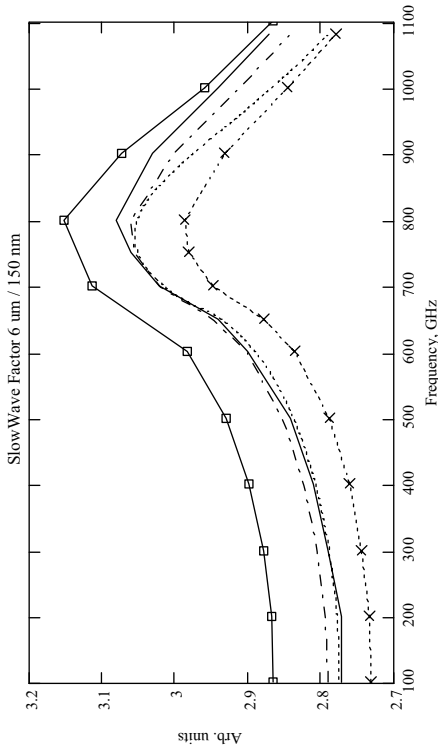


Figure 19. SML impedance for the 6 μm wide strip on 150 nm thick SiO_2 . Legend: solid line - HFSS, dot line - the new model, dot line with crosses - [7], dash-dot line - SuperMIX, solid line with rectangulars - Chang with $\lambda(f)$.

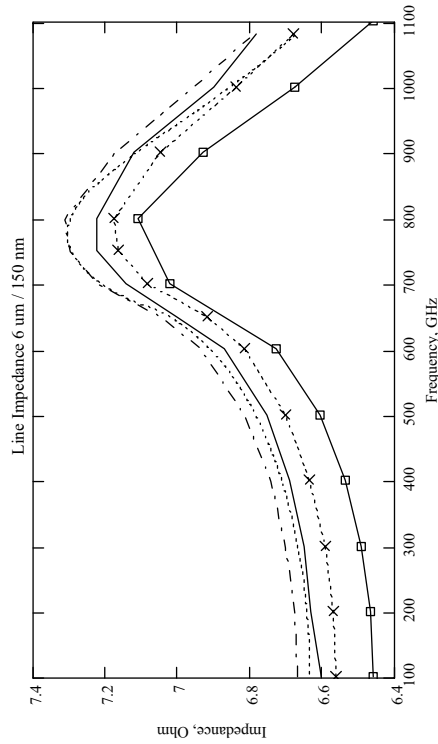


Figure 20. SML slow-wave factor for the 6 μm wide strip on 150 nm thick SiO_2 . Legend: solid line - HFSS, dot line - the new model, dot line with crosses - [7], dash-dot line - SuperMIX, solid line with rectangulars - Chang with $\lambda(f)$.

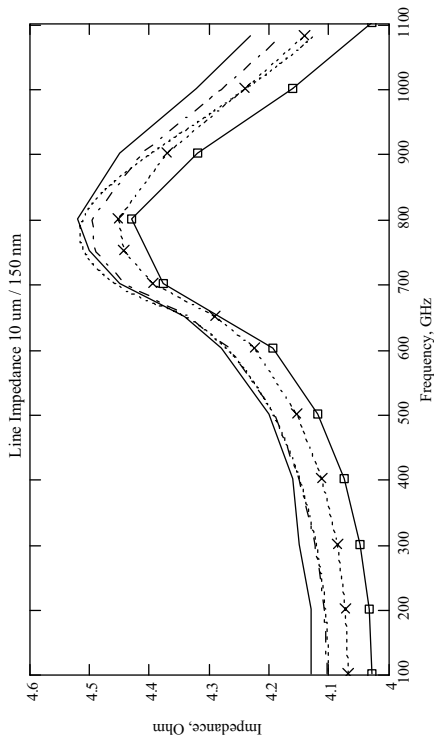


Figure 21. SML impedance for the 10 μm wide strip on 150 nm thick SiO_2 . Legend: solid line - HFSS, dot line - the new model, dot line with crosses - [7], dash-dot line - SuperMIX, solid line with rectangulars - Chang with $\lambda(f)$.

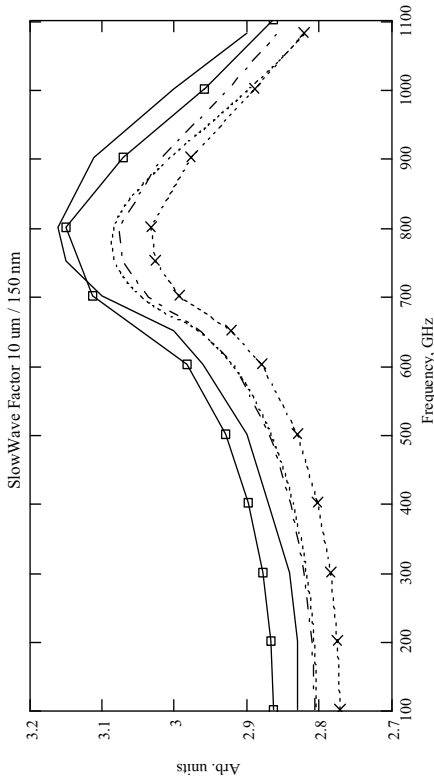


Figure 22. SML slow-wave factor for the 10 μm wide strip on 150 nm thick SiO_2 . Legend: solid line - HFSS, dot line - the new model, dot line with crosses - [7], dash-dot line - SuperMIX, solid line with rectangulars - Chang with $\lambda(f)$.

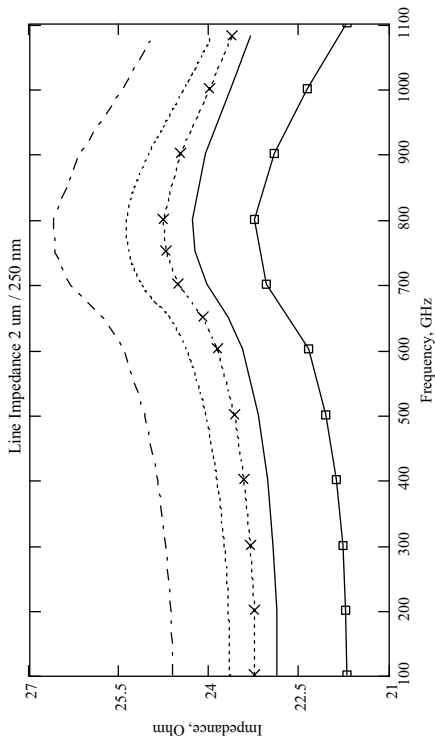


Figure 23. SML impedance for the 2 μm wide strip on 250 nm thick SiO₂. Legend: solid line - HFSS, dot line - the new model, dot line with crosses - [7], dash-dot line - SuperMIX, solid line with rectangles - Chang with λ(f).

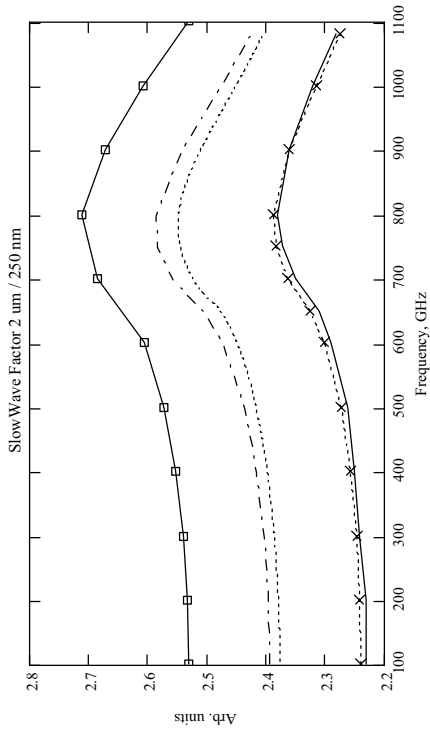


Figure 24. SML slow-wave factor for the 2 μm wide strip on 250 nm thick SiO₂. Legend: solid line - HFSS, dot line - the new model, dot line with crosses - [7], dash-dot line - SuperMIX, solid line with rectangles - Chang with λ(f).

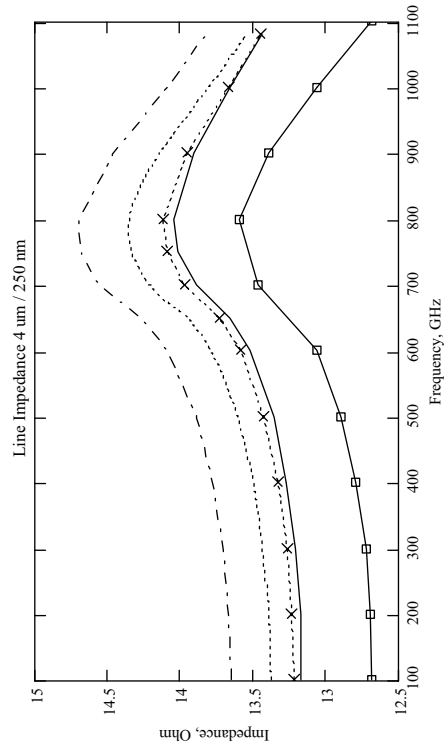


Figure 25. SML impedance for the 4 μm wide strip on 250 nm thick SiO₂. Legend: solid line - HFSS, dot line - the new model, dot line with crosses - [7], dash-dot line - SuperMIX, solid line with rectangles - Chang with λ(f).

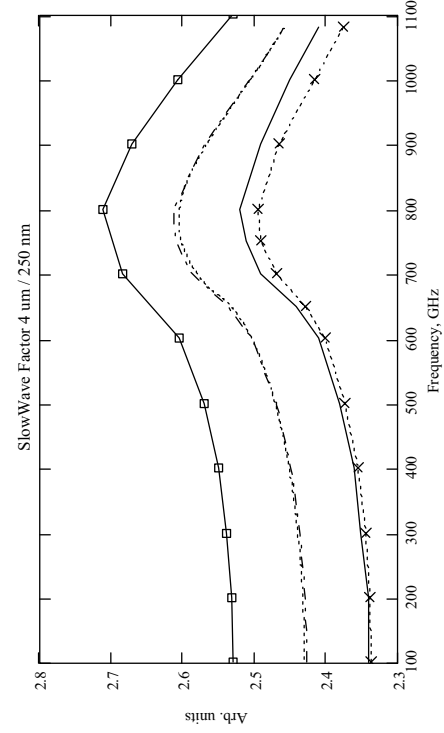


Figure 26. SML slow-wave factor for the 4 μm wide strip on 250 nm thick SiO₂. Legend: solid line - HFSS, dot line - the new model, dot line with crosses - [7], dash-dot line - SuperMIX, solid line with rectangles - Chang with λ(f).

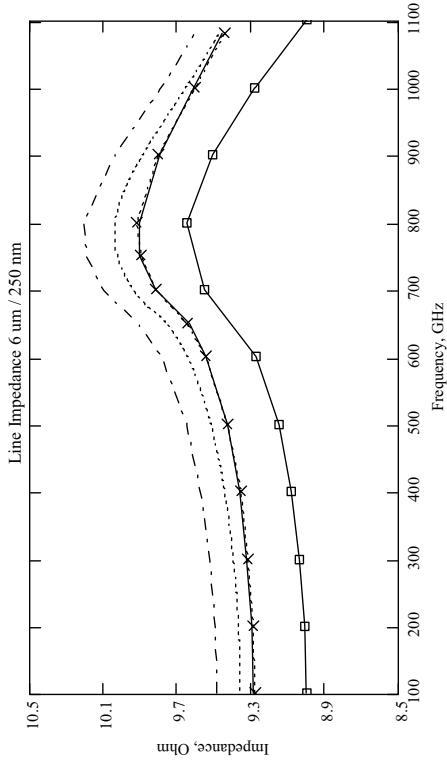


Figure 27. SML impedance for the 6 μm wide strip on 250 nm thick SiO₂. Legend: solid line - HFSS, dot line - the new model, dot line with crosses - [7], dash-dot line - SuperMIX, solid line with rectangulars - Chang with $\lambda(f)$.

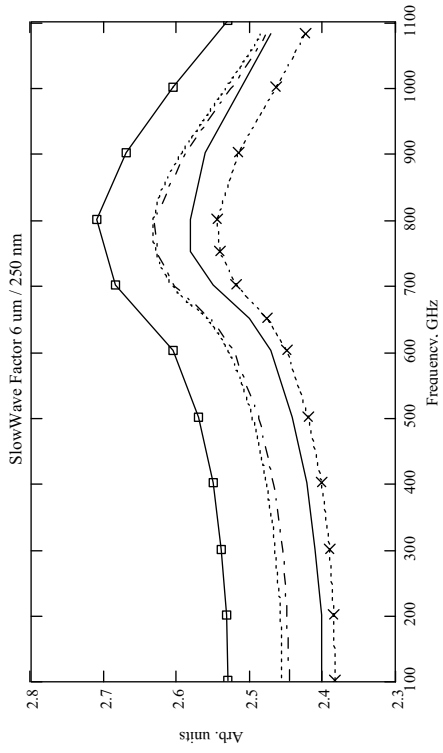


Figure 28. SML slow-wave factor for the 6 μm wide strip on 250 nm thick SiO₂. Legend: solid line - HFSS, dot line - the new model, dot line with crosses - [7], dash-dot line - SuperMIX, solid line with rectangulars - Chang with $\lambda(f)$.

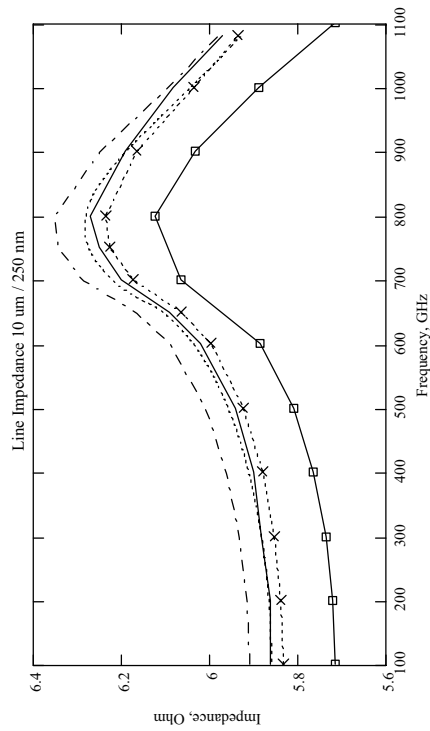


Figure 29. SML impedance for the 10 μm wide strip on 250 nm thick SiO₂. Legend: solid line - HFSS, dot line - the new model, dot line with crosses - [7], dash-dot line - SuperMIX, solid line with rectangulars - Chang with $\lambda(f)$.

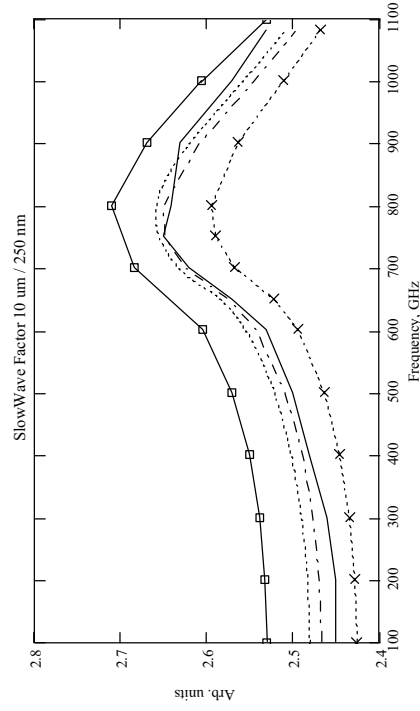


Figure 30. SML slow-wave factor for the 10 μm wide strip on 250 nm thick SiO₂. Legend: solid line - HFSS, dot line - the new model, dot line with crosses - [7], dash-dot line - SuperMIX, solid line with rectangulars - Chang with $\lambda(f)$.

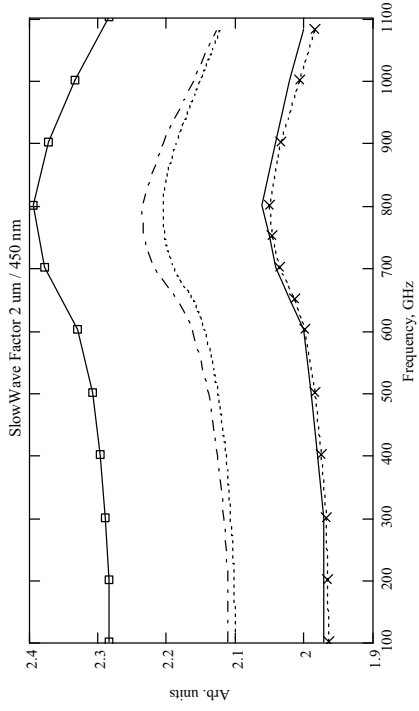


Figure 31. SML impedance for the 2 μm wide strip on 450 nm thick SiO_2 . Legend: solid line - HFSS, dot line - the new model, dot line with crosses - [7], dash-dot line - SuperMIX, solid line with rectangulars - Chang with $\lambda(f)$.

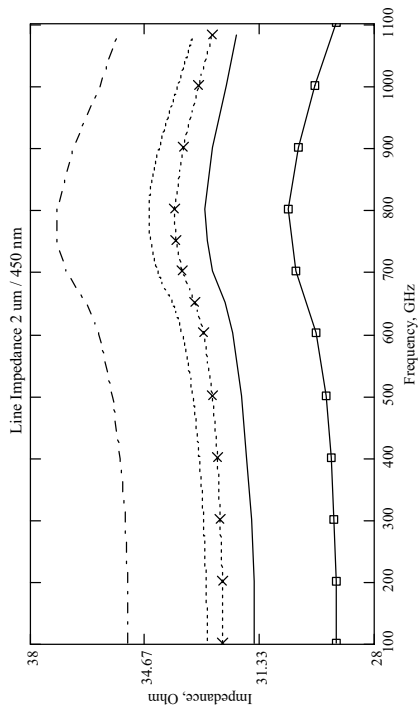


Figure 32. SML slow-wave factor for the 2 μm wide strip on 450 nm thick SiO_2 . Legend: solid line - HFSS, dot line - the new model, dot line with crosses - [7], dash-dot line - SuperMIX, solid line with rectangulars - Chang with $\lambda(f)$.

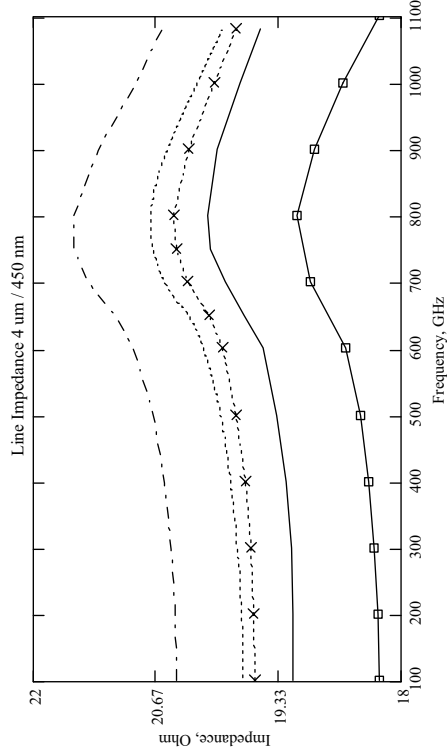


Figure 33. SML impedance for the 4 μm wide strip on 450 nm thick SiO_2 . Legend: solid line - HFSS, dot line - the new model, dot line with crosses - [7], dash-dot line - SuperMIX, solid line with rectangulars - Chang with $\lambda(f)$.

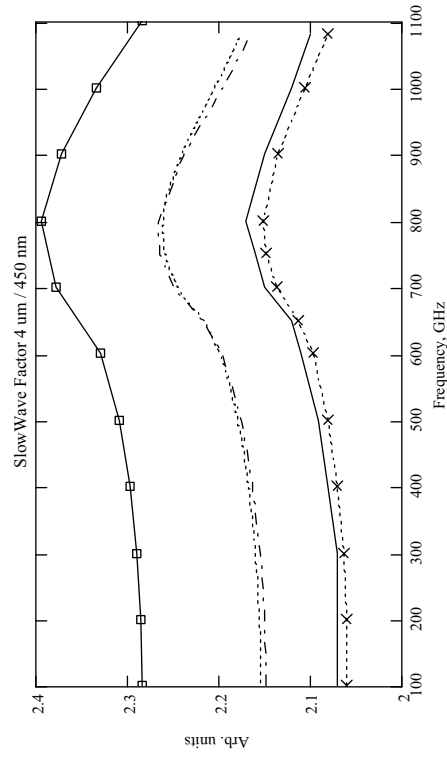


Figure 34. SML slow-wave factor for the 4 μm wide strip on 450 nm thick SiO_2 . Legend: solid line - HFSS, dot line - the new model, dot line with crosses - [7], dash-dot line - SuperMIX, solid line with rectangulars - Chang with $\lambda(f)$.

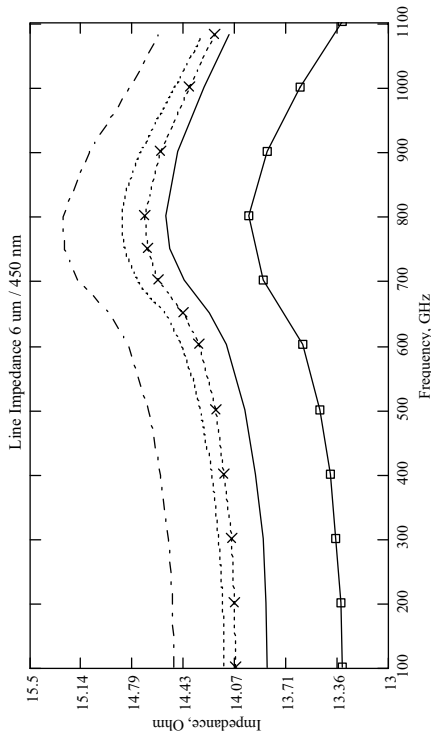


Figure 35. SML impedance for the 6 μm wide strip on 450 nm thick SiO₂. Legend: solid line - HFSS, dot line - the new model, dot line with crosses - [7], dash-dot line - SuperMIX, solid line with rectangles - Chang with λ(f).

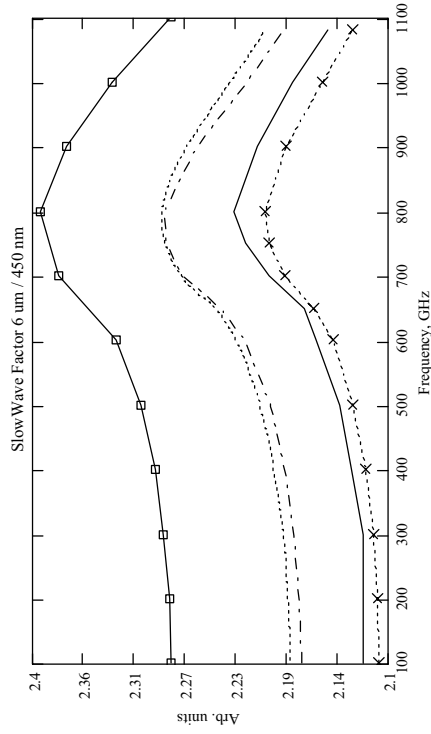


Figure 36. SML slow-wave factor for the 6 μm wide strip on 450 nm thick SiO₂. Legend: solid line - HFSS, dot line - the new model, dot line with crosses - [7], dash-dot line - SuperMIX, solid line with rectangles - Chang with λ(f).

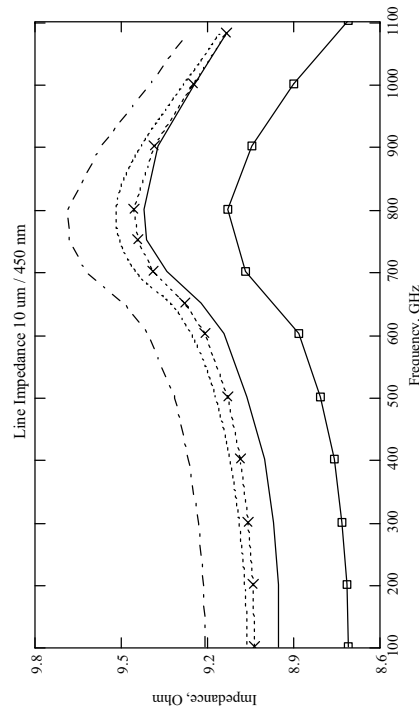


Figure 37. SML impedance for the 10 μm wide strip on 450 nm thick SiO₂. Legend: solid line - HFSS, dot line - the new model, dot line with crosses - [7], dash-dot line - SuperMIX, solid line with rectangles - Chang with λ(f).

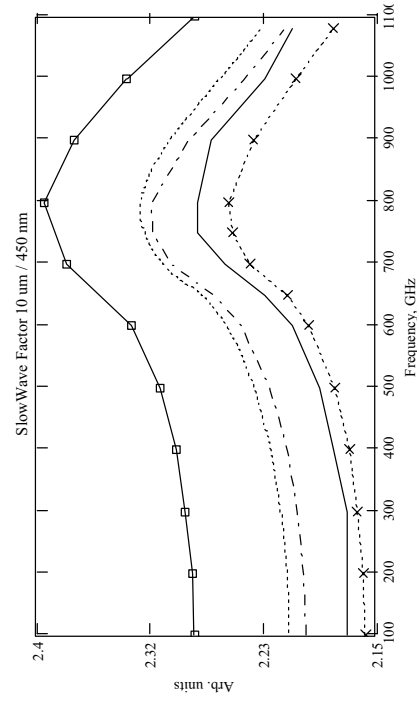


Figure 38. SML slow-wave factor for the 10 μm wide strip on 450 nm thick SiO₂. Legend: solid line - HFSS, dot line - the new model, dot line with crosses - [7], dash-dot line - SuperMIX, solid line with rectangles - Chang with λ(f).

Interestingly, the new model that initially doesn't take into account increasing loss in the superconductors around and above the gap frequency anyway produces *correct* values of the impedance and the slow-wave factor as compared to the models, which take use of the surface impedance of the superconductor and therefore include these losses. This opens possibility to use the suggested model even in the *wider* frequency band by adding conventional multiplicative loss factor [29].

Acknowledgements

Authors would like to thank Prof. R. Booth for his remarkable support over years. We are thankful to Dr. A.R. Kerr for useful discussions regarding numerical simulations of the SML using commercial CAD packages. We would like to thank colleagues from Caltech for generous sharing of the *SuperMIX* software package.

References

- [1] J.R. Tucker, M.J. Feldman, "Quantum detection at millimeter wavelengths", *Rev. Modern Phys.*, Vol. 4, pp. 1055–1113 (1985).
- [2] M. J. Wengler, "Submillimeter-Wave Detection with Superconducting Tunnel Diodes," *IEEE Proc.*, Vol. 80, pp. 1810-1826 (1992).
- [3] R. Blundell and C.-Y. Tong, "Submillimeter Receivers for Radio Astronomy," *IEEE Proc.*, Vol. 80, pp. 1702-1720 (1992).
- [4] W.H. Chang, "The inductance of a superconducting strip transmission line", *J. Appl. Phys.* **50** (12), December 1979, pp. 8129 – 8134.
- [5] J. Zmuidzinas, H.G. LeDuc, "Quasi-Optical Slot Antenna SIS Mixers", *IEEE Trans. Microwave Theory Tech.*, v. **40**, pp. 1797-1804, 1992.
- [6] M. Bin, "Low Noise THz Niobium SIS Mixers", PhD Thesis, Caltech, October 1997.
- [7] G. Yassin and S. Withington, "Electromagnetic models for superconducting millimetre-wave and sub-millimetre-wave microstrip transmission lines", *J. Phys. D: Appl. Phys.* **28**, pp. 1983-1991, 1995.
- [8] C.-Y. Tong, R. Blundell, S. Pain, D.C. Papa, J. Kawamura, X. Zhang, J.A. Stern, H.G. LeDuc, "Design and Characterization of a 250-350 GHz Fixed-Tuned Superconductor-Insulator-Superconductor Receiver", *IEEE Trans. Microwave Theory and Tech.*, v. 44, Iss.9, pp. 1548 - 1556, 1996.
- [9] T. Imamura, T. Shiota and S. Hasuo, "Fabrication of High Quality Nb/AlO_x-Al/Nb Josephson Junctions: I - Sputtered Nb films for junction electrodes.", *IEEE Trans. on Appl. Superconductivity*, Vol. 2, N. 1, pp. 1-14, 1992.
- [10] T. Imamura, S. Hasuo, "Fabrication of High Quality Nb/AlO_x-Al/Nb Josephson Junctions: II - Deposition of Thin Al Layers on Nb Films", *IEEE Trans. on Appl. Superconductivity*, Vol. 2, N. 2, pp. 84-94, 1992.
- [11] Agilent High-Frequency Structure Simulator (HFSS), Agilent Technologies, 395 Page Mill Road, Palo Alto, CA 94304, U.S.A.
- [12] A.R. Kerr, "Surface Impedance of Superconductors and Normal Conductors in EM Simulators", NRAO, Electronics Division Internal Report No. 302, February 1996.

- [13] G.S. Lee and A. T. Barfknecht, "Geometrical and Material Dispersion in Josephson Transmission Lines," *IEEE Trans. on Appl. Superconductivity*, Vol. 2, pp. 67-72, 1992.
- [14] H.H.S. Javadi, W. R. McGrath, B. Bumble, and H. G. LeDuc, "Onset of Dispersion in Nb Microstrip Transmission Lines," *Proceedings of the III Int. Symp. on Space Terahertz Technology*, pp. 362-381, Univ. Of Michigan, Ann Arbor, USA, 1992.
- [15] V. Belitsky, S. W. Jacobsson, L.V. Filippenko, E.L. Kollberg, "Theoretical and Experimental Studies of Nb-based Tuning Circuits for THz SIS Mixers", *Proceedings of the 6th Space Terahertz Technology Symposium*, pp. 87-102, Caltech, Pasadena USA, March 21-23, 1995.
- [16] R.L. Kautz, "Picosecond pulses on superconducting striplines," *J. Appl. Phys*, Vol. 49, pp. 308-314, 1978.
- [17] R. Pöpel, "Surface impedance and reflectivity of superconductors," *J. Appl. Phys*, Vol. 66, pp. 5950-5957, 1989.
- [18] D.C. Mattis and J. Bardeen, "Theory of anomalous skin effect in normal and superconducting metals", *Phys. Rev.*, Vol. 111, pp. 412-417 (1958).
- [19] V. Belitsky, S.W. Jacobsson, L.V. Filippenko, C. Holmstedt, V.P. Koshelets, E.L. Kollberg, "Fourier Transform Spectrometer Studies (300-1000 GHz) of Nb-based Quasi-Optical SIS Detectors", *IEEE Trans. on Appl. Supercond.*, Vol. 5, pp. 3445-3451, Nov. 3, 1995.
- [20] J.C. Swihart, "Field Solution for a Thin-Film Superconducting Strip Transmission Line", *J. Appl. Phys.*, Vol. 32, No. 3, pp.461-469, March 1961.
- [21] F. Schnieder, W. Heinrich, "Model of Thin-Film Microstrip Line for Circuit Design", *IEEE MTT*, Vol. 49, No. 1, January 2001.
- [22] E.O. Hammerstad and Ø. Jensen, "Accurate Models for Microstrip Computer Aided Design", *IEEE MTT-S International Microwave Symposium Digest*, pp.407-409, 1980.
- [23] R.A. Pucel, D.J. Massé and C.P. Hartwig, "Losses in microstrip", *IEEE Trans. Microwave Theory Tech.*, Vol. 16, pp. 342-350, 1968; see also correction in vol. 16, p. 1064, 1968.
- [24] Jacobsson S.W., Belitsky V., Filippenko L.V., Kovtonjuk S.A., Koshelets V.P., Kollberg E.L., "Quasi-optical 0.5 THz SIS Receiver with Twin Junctions Tuning Circuit.", *The 18th Int. Conf. on Infrared and Millimetre Waves*, Univ. of Essex, UK, Vol. SPIE 2104, pp. 267-268, 1993.
- [25] V. Belitsky, I.L. Serpuchenko, M.A. Tarasov, A.N. Vystavkin, "MM Waves Detection Using Integrated Structure with SIS Junction, Stripline Transformer and Spiral Antenna", *Extended Abstracts of ISEC'89*, Tokyo, Japan, 1989, pp. 179-182.
- [26] V. Belitsky, M.A. Tarasov, S.A. Kovtonjuk, L.V. Filippenko, O.V. Kaplunenko, "Low Noise Completely Quasioptical SIS Receiver for Radioastronomy at 115 GHz", *Int. J. Infrared and Millimetre Waves*, 1992, v. 13, 4, pp. 389-395.
- [27] MathCAD 2000i, Mathsoft Corp., <http://www.mathsoft.com>.
- [28] SuperMix software library, <http://www.submm.caltech.edu/supermix/default.html>.
- [29] S.R. Pennock, P.R. Shepherd, "Microwave Engineering with Wireless Applications", Macmillan Press, ISBN 0-333-72801-7, 1998.

Local Oscillator Systems for (sub)millimetre Spectroscopy

S. Andersson, A. Emrich, J. Embretsen
Omnisys Instruments AB, Gruvgatan 8, 421 30 Göteborg, Sweden

ABSTRACT

One of the most critical subsystems in a (sub)millimetre heterodyne radiometry instrument is the Local Oscillator (LO) system, especially for high resolution spectroscopy. For space applications, requirements such as low power consumption, compactness and reliability concerns add an additional dimension to the system design issues.

Design aspects of a complete LO system will be described below. This includes trade-offs between phase noise characteristics of Gunn oscillators and harmonic reference oscillators, bandwidth requirements of tuning ports as well as power supply filtering and general protection of various components. As an example, the complete LO system of the ODIN satellite will be described, a system with very high resolution requirements, and for SMILES.

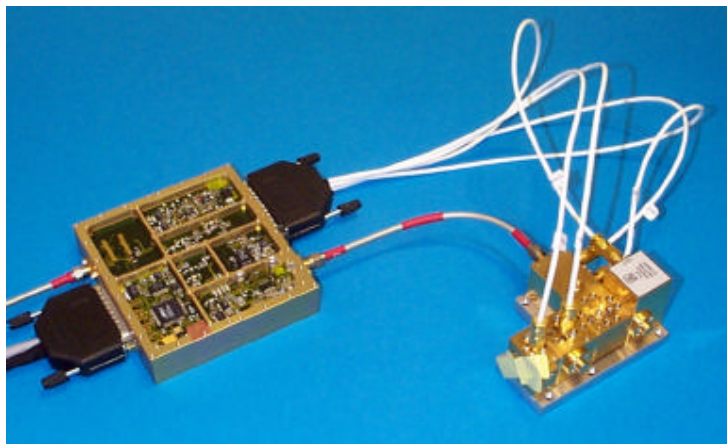


Figure 1. Breadboard of the SMILES phaselock and control system.

SYSTEM COMPONENTS

Harmonic reference oscillator (HRO). The harmonic reference oscillator is a low phase-noise frequency synthesizer in the 2-10 GHz band. This signal is mixed harmonically with the Gunn oscillator in order to produce a low IF frequency. The harmonic IF is then used for the phase-locking of the Gunn oscillator.

PLL reference oscillator (PRO). This synthesizer is used to create a signal in the 50-500 MHz range. This signal is used in the main PLL as a reference for the phase detector. The PRO will typically set the system frequency step size.

Main PLL. The main PLL consists of a high performance phase- frequency discriminator feeding the main active loop filter. PLL requirements are dependent on the quality of the Gunn oscillator and the receiver phase-noise specification. Loop bandwidths can range from 100 kHz to 10 MHz.

Main reference source. This reference is usually an OCXO or a TCXO with stability in the order of 10^8 or better.

Biasing and monitoring. The biasing system of a front-end controller is often over-looked. In a typical receiver, bias shall be provided to Gunn oscillators, harmonic mixers, multipliers, cryogenic mixers and cryogenic IF amplifiers. Bias points on all these units should be monitored together with temperatures. 30 bias and 50 monitor channels are used in ODIN.

The most critical elements of the LO system is the HRO and the PLL loop filter. Given a typical gunn oscillator, these units limit the maximum resolution of the receiver. In order to analyze how different noise contributors affects the overall phase-noise performance of an LO system, a MatLab simulation program has been developed. The program simulates a large number of noise sources and transforms the result to the operating frequency. Performance is evaluated and compared with the specification.

THE ODIN SYSTEM

The ODIN satellite is a joint aeronomy and astronomy mission. The main payload consist of four tunable heterodyne schottky receivers in the frequency range 480-570 GHz and one fixed tuned 119 GHz heterodyne system.

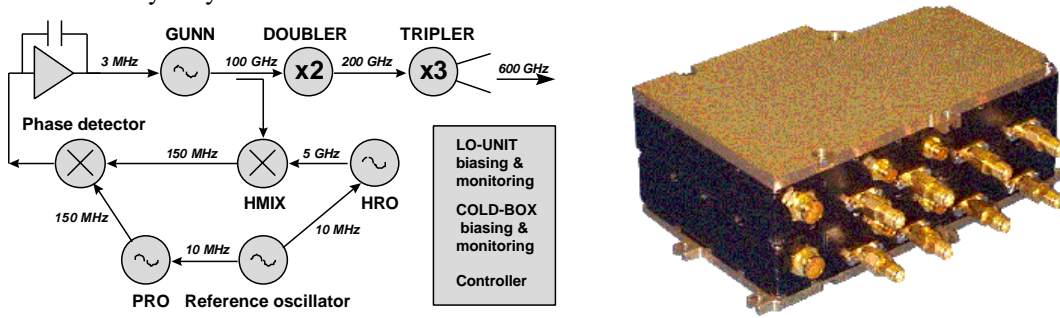


FIGURE 3. Block diagram for the ODIN control system. The box on the right incorporates four complete phase-lock and control systems.

SMILES

Based on the experience from the ODIN satellite, a phase-lock and control system for the Japanese SMILES experiment, scheduled for operation on the International Space Station has been developed. Although the basic design is similar to the ODIN version, it differs in frequencies, interfaces as well as specification.

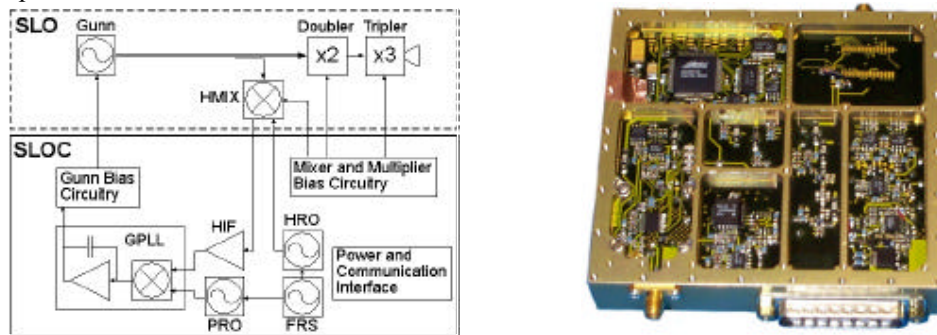


Figure 4. Block diagram of the phase lock and bias system for the SMILES LO to the left, and top view of the physical realization to the right.

6. CONCLUSION

When designing a controller for a (sub)millimetre front-end, one must realize that this is a complex system. One of the most over-looked issues is the great number of biasing and monitoring circuits needed. These circuits play an important roll for the phase-noise budget. They also serve as protection circuits for the very sensitive front-end components such as multipliers and mixers.

In order to transform the resolution requirements of the receiver to specifications at component level, a MatLab program has been developed. This program takes into account many sources of noise and different filter functions through out the system.

Equivalent Circuit for Photomixing In Resonant Laser-Assisted Field Emission

M. J. Hagmann^a, M. S. Mousa^b, M. Brugat^c, E. P. Sheshin^d, and A. S. Baturin^d

^aDeseret Electronics Research Corporation, North Salt Lake, Utah,

^bDepartment of Physics, Mu'tah University, Al-Karak, Jordan

^cImage Instrumentation Inc., Cooper City, Florida

^dMoscow Institute of Physics and Technology, Moscow, Russia

Abstract

Resonant Laser-Assisted Field Emission is a new technology for wide-band tunable and pulsed terahertz sources. Microwave prototypes have been made to demonstrate proof of concept. Equivalent circuits are developed to extend the quantum simulations to optimize designs for maximum power and bandwidth. Calculations with the equivalent circuits are consistent with the experimental data.

Summary of the new technology

Quantum simulations [1] recently confirmed by others [2,3] show that tunneling electrons have a resonant interaction with optical radiation. By means of the resonance, a TTL amplitude-modulated laser diode (30 mW, 690 nm) maximally focused ($P = 10^6$ - 10^8 W/m²) at a field emitter tip causes current oscillations that may be seen on an oscilloscope [4]. When optical radiation is focused on a field emitter tip, the tip rises and falls in potential following each cycle because it is much smaller than the wavelength. The field emission current follows the instantaneous electric field with a delay $\tau \approx 2$ fs [5], and the I-V characteristics of field emission are highly nonlinear, so photomixing in laser-assisted field emission can generate current oscillations up to 500 THz ($1/\tau$). We have studied several means to couple signals from these current oscillations [6].

Development of an equivalent circuit

The Fowler-Nordheim equation for current density in field emission is used in order to obtain closed-form expressions [10,11]. The current density is given by the following expression, where E is the electric field and parameters A and B depend on the work function of the tip.

$$J = AE^2 e^{-B/E} \quad (1)$$

The response to a time-dependent field is found by setting

$$E = E_0 + E_1 \cos(\omega_1 t) + E_2 \cos(\omega_2 t) \quad (2)$$

where E_0 is the static field and the other two terms may represent the radiation. A Taylor series expansion of Eq. (1) about operating point (E_0, J_0) where there is only the static field E_0 gives the following expression for the current:

$$I = I_0 + I_D + I_M \quad (3)$$

$$\text{where } I_D = \frac{I_0}{2} \left(1 + \frac{B}{E_0} + \frac{B^2}{2E_0^2} \right) \left[\left(\frac{E_1}{E_0} \right)^2 + \left(\frac{E_2}{E_0} \right)^2 \right] \quad (4)$$

$$\text{and } I_M = I_0 \left(1 + \frac{B}{E_0} + \frac{B^2}{2E_0^2} \right) \left(\frac{E_1}{E_0} \right) \left(\frac{E_2}{E_0} \right) \cos[(\omega_1 - \omega_2)t] \quad (5)$$

All terms at frequencies above the mixer frequency are neglected because they would be highly attenuated. This derivation is only valid at low frequencies where the effects of photon exchange may be neglected. However, the resonance for optical radiation [1] increases I_D and I_M by ≈ 40 dB while their ratio remains consistent with Eqs (4) and (5).

The three components of the current in Eqs. (3-5) are represented by separate parallel paths in the following equivalent circuit. This circuit also contains an external voltage source V_0 , load and ballast resistances R_{L1} , R_{L2} , and R_b , and anode and tip capacitances C_A and C_T . The beam impedance is defined by $R_B \equiv V_{AT}/I_0$, where V_{AT} is the anode-to-tip potential with the static field E_0 at the surface of the tip. From Ohm's Law, $R_B = V_0/I_0 - R_b - R_{L1}$. It is assumed that $R_{L1} \ll R_B$ so the feedback of I_D and I_M through R_B may be neglected.

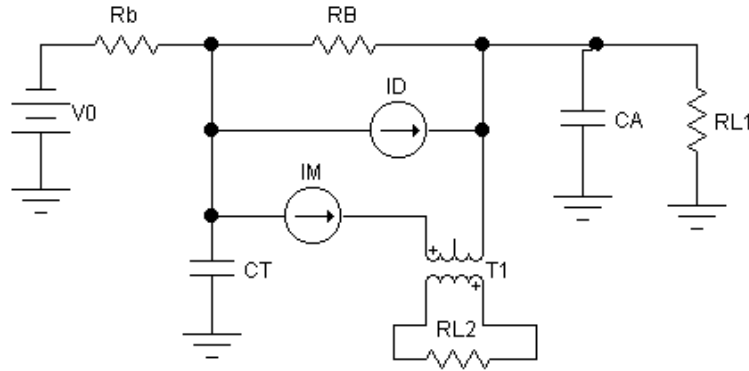


Fig. 1. Equivalent circuit for resonant laser-assisted field emission.

Application of the equivalent circuit to previous experiments

When field emission current is gated with an amplitude-modulated laser [4] the emitted current is gated at the modulation frequency of the laser, with a peak-to-peak value that is proportional to the power flux density. The magnitude and waveform of the gated current in the external circuit have the characteristics of a low-pass filter. These results are consistent with the model. For example, shunting of the current by the anode capacitance causes the external current to roll-off with increasing frequency.

Direct coupling from the tip to obtain maximum bandwidth and power

Signals may be coupled directly from the tip by (1) exciting surface waves that are propagated to the load, (2) forming antennas on the tip so the currents cause radiation to the load, or (3) exciting signals in a dielectric waveguide attached to the apex. Figs. 2

and 3 show microwave prototypes that use the first and second methods, respectively.



Fig. 2. First microwave photomixer using resonant laser-assisted field emission.

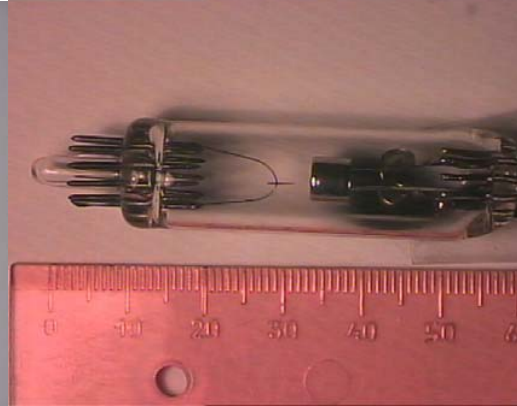


Fig. 3. Microwave source using a looped filament as an antenna.

The equivalent circuit shows how the effects of shunting by the anode capacitance, which cause the current in the external circuit to roll-off with increasing frequency, can be avoided to obtain the full bandwidth that is inherent in resonant laser-assisted field emission. At microwave frequencies the anode and tip capacitances are effective shunts to ground, and at terahertz frequencies we need not be concerned about the impedance of the ground path return because the current is dissipated by attenuation and dispersion. The transformer in Fig. 1 represents the coaxial horn transition in the prototype in Fig. 2, transforming the surface wave to a coaxial output matched to load R_{L2} . The power propagating on the tip is approximately equal to the product of the characteristic impedance of this line and the square of the current in the surface wave:

$$P = \frac{1}{2} Z_0 I_0^2 \left(1 + \frac{B}{E_0} + \frac{B^2}{2E_0^2} \right)^2 \left(\frac{E_1}{E_0} \right)^2 \left(\frac{E_2}{E_0} \right)^2 \quad (6)$$

Equation 6 shows that the output power is proportional to the product of the power flux densities produced at the tip by the two lasers. Using typical values for field emission, and allowing for the resonance, it appears possible to generate mW levels of power at THz frequencies by photomixing in resonant laser-assisted field emission.

References:

- [1] M. J. Hagmann, *J. Appl. Phys.* 78 (1995) 25.
- [2] A. Mayer and J.-P.-Vigneron, *Phys. Rev. B*, 62 (2000) 16138.
- [3] A. Mayer, N. M. Miskovsky and P. H. Cutler, *Phys. Rev. B* 65 (2002) 195416.
- [4] M. Brugat and M. J. Hagmann, *Ultramicroscopy* 79 (1999) 181.
- [5] M. J. Hagmann, *Int. J. Quant. Chem.* 70 (1998) 703.
- [6] K. Alonso and M. J. Hagmann, *J. Vac. Sci. Technol. B*, 19 (2001) 68.
- [10] R. H. Fowler and L. W. Nordheim, *Proc. R. Soc. London A* 119 (1928) 173.
- [11] L. W. Nordheim, *Proc. R. Soc. London A* 121 (1928) 626.

Effect of Finite Spectral Width on Photomixing In Resonant Laser-Assisted Field Emission

Mark J. Hagmann

Deseret Electronics Research Corporation, North Salt Lake, Utah

Abstract

Resonant Laser-Assisted Field Emission is a new technology for wide-band tunable and pulsed terahertz sources. Simulations are made to determine the effect of laser linewidth on photomixing with this technique. The results show that single mode tunable laser diodes may be used in early prototypes.

Argument for unusually high bandwidth with this New Technology

Photomixing with low-temperature-grown GaAs generates $1 \mu\text{W}$ at 1 THz, rolling off as $1/f^4$ at higher frequencies— $1/f^2$ from finite carrier lifetime in the semiconductor and $1/f^2$ from capacitive shunting [1]. Photomixing in laser-assisted scanning tunneling microscopy (STM) has a roll-off of only $1/f^2$ because the tip is closely coupled to the sample but there is no semiconductor [2]. It is reasonable to suppose that by moving the sample away from the tip in a STM, for laser-assisted field emission, the capacitive shunting of the tunneling junction would be eliminated so there would be no inherent roll-off of power with increasing frequency. This conclusion is supported by quantum simulations [3,4].

Advantages of THz sources using the new technology

In addition to the potential for large bandwidth, simulations also suggest that output powers at the mW level are possible. Furthermore, field emission is insensitive to environmental temperature, ionizing radiation, and electrostatic discharge (ESD).

Method for the simulations allowing for finite spectral width

We simulate photomixing as a stationary stochastic process in which the frequencies and phases of two sources of optical radiation are random variables changing at the ends of their respective periods of coherence. Lorentzian and Gaussian line shapes are modeled, to simulate different mechanisms for line broadening [5]. The center wavelength (λ_0), linewidth (FWHM) and power flux density (P) for each radiation source are specified, and the coherence times are calculated. The metal for the field emitter tip and the applied static field are specified. The waveform of the field emission current is sampled with 5 points per cycle at the highest frequency in the incident radiation to exceed the Nyquist criterion at the second harmonics. An adiabatic solution of the Schrödinger Equation is used to obtain these sample points [4], in which the Fowler-Nordheim expression for the potential barrier [6,7] is modified by superimposing the instantaneous value of the radiation field. Pseudorandom deviates are used to change the frequencies and phases of the two radiation sources as random variables at the ends of their respective periods of coherence. The one-sided power spectral density of the current

is calculated with the current vs. time data partitioned into K segments, each with 2^N consecutive samples, for a total of $K \times 2^N$ points with no overlapping. Square windowing is applied to the data and the FFT is used to produce a periodogram estimate for each segment. Finally, the K periodogram estimates are averaged at each frequency to reduce the variance of the estimate [8]. Routines for the periodogram estimates are from [9]. The normalized current densities, which are reported, may be integrated over a frequency interval and multiplied by the DC current density to give the RMS current density in that frequency interval.

Presentation of the data

The first four figures show the normalized current density for photomixing with a tungsten tip having an applied static field of 5 V/nm when each laser has $P = 10^{12}$ W/m². In each case the simulated period exceeds 100 times each coherence time. In Figs. 1a and 1b, $\lambda_0 = 670.00$ and 668.51 nm, and FWHM = 0.1 nm. In these calculations $K = 20$ and $N = 18$ for 5,242,880 sample points to simulate 2.34 ns of the waveform. In Figs. 2a and 2b, $\lambda_0 = 670.00$ and 655.35 nm, and FWHM = 1.0 nm. In these calculations $K = 40$ and $N = 17$ for 5,242,880 sample points to simulate 2.29 ns of the waveform. Figure 2A shows peaks for the two lasers, the mixer (difference) frequency, the second harmonics for each laser, and the sum frequency. Each of these features is also present in the data for Fig. 1A, although some of the peaks are too close to be seen in the figure.

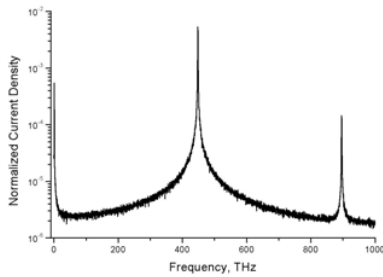


Fig. 1a

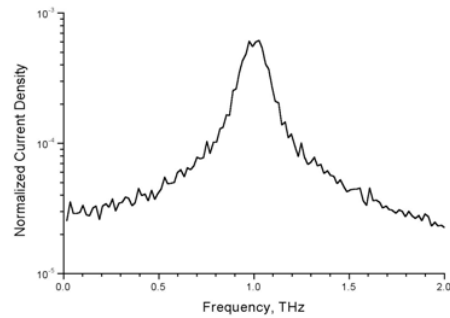


Fig. 1b

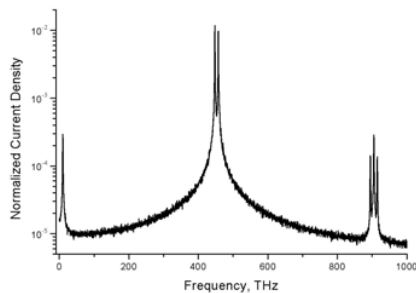


Fig. 2a

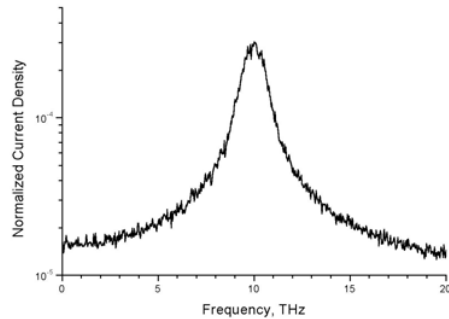


Fig. 2b

A series of simulations like those shown on the previous page was made to determine the linewidth for either 1 THz or 10 THz mixer outputs using radiation sources having different values of linewidth. In each case one source had a center wavelength of 670 nm, and the second was shifted to obtain the chosen mixer frequency. The results are shown as solid squares in Figs. 3 and 4. An analytical solution for mixing with a quadratic law device when the sources have Gaussian line shapes shows that the spectral widths of the two input signals and the mixer output are related by $\sigma_M^2 = \sigma_1^2 + \sigma_2^2$. The solid line in each figure shows this result, marked as a “Semiclassical Approximation”.

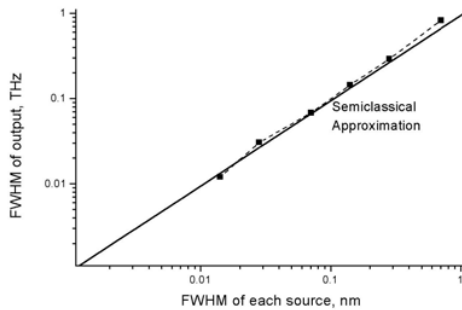


Fig. 3. Mixer output at 1 THz.

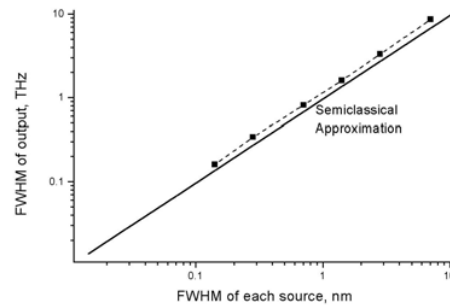


Fig. 4. Mixer output at 10 THz.

Discussion and conclusions

The “semiclassical” relation for the linewidth is consistent with the simulations. We find no significant difference in the relation between the linewidth of the mixer output to the linewidths of the two radiation sources when Lorentzian or Gaussian line shapes are used consistently in the simulations. The adiabatic approximation used in the simulations may be corrected by a frequency-dependent multiplier increasing these values by as much as 40 dB [3,4]. We have not included the effects of instabilities and noise in these simulations.

References:

- [1] E. R. Brown, F. W. Smith and K. A. McIntosh, *J. Appl. Phys.* 73 (1993) 1480.
- [2] L. Arnold, W. Krieger and H. Walther, *J. Vac. Sci. Technol. A*, 6 (1988) 466-469.
- [3] M. J. Hagmann, *J. Vac. Sci. Technol. B*13 (1995) 1348.
- [4] M. J. Hagmann, *Ultramicroscopy* 79 (1999) 115.
- [5] B. E. A. Saleh and M. C. Teich, *Fundamentals of Photonics*, New York, John Wiley, 1991, pp. 351, 444-449.
- [6] R. H. Fowler and L. W. Nordheim, *Proc. R. Soc. London A* 119 (1928) 173.
- [7] L. W. Nordheim, *Proc. R. Soc. London A* 121 (1928) 626.
- [8] P. M. T. Boersen, *IEEE Trans. Instrum. Meas.* 49 (2000) 766.
- [9] W. H. Press, S. A. Teukolsky, W. T. Vetterling and B. P. Flannery, *Numerical Recipes in FORTRAN*, New York, Cambridge University Press, 2nd ed., 1992, pp. 269-280, 542-551.

Terahertz quantum cascade laser based on LO-phonon-scattering assisted depopulation.

Benjamin S. Williams, Hans Callebaut, Sushil Kumar, and Qing Hu

Department of Electrical Engineering and Computer Science and Research Laboratory of Electronics, Massachusetts Institute of Technology, Cambridge, MA 02139

John L. Reno

Sandia National Laboratories, Dept 1123, MS 0601, Albuquerque, NM 87185-0601

In a recent breakthrough,¹ we have developed the longest wavelength quantum cascade laser to date, at $\lambda = 87.2 \mu\text{m}$ corresponding to 3.44 THz or 14.2 meV photon energy. The laser is based on GaAs/Al_{0.15}Ga_{0.85}As multiple quantum well structures, and it utilizes resonant LO-phonon scattering for depopulation of the lower radiative level to achieve population inversions. The core structure, a four-well module, is shown within the dashed box in Fig. 1. The radiative transition takes place between levels 5 and 4, highlighted by thicker lines. 175 nominally identical such modules are cascade connected in series. Under designed bias, the ground level 1' of a previous module is aligned with level 5, selectively injecting electrons to this upper level. The lower level 4 is at resonance with a level in the adjacent well, where very fast LO-phonon scattering (~ 0.5 ps) takes place, keeping this level mostly empty.

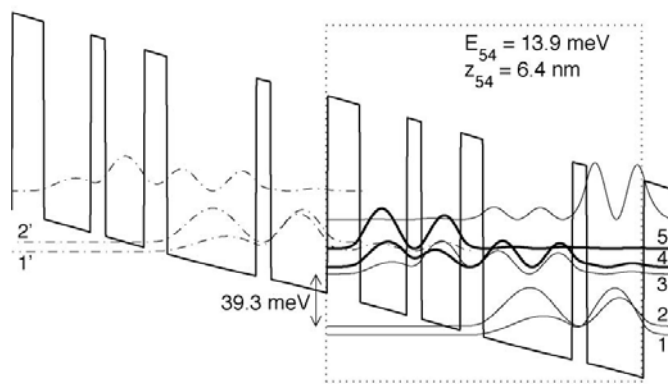


Figure 1. Conduction band profile of the THz quantum cascade laser structure under a bias of 64 mV/module, corresponding to a total bias voltage of 11.2 V.

Lasing at 3.437 THz ($\lambda = 87.2 \mu\text{m}$) was obtained in this device at a threshold current density of 840 A/cm^2 at 5 K heat sink temperature. Typical emission spectra above threshold are shown in Fig. 2. The emission frequency corresponds to a photon energy of 14.2 meV, close to the calculated value of 13.9 meV. For much of the bias range, the emission is dominated by a single mode, and the spectrum shifts towards higher energy longitudinal modes with increasing bias (inset, Fig. 2) due to Stark shift.

Measured optical power versus current (P-I) curves at low duty cycle are plotted in Fig. 3(a). Lasing is observed up to 64 K with a power level of $25 \mu\text{W}$, compared to the 2.5 mW observed at 5 K. Fig. 3(b) displays the voltage versus current, as well as several P-I curves taken at

different duty cycles. The peak power remains largely unchanged for duty cycle below 1%, and gradually drops to 0.5 mW at 50% duty cycle.

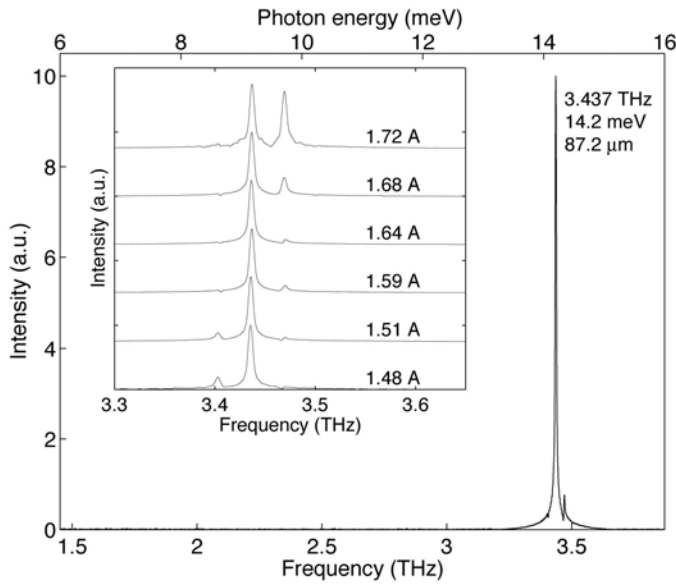


Figure 2. Emission spectrum above threshold biased at 1.64 A at 5 K. The inset shows an expanded view of spectra at various bias points, offset for clarity.

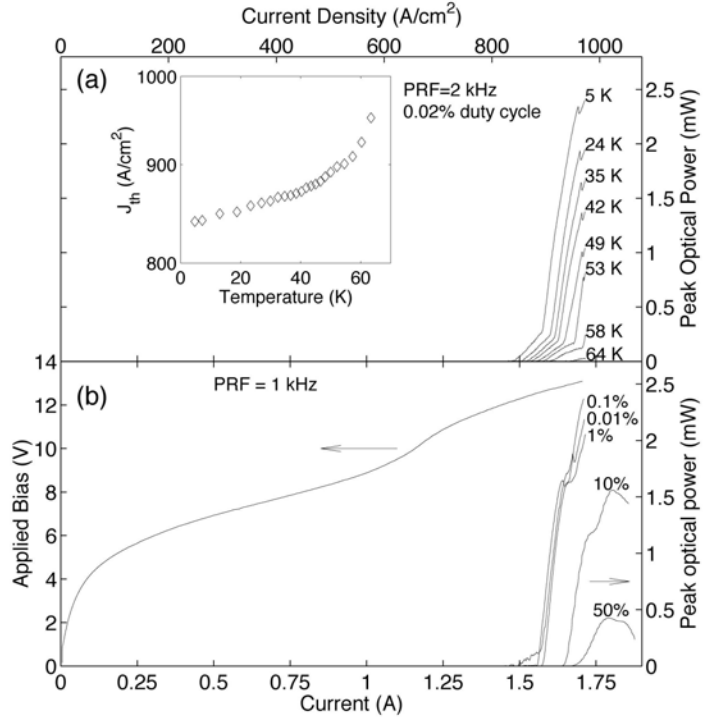


Figure 3. (a) Emitted power versus current at various heat sink temperatures with a 0.02% duty cycle. (b) Applied bias voltage and peak emission power versus current, collected at various duty cycles and heat sink temperature from 8 K to 15 K.

The performance of this device is quite promising, as a first attempt to develop THz quantum cascade lasers based on LO-phonon assisted depopulation and at this long wavelength. Minor improvements such as fabrication of narrower ridges and improved heat sinking should lead to CW operations. Further refinement of the injector design should improve efficiency and reduce the threshold current density. We believe that resonant LO-phonon assisted depopulation is a robust scheme that will enable operation at even higher temperatures and still longer wavelengths. We are currently developing quantum cascade lasers for the important 2.5-THz frequency range based on the same operating principle. Given the remarkable success at 3.4 THz, we are optimistic about the outcome of this new development. The result will be presented at the symposium.

1. B. S. Williams, H. Callebaut, S. Kumar, Q. Hu, and J. L. Reno, to be published in Appl. Phys. Lett., February 24 (2003).

Terahertz Backward Wave Oscillator Development

Lawrence Ives, David Marsden, Malcom Caplan, Carol Kory, Jeff Neilson,

Calabazas Creek Research, Inc.

20937 Comer Drive, Saratoga, CA 95070-3753, USA

(408) 741-8680, Fax: (408) 741-8831

S. Schwartzkopf, RWI, Inc.

Calabazas Creek Research, Inc. is funded by the National Aeronautics and Space Administration to develop efficient, light-weight, backward wave oscillators (BWOs) for applications from 300 GHz to more than 1 THz. These devices are needed as local oscillator (LO) sources in heterodyne receivers. Very low noise heterodyne receivers are needed at submillimeter wavelengths for low-background radioastronomy observations and remote sensing of comets, Earth and other planetary atmospheres. Important molecules play a key role in the energy balance, chemistry, and dynamics of interstellar molecular clouds, planetary atmospheres, and cometary coma. High resolution observations of these species are needed to understand the structure and evolution of the galactic and nearby extragalactic interstellar medium. Heterodyne instruments are required for these observations at ground-based observatories such as the Caltech Submillimeter Observatory, airborne observatories such as the upcoming NASA SOFIA (a 747 aircraft with a 2.5 m telescope), and the ESA Far Infrared and Submillimeter Telescope mission. Currently there are no compact, low-power, broadband LO sources, even above a few hundred GHz. Such a source would enable new science missions and enhance the science return of a given mission as well as expedite the laboratory development of the receiver system. Above 100 GHz, only BWOs have broad tunability (over 100 GHz) and high output power (~1 mW); however, existing BWOs are heavy (over 20 kg), consume a lot of power (270 W), require water cooling, and have poor output mode purity.

The technical objectives of the current program are as follows:

- Utilize advanced manufacturing techniques to extend the operating range to frequencies exceeding 1 THz.
- Incorporate a depressed collector to improve the efficiency and eliminate water cooling,
- Improve the output coupling to increase coupling efficiency and mode purity,
- Reduce the magnet system size and weight.

Previous presentations described the design of the 600-700 GHz BWO¹. The prototype is currently being assembled by CCR and RWI. A number of issues arose during the construction of components that required significant technological development.

Circuit: The slow wave circuit requires creation of 1500 metallic “towers,” or pintles, that are 30 microns by 20 microns in cross section and 80 microns high. These are separated by approximately 20 microns. Machining these structures presented a significant challenge, so two separate approaches were undertaken. CCR worked with Sandia National Laboratory to develop a lithographic process using LIGA; which could provide mass production of slow wave circuits up to 1.5 THz. This development proved more difficult than anticipated due to a number of processing steps. Never the less, Sandia was able to solve most problems and accurately expose and electro-

plate the desired structures. Unfortunately, the wafer failed to complete the final process successfully. Additional funding was provided to continue this development, and Sandia is continuing this research. This development will be crucial to increase frequencies above 1 THz.

In parallel, RWI successfully implemented advanced electric discharge machining (EDM) procedures using 8 micron wire. This allowed machining of the structures with the required accuracy, so four circuits are currently being produced. RWI is investing in more advanced equipment to manufacture even smaller structures.

Output Waveguide System: The BWOs incorporate fundamental waveguide coupling from the slow wave structure, transitioning to a Gaussian mode antenna for coupling to external devices. The system requires manufacture of the BWO body in halves to incorporate the matching structures, which contain 2 micron features. RWI developed special procedures to manufacture these structures, which were successfully tested at the Jet Propulsion Laboratory. A photograph of one half the 600-700 GHz body is shown in Figure 1.

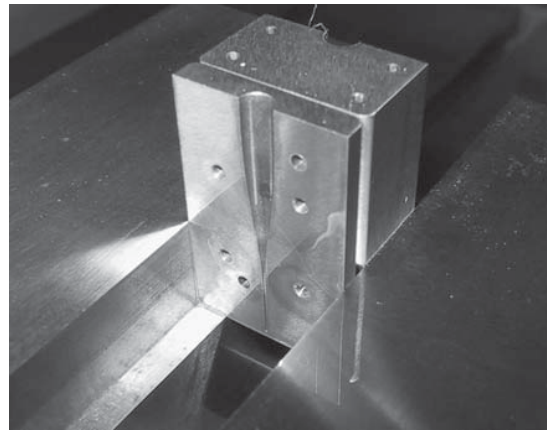


FIGURE 1. Body half with output waveguide system

Window: Initially, the program planned to use RF windows manufactured by Istok Company, the original developer of the BWOs; however, the thickness was not appropriate for the advanced output waveguide system. Consequently, CCR developed a procedure for manufacturing the 100 micron thick windows using sapphire ceramics. Because of the small window thickness, special brazing and lapping procedures were developed to make the window assemblies. A solid model of the window assembly is shown in Figure 2.



FIGURE 2. Solid model of window assembly

Depressed collector: An important feature of the BWO is the depressed collector. Successful implementation will significantly increase the operating efficiency and eliminate the current requirement for water cooling. Special adhesives were investigated for connecting the ceramic insulator to the body section for conductive cooling. Components of the collector are shown in Figure 3.



FIGURE 3. Metal components of the depressed collector

1. Lawrence Ives, Jeff Neilson, Malcom Caplan, Carol Kory, David Marsden, "Advanced Terahertz Backward Wave Oscillators," International Vacuum Electronics Conference, Monterey California, June 2002

This development is funded by National Aeronautics and Space Administration Grant NAS3-01014.

Design and operational considerations for robust planar GaAs varactors: A reliability study

Frank Maiwald, Erich Schlecht, John Ward, Robert Lin, Rosa Leon, John Pearson, and Imran Mehdi

Jet Propulsion Laboratory, MS 168-314, 4800 Oak Grove Drive, Pasadena, CA 91109

Abstract — Fix-tuned, broadband local oscillator (LO) sources to 1900 GHz have been developed for the HIFI instrument on the Herschel Space Observatory. Each LO chain consists of cascaded multipliers (doublers or triplers) being pumped with high-power (>100 mW) power amplifier modules in the 70 to 110 GHz frequency range. For long-term mission reliability it is important to quantify the safe operating conditions for these multipliers, especially when pumped with high input power. This paper will describe on-going investigations into the effects of excessive reverse currents in Schottky diodes along with presenting a methodology for determining safe bias conditions for a given multiplier.

I. INTRODUCTION

In recent years tremendous progress has been made in demonstrating broadband all planar solid-state LO chains to 1.9 THz [1,2,3] for the heterodyne instrument on the Herschel Space Observatory [4]. In order to produce sufficient output power at frequencies above 1 THz, the first stage multipliers are being pumped with power levels of more than 100 mW at W-band with power-combined GaAs based power amplifiers [5]. The multipliers must be designed and operated keeping this high RF input power requirement in mind. Though there have been some general studies regarding the reliability of GaAs Schottky diodes [6,7,8] we are not aware of any systematic study on the reliability of planar high power GaAs varactors. The situation is further complicated due to the fact that reliability of the devices is intimately dependent on the fabrication technology as well as the RF design. The goal of the present study is to determine what constitutes a safe RF and bias range for a given multiplier.

II. ELECTRICAL STRESS

Excessive amounts of either forward or reverse currents can cause the GaAs/metal contact to degrade. Catastrophic failure of GaAs Schottky contacts with forward current of $14\text{mA}/\mu\text{m}^2$ has been reported in [8] for whisker-contacted diodes. For planar diodes it is observed that the forward current limit is often imposed by the metal trace connecting the anode (diode finger), which acts as a fuse. However, the effect of reverse currents on diode characteristics is more difficult to predict. In the presence of constant reverse currents we have observed the diode bias voltage at constant current degrade even before there is avalanche breakdown at room temperature.

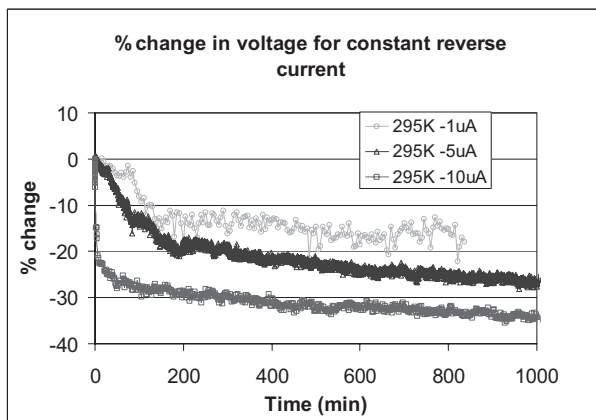


Figure 1: Measured reverse bias voltage for constant reverse currents of $-1\mu\text{A}$, $-5\mu\text{A}$, and $-10\mu\text{A}$. The diodes used have anode areas of $1.5\mu\text{m}^2$ with $2 \times 10^{17}\text{cm}^{-3}$ doping.

Degradation of the Schottky contact due to reverse current is investigated by passing a constant reverse current through a device while monitoring the required voltage over an extended period of time. This is depicted for three different current

levels at room temperature in Figure 1. The anode area is $1.5 \mu\text{m}^2$ and thus the current densities are $0.67 \mu\text{A}/\mu\text{m}^2$ for $-1 \mu\text{A}$, $3.3 \mu\text{A}/\mu\text{m}^2$ for $-5 \mu\text{A}$, and $6.7 \mu\text{A}/\mu\text{m}^2$ for $-10 \mu\text{A}$. The measurements at $-1 \mu\text{A}$ are more scattered than the others due to the low current but it follows the trend indicating that lower reverse currents do not result in as severe of degradation as higher reverse currents. However, it is clear that even at $-1 \mu\text{A}$ of reverse bias current, the reverse voltage will gradually degrade. For all three current values, the reverse voltage approaches a fixed value after a few hundred minutes. Similar fixed-current reverse voltage behavior with time is observed when high RF power is applied. Furthermore, the degradation occurs at lower negative bias voltages, indicating as one would expect that the RF input power aggravates the reverse current damage to the device. The rate of degradation is expected to depend on the reverse current amplitude, RF power, device doping, operating frequency and device technology. These effects will be measured quantitatively in the future.

III. DIODE CURRENTS IN THE PRESENCE OF RF POWER

To better understand appropriate bias conditions for a varactor it is essential to investigate the RF induced current and voltage waveform on the diodes. This can be done by analyzing the circuit iteratively with harmonic balance code [9,11, 11]. The solid line in Figure 2 represents a measured I(V) curve for a $3 \times 12 \mu\text{m}^2$ anode with $2 \times 10^{17} \text{cm}^{-3}$ n carrier concentration. This anode is part of a 200 GHz balanced doubler chip, which has three such anodes in series and two parallel branches for a total of six anodes. During the circuit simulation, the bias voltage is optimized at each frequency to maximize the RF output power. However, it is obvious that the bias voltage must not exceed a certain range in order to avoid excessive currents in the positive or reverse directions. In the presence of RF input power, a voltage is induced on the device. The voltage waveform is shown as a dashed line in Figure 2. This waveform is simulated for an input power of 25 mW/anode and the anode biased with -2.5 Volts. The breakdown voltage V_{br} , which is for the purposes of this paper defined as reverse bias voltage necessary to produce $-10 \mu\text{A}$ of reverse current, for the single anode is measured to be -9.1 Volts. The shape of the induced RF swing depends on the embedding impedance of the multiplier circuit, the input power level, the frequency, and the bias voltage. The sinusoidal RF swing gets deformed due to the non-linearity of the device. The peaks of the voltage swing cannot be measured directly; only measurements of the average voltage and current are possible at these frequencies.

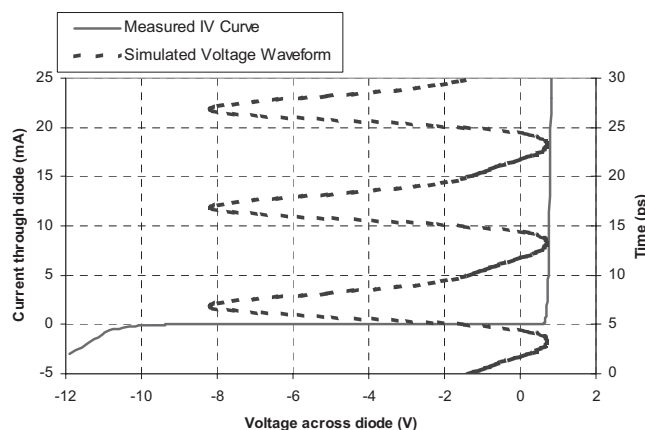


Figure 2: 200 GHz doubler anode ($3 \times 12 \mu\text{m}^2$ anodes and $2 \times 10^{17} \text{cm}^{-3}$ doping). The I(V) curve was measured at 295 K on a single diode. The voltage waveform is calculated (295 K) for a single diode with 25 mW input power per diode (150 mW total) biased at -2.5 V per anode (-7.5 V total).

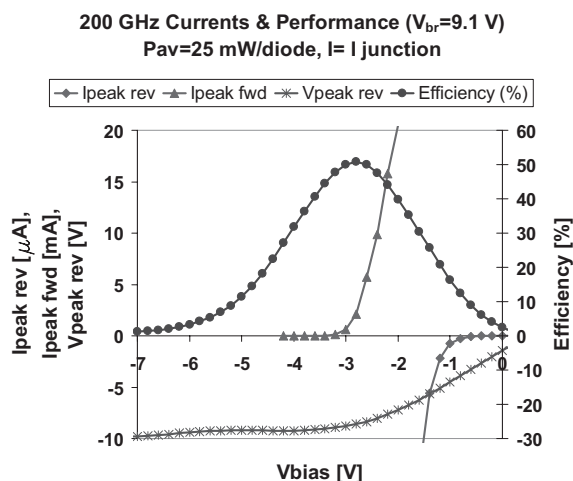


Figure 3: Simulation of the current and voltage at 295 K induced in a single diode of a balanced varactor doubler with 25 mW per diode input power at 100 GHz. The calculated peak currents and the efficiency are displayed as a function of bias voltage (V_{bias}).

Along with the voltage waveform, it is also important to study currents in the device while RF power is present. Such a simulation for a fixed input frequency of 100 GHz, is shown in Figure 3. As the bias voltage (V_{bias}) is swept from positive towards negative, a sharp increase in the peak reverse current ($I_{\text{peak rev}}$) is observed. Even when biased at only 20 percent of the breakdown voltage V_{br} , the peak reverse voltage ($V_{\text{peak rev}}$) swings close to the breakdown voltage. Though the maximum efficiency based on this simulation alone would require a bias voltage of about 0.28 V_{br} this would clearly be courting danger. In practice, such a diode should be biased close to 0.15 to 0.18 of V_{br} in order to avoid excessive reverse currents, which can lead to device failure. One should use caution in interpreting this plot since it does not include the temperature and frequency dependence. Moreover, due to the lack of a satisfactory model for predicting the reverse currents through Schottky diodes it is believed that the predicted currents are somewhat higher than what actually occurs in the laboratory. These current simulations are probably pessimistic [9], since $I(V)$ measurements indicate that it overestimates the reverse current by about an order of magnitude. The rise in peak reverse current therefore probably occurs at more negative bias voltages than plotted in Figure 3. Simulations like these along with empirical results are both needed to determine safe and useable bias limits for these particular multipliers.

IV. PROPOSED METHOD FOR THE EXPERIMENTAL DETERMINATION OF BIAS LIMITS

Since the direct measurement of the peak reverse current is not possible, the following measurements were made to determine the safe operating conditions of a 200 GHz doubler. At a fixed frequency, the input RF power was increased from 10 mW to 170 mW in 10 mW steps. At each input power the bias voltage was recorded at four different bias currents. First, the bias was adjusted to obtain maximum output power. Second, the bias was adjusted to obtain +7 mA bias current. Third, the bias was adjusted to obtain +0 mA through the device. Finally the bias was adjusted to give $-5 \mu\text{A}$ through the device. These measurements are shown in Figure 4a. The forward current at this level poses no risk to the device and is below $1 \text{ mA}/\mu\text{m}^2$ current density. However, reverse current of $-5 \mu\text{A}$ will be detrimental to the device and thus the safe bias voltage limit must be more positive. Figure 4b shows the estimated safe operating zone for this particular multiplier and for this particular frequency. The $-5 \mu\text{A}$ bias line is de-rated to 75% to provide a safer operating condition. The dashed trapezoid in this figure indicates the approximate safe operating bias zone for this device.

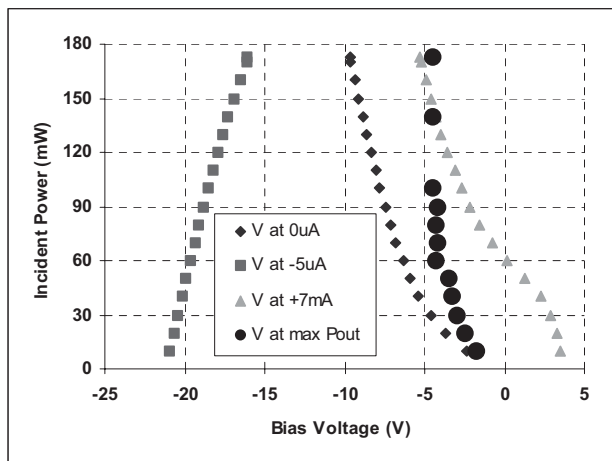


Figure 4a: 200 GHz doubler with six $3 \times 12 \mu\text{m}^2$ anodes and $2 \times 10^{17} \text{ cm}^{-3}$ n carrier concentration. Measurement of bias voltage for various bias currents and RF input powers.

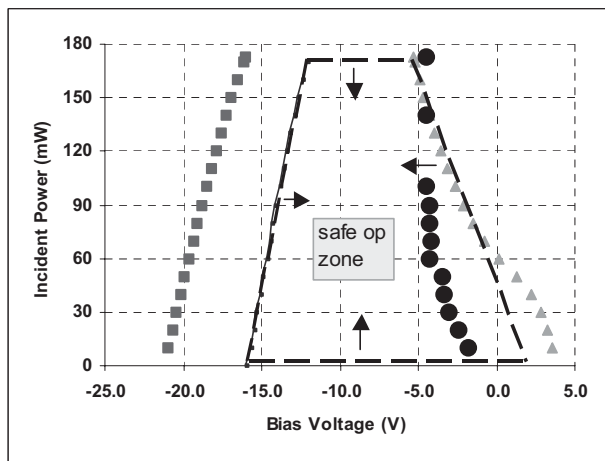


Figure 4b: Definition of safe operational range. The maximum safe RF input power is limited by the design specification of the thermal dissipation.

V. CONCLUSION

Reverse currents through Schottky diodes can degrade the breakdown voltage thus ultimately leading to device performance failure. The amplitude of the current along with the device technology will determine how long it takes for catastrophic failure. A preliminary procedure for determining safe operating conditions for a given multiplier has been outlined in this paper. A quantitative approach is under development that will be based both on simulated and experimental behaviors and will define safe operating bias conditions for any given multiplier.

VI. ACKNOWLEDGEMENTS

We thank Peter Siegel (JPL) and Neal Erickson (U-Mass) for fruitful technical discussions. The research described in this publication was carried out at the Jet Propulsion Laboratory, California Institute of Technology, under a contract with the National Aeronautics and Space Administration.

VII. REFERENCES

1. J.C. Pearson, I. Mehdi, E. Schlecht, F. Maiwald, A. Maestrini, J. Gill, S. Martin, D. Pukala, J. Ward, J. Kawamura, W.R. McGrath, W.A. Hatch, D. Harding, H.G. Leduc, J.A. Stern, B. Bumble, L. Samoska, T. Gaier, R. Ferber, D. Miller, A. Karpov, J. Zmuidzinis, T. Phillips, N. Erickson, J. Swift, Y.-H. Chung, R. Lai, and H. Wang, "THz Frequency Receiver Instrumentation for Herschel's Heterodyne Instrument for Far Infrared (HIFI)," *SPIE conference, Astronomical Telescopes and Instrumentation*, Waikoloa, Hawaii, 22-28 August 2002.
2. N. Erickson, A. Maestrini, E. Schlecht, G. Chattopadhyay, J. Gill, and I. Mehdi, "1.5 THz all-Planar Multiplied Source," *presented at the 13th International Symposium on Space THz Technology*, Harvard, March 2002.
3. Alain Maestrini, John Ward, John Gill, Goutam Chattopadhyay, Frank Maiwald, Katherine Ellis, Hamid Javadi, and Imran Mehdi, "A Planar-Diode Frequency Tripler at 1.9THz," *IEEE MTT-S International Microwave Symposium*, Philadelphia, Pennsylvania, June 13, 2003.
4. N. D. Whyborn, "The HIFI Heterodyne Instrument for FIRST: Capabilities and Performance," *Proc. ESA Symposium, The Far Infrared and Submillimetre Universe*, 1997, ESA SP-401.
5. Robert R. Ferber, John C. Pearson, Todd C. Gaier, Lorene A. Samoska, Frank W. Maiwald, Mary Wells, April Campbell, Gerald Swift, Paul Yocom, and K. T. Liao, "W-Band MMIC Power Amplifiers for the Herschel HIFI Instrument," *14th Int. Symposium on Space THz Technology*, Tucson, 22 April 2003.
6. B.K. Sehgal, B. Bhattacharya, S. Vinayak, R. Gulati, "Thermal reliability of n-GaAs/Ti/Pt/Au Schottky contacts with thin Ti films for reduced gate resistance," *Elsevier, Thin Solid Films*, pp. 146-149, 1998.
7. M. Schuessler, V. Krozer, K.H. Bock, M. Brandt, L. Vecchi, R. Losi, and H.L. Hartnagel, "Pulsed Stress Reliability Investigations of Schottky Diodes and HBTS," *Pergamon, Microelectron. Reliab.* Vol. 36, No. 11/12, pp. 1907-1910, 1996.
8. A. Grub, V. Krozer, A. Simon, and H.L. Hartnagel, "Reliability and Micro-structural Properties of GaAs Schottky Diodes for Submillimeter-wave Applications," *Solid-State Electronics*, Vol. 37, No. 12, pp. 1925-1931, 1994.
9. E. Schlecht, G. Chattopadhyay, A. Maestrini, D. Pukala, J. Gill and I. Mehdi, "Harmonic Balance Optimization of Terahertz Schottky Diode Multipliers Using an Advanced Device Model," *13th Int. Symp. on Space THz Technology*, Cambridge, MA, March 2002.
10. E. Schlecht, G. Chattopadhyay, A. Maestrini, A. Fung, S. Martin, D. Pukala, J. Bruston and I. Mehdi, "200, 400 and 800 GHz Schottky Diode 'Substrateless' Multipliers: Design and Results," *IEEE Int. Microwave Symp. Digest*, pp. 1649-1652, Phoenix, AZ, May 2001.
11. E. Schlecht, F. Maiwald, G. Chattopadhyay, S. Martin and I. Mehdi, "Design Considerations for Heavily-Doped Cryogenic Schottky Diode Varactor Multipliers," *12th Int. Sym. on Space THz Tech.*, San Diego, CA, Feb 2001.

A Design Theory for a Terahertz-Frequency Quantum Oscillator that Operates in the Positive Differential Resistance Region

Dwight Woolard

US Army Research Lab., ARO, Research Triangle Park, NC, USA

Peiji Zhao

Department of Electrical and Computer Engineering, NCSU, Raleigh, NC 27696 USA

H. L. Cui

*Department of Physics and Engineering Physics, Stevens Institute of Tech
Hoboken, NJ 07030 USA*

Abstract

The traditional implementation of resonant tunneling diodes (RTD) as high-frequency power sources always requires the utilization of negative-differential resistance (NDR). However, there are inherent problems associated with effectively utilizing the two-terminal NDR gain to achieve significant levels of output power. This paper will present a new design methodology where resonant tunneling structures (RTS) are engineered to exhibit electronic instabilities within the positive-differential-resistance (PDR) region. As will be demonstrated, this approach utilizes a microscopic instability that alleviates the need to reduce device area (and therefore output power) in an effort to achieve low-frequency stabilization.

Terahertz frequency systems have previously found applications in radio astronomy, atmospheric monitoring, plasma diagnostics, imaging and surveillance, etc. Though terahertz technology already has potential importance for some civilian and military applications, this region of the electromagnetic spectrum has not reached maturity for commercial exploitation. The main reason for this is the general absence of reliable, low-cost, miniaturized solid-state power sources.

To date, most of the two-terminal devices can only provide significant power for applications at the very lower limit of the terahertz electromagnetic spectrum.

The RTD, when implemented in the traditional manner, have been shown capable of reaching frequencies up to 712 GHz with output power of $\sim 0.3 \mu\text{W}$. However, the conventional RTD oscillators have some inherent drawbacks. In the traditional implementation, a RTD is utilized as the gain component in a traditional two-terminal oscillator configuration. Here, the RTD is biased in its negative differential resistance (NDR) region. This leads to several problems that severally influence the output power performance. First, any noise fluctuations will be amplified when the RTD and its inherent charge storage capacitance resonates in an unstable manner with some external charge-storage element (e. g., inductance of the contact lead). This effect will finally drive the balance point of the oscillation to the edge of the NDR region. Second, since a RTD acts as an unstable gain mechanism, the oscillation can only be produced through an energy exchange with an external element. Hence, the energy associated with the oscillation

must pass through a physical contact, which will always possess some loss. Third, the NDR of a RTD will encourage oscillation in the bias circuitry down to zero frequency. Therefore, one must design the circuit coupled to the RTD-based oscillator so that it is low-frequency stable to prevent energy losses to lower frequency modes. This requires the designer to reduce the RTD capacitance thereby the cross-sectional area of the RTD. This reduction in RTD device area significantly limits the available output power of the oscillator at high frequencies.

In previous numerical experiments, intrinsic current oscillations at terahertz frequency in a double barrier quantum well (DBQW) system have been observed [1]. However, the bias voltage window in which the current oscillates for the device structure studied earlier occurs in the NDR region. This situation occurs because the oscillation criteria are satisfied when an emitter quantum well (EQW) is being created by the interference between the injected and the reflected electron waves just as the bias voltage passes the resonance bias voltage (i.e., when the energy level in the main quantum well is passing the Fermi level in the emitter). As stated earlier, current oscillations that arise within the NDR region will be severally limited in power since the area of the cross-section of the device has to be made small to reduce the capacitance of the device. This work will consider an emitter engineering technique that induces microscopic instabilities within resonant tunneling structures (RTSs). An artificial shallow well is “induced” in front of the emitter barrier. This shallow well enhances the formation of the EQW (and subsequent the instability

mechanisms), so that the criteria for the creation of the intrinsic current oscillation in the RTS system can be realized at bias voltages outside of the NDR region. Therefore, bias voltage windows for intrinsic oscillations can be created in the positive differential resistance (PDR) region as long as the underlying oscillation criteria can be satisfied.

To illustrate the potential design of a new quantum oscillator in the PDR region, we have performed Wigner-Poisson based numerical simulation studies. The device structure used in the simulation is based on that used in our previous research [1]. An emitter-engineering method is used to modify the device structure so that the oscillation can be obtained in the PDR region. Specifically, a small pre-well is built in front of the emitter barrier as shown by Fig. 1. The depth of the pre-well is 0.05eV. The length of the pre-well is 200Å. Grading of the Al in the well is used to achieve potential dip.

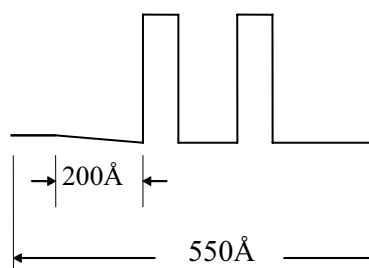


Fig.1 Band structure of the double barrier quantum well structure.

In order to analyze the device, the one-dimensional Wigner-Poisson model has been applied. This model was used to derive the potential profiles, electron distributions and current density. The simulation results are given in Figs. 2 and 3. Fig. 2 shows the average I-V

characteristics and demonstrates that there are two bias voltage windows (BVWs). Fig. 3 shows the current oscillatory behavior at select bias voltages. In the lowest BVW, the oscillations are damped. In the higher BVW, the oscillations are significant. Most importantly, the oscillations are located in a PDR region. These studies demonstrate intrinsic current oscillations in the PDR region of a tunneling diode for the first time. Fig. 2 and Fig. 3 show the salient features of the suggested terahertz power source. These features can be outlined as follows. First, the BVW for current instabilities can be located in the PDR region. This feature of the oscillation can be used to overcome the bias-point-shift problem in the engineering design of two-terminal oscillators. Furthermore, there is no broadband gain since the mechanism is not related to negative resistance. This will allow *the area of the cross-section of the device to remain large*. Finally, the operation temperature of the oscillator is in the temperature region of liquid nitrogen. In contrast, QC lasers can provide terahertz power output on the order of pico-watts only at very low temperature, such as $5 K^0$.

In conclusion, we have presented a new design method for two-terminal high frequency power sources. Since the gain mechanism is not related to negative resistance and the oscillations are designed in positive resistance region, the oscillators based on this design method should lead to enhanced levels of output power.

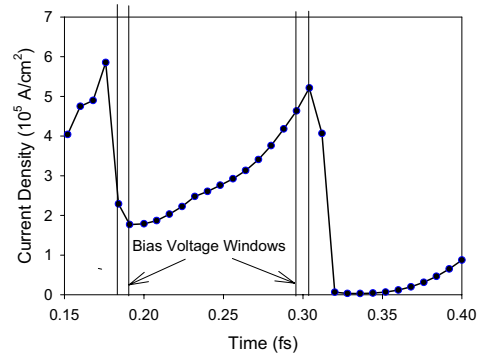


Fig. 2. The I-V characteristics of the new device structure. In the denoted bias voltage windows, the current density oscillates. The values of the current density in the bias voltage window in this figure are the time-average of the time-dependent current density.

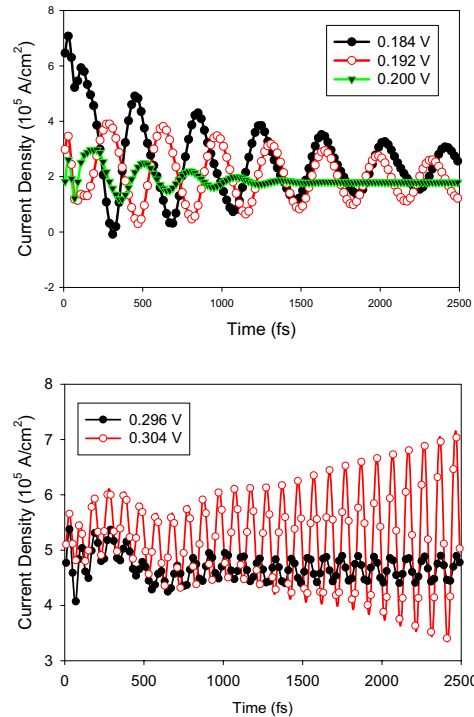


Fig.3. The time-dependent current density in the bias voltage windows. For the oscillation in positive differential resistance region, the oscillation frequency is 16.7 THz.

Reference:

[1] Peiji Zhao, H. L. Cui and D. Woolard, Physical Review B63, 75302(2001); Peiji Zhao, D. Woolard, and H. L. Cui, Phys. Rev. B67, 085312(2003).

A Multi-Subband Design Theory for a Terahertz-Frequency Double-Barrier Quantum-Well Oscillator

Peiji Zhao¹ and D.L. Woolard^{1,2}

¹ North Carolina State University, Raleigh, NC

² Army Research Laboratory, Army Research Office, Research Triangle Park, NC

ABSTRACT

This paper presents a theory of the creation of current oscillation in a multi-subband system. The oscillation in the system originates from the intersubband coupling. The relationship between the oscillation frequency and the subband structure can be used as a design criterion for a new class of intrinsic oscillators.

The search for compact solid-state, high-frequency power sources has been an important research subject for many years. Since the end of 1980's, resonant tunneling diodes (RTD) have been treated as a possible high frequency power sources. However, as it is well known, the traditional implementation of a RTD has not been successful as a power source at terahertz (THz) frequency. This failing is due to the extrinsic design manner of the oscillator that utilizes external circuit elements to induce the oscillation. In contrast to the extrinsic design of RTD oscillators, the intrinsic design of RTD oscillators makes use of the microscope instability of RTDs directly. This type of an approach will avoid the drawbacks associated with the extrinsic implementation of RTD's. It is believed that if the dynamics surrounding the intrinsic oscillation can be understood and controlled, RTD sources based on the self-oscillation process should yield milliwatt levels of power in the THz

regime. However, the exact origin of the intrinsic high-frequency current oscillation has not yet been fully established. The lack of knowledge related to the origin of the intrinsic instabilities in double-barrier quantum-well structures (DBQWSs) directly hampers realizing an optimal design (device and circuit) of a RTD-based oscillator. Thus, it is extremely important to understand the creation mechanism of the intrinsic instability in DBQWSs.

Previously, a new theory was presented by our group that provided a basic idea for the origin of the intrinsic oscillation in a DBQWSs [1]. This theory revealed that the current oscillation, hysteresis and plateau-like structure in I-V curve are closely related to the quantum mechanical wave/particle duality nature of the electrons. In addition, these effects were shown to be a direct consequence of the development and evolution of a dynamical emitter quantum well (EQW), and the ensuing coupling of the quasi-discrete energy levels that are shared between the EQW and the main quantum-well (MQW) formed by the DBQWS. This paper will extend the earlier theory through the application of basic quantum mechanical model. A multi-subband model for the describing the electron dynamics in DBQWSs is given. The multi-subband based theory will provide a simple relationship

between the oscillation frequency and the energy-level structure of the system.

Our previous research showed that a DBQWS becomes a multi-subband system once the emitter quantum well (EQW) is crested. For a multi-subband system, the wavefunctions of the system can be written as

$$\psi(z, t) = \sum_{k=1}^n \psi_k(z, t) e^{-\frac{2\pi i}{h} F_k(t)} \quad (1)$$

where

$$F_k(t) = \int_0^t dt' E_k(t') \quad (2)$$

In terms of the fundamental definitions of current and density, the density and current can be expressed as

$$j(t) = \sum_k \langle \psi_k | \hat{j} | \psi_k \rangle + 2 \operatorname{Re} \sum_{k, j (l < k)} \langle \psi_k | \hat{j} | \psi_j \rangle e^{-\frac{2\pi i}{h} (F_l(t) - F_k(t))}$$

$$\rho(t) = \sum_k \psi_k^* \psi_k + 2 \operatorname{Re} \sum_{k, j (l < k)} \psi_k^* \psi_j e^{-\frac{2\pi i}{h} (F_l(t) - F_k(t))}$$

Generally speaking, these two formulas show that there are no oscillations in a multi-subband system. However, if a system meets the following criteria, the oscillations do exist in the system.

Energy criteria: There are three conditions regarding to the relationship between the subband energies. If current oscillations exist in a multi-subband system, one of the conditions has to be satisfied. The following are the conditions.

1. Maximum Subband Coherence: The energy differences between the subbands are equivalent, that is,

$$\Delta E(t) = \Delta E_{lk}(t) = |E_l(t) - E_k(t)| = \text{const}$$

Here, $l \in \{l_i\}, k \in \{k_j\}$, and $l < k$. The sets $\{l_i\}$ and $\{k_j\}$ are of equal number

and assume all possible values from the number sequences $1, 2, \dots, n$.

2. Partial Subband Coherence: A finite and countable number of energy differences are equivalent, that is,

$$\Delta E(t) = \Delta E_{lk}(t) = |E_l(t) - E_k(t)| = \text{const}$$

Here, $l \in \{l_i\}, k \in \{k_j\}$, and $l < k$. The sets $\{l_i\}$ and $\{k_j\}$ are of equal number and assume some of the values from the number sequences $1, 2, \dots, n$.

3. Minimum Subband Coherence. The intrinsic oscillation is characterized by the condition in which only a single set of subbands contributes to the instability, that is,

$$\Delta E(t) = \Delta E_{lk}(t) = |E_l(t) - E_k(t)| = \text{const}$$

where l and k can assume only one set of values from the energy level index $1, 2, \dots, n$ and $l < k$.

Wavefunction criterion: The wavefunctions of the energy levels that cause the oscillation should be spatial overlapped. That is $\psi_i \psi_j \neq 0$ if the i th and the j th energy levels are able to cause the oscillation.

If the energy criteria and the wavefunction criterion can be satisfied simultaneously, the current and density can be expressed as

$$j(t) = \sum_k \langle \psi_k | \hat{j} | \psi_k \rangle + 2 \operatorname{Re} \left\{ e^{-\frac{2\pi i}{h} \Delta F(t) + i\alpha(t)} Q(z, t) \right\}$$

$$\rho(t) = \sum_k \psi_k^* \psi_k + 2 \operatorname{Re} \left\{ e^{-\frac{2\pi i}{h} \Delta F(t) + i\beta(t)} H(z, t) \right\}$$

where $\Delta F(t) = \int_0^t dt' \Delta E(t')$ and α and β are periodical functions of time.

Obviously, these formulas show that *the intrinsic current oscillation in a multi-subband system originates from the intersubband coupling*. The previous derivations lead to a simple relation, $\nu = \Delta E_0/h$ for defining the oscillation frequency. This relationship can be regarded as the basic design formula for the oscillator.

In order to verify our theory, a self-consistent, time-dependent Wigner-Poisson numerical investigation has been used to reveal sustained current oscillations in an isolated DBQWS-based device. The structure of the device has been described elsewhere [1]. The potential profiles obtained are then used in a Schroedinger-based approach to derive the energy level structure and the associated wavefunctions as shown in Figs. 1 and 2. From Fig. 1, we can see that only E_2 and E_3 contribute to the oscillation since the wavefunctions of these states are located in the same spatial region. Calculations show there is only 1% difference between the frequency from the Wigner-Poisson simulation and that from the formula $\nu = \Delta E_0/h$.

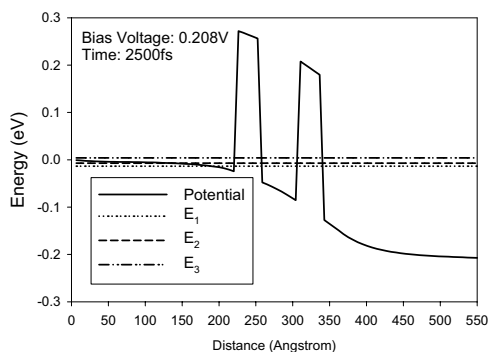


Figure 1. The quantum subband structure that is used to reveal the underlying source of the oscillations.

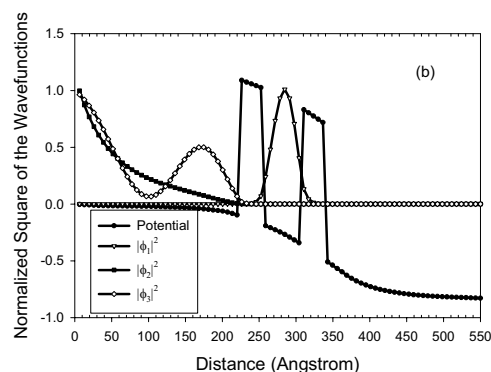


Figure 2. The wavefunctions of the subbands in the system.

Insight into DBQWSs as potential devices for very high-frequency oscillators is facilitated through two simulation studies. Together, these studies establish the fundamental principals and basic design criterions for the future development and implementation of DBQW-based oscillators. Further, this paper provides physical interpretations of the instability mechanisms and explicit guidance for defining new structures that will admit enhanced oscillation characteristics. Also, the theory has been used to probe the possible device structures that can create oscillations in the positive differential resistance region of the average I-V curve. These physics-based models and design criteria will be used in the future to facilitate the design of a realistic oscillator where a tunneling structure is integrated and optimized within an embedding circuit.

References

- [1] Peiji Zhao, H. L. Cui and D. Woolard, Physical Review B63, 75302(2001); Peiji Zhao, D. Woolard, and H. L. Cui, Phys. Rev. B67, 085312(2003).

argon atmosphere. The background pressure in a vacuum chamber prior to deposition was about 3×10^{-7} mbar. The argon working pressure was 6×10^{-3} mbar and 9×10^{-3} mbar during Mo and Cu deposition correspondingly. The deposition rate was 1.7 nm/sec for Mo and 0.9 nm/sec for Cu. The calibration has been done independently using specially deposited films measured by alpha step profilometer. Finally samples were cut into pieces of 24×1.5 mm² size to provide measurements.

Samples with the following Mo/Cu thickness values (nm) have been fabricated:

- (1) 8/0, 8/30, 8/50, 8/100;
- (2) 12/0, 12/30, 12/50, 12/100;
- (3) 15/50, 25/50, 35/50, 50/50;
- (4) 10/40, 15/35, 20/30, 30/20.

Dependencies of resistance versus temperature $R(T)$ have been measured in ³He/⁴He dilution refrigerator using four-probe method. The transition edge temperature of samples with Mo thickness 12 – 15 nm turned out to be the most sensitive to Cu thickness. Such samples have shown the transition edge temperature in the range $\approx 0.075 - 0.4$ K, which is required for bolometer operation. Samples with thinner Mo layer haven't demonstrated the superconducting transition at all. $R(T)$ dependencies for Mo/Cu thickness values 15/35 and 12/100 (nm/nm) are shown on Fig.1 together with $R(T)$ dependence for pure Mo film of 12 nm thickness.

The effect of proximity is clearly seen from the Fig.1. The transition edge temperature decreases with thickening of the Cu layer, simultaneously the resistance of bi-layer structure getting smaller. The pure Mo film has shown transition temperature of ≈ 0.93 K, which is expected value for Mo.

The parameter $\alpha = T / R \cdot dR / dT$, which characterizes the abruptness of superconducting transition, has been estimated in the vicinity of the superconducting transition edge temperature (T_c) for three measured samples. It was found to be $\alpha \approx 1070$ for $T_c \approx 0.93$ K, $\alpha \approx 150$ for $T_c \approx 0.4$ K and $\alpha \approx 510$ for $T_c \approx 0.08$ K. This parameter determines the speed response: the larger α the smaller response time of bolometer [3]. The value of α found in our measurements for $T_c \approx 0.08$ K and 0.4 K is about two times smaller in comparison with this value reported in [3] for similar bi-layer structure. Probably it can be explained by nonuniformity of our sputtered thin films.

Obtained results will provide the basis for subsequent developments of bolometer microcircuits with transition edge sensor of micrometer and sub-micrometer size.

It is pleasure to acknowledge V.V. Dmitriev and V.V. Zavialov for participation in measurements. This work was supported by ISTC (project № 1239).

Beam Lead Fabrication for Submillimeter-wave Circuits Using Vacuum Planarization

R.B. Bass¹, J.C. Schultz¹, A.W. Lichtenberger¹, J.W. Kooi², C.K. Walker³

¹Department of Electrical and Computer Engineering, University of Virginia, Charlottesville, VA

²Division of Physics, Mathematics, and Astronomy, California Institute of Technology, Pasadena, CA

³Department of Astronomy, University of Arizona, Tucson, AZ

The assembly of superconducting millimeter and submillimeter-wave circuits becomes increasingly difficult as chip dimensions and design tolerances shrink with increased operating frequency. Currently, RF ground connections are made by soldering, wire bonding or with conductive wire gaskets^{1,2}. To facilitate assembly and throughput, we are developing a beam lead process for quartz chips. Such processes already exist for silicon and gallium arsenide wafers³⁻⁵. However, niobium circuits on quartz substrates present unique difficulties. SIS junctions introduce additional thermal and chemical constraints to process development. For quartz, wet etches are isotropic and dry etches with high etch rates require large ion energies. We have developed a new, top-side approach to beam lead fabrication suitable for whole wafer processing.

Introduction

We have developed a new, top-side approach to beam lead fabrication suitable for whole wafer processing. The new process, reported for the first time in this paper, differs from our original approach in which a sacrificial epoxy resin is planarized within the trenches using a sodium chloride optical flat⁶. The new process still uses a sacrificial epoxy to fill the trenches, but the method of epoxy planarization is much improved.

Process

After the mixer circuits are completed, trenches are cut along the perimeter of the chips using a standard wafer dicing saw. The trenches are diced only partly through the wafer, to a depth slightly greater than the desired chip thickness. Multiple passes with the dicing saw are used to achieve the desired trench width. Trenches are, on average, 143 μ m wide with a standard deviation of 12 μ m.

Planarization is accomplished by filling the diced trenches with a sacrificial epoxy. This is done by isolating the trench volume from the surface of the wafer and then injecting the epoxy into the trench volume. To isolate the trench volume from the wafer surface, a relatively smooth piece of silicone rubber is placed atop the wafer. The silicone is naturally attracted to the wafer surface by Van der Waals forces, creating a seal at the wafer-silicone interface. Once sealed, the wafer is placed in a metal support jig with the backside of the wafer facing up. Because the trenches run to the edge of the wafer, there is a unique opportunity to “inject” the epoxy into this unsealed region. This is accomplished by first placing the jig under vacuum along with an attached reservoir of epoxy. After the air is removed, the vacuum chamber is tilted in such a way that the epoxy runs from the reservoir, into the jig and over the wafer. The epoxy is allowed to

flow over the wafer until the perimeter of the wafer is thoroughly coated. When the vacuum is released, air pressure forces the epoxy into the trenches. The excess epoxy on the backside is then cleaned off. Next, the wafer and jig are oven-baked to cure the epoxy. After curing, the silicone rubber is gently peeled away, revealing a clean quartz surface and epoxy-filled trenches. Because the silicone rubber seals the surface very tightly and uniformly, every trench fills in the same manner resulting in consistent epoxy planarization across the wafer. The open quartz surfaces are completely devoid of any residual epoxy.

The vacuum planarization process produces excellent results. The level of the epoxy does dip below the level of the quartz, but this dipping is slight compared to the depth of the trench. After planarizing once, we find an average dip in the epoxy of $3.83\mu\text{m}$, with a standard deviation of 630nm . To further improve planarization, the epoxy is etched back by $30\mu\text{m}$ using an oxygen plasma. The process is then repeated once again, resulting in an average epoxy dip of only $1.58\mu\text{m}$ below the quartz, with a standard deviation of 470nm , as seen in Figure 1.

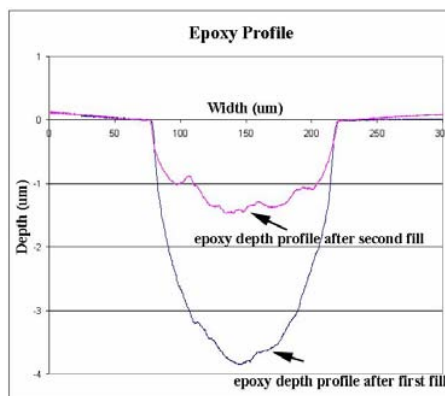


Figure 1 Trench depth is improved by performing the vacuum planarization process twice. After one fill, the maximum depth of the epoxy is, on average, $3.83\mu\text{m}$. After a second fill, this is improved to $1.58\mu\text{m}$.

After the epoxy is fully cured, 15nm of titanium and 50nm of gold are sputter deposited over the wafer using DC magnetron sputtering. The titanium serves as an adhesion layer for the gold atop the quartz and epoxy surfaces. The gold serves as a plating seed layer, providing electrical continuity across the wafer during the plating step.

The beam lead patterns are defined using an ultra-thick resist, and are designed to straddle the quartz-epoxy boundary. Thick ($10\mu\text{m}$) gold beam leads are plated atop the seed layer within the resist patterns. After plating, the resist is stripped with acetone. The gold seed layer and titanium are removed using wet chemical etchants. The wafer is then mounted, beam lead side down, to a silicon carrier wafer. With the wafer mounted face-down, the quartz is lapped to the desired chip thickness, usually around $100\mu\text{m}$ or less. Since the trenches are deeper than the final chip thickness, the lapping process separates the chips from one another. The sacrificial epoxy is then removed from between the chips using an oxygen plasma. The mounting wax is then dissolved using TCE. At this point, the

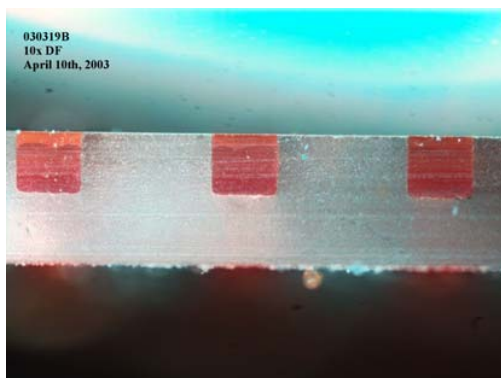


Figure 2 Epoxy-filled trenches are shown in the above cross-section of a quartz chip. The wafer thickness is $250\mu\text{m}$. The cross-section was made using a wafer dicing saw.

chips are completed. The beam leads extend 40 μ m beyond the chip perimeter, and are rigid enough to support the chip when gripped with fine tweezers.

Conclusion

This process was developed specifically for quartz, but its implementation is independent of the substrate. The technology is easily transferable to other substrates such as silicon or gallium arsenide. Moreover, this fabrication process is also suitable for substrates for which beam lead processes have yet to be developed, such as sapphire and glass. We have found a device yield of greater than 60%, which is much improved with respect to the process of [6]. However, the device yield is not limited by the planarization process; beam lead failures are attributed to seed layer adhesion and plating issues.

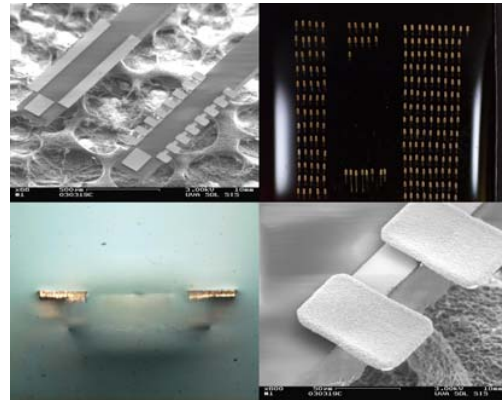


Figure 3 A composite picture of quartz chips with gold beam leads. In the upper left is an SEM image of two beam lead chips. A close-up SEM image is shown in the lower right. In the upper right is a completed batch of chips. In the lower left is an end-on picture of gold beam leads extending off of a quartz chip.

Submillimeter-wave circuits with beam lead RF ground connections greatly simplify the assembly of receivers. Beam leads make it possible to quickly test receivers, and allow for replacement of nonfunctioning chips without having to deal with conductive adhesives, wire bonding or soldering. In turn, the ability to assemble large arrays of submillimeter devices is enhanced, since the burden of fabricating a large, functional array of devices on a single chip is eliminated. Instead, individual beam lead chips may be placed into micro-machined waveguides and then tested. Non-functioning devices may then be removed and replaced. The size of the array is then no longer limited by the yield statistics of the device fabrication process.

References

1. A.R. Kerr, S.-K. Pan, S. Whiteley, M. Radparvar, S. Faris, IEEE International Microwave Symposium Digest, pp. 851-854, May 1990
2. A.R. Kerr, S.-K. Pan and A.W. Lichtenberger, D.M. Lea, IEEE Microwave and Guided Wave Letters, **2** (11), pp. 454-456, November 1992
3. B.J. Rizzi, K.K. Rausch, T.W. Crowe, P.J. Koh, W.C.B. Peatman, J.R. Jones, S.H. Jones, G. Tait, Fourth International Symposium on Space Terahertz Technology, Los Angeles, CA, March 1993
4. E. Schlecht, G. Chattopadhyay, A. Maestrini, A. Fung, S. Martin, D. Pukala, J. Bruston, I. Mehdi, IEEE MTT-S International Microwave Symposium Digest, Phoenix, AZ, pp. 1649-1652, May 2001
5. K.W. Nye, Q.Xiao, J.L. Hesler, T.W. Crowe, Proceedings of the 27th IEEE International Conference on Infrared and Millimeter Waves, San Diego, California, September 2002
6. R.B. Bass, J.Z. Zhang, W.L. Bishop, A.W. Lichtenberger, Proceedings of the SPIE Astronomical Telescopes and Instrumentation Conference, Waikoloa Village, HI, August 2002

This work was supported by grants from the National Science Foundation (9987330) and the National Aeronautics and Space Administration (NAG5-9100).

Wide Band Cryogenic IF Amplifiers for ALMA and Herschel Receivers

Isaac López-Fernández, Carmen Diez, Juan Daniel Gallego, Alberto Barcia
Centro Astronómico de Yebes, OAN-IGN, Apartado 148, 19080 Guadalajara, SPAIN

1. INTRODUCTION

This work describes the design, construction and measured results of the cryogenic IF amplifiers developed for band 7 (275-370 GHz) receivers of ALMA (Atacama Large Millimeter Array) built by IRAM. The present approach for this channel is to use 2SB (sideband-separating) mixers. In that case, the bandwidth allocated for each individual sideband and polarization will be 4 GHz. The design and the results obtained are compared with those from the amplifiers built for the instrument HIFI (Heterodyne Instrument for the Far Infrared) of Herschel Space Mission¹. In both cases, the required band is from 4 to 8 GHz. There is no need to integrate the amplifier with the mixer, since a cryogenic isolator has been developed for that band and it is commercially available.

2. DESIGN

Both amplifiers use a high quality **InP HEMT** device in the first stage to obtain the ultimate noise performance. The subsequent stages also employ InP transistors to overcome the severe power dissipation requirements of the two projects: HIFI mission lifetime is limited by the amount of liquid He, and in ALMA dewars the thermal load is important due to the great number of channels. ALMA amplifiers are made of three stages to obtain more gain and to overcome the noise of the next uncooled amplifier in the IF chain, while HIFI amplifiers were built with only two stages. The disadvantages of using InP HEMTs against commercial GaAs devices are their sensitivity to ESD, their larger gain fluctuations and the difficulties in its procurement.

The amplifier designed for ALMA (fig. 2) is smaller and lighter than the one of Herschel (fig. 1), although it has one stage more. Three stages give more degrees of freedom and made possible a new design of the interstage networks, which allows reducing the overall length while keeping the gain flat. In addition, an extra cavity in the bottom of the Herschel amplifier was suppressed. The cavity was introduced to have the possibility of adding a filter for rejection of interference in the bias cables.

	HIFI DMS	ALMA PROTOTYPE
Dimensions	58 × 32 × 15 mm	46 × 29 × 9 mm
Weight	65 g	31 g
Transistors	1 st = TRW IREL1 2 nd = TRW IREL1	1 st = TRW CRYO4 2 nd & 3 rd = ETH run1
Technology	Hybrid microstrip, soft substrates	
Construction	Gold plated aluminium	
RF connectors	SMA O-ribbon junction	SMA sliding pin
Bias connector	ITT-Cannon MDM	

Table 1: Design features of HIFI DMS and ALMA prototypes

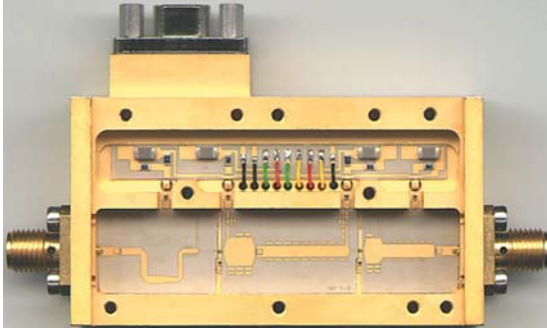


Figure 1: 2-stages 4-8 GHz HIFI cryogenic LNA Development Model (DM) YCF 6.

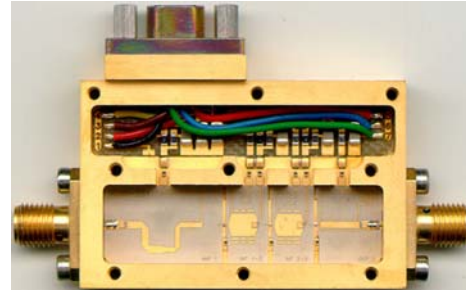


Figure 2: 3-stages 4-8 GHz cryogenic LNA prototype for ALMA band 7.

Reliability was a concern in the construction of the amplifiers for Herschel. The lessons learned in the process of space qualification have been applied to the design of the ALMA amplifiers. Herschel amplifiers have been tested for thermal cycling, vibration, radiation, ESD and EMC. Power connectors were carefully selected, and the junction of SMA connectors to the circuit was identified as a critical point. The junction was implemented using the O-ribbon technique to avoid any stress in thermal cycles. The ESD damage level of the HEMT devices was measured, and the bias circuit was designed with a combination of charge and voltage divider to reduce the sensitivity to a level of ~ 38000 V at the power connector, which can be considered safe for manipulation with standard ESD precautions. EMC measurements were performed on the Herschel amplifiers in the range from 1 MHz to 18 GHz and were found acceptable. It was identified that the weakest point was due to radiation picked up by bias cables, in particular at frequencies below 2 GHz. Special attention was paid in both amplifiers to obtain unconditional stability (no oscillation under any passive loading condition).

3. RESULTS

Table 2 shows the performance of HIFI and ALMA amplifiers. Noise and gain curves, measured in our 350 cold attenuator system are presented in figs. 3 and 4. The noise results are comparable, at the level of 3.6 K (NF=0.05 dB). Notice the improvement in gain flatness and output return losses in ALMA prototype, and the 11 dB higher gain, because of the extra stage and a perfected design.

The measurements were taken without **input isolator**. PAMTECH developed the cryo-isolator CTH-1365 K10 for the 4-8 GHz band. The performance of a number of units of

PARAM. @15 K, 4-8 GHz	YCF 6 DMS AVERAGE	YCA 1003 PROTOT.
Average Noise Temperature	3.6 K	3.6 K
Average Gain	27.1 \pm 1.1 dB	38.0 \pm 0.5 dB
Worst Output reflection	< -13 dB	< -16 dB
Norm. Gain Fluctuations. @ 1 Hz	9.4 \cdot 10 ⁻⁵ Hz ^{-1/2}	6.2 \cdot 10 ⁻⁵ Hz ^{-1/2}
Total power dissipation	4 mW	9 mW

Table 2: Comparison of the performance of HIFI (average) and ALMA amplifiers.

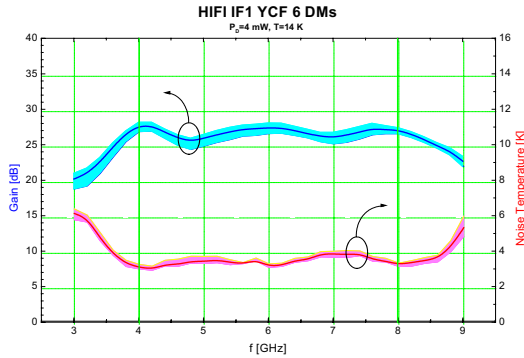


Figure 3: Noise and gain plots of all DMs built for HIFI. The colored bands represent the dispersion.

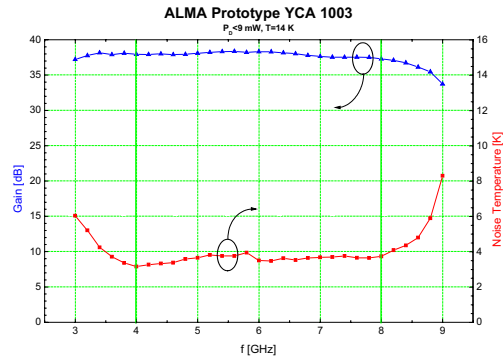


Figure 4: Noise and gain plots of prototype YCA 1003 for ALMA (see features in tables).

this type has been measured in our labs at 15 K. Typical insertion loss (worst case in the band) is 0.5 dB, which result in an estimated noise increment for an isolator-amplifier unit of 1.3 K. Typical input and output reflection and isolation are higher than 15 dB.

A series of measurements of the ALMA amplifier **gain fluctuations** were taken to evaluate the dependence with the bias point (see fig. 5). This parameter can become a key issue in these projects, where large bandwidths and very low noise temperatures are needed. It depends mainly on the transistors and we have seen a great dispersion in the results of different devices. Therefore, apart from device selection, bias optimization appears as the only procedure to reduce the fluctuations. We have found a remarkable dependence of the gain fluctuations with the drain voltage of the transistor, especially at low drain currents. Above 0.5 volts the fluctuations are rather constant, while below the variation is steep. There is no direct link between power dissipation and fluctuations: the fluctuations increase with drain voltage and decrease with drain current. The optimum bias point for gain fluctuations is not related with the optimum bias for noise measurements and is more critical. It is important to notice that small changes in bias, which may not affect significantly the noise temperature, may lead to great variations in gain fluctuations.

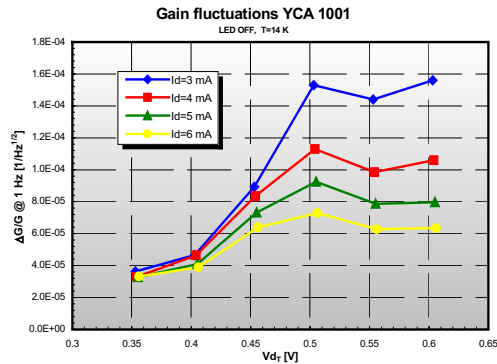


Figure 5: Measurements of the gain fluctuations of an ALMA prototype amplifier at different bias of the 1st stage. TRW IREL1 transistor is used in the 1st stage and ETH run1 in the 2nd and 3rd stages. The parameter used to characterize the fluctuations is the spectral density of the normalized gain at 1 Hz. The data is obtained averaging several spectra of the time domain data taken at 6 GHz with a HP8510C VNA.

¹ This work is funded in part by the Spanish MCyT under projects DGES/AYA2000-927, ESP2001-4519-PE and ESP2002-01693, and European FEDER funds. It is described in detail in I. López-Fernández, J. D. Gallego, C. Diez, A. Barcia, J. Martín-Pintado, "Wide band, ultra low noise cryogenic InP HEMT amplifiers for the Herschel mission radiometers", *Millimeter and Submillimeter Detectors for Astronomy, Proc. SPIE Vol. 4855*, pp. 489-500, 2003 (available at http://www.oan.es/cay/tech/SPIE2002_paper.pdf).

Investigation of superconducting transition in the molybdenum-copper thin film structure showing the proximity phenomenon with the purpose of constructing TES bolometer

S.A.Kovtonyuk, A.G.Kovalenko, A.A.Chebotarev, A.N.Vystavkin¹
Institute of Radioengineering and Electronics of RAS
11 Mokhovaja Str., 125009 Moscow, Russia

Abstract. We are developing highly sensitive direct detectors based on Mo/Cu superconducting transition edge sensor (TES) for submillimeter radio astronomy and spectroscopy. Toward this end Mo/Cu bi-layers with different layers thickness values showing the superconducting transition in the temperature range $\approx 0.075 - 1.0$ K have been experimentally tested. We have shown that the temperature of the superconducting transition edge can be adjusted because of proximity phenomenon by varying the thickness of Mo and Cu layers. We present details of measurements and fabrication of these devices.

For the purpose of equipping of radio telescopes for ground based, airborne and space based radio astronomical observation we are developing highly sensitive receivers based on direct detectors of sub-millimeter range [1, 2]. Use of transition edge sensor bolometer with ultra low ($\approx 0.3-0.1$ K) temperature of operation is one of the most promising way to achieve appropriate sensitivity and low time constant [3]. The transition edge sensor inserted into the center of planar antenna works as an absorber of incoming radiation and simultaneously as a signal detector. For signal read-out and amplification the SQUID's based circuits are used. The temperature of operation is set near the superconductor-normal metal transition edge temperature. A sensor is voltage biased to provide the electro-thermal feedback mode of operation with very low time constant [3].

Since it is very important to have temperature of superconducting transition edge in the range of stable operation of used refrigerator it has been proposed to use the superconductor-normal metal bi-layers [3] showing the proximity phenomenon [4]. Changing the thickness of superconductor and normal metal layers the temperature of superconducting transition edge of the bi-layer structure can be adjusted to the desired value. According to estimations [2, 3, 5] using this strategy the best ultimate sensitivity and fast response can be achieved simultaneously.

Toward this end Mo/Cu the bi-layers with different layers thickness values showing the superconducting transition in the temperature range $\approx 0.075 - 1.0$ K have been experimentally tested. The sample fabrication procedure was as follows. Two layers of Mo and Cu were deposited successively on the polished silicon wafer of 24×15 mm² size and 430 μ m thick, kept at ambient temperature, using the dc magnetron sputtering in

¹ Corresponding author: vyst@hitech.cplire.ru

argon atmosphere. The background pressure in a vacuum chamber prior to deposition was about 3×10^{-7} mbar. The argon working pressure was 6×10^{-3} mbar and 9×10^{-3} mbar during Mo and Cu deposition correspondingly. The deposition rate was 1.7 nm/sec for Mo and 0.9 nm/sec for Cu. The calibration has been done independently using specially deposited films measured by alpha step profilometer. Finally samples were cut into pieces of 24×1.5 mm² size to provide measurements.

Samples with the following Mo/Cu thickness values (nm) have been fabricated:

- (1) 8/0, 8/30, 8/50, 8/100;
- (2) 12/0, 12/30, 12/50, 12/100;
- (3) 15/50, 25/50, 35/50, 50/50;
- (4) 10/40, 15/35, 20/30, 30/20.

Dependencies of resistance versus temperature $R(T)$ have been measured in ³He/⁴He dilution refrigerator using four-probe method. The transition edge temperature of samples with Mo thickness 12 – 15 nm turned out to be the most sensitive to Cu thickness. Such samples have shown the transition edge temperature in the range $\approx 0.075 - 0.4$ K, which is required for bolometer operation. Samples with thinner Mo layer haven't demonstrated the superconducting transition at all. $R(T)$ dependencies for Mo/Cu thickness values 15/35 and 12/100 (nm/nm) are shown on Fig.1 together with $R(T)$ dependence for pure Mo film of 12 nm thickness.

The effect of proximity is clearly seen from the Fig.1. The transition edge temperature decreases with thickening of the Cu layer, simultaneously the resistance of bi-layer structure getting smaller. The pure Mo film has shown transition temperature of ≈ 0.93 K, which is expected value for Mo.

The parameter $\alpha = T / R \cdot dR / dT$, which characterizes the abruptness of superconducting transition, has been estimated in the vicinity of the superconducting transition edge temperature (T_c) for three measured samples. It was found to be $\alpha \approx 1070$ for $T_c \approx 0.93$ K, $\alpha \approx 150$ for $T_c \approx 0.4$ K and $\alpha \approx 510$ for $T_c \approx 0.08$ K. This parameter determines the speed response: the larger α the smaller response time of bolometer [3]. The value of α found in our measurements for $T_c \approx 0.08$ K and 0.4 K is about two times smaller in comparison with this value reported in [3] for similar bi-layer structure. Probably it can be explained by nonuniformity of our sputtered thin films.

Obtained results will provide the basis for subsequent developments of bolometer microcircuits with transition edge sensor of micrometer and sub-micrometer size.

It is pleasure to acknowledge V.V. Dmitriev and V.V. Zavialov for participation in measurements. This work was supported by ISTC (project № 1239).

REFERENCES

1. I. A.N. Vystavkin, D.V. Chouvaev, T. Claeson, D.I. Golubev, V.D. Gromov, N.S. Kardashev, A.G. Kovalenko, V.G. Kurt, L.S. Kuzmin, M.A. Tarasov, A.G. Trubnikov, M. Willander, Submillimeter Cryogenic Telescope with Andreev Type Microbolometer for the International Space Station. Project Submillimeteron, 10-th Intern. Symp. on Space Terahertz Technology, 16-18 March, 1999, Charlottesville, USA.
2. A.N. Vystavkin. Highly sensitive hot electron microbolometer with Andreev reflection for sub-millimeter radio astronomy, Radiotekhnika i Elektronika (in Russian), 2001, т.46, № 7, cc. 806-815.
3. K.D. Irwin, G.C. Hilton, D.A. Wollman, John M. Martinis, X-ray Detection using a Superconducting Transition-Edge Sensor Microcalorimeter with Electrothermal Feedback, Appl. Phys. Lett., 1996, 23 September, 69 (13), pp. 1945-1947.
4. N.R. Werthamer, Theory of the superconducting transition temperature and energy gap function of superposed metal films, Physical Review, 1963, v. 132, № 6, pp. 2440-2445.
5. B.S. Karasik, W.R. McGrath, H.G. LeDuc, M.E. Gershenson, A hot-electron direct detector for radio astronomy, Supercond. Sci. & Technol., 1999. v. 12, p.745.

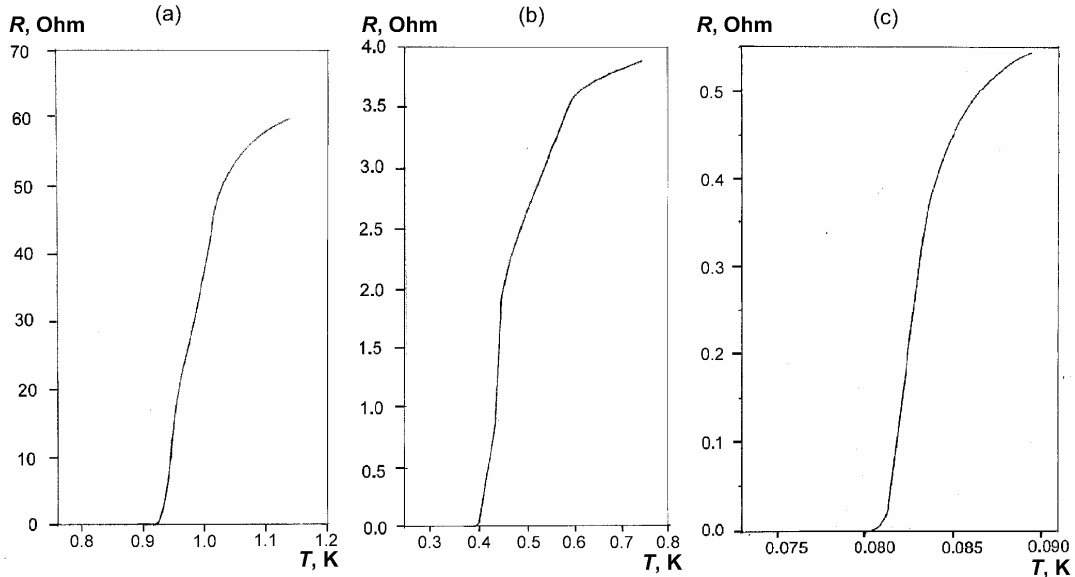


Fig.1 Dependencies $R(T)$ for three Mo/Cu samples of $24 \times 1.5 \text{ mm}^2$ size with the following Mo and Cu thickness values (nm/nm): (a) 12/0, (b) 15/35 and (c) 12/100.

Full-Waveguide Band Orthomode Transducer for the 3 mm and 1 mm Bands

Gopal Narayanan¹, and Neal Erickson

Department of Astronomy, University of Massachusetts, Amherst, MA 01003

Abstract

The design of a novel, full-waveguide band orthomode transducer (OMT) for the 3 mm (75 - 110 GHz) waveguide band was previously reported [1]. Here, the fabrication details and test results from OMTs made for the 3 mm band are presented. New optimized designs for the 1 mm band are also shown.

1 Introduction

An orthomode transducer (OMT) is a device that separates orthogonal polarizations within the same frequency band. The traditional way of separating orthogonal polarizations, the wire-grid diplexer, is large and bulky. A broadband waveguide-based OMT would be a preferable alternative as it would be much smaller, can be cryogenically cooled, and it would be a good match to available high-performance dual-polarized broadband corrugated feedhorns. The design of a novel waveguide-based OMT was previously presented [1]. In this paper, the measured results of a 3 mm prototype are shown, and new optimized designs for the 1 mm band are presented.

2 Fabrication and Testing of 3 mm Band OMT

With improved fabrication techniques [2], high-quality waveguide blocks can be directly machined to 1 THz and beyond. One of the principal requirements in our design is the scalability of the design to terahertz frequencies. To verify the design, a 3 mm prototype was built using split-block techniques. Figure 1 shows the split-block view of the WR-10 OMT, and a close-up view of the septum. Design details and dimensions are summarized in [1]. The split-block was fabricated in Aluminum using NC machining on a conventional Haas milling machine. The only major challenge is the long (~ 9.5 mm) oval waveguide for the vertical (main arm) polarization. This latter feature was milled from both sides of the block to meet in the middle. The septum is 0.254 mm (0.010 inches) thick, and was fabricated using the micro-milling technique described in [2] from a 0.010 inch thick Aluminum shimstock. The septum is placed in a 0.127 mm deep pocket on the split-plane, and the two split blocks are tightened together using fasteners. Recessed 0.127 mm deep pockets on either split block outside the waveguide features (see Figure 1a) allows enough pressure to be applied to ensure adequate grounding of the septum to the block.

¹e-mail: gopal@astro.umass.edu

The assembly is very simple, and the measurements are quite repeatable when the OMT is disassembled and then reassembled.

Figure 1b shows the results for the fabricated 75–110 GHz band OMT. Measurements were performed using a scalar network analyzer setup. While the OMT was designed originally using a square waveguide at the input, at the time of fabrication, a circular-square transition was built in to the input of the OMT (see Figure 1a). The measurement setup employed a WR-10 rectangular to circular transition at the input. Two back-to-back rectangular to circular transitions were first measured to calibrate the insertion loss (~ 0.1 dB across the band) of the single transition. The losses in the measurement setup have thus been removed in the insertion loss plot shown in Figure 1b. The insertion loss is ~ 0.2 to 0.3 dB across the band.

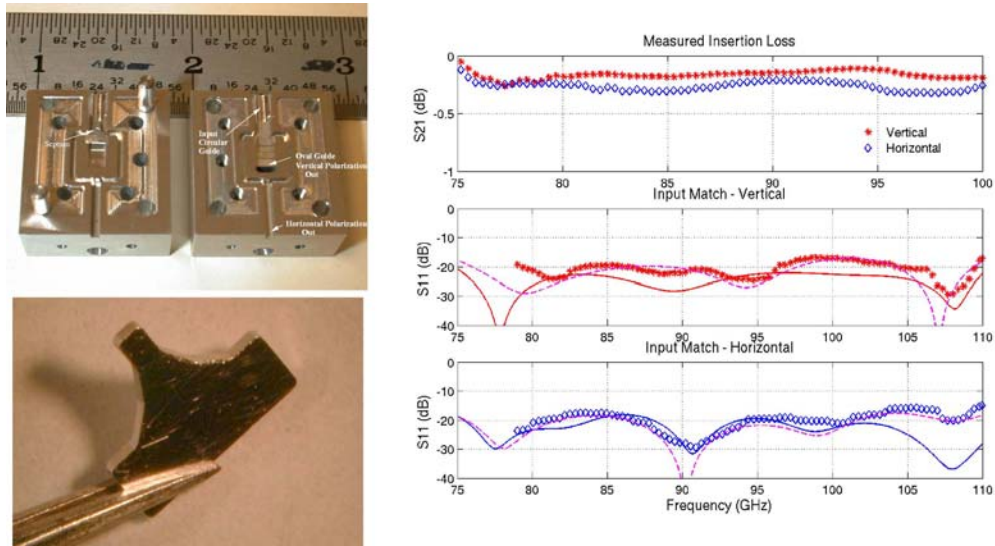


Figure 1: (a) Top. Split-block view of the 3 mm band OMT. Bottom. Zoomed-in photograph of the septum used in the OMT. (b) Scalar network analyzer measurements of the 3 mm OMT. Top panel. Insertion Loss in dB for each polarization. Bottom two panels. The measured input match for both polarizations is shown along with two simulated curves. The measurements points are shown as stars. The solid curves show the simulation for the designed OMT with an input square waveguide. The dashed curves show the effect of simulating the full OMT with the circular-to-rectangular transition that was added in the prototype model to facilitate the measurements.

The bottom two panels of Figure 1b show the measured input match for both polarizations, measured at the input circular waveguide angle. The match looked somewhat worse than that predicted by the original design (shown in solid lines in the bottom two panels). However, in the original design we did not simulate the circular-to-square transition. If

we simulate the circular-to-square transition that was added at the input to the fabricated prototype, the agreement is much better. This circular-to-square transition is necessary to test the OMT, and was added at the fabrication stage without fully accounting for its effect on the OMT. Measured S11 points below 79 GHz have been removed from the plot in Figure 1b, as the source used in the scalar measurements did not have enough power to provide adequate dynamic range for the measurements. This same dynamic range problem in the measurement setup is present at other frequencies as well, which probably explains why the measurements are not able to reproduce the deep dips seen in the simulations. Even with a poorly matched circular to square transition, the prototype OMT has good input match (< 17 dB across the band). An optimized transition will yield better performance. The good match with the simulations indicate that there were no major errors in the fabrication.

Compared to the Bifot OMT design outlined by Wollack et al. in [3], the OMT reported in this work offers the following advantages: (1) The Wollack NRAO OMT design had very tight mechanical tolerances and difficult assembly, and is not suitable for scaling much above ~ 150 GHz. The new OMT design presented here can be scaled up to 1 THz without posing significant fabrication difficulties. (2) The waveguide pins (0.127 mm for W-band) that was used in the Wollack design has been replaced with simple capacitive steps in waveguide walls, considerably easing assembly and fabrication issues. (3) The new design also has a septum that is over four times thicker than that used in the Wollack design, which is easier to fabricate, provides better stiffness, alleviates mode conversion problems and provides better grounding to the block.

3 1 mm Band OMT Design

The most challenging part of the fabrication of the OMT is the long oval guide (9.5 mm) required for the vertical polarization to exit the block. This length is required to accommodate a normal UG-387 19 mm diameter cone on all three ports of the OMT. For the 3 mm band OMT, the tooling required for this guide is not specialized, but for the corresponding 1 mm band OMT, special tooling is required to mill the oval guide. One way around the problem is to split the block another time at the location of the output oval guide. The two side arm waveguides will then need to be bent by a H-plane bend and then recombined together. Figure 2a (bottom) shows such a “symmetric” configuration, with the two output rectangular output ports located on either side symmetrically from the input square waveguide. This latter structure has two split-planes, one on the YZ-plane as in Figure 2a (top), and one parallel to the XZ-plane and shown with a dark line in Figure 2b (bottom). On this latter split-plane, there is an E-plane bend and a H-plane bend, both of which can be optimized quite well, since we can utilize the entire waveguide height and width respectively for the bends.

Both types of OMT shown in Figure 2a were designed and optimized using CST Microwave Studio (CST MWS)[4], a time-domain finite-element analysis software suite. The predicted input match for both types of OMTs for either polarization are shown in Figure 2b. In a real receiver system, the input to the OMT will be a corrugated feed-

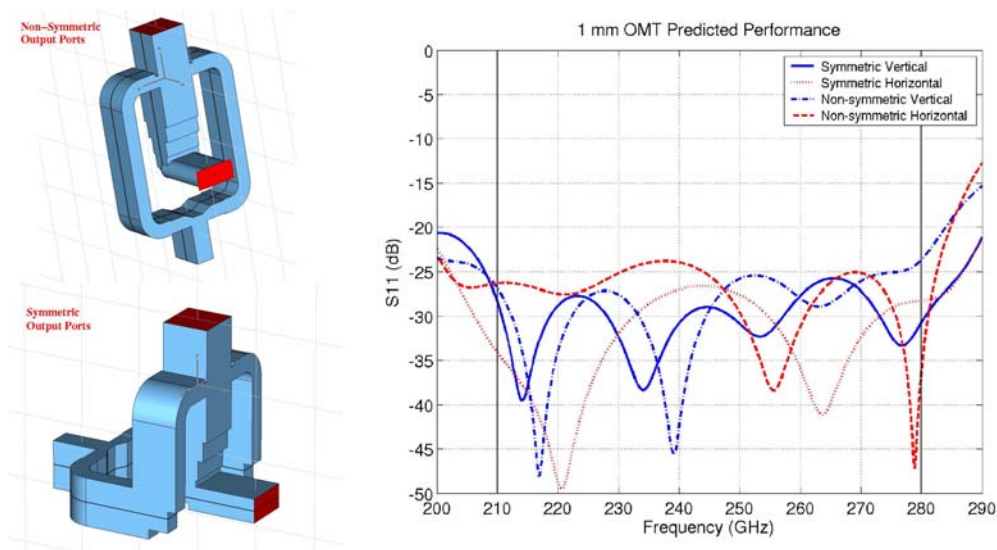


Figure 2: (a) *Left*: Two different designs for the 1 mm band OMT. The top figure shows essentially a scaled version of the 3 mm design with the two output ports orthogonal to each other (dubbed the “Non-Symmetric” type). The split-block plane is shown as a dark line and coincides with the YZ plane. The bottom figure shows the two side-arm guides bend through a H-plane bend and recombined to yield the two rectangular waveguide output ports located symmetrically with respect to the input square waveguide port. In addition to the YZ split-plane, another split plane is used (a plane parallel to the XZ plane, and shown as a dark line). The “symmetric” configuration does not need the oval waveguide. For the vertical (main-arm) polarization, the split-plane occurs where the current flow is at a maximum, so care is required in fabrication and assembly. (b) *Right*: Simulated input return loss for the “symmetric” and “non-symmetric” configurations of the 1 mm band OMTs shown to the left.

horn, so a waveguide angle will not be required at the input. This can ease the task of putting angle patterns on the other two ports, as also the required real-estate on the blocks for fasteners and alignment pins. The two split-plane “symmetric” configuration shows slightly better performance than the single split-plane “non-symmetric” configuration. But the “symmetric” configuration is more complex to fabricate and assemble.

4 Conclusions

A novel full-waveguide band orthomode transducer has been designed, fabricated and tested. The W-band prototype has > 17 dB return loss and < 0.3 dB insertion loss over the full design band of 75 – 110 GHz ($\sim 40\%$ bandwidth). This new OMT is simple to fabricate and assemble and is scalable to frequencies of ~ 1 THz. New optimized designs for the 1 mm band were also presented.

5 References

- [1] G. Narayanan, and N. R. Erickson, 2002, "A Novel Full Waveguide Band Orthomode Transducer", Proc. of the 13th International Space Terahertz Symposium, held at Harvard University.
- [2] G. Narayanan, N. R. Erickson, and R. M. Grosslein, "Low Cost Direct Machining of Terahertz waveguide Structures," Tenth International Symposium on Space Terahertz Technology, pp. 518-528, Mar. 99.
- [3] E. J. Wollack, W. Grammer, and J. Kingsley, "The Bifot Orthomode Junction", ALMA Memo Series 425.
- [4] Computer Simulation Technology (CST) Microwave Studio (MWS) v3.4, CST of America, Inc., Wellesley MA.

Precision measurements of the properties of thin-film superconducting microstrip lines at 100-500 GHz

Anastasios Vayonakis¹, Alexey Goldin², Henry Leduc², Chiyan Luo³, Jonas Zmuidzinas¹

¹California Institute of Technology, Pasadena, CA

²Jet Propulsion Laboratory, Pasadena, CA

³Massachusetts Institute of Technology, Cambridge, MA

ABSTRACT

We have developed a novel technique for making high quality measurements of the millimeter-wave properties of superconducting thin-film microstrip transmission lines. Our experimental technique currently covers the 75–120, 220–320, and 450–550 GHz frequency bands. The method is based on standing wave resonances in an open ended transmission line. We measure the characteristic impedance, phase velocity, and loss of the microstrip. Our data for Nb/SiO/Nb lines, taken at 4.2 K and 1.5 K, can be explained by a single set of physical parameters, with a temperature-independent loss tangent of $\tan \delta_{SiO} = 1.3 \pm 0.3 \times 10^{-3}$ for our lowest loss samples. The corresponding amplitude $1/e$ attenuation length is about 30 cm at 100 GHz. In the region 100–500 GHz, we do not observe any significant frequency variation of the loss per wavelength.

INTRODUCTION

Superconducting thin-film microstrip transmission lines are of major importance in superconducting electronics, but their high-frequency properties, especially their losses, are not well measured. Such thin-film microstrip lines are currently used for tuning circuits in SIS mixers, pulse propagation in RSFQ superconducting digital electronics, and are of also of great interest for use in new architectures for millimeter and submillimeter direct-detection focal plane arrays. The transmission losses of the superconducting microstrip lines are a key issue for the feasibility of such architectures. While, the properties of superconducting microstrip lines have been investigated previously, the method that we present here provides much higher quality data, and provides a complete characterization of all relevant electrical parameters.

EXPERIMENTAL METHOD

Our method is based on standing-wave resonances in an open ended microstrip stub. The entire circuit is fabricated on a thick silicon substrate (400 μ m), and the millimeter-wave radiation is coupled onto the chip quasi-optically using a silicon substrate lens. There are two Nb/Al-oxide/Nb SIS junctions on the chip which serve as direct detectors. One of the junctions is connected to an open-ended Nb/SiO/Nb microstrip stub (Figure 1). Having two SIS junctions on the chip allows us to calibrate out changes in the power that

is coupled onto the chip from the external signal source. The ratio of the signal from the junction connected to the stub, to the signal from the other junction, gives us a precise relative power response, whose frequency dependence carries information about the properties of the microstrip stub.

The Agilent 83751B microwave signal generator, paired with the Agilent 83558A millimeter-wave source module, allows us to easily generate millimeter-waves in the 75–123 GHz range (Figure 2a). We generate mm-wave signals in the 220–320 and 450–550 GHz bands by coupling the Agilent mm-wave module with a Virginia Diodes tripler and quintupler respectively. We generate the readout signals by AM modulating the microwave source at 100 kHz, and using lock-in detection of the SIS currents.

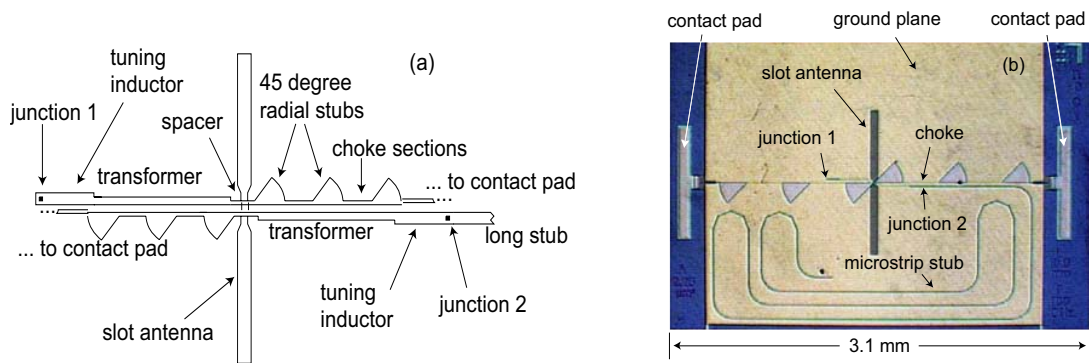


Figure 1: (a) Schematic diagram of test device. (b) Photograph of a 100 GHz test device with a 10 mm long microstrip stub. The Nb top strip is 5 μm wide, and 4000 \AA thick. The thickness of the Nb ground plane layer is 2000 \AA . The thickness of the SiO dielectric is 4000 \AA .

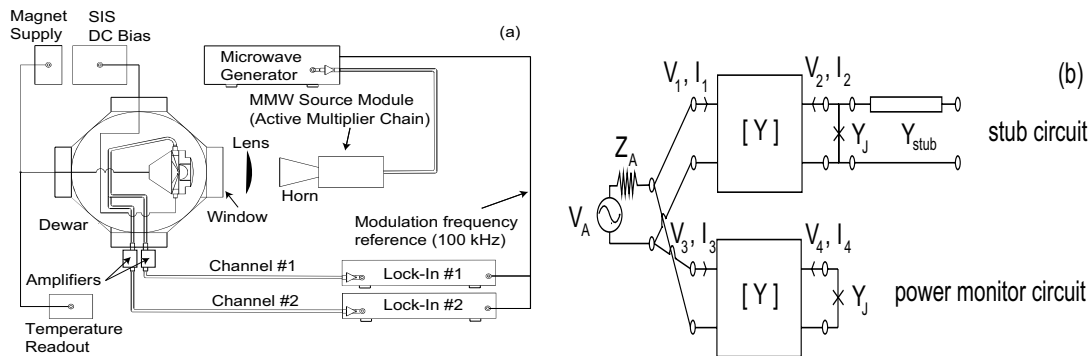


Figure 2: (a) Schematic diagram of experimental setup. (b) Equivalent circuit model of the device. The two junctions are connected in parallel to the slot antenna through two identical matching circuits, which we treat as two-port black box linear circuits, characterized by an unknown admittance matrix Y .

The relative power response is given by the detected power ratio of the two junctions, which can be shown to be (Figure 2b):

$$P_{\text{dB}}(\nu; \bar{c}, \text{PPL}/\lambda, w, L) = 10 \log_{10} \left| \frac{V_2}{V_4} \right|^2 = -20 \log_{10} \left| 1 + w \frac{1 - \exp \left[\frac{\nu L}{\bar{c}} \left(\ln \left(1 - \frac{\text{PPL}/\lambda}{100} \right) - j4\pi \right) \right]}{1 + \exp \left[\frac{\nu L}{\bar{c}} \left(\ln \left(1 - \frac{\text{PPL}/\lambda}{100} \right) - j4\pi \right) \right]} \right|,$$

where the complex parameter w is defined from:

$$Y_J = \frac{1}{Z_0} \frac{1}{w} - Y_{22}.$$

We assume that the phase velocity, the percent power loss per wavelength (PPL/ λ), and the parameter w remain essentially constant over a narrow frequency range of a single resonance, and obtain their values using a least-squares fit to the data. Since $1/w$ scales as the admittance of the junction Y_J (which can be calculated from the dc I-V curve), the scaling factor yields the characteristic impedance of the microstrip.

RESULTS

We have taken data in the 75–120, 220–320, and 450–550 GHz bands, at 4.2 K and 1.5 K, for a wide range of junction bias voltages both below and above the gap voltage. Figure 3 shows the measured loss at the two temperatures (for various frequency bins). Although the junction impedance varies greatly from 2.0 mV to 4.0 mV, the extracted values of the loss are essentially independent of bias voltage. The difference of about 1.5% power loss per wavelength between the two temperatures is accounted for by the theoretical (Mattis-Bardeen) loss difference in the superconductor. The remaining loss is attributed to the dielectric, with a temperature-independent loss tangent $\tan \delta_{\text{SiO}} = 1.3 \pm 0.3 \times 10^{-3}$. We do not observe any significant frequency variation of the loss per wavelength, which can be attributed to a constant loss tangent in the range 100–500 GHz. The scaling factor of $1/w$ yields the characteristic impedance of the microstrip, which we measure to be $Z_0 = 11.0 \pm 0.6 \ \Omega$.

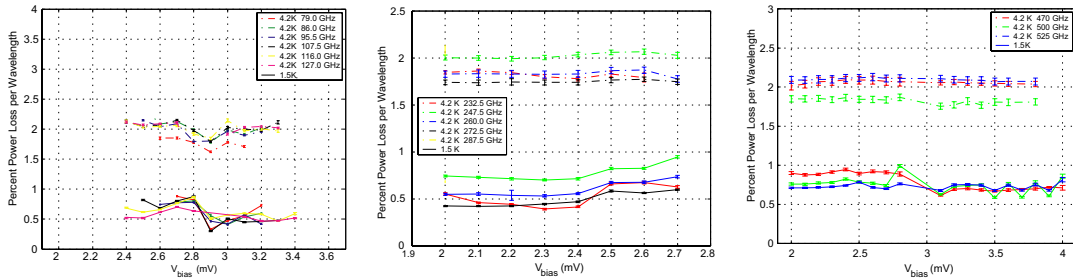


Figure 3: Percent power loss per wavelength at 4.2 K and 1.5 K, for the three frequency ranges measured: (a) 75–120 GHz, (b) 220–320 GHz, (c) 450–550 GHz.

Acknowledgments: This work was supported in part by NASA grant: NAG5-8589 to Yale University, subcontract Y-99-0019 to Caltech, and NASA grants NAG5-10358 and NAG5-10317 to Caltech. We are grateful for the generous support of Alex Lidow, Caltech Trustee.

Propagation in Lossy and Superconducting Cylindrical Waveguides

G. Yassin, C.Y. Tham, and S. Withington
Cavendish Laboratory, University of Cambridge
Madingley Road, Cambridge, CB3 0HE, UK

Abstract – We present rigorous analysis of guided propagation in cylindrical waveguides with finite conductivity and superconducting walls. Our calculations are based on a method by Stratton which solves Maxwell’s equations in cylindrical coordinates. The transcendental equation gives the complex propagation constant as a function of frequency, geometry and conductivity. The complex conductivity of the superconducting waveguide is obtained from BCS theory. We computed the attenuation and cutoff frequencies in different materials at microwaves and submillimetre-wave frequencies and compared with those obtained from the commonly used approximate computations.

1 Introduction

While the electromagnetic behaviour of planar superconducting transmission lines have been thoroughly investigated [1] – [4], little has been reported on superconducting waveguides. Waveguides are fundamentally different from the microstrip. A microstrip can support a single TEM with complex propagation constant that remains constant below the superconducting gap. A cylindrical waveguide however supports multimode operation and the complex conductivity influences propagation via surface impedance dependency and also by modifying the modes cutoff. Consequently we expect superconductivity to influence attenuation significantly, not only near the gap but also near cutoff.

The commonly used method for calculating the complex propagation constant in a waveguide is to first obtain the fields by assuming infinite conductivity. This allows separating the solution into TE and TM modes. The cutoff frequencies and phase velocity are obtained by solving a simple characteristic equation. To calculate attenuation, the fields are assumed to penetrate the conductor surface and energy dissipated rapidly within a thin layer. This analysis is only valid if the decay of the field within the surface is much faster than its variation in the tangential plane, an assumption that applies for good conductors.

In a waveguide of finite conductivity, pure TE or TM modes cannot be excited separately. A valid solution of the wave equation must be expanded in terms of both TE and TM mode functions. Equating the tangential components of the fields at the boundary within and outside the conductor surface yields characteristic equations far more complicated than those for the perfect conductor.

2 Propagation in lossy cylindrical waveguides

Approximate solution: The electric and magnetic fields propagating in the z -direction in a waveguide with uniform cross section are expressed as -

$$\mathbf{E} = \mathbf{E}_0 e^{-(\alpha + j\beta)z} \quad \text{and} \quad \mathbf{H} = \mathbf{H}_0 e^{-(\alpha + j\beta)z}, \quad (1)$$

where α and β are respectively the attenuation and phase constants. By considering the average power per unit area along the waveguide and using the Poynting theorem, the attenuation constants for the TM and TE modes respectively are given by the approximate expressions [5] -

$$\alpha = \operatorname{Re} \left[\frac{Z_S}{a\eta\sqrt{1-(f_c/f)^2}} \right], \operatorname{Re} \left\{ \frac{Z_S}{a\eta\sqrt{1-(f_c/f)^2}} \left[(f_c/f)^2 + \frac{(n/p'_{nl})^2}{1-(n/p'_{nl})^2} \right] \right\}, \quad (2)$$

where a is the radius, Z_S the surface impedance, η the intrinsic impedance, f the frequency, f_c the cutoff frequency, and p'_{nl} is the l -th root of the first derivative of the Bessel function J'_n .

Exact solution: The field in the cylindrical waveguide may be written as a combination of elementary waves having the general functional form -

$$\psi = e^{jn\phi} F_n(k_c r) e^{\pm j\gamma z - j\omega t}, \quad (3)$$

where F_n is a cylindrical function, $\gamma = \alpha + j\beta$ is the propagation constant, $k_c^2 = k^2 - \gamma^2$, $k = \sqrt{\mu\varepsilon\omega^2 - j\mu\omega\sigma}$, and σ is the complex conductivity of the lossy waveguide wall. For superconducting waveguide the complex conductivity is obtained from BCS theory [7]. Within the waveguide ($0 \leq r \leq a$), F_n takes the form of a Bessel function J_n and outside the guide (dielectric or lossy conductor), the Hankel function of the first kind $H_n^{(1)}$ is used to satisfy the radiation condition at $r \rightarrow \infty$. The boundary condition that the tangential fields are continuous across the waveguide wall yields four linear-homogeneous equations in four unknown coefficients. A non-trivial solution is only obtained if the determinant of the equations vanishes. This yields the transcendental equation [7] -

$$\left[\frac{\mu_1 J'_n(u)}{u J_n(u)} - \frac{\mu_2 H_n^{(1)'}(v)}{v H_n^{(1)}(v)} \right] \left[\frac{k_1^2 J'_n(u)}{\mu_1 u J_n(u)} - \frac{k_2^2 H_n^{(1)'}(v)}{\mu_2 v H_n^{(1)}(v)} \right] = n^2 \gamma^2 \left(\frac{1}{v^2} - \frac{1}{u^2} \right)^2. \quad (4)$$

In the above $u = k_c^1 a$, $v = k_c^2 a$ and the superscripts 1, 2 refers to the regions inside and outside the waveguide respectively. The above equation can be solved numerically for the propagation constant γ for TE modes. For TM modes an alternate form of the equation is required -

$$\left[\frac{J_n(u)}{J'_n(u)} \right]^2 \left[\frac{H_n^{(1)'}(v)}{H_n^{(1)}(v)} \right]^2 \frac{k_2^2}{v^2} + \frac{k_1^2}{u^2} - \frac{1}{uv} \frac{J_n(u)}{J'_n(u)} \frac{H_n^{(1)'}(v)}{H_n^{(1)}(v)} \left(\frac{\mu_1 k_2^2}{\mu_2} + \frac{\mu_2 k_1^2}{\mu_1} \right) = \left[\frac{J_n(u)}{J'_n(u)} \right]^2 n^2 \gamma^2 \left(\frac{1}{v^2} - \frac{1}{u^2} \right)^2 \quad (5)$$

3 Results & Conclusion

The results are depicted in Fig. 1 – 6. Our analysis reveals that in practical applications, the modes in a superconducting waveguides could be approximated to those in a perfect conductor, which is consistent with recently reported experimental results. We also found that for good conductors, the attenuation computed by the surface impedance method is very close to the rigorous solution. However the results from the two methods differ significantly in two regions. They deviate near cutoff and at extremely high frequencies. At $\omega = \omega_c$ the attenuation given by the approximate method becomes singular. In the

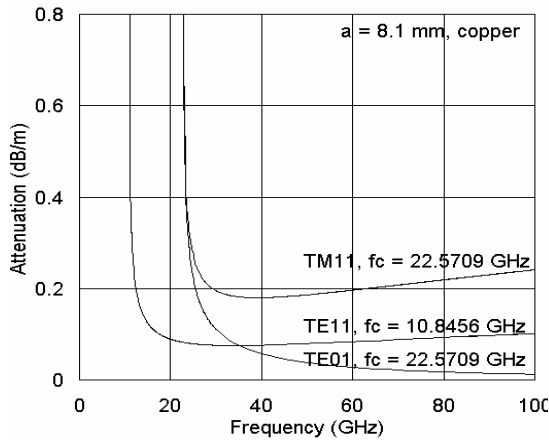


Fig. 1 Attenuation for TE₁₁, TE₀₁ and TM₁₁ modes in a copper waveguide of radius 8.1 mm at low frequencies. Results by both the exact and the approximate surface impedance methods are in very good agreement.

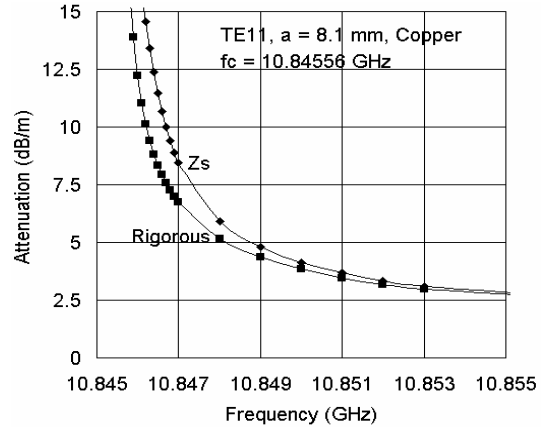


Fig. 2 Attenuation for TE₁₁ mode in a copper waveguide of 8.1 mm as in Fig. 1 showing discrepancy between the results of the rigorous and the surface impedance methods near the cutoff frequency.

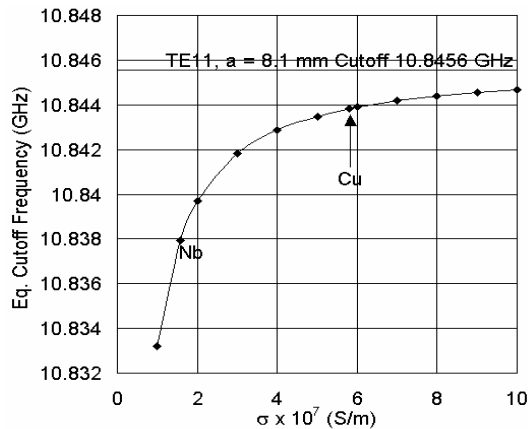


Fig. 3 Cutoff frequency as a function of conductivity. Notice that the cutoff calculated by the approximate method does not vary with conductivity.

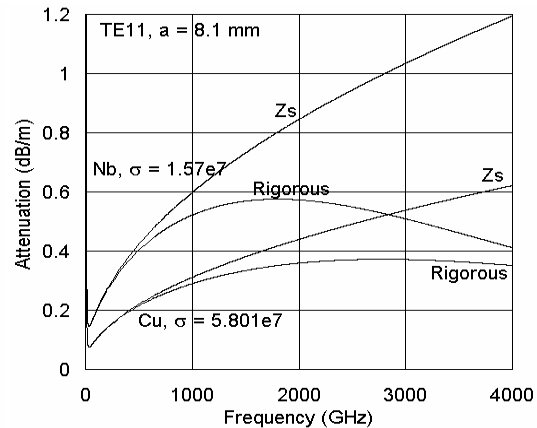


Fig. 4 Attenuation for TE₁₁ mode in a copper waveguide of 8.1 mm as that in Fig. 1 at extremely high frequencies.

exact solution such singularity does not exist and the attenuation diverges sharply but continuously. The differences turn out to be significant even for good conductors. This difference in the attenuation results is large enough to be easily measurable. Next, at very high frequencies, with the approximate method we can still assume that only the TE₁₁ mode is excited and hence the attenuation as a function of frequency diverges to infinity. The exact solution however gives a finite loss, which is clearly a more realistic behaviour. We attribute these differences to the fact that in those cases the field can no longer be approximated to those of a perfect conductor. In particular the solutions are no longer separable as either TE or TM modes.

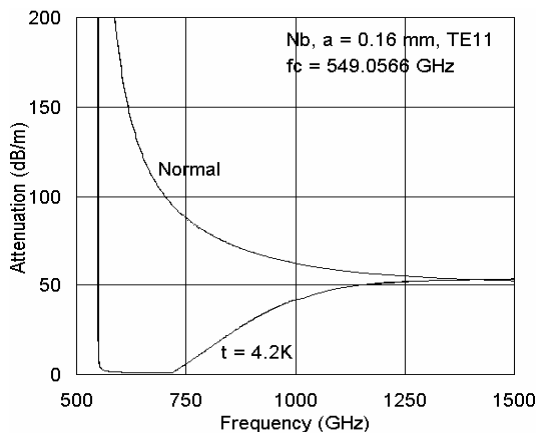


Fig. 5 Attenuation for TE11 mode in a Nb waveguide of 0.16 mm. Both the rigorous and surface impedance methods agree well for both normal and non-superconducting states.

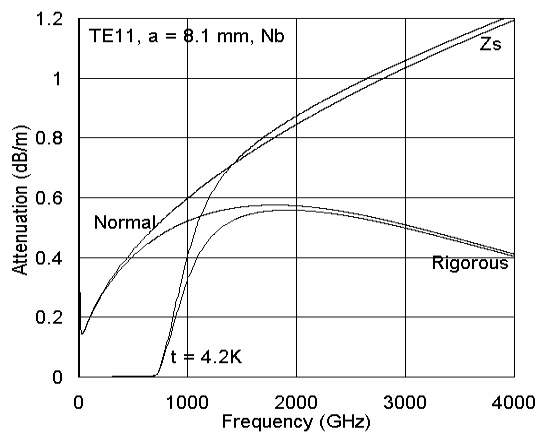


Fig. 6 Attenuation for TE11 mode in a Nb waveguide of 8.1 mm. Both normal and superconducting behaviours are shown. At low frequencies both the rigorous and surface impedance methods agree well. There are deviations between the two methods at high frequencies above the gap.

References

- [1] G. Yassin and S. Withington, "Electromagnetic models for superconducting millimetre-wave and sub-millimetre-wave microstrip transmission lines", *J. Phys. D: Appl. Phys.*, **28**, 1995, pp. 1983 – 1991.
- [2] G. Yassin, G. Jung, V. Dikovskiy, I. Barbov, M. Kambara, D. A. Cardwell, and S. Withington, "Investigation of microwave propagation in high-temperature superconducting waveguides", *IEEE Microwave Guided Wave Lett.*, Vol. 11, 2001, pp. 413 - 415.
- [3] P. L. Kautz, "Picosecond pulses on superconducting striplines", *J. Appl. Phys.*, **49**(1), Jan. 1978, pp. 308 – 314.
- [4] Simon Ramo, John R. Whinnery, and Theodore Van Duzer, *Fields and waves in communication electronics*, 3rd edn., John Wiley & Sons, Inc., 1994.
- [5] D. C. Mattis and J. Bardeen, "Theory of the anomalous skin effect in normal and superconducting metals", *Physical Review*, Vol. 111, No. 2, July 1958, pp. 412 – 417.
- [6] Julius Adams Stratton, *Electromagnetic Theory*, McGraw-Hill Book Co., Inc., 1941.

Autocorrelation Spectrometers for (sub)millimetre Spectroscopy

A. Emrich, S. Andersson, J. Embretsén, J. Dahlberg, L. Landen, C. Tegnander
OmniSys Instruments AB, Gruvgatan 8, 421 30 Göteborg, Sweden

ABSTRACT

The autocorrelation spectrometer is one of four types of spectrometers being considered for space based (sub)millimetre heterodyne systems. The advantages of the digital autocorrelation spectrometer compared to Chirp Transform, Acousto Optical and Filterbank spectrometers are; stability, compactness, high reliability and variability in bandwidth and resolution.

The detailed design of three autocorrelation spectrometers will be described, from the ODIN spectrometer currently in operation in space, the TELIS spectrometer delivered to DLR, and for an experiment under development for Venus Express.

ODIN SPECTROMETER

The ODIN satellite is a joint aeronomy and astronomy mission. The main payload consists of four tunable heterodyne schottky receivers in the frequency range 480-570 GHz and one fixed tuned 119 GHz heterodyne system. In addition, there is an UV-spectrometer.

There are four back-end spectrometers connected to the five heterodyne systems, two autocorrelation spectrometers, one AOS and one filterbank. The autocorrelation spectrometer and AOS power consumption are the same, while the size and mass of the AOS is 7 times the correlation spectrometer. The filterbank only consumes 2 W.

The ODIN satellite has been in successful operation for more than 2 years, the design lifetime, and a decision has been made to operate for an additional 2 years.

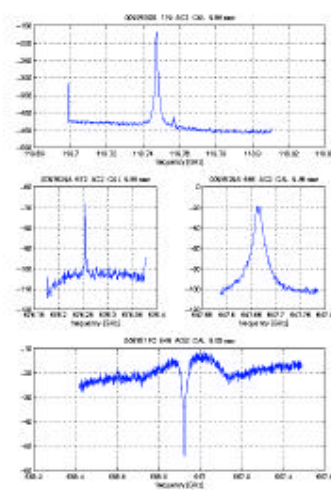
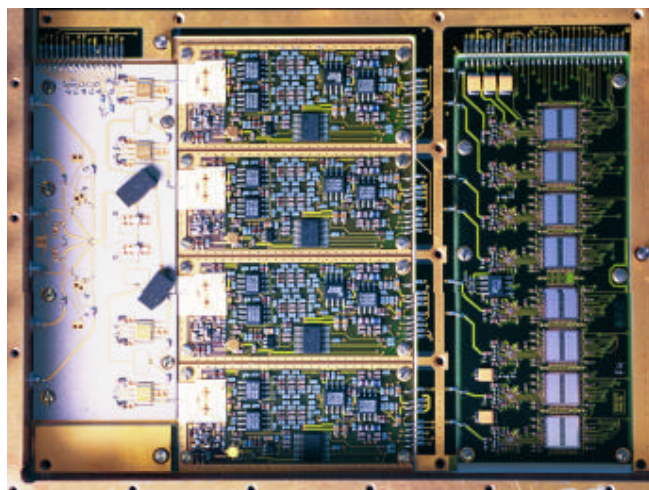


Figure 1. The ODIN spectrometer core. The complete spectrometer has 100-800 MHz bandwidth in steps with 0.13-1.1 MHz resolution. Other specifications are: 1 kg, 220x180x30 mm and 18 W power consumption. The spectra is "first light" from the satellite.

DLR/TELIS SPECTROMETERS

Based on a chip-set developed during 1998-1999, motivated by MASTER and FIRST, 600 MHz coverage and 256 channels resolution is possible with only two chips, one quantiser and one correlator chip.

A “standard” spectrometer with 2x2 GHz bandwidth, and 2 x 1024 channels has been designed, and two of those has been ordered for the DLR TELIS project. These will be shared between three front-ends, through an IF processor, also produced by Omnisys.



Figure 2. The current generation of spectrometers, with top and bottom views, based on a 256 channel correlator chip and quantizer with 1200 MHz effective sample rate. The box incorporates 2048 channels and could be configured with 1 x 4 GHz bandwidth, 2 x 2 GHz etc. The mass is 900 grams, the size 170 x 110 x 30 mm, and the power consumption is 18 W.

VENUS EXPRESS

Currently a development for a radiometer for the Venus Express mission is under development. For Omnisys part it is based on preliminary design for a similar instrument, Mambo, planned for a Mars mission. The instrument will cover 546-576 GHz, and the autocorrelation spectrometers will be flexible, but covering up to 12 lines between 6-13 GHz, with resolutions from 100 kHz to 20 MHz. The mass will be 500-700 grams, and the power consumption variable, depending on mode, but between 6-12 W.



Figure 3. Test set-up of the Venus Express chip-set to the left. This chip set can process up to 2 GHz bandwidth, with 1024 channels. To save power, the number of channels used can be controlled, starting from 128. On the right side, the MCM is shown.

CONCLUSION

Now, as a result from the development described above, a general conclusion is that autocorrelation spectrometers are very competitive with other type of spectrometers for space based (sub)millimeter radiometry. The main advantages are: compact implementations, scalability and versatility in bandwidth and resolution, combined with potentially very high stability. In addition, it uses no special technologies and components, such as CCD's, Bragg Cell's or Chirp filters, with concerns regarding availability, radiation tolerance and other quality concerns.

The chip set developments has been supported by the Swedish National Space Board and by ESA.

Chip set for autocorrelation spectrometer applications

L. Landén^{*+}, J. Dahlberg^{*}, A. Emrich^{*}

^{*}Omnisys Instruments AB, Gruvgatan 8, 421 30 Göteborg, Sweden

⁺Chalmers University of Technology, MEL, 412 96 Göteborg, Sweden

INTRODUCTION

Three integrated circuits for autocorrelation spectrometer applications have been designed and manufactured. The first circuit is an IQ-converter that provides down conversion to baseband and quadrature. The second circuit is a digitizer that transforms analog information to digital information. The last circuit is a digital signal processing circuit that calculates the autocorrelation function for digital input data. The IQ-converter and the digitizer have been manufactured using a bipolar silicon process and the autocorrelator has been manufactured in a 0.25 μm CMOS process. This paper will first describe the autocorrelator system and then describe the three integrated circuits and a multi chip module that has been used. At last, future projects will be described.

AN AUTOCORRELATION SPECTROMETER SYSTEM

The autocorrelation function of a discrete sequence, $x(n)$, of length N is defined as:

$$R_{xx}(l) = \sum_{l=0}^{N-1} x(n)x(n-l), l, n \in Z$$

By applying the discrete Fourier transform to the autocorrelation function the power spectrum is obtained. The resolution of the spectrum is improved by increasing the length, l , of the function. The autocorrelation function can be realized using a digital integrated circuit.

The input to the spectrometer is some analog frequency band that is being observed. This band is down converted and split into subbands. The subbands are individually down converted to baseband with the IQ-converter. The baseband information is quantized by the digitizer and then fed to the autocorrelation circuit.

THE IQ-CONVERTER

The IQ-converter is used to convert the subbands to the baseband. It also provides quadrature meaning that two identical signals shifted in phase by 90° is produced. The quadrature is used to analyze the upper and lower sidebands at the same time.

The IQ-converter was manufactured using a 0.6 μm silicon bipolar process. The circuit consists of two doubly balanced mixers and buffer amplifiers to amplify the IF -signals at the output.

Experimental results showed that the IQ-converter could be used up to 10 GHz input frequency and up to 1 GHz output frequency. However, the performance of the IQ-converter was not satisfactory due to badly balanced output buffers. This means that commercial circuits are used in this version of the autocorrelation spectrometer system.

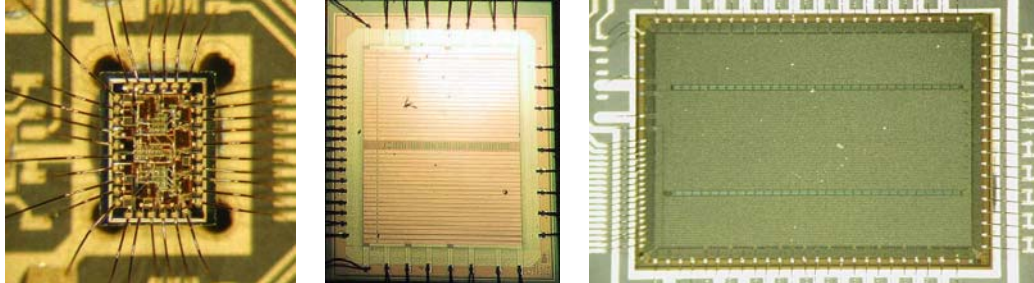


Figure 1. The digitizer (left), the low resolution chip (middle) and the high resolution chip (right)

THE DIGITIZER

The signals produced by the IQ-converter are analog and need to be converted to digital data in order to be manageable by the digital autocorrelator. For this, a digitizer is used. Time multiplexing may be used since the quantization is possible to achieve at higher frequencies than the following digital signal processing.

The digitizer was manufactured using the same 0.6 μm silicon bipolar process mentioned in the previous paragraph. A bipolar process was chosen due to the possibility to design high speed high precision comparators. This circuit was designed to be used in parallel with the correlator, meaning that I/O and functionality is matched. In order to reduce the influence of noise on the data and reference ports, a differential interface was chosen. The chip consumes 200 mW and its size is 1.175 \times 0.775 mm².

THE AUTOCORRELATOR

The serial output data from the digitizer is fed to the autocorrelator. This data is then split in two identical parts and fed to a multiplier that calculates the autocorrelation function for zero delay, $l=0$. One of the serial data paths is then delayed one clock cycle and multiplied with the initial data to produce the function for $l=1$. This procedure is then repeated until the desired resolution is obtained.

Two autocorrelation chips have been manufactured using a 0.25 μm CMOS process from STMicroelectronics, one low resolution correlator with 128 channels and one high resolution correlator with 1024 channels. The number of channels corresponds to the number of delay blocks described in the previous paragraph. The autocorrelation circuits can analyze a maximum bandwidth of 1.5 GHz. Synchronization blocks have been introduced each sixteen channels in order to synchronize the data and the clock. The low resolution correlator has a DC-power consumption of 300 mW and its size is 2.5 \times 3 mm². The high resolution correlator has a DC-power consumption of 1.5 W and its size is 7 \times 5 mm². A possibility to switch off channels to reduce the power consumption has been implemented on both versions. When the high resolution correlator works at its maximum frequency it performs 3 \times 10¹² operations per second.

THE MULTI CHIP MODULE

Digitizer and correlator were together with mixers bias circuits and digital control circuits implemented on a PCB. The naked chips were mounted and bonded to a ceramic carrier. In order to protect the chips and bond wires from the environment, a glob of epoxy was placed on this carrier. By placing the chips in module the test possibilities are improved since the module is possible to move between different PCBs.

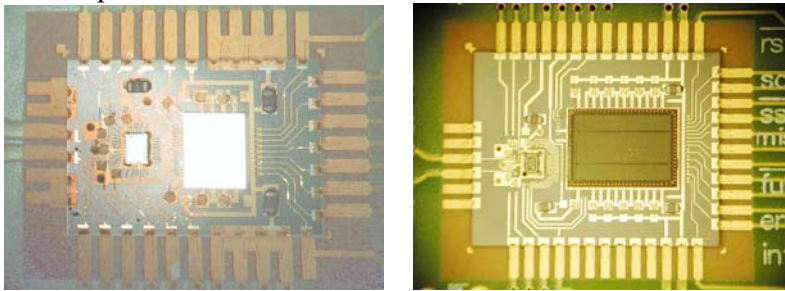


Figure 2. The multi chip modules for the low resolution correlator (left) and for the high resolution correlator (right)

FUTURE WORK

Some efforts have been made to implement bipolar and CMOS functions on the same chip using a SiGe BiCMOS process. Some improvements are expected when using this technology since the bipolar transistors have a higher frequency of operation.

CONCLUSIONS

The digitizer and correlator chips described in this paper show good performance and they will be used in future spectrometer applications. Quadrature, time multiplex and sampling methodology have improved the performance of the spectrometers. The multi chip module provides easy handling and testing of the circuits. The power consumption is exceptional and an order of magnitude better than comparable solutions. A future implementation on SiGe BiCMOS looks promising.

The chip set developments has been supported by ESA.

THIS - A Quantum-Cascade-Laser pumped Mid-Infrared Heterodyne Receiver

D. Wirtz¹, G. Sonnabend², V. Vetterle¹, M. Olbrich¹, R. Schieder¹

¹I. Physikalisches Institut, Universität zu Köln, D-50937 Köln, Germany
²NASA Goddard Space Flight Center, Greenbelt, MD, USA

A brief description of the current status of the Cologne Tuneable Heterodyne Infrared Spectrometer **THIS** is given. By using quantum-cascade lasers (QCL) [1,2] as local oscillator (LO) **THIS** opens the mid-infrared wavelength region from 5 to 28 μm for ultra-high-resolution spectroscopy with a system sensitivity equivalent to CO_2 -laser based heterodyne instruments [3-6] (noise temperatures about three times the quantum limit of 1440 K @ 10 microns, see fig. 2). The current bandwidth of 1.4 GHz is

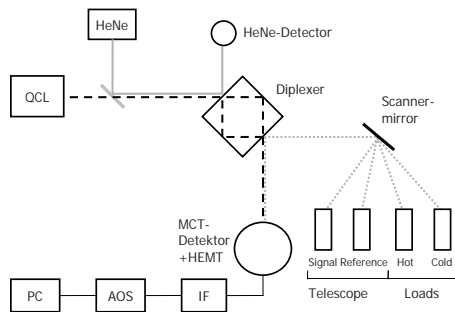


Figure 1: Setup scheme of the receiver: QC-laser and signal (switchable between telescope and two loads for calibration) are combined and focussed on the detector. After filtering and amplification the frequency-analysis is done using an AOS.

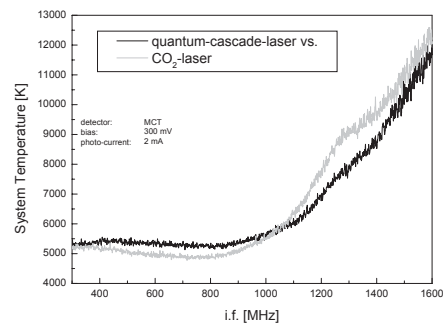


Figure 2: Comparison between QC- and CO_2 -laser: system performance is equal, above 1000 MHz i.f. the performance of the detector drops.

provided by an acousto-optical spectrometer (AOS). The frequency resolution is $R = 2 \cdot 10^7$. (This corresponds to a 14 km/sec bandwidth at a wavelength of 10 microns). **THIS** is the only widely tuneable infrared heterodyne receiver to date.

THIS consists of an optical receiver and common back-end electronics including the AOS. Inside the receiver the QCL is very efficiently superimposed with the telescope beam on a confocal travelling wave ring-resonator (the diplexer) and mixed on a fast Mercury-Cadmium-Telluride detector (MCT) [7,8]. The performance of **THIS** using a CO₂-laser LO in comparison with a QCL is practically identical as is shown in fig. 2. A scheme of the receiver is shown in fig. 1.

Various measurements at different ground based telescopes (e.g. the west auxiliary telescope of the McMath-Pierce Solar Observatory near Tucson, Az.) including the analysis of trace gases in the Earth's atmosphere, observations of molecular features in sunspots (see fig. 3), and detection of non-LTE CO₂ emission from the Venus atmosphere (see fig. 4) have been performed. These observations demonstrate the instrument's capabilities with regards to astronomical observations at both, ground based telescopes and the stratospheric observatory **SOFIA** in the near future.

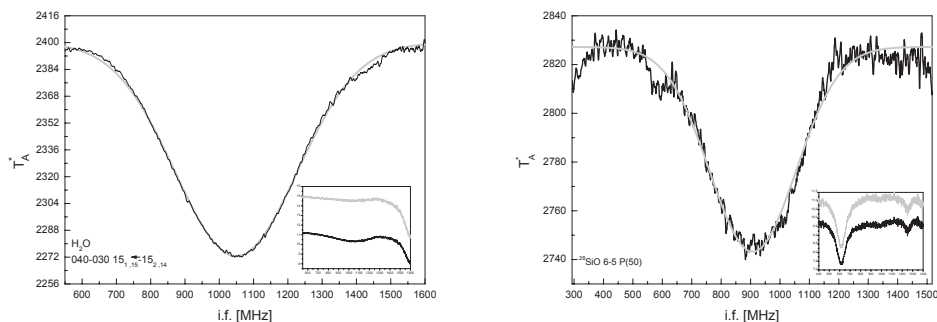


Figure 3: measurements (black) in a sunspot (11/21/2002) and Voigt-fits (light gray), left: 040–030 $15_{1,15}$ – $15_{2,14}$ transition of H₂O, right: ^{28}SiO 6-5 P(50) absorption at 1088.80925cm^{-1} , Insets: Spectra taken on (black) / off (gray) the sunspot. The SiO-spectrum still shows residuals from atmospheric ozone around 600 MHz i.f.

Besides incorporating new laser-technology it is also important to increase the presently available IF-bandwidth of MCT-mixer detectors. Therefore, in collaboration with the Fraunhofer IAF institute in Freiburg, Germany, first experiments with Quantum Well IR-Photodetectors (QWIPs) began [9,10]. Those devices might be able to reach MCT-mixers in terms of quantum-efficiency but will probably provide a significantly larger bandwidth (fig. 5 shows one of the first test measurements). As future backend a Wide-Band-Spectrometer (WBS) is currently under development at KOSMA based on the well known AOS-design. It will double the available bandwidth to 3 GHz. Further increase in bandwidth is achieved by stacking several spectrometers in an array-setup.

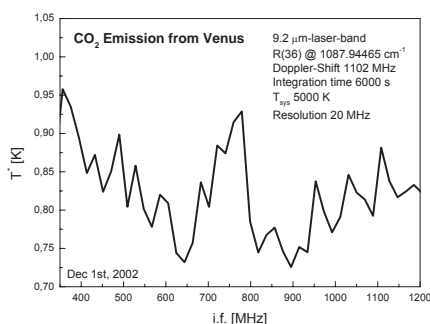


Figure 4: *Non-LTE R(36) transition of CO₂ from the illuminated arc of Venus. The emission is located in the middle of the broad CO₂-absorption peak. Data are binned to 20 MHz resolution.*

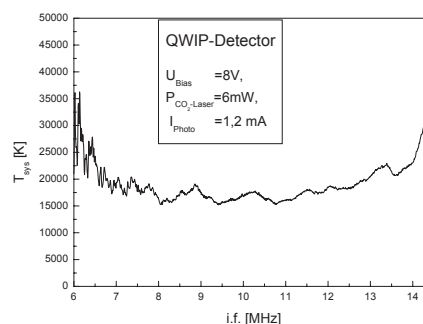


Figure 5: *First test of a QWIP-detector: the overall performance is still well below MCT-mixers but new developments promise good quantum-efficiencies and large bandwidths.*

The long-term goal is the operation of THIS on the stratospheric observatory SOFIA from roughly 2007 on. Here the detection of the two lowest lying pure rotational transitions of cold interstellar H₂ against moderately hot IR sources at wavelengths around 17 and 28 μm will be the prime target. Moreover since QC-lasers are being developed for the THz-regime as well, THIS might serve as a prototype for QCL-pumped THz-receivers in the future.

- [1] J. Faist, F. Capasso, D.L. Sivco, C. Sirtori, A.L. Hutchinson and A. Cho, "Quantum cascade laser" *Science* **264**, 553–555 (1994)
- [2] M. Beck, D. Hofstetter, T. Aellen, J. Faist, U. Oesterle, M. Ilegems, E. Gini, and H. Melchior "Continuous Wave Operation of a Mid-Infrared Semiconductor Laser at Room Temperature" *Science* **295**, 301–305 (2002)
- [3] T. Kostiuk and M. J. Mumma: "Remote sensing by IR heterodyne spectroscopy", *Applied Optics* (22), 2644–2654 (1983)
- [4] A.L. Betz, M.A. Johnson, R.A. McLaren, and E.C. Sutton "Heterodyne detection of CO₂ emission lines and wind velocities in the atmosphere of Venus" *Astrophys.J.Lett.*, **208**, No.3, L141–L144 (1976)
- [5] R. T. Menzies, "Laser heterodyne detection techniques" in *Laser Monitoring of the Atmosphere*, ed. E. D. Hinkley, Springer, 297–353 (1976)
- [6] T. Kostiuk, K.E. Fast, T.A. Livengood, T. Hewagama, J.J. Goldstein, F. Espenak and D. Buhl "Direct Measurement of Winds on Titan" *Geophys. Res. Lett.* **28**, No. 12, 2361–2364 (2001)
- [7] F. Schmölling, B. Klumb, M. Harter, R. Schieder, B. Vowinkel and G. Winnewisser "High-sensitivity mid-infrared heterodyne spectrometer with a tunable diode laser as a local oscillator" *Applied Optics* **37**, 5771–5776 (1998)
- [8] G. Sonnabend, D. Wirtz, F. Schmölling and R. Schieder "Tuneable Heterodyne Infrared Spectrometer for Atmospheric and Astronomical Studies" *Applied Optics* **41**, 2978–2984 (2002)
- [9] H. Schneider, P. Koidl, M. Walther, J. Flessner, R. Rehm, E. Diwo, K. Schwarz and G. Weimann "Ten years of QWIP development at Fraunhofer IAF" *Infrared Physics & Technology* **42** 283–289 (2001)
- [10] H.C. Liu, R. Dudek, A. Shen, E. Dupont, C.Y. Song Z.R. Wasilewski and M. Buchanan "High absorption (>90 %) quantum-well infrared photodetectors" *App. Phys. Lett.* **79** 4237–4239 (2001)

HETERODYNE RECEIVER REQUIREMENTS FOR THE SINGLE APERTURE FAR-INFRARED (SAFIR) OBSERVATORY

Dominic J. Benford

NASA – Goddard Space Flight Center, Code 685, Greenbelt, MD 20771

Jacob W. Kooi

Caltech, MC 320-47, Pasadena, CA 91125

In the next few years, work will commence in earnest on the development of technology for the next generation large cryogenic far-infrared telescope: the Single Aperture Far-Infrared (SAFIR) Observatory. SAFIR's science goals are driven by the fact that youngest stages of almost all phenomena in the universe are shrouded in absorption by cool dust, resulting in the energy being emitted primarily in the far-infrared. The earliest stages of star formation, when gas and dust clouds are collapsing and planets forming, can only be observed in the far-infrared. Spectral diagnostics in the far-infrared are typically quite narrow (~ 1 km/s) and require high sensitivity to detect them. SAFIR is a 10m-class telescope designed for cryogenic operation at L2, removing all sources of thermal emission from the telescope and atmosphere. Despite its limited collecting area and angular resolution as compared to the ALMA interferometer, its potential for covering the entire far-infrared band cannot be matched by any ground-based or airborne observatory. This places a new challenge on heterodyne receivers: broad frequency coverage. The ideal mixer would be able to detect frequencies over several octaves (e.g., 0.6THz-12THz) with near quantum-limited performance at all frequencies. In contrast to ground-based observatories, it may not be necessary to strive for high instantaneous bandwidth, as direct detection spectroscopy is preferable for bandwidths of $\Delta\nu/\nu \geq 10^{-4}$ (e.g., 1GHz at 10THz). We consider likely directions for technology development for heterodyne receivers for SAFIR.

Keywords: heterodyne receiver, SIS mixer, HEB mixer, SAFIR, far-infrared, submillimeter

JUSTIFICATION FOR SAFIR

The earliest stages of star formation occur when thick, dusty gas clouds collapse towards the central protostar. The beginnings of this central star can only be observed at wavelengths in the far-infrared and longward. A host of diagnostics of the physical and chemical parameters of protostars can teach us about the processes that allow stars to form. Additionally, the cool dust that will eventually form planetary systems, as well as the cool debris disks that indicate the likelihood of planet-sized bodies around more developed stars, can only be observed at wavelengths longward of $20\mu\text{m}$. A hint of the richness of the far-infrared spectrum is given below in Figure 1.

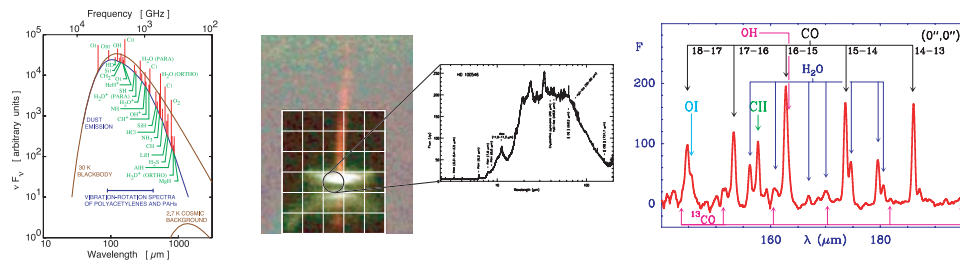


FIGURE 1. [Left] Synthetic molecular cloud spectrum, from Phillips & Keene (1992).
 [Center] Zooming in on a protostar with SAFIR (Burrows et al. 1996; Malfait et al. 1998)
 [Right] ISO/LWS spectrum of Orion-IRC2 (from Cernicharo et al. 1999).

SAFIR MISSION CONCEPT

SAFIR is best thought of as a set of scientific objectives that answer key questions in astrophysics by means of measurements in the far-infrared. Its implementation can be determined only by thoughtful study of multiple mission concepts, taking into account the science goals, technological capabilities, and programmatic feasibility. Several preliminary concepts have been produced, at varying levels of fidelity, as shown in Figure 2 below (all to scale).

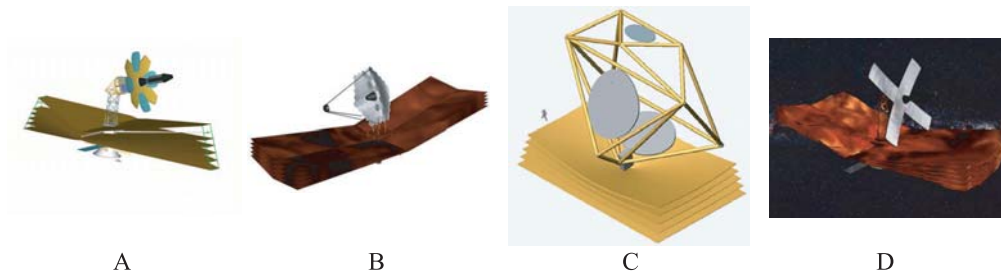


FIGURE 2. SAFIR concepts [A] Petal-deployed telescope based on the NGST Strawman Design (Amato et al. 2002); developed at NASA/GSFC. [B] Table-fold telescope based on the JWST (TRW) Design; developed at NASA/GSFC. [C] Stretched membrane telescope "DART" (Dragovan 2002); developed at NASA/JPL. [D] Strip-mirror mission concept using a sparse-aperture telescope for high angular resolution; developed at NASA/GSFC.

More in-depth consideration of SAFIR mission designs will be needed before a single approach can be selected. A high-fidelity but preliminary mission concept for SAFIR has been developed, derived from the technology heritage of JWST (Amato et al., SPIE, 2002). A full discussion of this mission is beyond the scope of this paper, but a few points are important. First of all, the design provides for a 10m diameter with >80% effective area used. Furthermore, the entire optical surface is cooled to 4 K, so that thermal emission in the far-infrared is negligible.

REQUIRED HETERODYNE RECEIVER PERFORMANCE

In order to satisfy the science goals listed above, SAFIR needs high resolution ($\lambda/\delta\lambda\sim 10^6$) spectrometer covering the wavelength range 25-520 μm (575GHz-12THz). An instrument with a small number of diffraction-limited beams in a sparse pattern would be sufficient to provide a reasonable imaging speed, but the detectors, if heterodyne, will need to be nearly quantum-limited so that the spectrometer can take advantage of the very low background in space.

When building a high resolution spectrometer for a wavelength longward of $\sim 300\mu\text{m}$ ($\nu < 1\text{THz}$), it is common to use coherent spectrometers. If the instantaneous bandwidth desired is narrower than $\lambda/\Delta\lambda = 10^4$ (30km/s), the bandwidth of the intermediate frequency amplifier and backend spectrometer need be only $\sim 100\text{MHz}$, easily achievable by today's standards. Given sufficient technology investment, could a coherent spectrometer be developed to cover the SAFIR bands (25 μm -520 μm) to provide information via very high resolution observations? This is possible for the case of Galactic observations, where line strengths relatively large though line widths are narrow. SAFIR's detection limit in a 1km/s line in 10^4s is about 1mK at 300 μm with a heterodyne spectrometer. However, in distant, extragalactic sources where linewidths are larger but sources are fainter, the quantum limit makes the detection of lines a difficult proposition.

Using the background power for a 4K, 10m telescope, we calculate a total effective power (including quantum noise fluctuation power) to produce a photon-limited noise equivalent flux density (NEFD). The result is shown in Figure 3 below for a spectral resolution of $\lambda/\Delta\lambda = 3 \cdot 10^5$, or a 1 km/s resolution. To put the comparison into scientific terms, the predicted fluxes of bright far-infrared fine-structure lines as they are redshifted towards submillimeter wavelengths are also shown. It is clear that a heterodyne spectrometer will pay a severe sensitivity penalty as compared to the natural photon background. In the quantum-limited case, a 270K telescope is about as good as a 4K telescope, and so ALMA will be more sensitive than SAFIR anywhere they overlap. However, practical issues mandate that at very high spectral resolutions, heterodyne spectroscopy is preferred (see, e.g., Zmuidzinas (2003) for details).

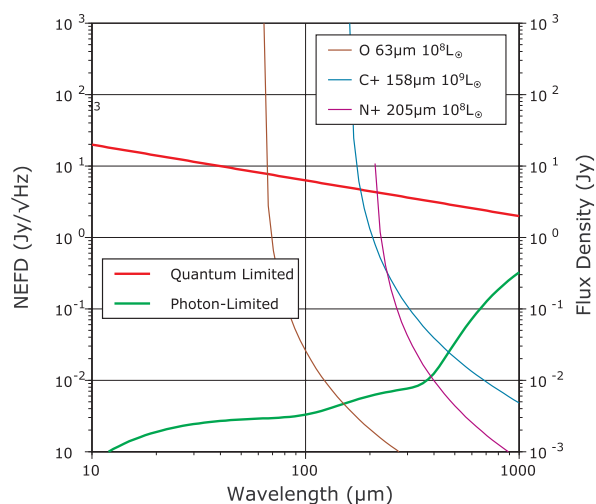


FIGURE 3. NEFD for a $\lambda/\Delta\lambda = 3 \cdot 10^5$ (1km/s resolution) spectrometer using photon-limited direct detectors compared with quantum-limited coherent detectors. Predicted fluxes for redshifted fine-structure lines are shown for reference.

FUTURE SUBMILLIMETER FACILITIES

We compare the predicted sensitivity of SAFIR's heterodyne spectrometer to those of other facilities available in the next decade. In Figure 4 below, we have made an estimate of the NEFD for an upgraded CSO instrument suite (Kooi et al. 2003), a hypothetical ALMA suite with receivers at all frequencies available from the ground, a hypothetical optimized SOFIA heterodyne spectrometer covering the whole 300 GHz – 3 THz band, and the HIFI instrument on Herschel. NEFD is chosen rather than noise temperature, as the point source sensitivity of each facility is the more relevant parameter. As can be seen, SAFIR will provide a substantial gain in sensitivity at frequencies above 1THz, enabling new science at these frequencies. Where ALMA is operational, its sensitivity and high angular resolution are superior, but the availability of the >1THz windows is not common.

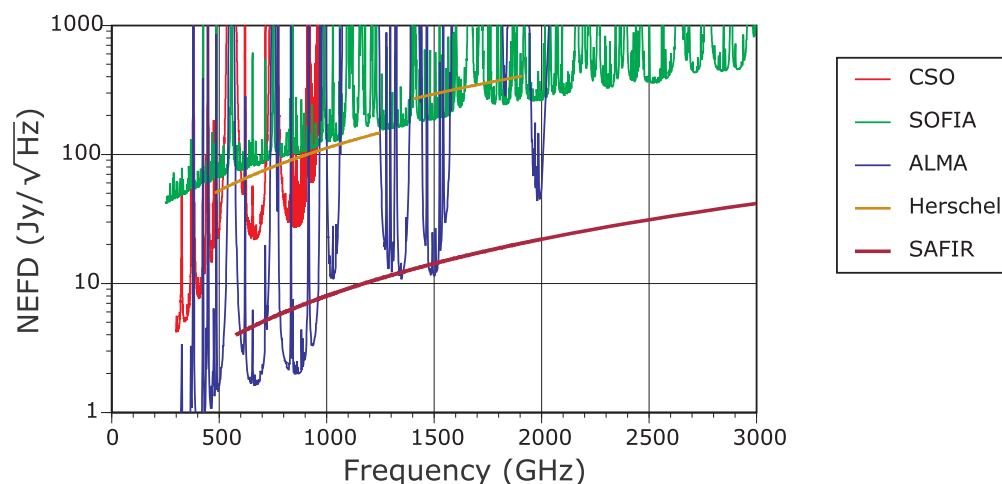


FIGURE 4. Flux density sensitivity at 1km/s resolution from 300 GHz to 3 THz (100 μ m to 1 mm) of several facilities envisioned for the coming decade, as compared to the sensitivity of the SAFIR observatory.

It is worth noting that all of these facilities are quantum-limited except where the atmospheric emission is strong. For this reason, a warmer but larger implementation of SAFIR would yield better sensitivity for its heterodyne instruments. Figure 2(C) shows a tensioned membrane telescope, which yields a very low areal density but more difficult cooling problems. This, the NASA/JPL "DART" concept, might be easily scaled to a larger (10-30m), warmer (\sim 30K) telescope than the baseline 10m, 4K SAFIR.

TECHNOLOGIES FOR HETERODYNE INSTRUMENTS

Significant progress on the development of heterodyne technologies has been made (see, e.g., Siegel 2002). However, to achieve the required sensitivity and bandwidth for SAFIR, many of the needed components will need to be developed by NASA. These include:

- Tunerless (waveguide or quasioptical) mixers (SIS and HEB) with large fractional RF bandwidth
- High efficiency local oscillators for the 0.6 THz – 12 THz range (e.g., laser photomixed sources)
- Low noise cryogenic amplifier (e.g., 4 – 8 GHz)
- Combined wideband (e.g., also 4 – 8 GHz) IF matching network, DC-break, bias tee, etc.
- Broadband coupling techniques
- Low power, compact multichannel backend spectrometers

One of the most difficult aspects of the development of a heterodyne spectrometer for SAFIR is the broad wavelength coverage required. It is typically possible to achieve a bandwidth of nearly an octave with a single tuning and amplifier network. SAFIR's requirement of 4.3 octaves implies that >5 bands will be needed, all well-matched to each other. An example of this approach is given by Kooi et al. (2003), and is reproduced here (Figure 5). The calculations assume optimized balanced twin-junction Nb SIS receivers. Further development of broadband quasioptical coupling techniques may enable mixers to operate over even broader ranges.

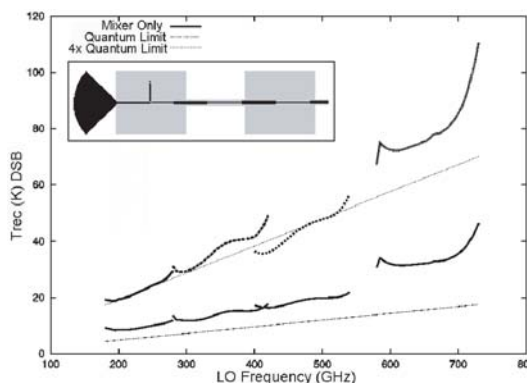


FIGURE 5. Predicted noise temperatures for next-generation mixers and receivers at the Caltech Submillimeter Observatory (Kooi et al. 2003).

As shown above, across the 200–700 GHz (430 μ m–1.5mm) range, the predicted receiver temperature is about four times the quantum limit. If we extrapolate the calculation to the SAFIR bands, the entire region from 575 GHz–12 THz (25 μ m–520 μ m) can be covered with seven contiguous bands. We have assumed similar performance: a noise level of four times the quantum limit over the entire frequency span, and coupling limited in bandwidth by waveguide techniques. Considering the 575 GHz–8 THz (38–520 μ m) bands, we find the receiver noise shown in Figure 6.

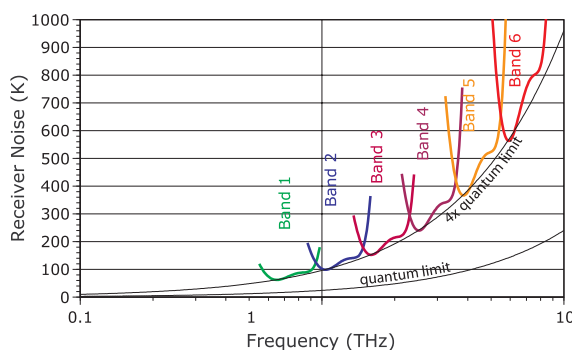


FIGURE 6. Layout of the lowest six bands of the SAFIR heterodyne spectrometer. Each receiver is assumed to operate at four times the quantum limit at its best frequency.

STATE-OF-THE-ART

The current state-of-the-art receiver performance (Figure 7) is excellent for SIS mixers operated at frequencies below ~ 500 GHz ($600\mu\text{m}$). Once into the SAFIR bands, however, the best receivers are HEBs, which typically have substantially more noise. This sensitivity reduction is so substantial that it may reduce the advantage SAFIR has over a larger ground-based facility such as ALMA. Technology to fill this sensitivity gap must be developed to enable a heterodyne instrument for SAFIR.

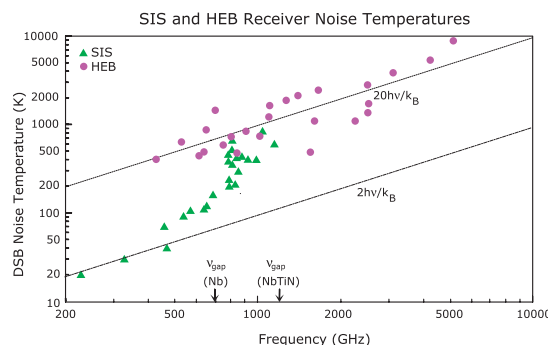


FIGURE 7. Current (early 2003) state of the art performance for heterodyne receivers.

CONCLUSION

For SAFIR, single-mode coherent detectors operating near the quantum limit over the $575\text{GHz}–12\text{THz}$ ($25–520\mu\text{m}$) range are needed. To this end, increasing the tunable bandwidth of detectors and local oscillator sources is a key research investigation to be undertaken. HEB or SIS mixers are the most promising current technology for this purpose, if they can be manufactured with near-quantum noise at such high frequencies. Additionally, backend spectrometers using low-power digital autocorrelators should be developed.

REFERENCES

- Amato, M.J., Benford, D.J., Moseley, S.H., & Roman, J.A. 2002, "An Engineering Concept and Enabling Technologies for a Large Single Aperture Far-Infrared Observatory (SAFIR/FAIR)," Proc. SPIE #4850, pp.1120-1131
- Burrows, C.J., Stapelfeldt, K.R., Watson, A.M., Krist, J.E., Ballester, G.E., Trauger, J.T. & Westphal, J.A. 1996, "Hubble Space Telescope Observations of the Disk and Jet of HH30," ApJ, 473, p.437
- Cernicharo, J., et al. 1999, "The Water Vapour Abundance and Its Spatial Distribution in Orion and SgrB2," in "The Universe as Seen by ISO," ed. P. Cox & M. F. Kessler (ESA SP-427; Noordwijk: ESA/ESTEC), p.565
- Dragovan, M. 2002, "The DART System for Far-IR/Submillimeter Space Missions," in "New Concepts for Far-Infrared and Submillimeter Space Astronomy", ed. D.J. Benford & D.T. Leisawitz (NASA/CP-212233), in press
- Kooi, J.W., Kovács, A., Kaye, S., Dama, J., Edgar, M.L., Zmuidzinas, J. & Phillips, T.G. 2002, "Heterodyne Instrumentation Upgrade at the Caltech Submillimeter Observatory," Proc. SPIE #4855, pp.265-278
- Malfait, K., Waelkens, C., Waters, L.B.F.M., Vandenbussche, B., Huygen, E. & de Graauw, M.S. 1998, "The Spectrum of the Young Star HD100546 Observed with the Infrared Space Observatory," A&A 332, pp.L25-L28
- Phillips, T.G. & Keene, J.B. 1992, "Submillimeter Astronomy," Proc. IEEE #80, p.1662
- Siegel, P.H. 2002, "Terahertz Technology," IEEE-MTT, 50, 3, pp.910-928
- Zmuidzinas, J. 2003, "The Role of Coherent Detection," in "New Concepts for Far-Infrared and Submillimeter Space Astronomy", ed. D.J. Benford & D.T. Leisawitz (NASA/CP-212233), in press

Cartridge-type receiver system on ASTE

Masahiro Sugimoto, Yutaro Sekimoto,

Sozo Yokogawa, Takeshi Okuda,

Ken'ichi Tatematsu, Takashi Noguchi

National Astronomical Observatory of Japan

Kotaro Kohno

Institute of Astronomy, The University of Tokyo

Hideo Ogawa, and Kimihiro Kimura

Department of Earth and Life Sciences,

College of Integrated Arts and Sciences

Abstract

We have developed a cartridge-type receiver system composed of three cartridge-type receivers and a cryostat, which is designed to test on the Atacama Submillimeter Telescope Experiment (ASTE). It was preliminarily evaluated at Pampa la Bola (alt. 4800 m) in the northern Chile since November 2002. The cryostat, which can house 3 cartridge-type receivers, has been developed with following technologies; a central pipe and bellows structure to reduce mechanical vibration; simple and efficient thermal links for plug-in cartridges; 3-stage Gifford McMahon cryocooler and an outdoor compressor. Engineering models of band 3 (100 GHz), band 8 (500 GHz), and band 10 (800 GHz) cartridge-type receivers were independently developed with cartridge-test cryostats. They were integrated into the cryostat at NAOJ,

then the system was shipped to the site. We confirmed that the system including three receivers operates as designed and the concept of cartridge-type receiver system is very promising for the ALMA.

Instruments

A cartridge-type cryostat, which can house 3 cartridge-type receivers, has been developed for the ASTE. The ASTE 10 m telescope has been developed as a prototype antenna of the Large Millimeter Submillimeter Array. It was installed on Pampa la Bola following evaluation at Nobeyama. The detail of this cryostat was described by Yokogawa et al. (2003)[1]. The cryostat is shown in Figure 1. The cylindrical cryostat can accommodate 2 cartridges of 170 mm diameter and 1 cartridge of 140 mm diameter. The cryostat is composed of 3 stages, which

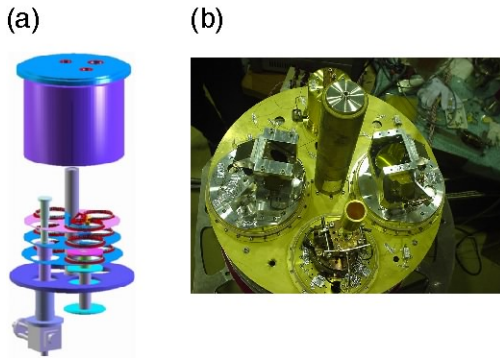


Figure 1: (a) A schematic drawing of a cryogenic system for the ASTE, which houses 3 cartridge-type receivers. (b) A photograph of the cryostat. 3 cartridge-type receivers (from right to left, 800 GHz, 100 GHz, 500 GHz) are installed.

are connected with corresponding stages of a cryocooler.

The concept of the thermal link for the ALMA receiver was proposed by the Rutherford Appleton Laboratory (RAL)[2]. We have designed and developed a simple and efficient thermal link with high heat conductivity [3]. Measured thermal conductance of $\phi 170$ mm links is 1.7, 5.6, 3.3 W K⁻¹ for 4, 12, and 80 K stages. This simple and compact links have good performance and can be easily fabricated.

The concept of the cartridge for the ALMA was proposed by the RAL [2]. NAOJ have developed cartridges which have compatible interface to the ALMA receiver cartridges. The cartridge structure is supported by the central pipe as shown in Figure 2a, b. One can assemble and maintain receivers without decomposition of the NAOJ cartridge. The $\phi 140$ mm cartridge has been designed and

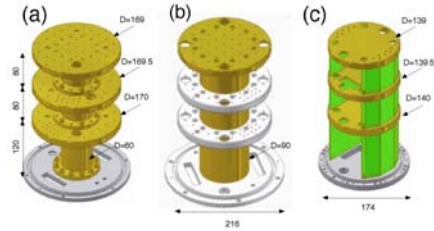


Figure 2: (a) A schematic drawing of the $\phi 170$ mm cartridge made by NAOJ. (b) The same in (a), but for $\phi 90$ mm central pipe. (c) A schematic drawing of the $\phi 140$ mm cartridge made by Osaka Prefecture University/Nagoya University.

developed by Osaka Prefecture University/Nagoya University is shown in Figure 2c. Support structure of their cartridge is composed of divided plates placed on the circumference. This cartridge provides accessibility and spaciousness.

An engineering model of band 10 cartridge-type receiver has been developed. We designed and developed a single mirror optics which couples between a feed horn and the subreflector of the antenna. The dielectric is used for coupling the RF signal with the LO signal. Receiver noise temperature was about 1000 K in DSB at a LO frequency of 812 GHz.

An engineering model of band 8 cartridge-type receiver has been developed. The optics is similar to that of the band 10 receiver. Receiver noise temperature was about 240 K (DSB) at 498 GHz. This receiver was used for noise measurements of hybrid photonic LO (for details, see [4]).

A engineering model of band 3 cartridge-type receiver has been devel-

oped as a scaled model of band 4 by Osaka Prefecture University and Nagoya University [5]. We designed flat and ellipsoidal mirror of room temperature and adopted frequency independent solution for receiver optics. The SIS mixer device of band 3 receiver is a parallel-connected twin-junction [6][7]. The measured receiver noise temperature is less than 25 K (DBS) in the frequency range of 95 – 120 GHz.

Integration and test observation

Three cartridge-type receivers have been independently developed with cartridge-test cryostats, which are developed for tests in laboratories [8]. Then, three receivers were integrated into the cryostat at the Mitaka campus of NAOJ. We confirmed that their performance is almost same as that measured with the cartridge-test cryostat. After the integration, the system was shipped to the ASTE site.

In November 2002, 3 cartridge-type receivers were installed to the ASTE. On 17 November 2002, we detected continuum signals from the moon with all three receivers. The moon and Jupiter efficiency of the band 3 receiver were 90 % and 73 % at 100 GHz, respectively. In spite of not adjusting tilt parameters of the subreflector, the moon and Jupiter efficiency were 82 % and 42 %, respectively at 498 GHz. The pointing accuracy was about $1''$, which derived from measurements of the Jupiter and the Saturn. On 9 December 2002, we observed a spectrum of CI (rest frequency = 492.16 GHz) from Orion (Figure 3). At that night, the optical depth at zenith was ~ 1.0 and the system noise temperature was around

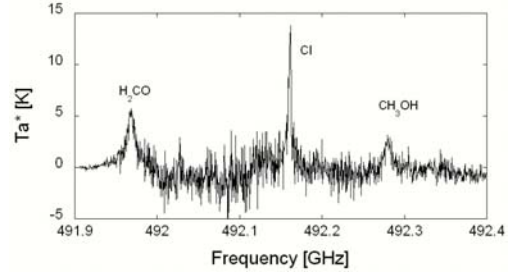


Figure 3: A spectrum of CI (${}^3P_1 - {}^3P_0$) from Orion KL.

1000 K.

We have confirmed that the engineering models of three cartridge-type receivers work as designed and the cartridge-type receivers are very promising for ALMA.

References

- [1] Yokogawa, S., Sekimoto, Y., Sugimoto, M., et al. 2003, PASJ, 55, 519.
- [2] Orłowska, A., Harman, M., Ellison, B. 2002, ALMA project book, Chapter 6.
- [3] Sugimoto, M., Sekimoto, Y., Yokogawa, S., et al. 2003, Cryogenics, in press.
- [4] Sekimoto Y, Ueda A, Okuda T, et al. 2003a ALMA memo 449.
- [5] Ogawa, H., Yonekura, Y., Asayama, S., et al. 2002, Proc. IAU 8th APRM.
- [6] Asayama, S., Noguchi, T., Ogawa, H. 2003a, International Journal of Infrared and Millimeter Waves, in press.
- [7] Asayama, S., Ogawa, H., Noguchi, T., et al. 2003b, ALMA memo 453.
- [8] Sekimoto, Y., Kamba, T., Yokogawa, S., et al. 2003b, ALMA memo 455.

Current Status of the Antarctic Submillimeter Telescope and Remote Observatory

Kecheng Xiao, Antony A. Stark, Adair P. Lane,
Christopher L. Martin, Wilfred M. Walsh (SAO)
Christopher K. Walker (U. Arizona)
Jacob W. Kooi (Caltech)

ABSTRACT

The Antarctic Submillimeter Telescope and Remote Observatory (AST/RO) is a 1.7-m diameter offset Gregorian instrument operating year-round at the NSF Amundsen-Scott South Pole Station. During the Austral winter of 2002, there were five submillimeter heterodyne receivers mounted on its optical table: 1) a 230 GHz SIS receiver, 2) a 450-495 GHz SIS quasi-optical receiver, 3) a 450-495 GHz SIS waveguide receiver, 4) a 800-820 GHz fixed-tuned SIS waveguide receiver and 5) a 2x2 804-810 GHz fixed-tuned SIS array receiver (PoleSTAR). Observations were conducted at 230 GHz, 460-490 GHz and 810 GHz towards Galactic Center region and Magellanic Clouds. After an upgrade of PoleSTAR and a successful installation of a 1.5 THz heterodyne receiver (TREND) during the last Austral summer, AST/RO is currently able to measure the sky at wavelengths from 1.3 mm to 200 μm .

AST/RO could be used in future as an observational test bed for additional prototype Terahertz instruments. Observing time on AST/RO is available on a proposal basis (see http://cfa-www.harvard.edu/~adair/AST_RO).

I. Introduction

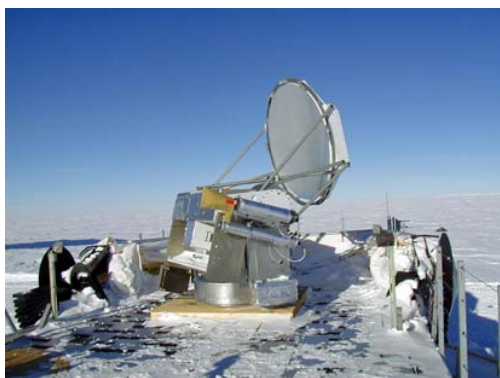


Fig. 1. The Antarctic Submillimeter Telescope and Remote Observatory atop its building at the South Pole in 2002 February.

The Antarctic Submillimeter Telescope and Remote Observatory (AST/RO) is a 1.7-m diameter offset Gregorian telescope with optics designed for wavelengths between 3 mm and 200 μm . It is the first submillimeter-wave telescope to operate year-round on the Antarctic plateau and is open to the astronomical community on a proposal basis. The South Pole is the best ground-based observatory site for the millimeter, submillimeter, and far-infrared, due to its extremely cold, dry conditions. Since AST/RO became operational in January 1995 at the United States National Science Foundation Amundsen-Scott South Pole Station, over 800,000 raw spectra have been obtained, including maps of the Magellanic Clouds, Carina molecular clouds, and the Galactic Center region in the 230 GHz line of CO (2-1), 492 GHz line of C I, 461 GHz line of CO (4-3) and 807 GHz line of CO (7-6). Figure 1 is a photograph

of AST/RO, which located on the roof of a dedicated support building about 1 km from the Geographic South Pole. In this paper we report the current status of AST/RO.

II. The AST/RO Optics and Calibration System

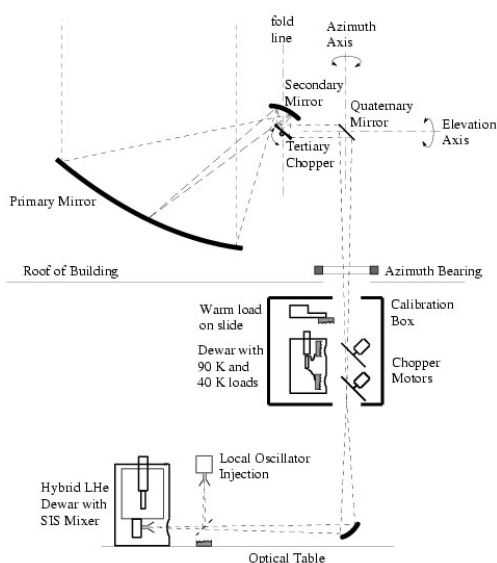


Fig. 2. Schematic of the AST/RO optical system.

mounted on a linear actuator and can be moved to block the beam from the sky. The cooled loads are in a Dewar to the side of the beam coming into the Coudé room and are switched into the beam by flat chopper mirrors (Stark 1997).

III. The AST/RO Submillimeter-wave Receivers

During the 2002/2003 Austral summer season, we upgraded PoleSTAR and replaced the 450-495 GHz SIS quasi-optical receiver (165-250 K DSB, Engargiola, Zmuidzinas, & Lo 1994) with a 1.5 THz heterodyne HEB receiver (TREND). Figure 3 shows the AST/RO receivers mounted on optical table.

- **230 GHz SIS receiver (Kooi et al 1992)**

The 230 GHz SIS receiver has a full height rectangular waveguide mixer with two tuning elements: E-plane tuner and backshort. The mixer, which uses a small size $0.25 \mu\text{m}^2$ Nb/AlOx/Nb SIS tunnel junction with $\omega RC \sim 1.7$ at 230 GHz and a wideband integrated IF matching network, is able to work in a frequency range of 225-255 GHz with the current local oscillator (LO). The LO power is injected to the junction via a $12 \mu\text{m}$ thick Mylar beamsplitter. Since the upgrade in 2001, this receiver has been working stably for CO (2-1) observations, with a typical DSB receiver noise temperature of 80 K. A novel Millitech 230 GHz multiplier, which is a combination of an X-band power amplifier and an 18th-order harmonic generator with signal input from a frequency synthesizer, has been successfully used as an alternative LO source for CO, ^{13}CO and C^{18}O (2-1) observations. With this ultra-compact LO unit, no high frequency phase-lock control loop is necessary.

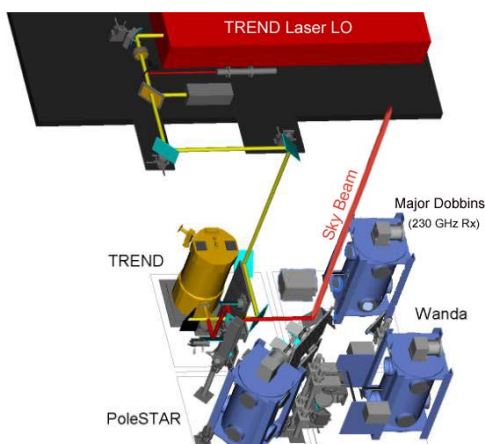


Fig. 3. A 3-d view of current AST/RO receiver room configurations with 1.5 THz HEB receiver TREND and its laser local oscillator installed, looking downwards to the Coudé focus. (Created: Dathon Golish, modified: Kecheng Xiao)

- **450-495 GHz/800-820 GHz dual channel SIS receiver (Wanda) (Walker et al. 1992, Honinggh et al. 1997)**

This dual channel receiver was built by Steward Observatory Radio Astronomy Laboratory (SORAL), University of Arizona, in 1996. The “Wanda” 450-495 GHz SIS mixer (Caltech) has a double tuning structure of E-plane tuner and backshort, while the “Wanda” 810 GHz mixer (U. Koln) is fixed-tuned. The two mixers have been built into a single dewar and are used in a two channel configuration. Two phase-locked RPG-made LO chains (77 GHz-Gunn $\times 2 \times 3$ and 135 GHz-Gunn $\times 2 \times 3$) provide LO power for both channels via 45° Mylar beamsplitters. A wire-grid polarizer splits the RF signals and allows simultaneous measurement of the atomic carbon [C I] 3P_1 - 3P_0 and [C I] 3P_2 - 3P_1 lines or the CO (4-3) and the CO (7-6) molecular rotation lines. The DSB uncorrected receiver noise

temperatures are 250K and 1100 K. An extensive survey towards the Galactic Center region was carried out using this receiver during the 2001 and 2002 Austral winter seasons (Martin et al. 2003).

- **800-820 GHz 2 x 2 array SIS receiver (PoleSTAR) (Groppi et al. 2000)**

This SORAL-built 4-channel receiver has been installed on AST/RO since November-December 2000. It has a unique optical system with a pair of parabolic mirrors and two flats, to reimage AST/RO’s focal plane onto a compact 2x2 array of lenses located in the array cryostat and to efficiently inject local oscillator power into each mixer. A quasi-optical LO power divider is used to split the focused LO beam into 4 equal parts. A JPL-supplied LO unit which comprises a 100 GHz Gunn oscillator, a 100 GHz power amplifier and a $\times 2 \times 2 \times 2$ doubler chain, together with a simple Mylar beamsplitter are now used to pump the array.

The SIS mixers used in PoleSTAR were made by KOSMA (Honinggh et al. 1997). Each mixer uses a Potter horn with a circular-to- $\frac{1}{2}$ height rectangular waveguide transition to couple radiation to a Nb SIS junction. The junctions achieve low noise performance through the use of an on-substrate Al tuning structure and a fixed waveguide backshort. The mixers have embedded magnets to suppress the Josephson effect. After a recent upgrade, three mixers are on the sky with receiver temperatures less than 600 K, including all losses in the system.

- **1.5 THz heterodyne HEB receiver (TREND) (Gerecht et al. 1999, Yngvesson et al. 2001)**

During the 2002/2003 Austral summer season, TREND was successfully installed and initialized on AST/RO. The TREND optics, dewar and its laser LO can be seen in Figure 3. TREND is a single-pixel THz receiver and its LO frequency can be changed by choosing different pumping gases in the submm laser LO. Details of the TREND receiver will be described elsewhere in these proceedings.

- ***Acousto-Optical Spectrometers (AOSs) on AST/RO***

Two low-resolution spectrometers (LRSs) with a bandwidth of 1 GHz (bandpass 1.6-2.6 GHz), one high-resolution AOS (HRS) with a 60 MHz bandwidth (bandpass 60-120 MHz) (Schieder et al 1989).

An array AOS having four low-resolution spectrometer channels with a bandwidth of 1 GHz (bandpass 1.6-2.6 GHz) for the PoleSTAR array (Horn et al. 1999).

IV. Cryostat

The cryostats on AST/RO (except for TREND) were constructed by Precision Cryogenics and are based on the successful CSO hybrid design. They use a CTI model 350 coldhead to cool the outer and inner radiation shields to ~77 and ~14 K, respectively and a 4 liter liquid helium reservoir to maintain the mixers at their ~ 4 K operating temperature. In the single pixel AST/RO receivers, 30.5 mm diameter, Teflon coated, crystalline quartz windows are used at 300 and 77 K. Zytex is used as the IR filter on the 12 K radiation shield. Holding times of ~ 5 days can be achieved. With the array receiver PoleSTAR, an additional layer of Zytex has been substituted for the 50-mil quartz windows at 77 K. This past Austral summer, we replaced the original Zotefoam vacuum window with a lower-loss crystalline quartz window which has an IR-reflective coating. With all 4 mixers and amplifiers operating in the cryostat, the measured LHe hold time is ~ 4 days.

References

- Engargiola, G., Zmuidzinas, J., & LO, K.-Y. 1994, *Rev. Sci. Inst.*, 65, 1833
- Gerecht, E., Musante, C. F., Zhuang, Y., Yngvesson, K. S., Goyette, T., Dickinson, J., Waldman, J., Yagoubov, P. A., Gol'tsman, G. N., Voronov, B. M., & Gershenson, E. M. 1999, *IEEE Trans.*, MTT-47, 2519
- Groppi, C., Walker, C., Hungerford, A., Kulesa, C., Jacobs, K., & Kooi, J. 2000, in *ASP Conf. Ser.* 217, *Imaging at Radio through Submillimeter Wavelengths*, ed. J. G. Mangum & S. J. E. Radford (San Francisco: ASP), 48
- Honinggh, C. E., Haas, S., Hottgenroth, K., Jacobs, J., & Stutzki, J. 1997, *IEEE Trans. Appl. Superconductivity*, 7, 2582
- Horn, J., Siebertz, O., Schmulling, F., Kunz, C., Schieder, R., Winnewisser, G. 1999, *Exp. Astron.* 9, 17
- Kooi, J. W., Chan, M., Phillips, T. G., Bumble, B., & LeDuc, H. G. 1992, *IEEE Trans. Microwave Theory and Techniques*, 40, 812
- Martin, C. L., Walsh, W. M., Xiao, K., Lane, A. P., Walker, C. K., Stark, A. A. 2003, accepted by *ApJ* (astro-ph 0211025)
- Schieder, R., Tolls, V. & Wimmewisser, G. 1989, *Exp. Astron.* 1, 101
- Stark, A. A. 1995, in *proceeding of Sixth International Symposium on Space Terahertz Technology* (Pasadena: Caltech), 150
- Stark, A. A., Chamberlin, R. A., Cheng, J., Ingalls, J., & Wright, G. 1997, *Rev. Sci. Instr.*, 68, 2200
- Walker, C. K., Kooi, J. W., Chan, W., LeDuc, H. G., Schaffer, P. L., Carlstrom, J. E., & Phillips, T. G. 1992, *Int. J. Infrared and Millimeter Waves*, 13, 785
- Yngvesson, K. S., Musante, C. F., Ji, M., Rodriguez, F., Zhuang, Y., Gerecht, E., Coulombe, M., Dickinson, J., Goyette, T., Waldman, J., Walker, C. K., Stark, A. A., & Lane, A. P. 2001, in *Twelfth Int. Symp. Space THz Tech.*, (I. Medhi, Ed.), San Diego, CA, Feb. 14-16, 2001, p. 26

Efficient Side-band Ratio Measurement of a Submm Wave Mixer Using a Fourier Transform Spectrometer.

A. Baryshev¹, R. Hesper¹, G. Gerlofsma¹, M. Kroug², W. Wild³

¹NOVA/SRON/RuG

²DIMES/TuD

³SRON / RuG

Abstract

The sideband ratio is an important parameter for the sensitivity calibration of a DSB heterodyne receiver at a telescope. A number of techniques can be used for measuring this parameter. We present sideband ratio measurements of a submm receiver in the 600-720 GHz band. A Michelson Fourier transform spectrometer with long path length difference is used. A frequency resolution of up to 0.75 GHz is achieved. The sideband ratio is measured at many points across the receiver band making use of an electronically tuneable LO and automatic receiver tuning procedures. The direct response of the same mixer is measured using the same interferometer. We will compare the side-band ratio obtained in the heterodyne mode with an estimate that can be obtained from a direct detection mode, and evaluate if the direct detection curve can be a good indication of the receiver quality. Comparison with estimates for the side-band ratio applying the full Tucker theory will be made.

Preference: poster

Corresponding author A. Baryshev -- andrey@srn.rug.nl

Transmission and Reflection Characteristics of Slightly Irregular Wire-Grids for Arbitrary Angles of Incidence and Grid Rotation

Takeshi Manabe[†] and Axel Murk[‡]

[†] Communications Research Laboratory
Koganei, Tokyo 184-8795, Japan (e-mail: manabe@crl.go.jp)

[‡]Institute of Applied Physics, University of Berne,
Silderstrasse, CH-3012 Berne, Switzerland (e-mail: axel.murk@mw.iap.unibe.ch)

1 Introduction

Although there has been many different theoretical studies developed for calculating the transmission and reflection characteristics of freestanding wire-grids, most of them, to the authors' knowledge, were approximate ones only applicable to the cases where the diameter of the wire is much smaller than the wavelength or the spacing between wires [1][2]. It was only rather recently that more exact treatment of wire-grid without such approximations became possible by the Green-function method [3] or the lattice-sum method [4]. In the first half of this paper, a method for calculating transmission and reflection characteristics of wire-grids consisting of a periodic array of cylinders for arbitrary directions of incidence and grid rotation is presented by extending a very accurate and efficient calculation method for wire-grids based on the lattice-sum method proposed by Yasumoto *et al.*[5].

In most of the theories which include the one presented in the first half of this paper, the wire-grid has been assumed to be a periodic array of parallel cylindrical wires with a constant spacing between them. In actual wire-grids used in millimeter- and submillimeter-wave regions, the grids are never free from irregularity in wire spacing due to the difficulty in producing evenly spaced grids as the spacing decreases[6][7]. There have been almost no detailed theoretical studies made about the effects of grid imperfection on its performance except the one by Houde *et al.* [8].

In the latter half of this paper, a perturbation theory for calculating the characteristics of wire-grid with slight random irregularity in its spacing is proposed. In this theory, the irregularity in wire-grid is modeled as random errors in wire positions from regular positions, and is treated as a perturbation to the exact theory of periodic wire-grid by assuming that the positional errors of wires are zero-mean statistically uncorrelated independent variables from wire to wire. In order to validate the applicability of the proposed theory for actual irregular wire-grid, results of measurements made for actual wire-grids with different degrees of irregularity at millimeter and sub-millimeter wavelengths are compared with those of the theoretical calculations.

2 Definition of the Coordinate System

In this paper, we define the coordinate systems as shown in Fig. 1 relating the geometry of the wire-grid and the incident wave. The wire-grid is a periodic array of parallel wires of radius a with a period h . In the x - y - z coordinate system, the plane of wire-grid lies in the x - z plane. Each wire supposed to be an infinitely long cylinder is directed along the z -axis. The plane of incidence in which the incident wavenumber vector \mathbf{k}_0

lies is defined as the X - Y plane ($Y \equiv y$) which is made by rotating the x - y plane by ϕ_g around the y -axis. We refer to the rotation angle ϕ_g as the grid rotation angle.

In reference to the X - Y - Z coordinate system, the incident wavenumber vector \mathbf{k}_0 lying in the X - Y plane is given by $\mathbf{k}_0 = -\mathbf{i}_X k_0 \sin \chi - \mathbf{i}_Y k_0 \cos \chi$ where χ is the angle of incidence. If we define the angles θ_{in} and ϕ_{in} as in Fig. 1 such that the incident wavenumber vector \mathbf{k}_0 is expressed in the (x, y, z) coordinate system as

$$\mathbf{k}_0 = -k_0 \sin \theta_{in} (\cos \phi_{in} \mathbf{i}_x + \sin \phi_{in} \mathbf{i}_y) + k_0 \cos \theta_{in} \mathbf{i}_z, \quad (1)$$

the relationship between (χ, ϕ_g) and (θ_{in}, ϕ_{in}) can be written as

$$\theta_{in} = \cos^{-1}(\sin \chi \sin \phi_g), \quad (2)$$

$$\phi_{in} = \tan^{-1}(\cot \chi \sec \phi_g). \quad (3)$$

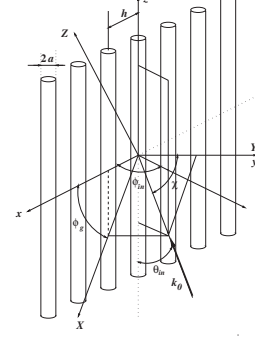


Figure 1: Coordinate system defining grid orientation and \mathbf{k}_0 .

3 T Matrix of Isolated Cylindrical Wire for Arbitrary Angle of Incidence

Before considering an array of cylinders, let us consider the scattering of a plane wave by a single isolated cylinder whose axis coincides with the z -axis in Fig 1.

In order for the theory to be applicable not only to metallic wires but also to dielectric cylinders, we assume that the material of wire is a lossy dielectrics characterized by a relative complex permittivity ϵ_r . When the material of the wire is a metallic conductor with a finite conductivity σ , the relative complex permittivity given by $\epsilon_r = 1 + j\sigma/(\omega\epsilon_0)$ should be substituted¹.

3.1 Incident Wave

For later discussions, let us decompose the field of the incident wave into the TM (transverse magnetic) and TE wave components whose electric field are polarized in a plane parallel and perpendicular to the direction of wire, respectively.

For the case of TM incident wave, the incident field at (ρ_0, ϕ_0, z) in the cylindrical coordinate system can be generated by the electric Hertz potential [9] given by

$$\Pi_{zi} = \sum_{n=-\infty}^{\infty} A_i e^{jk_0 z \cos \theta_{in}} J_n(k_0 \rho_0 \sin \theta_{in}) e^{jn(\phi_0 - \phi_{in} - \pi + \frac{\pi}{2})} = e^{jk_0 z \cos \theta_{in}} \mathbf{P}_0^T \cdot \mathbf{a}^{in} \quad (4)$$

where $\mathbf{P}_0 = [J_m(k_0 \rho_0 \sin \theta_{in}) e^{jm\phi_0}]$ and \mathbf{a}^{in} is the TM -incident-wave amplitude vector defined as $\mathbf{a}^{in} = A_i [(-j)^m e^{-jm\phi_{in}}]$, and A_i is the incident field amplitude related with the incident electric field E_0 by $A_i = E_0 / (k_0^2 \sin \theta_{in})$.

On the other hand, for the case of the TE incident wave, the incident field can be generated by the electric Hertz potential given by

$$\Pi_{mzi} = e^{jk_0 z \cos \theta_{in}} \mathbf{P}_0^T \cdot \mathbf{b}^{in}, \quad (5)$$

where \mathbf{b}^{in} is the TE -incident-wave amplitude vector defined as $\mathbf{b}^{in} = B_i [(-j)^m e^{-jm\phi_{in}}]$, and B_i is the incident field amplitude related with the incident electric field E_0 by $B_i = E_0 / (\eta k_0^2 \sin \theta_{in})$ where $\eta (= \sqrt{\mu_0 / \epsilon_0})$ is the impedance of free space.

¹The time dependence of field is assumed to be $\exp(-j\omega t)$ and is omitted throughout this paper.

3.2 Scattered Wave

We express the TM and TE components of the scattered wave by the electric Hertz potential Π_{zs} and the magnetic Hertz potential Π_{mzs} , respectively, by using unknown coefficient A_{sn} and B_{sn} as

$$\Pi_{zs} = e^{jk_0z \cos \theta_{in}} \mathbf{Q}_0^T \cdot \mathbf{a}_0^{sc}, \quad \text{and} \quad \Pi_{mzs} = e^{jk_0z \cos \theta_{in}} \mathbf{Q}_0^T \cdot \mathbf{b}_0^{sc}, \quad (6)$$

where $\mathbf{a}_0^{sc} = [(-j)^m A_{sm} e^{-jm\phi_{in}}]$, $\mathbf{b}_0^{sc} = [(-j)^m B_{sm} e^{-jm\phi_{in}}]$ and $\mathbf{Q}_0 = [H_m^{(1)}(k_0\rho_0 \sin \theta_{in}) e^{jm\phi_0}]$.

3.3 Field Inside the Wire

Inside the wire, we express the electric Hertz potential Π_{ze} and the magnetic Hertz potential Π_{mze} using the unknown coefficients A_{en} and B_{en} , respectively, as

$$\Pi_{ze} = \sum_{n=-\infty}^{\infty} A_{en} e^{jk_0z \cos \theta_{in}} J_n(k_1\rho_0 \sin \theta_1) e^{jn(\phi_0 - \phi_{in} - \pi + \frac{\pi}{2})}, \quad (7)$$

$$\Pi_{mze} = \sum_{n=-\infty}^{\infty} B_{en} e^{jk_0z \cos \theta_{in}} J_n(k_1\rho_0 \sin \theta_1) e^{jn(\phi_0 - \phi_{in} - \pi + \frac{\pi}{2})}, \quad (8)$$

where $k_1 = \sqrt{\epsilon_r} k_0$ and $k_1 \sin \theta_1 = \sqrt{k_1^2 - k_0^2 \cos^2 \theta_{in}}$.

3.4 T -Matrix for Isolated Cylinder

If we define the T -matrix [9] relating the m -th mode of the scattered amplitude with the incident amplitude as

$$\begin{pmatrix} A_{sm} \\ B_{sm} \end{pmatrix} = \begin{pmatrix} T_{AA}^{(m)} & T_{AB}^{(m)} \\ T_{BA}^{(m)} & T_{BB}^{(m)} \end{pmatrix} \begin{pmatrix} A_i \\ B_i \end{pmatrix}, \quad (9)$$

the the elements of the T -matrix are derived from the boundary conditions on the surface of cylinder for each modes as [9]:

$$\begin{pmatrix} T_{AA}^{(m)} & T_{AB}^{(m)} \\ T_{BA}^{(m)} & T_{BB}^{(m)} \end{pmatrix} = \mathbf{U} \mathbf{M}^{(m)-1} \mathbf{N}^{(m)}, \quad (10)$$

where the elements of the 2×4 matrix \mathbf{U} , the 4×4 matrix $\mathbf{M}^{(m)}$, and the 4×2 matrix $\mathbf{N}^{(m)}$ are given as:

$$\begin{aligned} U_{11} = U_{23} = 1, \quad U_{12} = U_{13} = U_{14} = U_{21} = U_{22} = U_{24} = 0, \quad \text{and} \quad (11) \\ \begin{aligned} M_{11}^{(m)} &= M_{23}^{(m)} = k_0^2 \sin^2 \theta_{in} H_m^{(1)}(k_0 a \sin \theta_{in}), & M_{41}^{(m)} &= j\omega \epsilon_0 k_0 \sin \theta_{in} H_m^{(1)'}(k_0 a \sin \theta_{in}), \\ M_{12}^{(m)} &= M_{24}^{(m)} = -k_1^2 \sin^2 \theta_1 J_m(k_1 a \sin \theta_1), & M_{42}^{(m)} &= -j\omega \epsilon_r \epsilon_0 k_1 \sin \theta_1 J_m'(k_1 a \sin \theta_1), \\ M_{13}^{(m)} &= M_{14}^{(m)} = M_{21}^{(m)} = M_{22}^{(m)} = 0, & N_{11}^{(m)} &= N_{22}^{(m)} = -k_0^2 \sin^2 \theta_{in} J_m(k_0 a \sin \theta_{in}), \\ M_{31}^{(m)} &= M_{43}^{(m)} = -\frac{k_0 m \cos \theta_{in}}{a} H_m^{(1)}(k_0 a \sin \theta_{in}), & N_{12}^{(m)} &= N_{21}^{(m)} = 0, \\ M_{32}^{(m)} &= M_{44}^{(m)} = \frac{k_0 m \cos \theta_{in}}{a} J_m(k_1 a \sin \theta_1), & N_{31}^{(m)} &= N_{42}^{(m)} = \frac{k_0 m \cos \theta_{in}}{a} J_m(k_0 a \sin \theta_{in}), \\ M_{33}^{(m)} &= -j\omega \mu_0 k_0 \sin \theta_{in} H_m^{(1)'}(k_0 a \sin \theta_{in}), & N_{32}^{(m)} &= j\omega \mu_0 k_0 \sin \theta_0 J_m'(k_0 a \sin \theta_{in}), \\ M_{34}^{(m)} &= j\omega \mu_0 k_1 \sin \theta_1 J_m'(k_1 a \sin \theta_1). & N_{41}^{(m)} &= -j\omega \epsilon_0 k_0 \sin \theta_0 J_m'(k_0 a \sin \theta_{in}). \end{aligned} \end{aligned}$$

For the discussion that follows, if we define the incident amplitude vector $\boldsymbol{\alpha}^{in}$ and the scattered amplitude vector $\boldsymbol{\alpha}_0^{sc}$ as

$$\boldsymbol{\alpha}^{in} = \begin{pmatrix} \mathbf{a}^{in} \\ \mathbf{b}^{in} \end{pmatrix}, \quad \boldsymbol{\alpha}_0^{sc} = \begin{pmatrix} \mathbf{a}_0^{sc} \\ \mathbf{b}_0^{sc} \end{pmatrix}, \quad (12)$$

and the T -matrix $\boldsymbol{\Upsilon}$ relating $\boldsymbol{\alpha}_0^{sc}$ with $\boldsymbol{\alpha}^{in}$ as

$$\boldsymbol{\alpha}_0^{sc} = \boldsymbol{\Upsilon} \boldsymbol{\alpha}^{in}, \quad \text{where} \quad \boldsymbol{\Upsilon} = \begin{pmatrix} \mathbf{T}^{(AA)} & \mathbf{T}^{(AB)} \\ \mathbf{T}^{(BA)} & \mathbf{T}^{(BB)} \end{pmatrix}, \quad (13)$$

the elements of $\boldsymbol{\Upsilon}$ are given by using the elements of the T -matrix for the m -th mode given in (10) as

$$T_{mn}^{(AA)} = \delta_{mn} T_{AA}^{(m)}, \quad T_{mn}^{(AB)} = \delta_{mn} T_{AB}^{(m)}, \quad T_{mn}^{(BA)} = \delta_{mn} T_{BA}^{(m)}, \quad T_{mn}^{(BB)} = \delta_{mn} T_{BB}^{(m)}. \quad (14)$$

As is found from (10), for cylinders with finite conductivity, there exists coupling between the TM and TE components when $\theta_{in} \neq \pi/2$.

4 Scattering of Plane Wave by a Regular Wire-Grid for Arbitrary Angle of Incidence and Grid Rotation

Before considering irregular wire-grids, let us consider a regular wire-grid of a periodic array of equally spaced cylinders with a spacing of h as shown in Fig. 1. In this case, the x - y dependence $\Psi^{sc}(x, y)$ of the scattered field

$$\Psi^{sc}(x, y, z) = e^{jk_0 z \cos \theta_{in}} \Psi^{sc}(x, y) \quad (15)$$

at a point (x, y, z) outside the cylinders is given by using Floquet's theorem as

$$\Psi^{sc}(x, y) = \sum_{l=-\infty}^{\infty} \mathbf{Q}_l^T \cdot \mathbf{a}_0^{sc} e^{-jlk_0 h \sin \theta_{in} \cos \phi_{in}}, \quad (16)$$

where $\mathbf{Q}_l = [H_n^{(1)}(k_0 \rho_l \sin \theta_{in}) e^{jn\phi_l}]$ with $\rho_l = \sqrt{(x - lh)^2 + y^2}$ and $\phi_l = \cos^{-1}[(x - lh)/\rho_l]$. By using Gegenbauer's addition theorem of Hankel functions given as

$$H_n^{(1)}(k_0 \rho_l \sin \theta_{in}) e^{jn\phi_l} = \sum_{m=-\infty}^{\infty} J_m(k_0 \rho_0 \sin \theta_{in}) e^{jm\phi_0} H_{n-m}^{(1)}(k_0 h l \sin \theta_{in}), \quad (17)$$

\mathbf{Q}_l is expressed as

$$\mathbf{Q}_l^T = \mathbf{P}_0^T \cdot \boldsymbol{\xi}_l \quad (l \neq 0) \quad (18)$$

where $\xi_{l,mn} = H_{n-m}^{(1)}(k_0 h l \sin \theta_{in})$.

The x - y dependence $\Psi(x, y)$ of the total field $\Psi(x, y, z) = \Psi(x, y) e^{jk_0 z \cos \theta_{in}}$ is given by

$$\Psi(x, y) = \mathbf{P}_0^T \cdot (\mathbf{a}^{in} + \mathbf{L} \cdot \mathbf{a}_0^{sc}) + \mathbf{Q}_0^T \cdot \mathbf{a}_0^{sc}. \quad (19)$$

The first and the second terms of the right-hand side of (19) are regarded as the field incident on the 0-th wire and the field scattered by the 0-th wire, respectively.

By considering the coupling between the TM and TE components given in (9), the scattered field amplitude α_0^{sc} can be expressed

$$\alpha_0^{sc} = \Upsilon \cdot (\alpha^{in} + \Lambda \cdot \alpha_0^{sc}) \quad (20)$$

by using the T -matrix Υ for isolated single wire. In (20), Λ is the lattice-sum matrix given as follows:

$$\Lambda = \begin{pmatrix} \mathbf{L} & 0 \\ 0 & \mathbf{L} \end{pmatrix}, \quad (21)$$

where the elements of \mathbf{L} are given by the lattice sum as

$$L_{m,n} = \sum_{l=-\infty, l \neq 0}^{\infty} H_{m-n}^{(1)}(lk_0 h \sin \theta_{in}) e^{-jlk_0 h \sin \theta_{in} \cos \phi_{in}}. \quad (22)$$

By solving (20) in terms of α_0^{sc} , we obtain the scattered amplitude as

$$\alpha_0^{sc} = (\mathbf{I} - \Upsilon \cdot \Lambda)^{-1} \cdot \Upsilon \cdot \alpha^{in}. \quad (23)$$

The sum of the infinite series in the right-hand side of (22), which is usually referred to as the lattice sum and is notorious for its desperately slow convergence in problems of periodic Green's functions, can be numerically calculated by an accurate and efficient method based on the Fourier integral representation of Hankel functions proposed by Yasumoto *et al.*[5] and [4].

4.1 Reflected and Transmitted Waves

From the scattered amplitude α_0^{sc} obtained above, the TM components of the reflected wave Ψ^r and the transmitted waves Ψ^t can be obtained as follows:

$$\Psi_{TM}^r(x, y, z) = \sum_{\nu=-\infty}^{\infty} \mathbf{p}_\nu^T \cdot \mathbf{a}_0^{sc} e^{j(k_{x\nu}x + k_{y\nu}y + k_0z \cos \theta_{in})} \quad (24)$$

$$\Psi_{TM}^t(x, y, z) = \sum_{\nu=-\infty}^{\infty} (\delta_{\nu 0} + \mathbf{q}_\nu^T \cdot \mathbf{a}_0^{sc}) e^{j(k_{x\nu}x - k_{y\nu}y + k_0z \cos \theta_{in})} \quad (25)$$

where

$$\mathbf{p}_\nu = \begin{bmatrix} \frac{2(-j)^m (k_{x\nu} + jk_{y\nu})^m}{hk_{y\nu}k_0^m \sin^m \theta_{in}} & (m \geq 0) \\ \frac{2j^{|m|} (k_{x\nu} - ik_{y\nu})^{|m|}}{hk_{y\nu}k_0^{|m|} \sin^{|m|} \theta_{in}} & (m < 0) \end{bmatrix} \quad \text{and} \quad \mathbf{q}_\nu = \begin{bmatrix} \frac{2(-j)^m (k_{x\nu} - ik_{y\nu})^m}{hk_{y\nu}k_0^m \sin^m \theta_{in}} & (m \geq 0) \\ \frac{2j^{|m|} (k_{x\nu} + ik_{y\nu})^{|m|}}{hk_{y\nu}k_0^{|m|} \sin^{|m|} \theta_{in}} & (m < 0) \end{bmatrix}$$

with $k_{x\nu} = \frac{2\nu\pi}{h} - k_0 \sin \theta_{in} \cos \phi_{in}$ and $k_{y\nu} = \sqrt{k_0^2 \sin^2 \theta_{in} - k_{x\nu}^2}$. The TE components of the reflected wave Ψ^r and the transmitted waves Ψ^t can be obtained similarly just by replacing \mathbf{a}_0^{sc} with \mathbf{b}_0^{sc} in (24) and (25).

It should be noted that, if $h|\sin \theta_{in}|(1 + \cos \phi_{in}) < \lambda$, only the modes with $\nu = 0$ of the transmitted and reflected waves are propagated, and other modes with $\nu \neq 0$ are

evanescent. In this particular case, the power reflection coefficient R and the power transmission coefficient T of the grid are given as

$$R_{TM} = |\mathbf{p}_0^T \cdot \boldsymbol{\alpha}_0^{sc}|^2, \quad \text{and} \quad T_{TM} = |1 + \mathbf{q}_0^T \cdot \boldsymbol{\alpha}_0^{sc}|^2, \quad (26)$$

for the TM components of reflected and transmitted waves, respectively. The power reflection coefficient R_{TE} and the power transmission coefficient T_{TE} for the TE component can be obtained similarly by replacing $\boldsymbol{\alpha}_0^{sc}$ with \boldsymbol{b}_0^{sc} in (26).

You can try calculations of regular grids on our web site[10].

5 Perturbation Theory for Slightly Irregular Wire-Grids

So far, we have assumed the wire-grid as a perfectly periodic array of equally spaced parallel wires. In this section, we consider an irregular wire-grid whose wire spacing is not perfectly uniform with slight random displacement of each wire position from its nominal position keeping the parallelism with each other. Although there might be other types of irregularity in wire-grids such as the nonuniformity in wire diameter or the nonflatness of the grid plane, experience shows that they are less significant as compared with the nonuniformity in wire spacing considering the usual fabrication method in which wire is wound on a precisely fabricated metallic frame. We, therefore, focus on the effects of irregularity in wire spacing ignoring other irregularities.

Let the random irregularity in wire spacing of a wire-grid be given by a column vector $\boldsymbol{\eta} = (\cdots, \eta_{-1}, \eta_0, \eta_1, \cdots, \eta_l, \cdots)^T$ where η_l is a random error in the x position of the center of the l -th wire from the right position lh as shown in Fig. 2. The scattering amplitude of the 0th wire given by (23) is modified for this irregular grid can be expressed as

$$\boldsymbol{\alpha}_0^{SC}(\boldsymbol{\eta}) = (\mathbf{I} - \boldsymbol{\Upsilon} \cdot \boldsymbol{\Lambda}(\boldsymbol{\eta}))^{-1} \cdot \boldsymbol{\Upsilon} \cdot \boldsymbol{\alpha}^{in}, \quad (27)$$

where $\boldsymbol{\Lambda}(\boldsymbol{\eta})$ is the lattice-sum matrix for irregular grid given by replacing lh in the lattice sum matrix given by (21) through (22) with $lh + \eta_l$. If we assume the positional errors are small variables such that $\eta_l \ll h$ ($l = \cdots - 1, 0, 1, \cdots$), $\boldsymbol{\alpha}_0^{SC}(\boldsymbol{\eta})$ can be approximated to the second order of $\boldsymbol{\eta}$ as

$$\boldsymbol{\alpha}_0^{SC}(\boldsymbol{\eta}) \simeq \boldsymbol{\alpha}_0^{SC}(\boldsymbol{\eta} = 0) + \sum_{l=-\infty}^{\infty} \left. \frac{\partial \boldsymbol{\alpha}_0^{SC}(\boldsymbol{\eta})}{\partial \eta_l} \right|_{\boldsymbol{\eta}=0} \eta_l + \frac{1}{2} \sum_{l=-\infty}^{\infty} \left. \frac{\partial^2 \boldsymbol{\alpha}_0^{SC}(\boldsymbol{\eta})}{\partial \eta_l^2} \right|_{\boldsymbol{\eta}=0} \eta_l^2, \quad (28)$$

where the partial derivatives in the right-hand side of (28) can be obtained as follows after some algebra:

$$\frac{\partial \boldsymbol{\alpha}_0^{SC}(\boldsymbol{\eta})}{\partial \eta_l} = (\mathbf{I} - \boldsymbol{\Upsilon} \boldsymbol{\Lambda}(\boldsymbol{\eta}))^{-1} \boldsymbol{\Upsilon} \frac{\partial \boldsymbol{\Lambda}}{\partial \eta_l} \boldsymbol{\alpha}_0^{SC}(\boldsymbol{\eta}), \quad (29)$$

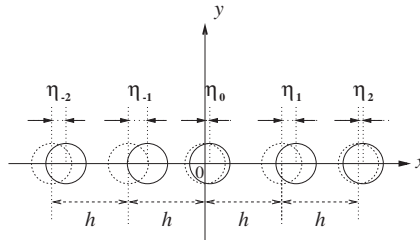


Figure 2: Irregular wire-grid with random displacements of grid positions

$$\frac{\partial^2 \alpha_0^{SC}(\boldsymbol{\eta})}{\partial \eta_l^2} = \left[(\mathbf{I} - \boldsymbol{\Upsilon} \boldsymbol{\Lambda}(\boldsymbol{\eta}))^{-1} \boldsymbol{\Upsilon} \frac{\partial^2 \boldsymbol{\Lambda}}{\partial \eta_l^2} + 2 \left\{ (\mathbf{I} - \boldsymbol{\Upsilon} \boldsymbol{\Lambda}(\boldsymbol{\eta}))^{-1} \boldsymbol{\Upsilon} \frac{\partial \boldsymbol{\Lambda}}{\partial \eta_l} \right\}^2 \right] \cdot \alpha_0^{SC}(\boldsymbol{\eta}). \quad (30)$$

If we assume that the positional errors of wires $(\dots, \eta_{-1}, \eta_0, \eta_1, \dots, \eta_l, \dots)$ are zero-mean statistically independent variables from wire to wire, we obtain the ensemble average of the scattering amplitude $\alpha_0^{SC}(\boldsymbol{\eta})$ as

$$\overline{\alpha_0^{SC}(\boldsymbol{\eta})} \simeq \alpha_0^{SC}(0) + \frac{1}{2} \sum_{l=-\infty}^{\infty} \frac{\partial^2 \alpha_0^{SC}(\boldsymbol{\eta})}{\partial \eta_l^2} \Big|_{\boldsymbol{\eta}=0} \overline{\eta^2}, \quad (31)$$

where $\alpha_0^{SC}(0) \equiv \alpha_0^{SC}(\boldsymbol{\eta} = 0)$, and $\overline{\eta^2}$ is the variance of the random positional errors of wires from their nominal positions.

By substituting (30) into (31), we obtain

$$\begin{aligned} \overline{\alpha_0^{SC}(\boldsymbol{\eta})} \simeq & \left[1 + \frac{\overline{\eta^2}}{2} \left[(\mathbf{I} - \boldsymbol{\Upsilon} \boldsymbol{\Lambda}(0))^{-1} \boldsymbol{\Upsilon} \sum_{l=-\infty}^{\infty} \frac{\partial^2 \boldsymbol{\Lambda}(\boldsymbol{\eta})}{\partial \eta_l^2} \Big|_{\boldsymbol{\eta}=0} \right. \right. \\ & \left. \left. + 2 \sum_{l=-\infty}^{\infty} \left\{ (\mathbf{I} - \boldsymbol{\Upsilon} \boldsymbol{\Lambda}(0))^{-1} \boldsymbol{\Upsilon} \frac{\partial \boldsymbol{\Lambda}(\boldsymbol{\eta})}{\partial \eta_l} \Big|_{\boldsymbol{\eta}=0} \right\}^2 \right] \right] \alpha_0^{SC}(0). \end{aligned} \quad (32)$$

In (32), the partial derivatives are taken at $\boldsymbol{\eta} = 0$, and $\boldsymbol{\Lambda}(\boldsymbol{\eta})$ is given by

$$\boldsymbol{\Lambda}(\boldsymbol{\eta}) = \begin{pmatrix} \mathbf{L}(\boldsymbol{\eta}) & 0 \\ 0 & \mathbf{L}(\boldsymbol{\eta}) \end{pmatrix}, \quad (33)$$

where $\mathbf{L}(\boldsymbol{\eta})$ is given by

$$L_{m,n}(\boldsymbol{\eta}) = S_{m-n}(\boldsymbol{\eta}) = \sum_{l=-\infty, l \neq 0}^{\infty} H_{m-n}^{(1)}(k_0(lh + \eta_l) \sin \theta_{in}) e^{-jk_0(lh + \eta_l) \sin \theta_{in} \cos \phi_{in}}. \quad (34)$$

With the aid of the recurrence formula and the Fourier integral representation of the Hankel functions as in [5], we can calculate the partial derivatives of the components of the lattice-sum matrix by using

$$\frac{\partial S_n}{\partial \eta_l} \Big|_{\boldsymbol{\eta}=0} = (-1)^n \frac{j e^{jk_x lh}}{k_0^n \sin^n \theta_{in}} \times \int_{-\infty}^{\infty} \frac{[\xi + j\kappa(\xi)]^m [k_x + \kappa(\xi)]}{\kappa(\xi)} e^{j\kappa(\xi)lh} d\xi, \quad (35)$$

and

$$\sum_{l=-\infty}^{\infty} \frac{\partial^2 S_n}{\partial \eta_l^2} \Big|_{\boldsymbol{\eta}=0} = (-1)^{n+1} \frac{e^{jk_x h}}{\pi k_0^n \sin^n \theta_{in}} \times \int_{-\infty}^{\infty} \frac{[\xi + j\kappa(\xi)]^m [k_x + \kappa(\xi)]^2}{\kappa(\xi)} \frac{e^{j\kappa(\xi)h}}{1 - e^{j[k_x + \kappa(\xi)]h}} d\xi, \quad (36)$$

where $k_x = -k_0 \sin \theta_{in} \cos \phi_{in}$ and

$$\kappa(\xi) = \begin{cases} \sqrt{k_0^2 \sin^2 \theta_{in} - \xi^2} & \text{for } k_0 \sin \theta_{in} \geq |\xi|, \\ j\sqrt{\xi^2 - k_0^2 \sin^2 \theta_{in}} & \text{for } k_0 \sin \theta_{in} < |\xi|. \end{cases} \quad (37)$$

Once the scattered amplitude vector $\overline{\alpha_0^{sc}}$ is obtained from (32), the reflection and transmission coefficient of the irregular wire-grid can be obtained from (26), and corresponding equations for the *TE* components with (32) and (12).

6 Comparison of Numerical Calculations with Measurements

To validate the effectiveness of the proposed theory in estimating the characteristics of practical freestanding wire-grids, results of numerical calculations are compared with results of measurements made for actual wire-grids with different irregularities.

The conditions for the numerical calculations and the measurements were as follows:

- the material of wires: tungsten ($\sigma^{-1} = 5.5 \times 10^{-8} \Omega\text{m}$ [6]).
- the wire diameter: $2a = 10 \mu\text{m}$, the nominal spacing between wires: $h = 25 \mu\text{m}$.
- the angle of incidence: $\chi = 45^\circ$.

Measurements were made for two wire-grids with different degree of irregularity. We, hereafter, refer to the one with less irregularity as Grid #1 and to the other as Grid #2. Figures 3 show the microscopic images of the grid planes of Grid #1 and #2 along with their probability distributions of the displacements of wires from nominal positions. From Figs. 3(b1) and (b2), the standard deviations $\sigma_\eta (= \sqrt{\eta^2})$ of the displacements of wires from their nominal positions are estimated to be 22.7 % and 52 %, respectively, of the nominal wire spacing ($h = 25 \mu\text{m}$).

Figs. 4(a) and (b) show the transmission and reflection coefficients, respectively, for the case of TE -wave incidence where the incident electric field is orthogonal to the direction of wires. The solid curves show the characteristics calculated for ideal grid without irregularity, and the dashed, dash-dot, and dotted curves show the characteristics calculated for irregular grids whose irregularities σ_η are assumed to be 20% ($\sigma_\eta = 0.20 h$), 40% ($\sigma_\eta = 0.40 h$), and 50 % ($\sigma_\eta = 0.50 h$) of the nominal wire spacing. Calculated results are shown for two different grid rotation angles, $\phi_g = 0^\circ$ (denoted as G_{perp}) and 90° (denoted as G_{para}), by thin and thick curves, respectively. In these Figures, E_{perp} and E_{para} denote the characteristics for the transmitted or reflected electric field component perpendicular and parallel to the plane of incidence,

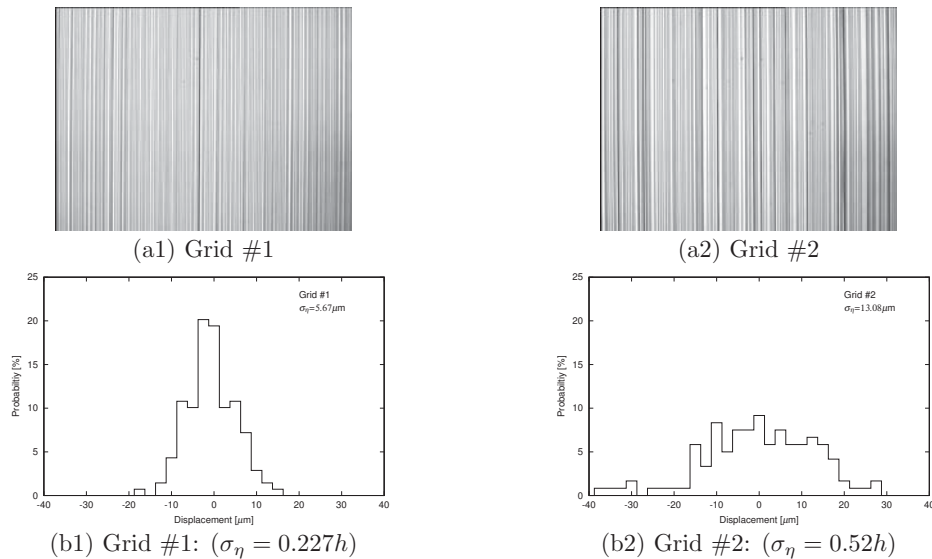


Figure 3: Microscopic images (top), and the probability distributions of the positional errors of wires from nominal positions (bottom) of measured wire-grids.

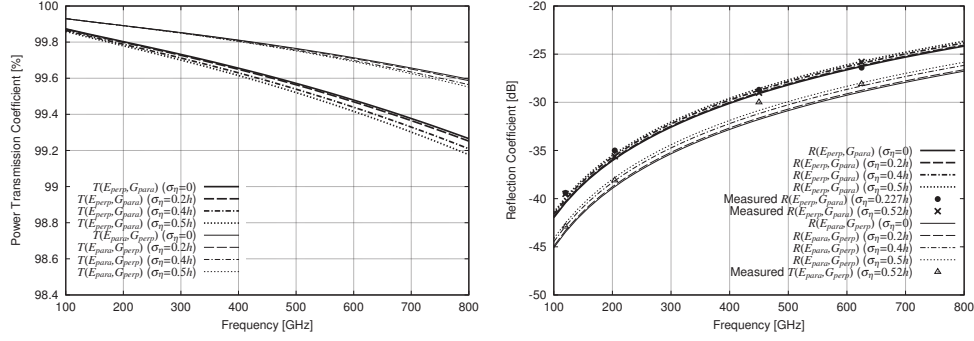


Figure 4: Transmission and reflection coefficients of regular ($\sigma_\eta = 0$) and irregular wire-grids for TE wave incidence. ($2a = 10\mu\text{m}$, $h = 25\mu\text{m}$, $\chi = 45^\circ$). E_{perp} and E_{para} denote the cases that the incident electric field is perpendicular and parallel to the plane of incidence, respectively. G_{perp} and G_{para} denote the cases that the wire is perpendicular ($\phi_g = 0^\circ$) and parallel ($\phi_g = 90^\circ$) to the plane of incidence, respectively.

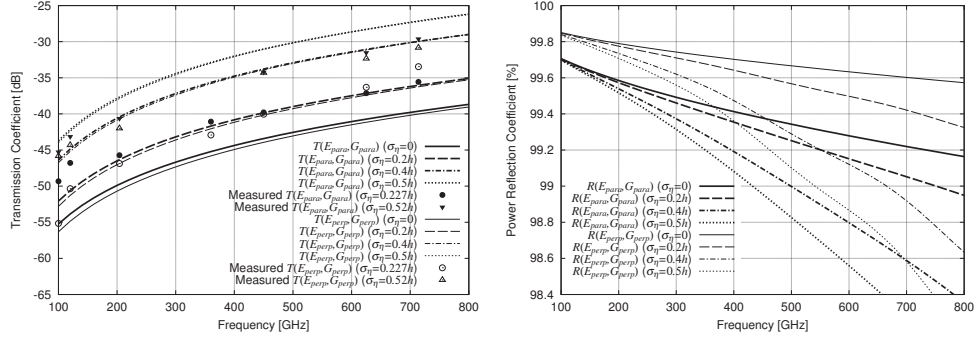


Figure 5: Transmission and reflection coefficients of regular ($\sigma_\eta = 0$) and irregular wire-grids for TM wave incidence. Same as in Fig. 4.

respectively. Measurement results for Grid #1 and Grid #2 are also shown in these Figures. The corresponding results of calculations and measurements for the case of TM -wave incidence are also shown in Figs. 5(a) and (b).

By comparing Fig. 4 and Fig. 5, it is found that the transmission and reflection characteristics of wire-grid are significantly affected by the grid irregularity when the incident wave has electric field component parallel to the grid wires (TM -wave incidence) as shown in Fig. 5, while the grid irregularity has little effect on its characteristics when the electric field of the incident wave was perpendicular to the grid wires (TE -wave incidence) as shown in Fig. 4. This can be explained by the fact that large currents are effectively induced on grid wires in the TM -wave incident case where the incident wave has a electric field component parallel to the wires, while currents are not effectively induced on grid wires in the TE -wave incident case where the incident wave does not have electric field component parallel to the wires.

Measurement results for Grid #1 and Grid #2 are also shown in Figs. 4(b) and 5(a) for comparison. From comparison between these measurement and calculation results, it is found that the measurement results for Grid #1 whose standard deviation of wire position irregularity σ_η was 22.7 % of the nominal wire spacing h agrees well with the theoretically calculated characteristics for $\sigma_\eta = 0.20h$. For the more irregular Grid #2

whose standard deviation of wire position irregularity was 52 % of h , the general trend of the different dependence of the characteristics on the grid irregularity between the TM and TE -wave incident cases agrees well with the measurement results, although the theoretical calculation results are found to overestimate the effects of irregularity as compared with the measurement results. This suggests that the irregularity of 52 % of wire spacing might be too large for the perturbation theory of irregular grid presented in Section 5 to be applicable.

7 Conclusion

In the first half of this paper, an accurate and computationally efficient method was presented for calculating the transmission and reflection characteristics of wire-grids of a periodic array of cylinders for arbitrary angles of incidence and grid rotation.

In the latter half of this paper, a method to calculate the effects of slight irregularity in wire spacing of grid was proposed by treating the irregular displacements of wire positions as a small perturbation to the theory of regular grid derived in the first half of this paper. Measurements made for actual wire-grids in millimeter- and submillimeter wavelengths have demonstrated that this perturbation theory was applicable to slightly irregular wire-grids whose standard deviation of the displacements of wire positions is less than about 30 % of the nominal wire spacing.

Acknowledgment

The authors would like to thank Prof. Kiyotoshi Yasumoto of Kyushu University for his elucidating comments and discussions on the use of an efficient calculation method that utilizes the lattice sums and T -matrix developed by him.

References

- [1] T. Larsen, "A Survey of the Theory of Wire Grids," *IRE Trans. Microwave Theory Tech.*, vol. 10, pp. 191-201, 1962.
- [2] J. Wait, "Reflection at arbitrary incidence from a parallel wire grid," *Appl. Sci. Research*, vol. B4, pp. 393-4000, 1955.
- [3] W. G. Chambers, C. L. Mok, and T. J. Parker, "Theory of the scattering of electromagnetic waves by regular grid of parallel cylindrical wires with circular cross section," *J. Phys. A: Math. Gen.*, vol. 13, pp. 1433-1441, 1980.
- [4] K. Kushta and K. Yasumoto, "Electromagnetic scattering from periodic arrays of two circular cylinders per unit cell," *Progress in Electromagnetics Research PIERs*, vol. 29, pp. 69-85, 2000.
- [5] K. Yasumoto and K. Yoshitomi, "Efficient calculation of lattice sums for free-space periodic Green's function," *IEEE Trans. Antennas Propagat.*, vol. 47, no. 6, pp. 1050-1055, June, 1999.
- [6] W. G. Chambers, T. J. Parker, and A. E. Costley, "Freestanding fine-wire grids for use in millimeter and submillimeter-wave spectroscopy," in *Infrared and Millimeter Waves*, vol. 16, K. J. Button, Ed. New York: Academic Press, 1986, pp. 77-106.
- [7] J. B. Shapiro and E. E. Bloemhof, "Fabrication of wire-grid polarizers and dependence of submillimeter-wave optical performance on pitch uniformity," *Int. J. Infrared Millimeter Waves*, vol. 11, no. 8, pp. 973-980, Aug. 1990.
- [8] M. Houde, R. L. Akeson, J. E. Carlstrom, J. W. Lamb, D. A. Schleuning, and D. P. Woody, "Polarizing grids, their assemblies and beams of radiation," *Publ. Astron. Soc. Pacific.*, vol. 113, pp. 622-638, May, 2001.
- [9] A. Ishimaru, *Electromagnetic Wave Propagation, Radiation, and Scattering*, Chap. 11 and Chap. 12, Prentice Hall, Englewoods Cliffs, 1991.
- [10] <http://www.crl.go.jp/dk/c214/smiles/grid/grid-calc.html>

Sinichiro Asayama
Osaka Prefecture University
1-1 Gakuen-Cho
Sakai-City, Osaka 599-8531
Japan
Phone: +72 (254) 9726
Fax: +72 (254) 9726
Email: *asayama@deal.cias.osakafu-u.ac.jp*

Andrey Baryshev
SRON/NOVA
Landleven 12 Postbus 800
Groningen 9700AV
Netherlands
Phone: +315 (0) -363-8287
Fax: +315 (0) -363-4033
Email: *andrey@sron.rug.nl*

Jochem Baselmans
SRON
Landleven 12
Groningen 9747 AV
Netherlands
Phone: +315 (0) -363-6648
Fax: +315 (0) -363-4033
Email: *j.baselmans@sron.nl*

Robert Bass
University of Virginia
351 McCormick Rd.
Charlottesville, VA 22904
United States of America
Phone: (434) 982-2262
Fax: (434) 924-8818
Email: *rbass@virginia.edu*

Jean Baubert
Chalmers University of Technology
MC2 Chalmers T.U.
Gothenburg SE-41296
Sweden
Phone: +46 (0) -31-772535
Fax: +46 (0) -31-164513
Email: *jbbaubert@yahoo.fr*

Dominic Benford
NASA GSFC
NASA/GSFC Code 685
Greenbelt, MD 20771
United States of America
Phone: (301) 286-8771
Fax: (301) 286-1617
Email: *dominic.benford@nasa.gov*

Rachel Berry
MRAO, University of Cambridge
MRAO
Madingley Rd.
Cambridge CB3 0HE
United Kingdom
Phone: +44- (0) -1223-337372
Fax: +44- (0) -1223-354599
Email: *rhb21@cam.ac.uk*

Albert Betz
University of Colorado
CASA 1255 38th St.
Boulder, CO 80309
United States of America
Phone: (303) 492-4880
Fax: (303) 492-5941
Email: *betz@casa.colorado.edu*

Dan Bock
Carnegie Mellon University
Department of Physics
Carnegie Mellon University
Pittsburgh, PA 15213
United States of America
Phone: (412) 268-1866
Fax: (412) 681-0648
Email: *dbock@andrew.cmu.edu*

Edward Campbell
Cambridge University
Cavendish Lab
Madingley Rd.
Cambridge CB3 0HE
United Kingdom
Phone: +44 (1223) 337247
Fax: +44 (1223) 354594
Email: esc24@mrao.cam.ac.uk

Goutam Chattopadhyay
Caltech/JPL
320-47, Caltech
Pasadena, CA 91125
United States of America
Phone: (626) 395-3741
Fax: (626) 796-8806
Email: goutam@caltech.edu

Hong-Wen Cheng
Academia Sinica Institute of Astronomy
and Astrophysics
ASIAA, P.O. Box 23-141
Taipei 106
Taiwan
Phone: +886 (2) 33652200
Fax: +886 (2) 23677849
Email: hwcheng@asiaa.sinica.edu.tw

Jingquan Cheng
NRAO
949 N. Cherry Ave.
Tucson, AZ 85721
United States of America
Phone: (520) 882-8250 x130
Fax: (520) 882-7955
Email: jcheng@nrao.edu

Chi Chin
Hertzberg Institute of Astrophysics
5071 W. Saanich Rd.
Victoria, BC V9E 2E7
Canada
Phone: (250) 363-0039
Fax: (250) 363-0045
Email: chi-chung.chin@nrc.ca

Stephane Claude
NRC
5071 W. Saanich Rd.
Victoria, BC V9E 2E7
Canada
Phone: (250) 363-0030
Fax: (250) 363-0045
Email: stephane.claude@nrc.ca

Charles Cunningham
NRC
5071 W. Saanich Rd.
Victoria, BC V9E 2E7
Canada
Phone:
Fax:
Email: charles.cunningham@nrc.ca

Larry D'Addario
NRAO
949 N. Cherry Ave.
Tucson, AZ 85721
United States of America
Phone: (520) 882-8250 x123
Fax: (520) 882-7955
Email: ldaddari@nrao.edu

Thijs de Graauw
SRON
P.O. Box 800
Groningen 9700AV
Netherlands
Phone: +31 (50) 363 4031
Fax: +31 (50) 363 6100
Email: thijsdg@sron.rug.nl

Gerhard de Lange
SRON
Landleven 12
Groningen 9747 AD
Netherlands
Phone: +31 (50) 3634051
Fax: +31 (50) 3634033
Email: gert@sron.rug.nl

Carmen Diez
Observatorio Astronomico Nacional
Centro Astronomico de Yeres Appo. 148
Guadalajara 19080
Spain
Phone: +34 (94) 929 0311
Fax: +34 (94) 929 0063
Email: *m.diez@oan.es*

Yiwei Duan
Univerisity of Virginia
112C Chelsea Dr.
Charlottesville, VA 22903
United States of America
Phone: (434) 982-2377
Fax: (434) 924-8818
Email: *yd3v@virginia.edu*

Erik Duerr
MIT Lincoln Laboratories
244 Wood St. E124F
Lexington, MA 02420
United States of America
Phone: (781) 981-0119
Fax: (781) 981-3867
Email: *duerr@ll.mit.edu*

Jack East
University of Michigan
2301 EECS
University of Michigan
Ann Arbor, MI 48109
United States of America
Phone: (734) 763-0212
Fax:
Email: *jeast@eecs.umich.edu*

Mick Edgar
Caltech
Downs 320-47
Pasadena, CA 91125
United States of America
Phone: (626) 395-3740
Fax: (626) 796-8806
Email:

Geoffrey Ediss
NRAO
2015 Ivy Rd. Ste. 219
Charlottesville, VA 22903
United States of America
Phone: (434) 296-0245
Fax: (434) 296-0324
Email: *gediss@nrao.edu*

Anders Emrich
Omnisys
Gruvgatan 8
Vastra Frolunda 421 30
Sweden
Phone: +46 (31) 734 3401
Fax: +46 (31) 734 3429
Email: *ae@omnisys.se*

Neal Erickson
University of Massachussets
University of Massachussets
Lederle 619
Amherst, MA 01003
United States of America
Phone: (413) 545-1873
Fax: (413) 545-4223
Email: *neal@astro.umass.edu*

Robert Ferber
JPL
4800 Oak Grove Dr.
Pasadena, CA 91109
United States of America
Phone: (818) 354-3463
Fax: (818) 393-6984
Email: *robert.r.ferber@jpl.nasa.gov*

Paolo Focardi
JPL
4800 Oak Grove Dr.
Pasadena, CA 91109
United States of America
Phone: (818) 354-0781
Fax: (818) 393-4683
Email: *paolo@merlin.jpl.nasa.gov*

Andy Fung
JPL
4800 Oak Grove Dr.
Pasadena, CA 91109
Phone: (818) 354-1832
Fax: (818) 393-4683
Email: *andy.fung@jpl.nasa.gov*

J. Gallego
Observatorio Astronomico Nacional
Centro Astronomico de Yebes
Guadalajara, APDO 148 14080
Spain
Phone: +34 (94) 929 0311
Fax: +34 (94) 929 0063
Email: *jd.gallego@oan.es*

Jianrong Gao
SRON/T.U. Delft
Lorentzweg 1
Delft 2628-CJ
Netherlands
Phone: +31 (15) 278 1570
Fax: +31 (15) 278 1413
Email: *j.r.gao@tnw.tudelft.nl*

Eyal Gerecht
NIST
325 Broadway
Boulder, CO 80305
United States of America
Phone: (303) 497-4149
Fax: (303) 497-3970
Email: *gerecht@boulder.nist.gov*

Gregory Gol'tsman
Moscow State Pedagogical University
29 M. Pirogovskaya Str.
Moscow 119 992
Russia
Phone: +71 (095) 246 1202
Fax: +71 (095) 246 6321
Email: *goltsman00@mail.ru*

Urs Graf
KOSMA, University of Cologne
Zuelpicher Str. 77
Koeln 50937
Germany
Phone: +49 (221) 470 4092
Fax: +49 (221) 470 5162
Email: *graf@ph1.uni-koeln.de*

Paul Grimes
Astrophysics Group, University of
Cambridge
Cavendish Laboratories, Madingley Rd.
Cambridge CB3 0HE
United Kingdom
Phone: +44 (1223) 337278
Fax:
Email: *p.grimes@mrao.cam.ac.uk*

Christopher Groppi
University of Arizona
933 N. Cherry Ave.
Tucson, AZ 85721
United Kingdom
Phone: (520) 621-6535
Fax: (520) 621-1532
Email: *cgroppi@as.arizona.edu*

Dazhen Gu
University of Massachusetts
55 Colonial Village
Amherst, MA 01002
United States of America
Phone: (413) 545-2170
Fax:
Email: *dgu@ecs.umass.edu*

Robert Hadfield
NIST
325 Broadway
Boulder, CO 80305
United States of America
Phone: (303) 497-5309
Fax:
Email: *hadfield@boulder.nist.gov*

Mark Hagmann
Deseret Electronics Research Corp.
762 Lacey Way
North Salt Lake, UT 84054
United States of America
Phone: (801) 936-0676
Fax: (801) 936-0676
Email: *dercorp@yahoo.com*

Merlijn Hajenius
SRON
Apothekersweg 282
Delft 2625 DZ
Netherlands
Phone: +31 (62) 757 6285
Fax: +31 (15) 278 1513
Email: *m.hajenius@tnw.tudelft.nl*

William Hatch
JPL
4800 Oak Grove Dr.
Pasadena, Ca 91109
United Kingdom
Phone: (818) 354-6387
Fax: (818) 393-4683
Email: *william.hatch@jpl.nasa.gov*

Jeffrey Hesler
Virginia Diodes Inc.
321 W. Main St.
Charlottesville, VA 22903
United States of America
Phone: (434) 924-6106
Fax: (434) 924-8818
Email: *jlh6r@virginia.edu*

Ronald Hesper
SRON/NOVA
Postbus 800
Groningen 9700 AV
Netherlands
Phone: +31 (50) 363 8287
Fax: +31 (50) 363 4033
Email: *hesper@sron.rug.nl*

John Hong
Astronomy and Physics Directorate
Jet Propulsion Laboratory
MS 180-704
4800 Oak Grove Dr.
Pasadena, CA 91109
United States of America
Phone: (818) 354-0720
Fax: (818) 354-2964
Email: *john.h.hong@jpl.nasa.gov*

Rudy Hoogeveen
SRON
Sorbonelaan 2
Utrecht 3584 CA
Netherlands
Phone: +31 (20) 253 5703
Fax: +31 (20) 254 0860
Email: *r.hoogeveen@sron.nl*

Heinz-Wilhelm Hubers
German Aerospace Center (DLR)
Rutherfordstr. 2
Berlin 12489
Germany
Phone: +44 (30) 670 55596
Fax: +49 (30) 670 55507
Email: *heinz-wilhelm.hubers@dlr.de*

Mattias Ingvarson
Microwave Electronics Laboratory,
Chalmers University
Kemivagen 9
Goteborg SE-41296
Sweden
Phone: +46 (31) 772 1836
Fax: +46 (31) 164513
Email: *mattias.ingvarson@ep.chalmers.se*

Hiroshi Ito
NTT Photonics Laboratories
3-1 Morinosato Wakamiya
Atsugi, Kanagawa 243-0198
Japan
Phone: +81 (46) 240 2885
Fax: +81 (46) 240 4306
Email: *hiro@aecl.ntt.co.jp*

Karl Jacobs
KOSMA, University of Cologne
Zuelpicher Str. 77
Koeln D-50937
Germany
Phone: +49 (221) 470 3484
Fax: +49 (221) 470 5162
Email: *jacobs@ph1.uni-koeln.de*

Hamid Javadi
JPL
4800 Oak Grove Dr.
Pasadena, CA 91109
United States of America
Phone: (818) 354-5655
Fax: (818) 393-4683
Email: *hamid.h.javadi@jpl.nasa.gov*

Boris Karasik
JPL
4800 Oak Grove Dr.
Pasadena, CA 91109
United States of America
Phone: (818) 393-4438
Fax: (818) 393-4683
Email: *boris.s.karasik@jpl.nasa.gov*

Alexandre Karpov
Caltech
Downs Lab 320-47
Pasadena, CA 91125
United States of America
Phone: (626) 395-8588
Fax: (626) 796-8806
Email: *karpov@submm.caltech.edu*

Jonathan Kawamura
JPL
4800 Oak Grove Dr.
MS 168-314
Pasadena, CA 91109
United States of America
Phone: (818) 393-4779
Fax: (818) 393-4683
Email:
jonathan.h.kawamura@jpl.nasa.gov

Anthony Kerr
NRAO
2015 Ivy Rd. Ste. 219
Charlottesville, VA 22903
United States of America
Phone: (434) 296-0363
Fax: (434) 296-0324
Email: *akerr@nrao.edu*

Pete Kirby
Georgia Institute of Technology
855 W. Peachtree St. Unit 1133
Atlanta, GA 30308
United States of America
Phone: (404) 385-3018
Fax: (404) 894-0222
Email: *pkirby@ece.gatech.edu*

Erik Kollberg
Chalmers University of Technology
Chalmers University of Technology
Department of Microelectronics
Gothenburg SE-41296
Sweden
Phone: +46 (31) 772 1841
Fax: +46 (31) 164513
Email: *kollberg@ep.chalmers.se*

Jacob Kooi
Caltech
Caltech
MS 320-47
Pasadena, CA 91125
United States of America
Phone: (626) 395-4286
Fax: (626) 796-8806
Email: *kooi@submm.caltech.edu*

Attila Kovacs
Caltech
Caltech
MS 320-47
Pasadena, CA 91125
United States of America
Phone: (626) 395-2648
Fax: (626) 796-8806
Email: *attila@submm.caltech.edu*

Jean-Michel Krieg
LERMA - Observatoire de Paris
77 avenue Deufert Rochereau
Paris 75014
France
Phone: +33 (140) 512109
Fax: +33 (140) 40512002
Email: *krieg@mesio.observ.iaa.fr*

Matthias Kroug
Delft University of Technology
Feldmannweg 17
Delft 2628 CT
Netherlands
Phone:
Fax:
Email: *kroug@tnw.tudelft.nl*

Lars Landen
Microwave Engineering Laboratory,
Chalmers Univ. / Omnisys Instruments
AB
Kemivagen 9
Goteborg SE-41296
Sweden
Phone: +46 (31) 773612
Fax: +46 (31) 164513
Email: *landen@ep.chalmers.se*

Mark Lee
Bell Laboratories - Lucent Technologies
Rm, 1C-360
600 Mountain Ave.
Murray Hill, NJ 07922
United States of America
Phone: (908) 582-7697
Fax: (908) 582-4868
Email: *markl@lucent.com*

Bruno Leone
European Space Agency
Keplerlaan 1
Noordwijk 2201 AZ
Netherlands
Phone: +31 (71) 565 3185
Fax: +31 (71) 565 5430
Email: *bruno.leone@esa.int*

Dan Lester
University of Texas
University of Texas
Department of Astronomy C1400
Austin, TX 78712
United States of America
Phone: (512) 471-3442
Fax: (512) 471-6016
Email: *dfl@astro.utexas.edu*

Arthur Lichtenberger
University of Virginia
University of Virginia
Department of Electrical Engineering
Charlottesville, VA 22903
United States of America
Phone: (434) 989-2000
Fax: (434) 924-6085
Email: *awll1@virginia.edu*

Fred Lo
NRAO
NRAO Headquarters
520 Edgemont Rd.
Charlottesville, VA 22903
United States of America
Phone: (434) 296-0241
Fax:
Email: *flo@nrao.edu*

Isaac Lopez-Fernandez
Observatorio Astronomico Nacional
Centro Astronomico de Yebes, Apartado
148
Guadalajara 19080
United States of America
Phone: +34 (94) 929 0311
Fax: +31 (94) 929 0063
Email: *i.lopez@oan.es*

Frank Maiwald
JPL
4800 Oak Grove Dr.
#168-314
Pasadena, CA 91109
United States of America
Phone: (818) 354-0214
Fax: (818) 393-4683
Email: *fmaiwald@mail1.jpl.nasa.gov*

Takeshi Manabe
Communications Research Laboratory
4-2-1 Nukui-Kitamachi
Koganei, Tokyo 184-8795
Japan
Phone: +81 (42) 327 7544
Fax: +81 (42) 327 6110
Email: *manabe@crl.go.jp*

Robert Martin
ASIAA - Hawaii Operations
82 Pu'uuhonu Pl. Ste. 210
Hilo, HI 96720
United States of America
Phone: (808) 933-8126
Fax:
Email: *robert@asiaa.sinica.edu.tw*

Imran Mehdi
JPL
4800 Oak Grove Dr.
168-314
Pasadena, CA 91109
United States of America
Phone: (818) 354-2001
Fax: (818) 393-4683
Email: *imran.mehdi@jpl.nasa.gov*

Harald Merkel
Chalmers University of Technology
Kemigarden 9
Goteborg 412 96
Sweden
Phone: +46 (31) 772 1848
Fax: +46 (31) 164513
Email: *harald@ep.chalmers.se*

Harvey Moseley
NASA GSFC
NASA GSFC
Code 685
Bldg. 21
Rm. 066
Greenbelt, MD 20678
United States of America
Phone: (301) 286-2347
Fax: (301) 286-7230
Email: *moseley@stars.gsfc.nasa.gov*

Eric Mueller
Coherent Inc.
Coherent DEOS
Hartford, CT
United States of America
Phone: (860) 243-9557
Fax:
Email: *eric.mueller@coherentinc.com*

Alessandro Navarrini
Radio Astronomy Laboratory, Berkeley
601 Campbell Hall
Berkeley, CA 94720
United States of America
Phone: (510) 642-6839
Fax: (510) 642-3411
Email: *navarrin@astro.berkeley.edu*

Takashi Noguchi
Nobeyama Radio Observatory
462-2 Nobeyama, Minamimaki
Nagano 384-1305
Japan
Phone: +81 (26) 798 4364
Fax: +81 (26) 798 2927
Email: *noguchi@nro.nao.ac.jp*

Hideo Ogawa
Osaka Prefecture University
1-1 Gakuen Cho
Sakai City, Osaka 599 8531
Japan
Phone: +81 (72) 264 9726
Fax: +81 (72) 254 9726
Email: *ogawa@el.cias.osakafu-u.ac.jp*

Michael Olbrich
University of Cologne
Zuelpicher Str. 77
Koeln D-50937
Germany
Phone: +49 (221) 470 6147
Fax: +49 (221) 470 6727
Email: *olbrich@ph1.uni-koeln.de*

John Papapolymerou
Georgial Tech
777 Atlantic Dr.
Atlanta, GA 30332
United States of America
Phone: (404) 894-5250
Fax: (404) 894-0222
Email: *papapol@ece.gatech.edu*

Ferdinand Patt
ASIAA - Hawaii
82 Pu'uhonu Pl. #210
Hilo, HI 96720
United States of America
Phone: (808) 933-6964
Fax: (808) 933-6948
Email: *fpatt@sma.hawaii.edu*

John Payne
NRAO
949 N. Cherry Ave.
Tucson, AZ 85721
United States of America
Phone: (520) 882-8250 x118
Fax: (520) 882-7955
Email: *jpayne@nrao.edu*

John Pearson
JPL
4800 Oak Grove Dr.
Pasadena, CA 91109
United States of America
Phone: (818) 354-6822
Fax: (818) 398-2430
Email: *jep@spec.jpl.nasa.gov*

Antonio Pefetto
NRAO
949 N. Cherry Ave.
Tucson, AZ 85721
United States of America
Phone: (520) 882-8250 x140
Fax: (520) 882-7955
Email: *aperfett@nrao.edu*

David Pukala
JPL
4800 Oak Grove Dr.
168-314
Pasadena, CA 91109
United States of America
Phone: (818) 354-4602
Fax: (818) 393-4683
Email: *david.pukala@jpl.nasa.gov*

Simon Radford
NRAO
949 N. Cherry Ave.
Tucson, AZ 85721
United States of America
Phone: (520) 882-8250 x125
Fax: (520) 882-7955
Email: *sradford@nrao.edu*

Matthew Reese
Yale University
15 Prospect St.
Room 405 B.C.
New Haven, CT 06511
United States of America
Phone: (203) 432-4270
Fax: (203) 432-4283
Email: *matthew.reese@yale.edu*

Fernando Rodriguez-Morales
University of Massachusetts
University of Massachusetts
Department of Electrical and Computer
Engineering
Amherst, MA 01003
United States of America
Phone:
Fax:
Email:

Aric Sanders
Yale University
15 Prospect St. Room 405 B.C.
New Haven, CT 06520
United States of America
Phone: (203) 432-4270
Fax: (203) 432-4283
Email: *aric.sanders@yale.edu*

Erich Schlecht
JPL
4800 Oak Grove Dr.
168-314
Pasadena, CA 91109
United States of America
Phone: (818) 354-4887
Fax: (818) 393-4683
Email: *erich.schlecht@jpl.nasa.gov*

Jonathan Schultz
University of Virginia
351 McCormick Rd.
Charlottesville, VA 22904
United States of America
Phone: (434) 982-2262
Fax: (434) 924-8818
Email: *jcs4x@virginia.edu*

Karl Schuster
IRAM
300 Rue de la Piscine
St. Martin d'Herès 38406
France
Phone: +33 (47) 682 4900
Fax: +33 (47) 651 5938
Email: *schuster@iram.fr*

Masumichi Seta
Communications Research Laboratory
4-2-1 Nukui-Kitamachi
Koganei, Tokyo 184-8795
United States of America
Phone: +81 (42) 327 5367
Fax: +81 (42) 327 6110
Email: *seta@crl.go.jp*

Mark Sherwin
UC Santa Barbara
Physics Department
University of California
Santa Barbara, CA 93106
United States of America
Phone: (805) 893-3774
Fax: (805) 893-3307
Email: *sherwin@physics.ucsb.edu*

Anders Skalare
JPL
4800 Oak Grove Dr.
168-314
Pasadena, CA 91109
United States of America
Phone: (818) 354-9383
Fax: (818) 393-4683
Email: *anders.skalare@jpl.nasa.gov*

Jan Stake
Microwave Electronics Laboratory,
Chalmers University
Kemivägen 9
Göteborg SE-41296
Sweden
Phone: +46 (31) 772 4983
Fax: +46 (31) 164513
Email: *jan.stake@ep.chalmers.se*

Antony Stark
Smithsonian Astrophysical Observatory
60 Garden St.
MS12
Cambridge, MA 02138
United States of America
Phone: (617) 496-7648
Fax:
Email: *aas@cfa.harvard.edu*

Robert Stupak
University of Arizona
933 N. Cherry Ave.
Tucson, AZ 85721
United States of America
Phone: (520) 621-7928
Fax: (520) 621-1532
Email: *rstupak@cfa.harvard.edu*

Masahiro Sugimoto
University of Tokyo / National
Astronomical Observatory of Japan
2-21-1 Osawa
Mitaka, Tokyo 181-8588
Japan
Phone: +81 (42) 234 3972
Fax: +81 (42) 234 4764
Email: *masahiro.sugimoto@nao.ac.jp*

Rafael Teipen
KOSMA/University of Cologne
Zuelpicher Str. 77
Koeln 50937
Germany
Phone: +49 (221) 470 3489
Fax: +49 (221) 470 5962
Email: *rteipen@ph1.uni-koeln.de*

Dorsey Thacker
NRAO
2015 Ivy Rd.
Charlottesville, VA 22903
United States of America
Phone: (434) 296-0214
Fax: (431) 296-0324
Email: *sthacker@nrao.edu*

Yoshinori Uzawa
Kansai Advanced Research Center, CRL
588-2 Iwaka, Iwaka-cho, Nishi-ku
Kobe 651-2492
Japan
Phone: +81 (78) 969 2159
Fax: +81 (78) 969 2199
Email: *uzawa@crl.go.jp*

Anastasios Vayonakis
Caltech
Downs Lab 320-47
Pasadena, CA 91125
United States of America
Phone: (626) 395-2601
Fax: (626) 796-8806
Email: *avayonak@submm.caltech.edu*

Christopher Walker
University of Arizona
933 N. Cherry Ave.
Tucson, AZ 85721
United States of America
Phone: (520) 621-8783
Fax: (520) 621-1532
Email: *cwalker@as.arizona.edu*

John Ward
JPL
4800 Oak Grove Dr.
168-314
Pasadena, CA 91109
United States of America
Phone: (818) 393-5902
Fax: (818) 393-4683
Email: *john.ward@jpl.nasa.gov*

Nick Whyborn
SRON
PO Box 800
Groningen 9700 AV
Netherlands
Phone: +31 (50) 363 4074
Fax: +31 (50) 363 4033
Email: *nick@sron.rug.nl*

Wolfgang Wild
SRON
PO Box 800
Groningen NL-9700 AV
Netherlands
Phone: +31 (50) 363 4074
Fax: +31 (50) 363 4033
Email: *wild@astro.rug.nl*

Daniel Wirtz
KOSMA, University of Cologne
Laudahn Str. 6
Koeln 50937
Germany
Phone: +49 (221) 470 3560
Fax: +49 (221) 470 5162
Email: *wirtz@ph1.uni-koeln.de*

Edward Wollack
Nasa GSFC
NASA GSFC
Code 685
Bldg 21
Rm 064
Greenbelt, MD 20771
United States of America
Phone: (301) 286-1379
Fax: (301) 286-7230
Email:
edward.wollack.1@gsfc.nasa.gov

Ge Wu
University of Wuppertal
Ranier-Gruenter-Str. 21
Wuppertal 42119
Germany
Phone: +49 (202) 439 1935
Fax: +49 (202) 439 1045
Email: *ge.wu@uni-wuppertal.de*

Kecheng Xiao
Harvard Smithsonian Center for
Astrophysics
60 Garden St.
MS-12
Cambridge, MA 01238
United States of America
Phone: (617) 496-7691
Fax: (617) 384-7830
Email: *kxiao@cfa.harvard.edu*

Qun Xiao
University of Virginia
Electrical Engineering Department
University of Virginia
Charlottesville, VA 22903
United States of America
Phone: (434) 924-6575
Fax:
Email: *qx9e@virginia.edu*

Ghassan Yassin
University of Cambridge
Cavendish Laboratory
Madingley Rd.
Cambridge CB3 0HE
United Kingdom
Phone: +44 (122) 333 7309
Fax: +44 (122) 335 4597
Email: *ghassan@mrao.cam.ac.uk*

Kieth Yeung
NRC, Canada
5071 W. Saanich Rd.
Victoria, BC V9E 2E7
Canada
Phone: (250) 363-0067
Fax: (250) 363-0045
Email: *keith.yeung@nrc.ca*

Sigfrid Yngvesson
University of Massachusetts
University of Massachusetts
Department of Electrical and Computer
Engineering
Amherst, MA 01003
United States of America
Phone: (413) 545-0771
Fax: (413) 545-4611
Email: *yngvesson@ecs.umass.edu*

Erick Young
University of Arizona
933 N. Cherry Ave.
Tucson, AZ 85721
United States of America
Phone: (520) 621-4119
Fax: (520) 621-9555
Email: *eyoung@as.arizona.edu*

Peiji Zhao
North Carolina State University
Department of ECE
North Carolina State University
Raleigh, NC 27695
United States of America
Phone: (919) 515-3984
Fax: (919) 515-5523
Email: *pzhao@ecs.ncsu.edu*

Xin Zhao
University of Massachusetts
1040 N. Pleasant St. Apt. 209
Amherst, MA 01002
United States of America
Phone: (413) 549-8661
Fax:
Email: *zhao_hippo@yahoo.com*